Transactions

of the

ASME

JULY, 1952

VOL. 74, NO. 5

Transactions

of The American Society of Mechanical Engineers

Published on the tenth of every month, except March, June, September, and December

---

Published monthly by The American Society of Mechanical Engineers. Publication office at 20th and Northampton Streets, Easton, Pa. The editorial department is located at the headquarters of the Society, 29 West Thirty-Ninth Street, New York 18, N. Y. Cable address, "Dynamic," New York. Price $1.50 a copy, $12.00 a year for Transactions and the *Journal of Applied Mechanics* to members and affiliates, $1.00 a copy, $6.00 a year. Changes of address must be received at Society headquarters four weeks before they are to be effective on the mailing list. Please send old as well as new address. . . . By-Laws: The Society shall not be responsible for statements or opinions advanced in papers or . . . printed in its publications (B13, Par. 4). . . . Entered as second-class matter March 2, 1928, at the Post Office at Easton, Pa., under the Act of August 24, 1912. . . .

The Development and Implementation of a Generation Program on the American Gas and Electric Company System

1—System Fundamentals[1]

By PHILIP SPORN,[2] NEW YORK, N. Y.

The paper discusses the fundamentals considered in the development of an optimum power supply for the American Gas and Electric Company System. The recent rapid growth in electric-power demand on this system has required the construction of five new generating plants in less than seven years; emphasis in this paper is on the two most recent additions, Kanawha River Plant of Appalachian Electric Power Company and Muskingum River Plant of The Ohio Power Company. The paper describes the American Gas and Electric Company System, a review of the plant sites and the reasons for selecting these sites, as well as considerations involved in selecting equipment of very large unit size, all of which have been projected in terms of mass production of electric power, with strong emphasis placed on plant location, transmission, and fuel supply to provide a reliable system power supply at the lowest possible cost.

Introduction

LATE in August, 1950, Appalachian Electric Power Company and American Gas and Electric Company announced plans to extend the generating capacity of Applachian and of the entire American Gas and Electric Company System with the construction by Appalachian of a new steam-electric power plant at Glasgow, West Virginia, on the Kanawha River about 22 miles upstream from Charleston, West Virginia. This development is now known as Kanawha River Plant. Then, in February, 1951, a similar announcement was made by The Ohio Power Company of the construction of a new plant near Beverly, Ohio, on the Muskingum River, about 46 miles downstream from Zanesville. This latter development was subsequently named Muskingum River Plant.

Each of these plants is being developed at a new site. In each case development of the site and the ultimate decision to build a new plant were preceded by long periods of exploration, including above all else exploration of the fundamentals requisite to an economical continuing fuel supply. Furthermore, these two developments are part of a long-range program looking toward a continuation of expansion of system generation facilities to a point considerably more than double present levels. The Kanawha and Muskingum Plants represent the fourth and fifth new major power-plant developments undertaken within a period of seven years on the American Gas and Electric Company System, the previous developments being Tidd, undertaken in 1944 (1),[3] Philip Sporn, begun in 1947 (2), and Tanners Creek, undertaken in 1948. This appears to be an appropriate time, therefore, to review system fundamentals behind and involved in these new developments.

American Gas and Electric Company System

A transmission map of the American Gas and Electric Company System, indicating principal transmission lines and principal power plants, including the two new plants, is presented in Fig. 1. This system serves smaller communities primarily. Not a single community on the system, for example, has a population as high as 150,000. Altogether, some 2165 communities are served with a total population of close to 4,250,000. The area served is, however, highly industrialized, with an abundance of both natural and human resources. Large, basic industrial operations including coal, steel, chemicals, and manufacturing operations are distributed over the entire territory. The growth of these industries is continuing at a rapid rate not only because of the basic industrial expansion that is going on throughout the country, but by virtue of a continued trend toward decentralization of industrial operations and the movement of industry toward smaller centers of population. This trend, coupled with an intensive area development program carried out on the AG&E System, has resulted in a very rapid growth of system load. The rapid increase in load can be clearly seen from an examination of Fig. 2 showing actual growth in system peak demand for the two-decade period 1930–1950, and a projection of peak demand through 1954. With a projected demand of 3,400,000 kw and an annual system input of 20.2 billion kwhr for 1954, it does not take an exaggerated optimism to realize not only the desirability, but the sheer necessity of planning now for future system demands up to as high as 6,000,000 kw.

The planning for such loads makes mandatory, however, not only the development of new concepts of mass or large-scale energy generation, but the devotion of much closer attention than in the past to the fuel component of total costs. Certainly where a difference in production costs of as little as $^1/_{10}$ of a mill per kwhr involves differences in annual operating costs of $2,000,000—which is the case with a system input of 20 billion kwhr—both thermal efficiency and ability to procure lowest cost fuel and, even more important, lowest unit fuel costs are indispensable to sound planning of the energy supply. Hence, on the American Gas and Electric Company System a great deal of effort has been directed toward the problem of fuel supply. Moreover, the

[1] Part 1 of three companion papers. The others are: Part 2—"Fuel Supply," by Philip Sporn and H. A. Kammer; and Part 3—"200,000-Kw, 2000-Psi, 1050 F–1050 F—An Advance in the Economics of Integrated Power-System Generation," by Philip Sporn and S. N. Fiala.

[2] President, American Gas and Electric Service Corporation. Fellow ASME.

Contributed by the Power Division and presented at the Annual Meeting, Atlantic City, N. J., November 25–30, 1951, of The American Society of Mechanical Engineers.

Note: Statements and opinions advanced in papers are to be understood as individual expressions of their authors and not those of the Society. Manuscript received at ASME Headquarters, September 10, 1951. Paper No. 52—A-115.

[3] Numbers in parentheses refer to the Bibliography at the end of the paper.

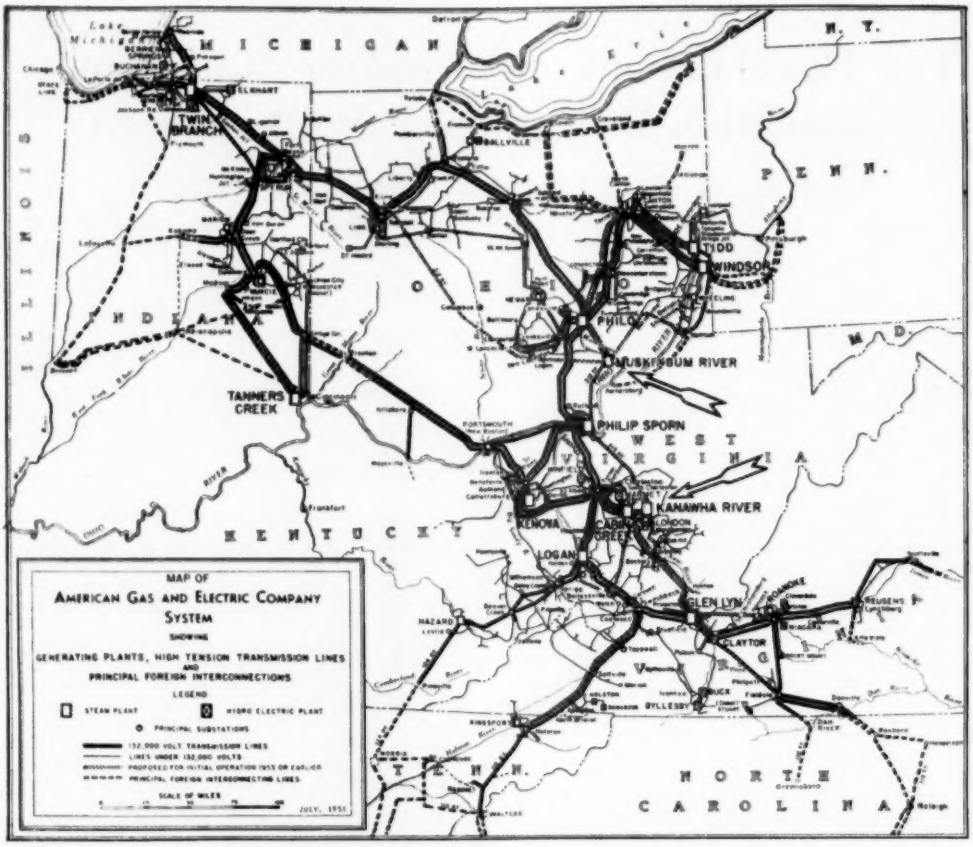

FIG. 1 MAP OF AMERICAN GAS AND ELECTRIC COMPANY SYSTEM SHOWING GENERATING PLANTS, HIGH-TENSION TRANSMISSION LINES, AND PRINCIPAL FOREIGN INTERCONNECTIONS
(Arrows point to the two new plants, Kanawha River and Muskingum River.)

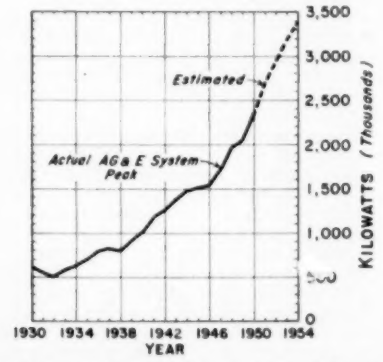

FIG. 2 GROWTH IN AMERICAN GAS AND ELECTRIC COMPANY SYSTEM ACTUAL PEAK DEMAND (ONE-HOUR INTEGRATED), 1930 TO 1950, AND ESTIMATED PEAK DEMAND THROUGH 1954

problem was materially facilitated by several major considerations: The fact that the Ohio River and a number of its very important and major tributaries flow through the very center of the AG&E System; the existence of major coal-producing areas along or immediately contiguous to these rivers; and the fact that the American Gas and Electric Company System is completely integrated. The system thus is capable of taking full advantage of all economies inherent in the most modern of steam power cycles, in large-size generating units, and in the maximum development of favorable sites to give an over-all optimum economy in system energy supply.

DISCUSSION OF SITES DEVELOPED

As stated previously, Kanawha River and Muskingum River represent the fourth and fifth new major power plants undertaken for development on the American Gas and Electric Company System within the past seven years. Each of these sites combines to an unusual degree all the fundamental requirements for a sound and economical generating center serving an integrated power system. Briefly, these requirements are:

Adequacy of Site. In each case ample acreage could be and was

assembled to provide not only all the area needed for plant, step-up substation, coal handling and coal storage, ash-handling and ash-disposal facilities, but in several cases, such as Sporn and Muskingum, additional land for prospective industrial developments which might find particularly attractive the ability to locate in close contiguity to a highly economical center of generation.

All the sites, moreover, are well located with regard to flood plain so that no expensive flood-protection structures would be involved.

Adequacy of Condensing Water Supply. Three of the plant sites are on the Ohio River, one on the lower reaches of the Muskingum, and one on the Kanawha River. On the Ohio River there was no question as to availability of sufficient condensing water for a capacity of 1,000,000 kw at each site when and if further plant expansion is necessary. In the case of the plants on the two Ohio River tributaries some auxiliary condensing water-cooling facilities might be involved if either development went beyond the 600-megawatt stage.

Adequacy of Coal Supply. Each of the sites is not only well located with regard to contiguity to major coal-producing areas but is especially well set up from the standpoint of being able to receive coal with minimum transportation and handling expense. This phase will be discussed fully in a companion paper (3).

Location With Regard to System. The sites are all particularly well placed from the standpoint of location in respect to System load centers and ability to integrate the new plant into the existing transmission network, as well as to make any necessary extensions to the network on a most economical basis. This, as a matter of fact, was one of the most important elements that influenced the final choice of any particular site when the other requisite factors were found to be satisfactory.

It is interesting, too, that the total initial development of these five sites, that is, the capacity installed in the initial phase of construction, will amount to close to 2,000,000 kw, being highest—600,000 kw in the case of Sporn, and lowest—220,000 kw in the case of Tidd. These sites, however, have a combined potential development of over 4,700,000 kw, and it is quite possible that if system requirements made it mandatory, they could be expanded further to a total of 5,000,000 kw. At 6000 hr annual use, full development of these sites would thus make possible a delivery to the system as high as 30 billion kwhr. This is further confirmation of the judgment that this setup justifies major effort and attention to improve the economics of mass production of electric energy.

Basic Features of Kanawha River and Muskingum River Plants—Continuity in the Ideas Behind Their Development

General. These two new plants are part of a much longer series of plant developments, each of which represented a progressive contribution to the art of electric-energy generation, with Kanawha River and Muskingum River merely marking another milestone in that forward march of progress. Many new features were incorporated in the designs of the three earlier plants. The design of the two latest plants is but a rational consolidation of the features introduced at various times in the earlier designs, with the addition of some novel elements which will result in an improved plant design, utilizing, however, all features proved in the older designs. It is confidently expected that the result will be a plant which will carry every proved idea or device to its present logical limit, and will give the most reliable and economical generating unit attainable for the mass production of electric energy, with a minimum of risk attendant upon experimentation.

All the foregoing applies equally to both Kanawha River and Muskingum River Plants. The principal differences in the two plants are in the basic setup for fuel supply. In view of these factors, and because construction of Kanawha River was initiated somewhat earlier, the discussions that follow, where they are not otherwise indicated, are directed to the Kanawha River Plant.

The new plant will serve the Appalachian Electric Power Company and the southern part of the American Gas and Electric Company System, as can be seen from the map in Fig. 1. This project calls for the immediate installation of two 200,000-kw units and an ultimate installation of five such units. Capacity ratings as used here refer to the net effective salable capability on the high-tension bus bars of the station after deduction of all losses and station uses. The first unit is scheduled to be brought into service early in 1953.

Briefly, the principal features of Kanawha River embrace a series of single cross-compound 217,260-kw (gross) turbine-generator sets, each supplied with steam from its own reheat boiler. These boilers require an unprecedented heat input of 1.84 billion Btu per hr in fuel. Each boiler will deliver steam to its high-pressure turbine at 2000 psi and 1050 F, and will reheat the steam for return to the high-pressure machine at 460 psi and 1050 F.

Basic Reason for Selection. In a discussion of the reasons for the decision to use 200,000-kw units, it is important to recognize that in sound generating-station design the struggle for novelty, which naturally pervades the thinking of progressive-minded engineers, must be relegated to its proper position. It is all very well to be able to point to a development as the biggest "this" or the first "that." Such reasoning or, more precisely, rationalizing, is, however, no justification for novelty. There must be an over-all economic merit which, from the viewpoint of reliability and cost, justifies the choice. Above all, the system aspect must never be lost sight of. The present AG&E System peak, now in excess of 2,480,000 kw, will, by the time the fourth of these projected units is on the line, have risen to close to 3,200,000 kw. This load is coupled with an annual system load factor close to the highest being experienced in the United States today—a figure just below 70 per cent. The trough of the daily load curve in 1953 is not expected to drop below about 1,200,000 kw on Sundays and 1,750,000 kw on weekdays. Such a load and its load-duration curve are in themselves practically sufficient ground to justify the selection of high-efficiency units of 200,000-kw capability.

The study of the rational size of unit for the AG&E System at this stage was helped materially by a consideration of the factors shown in Fig. 3. This gives, along the abscissa, the various capacity additions which have been made to the system since 1942. The ratios of net capability of the addition to the net capability of the system have been plotted as ordinates. Experience has demonstrated, as shown in these plots, that for the 90,000-kw, 110,000-kw, and 150,000-kw units variously installed, the ratio of net capability of any extension to the net capability of the system has ranged from a maximum of 7 per cent to a minimum of 5 per cent. The graph shows that whenever the ratio approached the lower value it has always been deemed desirable to increase the size of unit next to be installed. This critical minimum will again be reached when the second Tanners Creek Unit (the 7th 150,000-kw reheat unit) is brought on the line in 1952. Increasing the unit size to 200,000 kw at Kanawha River and Muskingum River serves the purpose of maintaining balance in size of units from a system fundamentals viewpoint.

It is not to be inferred from this that a fast arithmetical criterion such as indicated here has been used to determine size of units. On the contrary, this was farthest from having been controlling. It is, however, clear that in the process of giving full evaluation to all relevant factors that should influence size of unit on a well-planned integrated system, certain natural limits automatically tend to establish themselves. Independently of this, it

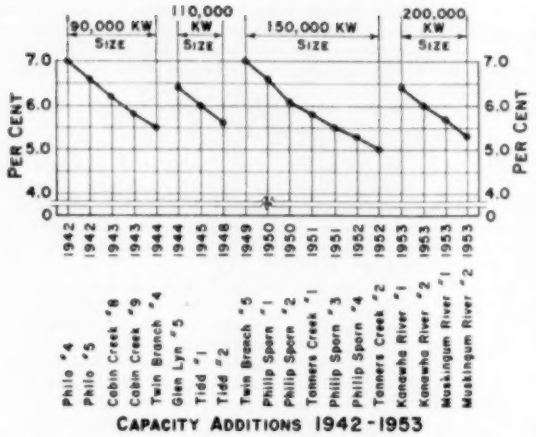

FIG. 3 CAPACITY ADDITIONS TO AMERICAN GAS AND ELECTRIC COMPANY SYSTEM, 1942 THROUGH 1953

(Capability of each addition plotted as a per cent of total system generating capability at the time of the addition.)

is clear otherwise that by the time Tanners Creek No. 2 will have been brought on the line a 200,000-kw unit will be capable of being used to maximum advantage. If a half dozen or so units of this design are eventually employed on the system—and four of that half dozen are now in process of construction—the co-ordinated maintenance schedules under which they will function will justify the purchase of not only the smaller necessary spare parts but even the large spare parts such as extra turbine rotors and generator fields.

With interchangeability thus possible among six or seven units, one part can always be available for rebuilding at any one of six or seven locations without loss of a single otherwise unnecessary outage hour and with minimum loss in production efficiency. The pattern is thus established for the next million and possibly two million kilowatts of needed additional system capacity, starting the count with the first of the Kanawha units.

A further examination of Fig. 3 also discloses that if the trend in size, and the criteria for determining size of system units are to be the same in the future as in the past, then units larger than 200,000 kw are indicated for installation in the relatively near future.

Thermal and Operating Economics. Thermal economies hitherto unattained are a basic inherent advantage realized by the units developed for Kanawha River. A heat rate of the order of 9000 Btu per kwhr, with fuel costing 16½ cents per million Btu, results in a unit fuel cost of less than 1.5 mills per kwhr—certainly an excellent performance in these days and times. There are also other operating savings which stem primarily from the use of large-size units with a single boiler serving a single turbine-generator set. These are to be found in the labor needed to run and maintain the larger units, and in material and supplies entering in the same operations. Thus this makes possible some savings to counterbalance in partial measure the general rising trend in wage and material costs.

The savings due to the selection of these large high-pressure reheat units extend also to the investment required. There are many contributory factors which in the aggregate make up the savings. Unit costs for both boiler and turbine are less than the unit costs of smaller machines because there are very few, if any, more component parts in a 200,000-kw unit than in a 100,000-kw unit. Piping is another striking example of the advantages which accrue from the use of the larger units. The expenditures for building substructures and superstructures are materially reduced as size of units increases. The preliminary layouts indicate an estimated building volume of 19.3 cu ft per kw, including machine shop and office building to house the two 200,000 kw units. This figure compares with its equivalent of 26.4 cu ft for the first two 150,000-kw units at the Philip Sporn Plant.

The larger units will thus reduce the needed building volume for each of the Kanawha units by 7.1 cu ft per kw. At a cost of 75 cents per cu ft for buildings this means a saving of over $1,000,000 per 200,000-kw unit.

Electrical Connections and Connections to the System. The fundamental principles utilized in developing the electrical connections of the units are the same at Kanawha River and Muskingum River as were developed for the first two 40,000-kw units built at Philo, Ohio, almost 30 years ago (4); no low-voltage buses or switches; direct connection to the high-voltage bus; treating either the two or three elements of a cross-compound machine as a single element; and switching on the high-voltage side of the step-up transformer. This is indicated in Fig. 4 showing the simplified electrical diagram for Kanawha River Plant. The one difference between the two plants is that in the case of Muskingum the second generating unit is switched to a 330-kv bus supplying a series of feeders at that voltage running to Lima, Ohio, and to the Philip Sporn Plant.

Within a relatively short distance of these two plants are located three other large plants on the AG&E System—Cabin Creek, Sporn, and Philo. The connections between these three plants and Kanawha River and Muskingum River, as they will exist upon the completion of the initial installations at Kanawha River and Muskingum River, are shown in Fig. 5. This close connection between such major plants materially simplified the problem of handling, from a transmission standpoint, the replacement of units under either scheduled outage or emergency conditions. But such close integration is not an unmixed blessing, since it carries with it the burden of higher short-circuit duty on the breakers at the point of maximum concentration of power, amounting to 6,000,000 kva on the 132-kv buses and 7,500,000 kva on the 330-kv bus bars. It is of major and significant interest that heavy as these short-circuit duties are, it does not appear that they will present any appreciable technical problems, particularly since the heavier duty is obtained at 330 kv. Nor does it appear, considering the greater concentration of power per circuit, that the increased cost of circuit-interrupting devices will in itself constitute any appreciable economic burden on the cost of transmission considered on a unit basis.

Development of Economical Fuel Supply. Because the fuel component is the most important item in production cost of electric energy, at least as far as costs at bus bars are concerned, more attention than is generally given to this phase of plant design was spent on this feature at both Kanawha River and Muskingum River, and because the item is so important it was felt best to treat it separately in a companion paper (3).

PRINCIPAL AIMS SOUGHT IN KANAWHA RIVER AND MUSKINGUM RIVER PLANT DESIGNS

In evaluating the discussions of the fundamental considerations in the development of these two plants, one must keep in mind that the basic aim sought was an over-all optimum power supply on an integrated system where energy requirements call for mass

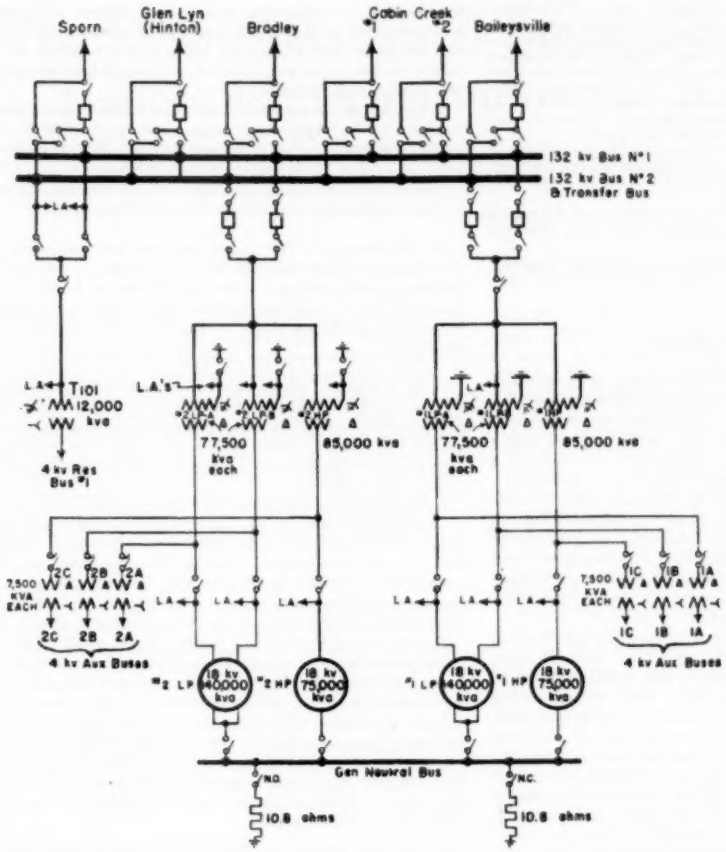

FIG. 4 (*left*) SIMPLIFIED DIAGRAM OF PRINCIPAL ELECTRICAL ARRANGEMENTS OF KANAWHA RIVER PLANT OF APPALACHIAN ELECTRIC POWER COMPANY, A MEMBER COMPANY OF THE AMERICAN GAS AND ELECTRIC COMPANY SYSTEM

or large-scale production of energy. To accomplish this, attention was given not only to thermodynamic cycle and plant-design features commonly associated with the design of a sound power plant, but unusual stress laid on location, transmission, size of units, and fuel supply. All of these elements, it is believed, have here been co-ordinated and brought together to provide an optimum result within presently existing technological limits. It remains for operating experience on these plants to indicate how well performance will agree with design. The author, at least, is confident that the deviation between the two will be of a relatively minor order.

BIBLIOGRAPHY

1 "The Tidd Plant of The Ohio Power Company," by S. N. Fiala and E. H. Krieg, *Power Plant Engineering*, March, 1947.

"Steam Generation at the New Tidd Plant," by S. N. Fiala and L. B. Schueler, *Combustion*, vol. 18, October, 1946, pp. 30–35.

"Modern Steam Electric Station (Tidd) Built on Riverside Site," by H. A. Kammer, *Engineering News-Record*, vol. 137, October 31, 1946, pp. 591–594.

"Simple Tidd Plant Efficient and Economical," by Philip Sporn, *Electrical World*, August 2, 1947.

"Tidd Generating Plant Electrical Features," by F. A. Lane, *Electrical World*, August 16, 1947, and August 30, 1947.

2 "The 2000-Psi, 1050 F, and 1000 F Reheat Cycle at the Philip Sporn and Twin Branch Steam-Electric Stations," by Philip Sporn, Trans. ASME, vol. 70, 1948, pp. 287–294.

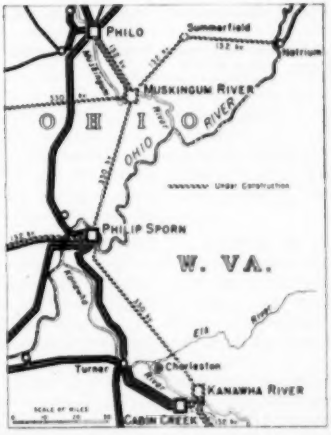

FIG. 5 MAP OF A PORTION OF AMERICAN GAS AND ELECTRIC COMPANY SYSTEM SHOWING CLOSE GEOGRAPHIC PROXIMITY AND TRANSMISSION TIES OF FIVE MAJOR PLANTS, PHILO, MUSKINGUM RIVER, PHILIP SPORN, CABIN CREEK, AND KANAWHA RIVER

"The Basic Concept Behind Philip Sporn Station," by Philip Sporn; "Sporn Heat Cycle Meets High Goal," by Theodore Baumeister; "(Philip Sporn Plant) Steam Generation Employs Reheat, Pressurization, Gas Recirculation," by S. N. Fiala; "Turbine, Condenser and Piping Fit Objectives," by S. N. Fiala; "Control of Units Centralized in Pairs for Effective Operation," by T. T. Frankenberg; "Simplicity Is the Keynote of Plant Electrical Features," by F. A. Lane; "Plant Construction and Architecture Keyed to Economy," by H. A. Kammer, *Electrical World*, vol. 133, June 5, 1950.

3 Companion paper, "The Development and Implementation of a Generation Program on the American Gas and Electric Company System, Part 2—Fuel Supply," by Philip Sporn and H. A. Kammer. Published in this issue, pp. 609–612.

4 "Philo Station Sets Record, General Conditions and Mechanical Features—I," by M. L. Sindeband and Philip Sporn, *Electrical World*, August 22, 1925.

"Philo Station Sets Record, Electrical Features and Control—II," by M. L. Sindeband and Philip Sporn, *Electrical World*, August 29, 1925.

Discussion

EDWIN H. KRIEG.[4] The author's stimulating and provocative exposition of system growth to about 15,000,000 kw, predicted for 1970, almost overshadows the unusual and interesting evolution of the fuel supply that contributes much in making such a large expansion possible. It is striking that when a new site is acquired, so much interest is given to the fuel which will be burned, not only now but 10, 20, and even 30 years from now. To the millions of tons of coal reserves that already existed at the Windsor, Philo, Tidd, and Sporn plants, have been added some 50,000,000 tons at Kanawha and 100,000,000 tons at Muskingum. One cannot help but feel that this approach and attention to long-range fuel procurement has much to do with the attainment of a coal cost of 16.5 cents per million Btu.

Although really large coal reserves are available near each of the six plants mentioned, perhaps enough for 30 or 40 years, still, of a 9,000,000-ton annual burn in 1954, 6,000,000 tons will be furnished by commercial operators. Thus the coal reserve is relatively untouched, assuring a future coal supply contiguous to the major plants. Fuel contracts expire; gas, oil, and even coal veins become exhausted; and if fuel may have to be brought considerable distances, transporting some 9,000,000 tons of coal per year could be costly. True it is that this country has ample coal resources, but unfortunately, the cost of transporting it costs the utilities more than the coal itself.

Conveying 80 per cent of the total coal to be used on the American Gas and Electric system over existing Ohio, Muskingum, and Kanawha River waterways upon which millions of dollars have been spent by the Federal Government to maintain all-year channel depth, and which have hitherto seen relatively little service for the investment involved, indicates a keen appreciation of long-range economics.

In Part 3 of this series, mention is made of studies of cycles using pressures up to 5000 psi and temperatures up to 1200 F. It would be of much interest if the authors would tabulate these as was done by Prof. T. Baumeister in an earlier paper.[5]

Messrs. Sporn, Kammer, and Fiala merit our real appreciation for their invigorating discussion of their generation program.

W. H. ROWAND.[6] The author mentions the desirability of installing units larger than 200,000 kw capability in the future. Studies of the problems involved in building a single reheat boiler for larger capacities indicate that a unit considerably bigger than 200,000 kw should be practical from a boiler-design standpoint.

G. B. WARREN.[7] The authors are to be complimented upon the preparation of what should be very valuable papers for the guidance of others planning large power-system developments, and also for this further evidence of important leadership in the development of outstanding power-plant facilities to serve the power needs of this country.

Mr. Sporn and his associates presented a similar program at a meeting of the Society four years ago and described a group of plants expecting at that time unprecedented efficiencies. These plants are now in successful operation. They, in turn, were the result of efforts on Mr. Sporn's part to reach new heights in such performance. The plants which are the subject of the current papers should make another step in this continuing progress.

The authors of these papers belong to that small group of utility executives who, one after the other, with the assistance of the equipment manufacturers, have pioneered first one, and then another, and then another, and so on, of the outstanding and forward-looking engineering developments which, in their aggregate, have made up the great progress which the utility industry has made in this country. Out of this progress have come the step-by-step improvements in power-plant economies and capacities which have made our present utility development outstanding in all the world.

[4] Consulting Engineer, Stone & Webster Engineering Corporation, Boston, Mass. Fellow ASME.

[5] "Sporn Heat Cycle Meets High Goal," by T. Baumeister, *Electrical World*, June 5, 1950, table 1, p. 89.

[6] Chief Engineer, The Babcock & Wilcox Company, New York, N. Y. Mem. ASME.

[7] Manager, Engineering, Turbine Division, General Electric Company, Schenectady, N. Y. Fellow ASME.

The Development and Implementation of a Generation Program on the American Gas and Electric Company System

2—Fuel Supply[1]

By PHILIP SPORN[2] and H. A. KAMMER,[3] NEW YORK, N. Y.

This paper discusses the engineering and economics of fuel supply for the generating plants of the American Gas and Electric Company System, and in particular the fuel supply for two new plants—Kanawha River of Appalachian Electric Power Company, and Muskingum River of The Ohio Power Company. The importance of adequately planning fuel supply for a large power system is stressed, and the fundamental considerations of adequacy of supply, reliability, characteristics of supply, coal storage, and transportation are discussed with reference to the System characteristics, and with special emphasis on the development of the fuel supply for the two new plants.

Introduction

In connection with the announcement late in the summer of 1950, and then in February, 1951, by Appalachian Electric Power Company and The Ohio Power Company, respectively, both member companies of the American Gas and Electric Company System, of plans for each to increase its generating capacity by constructing a new 400,000-kw steam-electric generating station, it seems appropriate to treat in a co-ordinated manner the three essential elements in the development of a sound generation program on an integrated system: System fundamentals; fuel; and the plant itself. System fundamentals and a discussion of the design features of the plant are treated in separate companion papers.[1] This paper will be devoted to a discussion of fuel supply in its broadest aspects.

The American Gas and Electric Company System Fuel Problem

The American Gas and Electric Company System is an integrated power system serving portions of the seven states of Michigan, Indiana, Ohio, West Virginia, Virginia, Kentucky, and Tennessee. The communities served by the System are primarily small communities, all of them being under 150,000 population and the average of all the 2165 communities being of the order of 2000. The area served is highly industrialized so that there is ample opportunity for exploiting heavy energy use. The availability of an adequate, in fact, an abundant, supply of energy has made possible the industrial development of the area. System energy input, which in 1950 amounted to some 13.5 billion kwhr, is now running at the rate of 16 billion kwhr and is expected to be 20.2 billion kwhr in 1954. The source of all this energy is primarily thermal with all of it dependent upon coal as the fuel source. Estimated coal consumption in 1954 will be 9,140,000 tons.

Coal thus presents a major problem in system planning, design, and operation. The great difficulty in planning fuel supply is, or can come from, a failure to recognize the scale of the problem. This is one of the items to which a great deal of thought and consideration was given when developing the details of the two new plants, Kanawha River Plant of Appalachian Electric Power Company, located about 22 miles upstream from Charleston, W. Va., and Muskingum River Plant of The Ohio Power Company, located near Beverly, Ohio, on the Muskingum River about 46 miles downstream from Zanesville. A review of the features of these plants presents an occasion for showing not only how the fuel problem will be handled there, but how that solution ties in with the handling of the fuel problem on the rest of the system.

Fundamentals of Coal Supply

The fundamental questions to which a proper answer must be given in any solution of the fuel-supply problem are as follows:

(*a*) Adequacy of supply.

(*b*) Reliability of supply. This includes the question of the reliability of the supplier and the question of fuel reserves.

(*c*) Characteristics of coal supply.

(*d*) The cost or economics of fuel supply.

Requirements (*a*) to (*d*) are general requirements which must be reasonably well met to do a good job. On the American Gas and Electric Company System the importance of these requirements has been realized for many years, and the means for meeting the requirements have had to be thoroughly and soundly worked out because of a number of special burdens and obligations that have developed as the System expanded. Among the most important are the following:

(*a*) Most of the 2165 communities served by the system are located relatively far from possible generating-plant sites.

(*b*) Industrial development in the area, particularly the development of heavy industry, including such industries as coal mining, chemicals, steel and alloys, and metallurgical operations, have imposed requirements for large blocks of power which, to be salable, had to be of relatively low cost.

(*c*) A good deal of the area is covered by extensive natural-gas deposits or natural-gas pipe lines. The competitive angle here makes necessary highly economical energy to permit electric-load development.

---

[1] Part 2 of three companion papers. The others are: "Part 1—System Fundamentals," by Philip Sporn; and "Part 3—200,000 Kw, 2000 Psi, 1050 F to 1050 F—An Advance in the Economics of Integrated Power System Generation," by Philip Sporn and S. N. Fiala.

[2] President, American Gas and Electric Service Corporation. Fellow ASME.

[3] Vice-President, American Gas and Electric Service Corporation.

Contributed by the Power Division and presented at the Annual Meeting, Atlantic City, N. J., November 25–30, 1951, of The American Society of Mechanical Engineers.

Note: Statements and opinions advanced in papers are to be understood as individual expressions of their authors and not those of the Society. Manuscript received at ASME Headquarters, September 10, 1951. Paper No. 51—A-116.

(*d*) The only feasible solution of the generation problem that all the foregoing requirements impose is large-scale centralized power generation. This, however, introduces concomitantly the handicap of distance, resulting in considerable transmission cost. To overcome this cost handicap, economical fuel and fuel utilization are essential. Translated to the fuel problem, this in turn leads to a solution calling for the use of local fuels wherever such fuels are available, because, generally speaking, these fuels can be developed to become the most economical fuels.

On the other hand, utilization of local fuels sometimes means accepting lower-grade fuels, with the handicap in quality being offset in a considerable measure by more favorable transportation costs. In most locations on the system such a supply can be obtained commercially. In other locations it has been necessary to stimulate local developments, and in some cases actually to carry out such developments under the direct sponsorship of the company. However, the predominant portion of fuel supply for 35 years or more has been and is expected to continue to be obtained from commercial coal sources; this is discussed later in the paper.

Means Available for the Job

There are three factors that materially assist in controlling the cost of fuel on the AG&E System:

(*a*) The location of the System with respect to the coal fields of the Eastern Coal Province.

(*b*) The proximity of a number of the System's major power plants to coal that can be strip-mined and trucked to the plants.

(*c*) The location of many of the major plants on the Ohio River or its tributaries.

The physical relationship between the major plants, the coal fields, and the Ohio River system is shown in Fig. 1.

Of the total steam-electric generating capacity in operation by 1954, including the units now under construction at the Kanawha and Muskingum plants, 72 per cent is or will be located in the coal fields of Ohio and West Virginia. These favorable plant locations materially assist in controlling the cost of transporting coal to the plant and, in the case of three plants, Philip Sporn, Windsor, and Muskingum, permit transporting the coal to the plant by belt conveyer.

Strip coal, with lower production cost than that of deep-mine coal, materially contributes to keeping the cost of fuel at a minimum. Of the total of approximately 3,600,000 kw installed thermal generating capacity available to feeders in 1954, almost 30 per cent will be operating on strip-mined coal.

Major steam-electric stations of the AG&E System totaling about 2,900,000 kw, or 80 per cent of the generating capacity available to feeders in 1954, are located on the Ohio River or

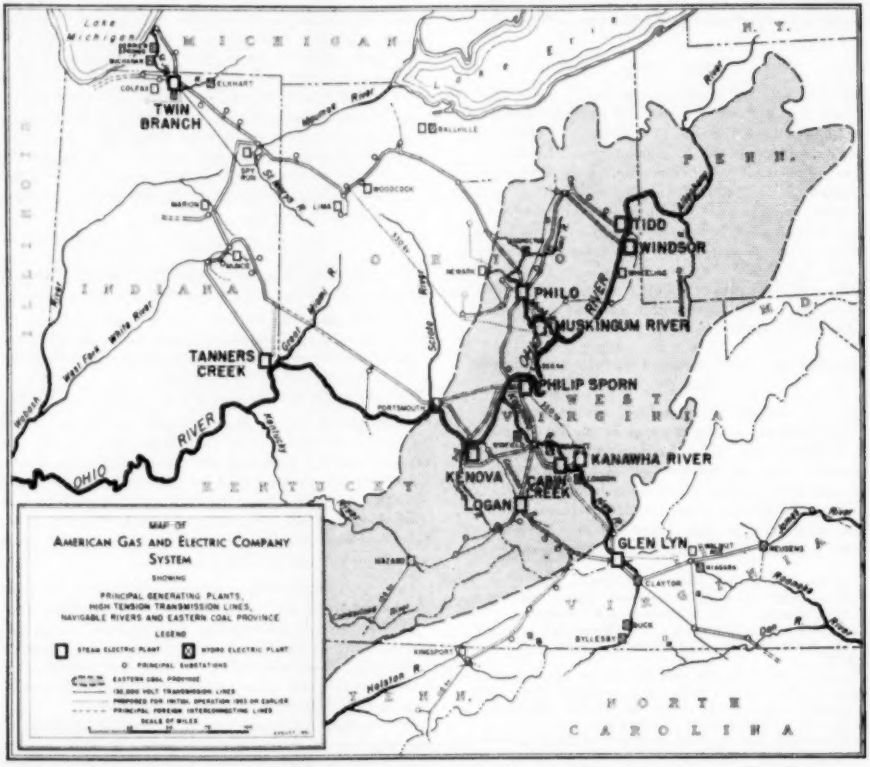

Fig. 1 Map of American Gas and Electric Company System, Showing Generating Plants, High-Tension Transmission Lines, the Ohio River and Its Navigable Tributaries, and the Eastern Coal Province

its navigable tributaries, the Muskingum, Kanawha, and Big Sandy Rivers. This not only is of material help in controlling transportation cost but, as discussed later, has an important bearing on the storage requirements at each plant.

Coal Requirements and Source of Supply

As of the present time coal is being burned at the major AG&E steam-electric plants at a rate of more than 8,000,000 tons per year. By 1954 the burn will increase to about 9,140,000 tons per year, about two thirds of which will be furnished to the plants by commercial suppliers, as shown in Table 1. As previously

TABLE 1 ESTIMATED ANNUAL COAL CONSUMPTION OF AG&E SYSTEM—1954

Plant	Estimated consumption, tons	To be furnished by commercial operators, tons
Tanners Creek	800000	800000
Philo	1430000	950000
Windsor	410000	60000
Tidd	730000	730000
Sporn	1740000	1300000
Kanawha River	950000	450000
Muskingum River	1070000	...
Cabin Creek	650000	380000
Twin Branch	610000	610000
Logan	220000	220000
Glen Lyn	440000	440000
Small plants	90000	90000
Total	9140000	6030000

mentioned, it has been the policy on the system to purchase the required fuel from commercial suppliers whenever such supply was available within the zone of economical transportation, as long as there was assurance that an adequate and economical supply of the required type of coal would continue to be available. However, it has not always been possible for commercial suppliers to meet these specifications. It therefore became necessary for the member companies of the system on occasion to acquire coal reserves in order to back up the existing commercial supply, and in some cases actually to develop the mining operation. But the program of obtaining the system fuel requirements from reliable commercial suppliers, and of sponsoring and developing technological improvements in coal utilization to promote the use of coal as a source of energy, has continued to be a consistent policy of the company throughout its entire system.

Coal Storage

To provide for operation of the plants during periods of interruption in the coal supply, either at the mines or in the transportation systems, substantial coal storage must be maintained at each of the system's steam plants. The amount of coal to be held in storage at a major plant is dependent on both economics of supply and the area available for storage purposes. Sufficient area for storing at least 100 days' consumption has been provided at all of the major plants of the AG&E System, and it is planned to maintain such storage at each location. Two exceptions are the Philip Sporn Plant, where coal storage will total 1,000,000 tons, equivalent to approximately 165 days' burn for the four units now installed, and the Logan Plant, where storage area is limited.

As of June, 1951, approximately 2,160,000 tons of coal were in storage at the steam plants, equivalent to a 99-day supply for the entire system. The distribution of this coal among the various plants is shown in Table 2. While some coal had to be taken from storage during the late summer and early fall, due to some local labor disturbances, coal storage has been built up since that time and soon will be at the total tonnage shown for June. By 1954 it is expected that some 3,130,000 tons, 125

TABLE 2 COAL STORAGE AT STEAM-ELECTRIC GENERATING STATIONS OF THE AG&E SYSTEM

Plant	Actual storage as of June 30, 1951		Expected storage 1954	
	Tons	No. day's supply	Tons	No. day's supply
Tanners Creek[a]	50000	41	220000	100
Philo[a]	435000	92	390000	100
Windsor[a]	250000	81	220000	100
Tidd[a]	223000	111	200000	100
Sporn[a]	296000	119	1000000	165
Kanawha River[a]	...	...	260000	100
Muskingum River[a]	...	...	280000	100
Cabin Creek[a]	251000	86	175000	100
Twin Branch	375000	153	170000	100
Logan	33000	37	60000	100
Glen Lyn	187000	94	120000	100
Small plants	60000	81	35000	100
Total	2160000	99	3130000	125

[a] Located on the Ohio River or its navigable tributaries.

days' supply for the entire System, will be in storage, apportioned among the various plants as shown in the table.

The first eight plants listed in Table 2 are located or are now under construction on the Ohio River and its navigable tributaries. As of June 30, 1951, the coal at these eight plants represented 68 per cent of all the coal in storage on the AG&E System; by 1954 the coal in storage at these eight plants, available for transfer from one plant to another by water transportation, will represent 88 per cent of the total coal in storage. Because of the favorable location of these plants, and the flexibility afforded by the river system, it was concluded that coal storage at each major plant sufficient for 100 days' operation would be satisfactory, provided that a minimum of 1,000,000 tons was maintained at the Sporn Plant. Thus coal could be transferred easily by barge from the Sporn Plant to all but three of the other major plants. Dock and coal-handling facilities provided at the Sporn Plant are so arranged that coal can be readily unloaded from or loaded into river barges. Although permanent coal-handling facilities at the other major Ohio River system plants provide only for unloading coal, portable temporary conveyers, stored at several of the plants, can be set up quickly for loading coal from storage piles to river barges for use at other plants

Coal at the Kanawha River Plant

When it became apparent in the latter part of 1946 that Appalachian Electric Power Company would soon require additional generating capacity in the western end of its system, a detailed study was made of that section of West Virginia for a new power-plant site which could be backed up with an economical coal supply, with sufficient condenser cooling water, and of favorable location with respect to the transmission picture of both Appalachian Electric Power Company and the American Gas and Electric Company System. As a result of these studies, coal reserves for the new plant were acquired in the middle of 1948, and the Kanawha Plant site was acquired in 1949.

The coal reserves, consisting of 20,000,000 tons of high-fusion and 35,000,000 tons of low-fusion coal, are located on Morris Creek, which is about six miles upstream from the Kanawha River Plant site and ten miles above the Cabin Creek Plant of Appalachian Electric Power Company.

In the spring of 1948 a commercial mining company was engaged to open and construct a mine in these reserves. This mine is now in operation, supplying coal to Cabin Creek and Philip Sporn Plants. It is fully mechanized, equipped with a washing plant and a 2½-mile 36-in. belt conveyer, which transports clean coal from the mine to a loading tipple located on the Kanawha River. This mine will supply approximately 50 per cent of the Kanawha fuel requirements; the balance will be obtained from commercial suppliers.

A dock to be installed at the Kanawha River Plant will be

equipped with a coal-hoisting tower for unloading the coal from barges at a rate of 700 tons per hr. Coal will be transported by belt conveyer from the hoisting tower either to storage at the west end of the plant or directly to the bunkers.

Coal at the Muskingum River Plant

Load studies made of The Ohio Power Company portion of the American Gas and Electric Company System in 1947 indicated that at a relatively early date it would become necessary to locate a new plant in the vicinity of the Philo Plant, since inadequate condensing water flow of the Muskingum River at Philo prevented further expansion of that plant. The area abounds in extensive coal deposits which have been under study for many years. With the decision that new facilities had to be installed, these studies were intensified. After considerable exploration of the area, options were obtained on coal lands in Morgan County, Ohio, and after the coal field had been proved by test drilling, the Muskingum River Plant site was acquired at Relief, Ohio. A total of 35,000 acres was assembled into a solid field, which is estimated to contain about 100,000,000 tons of Ohio No. 9 coal, 45,000,000 tons of which can be recovered by strip mining, the balance by a system of deep or auger mining.

A strip mine, now being opened in these reserves, is expected to be in operation late in the summer of 1952, producing at a rate of approximately 1,100,000 tons per year. This mine also will be equipped with a cleaning plant. A 36-in. rubber belt conveyer about $4^1/_2$ miles long will transport the coal from the cleaning plant direct to the powerhouse.

Coal-handling facilities at Muskingum are similar to those previously described for Kanawha River, with the exception that no river dock or unloading facilities are currently being provided. However, arrangements have been made so that river coal-handling facilities can be installed readily and quickly if needed in the future.

Summary and Conclusions

For the past fifteen years the fuel-procurement program for the steam-electric generating stations of the American Gas and Electric Company System has been scaled to the estimated growth of the System, and has received the same care and attention given to all of the other fundamentals basic to the sound development of any large thermal electric-power system. Emphasis has been and will continue to be given to the following axiomatic considerations:

1 For any system such as that of the American Gas and Electric Company wherein 95 per cent of the energy generated is produced from coal, the procurement of fuel must be developed on a long-term basis and must always be considered a basic element of the power-generation program. The fact that fuel usually represents between 65 and 80 per cent of the total production cost at modern plants must never be lost sight of.

2 Not only in providing for operation of present plants, but in planning future expansion of generation facilities, effort will be exerted to utilize commercial fuel sources to the maximum possible extent.

3 Utilization of local resources will be aided by designing steam generators to burn local fuels satisfactorily.

4 Location of future generating plants on the Ohio River and its tributaries will be developed further. Here the objective will continue to be not only better control over transportation costs, but also the reduction of coal storage required at each site by providing for the shuttling of coal between plants during emergency conditions.

It is only by careful and continued application of these ideas, considerations, and principles in the development of a fuel-procurement program that it has been and will continue to be possible to provide to the areas served the highly economical electric power supply that is so necessary to further develop these areas, and to develop greater energy use.

The Development and Implementation of a Generation Program on the American Gas and Electric Company System

3—200,000 Kw, 2000 Psi, 1050 F/1050 F—An Advance in the Economics of Integrated Power-System Generation[1]

By PHILIP SPORN[2] AND S. N. FIALA,[3] NEW YORK, N. Y.

This paper discusses the steam-electric generating units being installed at two new plants of the American Gas and Electric Company System, Kanawha River Plant of Appalachian Electric Power Company, and Muskingum River Plant of The Ohio Power Company. Reasons for the selection of unusually large single boiler-single turbine sets are presented in terms of the over-all generating requirements of the AG&E System. Basic considerations in the selection of component equipment for these units are developed, as well as the means by which these components have been combined to accomplish a very economical arrangement for mass generation of power for the System.

Introduction

IN the late summer of 1950, and then in February, 1951, the Appalachian Electric Power Company and The Ohio Power Company, both principal companies of the American Gas and Electric Company System, announced plans to extend generating capacity with the construction by Appalachian of a new steam-electric power plant in Glasgow, West Virginia, on the Kanawha River about 22 miles upstream from Charleston, West Virginia, and of a similar plant by The Ohio Power Company on the Muskingum River near Beverly, Ohio, about 46 miles downstream from Zanesville, Ohio. Since then the former plant has been named Kanawha River and the latter, Muskingum River. Because each of the plants carries forward the technology of mass production of electric energy by steam-electric methods to new frontiers of capital economy and operating efficiency, it seems appropriate at this time to deal on a co-ordinated basis with the three essential elements in the development of a sound generation program on an integrated system, namely, system fundamentals, fuel, and the plant itself. The first two items are covered in two companion papers (1). This paper will confine itself to dealing with the last item—the plant itself.

Design Objectives

The Kanawha and Muskingum plants are the direct results of studies which extended over a long period of time. These studies had as their objective the definition of a plant and plant cycle which would be the logical successor to the seven large units of 150,000 kw capability installed or under construction at Philip Sporn, Tanners Creek, and Twin Branch Plants (2, 3). Ever-increasing prices for fuel, labor, and equipment have necessitated developing a design to improve plant heat rates and reduce operating labor costs—in terms of mills per kwhr—without prohibitive increments in investment.

It was recognized at the outset that increased size of units would be of help. The long pioneering experience of the company with high pressures, high temperatures, high speeds, reheat, large sizes of units, and lower grades of fuels was a source of knowledge and confidence in the efforts to reach the objective.

In addition to the factors of system requirements (1) the boiler design had great influence on the size of the unit. The Philip Sporn boilers already had been operated for substantial periods of time with an hourly furnace heat input of 1.43 billion Btu. Successful operating experience at these rates of heat input indicated that an appreciable increase in this level of input could be achieved without introducing any particular difficulties.

With this assurance, serious consideration was given to a number of other possible avenues of improvement. Studies were made of (*a*) cycles with two reheats; (*b*) cycles using single-shaft high-speed units; (*c*) cycles using pressures higher than 2000 psi, to a maximum of 5000 psi; and (*d*) cycles using temperatures, primary and reheat, as high as 1200 F.

Each of these possibilities was analyzed, evaluated, and ultimately eliminated from consideration at this time. Two reheats were not favored because of radical changes in boiler, turbine, and piping designs which would be required. Single-shaft turbines could not give the assurance of best over-all economies which otherwise could be obtained. Cycles with ultrahigh pressures would introduce new and unexplored boiler problems which could not be accepted for solution in the short time available for development. Temperatures from 1050 F to 1200 F, while offering substantial thermal savings, introduce metallurgical problems which in turn introduce problems of procuring materials in critical supply. It was felt that such requirements could not be justified under a defense-mobilization-program condition such as the present.

The consequence of all these analyses was to resolve the decision in favor of the largest units which could be adapted to the system without disturbing reserve requirements or operating and maintenance schedules, and which would make possible consolidation of the many gains which had been introduced from time to time in the previous experience of the company. Thus the decision was reached to use 200,000-kw (net) cross-compound units, to limit the throttle pressure to 2000 psi, and to utilize ferritic steels in the construction of piping and turbines at 1050 F, both for primary and reheat-steam temperatures. This combi-

[1] Reference (1); numbers in parentheses refer to the Bibliography at the end of the paper.

[2] President, American Gas and Electric Service Corporation. Fellow ASME.

[3] Mechanical Engineer, American Gas and Electric Service Corporation. Mem. ASME.

Contributed by the Power Division and presented at the Annual Meeting, Atlantic City, N. J., November 25–30, 1951, of THE AMERICAN SOCIETY OF MECHANICAL ENGINEERS.

NOTE: Statements and opinions advanced in papers are to be understood as individual expressions of their authors and not those of the Society. Manuscript received at ASME Headquarters, September 10, 1951. Paper No. 51—A-117.

nation, as will be brought out in the description of the heat cycle, will be capable of developing a net continuous output of 200,000 kw at a heat rate of slightly over 9000 Btu per net kwhr. It is a logical culmination of the numerous forward steps taken previously at many points in the development of an optimum power supply on the AG&E System.

The Kanawha and Muskingum River Plants are being designed with the minimum possible variation between the two plants; they are thus very nearly alike except for differences in the boilers. The Kanawha River boilers will be of dry-ash pit design and the Muskingum boilers will be of fluid-bottom design.

Site Conditions and Structural Features

The Kanawha River Plant is being constructed on the north flood plain of the Kanawha River about 80 miles above its confluence with the Ohio River at Point Pleasant, West Virginia. Rock found at a depth of about 60 ft is overlain with about 15 ft of coarse sand and gravel and the materials above this stratum consist mainly of soft sandy clay, unsatisfactory for the foundation of any important structure.

Consideration was given to founding the entire powerhouse structure on caissons or piles driven to rock, but later studies indicated that the most economical scheme would be to drive wood piles for supporting the boiler room, heater bay, and office building portions of the structure, and founding the condenser pit, turbine room, turbine and other foundations, on the sand and gravel strata. The substructure of the powerhouse will be reinforced concrete. The superstructure is a structural steel frame which supports a composite masonry wall made up of Speed-a-backer tile and 4 in. of brick. It will be noted from the cross section of the powerhouse, Fig. 1, that all equipment is housed within the building except the fans, air heaters, dust collectors, and connecting ductwork. Studies made of outdoor and semioutdoor designs indicated no substantial saving over that finally adopted.

Equipment in the plant was arranged to give the most compact and economical layout attainable; that this had been accomplished is demonstrated by the low volume of building structure per kilowatt of installed generating capacity, 19.3 cu ft per kw, including all service and office facilities. The development of remote operation through centralized control rooms has reached a very satisfactory stage (4); this has made possible the location of the control room on the roof of the turbine room without detrimental effect on plant operation. It also has had a material effect on the total building volume and on volumetric economy.

Boiler ash and fly ash will be pumped from the plant to a pit which has been dug downstream from the plant and immediately landward of the present coal-storage pile. When the pit is finally filled some years hence, the coal-storage area will be extended landward over this filled area to provide the additional storage space needed for a 1,000,000-kw plant.

Earth excavated in order to create the ash storage pit was used to build up the plant and substation yards to an elevation above reasonable high water. To assure plant operation during the maximum floods which might be attained, bulkheading will be employed for the powerhouse, and electrical equipment in the substation and transformer yards susceptible to water damage will be raised above the maximum flood elevation.

At the Muskingum River Plant site better foundation conditions existed than at Kanawha River so that it was not necessary to use bearing piles to support any part of the structure, the bottom slab of the powerhouse being founded on sand and gravel which extends to rock.

The Cycle

Essential details of the cycle on which the plant is projected to operate are shown in Fig. 2. Over-all plant thermal economy is estimated at slightly above 9000 Btu per kwhr. These calculations are based on full-load conditions, and with average allowances for circulating-water temperature, steam losses, feed make-up, pressure drops, terminal temperature differences, blowdown losses, and auxiliary power requirements. The data in Fig. 2 are thus reflective of the realities which should obtain on the plant. Seven stages of extraction feed heating are planned with an extreme full-load feedwater temperature of 461 F.

The Turbine

The turbine generators are arranged cross compound. Gross capability of each complete unit is expected to reach 217,260 kw, operating with $1^1/_2$ in. Hg back pressure. Fig. 3 shows the general arrangement and various details of the 3600-rpm high-pressure element, and Fig. 4 shows a similar sectional view of the 1800-rpm tandem-compound double-flow low-pressure element.

Two emergency stop valves are being furnished for each unit to accommodate the large steam volumes. These are to be welded directly to either end of an external control-valve chest located below the turbine-room floor. Steam at 2000 psi and 1050 F will enter the emergency stop-valve inlets and flow to the turbine proper via six control valves and six connecting pipe lines. Four

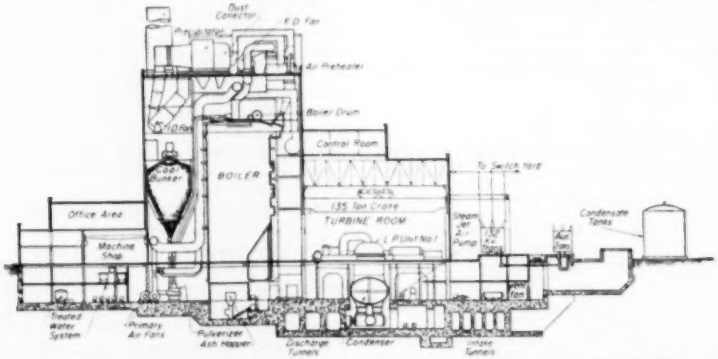

Fig. 1 Diagrammatic Cross Section of Kanawha River Plant of Appalachian Electric Power Company, a Member Company of the American Gas and Electric Company System

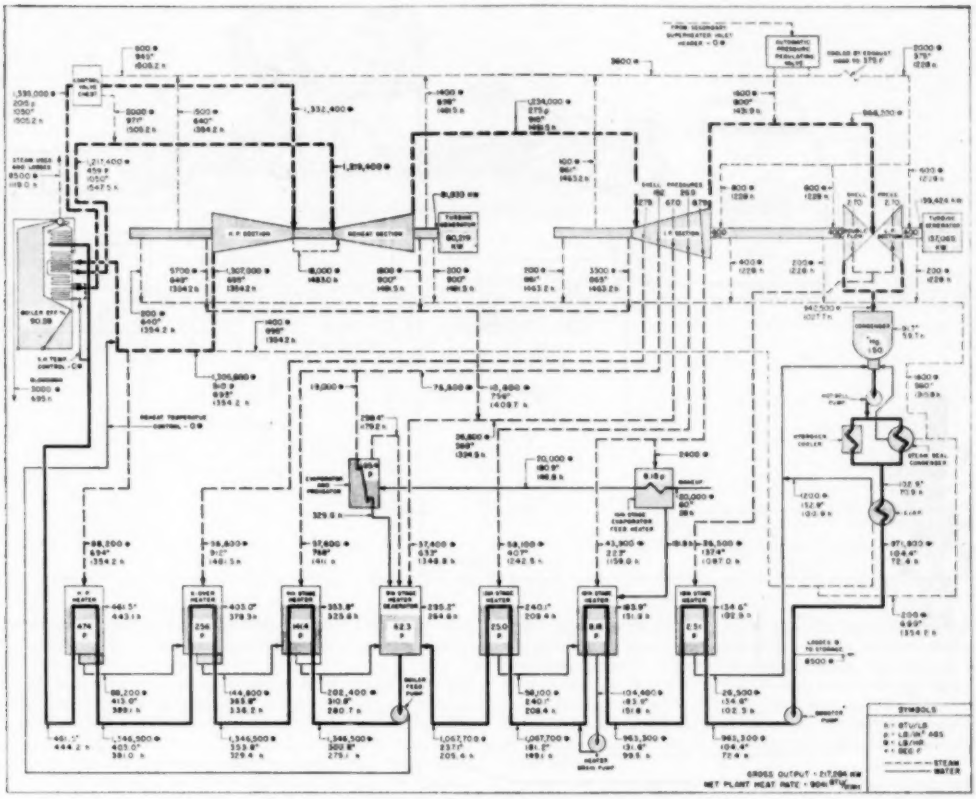

FIG. 2 PROJECTED HEAT CYCLE OF KANAWHA RIVER PLANT
(Indicated flows, temperatures, pressures, and enthalpies are for normal full-load operation.)

of these pipes will be attached to the lower turbine shell half and the other two to the upper half.

The use of an external valve chest with turbines of this size has several decided advantages. It makes possible the concentration of high temperatures on a relatively small and reasonably symmetrical portion of the high-pressure turbine shell and also makes feasible the use of a forged valve chest, fabricated in this case from a ferritic forging. Aside from internal valve parts of austenitic material in the emergency stop valves and control valves, all high-temperature elements operating in the range of 1050 F will be made of ferritic Cr-moly-vanadium material.

Initial and reheated steam will enter the turbine shell at adjacent belts located centrally in the high-pressure-turbine shell. This arrangement, in conjunction with the elimination of the intercept valves at the turbine reheat-steam inlet, has simplified many of the problems associated with high-temperature turbine design.

High-temperature steam, entering the high-pressure turbine shell near its mid-section, travels toward the front standard through eight stages and discharges to the steam reheater at 490 psi when operating at gross capability.

Returning from the reheater at 1050 F, the steam again enters the high-pressure-turbine shell mid-section at a belt adjacent to the initial steam inlet. From this point it flows toward the coupling end through four stages. The steam then leaves the high-pressure shell through two 24-in. lines and enters the single-flow or intermediate section of the low-pressure turbine through two massive intercept valves. Steam pressure at these valves when operating at maximum load will be about 260 psi. Passing through the intercept valves, the steam expands through sixteen single-flow stages followed by four similar double-flow stages. A large overhead duct will form the crossover between the single- and double-flow sections of the low-pressure turbine.

The four reheat-steam stages in the high-pressure shell were introduced to reduce reheat steam temperature prior to its entering the intercept-valve bodies and low-pressure turbine shell, avoiding serious thermal-stress problems associated with 1050 F reheat steam. However, the specific volume of the steam is nearly doubled, and this factor necessitated the unusually large physical size of the intercept valves.

The two intercept valves will be mounted at the top front of the low-pressure machine. Each will be operated by independent hydraulic cylinders and reach rods. In action, the valves will operate as shutoff or throttling elements. A speed governor activating the intercept valves will regulate overspeed of the low-pressure unit. Like the high-pressure emergency stop valves, the

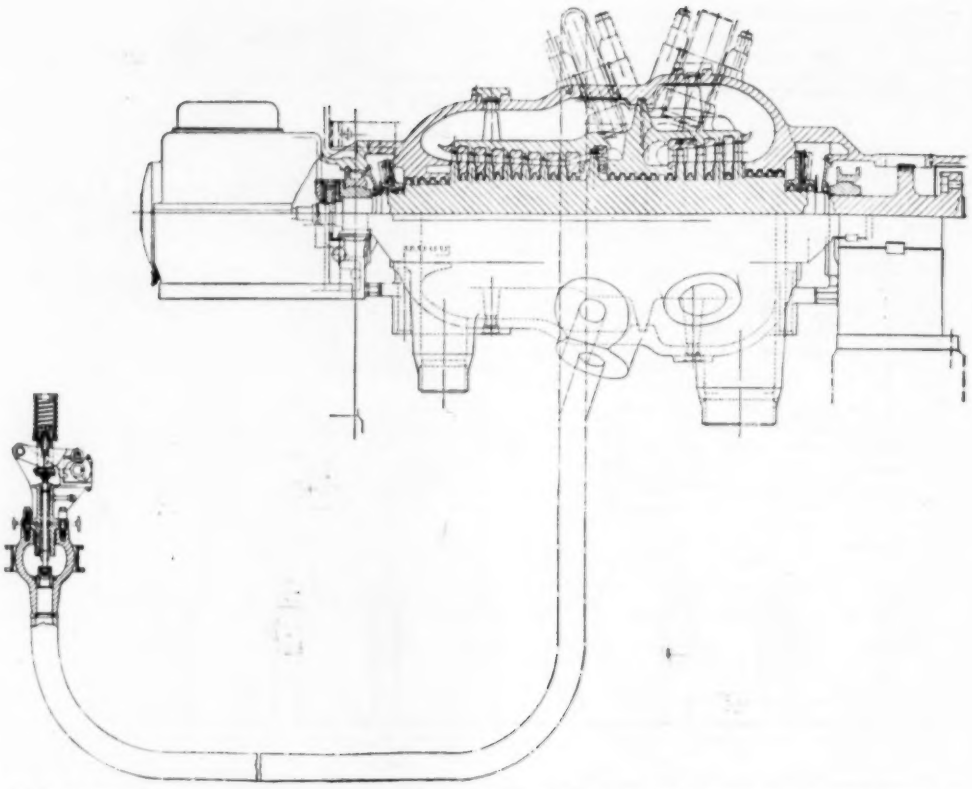

FIG. 3 GENERAL ARRANGEMENT CROSS SECTION OF THE 3600-RPM, 2000-PSI, 1050 F AND 1050 F REHEAT HIGH-PRESSURE TURBINE OF KANAWHA RIVER PLANT, SHOWING EXTERNAL CONTROL VALVES

intercept valves also are being furnished with a steam-sealing device which eliminates stem-bushing steam leakage when the valves are in their normal or fully open position.

Overheating of the low-pressure-turbine exhaust hood is expected to be more critical than on previous machines of similar design. For this reason automatically controlled water sprays are located in the low-pressure crossover duct and used for attemperating the steam leaving the single-flow low-pressure-turbine casing. Water will be injected during all no-load operations and for all loads up to 5 per cent of full load.

The lower half of the low-pressure-turbine exhaust hood is being fabricated from steel plate, rather than being built up from iron castings, as has been past practice. A considerable saving in weight is expected from this change. From an operating point of view, the final installation should be more rugged and less sensitive to temperature shocks. Originally the upper half of the exhaust hood was also to have been fabricated, as shown in Fig. 4. However, owing to the national emergency and the resulting scarcity of steel plate, it has been necessary to resort to castings for this section of the hood.

Adoption of steam seals in lieu of water seals is an interesting change from usual design standards. These seals will provide a number of operating and maintenance advantages over water seals. Greater operating flexibility is expected. The usual difficulty experienced in adjusting water seals while bringing units to synchronous speed or while changing load will be eliminated. Rapid starting of turbine units will be simplified. Serious thermal shocks to the turbine shafts can be avoided with ease. By the elimination of motor-operated valves and the water-runner parts required with water-seal operation, the system is simplified and less subject to mechanical trouble and maintenance.

A single high-pressure pump on the high-pressure-turbine shaft will furnish all hydraulic and bearing lubricating oil for the high- and low-pressure turbines. This pump will be of a new design having double suction. It will operate at 3600 rpm and deliver oil at 200 psi.

THE BOILER

In view of previous successful experience with natural circulation boilers operating above 2000 psi at Twin Branch and at Philip Sporn Plants, there was no concern regarding the adequacy of natural circulation for the conditions of this plant. Extensive circulation tests which were conducted on the 2300-psi Twin Branch Unit No. 3 demonstrated that the separation of steam and water provided by the cyclone steam separators assured a more than adequate differential head for proper circulation. These

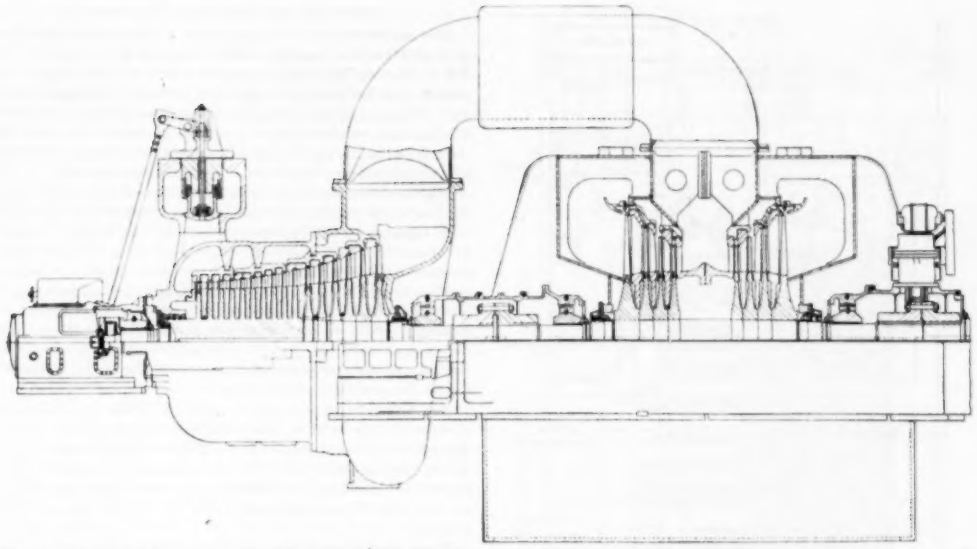

FIG. 4 GENERAL ARRANGEMENT CROSS SECTION OF 1800-RPM TANDEM-COMPOUND DOUBLE-FLOW LOW-PRESSURE TURBINE OF KANAWHA RIVER PLANT

(Upper half of exhaust hood will be built up from iron castings, rather than fabricated from steel plate as shown, due to scarcity of steel plate resulting from current national emergency.)

tests also demonstrated that circulating flow in individual tubes, as well as the over-all circulation rate, increases with increases in the rate of heat absorption.

Fig. 5 shows a cross section of one of the Kanawha River boilers. This boiler is equipped with a dry-bottom-type furnace in order to handle high-ash-fusion coals. Each boiler is designed for a furnace heat input of 1.84 billion Btu per hr almost one third greater than the heat-input requirements of the Philip Sporn units. In terms of heat input, these boilers may be classified among the largest, if not actually the largest, steam boilers ever projected. Primary steam flow is 1,335,000 lb per hr, and reheater flow is 1,216,000 lb per hr. The furnace will be 56 ft wide × 27 ft deep, with an average height of 90 ft.

Each boiler will consume approximately 80 tons of coal per hr. This high firing rate will be sustained by the use of eight pulverizers on each boiler, sized so that seven pulverizers will carry full load on the boiler even when burning the poorest quality of coal contemplated, namely, 15 per cent ash, 10 per cent moisture, and 40 grindability. One pulverizer thus will be available at all times for maintenance, which can be accomplished during regularly scheduled working hours, without reducing output capability.

Each boiler will be furnished with three Ljungstrom regenerative air preheaters which will bring the combustion air to a temperature of 550 F. There will be three induced-draft fans and two forced-draft fans, the latter being sized and motored for full pressurized furnace operation. The induced-draft fans are being equipped with tight shutoff dampers and bulkheading arrangements to permit maintenance on any one of the three fans while the boiler is in operation.

The boiler casing is designed for pressurized furnace operation. Such operation will provide better control over furnace combustion conditions, improved temperature control, and increased boiler efficiency through reduction of stack losses. An appreciable operating saving through reduction in induced-draft-fan power requirements also is anticipated. The induced-draft fans are provided to avoid any possibility of boiler outages during peak-load operation as a result of casing leakage. Investment in the induced-draft fans will furnish not only protection against unavailabilty but also a very desirable and most valuable degree of flexibility in operation, although it is expected that these boilers will operate without induced-draft fans approximately 95 per cent of the time.

Superheaters and reheaters are entirely in the form of convection surface. Experience with radiant superheater and reheater surface in various earlier installations has not been as favorable as that of convection surface. The problem of slag formation and removal, resulting from the higher gas temperature required for the all-convection surface arrangement, has been found to be controllable and the difficulties so introduced are more than offset by the advantages accruing from the complete elimination of radiant superheater and reheater surface.

Superheater and reheater surface has been divided and so arranged as to give the necessary temperature control with minimum use of reheat attemperation and without danger of overheating reheater tubes during periods of trip-out, starting, and shutting down of the boiler. Superheat and reheat control below full load will be obtained primarily by recirculation of flue gas from the economizer outlet to the furnace, with water-spray attemperation at the reheater inlet and between stages of the superheater for critical temperature control.

The Muskingum River boilers are designed for the same capacity, pressure, and temperature conditions as the Kanawha River boilers. Arrangement of superheater, reheater, economizer, and air-heater surface also will be identical. A two-stage slag-tap furnace design has, however, been selected in order to permit use of coals having relatively low ash-fusion characteristics. The primary furnace will be 56 ft wide, 15 ft deep, and 71 ft high; the open pass 56 ft wide × 9 ft deep with an average height of 80 ft.

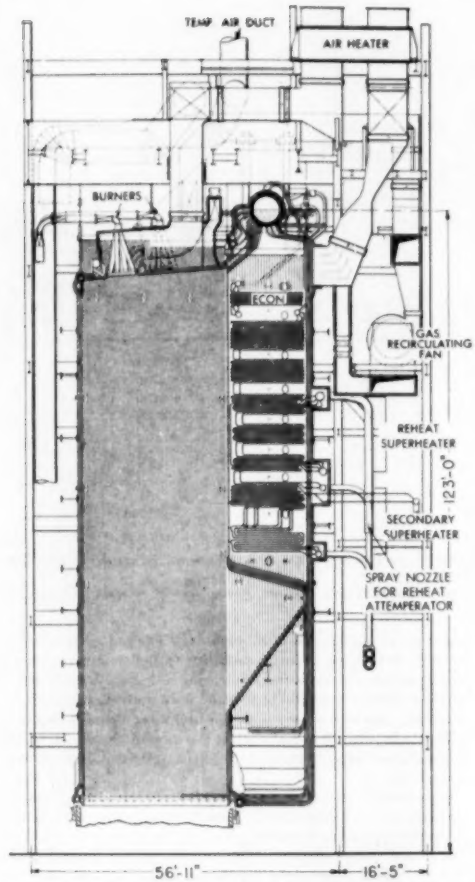

FIG. 5 CROSS SECTION OF ONE OF THE STEAM BOILERS OF KANAWHA RIVER PLANT

(These boilers are equipped with dry-bottom furnaces; boilers for Muskingum River Plant will have wet-bottom furnaces.)

These boilers also will be designed for full pressurized operation, and draft-fan capacities and arrangement will be similar to the Kanawha River units.

Each of the Kanawha River boilers will be arranged with an independent furnace ash-removal system, with no interconnections being provided. Ash from the two identical dry-bottom furnace hoppers of each boiler will be collected in twin water-filled ash pits, from where it will be discharged periodically through a double-roll clinker grinder to a common sump. From this sump the ash-water mixture will be pumped to a temporary storage area.

The Muskingum River boilers also will be arranged with independent furnace ash- and slag-removal systems, without interconnections. Molten slag from the primary furnace and dry ash from the open pass of each boiler will be collected in a relatively deep submerged double-discharge ashpit and piped to the storage area.

CONDENSERS AND ASSOCIATED EQUIPMENT

The condenser is of the single-pass divided-circulation type, with 90,000 sq ft of cooling surface consisting of $^{7}/_{8}$-in-OD × 18 BWG arsenical admiralty tubes, 30 ft 0 in. over-all length. A storage-type hot well is provided with 1100 cu ft of storage capacity. Condenser design provides for condensate deaeration, with the standard residual oxygen guarantee of 0.03 cc per liter, although operating experience with similar condensers indicates that oxygen removal will be considerably better than this.

The steam-jet air ejector is of the 2-stage triple-element type with separate inter- and aftercoolers, each element having sufficient capacity to handle normally expected air leakage. Steam for operating the air ejector is obtained normally from the high-pressure-turbine exhaust through a pressure regulator. During starting up and at loads below approximately one-half load, steam is obtained from the boiler intermediate-superheater header at 2150 psig 900 F reduced to 150 psig at the nozzles. Steam- and water-space priming ejectors also use steam from the intermediate-superheater header, reduced to 400 psig at the nozzles by means of a pressure-reducing orifice.

Two circulating-water pumps, each of 70,000 gpm capacity, provide cooling water for the condenser of each unit as well as general service water supply for washing traveling screens. Condensers are installed at an elevation low enough to permit siphon operation. To reduce basement depth, circulating-water pumps are installed in the screen house at the river at some distance from the plant.

Water flows through the two halves of the condenser in opposite directions, and provision is made to backwash the condenser at full load by means of two special butterfly-type reversing valves, operated simultaneously by a single switch on the control panel. Electrical protective features are provided to insure that the two valves at opposite ends of the condenser will operate together.

Space limitations made necessary the use of vertical circulating-water pumps. A standard dry-pit volute centrifugal-pump design was selected, with its shaft mounted in a vertical position. Such pumps have given entirely satisfactory experience over a long period of years, with very little maintenance or inspection required.

ELECTRICAL FEATURES

The Kanawha generators will be quite similar to those previously installed at the Philip Sporn and Tanners Creek Plants, although of larger size, with relatively minor differences in design details. The 1800-rpm double-winding low-pressure unit will be rated 140,000 kva at 0.8 power factor and 0.5 lb hydrogen pressure. Under these conditions the short-circuit ratio will be 0.8. The 3600-rpm high-pressure generator will be rated 75,000 kva at 0.85 power factor and 0.5 lb hydrogen pressure, with a short-circuit ratio of 0.7. At 30 lb hydrogen pressure the low-pressure generator will be rated 175,000 kva at 0.8 power factor, and the high-pressure machine 93,000 kva at 0.85 power factor.

Shaft-driven exciters on each generator will provide excitation current, supplemented by a motor-generator set for starting up the combined generator unit. A second such motor-generator set will be provided for emergency excitation in the event of failure of any of the main exciters. Voltage control for each unit will be provided by amplidyne regulators.

The large size of these generating units necessitated the selection of 18,000 volt terminal voltage, the economic upper limit in this case. Conventional aluminum bus structures will connect the 18,000-volt terminals of the high and low-pressure generators directly to three-phase power transformers, stepping up to 132 kv. Disconnect switches will be provided in these leads to permit convenient maintenance and testing of the units.

Three-phase auxiliary transformers will be connected to the

leads of each of the generator windings. These transformers will feed separate auxiliary bus sections, each of which will have an alternate power supply from a three-phase transformer stepping down from the 132-kv bus system. The major motor drives will be accommodated on these buses, operating at 4160 volts grounded neutral. To avoid outage of all major motor drives due to accidental grounding of one circuit, the auxiliaries are arranged into three groups, each fed by an independent source, so that the loss of one of the groups will not result in shutdown of the entire unit. The smaller 550-volt motors will be served from buses fed by three-phase transformers connected to the main auxiliary buses. Each 550-volt bus will have an emergency connection to one of the other main auxiliary buses to provide flexibility in operation and to assure an emergency 550-volt source in the event of loss of a transformer or main auxiliary bus.

Three main power transformers will be provided for each unit, one for the high-pressure generator and one for each of the two windings of the low-pressure generator. These transformers will be bussed on the 132-kv side, and then connected to the double-bus 132-kv yard immediately adjacent through two oil circuit breakers which also can serve as a bus tie. Initially, five 132-kv feeders will be employed, two to Cabin Creek, two to Glen Lyn, and one to Philip Sporn Plant. Each feeder will have a single breaker with selector switches to the two buses and a by-pass switch to one of them so that two 132-kv buses may be used as main and transfer bus for maintenance and for emergencies.

These three transformers will be forced-air, forced-oil cooled, located immediately adjacent to the station to give the shortest possible leads from generators to transformers. The transformers will be protected by the usual differential relay setups and by low-pressure carbon-dioxide fire-fighting equipment.

Provision will be made in the switchyard for installing a 330-kv double-bus system to take the output of future generating units, with a large transformer bank for tying between the 132-kv and 330-kv buses.

In this respect Muskingum River Plant will be similar in arrangement to Kanawha River, except that only one of the two initial generating units will be connected to the 132-kv bus. The second generating unit will step up to 330,000 volts through a bank of single-phase transformers. This bank will have a 330-kv winding rated 232,500 kva. Low-voltage windings will be in three sections, one for each generator. Auxiliary transformers will be connected to the generator leads as in the case of the other units connected to the 132-kv bus.

Two 150,000-kva three-phase auto transformers will be used to tie together the 132-kv and 330-kv systems. Tertiary windings on these transformers will serve to connect compensating-shunt reactors. This whole arrangement at Muskingum is shown diagrammatically in Fig. 6.

Operating and Maintenance Considerations

That basic design decisions have a major and frequently critical effect on operating and maintenance requirements and results would be too trite to mention were not these effects so frequently overlooked. Obviously this applies to such an item as thermal efficiency. But, to an even greater extent, these requirements and results are influenced by the kind of boiler and turbine selected, the arrangement of circulating pumps and condenser, heater location, instrumentation, automatic features, arrangement of equipment for ease of maintenance, and a host of similar features. All of these elements at Kanawha River and Muskingum River were studied thoroughly in the light of previous experience to assure not only safe operation, but maximum economy in operation and in maintenance. No truly sound development of economic mass generation of electric energy is possible without this thorough attention to operating and maintenance requirements.

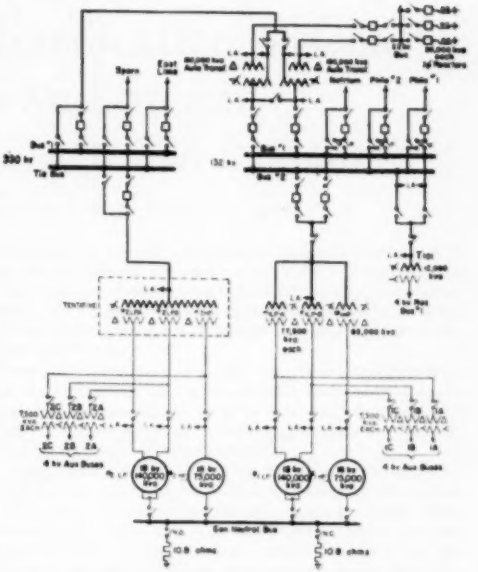

Fig. 6 Simplified Diagram of Principal Electrical Arrangements at Muskingum River Plant of The Ohio Power Company, Showing Connections to and Between the 132-Kv and 330-Kv Transmission Lines

BIBLIOGRAPHY

1 Companion papers, "The Development and Implementation of a Generation Program on the American Gas and Electric Company System—Part 1—System Fundamentals," by Philip Sporn, published in this issue, pp. 603–608; and "Part 2—Fuel Supply," by Philip Sporn and H. A. Kammer, published in this issue, pp. 609–612.

2 "Twin Branch Plant of Indiana & Michigan Electric Company (b) Twin Branch Extends High Pressure Economies," by Philip Sporn, *Electrical World*, vol. 116, October 18, 1941, p. 80.

"Twin Branch Plant of Indiana & Michigan Electric Company (i) Technically Sound and Commercially Workable," by Philip Sporn, *Electrical World*, vol. 116, October 18, 1941, p. 80.

"Operating History of the 2500-Psi Twin Branch Plant," by Philip Sporn and E. G. Bailey, Trans. ASME, vol. 66, 1944. (Special Pamphlet.)

"Twin Branch—A Study of Progress in Power Generation," by S. N. Fiala, H. A. Kammer, and F. A. Lane, *Power Generation*, vol. 53, November, 1949.

3 "The 2000-Psi, 1050 F, and 1000 F Reheat Cycle at the Philip Sporn and Twin Branch Steam-Electric Stations," by Philip Sporn, Trans. ASME, vol. 70, 1948, pp. 287–294.

"The Basic Concept Behind Philip Sporn Station," by Philip Sporn; "Sporn Heat Cycle Meets High Goal," by Theodore Baumeister; "(Philip Sporn Plant) Steam Generation Employs Reheat, Pressurization, Gas Recirculation," by S. N. Fiala; "Turbine, Condenser and Piping Fit Objectives," by S. N. Fiala; "Control of Units Centralized in Pairs for Effective Operation," by T. T. Frankenberg; "Simplicity Is the Keynote of Plant Electrical Features," by F. A. Lane; "Plant Construction and Architecture Keyed to Economy," by H. A. Kammer, *Electrical World*, vol. 133, June 5, 1950.

"Twenty-Five Years of Reheat Operating Experience on the American Gas and Electric Company System," by S. N. Fiala, Trans. ASME, vol. 74, 1952, pp. 561–568.

4 "Remote Operation Through Centralized Control Rooms—A New Concept Developed on the American Gas and Electric System," by T. T. Frankenberg, presented at the Semi-Annual Meeting, Toronto, Ont., Can., June 11–15, 1951, of The American Society of Mechanical Engineers.

Thermodynamics of Gasification of Coal With Oxygen and Steam

Charts for Material and Enthalpy Balance Calculations

By WAYNE C. EDMISTER,[1] HARRY PERRY,[2] R. C. COREY,[3] AND M. A. ELLIOTT[4]

Thermodynamic charts and tabulations are presented for calculating conveniently the heat balance, and product-gas yield and composition for the gasification of coal with oxygen and steam, on the assumption that water-gas shift equilibrium is attained by the product gases. These charts are of general applicability for any rank of coal; they cover a wide range of operating conditions through the use of multiple parameters, and may be used for pressures as high as 30 atm. Examples are given to illustrate the use and versatility of the charts. Charts and numerical examples are also given for a typical high-volatile C bituminous coal to illustrate the uses of such charts for a specific coal.

Introduction

INTENSIVE research and development work during the past few years have demonstrated the feasibility of producing carbon monoxide and hydrogen by the continuous and complete gasification of pulverized coal with oxygen and steam.[5,6,7] This has led to considerable interest in the thermodynamics of such systems, with the objectives of (1) comparing theoretical calculations with experimental results; (2) predicting reactor performance from known values of the feed rates and enthalpies of coal, oxygen, and steam; (3) evaluating the effect of a known change in one variable upon the other process variables; and (4) determining the process requirements and yields at given operating conditions.

In the course of experimental gasification work at the Bureau of Mines, Pittsburgh, Pa., extensive material and heat balances were made to compare the experimental results with the theoretical values, and to guide in the selection of the feed conditions necessary for optimum reactor performance. In addition, these calculations made it possible to evaluate the separate effects of the numerous variables, which are complexly interrelated. For example, if one examines the effect of increasing the preheat of the feed streams on any one process condition, assuming all other conditions constant, one finds that it results in (1) reduction of the oxygen required per pound of coal gasified; or (2) increase in the temperature of the exit gas; or (3) increase in the carbon conversion.

Repeated calculation of heat and material balances is tedious and time-consuming, and it was evident that thermodynamic charts would reduce considerably the numerical calculations and have the distinct advantage of showing more clearly the relationships between the process variables.

A significant step was made in this direction recently by Batchelder and Sternberg,[8] who made a thermodynamic analysis of the gasification of pulverized coal with oxygen and steam. They derived basic energy- and material-balance equations and constructed a series of graphs for a high-volatile A and a high-volatile C bituminous coal. Although the procedure can be applied to any general case, their graphs are limited to the special case of 95 per cent carbon conversion, two types of coal, and variations of heat loss expressed only in terms of steam preheat.

It is the purpose of this paper to present and discuss the development of more versatile thermodynamic charts, which are applicable to any coal for a wide range of operating variables. The charts are of the multiparameter type, designed to reduce to a minimum the numerical steps required for a solution. In addition to the charts for the general case, a specific chart has been developed for a particular coal.

The bases for these charts are material and heat balances for each set of feed conditions, and the major assumption that the product gases reach the water-gas shift equilibrium. No assumptions of the mechanism of the gasification process are necessary. When feed rates of the coal, oxygen, and steam are known, and elemental balances for carbon, oxygen, and hydrogen are made, the quantities of CO, CO_2, H_2, and H_2O leaving the reactor can be calculated for any assumed exit-gas temperature. The input enthalpy can be calculated from the quantities and the temperatures of the feed streams, and the output enthalpy from the quantities and the temperatures of the materials leaving the reactor.

The *actual* exit-gas temperature in an adiabatic reactor is the temperature required to balance the input and output enthalpies, and can be determined from calculations of the output enthalpy with successive assumed temperatures, or more conveniently, by graphical methods. In a nonadiabatic system, the difference between the input and output enthalpy corresponds to the heat lost.[9]

In the following sections the basic material- and energy-balance equations used in preparing the general thermodynamic charts are developed.

---

[1] Professor of Chemical Engineering, Carnegie Institute of Technology, and Consulting Chemical Engineer, Synthetic Liquid Fuels Branch, Bureau of Mines, Pittsburgh, Pa. Mem. ASME.

[2] Chemical Engineer, Synthetic Liquid Fuels Branch, Bureau of Mines, Pittsburgh, Pa.

[3] Supervising Engineer, Combustion Research Section, Coal Branch, Bureau of Mines, Pittsburgh, Pa. Mem. ASME.

[4] Assistant Chief, Research and Development Branch, Office of Synthetic Liquid Fuels, Bruceton, Pa. Mem. ASME.

[5] "Continuous Gasification of Pulverized Coal With Oxygen and Steam by the Vortex Principle," by H. Perry, R. C. Corey, and M. A. Elliott, Trans. ASME, vol. 72, 1950, pp. 599–610.

[6] "A Pilot Plant for Gasifying Powdered Coal Entrained in Oxygen and Steam," by J. P. McGee, L. D. Schmidt, and M. C. Stone, *Chemical Engineering Progress*, vol. 44, 1948, pp. 737–744.

[7] "The Continuous Gasification of Powdered Coal Suspension by Air-Oxygen and Air-Oxygen-Steam Mixture," by C. von Fredersdorff, Proceedings of the American Gas Association, 1949, pp. 705–724.

Contributed by the Fuels Division and presented at the Annual Meeting, Atlantic City, N. J., November 25–30, 1951, of THE AMERICAN SOCIETY OF MECHANICAL ENGINEERS.

NOTE: Statements and opinions advanced in papers are to be understood as individual expressions of their authors and not those of the Society. Manuscript received at ASME Headquarters, April 5, 1951. Paper No. 51—A-20.

[8] "Thermodynamic Study of Coal Gasification," by H. R. Batchelder and J. C. Sternberg, *Industrial and Engineering Chemistry*, vol. 42, 1950, pp. 877–882.

[9] This statement applies only to systems in which heat is not added through the walls of the gasifier.

Material-Balance Equations

It is assumed that (1) pure oxygen is used; (2) the sulphur in the coal appears as H_2S in the exit gas; (3) the nitrogen in the coal appears as N_2 in the exit gas; (4) no free oxygen appears in the exit gas; (5) any solids leaving the reactor consist of carbon and ash; and (6) no hydrocarbons appear in the exit gas. If oxygen of purity less than 100 per cent is used, the calculations can be modified easily since the inerts, which are mostly nitrogen, appear in the exit gas unchanged and can be treated accordingly.

Experimental evidence shows that assumptions 2 to 6 are essentially correct for any actual gasifier operating at atmospheric pressure, because the product gases consist of CO, CO_2, H_2, H_2O, H_2S, and N_2, and the solids leaving the reactor are unreacted carbon and ash. Furthermore, the calculations are affected only slightly by the small deviations from these assumptions that occasionally occur.

The elemental balances for H_2, O_2, C, and S for 100 lb of coal are

Hydrogen:

$$\frac{(H_2)_{net}}{2.016} + \frac{(H_2O)_{total}}{18.016} = H_2 + H_2O + H_2S \quad [1]$$

Oxygen:

$$\frac{(O_2)}{32.0} + \frac{(H_2O)_{total}}{36.032} = CO_2 + \frac{1}{2}CO + \frac{1}{2}H_2O \quad [2]$$

Carbon:

$$\frac{(C)_G}{12.0} = CO_2 + CO \quad [3]$$

Sulphur:

$$\frac{(S)}{32.0} = H_2S \quad [4]$$

where

$(H_2)_{net}$ = pounds of net hydrogen in 100 lb of coal = total hydrogen in coal minus 1/8 times[10] oxygen in coal

$(H_2O)_{total}$ = pounds of steam supplied per 100 lb of coal plus 9/8 times oxygen in coal

(O_2) = pounds of oxygen supplied per 100 lb of coal

(S) = pounds of sulphur per 100 lb of coal

$(C)_G$ = pounds of carbon *gasified* per 100 lb of coal

H_2, H_2O, CO_2, H_2S, and CO = moles of respective gases in product gases from 100 lb of coal

Combination and rearrangement of these equations gives

$$CO + H_2 = \frac{(C)_G}{6.0} - \frac{(O_2)}{16.0} + \frac{(H_2)_{net}}{2.016} - \frac{(S)}{32.0} \quad [5]$$

$$CO_2 + H_2O = \frac{(O_2)}{16.0} + \frac{(H_2O)_{total}}{18.016} - \frac{(C)_G}{12.0} \quad [6]$$

It is interesting to note from Equation [5] that the yield of carbon monoxide and hydrogen from a given coal depends upon the oxygen supplied and the carbon gasified, but is independent of the steam fed. Since experimental results have shown that the product gases from an entrained gasification system attain water-gas shift equilibrium, it is possible to calculate the composition of the product gases from Equations [5] and [6] and the water-gas shift equilibrium relationship which is

$$\frac{CO_2 \times H_2}{CO \times H_2O} = K \quad [7]$$

where K = water-gas shift equilibrium constant, which is a function of temperature only. The quantities of CO_2, H_2, CO, and H_2O are the mole concentrations of these respective gases.

Combining Equations [5], [6], and [7] and solving the resulting quadratic for the moles of CO, considering only the negative root, gives

$$CO = \frac{-\frac{\beta}{\alpha} - \sqrt{\left(\frac{\beta}{\alpha}\right)^2 - 4\frac{\gamma}{\alpha}}}{2} \quad [8]$$

where

$$-\frac{\beta}{\alpha} = (CO_2 + CO) + \frac{K}{1-K}(CO_2 + H_2O) + \frac{(CO + H_2)}{1-K} \quad [8a]$$

and

$$\frac{\gamma}{\alpha} = \frac{(CO_2 + CO)(CO + H_2)}{1-K} \quad [8b]$$

Although CO appears in each term of Equation [8], the bracketed terms in Equations [8a] and [8b] will be recognized as calculable from Equations [3], [5], and [6]. Therefore the moles of CO may be computed for any selected temperature, percentage carbon conversion, and set of feed condition. The value of K corresponding to the selected temperature may be found in Table 1.

TABLE 1 VALUES OF EQUILIBRIUM CONSTANT K FOR WATER-GAS SHIFT REACTION

$$K = \frac{CO_2 \times H_2}{CO \times H_2O}$$

Temperature, deg F	K
1800	0.610
1900	0.585
2000	0.480
2100	0.435
2200	0.396
2300	0.365
2400	0.337
2500	0.313
2600	0.292
2700	0.273
2800	0.258

Source: "Heats, Free Energies, and Equilibrium Constants of Some Reactions Involving O_2, H_2, H_2O, C, CO, CO_2, and CH_4," D. Wagman, J. Kilpatrick, W. Taylor, K. Pitzer, and F. Rossini, *Journal of Research*, National Bureau of Standards, vol. 34, February, 1945, pp. 143–161.

Enthalpy-Balance Equations

The type of gasification under consideration is basically a constant-pressure flow process in which there is no work done, and in which the changes in potential and kinetic energy are negligible. Accordingly, the net differences between the enthalpies of the charge and product streams represent the quantities of heat added or lost in the operation.[11] Enthalpy balances may be used to compute important gasification conditions such as heat loss and reaction temperature. These calculations are useful for design purposes, or for following the performance of a reactor under actual experimental conditions.

These enthalpy-balance calculations are based upon a datum of zero enthalpy for the *elements* at —459.6 F and 0 psia.

[10] These are approximate values used in engineering calculations. The exact values are 1.008/8 and 9.008/8.

[11] In this paper the calculations are applied to systems in which heat is lost from the generator but the methods used are general and can be applied also to systems in which heat is added through the walls of the generator.

With this datum the enthalpies of each stream include the heat of formation, so separate heat-of-reaction computations are not required. The quantity basis for the preparation of the charts is 100 lb of coal in the "as-received" condition. The unit enthalpies of all constituents, excepting coal, are given in Table 2 for temperatures between 77 F and 2800 F. The methods for computing the enthalpy of coal are discussed in the appropriate parts of this paper.

Input Enthalpy. The total enthalpy of the feed streams to the gasifier is the sum of the enthalpies of coal, oxygen, and steam, all above the datum of the elements at —459.6 F. The values for oxygen and steam are computed from the unit enthalpies given in Table 2. The enthalpy of coal at any temperature above the elements is:

$$\Delta H_{coal} = \Delta H_1 + \Delta H_2 - \Delta H_3 + \Delta H_4 \quad [9]$$

where

ΔH_1 = enthalpy of elements of coal substance at 77 F and above —459.6 F
ΔH_2 = enthalpy of combustion of elements of coal substance at 77 F
ΔH_3 = enthalpy of combustion of coal at 77 F
ΔH_4 = enthalpy of coal between 77 and t F

These terms are evaluated for 100 lb of as-received coal in the following manner

$$\Delta H_1 = 37.5\,(C)_c + 1800\,(H_2)_c + 115.6\,(O_2)_c + 78.1\,(S)_c + 132.3\,(N_2)_c + 107.5\,(A)_c \quad [10]$$

where the bracketed quantities are the number of pounds of carbon, hydrogen, oxygen, sulphur, nitrogen, and ash, respectively, in 100 lb of as-received coal (as indicated by the subscript c). The numerical coefficients for carbon through nitrogen are the enthalpies of the respective elements in Btu per lb, calculated from the unit molal enthalpies given in Table 2. The coefficient for ash is based upon a mean specific heat of 0.20 Btu/lb-deg F between —459.6 and 77 F.

$$\Delta H_2 = -14{,}087\,(C)_c - 60{,}958\,(H_2)_c - 3986\,(S)_c \quad [11]$$

where the numerical coefficients are the gross heats of combustion, Btu per lb, of each element.

ΔH_3 is the heat of combustion of the coal, determined calorimetrically, or calculated as follows from the Dulong formula

$$\Delta H_3 = 14{,}544\,(C)_c + 62{,}028\left[(H_2)_c - \frac{(O_2)_c}{8}\right] + 4050\,(S)_c \quad [12]$$

ΔH_4 may be estimated by using an average heat capacity for coal above 77 F of 0.325 Btu/lb-deg F, accordingly

$$\Delta H_4 = 32.5\,(t - 77) \quad [13]$$

Combining Equations [9], [10], [11], [12], and [13], i.e., using the Dulong formula to compute ΔH_3, gives the general expression for the enthalpy of 100 lb of as-received coal at any temperature, t deg F, between 77 and 2800 F

$$H_{coal} = 494\,(C)_c + 2870\,(H_2)_c - 7638\,(O_2)_c + 142\,(S)_c + 132.3\,(N_2)_c + 107.5\,(A)_c + 32.5\,(t - 77) \quad [14]$$

This equation may be simplified by weighing the coefficients of sulphur, nitrogen, and ash with respect to average quantities of these constituents in the coal, for example, 3, 0.5, and 10 per cent, respectively, which gives a weighted coefficient of 120. From the relations

$$H_c = 494\,(C)_c + 2870\,(H_2)_c - 7638\,(O_2)_c + 32.5\,(t - 77) + 120\,[(S)_c + (N)_c + (A)_c] \quad [15]$$

and since

$$(S)_c + (N_2)_c + (A)_c = 100 - (C)_c - (H_2)_c - (O_2)_c \quad [15a]$$

the approximate equation for the enthalpy of 100 lb of coal becomes

$$H_{coal} \doteq 374\,(C)_c + 2750\,(H_2)_c - 7758\,(O_2)_c + 32.5\,(t - 77) + 12{,}000 \quad [16]$$

The total enthalpy of coal may also be expressed in terms of the calorimetric heat of combustion of the coal, ΔH_c, which is used instead of the Dulong formula, i.e., Equation [12]. Combining Equations [9], [10], [11], and [13], then gives

TABLE 2 UNIT ENTHALPIES

Temp, deg F	Thousands of Btu per pound mol above elements at 0 R and 0 deg psia: C	O_2	H_2	H_2O	CO	CO_2	N_2	H_2S	S	Btu per lb, ash	Deg F
77	0.45	3.7	3.6	....	....	....	3.7	....	2.5	107.5	77
200	....	4.6	....	....	....	....	....	....	....	....	200
300	....	5.3	....	....	....	....	....	....	....	....	300
400	....	6.0	....	—95.8	....	....	....	....	....	....	400
500	....	6.8	....	—95.0	....	....	....	....	....	....	500
600	....	7.6	....	—94.2	....	....	....	....	....	....	600
700	....	8.4	....	—93.3	....	....	....	....	....	....	700
800	....	9.2	....	—92.5	....	....	....	....	....	....	800
900	....	10.0	....	—91.5	....	....	....	....	....	....	900
1000	....	10.8	....	—90.6	....	....	....	....	....	....	1000
1100	....	11.6	....	—89.7	....	....	....	....	....	....	1100
1200	....	12.4	....	—88.7	....	....	....	....	....	....	1200
1300	....	13.2	....	—87.7	....	....	....	....	....	....	1300
1400	....	14.0	....	—86.7	....	....	....	....	....	....	1400
1500	....	14.8	....	—85.7	....	....	....	....	....	....	1500
1600	....	15.7	....	—84.7	....	....	....	....	....	....	1600
1700	....	16.5	....	—83.7	....	....	....	....	....	....	1700
1800	8.0	17.4	15.9	—82.6	—32.2	—144.6	16.6	—63.4	....	520	1800
1900	8.5	18.3	16.7	—81.6	—31.4	—143.2	17.4	—62.2	....	....	1900
2000	9.1	19.1	17.4	—80.5	—30.5	—141.8	18.3	—61.1	....	590	2000
2100	9.7	....	18.2	—79.4	—29.7	—140.4	19.1	—59.9	....	....	2100
2200	10.2	....	19.0	—78.2	—28.8	—139.2	20.0	—58.7	....	665	2200
2300	10.8	....	19.8	—77.1	—28.0	—137.7	20.8	—57.5	....	....	2300
2400	11.4	....	20.5	—76.0	—27.2	—136.3	21.6	—56.3	....	743	2400
2500	12.0	....	21.3	—74.8	—26.3	—139.9	22.4	—55.0	....	....	2500
2600	12.6	....	22.1	—73.6	—25.5	—133.5	23.3	—53.8	....	887	2600
2700	13.2	....	22.9	—72.5	—24.6	—132.0	24.1	—52.5	....	....	2700
2800	13.8	....	23.7	—71.3	—23.8	—130.6	25.0	—51.2	....	....	2800

SOURCE: "Selected Values of Properties of Hydrocarbons," by F. D. Rossini, et al., Bulletin C-461 National Bureau of Standards, 1947.

$$H_{coal} = \Delta H_r - 14{,}050\,(C)_c - 59{,}158\,(H_2)_c - 3908\,(S)_c + 115.6\,(O_2)_c + 132.3\,(N_2)_c + 107.5\,(A)_c + 32.5\,(t - 77) \quad [17]$$

By grouping the oxygen, nitrogen, and ash terms, as was done previously for sulphur, nitrogen, and ash, a weighted coefficient of 116 is obtained for these terms, and Equation [17] simplifies to

$$H_{coal} = \Delta H_r + 14{,}166\,(C)_c + 59{,}274\,(H_2)_c - 4024\,(S)_c + 32.5\,(t - 77) + 11{,}600 \quad [18]$$

Since the Dulong formula is empirical, an enthalpy calculation by Equation [16] for a given coal may differ from one by Equation [18]. The maximum deviation of the Dulong formula is about 1.5 per cent,[12] which in certain instances may result in an enthalpy error that is significant. Therefore the use of Equation [16], which is somewhat simpler than Equation [18] because of one less term, will depend upon the error that can be tolerated for a given set of conditions.

It was of interest to calculate the enthalpy at 77 F of a typical subbituminous coal (sample No. 2, Table 3) by the equations that have been given to determine the errors incurred by using the Dulong formula and a weighted coefficient for certain terms. The reference enthalpy was obtained with Equation [9] by calculating values for ΔH_1 and ΔH_2, using the ultimate analysis given in Table 3, and using the calorimetric heating value, 1,336,000 Btu per 100 lb of coal, for ΔH_3. In comparison, the enthalpies were calculated by Equations [16] and [18], and the results given in Table 4 were obtained.

TABLE 3 ULTIMATE ANALYSES OF COALS (AS-RECEIVED) USED IN EXAMPLES

	Rock Springs, Wyoming coals			
	Sample 1		Sample 2	
	Weight, per cent	Moles per 100 lb	Weight, per cent	Moles per 100 lb
O_2	15.4	0.481	13.41	0.419
H_2	5.3	2.630	5.46	2.710
S	0.9	0.028	0.86	0.027
N	1.5	0.054	1.62	0.058
C	71.6	5.965	76.0	6.333
Ash	5.3	....	2.65	....
	100.0		100.00	
Gross heat of combustion, Btu/lb		12620		13360

TABLE 4 CALCULATION OF ENTHALPIES

Equation	Basis	Total enthalpy at 77 F of coal, Btu/100 lb coal. Above elements (carbon, hydrogen etc.) at —459.6 F and 0 psia	Deviation from results of Equation [9], Btu/lb coal
[9]	Calorimetric enthalpy of combustion of coal	56083	....
[16]	Dulong formula for enthalpy of combustion of coal with weighted coefficients for S, N_2, and ash	48596	—74.9
[18]	Calorimetric enthalpy of combustion of coal with weighted coefficients for O_2, N_2, and ash	56113	+ 0.3

Since the enthalpies obtained by Equations [9] and [18] differ only by the effect of using a weighted coefficient for oxygen, nitrogen, and ash, it is evident that the error due to combining these terms is negligible. Comparing the results for Equations [16] and [18], which differ only by the error of the Dulong formula, it is seen that for the conditions of this comparison the error is greater than that of the experimental determination of the heating value of coal, i.e., ± 40 Btu per lb of coal.

Output Enthalpy. The output enthalpy is the sum of the enthalpies of the gases and solids leaving the reactor. The unit enthalpies of the possible products are given in Table 2 where it should be noted that the unit enthalpy for ash above absolute zero is based upon mean specific heats at each temperature level. Since ash is assumed not to react chemically, its enthalpy of formation is not required.

The quantities of CO, CO_2, H_2, and H_2O in the product gas are obtained from Equations [3], [5], [6], and [8], and it is evident that these quantities depend upon the gasification conditions, that is, the feed rates, temperature, and the carbon gasified. The N_2 and H_2S in the product gases are computed from the nitrogen and sulphur in the coal, it being assumed that neither of these constituents appears in the solid residue. However, in the temperature range 1800 F to 2800 F, when the weight per cent of nitrogen in the coal is 2 to 3 times that of the sulphur in the coal, these terms may be omitted in the enthalpy calculations,[13] as the respective unit enthalpies of H_2S and N_2 at gasification temperature are of opposite sign and approximately cancel. When the weight ratio of nitrogen to sulphur is significantly outside the range of 2 to 3, it is recommended that the net enthalpy of nitrogen and H_2S be computed to determine if it is sufficiently large to be included in the total output enthalpy.

Further simplification of the output enthalpy is possible by using a mean unit enthalpy for carbon plus ash at various temperatures, calculated from Table 2 on the basis of equal weights of carbon and ash (Table 5).

TABLE 5 ENTHALPY OF RESIDUE, THOUSANDS OF BTU PER POUND ABOVE —459.6 F

Temperature, deg F	Carbon	Ash	Residue, (50% C + 50% ash)
1800	0.67	0.52	0.59
2000	0.76	0.50	0.63
2200	0.85	0.67	0.76
2400	0.95	0.74	0.85
2600	1.05	0.89	0.97
2800	1.15	1.04	1.10

Development of Thermodynamic Charts

To facilitate material and energy-balance calculations, seven charts, Figs. 1 to 7, were developed from Equations [5], [6], [8], [16], [18], and Table 3. These charts are applicable to any coal. However, as has been suggested previously, when many calculations are to be made for a specific coal it might be more convenient to construct a special "enthalpy-balance" chart for that coal. Such charts can be derived from the general charts. Accordingly, an additional chart, Fig. 8, was prepared for a Rock Springs, Wyoming, coal (Sample No. 1, Table 3) to illustrate the development of such charts.

Gas-Composition Charts. Fig. 1 is a graphical solution of Equations [5] and [6], which give the moles of ($CO + H_2$) and ($CO_2 + H_2O$). The two sections of the chart have a common oxygen scale, which gives the oxygen in terms of both standard cubic feet per 100 lb of coal and pounds per 100 lb of coal. The dashed lines illustrate the method for reading the scale.

Figs. 2, 3, and 4 graphically solve Equation [8] which gives the moles of CO for the operation. Figs. 2 and 3 solve the special functions in Equations [8a] and [8b], which are required for solution of Equation [8]. Fig. 4 gives the final solution for the moles of CO. The application of these charts is illustrated by the dashed lines.

Enthalpy Charts. The enthalpies of the feed and the product streams are represented on separate charts. Fig. 5 gives the input enthalpy when the enthalpy of the coal is calculated by

[12] "Chemistry of Coal Utilization," by H. H. Lowry, vol. 1, p. 138, John Wiley & Sons, Inc., New York, N. Y., 1945.

[13] These terms were omitted in preparing the charts.

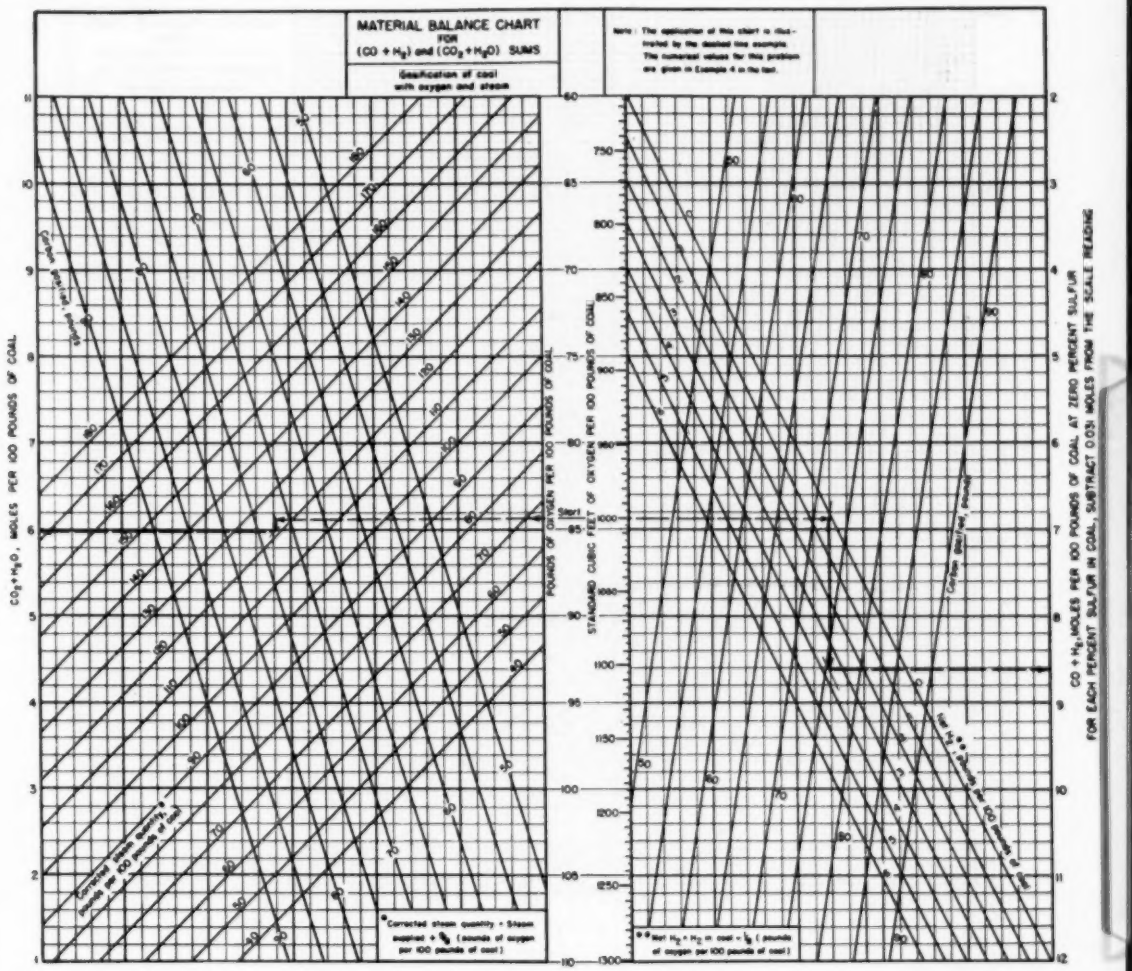

FIG. 1

Equation [16], which embodies the Dulong formula. Fig. 6 gives the coal enthalpy based upon Equation [18], i.e., using the experimental heat of combustion. The input enthalpy based upon the more accurate Equation [18] may be obtained graphically by the use of Figs. 5 and 6 together.

Fig. 7 gives the output enthalpy as a function of (*a*) the exit-gas temperature; (*b*) the amounts of oxygen and steam fed; (*c*) the amount of carbon gasified per 100 lb of coal; and (*d*) the amount of residue. Although the composition of the gases is implied in the results obtained by this chart, it will be noted that the gas composition is not required to obtain the output enthalpy. This convenient feature of Fig. 7 was obtained by making systematic calculations of product compositions and enthalpies for a range of conditions, and then correlating the results graphically as a function of the primary variables, oxygen, steam, exit-gas temperature, etc. The dashed lines illustrate the use of Fig. 7.

The enthalpy chart for a specific coal, Rock Springs subbituminous, is represented by Fig. 8. Since many of the variables of the previous enthalpy charts became constants for a coal of fixed composition, all of the parameters for computing the output enthalpy may be plotted on a single chart. Fig. 8 was prepared in the following manner: The total input and output enthalpies were computed for a wide range of the variables involved, and plotted on separate multiparameter charts. These charts then were connected by a heat-loss parameter, and the

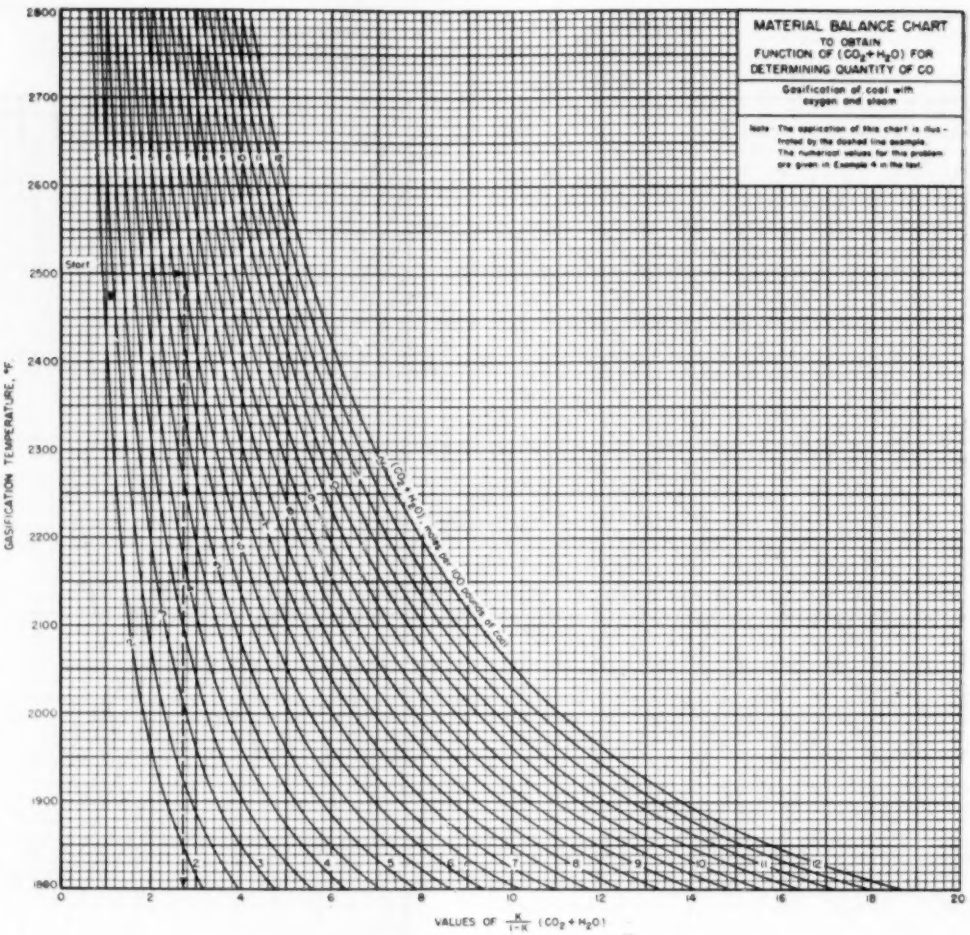

FIG. 2

input and output-enthalpy scales omitted to avoid unnecessary confusion. With this arrangement, the center section gives the heat loss required to balance the input and output enthalpies.

Practical examples of both the numerical and the graphical procedures are given in the following sections to illustrate the comparative ease with which a graphical solution can be made. Unless otherwise stated, the basis in all examples is 100 lb of as-received coal.

Illustrative Examples Using Numerical Methods

The following examples are based upon the gasification of 100 lb of Rock Springs coal (sample No. 2, Table 3) in the as-received condition with 10 SCF of pure oxygen per lb of coal, and 1.06 lb of steam per lb of coal, preheated to 1500 F. Assume that the product gases and residue leave the reactor at 2500 F, and that 95 per cent of the carbon is gasified. Calculate the composition and yield of the exit gases and the heat lost.

Example 1. Find the moles of CO, CO_2, H_2, and H_2O produced by 100 lb of coal. Basis: 100 lb as-received coal.

$$\text{Carbon gasified, } (C)_G = 76 \times 0.95 = 72.2 \text{ lb}$$

$$\text{Oxygen supplied, } (O_2) = 10 \times 0.084 \frac{\text{lb}}{\text{SCF}} \times 100 = 84.4 \text{ lb}$$

$$\text{Net } H_2 \text{ in coal, } (H_2)_{net} = 5.46 - \frac{13.41}{8} = 3.78 \text{ lb}$$

$$\text{Total steam, } (H_2O)_{total} = 106 + (1.125 \times 13.41) = 121.1$$

By Equation [3]

$$CO + CO_2 = \frac{72.2}{12} = 6.02 \text{ moles}$$

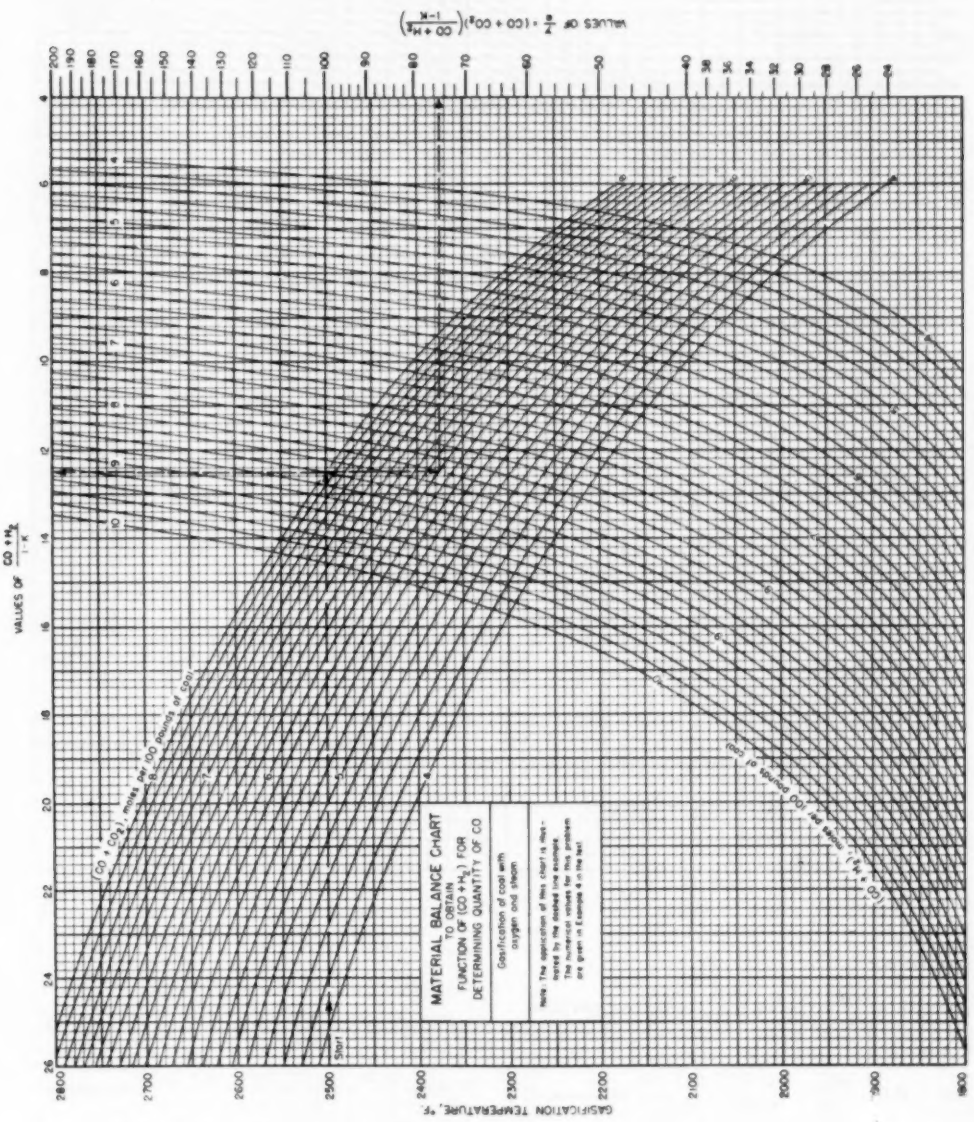
MATERIAL BALANCE CHART
TO OBTAIN
FUNCTION OF (CO + H2) FOR
DETERMINING QUANTITY OF CO
Gasification of coal with
oxygen and steam
Note: The application of this chart is illustrated by the following example. The material values for this problem are given in Example 4 in the text.
Start
(CO + CO2) - moles per 100 pounds of coal
(CO + H2) - moles per 100 pounds of coal
VALUES OF (CO + H2)/(1 - K)
VALUES OF (H - 1)/(CO + H2) (100 + CO2) = a/z
GASIFICATION TEMPERATURE, °F.

FIG. 3

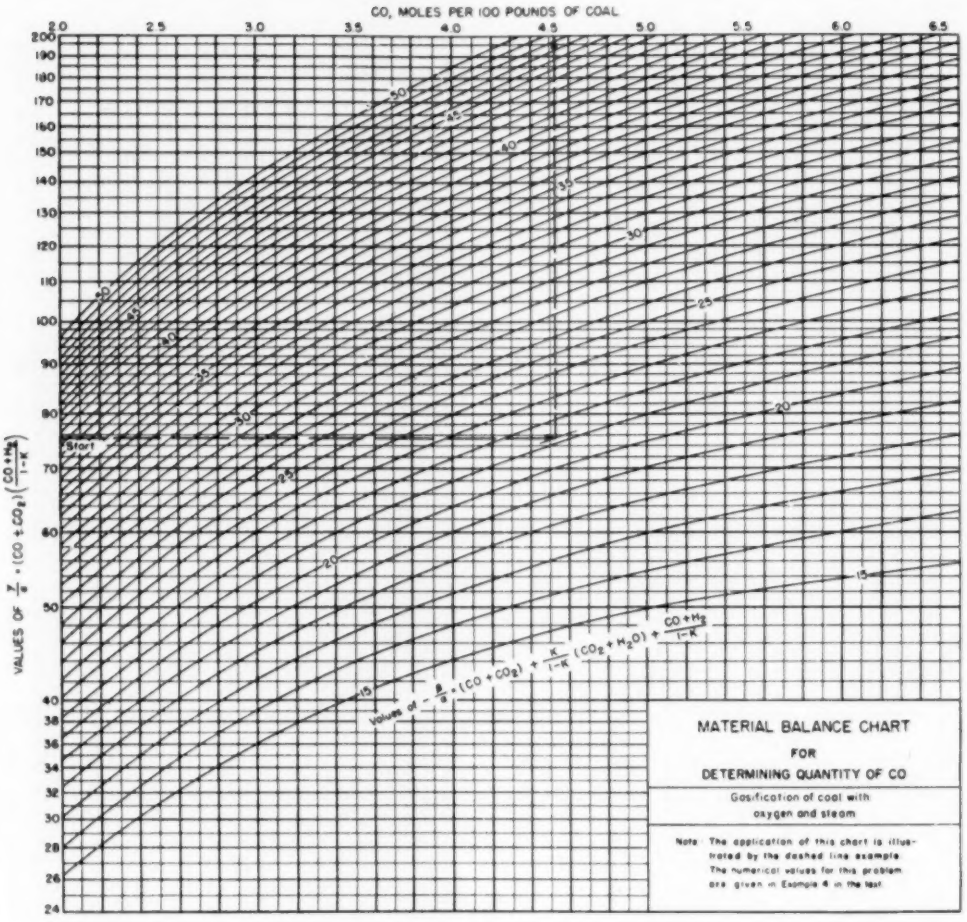

FIG. 4

By Equation [5]

$$CO + H_2 = \frac{72.2}{6} - \frac{84.4}{16} + \frac{3.78}{2.016} - \frac{0.86}{32} = 8.604 \text{ moles}$$

By Equation [6]

$$CO_2 + H_2O = \frac{84.4}{16} + \frac{121.1}{18.016} - \frac{72.2}{12} = 5.985 \text{ moles}$$

From Table 1, $K_{\text{max}} = 0.313$

$$1 - K = 0.687$$

$$\frac{K}{1-K} = 0.455$$

Therefore, by Equations [8*a*], [8*b*], and [8]

$$\frac{-\beta}{\alpha} = 6.02 + (0.455 \times 5.985) + \frac{8.604}{0.687} = 21.26$$

$$\frac{\gamma}{\alpha} = 6.02 \times \frac{8.604}{0.687} = 75.3$$

$$CO = \frac{21.26 - \sqrt{(21.26)^2 - (4 \times 75.3)}}{2} = 4.5 \text{ moles}$$

Then

$$CO_2 = 6.02 - 4.5 = 1.52 \text{ moles}$$
$$H_2 = 8.604 - 4.5 = 4.104 \text{ moles}$$
$$H_2O = 5.985 - 1.52 = 4.465 \text{ moles}$$

These values may be checked by substitution in Equation [7], which gives $K = 0.311$, compared to 0.313.

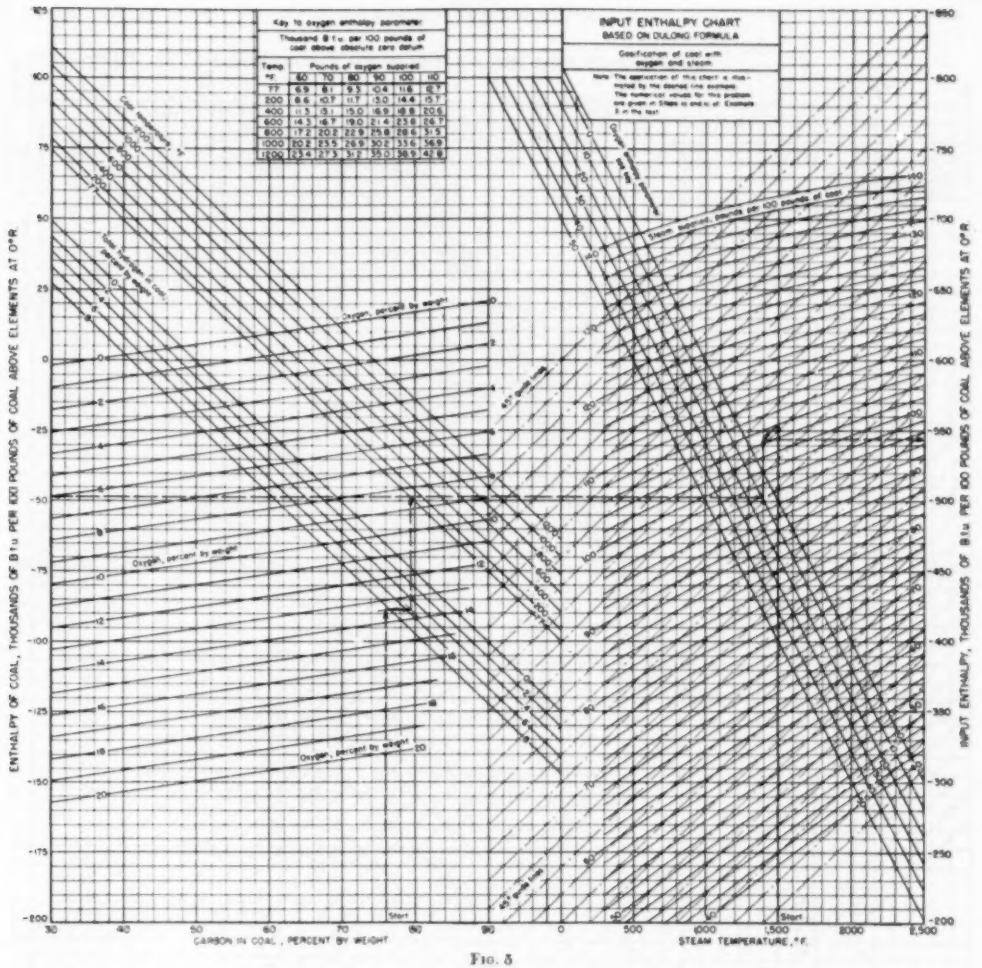

FIG. 5

The moles of H_2S and N_2 per 100 lb of coal, derived from Table 3, are 0.027 and 0.058, respectively. The composition of the dry nitrogen and sulphur-free exit gases in per cent by volume is CO_2, 15.0; CO, 44.5; H_2, 40.5.

Example 2. Find the input and output enthalpies and the heat loss for the conditions given previously.

If the H_2S and N_2 terms are neglected, and the mean unit enthalpy for the residue at 2500 F is used, the output enthalpy will be —564,130 Btu.

Heat loss = (—550,640) — (—564,151) = 13,511 Btu/100 lb coal. This heat loss is based upon the calorimetric heating value of the coal. If the Dulong formula were used, the heat loss would be approximately 7490 Btu per 100 lb of coal higher, or 21,001 Btu per 100 lb of coal.

Illustrative Examples Using Graphical Methods

Example 3. For the gasification of Rock Springs coal (sample No. 2, Table 3), find the "equilibrium reaction temperature" for

TABLE 6 INPUT AND OUTPUT ENTHALPIES AND HEAT LOSS

	Quantity—Lb	Quantity—Moles	Temperature, deg F	Unit enthalpy, Btu/mole	Total enthalpy, Btu/100 lb coal
Input enthalpy: Basis, 100 lb of coal					
Coal	100	...	77	— 561[a]	— 56100
Oxygen	84.4	2.638	77	3700	9760
Steam	106	5.884	1500	—85700	—504300
				Total input enthalpy	—550640
Output enthalpy: Basis, 100 lb of coal					
CO		4.5	2500	— 26300	—118400
CO_2		1.52	2500	—134900	—205000
H_2		4.104	2500	21300	87400
H_2O		4.465	2500	— 74800	—334000
H_2S		0.027	2500	— 55000	— 1485
N_2		0.058	2500	22400	1300
Carbon	3.8	0.317	2500	12000	3800
Ash	2.65	...	2500	815[b]	2160
				Total output enthalpy	—564151

[a] Btu per lb; calculated by Equation [18].
[b] Btu per lb.

ENTHALPY CHART FOR COAL
BASED ON EXPERIMENTAL HEAT OF COMBUSTION
Gasification of coal with oxygen and steam
Note The application of this chart is illustrated by the dashed line example. The numerical values for this problem are given in line 10 of Example 3 in the text.
ENTHALPY OF COAL, THOUSANDS OF B.t.u. PER 100 POUNDS OF COAL ABOVE ELEMENTS AT 0°R.
GROSS HEAT OF COMBUSTION OF COAL, THOUSANDS OF B.t.u. PER POUND OF COAL
Sulfur in coal, percent by weight
Hydrogen in coal, percent by weight
Carbon in coal, percent by weight
Coal temperature, °F

FIG. 6

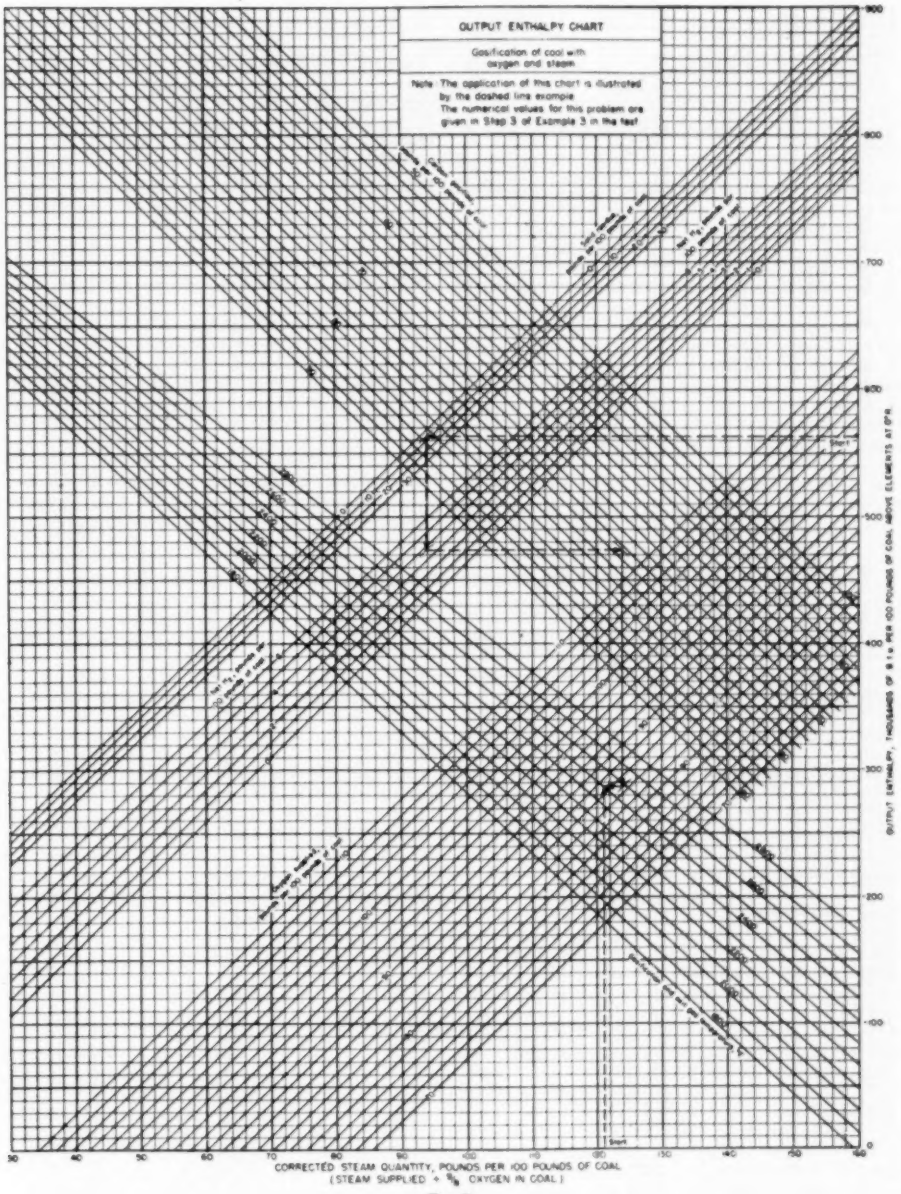
OUTPUT ENTHALPY CHART
Gasification of coal with oxygen and steam
Note: The application of this chart is illustrated by the dashed line example. The numerical values for this problem are given in Step 3 of Example 3 in the text
OUTPUT ENTHALPY, THOUSANDS OF B t u PER 100 POUNDS OF COAL ABOVE ELEMENTS AT 0°R
CORRECTED STEAM QUANTITY, POUNDS PER 100 POUNDS OF COAL
(STEAM SUPPLIED ÷ % OXYGEN IN COAL)

FIG. 7

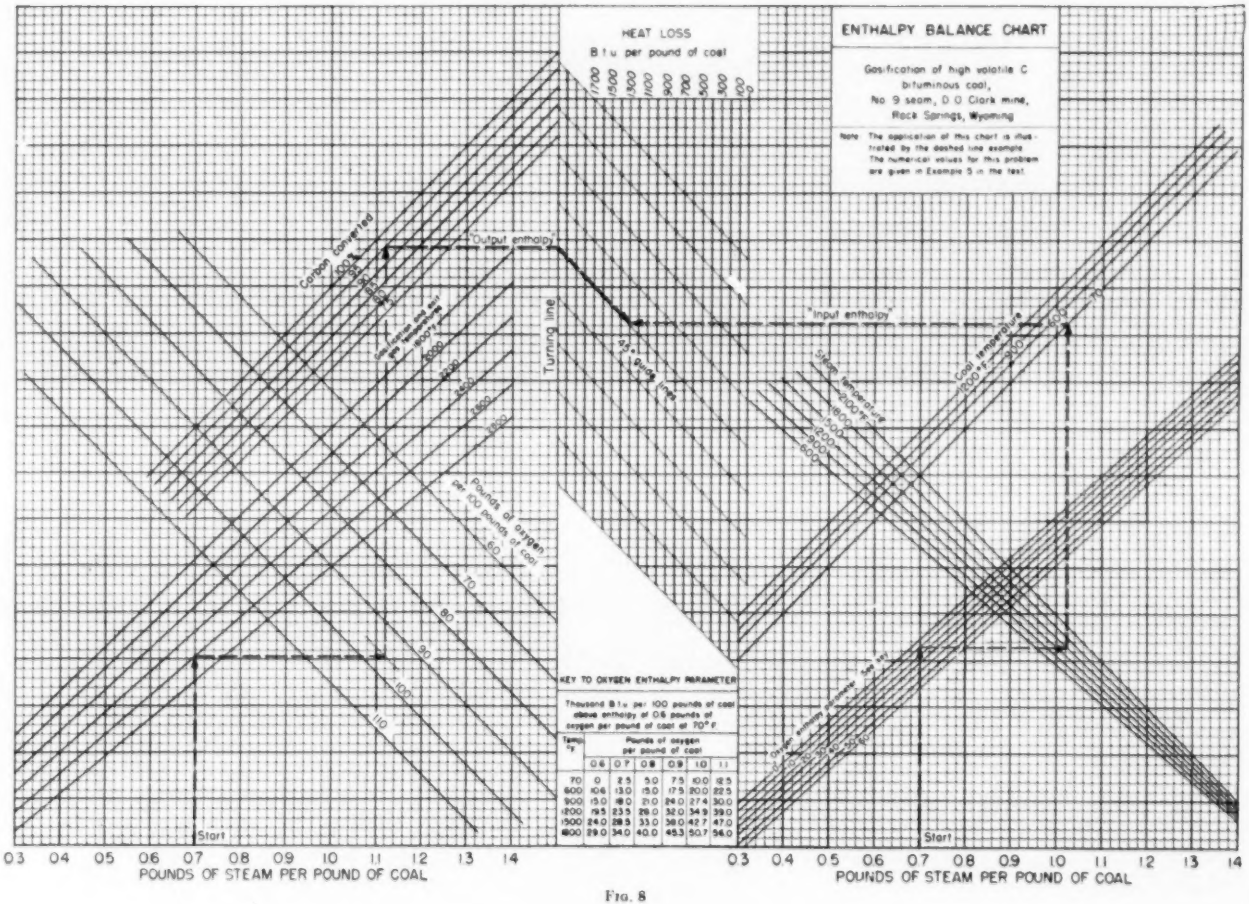

Temp., °F	Pounds of oxygen per pound of coal					
	0.6	0.7	0.8	0.9	1.0	1.1
70	0	2.5	5.0	7.5	10.0	12.5
800	10.6	13.0	15.0	17.5	20.0	22.5
900	13.0	18.0	21.0	24.0	27.4	30.0
1000	19.5	23.5	28.0	32.0	34.9	39.0
1500	24.0	28.5	33.0	38.0	42.7	47.0
1800	29.0	34.0	40.0	45.3	50.7	54.0

Fig. 8

the following conditions: 100 lb of coal at 77 F; 10 cu ft of pure oxygen per lb of coal, at 77 F; 1.06 lb of steam per lb of coal, preheated to 1500 F; 95 per cent carbon conversion; and a heat loss of 200 Btu per lb of coal.

The graphical solution of this problem involves three basic steps, i.e., finding (1) the input enthalpy, (2) the output enthalpy corresponding to the assumed heat loss, and (3) the temperature corresponding to the output enthalpy. The total input enthalpy is obtained on the basis of both the calculated heating value and the calorimetric heating value of the coal, to afford a comparison of the two methods.

Step 1(a): The enthalpy at 77 F of the coal, based upon Equation [16] and, therefore, the Dulong formula, is obtained from Fig. 5. For 76 per cent carbon, 13.41 per cent oxygen, and 5.46 per cent hydrogen, the dashed line to the left-hand scale shows the coal enthalpy to be —48,600 Btu per 100 lb of coal.

Step 1(b): The enthalpy at 77 F of the coal, based upon Equation [18], is obtained from Fig. 6 where the dashed lines connecting 13.36 thousand Btu per lb of coal (gross heating value), 76 per cent carbon, 5.46 per cent hydrogen, and 0.86 per cent sulphur, lead to a coal enthalpy on the right-hand scale of —56,000 Btu per 100 lb of coal.

Step 1(c): The total input enthalpy is obtained from Fig. 5 by following the dashed line from the coal-enthalpy scale through the appropriate oxygen-enthalpy and steam-enthalpy co-ordinates to the right-hand scale. For the coal enthalpy, based upon the Dulong formula, the total input enthalpy is —543,000 Btu per 100 lb of as-received coal. When the calorimetric heating value is used, the total input enthalpy is —551,000 Btu per 100 lb of coal. The latter is not illustrated on the chart.

Step 2: The total output enthalpy is found from the results of step 1(c) and the given heat loss of 20,000 Btu per 100 lb of coal to be —563,000.

Step 3: The gasification temperature is obtained from Fig. 7 by entering at the output enthalpy of —563,000 Btu obtained from the preceding step, and connecting with the following quantities which have already been computed at the beginning of Example 1: 6.45 lb (2.65 + 3.8) of solid residue, 3.78 lb of net hydrogen, 72.2 lb of carbon gasified, 84.4 lb of oxygen, and intersecting the vertical line representing 121.1 lb of total steam. For the coal enthalpy based upon the Dulong formula the intersection is at 2500 F. For the coal enthalpy based upon the calorimetric enthalpy of combustion it would be 2450 F.

Example 4: Find the exit-gas yield and composition for the preceding example. The moles of ($CO + H_2$) are obtained from the right side of Fig. 1 for 1000 cu ft (84.4 lb) of oxygen, 72.2 lb of carbon, and 3.78 lb of net hydrogen. Following the dashed line, the scale reading is 8.63 moles of ($CO + H_2$), which is reduced to 8.60 when the sulphur factor (0.31×0.86) is subtracted.

The ($CO_2 + H_2O$) is obtained from Fig. 1 for 84.4 lb (1000 cu ft) of oxygen, 72.2 lb of carbon gasified, and 121.1 lb of total steam. The dashed line to the left side of the figure gives 5.98 moles of ($CO_2 + H_2O$).

Using the sums $CO_2 + CO = 6.02$ moles, $CO_2 + H_2O = 5.98$ moles, and $CO + H_2 = 8.60$ moles, and the gasification temperature of 2500 F, the following calculations are made with Figs. 2, 3, and 4:

from Fig. 2

$$(CO_2 + H_2O)\frac{K}{1-K} = 2.7$$

from Fig. 3

$$\frac{CO + H_2}{1-K} = 12.52$$

and

$$\frac{\gamma}{\alpha} = 75.4$$

$$\frac{-\beta}{\alpha} = 2.7 + 12.52 + 6.02 = 21.24$$

Then from Fig. 4, CO = 4.52 moles per 100 lb of coal.

Accordingly, the gas yield becomes: CO = 4.52 moles, CO_2 = 1.50 moles, H_2 = 4.08 moles, H_2O = 4.48 moles; all per 100 lb of coal. The composition of the dry, nitrogen and sulphur-free exit gases in per cent by volume is CO_2, 14.8; CO, 44.8; H_2, 40.4.

It will be observed that for identical conditions the numerical example gives a heat loss of 210 Btu per lb for an assumed exit-gas temperature of 2500 F whereas the graphical example gives an exit-gas temperature of 2500 F for an assumed heat loss of 200 Btu per lb. If a heat loss of 210 Btu per lb had been assumed in the graphical example, the exit-gas temperature would have been about 7 deg F lower. These differences between the numerical and graphical values as well as those for the yield and composition of product gases are not significant in gasification calculations.

From either the numerical or the graphical examples the following material requirements per 1000 cu ft of $CO + H_2$ may be readily computed:

As-received coal, lb	30.7
Oxygen, cu ft	307
Steam at 1500 F, lb	32.5

The following example illustrates the use of Fig. 8, the enthalpy-balance chart for a specific Rock Springs, Wyoming coal. The analysis of this coal is represented by sample No. 1, Table 3. It should be emphasized that this chart does not apply to other Rock Springs coals whose analyses differ significantly from the one on which the chart is based. Charts similar to Fig. 8, which is included for illustrative purposes only, may be prepared from the other charts presented in the paper.

Example 5: Find the heat loss for the gasification of this coal under the following conditions: 100 lb of coal and 96 lb of oxygen at 70 F; 70 lb of steam preheated to 1500 F; 95 per cent carbon conversion, and an exit gas temperature of 2600 F.

Step 1: From the feed quantities and temperatures locate the horizontal "input-enthalpy" line on the right-hand segment of Fig. 8.

This is done in the following manner: Entering the chart with a steam-to-coal ratio of 0.7, and making the turns indicated, locates the input-enthalpy line. For this graphical calculation the oxygen parameter is established by interpolating in the insert oxygen enthalpy table and finding a value of 8.7 for 0.96 lb of oxygen per lb of coal, at 70 F.

Step 2: From the gasification conditions, locate the horizontal "output-enthalpy" line on the left-hand segment of Fig. 8.

Entering the chart with a steam-to-coal ratio of 0.7, and making the indicated turns, locates the output enthalpy.

Step 3: From the input and output-enthalpy levels, find the heat loss.

This is done by extending the output-enthalpy line horizontally to the "turning line," and then following a 45-deg guide line to the intersection of the horizontal extension of the input-enthalpy line. This gives a heat loss of 1300 Btu per lb of coal.

The foregoing examples apply to operations in which the feed streams are known. When one of the feed conditions, such as the oxygen-to-coal ratio, is to be determined it is necessary to use a method of successive approximation. For example, values of the unknown condition are assumed until the enthalpy balance

checks. The composition of the product gases may then be calculated in the usual manner.

Conclusions

A method has been presented for calculating the effect of any single or combination of variables in the gasification of coal with oxygen and steam, under conditions where water-gas shift equilibrium is reached. No assumptions regarding the gasification mechanism are required, all factors being derived from the material and energy relations of the input and the output items.

The thermodynamic charts are versatile and provide a graphical conception of the effects of the different variables. It will be found that gasifier performance can be predicted rapidly for a given set of conditions, or the results of a particular test can be evaluated in terms of approach to equilibrium. An additional advantage is the application of the charts to obtain the relative effects of different variables, for example, the amount of oxygen per pound of coal that is equivalent to a known heat loss from the gasifier.

The general charts in this paper can be used for any fuel for which the ultimate analysis is known. However, when a single kind of coal is under consideration, it will be found that the type of chart described in the latter portion of the paper is more convenient to use.

Although the thermodynamic methods employed are theoretically correct only at low pressure, i.e., 0 to 1 atm, the equations and charts presented are applicable at pressures as high as it is practical to gasify coal with oxygen and steam, because the effects of pressure on the equilibrium constant and the enthalpies are negligible. Thus these charts may be used up to 30 atm.

Acknowledgments

The authors wish to acknowledge gratefully the encouragement and helpful suggestions given by Dr. H. H. Storch, Chief, Research and Development Branch, Office of Synthetic Liquid Fuels; and the painstaking efforts of John Vidosh and Charles Siple of the Engineering Design Section, Bruceton Laboratories, in preparing the charts that form so important a part of this paper. The authors also wish to express their appreciation to H. R. Batchelder, Chemical Engineer, Coal-to-Oil Demonstration Branch, Louisiana, Missouri, and L. L. Newmann, Gas Engineer, Fuels and Explosives Division, Washington, D. C., for the suggestions resulting from their review of the manuscript.

Discussion

H. R. Batchelder.[14] It is believed that this paper represents an important contribution to the mathematical side of coal gasification. As the authors point out, repeated calculations are tedious and time-consuming. Because these are complex calculations, any graphical solution necessarily runs to a long series of single parameter charts or a few highly complex graphs. The present charts are for many purposes a distinct advance over those previously used.

There are points which can be discussed either to make the use of the charts easier or to avoid the possibility of errors in the results.

In the preparation of material of this sort, the inventors necessarily are guided primarily by their own needs. This method was developed in connection with experimental gasification work on a small scale entailing high heat loss, fairly high steam-to-coal ratios, and consequently high oxygen-to-coal ratios. In the calculation of gasification processes involving lower heat losses or especially lower steam-to-coal ratios, it will be found that the charts do not cover the required conditions. For example, in Fig. 7, the output-enthalpy chart, it will be seen that at any steam-to-coal ratio below about 70 lb per 100 lb and a gasification temperature, say, above 2000 F, the oxygen-to-coal ratio will be off scale. If the broadening of this scale would mean charts which are too bulky to use, then perhaps two sets embodying high and low steam ratios might be desirable.

The authors have used these charts in their own work primarily to determine heat loss or effective gasification temperature when all other process variables are known. Quite frequently we are called upon to calculate the required oxygen-coal ratio and the resultant gasification yields when the operating conditions such as temperature, steam-to-coal ratio, coal analysis, and the like are known. In order to use the authors' enthalpy charts, it is necessary to determine the approximate input enthalpy from Fig. 5 of the paper, by assuming an oxygen-coal ratio. This input enthalpy plus the assumed heat loss then equals the output enthalpy. From this and the known operating conditions, the required oxygen-to-coal ratio can be determined. If this is too far from the value originally estimated, a second approximation is necessary. Once the oxygen-coal ratio is determined in this fashion, the material-balance charts can be used to calculate yields.

It is our opinion that the warning, "It should be emphasized that this chart does not apply to other Rock Springs coals whose analyses differ significantly from the one on which the chart is based," is not stressed sufficiently. For example, the two Rock Springs coals whose analyses are given in Table 3 of the paper, to some people, may not show "significant differences," but to use Fig. 8 for coal No. 2 in Table 3 would result in an error of 440 Btu per lb heat loss, or at a constant heat loss, an error of 300 deg F in the gasification temperature. A chart such as Fig. 8 may be used reliably only for the specific coal on which it was based. It should be noted also that the coal with the lower carbon content and lower heat of combustion, under the same conditions, will give a higher calculated gasification temperature.

We consider the development of these charts an excellent piece of work. It is to be hoped, however, that this is not the end—that the present authors or others working in the field can pursue this work further, and develop calculation methods which are even simpler to use or still more precise in their results.

Wilhelm Gumz.[15] Calculations for the design or the performance of a gas producer are based on heat and material balances, and on equilibrium conditions. Such calculations are complex because of the many variables involved. Therefore, the ability to simplify the time-consuming computational work by the use of charts is strongly appealing. The title of this paper would indicate that the method presented is universally applicable; however, the method has been developed and used in connection with a pulverized-coal gasifier only. The authors undoubtedly will agree that the method does not apply to countercurrent fixed-bed producers because of their limitation of the methods described to systems "where the water-gas shift equilibrium is reached"—and invariably to systems where only this homogeneous reaction reaches equilibrium. In a deep fuel bed, however, with a large excess of carbon present, the heterogeneous water-gas reaction and the Boudouard reaction reach equilibrium with respect to the equilibrium or reaction temperature, as has been shown by a large number of comparisons of calculated and experimental data.[16]

[14] Chemical engineer, Synthetic Fuels Demonstration Plant, Bureau of Mines, Louisiana, Mo.

[15] Consultant, Battelle Memorial Institute, Columbus, Ohio.

[16] "Gas Producers and Blast Furnaces. Theory and Methods of Calculation," by W. Gumz, John Wiley & Sons, Inc., New York, N. Y., 1950.

One of the objectives listed in the beginning of the paper is "predicting reactor performance from known values of the feed rates and enthalpies of coal, oxygen, and steam." Either the temperature or the heat loss have to be known in a nonadiabatic system, otherwise the system would be indeterminate. The illustrative examples, indeed, show only such cases where either the temperature or the heat loss is known or can be estimated correctly.

It would be a valuable supplement to the paper if the authors would present comparisons of calculated and experimental data chosen from the results of their extensive experimental work and from published reports of the work of the Bureau of Mines at Morgantown, W. Va., and Louisiana, Mo.

The writer has used a different approach to the interpretation of results from pulverized-coal gasification. The reactions are primarily heterogeneous reactions which do not reach equilibrium. It has been shown[17] that the reason why equilibrium cannot be reached—even disregarding the kinetic aspect of the process—is the deficiency of carbon in the system. This interpretation at the same time hints of certain remedies in the process itself. It is certainly worth while and desirable to continue experimental work, to co-ordinate the results obtained by various workers, and to study the mechanism of pulverized-coal gasification in order to arrive at methods of calculation which will enable us to predict performance data with a minimum of deliberate assumptions.

L. L. Newman.[18] The thermodynamic charts presented in the paper provide ready means for the rapid prediction of the performance or for the evaluation of actual operations of generators in which pulverized fuel is gasified by means of oxygen and steam. In such operations, the pulverized coal is gasified in suspension and the products leave the generator at temperatures which may exceed 2000 F. Under such conditions, a negligible quantity of methane would be present in the gas produced at atmospheric pressure, or even at high operating pressures. Within the normal range of coal-oxygen-steam ratios, the sulphur in the coal is converted predominantly to hydrogen sulphide. It was, therefore, proper for the authors to omit from consideration the formation of hydrocarbons and sulphur compounds other than hydrogen sulphide in the interest of simplifying the charts and still retaining a degree of accuracy.

The assumption that the homogeneous water-gas reaction reaches equilibrium is supported fully in modern research on the kinetics of the gas reactions such as are being conducted at the Institute of Gas Technology and other educational and research institutions in the United States and abroad.

The charts in this paper, although they go considerably beyond the earlier charts constructed by Batchelder and Sternberg for two specific coals gasified under special conditions, and are applicable over a wide range of coals and operating variables, nevertheless, are not applicable to some of the lower ranking, high-oxygen-containing coals and lignites that may be of interest as a source of fuel for gas production. The authors, however, have provided sufficient basis for the construction of similar thermodynamic charts for different ranges of coal composition and operating conditions which other workers in the field may encounter, or for composite charts for any given coal.

It is undoubtedly possible to construct charts of universal range, but these would be too unwieldy for publication in technical periodicals, and might have to be distributed as supplements to future texts on gas engineering in about the same manner as Mollier's diagrams are distributed in conjunction with steam tables. It is hoped that such universal charts will be available eventually.

The use of these thermodynamic charts requires a knowledge of the ultimate analysis of the coal "as received." In the consideration of the ultimate analysis one must remember that the hydrogen and oxygen of the moisture in the sample are included with the hydrogen and oxygen in the dry-coal substance in Bureau of Mines bulletins. Since moisture content is variable, even in the same coal, under different conditions of handling and exposure, the coal carrying a definite percentage of moisture as delivered to the pulverizer may have an entirely different percentage of moisture as it enters the gasifier. Caution must be employed when using the charts to be sure that the ultimate analysis of the coal "as received" is that of the coal as it enters the gasifier.

A. A. Orning.[19] The authors have presented useful computational tools for the study of material and enthalpy balances in gasification systems. The fundamental assumptions involved are sound. Statements regarding application of the calculations, however, are too broad.

Thermodynamic calculations alone cannot lead to estimates of yields of reaction products in systems that do not attain complete thermodynamic equilibrium. Rather than this, the calculations give estimates of the gas yield, composition, and temperature as a function of the percentage of the carbon of the coal gasified. This becomes evident on examination of Fig. 8 of the paper. The right-hand side of the chart depends only on feed rates and feed temperatures. Heat loss will depend on temperatures in the system, but tentative values may be assumed subject to correction. The left-hand side of the chart, however, contains interdependent factors that leave one degree of freedom. The illustration shows 2600 F exit-gas temperature and 95 per cent carbon conversion. Closure might have been obtained equally as well with 2800 F and about 88 per cent carbon conversion.

Excepting an ultimate limit of complete equilibrium between gas and solids, the calculations alone offer no basis of selection among such alternatives. Operating experience or independent knowledge of the kinetics of the chemical reactions involved are the only basis of selection. Either 95 per cent carbon conversion at 1600 F exit-gas temperature or 50 per cent conversion at 3000 F would lie outside the expected range for the types of gasification systems considered. Gasification of carbon continues at a significant rate until the exit-gas temperature reaches such a low level that the added amount of gasification during the available time becomes negligible. The temperature level at which carbon gasification can be expected to "freeze" must be estimated for each gasification system considered.

Application to some systems might lead to the erroneous conclusion that the charts are not valid when the real fault might be that the system considered did not conform to the conditions for which the charts were designed. Thus the charts may be applied, with some limitations, to gasification in fixed beds. It might be necessary to assume exit conditions within the bed if the temperature falls to such a level that the water-gas shift tends to "freeze" before the gases leave the bed. With counterflow of fuel and gas, the fuel-feed temperature might approximate the exit-gas temperature at the limit of the "thermodynamic system" where the shift reaction was assumed to "freeze" and the enthalpy balance was taken.

Any significant evolution of volatile matter from the fuel at points downstream from the active gasification zone would cause deviations from the estimates of gas yield and composition.

[17] See footnote 16, pp. 124–129, with special reference to fig. 28, p. 127.

[18] Gas Engineer, Fuels and Explosives Division, Bureau of Mines, U. S. Department of the Interior, Washington, D. C.

[19] Coal Research Laboratory, Carnegie Institute of Technology, Pittsburgh, Pa. Mem. ASME.

Statements regarding application to systems at elevated pressures are valid provided exit-gas temperatures are high, in the range that has been observed in development of systems for gasification of coal in suspension, and provided that the gases, after leaving active gasification zones, contact only combustion residues and not fresh fuel. In systems involving fluidized beds under pressure, where feeding or recirculation present elements of counterflow, increasing pressure increases the yield of methane so that the basic assumptions underlying the calculations are no longer applicable.

Authors' Closure

The authors are glad to have the comments of Messrs. Batchelder, Gumz, Newman, and Orning, each of whom has made significant contributions to various phases of coal-gasification technology.

Mr. Batchelder makes the excellent suggestion that the range of certain parameters of the charts be extended to cover lower steam-to-coal ratios and higher exit-gas temperatures. Since the main purpose of this paper was to present the principles and procedures for constructing such charts, it was left to the reader to construct charts according to his particular requirements. He points out another important use for the charts, that is, calculation of the oxygen-coal ratio and make-gas yield when the operating conditions are known. Other uses will undoubtedly develop as experience with the charts is gained.

In reply to Dr. Gumz, the authors stipulated clearly that the charts applied only to systems in which water-gas shift equilibrium was attained. They agree, of course, that where only the Boudouard or heterogeneous water-gas equilibria are reached the charts are not applicable. In connection with the question regarding comparison of calculated and experimental results, it should be stated that the experimental results from both the vortex reactor, with which the authors worked, and the Koppers unit at the Bureau of Mines Coal-to-Oil Demonstration Plant, agreed closely with calculations from the charts. The primary significance of this is that the performance of both gasifiers satisfied the assumptions on which the thermodynamic charts are based.

Mr. Newman's remark concerning the ultimate analysis of the coal entering the reactor are important. Owing to the fact that in certain regions of the charts the parameters are relatively sensitive to the composition of the fuel, the as-charged composition may be sufficiently different from the as-received composition to cause some error in the calculations. In any event, representative sampling of the fuel close to the point where it enters the reactor is always desirable.

It might be inferred from Mr. Orning's comments that the authors intended the charts to provide a basis for reactor design—a matter that is determined by reaction kinetics and not thermodynamics. This was neither implied nor stated explicitly in the paper. The basic assumption was simply that water-gas shift equilibrium is attained, and the charts are not expected to apply under other circumstances. To go a step further, it is likely that the charts may be applied to any carbon-lean suspension system, since the experimental results from both the one ton per hour Koppers unit and the 100 lb per hr vortex gasifier fitted the charts with good accuracy.

Another paper that is soon to be published, based upon the experimental results of the vortex gasifier, will provide an approach to the rather difficult task of evaluating the kinetics of such systems.

Mr. Orning is correct in stating that "closure might have been obtained equally as well with 2800 F and about 88 per cent carbon conversion," as compared with 2600 F and 95 per cent carbon conversion, given by the authors. This is not a defect of the charts, since, other conditions being constant, the exit-gas temperature is a unique function of the carbon conversion. The authors' example 5 selected 2600 F and 95 per cent carbon conversion to illustrate the use of the charts; if the exit-gas temperature had been 2800 F, the carbon conversion would have to be 88 per cent to satisfy the 1300 Btu heat loss, other conditions being constant.

Summary of Investigation of Two-Stroke-Cycle Gas-Generator Aircraft Engine

By B. I. SATHER,[1] F. R. SCHURICHT,[1] and A. E. BIERMANN,[1] CLEVELAND, OHIO

An investigation of a two-stroke-cycle gas-generator type of aircraft engine is described. A theoretical analysis of the performance of the ideal gas-generator engine, an analysis of methods of achieving ideal performance when the engine components are fixed, and some experimental results are included. The experimental work was performed on the reciprocating component only and consisted of data obtained from three types of two-stroke-cycle single-cylinder test engines. Information presented in previously published NACA reports on the gas-generator engine together with some unpublished work on component requirements and gas-generator evaluation are summarized. Certain practical problems connected with the gas-generator type of engine are discussed also. The results of this investigation indicate that an engine of the two-stroke-cycle gas-generator type would provide a power plant of low specific weight and fuel consumption with favorable altitude performance characteristics. It was found possible to operate a two-stroke-cycle cylinder at the pressure and temperature levels required for the gas-generator engine. Mechanical functioning of the piston engine under gas-generator operating conditions was, in general, satisfactory.

Introduction

AMONG the prime requisites for an aircraft power plant are low specific fuel consumption and high specific output, two items usually difficult to attain simultaneously. Such an objective necessitates high cycle temperatures and pressures and high charge densities. These characteristics have been achieved to some extent in the conventional compound engine. In this type of engine the greatest portion of the work of the cycle is accomplished by the reciprocating component, which handles the portion of the cycle that involves high temperatures and pressures. Use of the turbine improves the efficiency of the cycle by increasing the effective expansion ratio. The turbine component of the conventional compound engine, however, may be viewed as a waste-energy-recovery device. Detailed information on this type of engine is presented in references (1 to 9).[2]

When the evolution of the compound engine is considered, a question as to the division of work arises, that is, how much of the work of the cycle should be accomplished by the reciprocating component and how much by the turbine. An analysis of a pressure- and temperature-limited compound engine has indicated that as the characteristically lightweight turbine is allowed to do more and more work of the cycle, the specific weight rapidly decreases, Fig. 1. As the degree of compounding is further increased, the reciprocating engine (the weight of which remains approximately constant) contributes a lesser percentage of the net work of the cycle and the specific weight begins to rise. Eventually, the reciprocating component does no work at all and may be replaced by a combustion chamber; the specific weight then drops to that of a turbine-propeller engine. During that portion of the division of work spectrum in which the reciprocating component is still included in the cycle, there is a division of work that results in a minimum specific weight. In this region of low specific weight, the specific fuel consumption is relatively low, being mainly determined by the over-all pressure ratio of the cycle. An engine constructed to operate at this division of work therefore would offer the advantages of both low specific weight and low specific fuel consumption. The point at which the power of the piston engine just equals the power required by the compressor is in the region of low specific weight and specific fuel consumption. At this design point the turbine may be uncoupled from the reciprocating engine so that the reciprocating engine merely generates high-energy gases for the turbine, which in turn furnishes the net work of the cycle. The reciprocating engine and the compressor are known as a gas generator, and the entire engine as a gas-generator engine. A diagrammatic sketch of this engine is presented in Fig. 2.

This type of gas-generator engine was investigated at the NACA Lewis Laboratory between November, 1945, and March, 1950. A portion of the program has previously been published in references (10 to 12).

The results of the gas-generator-engine program include a theoretical analysis of the ideal gas-generator engine and an analysis of methods of achieving the ideal performance when the engine components are fixed. Also included are experimental results from three types of two-stroke-cycle cylinders operating at gas-generator pressure and temperature levels.

Performance Analysis of Ideal Gas-Generator Engine

As a first step in the program, a theoretical analysis was made to determine the most advantageous cycle for the gas-generator engine, the probable operating conditions, and the performance of a theoretical gas-generator engine operating under these conditions.

Selection of Gas-Generator Cycle. Basic Considerations: As the division of work (a direct function of the manifold pressure) of a compound engine, limited by peak cylinder pressure and turbine-inlet temperature, is moved in the direction of greater percentage of turbine work, the inlet and exhaust pressures of the reciprocating component rise, the compression ratio becomes lower, and the fuel-air mixture becomes leaner. Because the resultant high pressures and temperatures at the end of compression and the relatively lean mixtures required would present knock and preignition problems in a spark-ignition engine, the reciprocating component is logically a compression-ignition engine. Furthermore, the capacity of the compression-ignition engine for operating with lean mixtures may make control of both turbine-inlet temperature and cylinder pressure feasible to some extent by varying the mixture strength and the injection-advance angle.

The piston engine under consideration may operate either on a constant-volume or constant-pressure cycle. Constant-volume

---

[1] Mechanical Engineer, Lewis Flight Propulsion Laboratory.

[2] Numbers in parentheses refer to the Bibliography at the end of the paper.

Contributed by the Oil and Gas Power and Gas Turbine Power Divisions and presented at the Annual Meeting, Atlantic City, N. J., November 25–30, 1951, of The American Society of Mechanical Engineers.

Note: Statements and opinions advanced in papers are to be understood as individual expressions of their authors and not those of the Society. Manuscript received at ASME Headquarters, October 4, 1951. Paper No. 51—A-131.

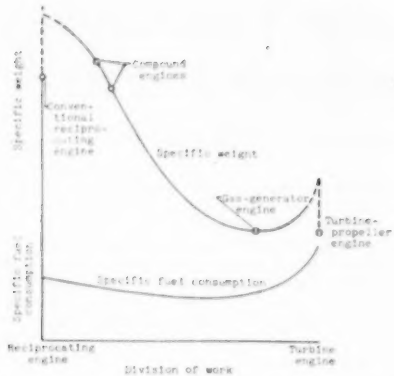

FIG. 1 EFFECT OF DIVISION OF WORK ON SPECIFIC WEIGHT AND SPECIFIC FUEL CONSUMPTION OF PRESSURE- AND TEMPERATURE-LIMITED COMPOUND ENGINE

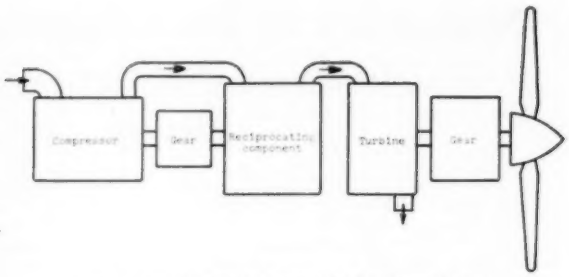

FIG. 2 DIAGRAMMATIC SKETCH OF GAS-GENERATOR ENGINE

combustion has been assumed for calculations of the gas-generator-engine performance because constant-volume combustion is easier to obtain than constant-pressure combustion in a high-speed compression-ignition engine.

Selection of Two-Stroke Cycle: The reciprocating component was further qualified to operate on a two-stroke-cycle basis because:

1 The high air-handling capacity of the two-stroke-cycle engine is of particular advantage in reducing the specific weight.

2 Engine design for operation at high-pressure and high-temperature levels is considerably simplified by use of a simple two-stroke-cycle, piston-ported cylinder.

Assumptions and Methods of Analysis. Analysis has shown that engine specific output is improved by keeping the magnitudes of the two engine limits (peak cylinder pressure and turbine-inlet temperature) as high as possible (10).

Maximum Cylinder Pressure: The maximum cylinder pressure was chosen as 1600 psia, which is considered to be well within a practical range for cylinders without poppet valves. Certain Diesel aircraft engines operate satisfactorily in this pressure range, and experimental work at the Lewis Laboratory has shown that no detrimental structural difficulties arise during operation at this pressure level.

Maximum Turbine-Inlet Temperature: At present, turbine-inlet temperatures of 2000 R are permissible in an aircraft engine. Because of a possible future increase in allowable turbine-inlet temperature, through the use of turbine cooling or possibly high-temperature materials, a maximum turbine-inlet temperature of 2260 R was assumed herein for the gas-generator engine.

Heat Loss to Coolant: If it is assumed that the compressor work equals the piston-engine work and if the maximum cylinder pressure and the turbine-inlet temperature are chosen, all other piston-engine variables, such as inlet-manifold pressure, compression ratio, and fuel-air ratio, are fixed automatically for any one altitude. The fuel-air ratio is determined uniquely by the exhaust-gas temperature and engine heat loss as indicated by a heat balance across the engine. A heat loss to the coolant of 18 per cent of the heat input was assumed; this value was selected after an examination of current engines and literature. With fuel-air ratio fixed, the compression ratio and the manifold pressure are then a function of only the maximum cylinder pressure.

Combustion Process: Constant-volume combustion with compression ignition was assumed for the piston engine. This type of combustion requires the use of Otto-cycle efficiencies. Use of Otto-cycle efficiencies is conservative because the actual combustion process may approach a dual cycle, the efficiency of which will be higher than that of the Otto cycle for fixed maximum cylinder pressures.

Over the altitude range considered (sea level to 50,000 ft), the gas generator is required to operate at over-all fuel-air ratios of about 0.034 for turbine-inlet temperatures of 2260 R, which results in a cylinder fuel-air ratio of about 0.054 for a loop-scavenged cylinder operating at a scavenging ratio of 1. This relatively high cylinder fuel-air ratio in compression-ignition operation should, however, still allow combustion efficiencies greater than 95 per cent (13).

Computation of the piston-engine performance was made using the methods of reference (10) which were corrected for losses to a real-cycle basis. Reference (14) was used to compute maximum cylinder pressures together with a correction factor to account for a finite combustion time.

Turbine and Compressor Efficiencies: Turbine and compressor adiabatic efficiencies of 0.85 based on inlet and outlet total pressures and temperatures were assumed for the ideal engine. These values were assumed constant except in certain phases dealing with off-design condition turbine and compressor-control problems. Because of flow-control problems with a fixed-nozzle-area turbine, the speed of the reciprocating component was kept constant except in one case where an off-design condition of greater than normal cruising power was desired.

A more complete discussion of the methods of calculation may be found in reference (10).

Performance of Ideal Gas-Generator Engine. Results of the theoretical analysis of the ideal gas-generator engine are presented in plots showing the effect of altitude, engine operating limits, and variation of component efficiencies. This engine is an ideal engine in that the components are varied so as to satisfy the engine requirements at every operating point. Thus compressor-pressure ratio, turbine-nozzle area, and pressure ratio, reciprocating-component compression ratio, and component sizes are at the required value at all times. Methods of attaining the performance of the ideal engine when the components are fixed are discussed subsequently.

Effect of Altitude: The cruising performance of the ideal gas-generator engine is shown in Fig. 3 as a function of altitude. As the altitude is increased, simultaneous adjustments must be made in manifold pressure and compression ratio in order to maintain the prescribed limits of peak cylinder pressure and turbine-inlet temperature of 1600 psia and 2260 R, respectively. The scavenging ratio was kept constant at 1.

The specific-power-output curve is rather flat up to an altitude of 30,000 ft, then drops at a more rapid rate at altitudes greater

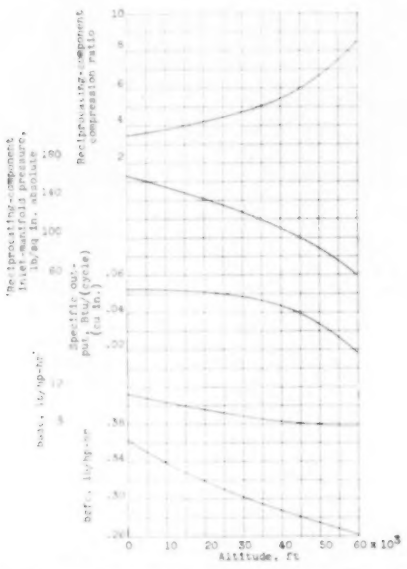

FIG. 3 EFFECT OF CHANGE IN ALTITUDE ON PERFORMANCE OF IDEAL GAS-GENERATOR ENGINE

(Peak cylinder pressure, 1600 psi; turbine-inlet temperature, 2260 R; compressor efficiency, 0.85; scavenging ratio, 1.)

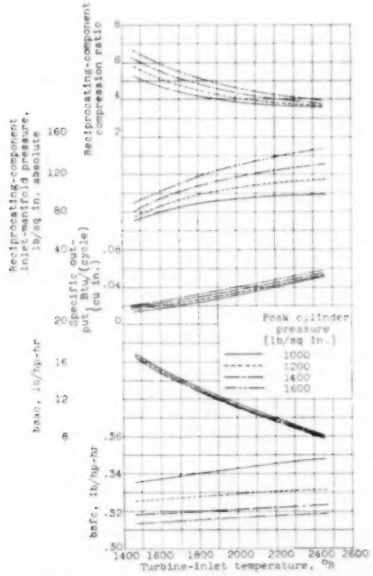

FIG. 4 EFFECT OF ENGINE OPERATING LIMITS ON PERFORMANCE OF IDEAL GAS-GENERATOR ENGINE

(Altitude, 20,000 ft; compressor efficiency, 0.85; scavenging ratio, 1.)

than 30,000 ft. This more rapid decrease in power with altitude is mainly due to the ambient-air temperature remaining constant at altitudes above the tropopause. The engine is pressure-limited; therefore the resulting increase in over-all pressure ratio causes an increase in efficiency with altitude, which is reflected in the brake-specific-fuel-consumption curve. The low order of brake specific fuel consumption is a result of the high over-all pressure ratio attainable with the gas-generator type of engine. At 20,000 ft altitude, the brake specific fuel consumption is about 0.32.

Effect of Varying Engine Operating Limits: The effect of varying the peak cylinder pressure and turbine-inlet temperature from the assumed values of 1600 psia and 2260 R on the performance of the ideal gas-generator engine is shown in Fig. 4 for an altitude of 20,000 ft and a scavenging ratio of 1.

Reducing the turbine-inlet temperature decreases the power output considerably. A small decrease in specific fuel consumption is apparent; this decrease is mainly a result of operation at lower fuel-air ratios. Although the mass flow through the engine is reduced because of decreased manifold pressure, the brake specific air consumption is increased. Reduction of turbine-inlet temperature therefore causes the engine specific weight to increase.

Reducing the peak cylinder pressure at constant turbine-inlet temperature results in lowering the over-all expansion ratio, which in turn results in higher specific fuel consumption: the power output decreases and the brake specific air consumption increases. Consequently, reducing the peak cylinder pressure produces an increase in both specific fuel consumption and specific weight.

Effect of Change in Component Efficiency: In the gas-generator engine, the effect of change in turbine efficiency is clearly apparent. The turbine delivers all the net work of the cycle; therefore the brake specific fuel consumption of the engine is inversely proportional and the power output is directly proportional to turbine efficiency.

The effect of changes in compressor efficiency is presented in Fig. 5 for an altitude of 20,000 ft and a scavenging ratio of 1. This figure indicates that such changes affect brake specific fuel consumption only slightly because the over-all efficiency is still largely determined by the over-all pressure ratio, which is unchanged. The specific power output is affected by changes in compressor efficiency to a much greater degree, however, indicating that compressor efficiency should be as high as possible.

The effect of changes in thermal efficiency of the piston engine is difficult to treat analytically because of the intimate relations that exist among thermal efficiency, peak cylinder pressure, and pressure rise during combustion. An approach to this problem can be made, however, by considering that the engine loses efficiency by burning part of the fuel at the end of expansion instead of all the fuel burning at the beginning of expansion. This condition of reduced piston-engine efficiency would be comparable to the use of over-rich-mixture ratios where some of the scavenging air is required to complete combustion. For instance, if the piston-engine efficiency were reduced by this method to 0.7 of the normal efficiency, the brake specific fuel consumption would rise only 6 per cent and the specific output would drop 21 per cent (10). The resulting decrease in over-all efficiency is thus relatively small compared with the reduction in piston-engine efficiency. The small decrease in efficiency is a direct consequence of the high over-all pressure ratio in the gas-generator engine. The decrease in specific output, is of course, significant; however, changes in specific output do not affect the ultimate range as much as changes in specific fuel consumption.

Effect of Change in Scavenging Ratio and Charging Efficiency: Two fundamental factors in two-stroke-cycle-engine operation indicate the effectiveness of engine breathing. These factors may

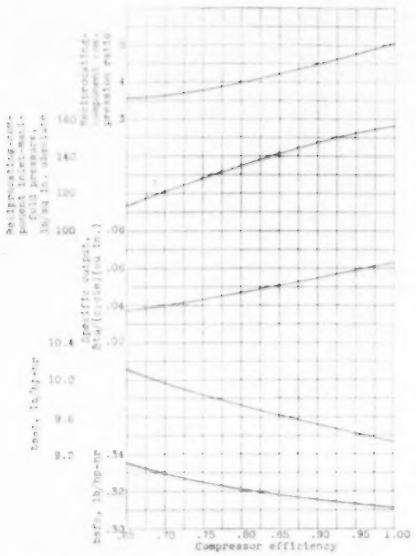

FIG. 5 EFFECT OF CHANGE IN COMPRESSOR EFFICIENCY ON PERFORMANCE OF IDEAL GAS-GENERATOR ENGINE
(Altitude, 20,000 ft; peak cylinder pressure, 1600 psi; turbine-inlet temperature, 2260 R; scavenging ratio, 1.)

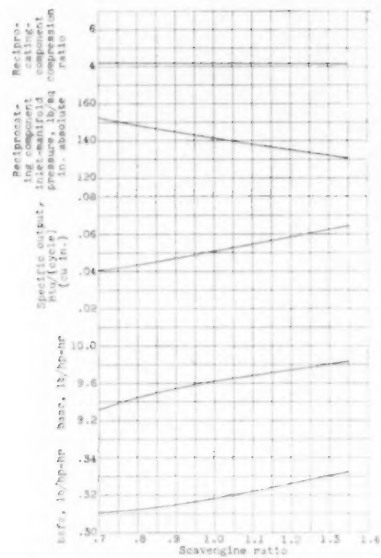

FIG. 6 EFFECT OF CHANGE IN SCAVENGING RATIO ON CALCULATED PERFORMANCE OF IDEAL GAS-GENERATOR ENGINE
(Altitude, 20,000 ft; peak cylinder pressure, 1600 psi; turbine-inlet temperature, 2260 R; compressor efficiency, 0.85.)

be defined as (*a*) the scavenging ratio, which is the ratio of the amount of charge air entering the cylinder per cycle to the product of total cylinder volume and inlet density (analogous to four-stroke-cycle volumetric efficiency); and (*b*) the charging efficiency, which is the ratio of the mass of fresh charge trapped in the cylinder after port closing to the product of total cylinder volume and inlet density. Charging efficiency is indicative of the amount of fresh charge in the cylinder available for combustion and thus determines the amount of exhaust-gas dilution. Charging efficiency is a function of scavenging ratio and the type of two-stroke-cycle cylinder being considered (8, 15).

Exhaust-gas dilution at low values of scavenging ratio and low combustion efficiency at high values of scavenging ratio distinctly limit the range of scavenging ratio over which the gas generator can operate. This limitation is a natural result of the gas-generator mode of operation. The over-all fuel-air ratio is fixed by the turbine-inlet temperature; therefore the cylinder fuel-air ratio increases in almost direct proportion to the increase in scavenging ratio (8). Eventually, a point is reached where there is more fuel in the cylinder than can be accommodated by the combustion air; thus an upper limit is imposed on the scavenging ratio. The lower limit of the scavenging ratio is determined by excessive dilution of charge air by the exhaust residuals at low scavenging ratios, which eventually cause the engine to stop firing; experimental results at this laboratory have indicated that the scavenging ratio should not be decreased below 0.7.

The effect of scavenging ratio on the performance of the ideal gas-generator engine is illustrated in Fig. 6. As the scavenging ratio is increased, the power output undergoes a large increase, which may be a convenient means of controlling power output of the engine. The manifold pressure, however, decreases with increase in scavenging ratio because the compressor load increases faster than the piston-engine output. The power output of the gas-generator engine therefore varies approximately as the product of manifold density and scavenging ratio.

The rise in fuel-consumption curve is caused by the decreased thermal efficiency of the piston engine with increased cylinder fuel-air ratios and by the increase in cylinder-pressure drop (difference between inlet and exhaust pressures) which is a function of scavenging ratio.

METHODS OF APPROACHING PERFORMANCE OF IDEAL GAS-GENERATOR ENGINE

The analysis so far presented has been idealized in that the components were varied so as to match theoretical operating requirements at every point. In order for the performance of the actual engine to approach that of the ideal curves, several steps must be accomplished: (*a*) A compressor and a turbine capable of operating over a range of air flows and pressure ratios must be provided; and (*b*) satisfactory methods of maintaining proper engine limits (peak cylinder pressure and turbine-inlet temperature) must be evolved.

Variation of Compressor-Pressure Ratio. Maintenance of Engine Limits: The pressure-ratio and flow requirements of the compressor are shown in Fig. 7 which shows that it would be almost impossible to design and to construct a compressor to satisfy the requirements of pressure ratio and air flow over the range of altitude from sea level to 50,000 ft.

A compressor can be designed, however, to deliver the proper pressure ratio and air flow at a specific critical altitude, and the engine operating limits (peak cylinder pressure and turbine-inlet temperature) will, of course, be satisfied at that altitude. If the altitude is decreased without altering the pressure ratio of the compressor, the peak cylinder pressure will rise to values well over the allowable limit. This situation may be alleviated and the peak cylinder pressure held constant at altitudes lower than criti-

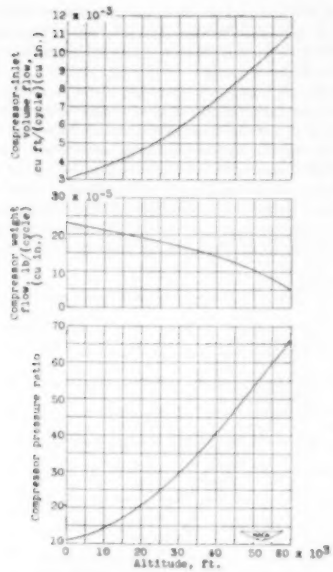

FIG. 7 COMPRESSOR REQUIREMENTS OF IDEAL GAS-GENERATOR ENGINE
(Scavenging ratio, 1.)

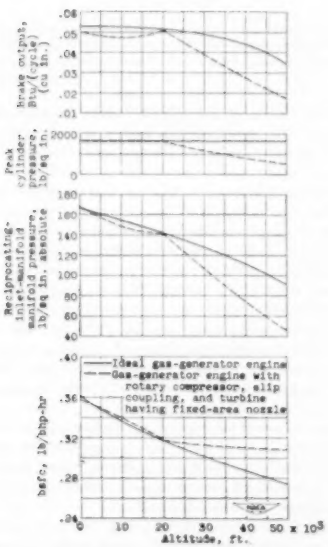

FIG. 8 COMPARISON OF PERFORMANCE OF IDEAL GAS-GENERATOR ENGINE INCORPORATING TWO-STAGE ROTARY COMPRESSOR WITH VARIABLE-SPEED FIRST STAGE DRIVEN BY SLIP COUPLING AND TURBINE HAVING FIXED-AREA NOZZLE

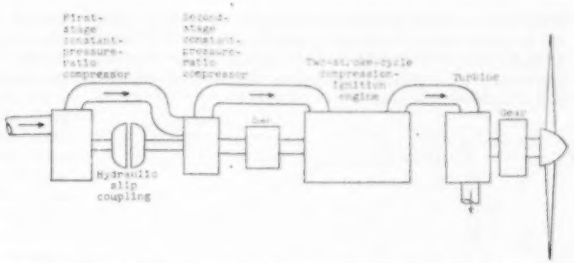

FIG. 9 SCHEMATIC DIAGRAM OF GAS-GENERATOR ENGINE USING MULTISTAGE CONSTANT-PRESSURE-RATIO COMPRESSOR WITH FIRST STAGE DRIVEN BY HYDRAULIC SLIP COUPLING

cal by throttling the inlet to the compressor; this method, however, is inefficient. A somewhat better method is to divide the compressor into two stages and drive the first stage (supercharging stage) by a variable-speed drive. As the altitude is decreased, the speed of the first stage would be reduced in order to reduce the manifold pressure and hence keep the peak cylinder pressure constant.

Compressor-System Analysis: A study of various compressor systems is made in reference (11). The results of the investigation showed that the best system appeared to be that in which the first stage of compression consisted of a variable-speed supercharger that was driven by a slip coupling. The second stage of compression could be either a constant-speed centrifugal-type or piston-type compressor. The performance of such a combination with a design altitude of 20,000 ft is shown in Fig. 8 in which the final stage is a constant-pressure-ratio compressor. Only a small loss in power between sea level and 20,000 ft occurs when the slip coupling is used. This small loss in power between sea level and altitude is a result of high coupling efficiency at altitude and approach of coupling load to zero at sea level. Furthermore, the load impressed on the coupling at any time is only a small fraction of the total compressor load.

For clarity, a diagrammatic sketch of the engine configuration is shown in Fig. 9.

A further result of the compressor-system study (11) was that when the second stage of this particular combination was a piston-type compressor, the time at which the piston-compressor valves open and close is substantially constant with changes in altitude so that mechanical valves with fixed timing can be substituted for automatic valves without incurring a penalty in performance.

A piston-type compressor was considered because, although the centrifugal-type compressor has the advantage of simplicity and light specific weight, the piston-type compressor conveniently fits into certain gas-generator-engine configurations as a second-stage compressor and because (*a*) with suitable valving arrangements it possesses a broader operating range (high efficiency over a wide range of air flows and pressure ratios) than equivalent rotary-compressor types; and (*b*) delivers a positive supply of air under all operating conditions including starting and idling.

The physical size of the piston-type compressor is dependent on the amount of supercharging produced by the first stage.

Variation of Turbine Flow Capacity. Fixed-Area Turbine Nozzle: In that part of the Analysis section dealing with the ideal gas-generator engine, the turbine-nozzle area was considered variable to allow for changes in air flow with altitude. Because a fixed-area nozzle would be desirable from the standpoint of simplicity, the cruising performance of the gas-generator engine also has been calculated for the case of a fixed-area turbine nozzle. The results are shown in Fig. 10 which indicates that only a small

reduction in cruising performance is incurred through the use of the fixed-area nozzle. Generally, a small drop in power occurs at altitudes below the 20,000-ft critical altitude (design altitude), and is caused by a change in scavenging ratio incurred through a lack of adequate flow control.

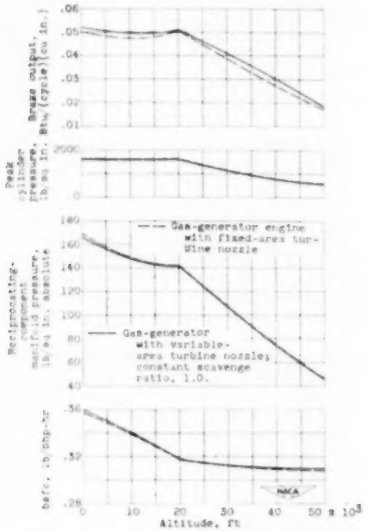

FIG. 10 EFFECT OF FIXED AND VARIABLE-AREA TURBINE NOZZLES ON PERFORMANCE OF GAS-GENERATOR ENGINES INCORPORATING TWO-STAGE ROTARY COMPRESSOR WITH FIRST STAGE DRIVEN BY SLIP COUPLING

Higher Than Cruising-Power Operation: An axial-flow, multistage fixed-nozzle-area turbine is perhaps the simplest type of turbine component suitable for the gas-generator engine. With this type of turbine, high power output (that is, higher than the cruise performance previously shown for engine limits of peak cylinder pressure of 1600 psia and turbine-inlet temperature of 2260 R) can be achieved only by increasing the engine limits. Attempts to increase the power output by increasing the generator speed or scavenging ratio without making the turbine nozzle larger will only result in increasing peak cylinder pressure or turbine-inlet temperature, or both. Because important engine limits are being exceeded under these conditions, this power output must be limited to periods of short duration.

One method of increasing the power level without affecting the engine limits is to increase the turbine-nozzle area. Increasing the turbine-nozzle area by means of a variable-area turbine nozzle requires a rather complicated nozzle section; therefore resort may be made to by-passing the initial turbine stages to obtain high mass flows and power outputs. In this manner the scavenging ratio (which is increased by increasing the turbine-nozzle area) and the generator speed may be increased with resulting increase in power output but without any additional temperature or pressure stresses on the generator. Some losses in efficiency are expected because of increased pressure drops through the system and reduced turbine efficiency.

When the by-pass valve is used, the flow from the generator divides into two parts—one part flowing through the first-stage turbine nozzle and controlled in quantity by turbine-inlet temperature and pressure, and the other part passing through the by-pass, which is opened sufficiently in each case to accommodate this flow. The two parts are then recombined in a mixing process and passed to the second stage.

For calculation of high power output by use of variable scavenging ratio and generator speeds, it is necessary to prepare operational maps of turbine-inlet pressure (engine-exhaust pressure) and mass flow for the various operating conditions. A sample map for 20,000 ft operation is shown in Fig. 11. After the entrance conditions to the turbine are determined by these curves, stage-by-stage calculations of enthalpy, drops, efficiencies, temperatures, and pressures may be made. Graphical solutions are necessary in order to match the mass flows through the various stages.

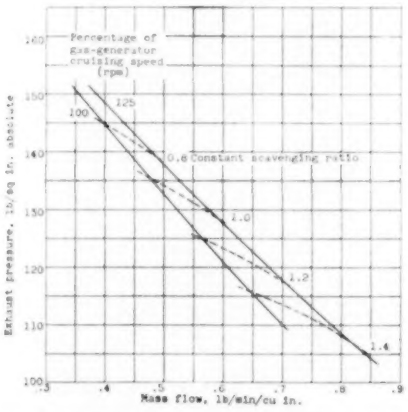

FIG. 11 OPERATIONAL MAP OF GAS GENERATOR FOR VARIABLE ENGINE SPEED AND SCAVENGING RATIO AT 20,000 FT
(Peak cylinder pressure, 1600 psi; turbine-inlet temperature, 2260 R; compressor efficiency, 0.85.)

From the results of the stage-by-stage calculations, the performance of the gas-generator engine may be computed and plotted, Fig. 12. Net brake specific fuel consumption and percentage of cruising power are shown as functions of scavenging ratio and generator speed, indicating that considerable extension of gas-generator performance range may be attained. For instance, when going from a point of 100 per cent cruising speed and a scavenging ratio of 1 to a point of 125 per cent cruising speed and a scavenging ratio of 1.4, the power output increases about 48 per cent, whereas the specific fuel consumption increases only about 17 per cent. All of the components except the turbine are operating at optimum design values. The over-all turbine efficiency at normal cruising conditions of a scavenging ratio of 1 and 100 per cent cruising generator speed is 85 per cent. The over-all efficiency decreases to 76 per cent at 125 per cent generator cruising speed and a scavenging ratio of 1.4.

For take-off conditions, increased power may be obtained by use of the methods just described. In addition, for short periods of time, the peak cylinder pressure may be raised, the engine fuel-air ratio increased, and water injection used to reduce the turbine-inlet temperature to a safe value.

Lower Than Cruising-Power Operation: With a fixed-nozzle-area turbine, low power output (lower than the cruising performance previously shown for engine limits at peak cylinder pressure of 1600 psia and turbine-inlet temperature of 2260 R) can best be obtained by reducing the engine limits. Consequently, because

economy is desirable for low-power operation, the effect of limits on brake specific fuel consumption must be determined. (A small variation in gas-generator speed could be used as an additional method of reducing power; however, scavenging-ratio requirements restrict the allowable range in speed.) With reduced engine limits, it is necessary to reduce the turbine speed for maximum turbine efficiency. The different turbine stages, however, require different speeds for optimum operation. Because all the stages must necessarily turn at the same speed, it is possible for the last stage to have a negative efficiency, or to act as a compressor. Consequently, the last turbine stage was assumed to have an over-run-

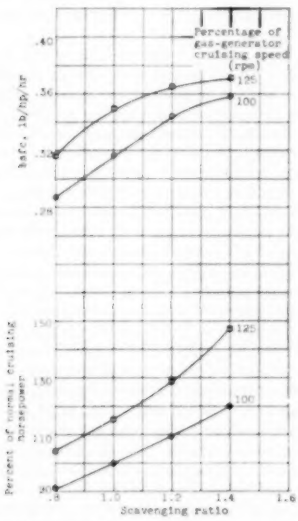

FIG. 12 BRAKE SPECIFIC FUEL CONSUMPTION AND PERCENTAGE OF NORMAL CRUISING POWER OF GAS-GENERATOR ENGINE FOR HIGH-POWER OPERATION WITH INCREASED ENGINE SPEED AND SCAVENGING RATIO AT 20,000 FT

(Peak cylinder pressure, 1600 psi; turbine-inlet temperature, 2260 R; compressor efficiency, 0.85; turbine speed, constant.)

ning clutch. In practice, however, this refinement may not be essential.

For low-power operation, operational maps may be prepared showing exhaust pressure and mass flow as functions of the variable engine limits of peak cylinder pressure and turbine-inlet temperature. With the entrance conditions determined by the operational map, stage-by-stage calculations are made, with an additional variable introduced—the percentage of rated turbine speed. From the results of the stage calculations, over-all power and specific fuel consumption are computed. Then, cross-plots are made at the point that corresponds to turbine speeds at minimum specific fuel consumption. The resulting cross-plot of percentage of cruising output against minimum brake specific fuel consumption for the range of reduced engine limits is shown in Fig. 13 for sea-level operation. The over-all turbine efficiency was found to range from the design point of 85 per cent to values as low as 75 per cent at a peak cylinder pressure of 1000 psia and a turbine-inlet temperature of 1600 R. Plots of this type may be made for any altitude at which operation is desired.

It is evident from Fig. 13 that considerable extension of gas-generator operating power range with reasonable efficiency is possible. It is, in fact, possible to change operating conditions from a turbine-inlet temperature of 2260 R and a peak cylinder pressure of 1600 psia to a turbine-inlet temperature of 1600 R and an absolute peak cylinder pressure of 1000 psia and by so doing to reduce the power approximately 50 per cent almost without increase in specific fuel consumption. If further reduction in power is

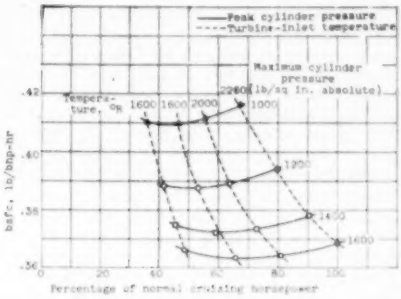

FIG. 13 BRAKE SPECIFIC FUEL CONSUMPTION AND PERCENTAGE OF NORMAL CRUISING POWER OF GAS-GENERATOR ENGINE FOR REDUCED ENGINE LIMITS AT SEA-LEVEL OPERATION

(Compressor efficiency, 0.85; turbine speed varied to obtain minimum brake specific fuel consumption.)

necessary, the peak cylinder pressure may be decreased to 1000 psia, resulting in a decrease in power output to about 37 per cent of normal cruising power and an increase in specific fuel consumption of about 11 per cent.

The turbine used so far was designed for an altitude of 20,000 ft. If this altitude is increased, the turbine design problems, of course, will become more acute.

Maintenance of Piston-Engine Limits. Among the control problems of the gas-generator engine is the one of maintaining proper engine limits (peak cylinder pressure and turbine-inlet temperature) in order that the performance of the actual gas-generator engine using a reciprocating component of fixed size and compression ratio may be made to approach that of the ideal engine. The peak cylinder pressure depends primarily on the manifold pressure (compressor load), engine-compression ratio, and fuel-air ratio. The exhaust temperature (turbine-inlet temperature) depends only on the fuel-air ratio provided that engine heat loss is a constant percentage of the heat input. The engine power output is determined by its thermal efficiency (a function of the compression ratio) and by the fuel-air ratio; this output must equal the compressor load. Consequently, control of engine limits resolves itself into a problem of regulating the thermal efficiency of the engine in relation to its pressure level.

In the simplest case, the compression ratio can be fixed at the optimum value for some set of operating conditions and at other conditions one engine limit may be held constant and the other allowed to vary. Also, the efficiency of the engine may be varied by burning part of the fuel at bottom dead center or preferably in the engine exhaust. A third instance of efficiency regulation is afforded by burning all the fuel at some time after top center on the engine expansion stroke; this arrangement allows an effective change in compression and expansion ratios by varying the time of fuel injection. This cycle is illustrated in Fig. 14.

Operation at Fixed Compression Ratio: As previously stated, one possible method of gas-generator control is to operate at a fixed compression ratio, keeping at least one engine limit constant. For instance, if the optimum compression ratio for the ideal engine at sea level is picked and held constant, at sea level both engine limits will be reached. As the operating altitude is

then increased, the peak cylinder pressure will decrease but the turbine-inlet temperature will be held constant at the limiting value of 2260 R. Power output and fuel consumption will depart from the ideal values, as shown in Fig. 15. In this figure the turbine and the compressor are assumed to operate at optimum design points although the piston engine has fixed characteristics. If the compression ratio required for 20,000-ft operation is used, as altitude is increased from sea level the peak cylinder pressure will remain constant at 1600 psia until the critical altitude is reached and will then decrease. The turbine-inlet temperature will increase from sea level to critical altitude until the limiting turbine-inlet temperature is reached and will stay constant as altitude is further increased. The turbine-inlet temperature is lower than the limiting value below critical-altitude operation because sufficient fuel cannot be admitted to the engine without raising the peak cylinder pressure above its allowable limit (1600 psia). This result is a direct consequence of the fact that a compression ratio picked at some altitude and fixed at that value will always be higher than the required compression ratio at lower altitudes. Operation at a fixed compression ratio picked at a critical altitude of 40,000 ft is also shown in Fig. 15.

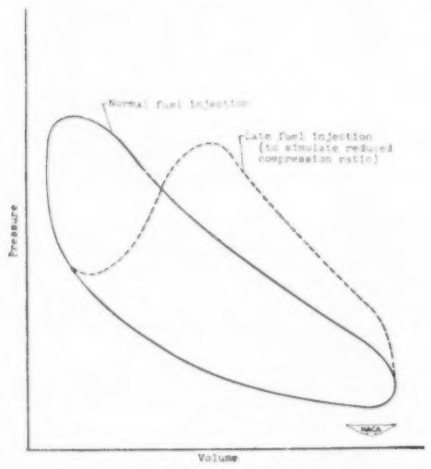

FIG. 14 REPRESENTATIVE PRESSURE-VOLUME INDICATOR CARD SHOWING EFFECT OF RETARDED INJECTION ADVANCE

The methods of reference (7) are used throughout this paper for computing the gas-generator performance; in this section dealing with the piston engine, however, a few refinements have been added for the purpose of greater accuracy. Therefore the results shown in this section do not agree exactly with the results previously shown herein. The shapes and the trends of the curves, however, are similar and differences in magnitude are slight.

Operation With Fixed Compression Ratio and Reheat: The specific output of the gas-generator engine with fixed-compression ratio operating at lower than rated turbine-inlet temperatures at altitudes less than the critical may be improved by burning enough extra fuel in the exhaust gases to bring the temperature up to the limiting value of 2260 R. Operation in this manner with reheat is shown in Fig. 16 for a 20,000-ft critical altitude. It is evident that with this system performance below the critical altitude is very close to the ideal. Of course, performance above the critical altitude departs greatly from the ideal; this departure is a direct consequence of fixed-compression-ratio operation.

Operation With Variable Injection Timing: Another possible method of control is to retard the injection, Fig. 14, which represents an effective means of decreasing the compression ratio. The engine would thus be built with a physical compression ratio equal to that required at the highest proposed altitude of operation. At lower altitudes, the time of injection would be retarded to vary the compression ratio to the required value.

Investigations were made at the Lewis Laboratory on a variable-compression-ratio compression-ignition engine to verify this type of operation. By running this engine at various compression ratios, injection-advance angles, and fuel-air ratios, data were obtained from which cross-plots of the engine power and the fuel consumption at constant peak cylinder pressure and exhaust temperature could be made to show the degree to which varying injection timing can simulate a physical change in compression ratio.

A typical result of these investigations follows: For a fuel-air

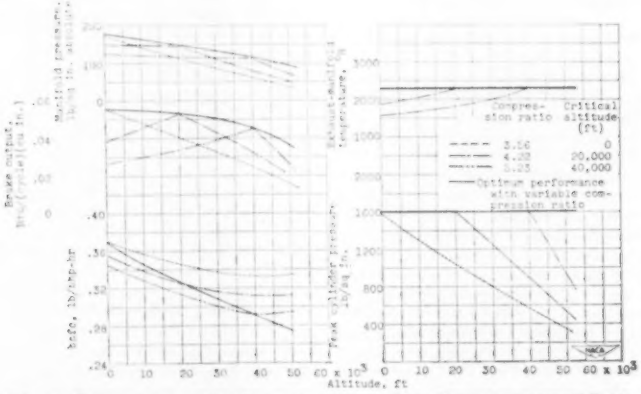

FIG. 15 PERFORMANCE OF GAS-GENERATOR ENGINE WITH FIXED COMPRESSION RATIO OPERATING AT LIMITING PEAK-CYLINDER PRESSURE OF 1600 PSI AND A LIMITING EXHAUST-MANIFOLD TEMPERATURE OF 2260 R
(Scavenging ratio, 1.)

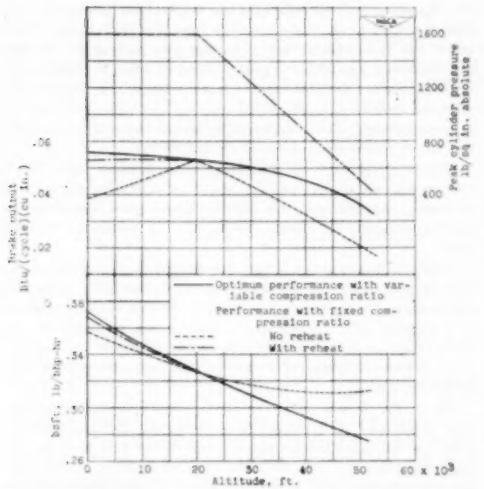

FIG. 16 PERFORMANCE OF GAS-GENERATOR ENGINE WITH FIXED COMPRESSION RATIO AND WITH REHEAT OPERATING AT A LIMITING PEAK OF CYLINDER PRESSURE OF 1600 PSIA AND LIMITING TURBINE-INLET TEMPERATURE OF 2260 R

(Critical altitude, 20,000 ft; compression ratio, 4.22; scavenging ratio, 1.)

ratio of 0.03, a cylinder having a physical compression ratio of 7.5 had a 1 per cent greater fuel consumption when operating at an effective compression ratio of 5 at retarded-injection conditions than the fuel consumption of the same cylinder operating with the compression ratio physically changed to 5; the power output was about 3.5 per cent less (peak cylinder pressure and exhaust temperature were maintained constant). Operation at other fuel-air ratios slightly increased these differences.

It was concluded that in the range of these investigations almost as good performance could be obtained at a compression ratio produced by retarding the injection as the performance obtained at the same compression ratio produced by changing actual physical engine dimensions. Performance of a fixed-compression-ratio gas-generator engine should thus be made to approach that of the ideal engine by suitable variation of the injection timing. Because the range of experimental data was limited, however, it is impossible to say that this conclusion will apply over the entire gas-generator operating range. The injection-timing method of controlling engine limits is therefore not assigned a preference over the fixed compression ratio with reheat method.

Cruising Specific Weight of Gas-Generator Engine. Specific weight is almost as important as specific output and specific fuel consumption in determining the over-all performance of the gas-generator engine; an analysis was therefore made of the specific weight of a gas generator engine that delivers 4000 hp cruising. The engine was assumed to operate at an altitude of 20,000 ft, a peak cylinder pressure of 1600 psia, a turbine-inlet temperature of 2260 R, a scavenging ratio of 1, an engine speed of 2400 cycles per minute (cpm), and at turbine and compressor efficiencies of 85 per cent. The weights of the various components were estimated from the weights of similar components in current aircraft engines.

The gas-generator engine will deliver a specific output of 0.051 Btu per cycle per cu in. at the assumed operating conditions, Fig. 3. From this value of specific output the piston displacement of the generator section may be calculated, and using a power-section specific weight of 0.65 lb per cu in. of piston displacement (obtained from a study of component weights of current aircraft engines weighted against operating pressures), the weight of the piston component of the gas-generator engine was estimated to be 862 lb.

For the air flow and pressure ratio required for the compressor, design estimates resulted in a weight of 150 lb for the first-stage centrifugal compressor. The weight of the second-stage compressor, assumed in this case to be an axial-flow compressor, was computed from the weight of a current aircraft axial-flow compressor using suitable corrections for differences in pressure ratio, air flow, and altitude; the weight was found to be 242 lb.

The turbine weight was determined by using a curve of stage weight against volume flow capacity given in reference (10); the weight of the three-stage turbine was calculated to be 210 lb.

The weight of the propeller reduction gear was calculated using a specific weight of 0.143 lb per hp, and the compressor reduction gear was assumed to have a specific weight of 0.7 of this value because of the lower speed ratio involved; because the compressor was divided into two stages, however, the weight of the compressor drive gear was increased by 30 per cent. These calculations resulted in a total reduction-gear weight of 922 lb.

The weight of the heat exchangers was estimated from the heat-rejection rate of the gas generator and data from reference (16). The total heat-exchanger weight was found to be 467 lb.

A weight of 200 lb was assumed for accessories and accessory drive gears and an installation weight of 10 per cent of the weights so far listed was assumed to take care of such weights as engine mounts, oil, coolant, fuel systems, and reinforcement of the inlet and exhaust manifolds.

These calculations resulted in a total engine weight without propeller of 3358 lb and a specific weight of 0.84 lb per cruising hp.

Details of the calculations may be found in the Appendix.

EXPERIMENTAL INVESTIGATIONS OF TWO-STROKE-CYCLE CYLINDERS

Gas-Generator-Engine Operating Pressures and Temperatures. In the foregoing discussion an indication of the potentialities of the gas-generator power plant has been presented. An inspection of the operating temperatures and pressures, however, will show more clearly the problems involved in making the gas generator a practical device.

Typical operating conditions of the ideal gas-generator engine at an altitude of 20,000 ft are shown in Fig. 17. Air at ambient pressure and temperature enters the compressor and is compressed up to inlet-manifold conditions of 140 psia and 702 F. In the piston engine, the charge is compressed and burned. The compression ratio is 4.2, the maximum cylinder pressure is 1600 psia, and the indicated mean effective pressure is 300 psi based upon the stroke above the ports (240 based on full stroke). The over-all fuel-air ratio is 0.033 and the cylinder fuel-air ratio is 0.052. The gases are discharged to the turbine at a pressure of 125 psia and a temperature of 1800 F, and are expanded in the turbine to atmospheric pressure. This cycle results in a brake specific fuel consumption of about 0.32.

A compression-ignition engine required to operate at the high inlet pressures, low compression ratios, and high inlet temperatures of the gas-generator engine is operating out of the range of conventional practice. Whether the heat and pressure loads are too great to permit satisfactory mechanical operation is a question that can be answered only by experimental investigation. Experimental investigations also will check the validity of the analytical work.

Experimental Apparatus and Techniques. It was considered

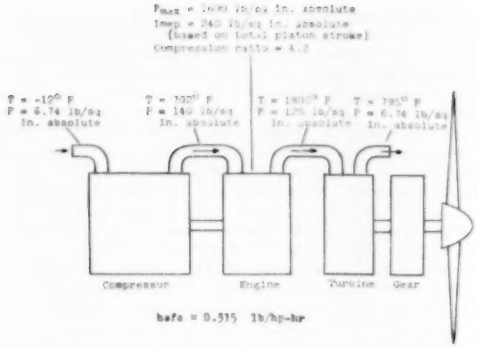

FIG. 17 TYPICAL GAS-GENERATOR PRESSURES AND TEMPERATURES AT 20,000 FT

best to obtain data from several types of two-stroke-cycle cylinder because of the questions raised in the preceding discussion. Therefore three different types of two-stroke-cycle compression-ignition liquid-cooled cylinders have been investigated to obtain the required data. These three types of cylinders are differentiated chiefly by the path taken by the scavenging air in its flow through the cylinder. The cylinders also differ in respect to displacement volume. A diagrammatic sketch illustrating the air-flow paths and port layouts of these three types of cylinders is shown in Fig. 18.

The first of these was a 37.4-cu-in. displacement cylinder of the so-called "Curtis loop-scavenged" type because the scavenging process is a combination of loop (path 1) and cross (path 2) scavenging. Rotative speeds up to 3600 rpm were run with this cylinder. Investigations at moderate pressure levels have been made elsewhere on cylinders of this type (17).

The second cylinder was a Schnüerle type loop-scavenged cylinder obtained from a 12-cylinder KHD (Klöckner-Humboldt-Deutz) engine of German manufacture. The Schnüerle type of scavenging eliminates the possibility of short-circuit scavenging (15), a phenomenon typical of cylinders that incorporate cross-flow scavenging in which charge air may blow directly from inlet to exhaust ports without removing combustion products. The Schnüerle type, although desirable from the scavenging standpoint, has the disadvantage of having only part of the cylinder circumference available for ports; thus, in order to obtain sufficient port area, the ports must be made longer, thereby cutting down on the effective stroke and necessitating larger cylinders for a given output. The cylinder investigated had a 195-cu-in. displacement and was run at speeds up to 2200 rpm.

The third cylinder was a single-cylinder Junkers Jumo 207-D uniflow opposed-piston cylinder of 186 cu in. displacement (both pistons). Scavenging in this cylinder is very good because of the uniflow design. This engine is capable of speeds up to 3000 rpm.

Details of construction of the three cylinders are not considered necessary to this paper as they are covered elsewhere. Complete information on construction of the Curtis-type cylinder is given in reference (12). Numerous references are available on the Junkers 207 uniflow cylinder (for example, reference 18), and discussion of the Schnüerle type can be found in the two-stroke-cycle literature (19).

The fuel-injection valves in the Curtis-type and Schnüerle-type cylinders were mounted in the center of the head; orifices were spaced uniformly around the nozzle tip and gave an umbrella-shaped spray, Fig. 19. The Junkers injection system used the original spray tips; however, instead of using four nozzles as in the commercial engine, only two, spaced 180 deg apart, were used in these investigations. Jerk-pump injection systems were used for all cylinders; one or more plungers, which were paralleled as necessary to give the required flow, were used. The plungers were 10 or 11 mm diam and each had a 10-mm stroke. Selection of the fuel-injection-pump cams was based upon the rate of injection required to give a period of injection of less than 30 deg at a fuel-air ratio of 0.035. The fuel used was a 50-cetane Diesel fuel of 0.835 specific gravity at 60/60 F with a hydrogen-carbon ratio of approximately 0.15. Fuel flow was measured with a rotameter.

High-pressure combustion scavenging air was obtained from the laboratory air system and was measured with ASME thin-plate orifices. Other instrumentation was similar to that used for

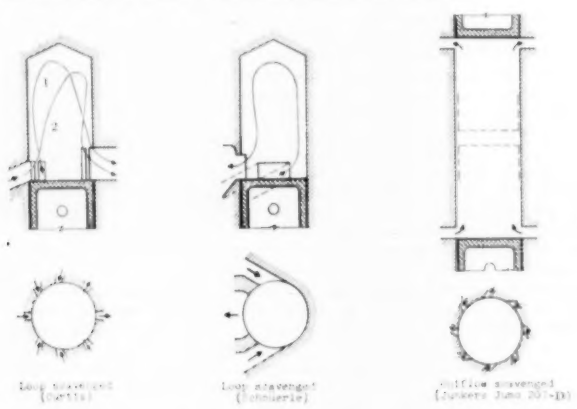

FIG. 18 DIAGRAMMATIC SKETCH OF THE THREE TYPES OF TWO-STROKE-CYCLE CYLINDER INVESTIGATED

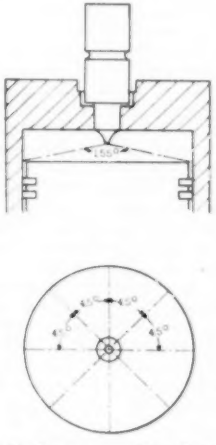

FIG. 19 LOCATION OF FUEL-INJECTION VALVE AND PATTERN OF FUEL SPRAYS IN CURTIS AND SCHNÜERLE CYLINDERS

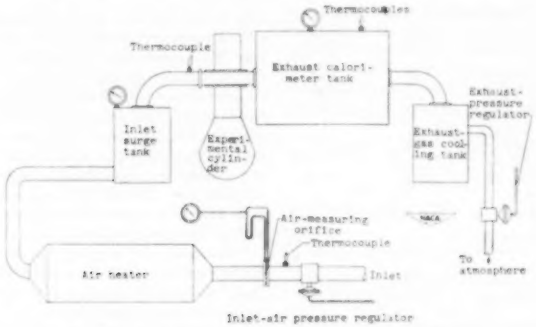

FIG. 20 DIAGRAMMATIC SKETCH OF TYPICAL TEST SETUP

internal-combustion engines as outlined in previous NACA reports.

A diagrammatic sketch of a typical test setup is shown in Fig. 20. The insulated exhaust tank illustrated is equipped with baffles to promote mixing of the exhaust gases for purposes of obtaining reliable exhaust-temperature measurements (12). Illustrations of the three engines mounted on their crankcases are shown in Fig. 21.

The injection-advance angle was 25 deg before top center for the Curtis-type cylinder, and 35 deg before top center for the Junkers and KHD cylinders.

Table 1 illustrates the range of data taken from these cylinders. Although not all the data taken are discussed here, it is evident that a wide range has been covered. The range of the Schnüerle and uniflow-cylinder data is not as great as that of the Curtis type because of termination of the tests due to failure of the air

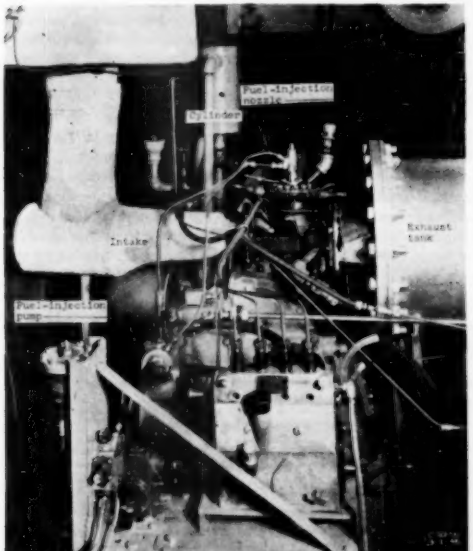

FIG. 21(a) TEST SETUP FOR CURTIS-TYPE SINGLE CYLINDER

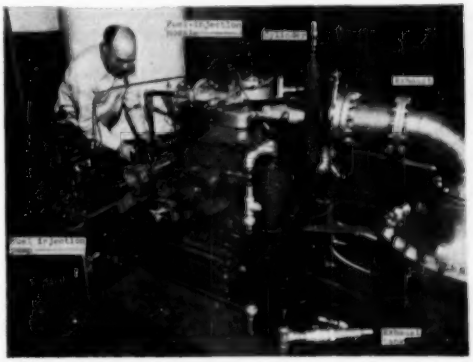

FIG. 21(b) TEST SETUP FOR SCHNÜERLE-TYPE SINGLE CYLINDER

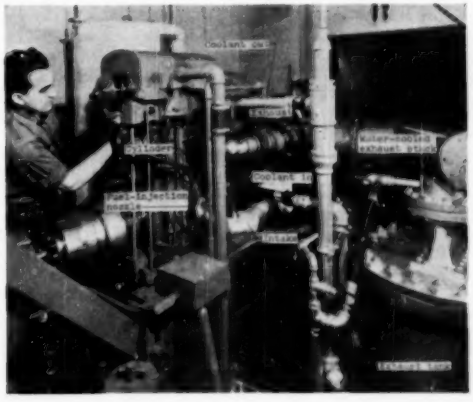

FIG. 21(c) TEST SETUP FOR JUNKERS JUMO 207-D UNIFLOW-TYPE SINGLE CYLINDER

TABLE 1 TEST DATA FOR VARIOUS-TYPE CYLINDERS

	Curtis cylinder	Schnüerle cylinder	Uniflow cylinder
Port timing, deg ATC:			
Exhaust opens	109 or 95	92	95
Intake opens	119	106	115
Intake closes	241	254	270
Exhaust closes	251 or 265	268	265
Compression ratio (based on volume above ports)	4, 4.5, 5.25, 7	6.02	4.98
Engine speed, rpm	1800-3000	1800-2200	1800-2400
Inlet-manifold pressure, psia	80, 100, 120, 135	50, 80	50, 80
Injection-advance angle, deg BTC	25	35	35
Fuel-air ratio (over-all)	0.01-0.06	0.01-0.05	0.01-0.04
Inlet-manifold temperature, deg F	300, 400, 500, 600	450	450
Coolant-inlet temperature, deg F	165	165	165
Scavenging ratio	0.7-1.6	0.7-1.6	0.7-1.6
Peak cylinder pressure, psia	800-2000	600-1200	600-1200

preheater. The compression ratios investigated are in the probable range required for the gas-generator engine.

Experimental Results: Because a more complete set of data is available, most of the data to be presented are from the Curtis-type cylinder. These data are typical of those obtained from the other cylinders.

Effect of Inlet Conditions: The effect of inlet-manifold pressure and over-all fuel-air ratio on the indicated mean effective pressure is shown for the Curtis-type cylinder in Fig. 22. At very lean fuel-air ratios, the indicated mean effective pressure is roughly proportional to fuel-air ratio. As the mixture is enriched, the indicated mean effective pressure approaches a maximum and then decreases. These peaks, which correspond to the condition of stoichiometric fuel-air ratio in the cylinder, occur at very low over-all fuel-air ratios because of the poor charging of this particular cylinder.

Poor charging is a direct consequence of insufficient exhaust lead and may be explained as follows: The mixture ratio in the cylinder is always richer than the over-all fuel-air ratio because of the inherent nature of the scavenging process (8). As the mixture in the cylinder approaches stoichiometric, there is always some fuel remaining unburned at the time of exhaust-port opening. With insufficient exhaust lead, the mixture of unburned fuel and combustion products does not have sufficient time to discharge before the fresh charge enters. The remaining unburned fuel thus undergoes combustion with the incoming charge, so that the cylinder is, in effect, being charged with products of combustion. This condition contributes to even higher fuel-air ratios in the cylinder and leads to rapid decrease of indicated mean effective pressure. All the fuel is burned at one time or another as evidenced by the continuous increase in exhaust-gas temperature with an increase in over-all fuel-air ratio (12).

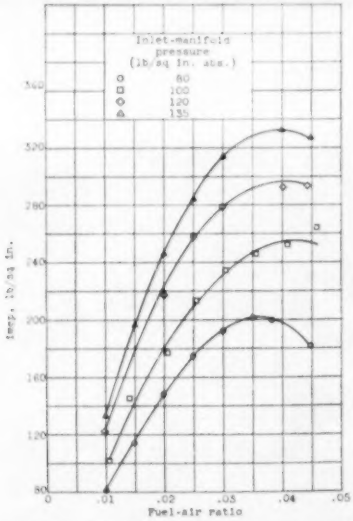

FIG. 22 EFFECT OF INLET-MANIFOLD PRESSURE AND OVER-ALL FUEL-AIR RATIO ON POWER OUTPUT OF CURTIS-TYPE CYLINDER (Compression ratio, 5.25; inlet-manifold temperature, 400 F; speed, 1800 rpm; scavenging ratio, 1; exhaust lead, 10 deg.)

This explanation is strengthened further by the fact that when the two-stroke cylinder was operated on a four-stroke-cycle basis (fuel is injected every other cycle) so that the unburned fuel and products of combustion were carried out of the cylinder during the nonfiring cycle, the indicated-mean-effective-pressure curves did not peak at all but became substantially flat as the over-all fuel-air ratio was increased, even out to an over-all fuel-air ratio of 0.10 (12). Unpublished investigations of this type of cylinder indicate that early peaking of the curves of indicated mean effective pressure against fuel-air ratio can be alleviated greatly by increasing the exhaust lead.

The effect of inlet-manifold temperature on indicated mean effective pressure for constant fuel-air ratio was also determined. Results showed that indicated mean effective pressure varied directly as the reciprocal of the manifold temperature. Indicated mean effective pressure is also a linear function of manifold pressure for constant fuel-air ratio; therefore it can be shown that indicated mean effective pressure is a linear function of the inlet density for constant fuel-air ratio.

Thermal Efficiency: The effects of pertinent engine variables on indicated specific fuel consumption are shown in Fig. 23 which illustrates that efficiency decreases with increasing fuel-air ratio. This change is caused by greater divergence of the properties of the working fluid from the properties of a perfect gas at the rich mixtures, the occurrence of more of the combustion at constant pressure, and burning continuing during the expansion stroke.

The variation of indicated specific fuel consumption with compression ratio is also presented. The trend is similar to that expected from theoretical considerations.

Heat Loss Exhaust-Gas Temperature: The heat loss to the coolant and the exhaust-gas temperature are shown in Fig. 24 as functions of fuel-air ratio. The heat losses decrease with an increase in fuel-air ratio. This variation probably results because the heat input increases faster than the temperature difference leading to heat transfer. All the heat-loss data of the Curtis-type cylinder are higher than 18 per cent, which is the value assumed for the theoretical work. Possible reasons for this difference are as follows:

1 The small Curtis-type cylinder has an unusually high surface-volume ratio (for instance, nearly two and one-half times as much as that of the KHD Schnüerle-type cylinder).

2 The particular data shown, Fig. 24, were for a rather low piston speed. Increasing the piston speed will reduce materially the percentage heat loss to the coolant.

3 The coolant temperature was held to a relatively low value in order to avoid the possibility of cooling difficulties during these preliminary investigations.

If the size of this small cylinder were increased to that of the Schnüerle cylinder and run at higher coolant temperatures and engine speeds, the percentage heat loss would probably be less than 18 per cent. The heat loss of the uniflow cylinder was down to 17 per cent, and that of the Schnüerle was around 20 per cent even at the low coolant temperatures used.

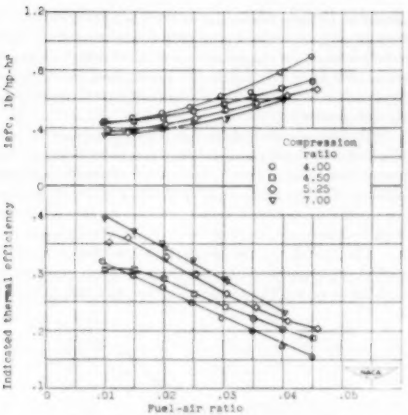

FIG. 23 EFFECT OF FUEL-AIR RATIO AND COMPRESSION RATIO ON INDICATED THERMAL EFFICIENCY OF CURTIS-TYPE CYLINDER
(Inlet-manifold temperature, 400 F; inlet-manifold pressure, 100 psia; speed, 1800 rpm; scavenging ratio, 1; exhaust lead, 10 deg.)

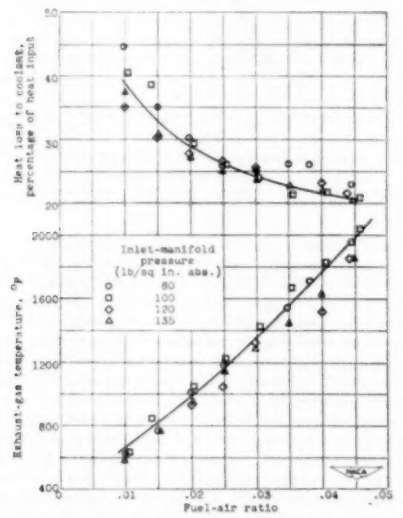

FIG. 24 VARIATION OF HEAT LOSS AND EXHAUST-GAS TEMPERATURE OF CURTIS-TYPE CYLINDER WITH FUEL-AIR RATIO
(Compression ratio, 5.25; inlet-manifold temperature, 400 F; speed, 1800 rpm; scavenging ratio, 1; exhaust lead, 10 deg.)

The exhaust-gas temperature is practically a linear function of fuel-air ratio. The slight upward curvature is caused by a decrease in engine efficiency as the fuel-air ratio is increased. It is interesting to note the wide range of temperature available from about 600 F at a fuel-air ratio of 0.01 to about 2000 F at a fuel-air ratio of 0.045.

Cylinder Pressure Drop: Typical cylinder-pressure-drop data obtained during the investigation of the three cylinders are shown in Table 2. These data were taken for representative engine conditions of fuel-air ratio of 0.03 and a scavenging ratio of 1.0. Because cylinder pressure drop is a function of engine speed and port design, data from the three cylinders are not comparable but are included to show what might be expected from engines of these types. Some data at an inlet-manifold pressure of 100 pounds per square inch absolute are included to show the effect of providing sufficient exhaust lead (24 deg in this case).

TABLE 2 TYPICAL CYLINDER-PRESSURE-DROP DATA

Cylinder type	Manifold pressure, psia	Cylinder pressure drop, psi	Engine speed, rpm
Curtis cylinder with 10 deg exhaust lead	80	7.2	1800
Schnuerle	80	3.5	1800
Uniflow	80	7.5	2400
Curtis cylinder with 10 deg exhaust lead	100	12.5	1800
Curtis cylinder with 24 deg exhaust lead	100	7.2	1800

Proper exhaust lead is necessary in two-stroke-cycle operation. With insufficient exhaust lead, not only does cylinder pressure drop increase with fuel-air ratio, but as previously discussed, scavenging is affected adversely. With sufficient exhaust lead, cylinder pressure drop is relatively insensitive to cylinder load (fuel-air ratio); in fact, this insensitivity serves as a good check on exhaust lead. There are also data which indicate that with insufficient exhaust lead the cylinder pressure drop increases faster with increase in inlet-manifold pressure than is the case with proper exhaust lead. Cylinder pressure drop is not too great a factor in the gas-generator engine, however, because the expansion ratio across the turbine is already so great that any reasonable increase in cylinder pressure drop can be tolerated.

Charging Efficiency: Charging efficiency, which is a fundamental factor in two-stroke-cycle operation, is a difficult item to measure. It can be determined, however, by taking samples of the cylinder gas through a sampling valve after injection of the fuel and before the ports open. Samples of the gas are led through the NACA mixture analyzer (20) which determines the fuel-air ratio of the gases from which calculations of charging efficiency can be made.

For a primarily loop-scavenged cylinder, such as the Curtis type, the theoretical value of charging efficiency is 0.63. Values determined by the sampling-valve method showed a charging efficiency of 0.60 at engine conditions of an over-all fuel-air ratio of 0.03, and an inlet-manifold pressure of 100 psia.

Effect of Speed: In general, most of the data were taken at constant speed (1800 rpm). For the purpose of determining the effect of speed on combustion, power, pressure drop, and heat losses, however, the speed range of the Curtis cylinder (with 24 deg exhaust lead) was increased up to approximately 3100 rpm. The results are shown in Fig. 25 for a compression ratio of 5, a scavenging ratio of 1, an inlet temperature of 400 F, a fuel-air ratio of 0.3, and a manifold pressure of 100 psia.

Apparently the increase in speed does not reduce performance materially; for instance, the performance is, in general, as good or better at the high speeds as at the low speeds. Although the specific fuel consumption of the reciprocating component is not too important with regard to over-all gas-generator-engine efficiency (because losses in the reciprocating component are more or less recovered by the turbine, which follows in the cycle), heat loss to the coolant is critical because increased heat loss directly decreases the available exhaust temperature for constant fuel-air-ratio operation or requires more fuel for constant-exhaust-temperature operation. An increase in engine speed, however, actually reduces percentage heat loss to the coolant. The decreased heat loss is reflected directly in higher exhaust temperature, as shown in Fig. 24. The increase in exhaust temperature coupled with the increase in mass flow (a consequence of increased engine speed at constant scavenging ratio) produces a substantial increase in ex-

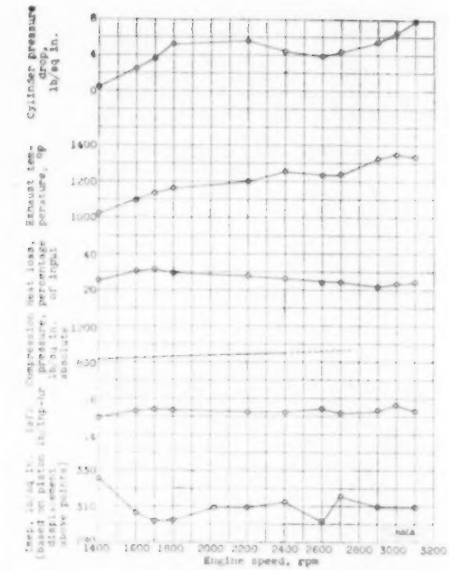

FIG. 25 EFFECT OF SPEED ON CURTIS-TYPE CYLINDER PERFORMANCE

(Compression ratio, 5; scavenging ratio, 1; inlet temperature, 400 F; fuel-air ratio, 0.03; manifold pressure, 100 psia; exhaust lead, 24 deg.)

haust energy. The compression pressure increases with engine speed because of either better ring-seal or inertia effects in the inlet or exhaust system. The cylinder pressure drop did not increase as rapidly as theory indicated, probably because of some inlet or exhaust inertia effect.

It can be concluded that operation at high rotative speeds (high for two-stroke-cycle compression-ignition engines) offers no particular problems in regard to combustion, power pressure drop, or heat losses, at least with this size and type of Curtis cylinder.

Effect of Fuel Quality: Because of advantages inherent in an engine not restricted to the use of a single fuel, an investigation was made with the Curtis-type cylinder to determine what effect fuel quality had on performance. The results are shown in Fig. 26 where indicated mean effective pressure is plotted against fuel-air ratio at constant manifold pressure. Four different fuels were used: laboratory Diesel fuel, jet-propulsion fuel (AN-F-32a), furnace oil (Federal spec. VV-O-326; grade F.S.2), and gasoline (AN-F-28). The use of the three nonvolatile fuels showed almost identical power outputs. Performance with gasoline was somewhat inferior. Roughness of engine running was not, however, apparent with any of these fuels.

The smooth running with these various types of fuel is attributed to the relatively low compression ratio of the gas-generator engine. Low compression ratio with corresponding large clearance volume results in a lower rate of volume change for a given crank angle than that of a high-compression engine. The lower rate of volume change in turn leads to lower rates of pressure rise, which obviates Diesel knock. Furthermore, in the low-compression engine, during the time of injection, the mean temperature and pressure are higher than in a high-compression engine operating at the same peak cylinder pressure. The higher mean temperatures and pressures are conducive to low ignition lag and smooth combustion.

Differences Between Observed and Predicted Performance: Inasmuch as the experimental investigation was conducted to determine the performance characteristics of a cylinder for gas-generator use as well as to investigate the mechanical feasibility of the cylinder, differences between experimental and theoretical results are of interest.

The cylinders operated under conditions of fuel-air ratio, compression ratio, and inlet and exhaust pressures required for the gas-generator engine. Furthermore, the cylinders investigated produced (*a*) the maximum indicated mean effective pressure required, (*b*) the maximum cylinder pressure required, and (*c*) the maximum exhaust-gas temperature required for the gas-generator engine. The cylinders investigated, however, did not produce all three of these required items at the same time, principally because of the impossibility of selecting the optimum injection advance. The time of injection controls all three of these items (that is, advancing the injection would increase the indicated mean effective pressure, reduce the exhaust temperature, and greatly increase the peak cylinder pressure). Selection of the proper advance angle for getting these three parameters at the required value would require cross-plots of the entire mass of data with the additional variable of injection-advance angle included. Because injection-advance angle was not made a variable in these investigations, such cross-plots are unavailable.

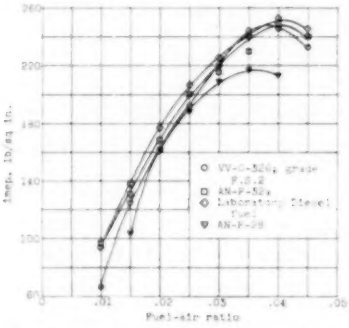

FIG. 26 EFFECT OF FUEL QUALITY ON CURTIS-TYPE CYLINDER PERFORMANCE

(Engine speed, 1800 rpm; compressor ratio, 5.25; scavenging ratio, 1; manifold pressure, 100 psia; inlet temperature, 400 F; exhaust lead, 10 deg.)

With proper injection timing, both engine limits (peak cylinder pressure and exhaust temperature) could be held at predetermined values. At the specified operating point, the indicated mean effective pressure and the indicated specific fuel consumption of the generator might not exactly agree with the values predicted by the theoretical equations (10) but with proper engine design it is believed that the differences would be small. Coolant heat loss, a principal shortcoming of the small Curtis cylinder, has been brought down to a practical value in the uniflow cylinder; although the Curtis cylinder showed poor scavenging at rich mixtures, investigation of the other two cylinders has shown improved results.

Mechanical Performance: Operation under the conditions of higher than conventional inlet pressures and temperatures and exhaust pressures and temperatures, as well as lower than conventional compression ratios indicated for the gas-generator engine, brings up such questions as mechanical reliability, combustion roughness, and wear of parts. The entire investigation covered about 1200 engine-hours, which permitted a reasonable estimate of the mechanical properties of the experimental set-

ups. During the lengthy operation of the engines investigated, no trouble was experienced with broken connecting rods, cylinder barrels, piston pins, or cylinder heads and, with proper selection of ring and barrel materials, no trouble was experienced with ring or barrel wear. Nearly 150 hr elapsed between overhauls on one setup and the rings were practically unworn at the end of this period. Ring sticking was no problem with use of keystone-section piston rings. Combustion roughness was lacking because of the low rate of pressure rise during combustion (approximately 30 lb/sq in./deg). A pressure rise rate of 50 psi per deg usually causes combustion roughness.

Conclusions

From the results of the theoretical and experimental investigations conducted on the gas-generator engine, the following conclusions were reached:

1 Theoretical analysis indicates that the two-stroke-cycle gas-generator engine promises an aircraft power plant of low specific weight combined with low specific fuel consumption. At an altitude of 20,000 ft, the specific fuel consumption was 0.32 lb per bhp-hr and the cruising specific weight was 0.84 lb per hp without the propeller.

2 Performance potentialities of this type of engine are not limited by knock or preignition over the range of compression ratios experimentally evaluated.

3 Moderate inefficiencies in the reciprocating component and the compressor result in only slight losses in the over-all efficiency of the gas-generator engine but produce relatively greater losses in specific output.

4 It was found possible to operate a two-stroke-cycle cylinder at the pressure and temperature levels required for the gas-generator engine.

5 Mechanical functioning of the piston engine under gas-generator operating conditions was generally satisfactory.

BIBLIOGRAPHY

1 "Effect of Exhaust Back Pressure on Engine Power," by Benjamin Pinkel, NACA CB 3F17, 1943.

2 "Calculated Performance of a Compression-Ignition Engine-Compressor-Turbine Combination Based on Experimental Data," by Alexander Mendelson, NACA TN 1774, 1948.

3 "A Theoretical Analysis of the Performance of a Diesel Engine-Compressor-Turbine Combination for Aircraft," by E. W. Hall, NACA ACR E5D10, 1945.

4 "Calculations of Economy of 18-Cylinder Radial Aircraft Engine With Exhaust-Gas Turbine Geared to the Crankshaft," by R. W. Hannum and R. H. Zimmerman, NACA Report 822, 1945.

5 "Performance of Blowdown Turbine Driven by Exhaust Gas of Nine-Cylinder Radial Engine," by R. L. Turner and L. B. Desmon, NACA Report 786, 1944.

6 "Effect of Valve Overlap and Compression Ratio on Variation of Measured Performance With Exhaust Pressure of Aircraft Cylinder and on Computed Performance of Compound Power Plant," by C. S. Eian, NACA TN 2025, 1950.

7 "Performance and Ranges of Application of Various Types of Aircraft-Propulsion System," by Cleveland Laboratory Staff, NACA TN 1349, 1947.

8 "Preliminary Evaluation of the Performance of a Uniflow Two-Stroke-Cycle Spark-Ignition Engine Combined With a Blowdown Turbine and a Steady-Flow Turbine," by B. I. Sather and H. H. Foster, NACA RM E7D29, 1947.

9 "An Analysis of a Highly Compounded Two-Stroke-Cycle Compression-Ignition Engine," by M. J. Tauschek, B. I. Sather, and A. R. Biermann, NACA RM E8L09, 1949.

10 "An Analysis of a Piston-Type Gas-Generator Engine," by M. J. Tauschek and A. E. Biermann, NACA RM E7I10, 1948.

11 "Study of Compressor Systems for a Gas-Generator Engine," by B. I. Sather and M. J. Tauschek, NACA RM E50H08, 1950.

12 "Experimental Study of Loop-Scavenged Compression-Ignition Cylinder for Gas-Generator Use," by H. H. Foster, F. R. Schuricht, and M. J. Tauschek, NACA RM E8L30, 1949.

13 "Hydrogen as an Auxiliary Fuel in Compression-Ignition Engines," by H. C. Gerrish and H. H. Foster, NACA Report 535 1935.

14 "Thermodynamic Charts for Internal-Combustion-Engine Fluids," by W. J. McCann; rev. by L. R. Turner and E. A. Bauer, NACA TN 1883, 1949.

15 "Scavenging of Two-Stroke Cycle Diesel Engines," by P. H. Schweitzer, The Macmillan Company, New York, N. Y., 1949.

16 "Aircraft Cooling Handbook," Harrison Radiator Division, General Motors Corporation, Lockport, N. Y., August, 1940.

17 "Scavenging a Piston-Ported Two-Stroke Cylinder," by A. R. Rogowski and C. L. Bouchard, NACA TN 674, 1938.

18 "Development of the Junkers-Diesel Aircraft Engine," by Dr. Gasterstädt, NACA TM 565, 1930.

19 "KHD Two-Cycle Engine Development With Schnürle Loop Scavenge System," by A. R. Pope, Jr., FIAT Final Report No. 683, Off. Division of Intelligence, U. S. Office Military Government, Germany, January 9, 1946. (Available from U. S. Department of Commerce as PB No. 30041.)

20 "The NACA Mixture Analyzer and Its Application to Mixture-Distribution Measurement in Flight," by H. C. Gerrish, J. Lawrence Meen, Jr., M. D. Scadron, and Anthony Colnar, NACA TN 1238, 1947.

Appendix

Analysis of Specific Weight of Gas-Generator Engine

The particular gas-generator engine selected for this analysis has a rating of 4000 bhp at an altitude of 20,000 ft. The limitations assumed to apply for continuous operation were a peak cylinder pressure of 1600 psia, a turbine-inlet temperature of 2260 R, and a generator speed of 2400 rpm. Component weights are evaluated for either altitude or sea-level conditions, whichever is the greater. The analysis follows the methods of reference (10) but certain changes were necessary because recent information indicates that some of the component weights selected in reference (10) were too great.

Piston Engine: The gas-generator engine will deliver a specific output of 0.051 Btu per cycle per cu in. at an altitude of 20,000 ft. In order to deliver 4000 hp, this specific output requires a piston-engine displacement volume above the ports of 1387 cu in. If a correction is made for the clearance volume and if 20 per cent of the stroke is allowed to be taken up by port height, the piston engine will have an actual piston displacement of 1328 cu in. Information on the specific weights of power sections of current reciprocating engines indicates that a specific weight of 0.65 lb per cu in. is a reasonable figure. The weight of the piston component of the gas-generator engine is thus 862 lb.

Compressor: The compressor of the gas-generator engine is assumed to be divided into two stages; the first stage (supercharger stage) is a centrifugal compressor, and the second stage is an axial compressor. From design estimates, a weight of 150 lb is assigned to the supercharger stage.

The weight of the axial-flow compressor was determined from the weight data of a current turbojet engine. This engine had a compressor weighing 466 lb, which was capable of handling a sea-level air flow of 50.5 lb per sec and used 11 stages to produce a pressure ratio of 4. The weight of this compressor was corrected for gas-generator application by use of the ratios of the air densities at sea level and 20,000 ft, the ratio of the required and actual weight-flow capacity of the compressor, and the ratio of the logarithms of the required and the actual compressor-pressure ratios. If the pressure ratio of the supercharging stage is assumed to be 3, the pressure ratio of the axial-flow stage will be 6.89 for operation at 20,000 ft. The required air flow will be 10.41 lb per sec. This calculation results in an axial-flow-compressor weight of 242 lb.

Turbine: The turbine weight was determined by using the relation of stage weight against volume-flow capacity shown in Fig.

9 of reference (10). The volume flow was calculated for the gas-generator engine by taking the arithmetical average of the turbine-inlet and turbine-outlet volume flows. The resultant stage weight was thus determined to be 70 lb. Because a three-stage turbine was assumed, the weight of the turbine was estimated to be 210 lb.

Reduction Gear: The reduction-gear weights were calculated by using 0.143 lb per transmitted horsepower, which was obtained from weight data on a current turbine-propeller engine. The gear weight is based upon the brake horsepower of the gas-generator engine at sea-level altitude. This computation resulted in a propeller reduction-gear weight of 583 lb.

Compressor Drive Gear: The weight of the compressor drive gear was calculated using a specific weight of 0.7 of that of the propeller-reduction gear because a smaller speed ratio is involved. Compressor-power requirements were calculated using the weight flows and pressure ratios at sea-level altitude as the compressor power required was higher there than at 20,000 ft. At sea level the required compressor-drive-gear horsepower is 2606 and results in a weight of 261 lb. The compressor is divided into two parts, necessitating two drive gears; therefore the weight was increased by 30 per cent, which resulted in a drive-gear weight of 339 lb.

Heat Exchangers: Heat-exchanger weights were determined using data from reference (16) which indicated heat-rejection rates of 2500 Btu per min per sq ft per 100 F initial temperature difference for oil coolers and 6000 Btu per min per sq ft per 100 F initial temperature difference for radiators. Wet weights of 48 and 54 lb per sq ft of frontal area, respectively, were used for these two coolers.

In determining the heat rejection of the gas-generator engines, 16 per cent of the heat input of the fuel was assumed to be rejected to the coolant and 2 per cent was assumed to be rejected to the oil. The heat input of the fuel was determined from the power output of the engine and the brake specific fuel consumption by use of a heating value for the fuel of 18,500 Btu per lb. Analysis showed that the sea-level condition was the limiting condition, where the heat-rejection rates for the gas-generator engine were 72,500 Btu per min to the coolant and 9070 Btu per min to the oil.

The radiator weight, which resulted from this calculation, was 343 lb, and the oil-cooler weight was 124 lb.

Miscellaneous Weights: A weight of 200 lb was assumed for accessories and accessory drive gears, and an installation weight of 10 per cent of the sum of the weights so far listed was assumed to take care of such items as engine mounting, oil, coolant, fuel systems, and reinforcements of the inlet and of the exhaust manifolds.

Total Installed Weight: The total installed weight of the gas-generator engine is then given by the sum of the components

TABLE 3 INSTALLED WEIGHT OF GAS-GENERATOR ENGINE

Component	Weight, lb
Power section	862
Supercharger stage	150
Axial-flow compressor	242
Turbine	210
Heat exchangers	467
Propeller-reduction gear	583
Compressor-drive gear	339
Accessories	200
	3053
Miscellaneous for installation	305
Total installed weight	3358

listed in Table 3. The specific weight for the 20,000-ft altitude, 4000-hp, gas-generator engine was then calculated to be 0.839 lb per hp.

Discussion

P. H. Schweitzer.[3] This paper raises the question whether the military is not making a mistake by putting all its eggs in the jet basket. For long-range flight with heavy pay load, that means bomb load, the compound engine beats the jet by a tremendous margin.

One hears that the predicted weight of a compound power plant is approximately 0.9 lb per hp. For a 100,000-lb-gross-weight airplane with four 4000-hp engines making a 2000-mile hop, the power plant would weigh approximately 14,000 lb. With 0.32 spec. fuel consumption and 375 mph the fuel would weigh 27,000 lb, which would leave for plane weight and load 59,000 lb. Using jet engines the power plant may weigh not more than 6000 lb but the fuel would weigh not less than 85,000 lb leaving 9000 lb for airframe and load combined. Even if this arithmetic is oversimplified, it illustrates the absurdity of transporting heavy loads to great distances with jet propulsion. The writer would like to see more than just paper research and relatively small-scale experimental work on compound power plants for aircraft.

The paper is a noble effort of a small NACA group in this direction. They deserve utmost encouragement. Although some of the assumptions are on the optimistic side, the calculated performance figures are realistic and are in rough agreement with those of the Schweitzer and Salisbury paper of 1949[4] as well as with the scarce experimental results. For instance, the authors calculated that a 4000-hp gas-generator engine running at 2400 engine rpm would have 1387 cu in. displacement, or 3.05 hp per cu in. The writer has calculated at 1200 rpm 1.485 hp per cu in., which is almost exactly the same.

As mentioned previously, some of the assumptions appear to be somewhat optimistic at present. A turbine-inlet temperature of 2260 R and 85 per cent compressor efficiency seem high. The authors' choice of the constant-volume cycle for their theoretical analysis seems unfortunate because such cycle is neither practicable nor desirable, and it robs the analysis of the flexibility offered by the variation of the point of cutoff in the limited-pressure cycle. By such procedure the inlet-manifold pressure and the compression ratio were fixed automatically for any one altitude. Previous NACA work, like the one cited in reference (12) of the paper, used the limited-pressure cycle; the writer wonders why the authors abandoned it in the present paper.

According to the assumptions, about 60 per cent of the air is short-circuited in the two-stroke-cycle engine, and the resultant 0.054 cylinder fuel-air ratio is considered adequate to permit good combustion efficiency. For an injection-type engine is such a fuel-air ratio not too rich to permit smokeless exhaust?

Was blowdown recovery ignored in the power analysis and if not, which was the method used to calculate it? In reference (12) of the paper, the turbine-inlet temperature was calculated by treating the reciprocating engine as a steady-flow machine. But, unless it has an infinitely large exhaust receiver, the reciprocating engine is not a steady-flow machine. If it has, no blowdown recovery is possible.

Referring to the experimental part of the paper, it is unfortunate that most of the tests were conducted with insufficient exhaust lead. Perhaps that could have been avoided if the observation that, with adequate exhaust lead, the pressure drop is insensitive to the fuel-air ratio, had been made earlier. This observation is identical with the statement that the Kadenacy effect increases with the engine load.

The writer disagrees with the authors in attributing the smooth

[3] Professor of Engineering Research, Pennsylvania State College, State College, Pa. Mem. ASME.

[4] "Compound Powerplants," by P. H. Schweitzer and J. K. Salisbury, Quarterly SAE Transactions, vol 3, 1949, pp. 656–669.

running of the gas-generator engine to the low compression ratio, and the increase of compression pressure with engine speed to better ring-seal or inertia effects.

The most gratifying result of the experimental work is the observation that conventionally designed two-stroke-cycle engines operated with such extreme manifold pressures (30–135 psia) and temperatures (300–600 F) can run for hundreds of hours without mechanical troubles and distress and without excessive ring and cylinder wear.

M. J. Tauschek.[5] While the gas-generator engine is proposed primarily for aircraft use, some consideration should be given to this power plant for railroad and marine propulsion. For that matter, it may even find application in heavy military equipment. The advantages of the gas-generator engine in these applications are incurred through its high specific output. For example, such an engine at 1800 rpm would deliver 2.2 hp per cu in. displacement, as contrasted to approximately 0.3 hp per cu in. for a conventional supercharged four-stroke Diesel engine. With these high outputs, it is possible to build a prime mover of substantial power within the space limitations imposed on propulsion machinery. At the same time the desirable fuel consumption of the conventional Diesel engine is not sacrificed.

A number of other advantages accompany the application of this power plant to surface transportation. The complication of controlling the engine with variation in altitude is no longer present, and the rather involved control schemes outlined in the subject paper are unnecessary. Again, the feature of the engine whereby losses in the compressor or Diesel engine are recovered partially by the turbine permits design compromises to be made which ordinarily would impair the performance of a conventional Diesel engine. For example, the fuel-injection system need not be critical. As a final point, a supply of hot gas at elevating pressure is readily available for heating and for powering auxiliary equipment.

Authors' Closure

The authors wish to thank Dr. Schweitzer and Mr. Tauschek for their interest in this paper and their kind comments thereon. While the NACA's interest in the gas-generator engine was primarily concerned with its possible use as an aircraft power plant, the paper was given to the ASME with the thought in mind that the information to be presented might be helpful in designing a power plant for applications other than in the aircraft field. Mr. Tauschek, who did much of the early NACA analytical work on the gas-generator engine, mentions some of these additional fields. It might also be pointed out that the gas generator in a ground vehicle, together with one or two turbines and suitable gearing to provide the torque conversion required, represents, in effect, a variable-speed transmission and, in addition, the need for a clutch is eliminated. By-pass valves (waste gates) for the turbines are required for such an installation.

In answer to Dr. Schweitzer's comments, a turbine-inlet temperature of 2260 deg R (1800 deg F), and a compressor efficiency of 85 per cent may seem high, but in the light of possible future developments of the art, these values serve as probable limitations to the ultimate performance of the gas-generator engine. In any event, curves are shown in the paper which allow conversion of the performance to other values of turbine-inlet temperature and compressor efficiency. Constant-volume combustion was assumed because such combustion is easiest to obtain in a high-speed compression-ignition engine and, because in a pressure-limited cycle, results obtained using an Otto cycle are more conservative than those obtained using a Diesel cycle.

The cylinder fuel-air ratio of 0.054 used in the analysis is probably near the clear exhaust limit. Whether this will affect the turbine blading is beyond our knowledge at this time.

No blowdown recovery was assumed in the analysis; preliminary work indicated that the results obtainable under the cycle used would not be worth the complication of providing suitable ducting to a blowdown turbine.

With regard to the operation with insufficient exhaust lead, it was known, after preliminary tests, that the lead was insufficient; however, the length of time required to machine another cylinder with suitable lead made it imperative to operate in the meantime with the old cylinder.

The authors still feel that the smooth combustion obtained with the gas-generator engine was due to the fact that a low compression ratio and heated inlet air resulted in a higher mean temperature and pressure during injection than obtainable with a high-compression engine with unheated inlet air.

[5] Thompson Products, Inc., Cleveland, Ohio.

Design Features of a 5000-Hp Gas Turbine

By B. O. BUCKLAND[1] and D. C. BERKEY[2], SCHENECTADY, N. Y.

A 5000-hp, one-compressor, two-turbine gas-turbine power plant is described, its features are discussed, and its expected capability and economy are given. The plant which is designed to have a maximum of flexibility in its application is intermediate in efficiency and complication between a simple one-compressor, one-turbine nonregenerative power plant and a two-compressor, two-turbine intercooled and regenerative power plant designed by the authors' company. The axial-flow compressor has 14 stages and operates at a pressure ratio of 5.5. The turbine has two stages. The second stage produces the useful load and has a nozzle arranged so that its effective flow area can be varied during operation. The six combustion chambers are expected to operate at 800 F preheat and at 650 F rise. The cylindrically shaped regenerator when used is mounted on end and outdoors. The lube-oil system is similar to that used for steam turbines. The plant can be supplied either with a motor-driven or a turbine-driven cranking assembly. The control means for starting and stopping the plant and for controlling the turbine speeds and temperatures during operation is described. The installation requirements such as weights, outline dimensions, and water requirements are given.

Introduction

A NEW combustion-gas turbine of 5000-hp rating has been designed by the authors' company, and several are being manufactured. The first one is expected to be in commercial operation early in 1952.

This is the third type of gas turbine designed by the company for other than aircraft application.

The first was a 4800-hp simple-cycle unit designed primarily for locomotive service. The design was completed in August, 1947, and its features were then described (1).[3] Experience in the further development of this unit has been reported from time to time (2 to 8).

The second design, with a capacity of 5000 kw, was described in 1948 (9). It is a compound-cycle unit, utilizing both intercooling and regeneration and was designed particularly for electric power generation.

This new gas turbine is intermediate in efficiency and complication between the other two, having been designed for maximum flexibility. It can be used with or without a regenerator and is easily applied to various arrangements involving the combined use of the steam and the gas-turbine cycles. Since the load turbine is not required to drive the compressor element, the load speed can be chosen over a wide range of values without affecting the capability of the unit. Thus the feature, sometimes valuable, of being able to bog down the load speed to a very low value (zero if required) without stalling the unit is available.

It is expected that the plant will be particularly useful for such industrial applications as gas-pipe-line pumping or driving compressors for repressurizing oil wells. It also should be useful for power generation of 3500 kw in which case the load turbine would drive an electric generator. This paper describes some of the features of the new plant.

Description of Plant

The plant is a one-compressor, two-turbine unit to be used with or without a regenerator. As a regenerative gas turbine the thermal efficiency at the output coupling will be 22.5 per cent based on the higher heating value of natural gas fuel or 25 per cent based on the lower heating value. The flow diagram for the regenerative plant is shown in Fig. 1.

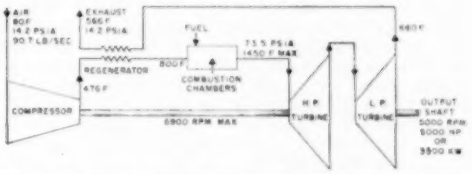

Fig. 1 Schematic Diagram of 5000-Hp Regenerative-Cycle Gas Turbine

The gas-generator-set speed and the initial temperature are maximum design values, and the conditions shown do not necessarily exist simultaneously. Thus they are not mutually consistent since they are not necessarily those required to give the rated output.

A semi cross section of the compressor and turbine is shown in Fig. 2. The first turbine stage drives the compressor, and this section of the machine is called the "gas-generator set" because it supplies the gas which furnishes the useful energy. The second turbine stage, which is in tandem but separate from the first stage makes use of the energy from the gas-generator set and drives the load only. This section of the machine is called the "load turbine." The arrangement allows the load speed to be independent of the gas-generator speed. Thus the output speed may be selected over a wide range to suit a variety of loads, and a good light load economy is obtained for any speed of the load turbine. In addition, the arrangement allows excess loads to be applied without stalling the gas-generator part of the plant, and thus excess loads do not stall the plant. They simply reduce the load-turbine speed, but the capability of the plant remains at its full value.

Performance

Fig. 3 shows the expected capability and fuel rates for 80 F ambient based on the higher heating value of a natural gas, which has a ratio of lower to higher heating value of 0.9. The flexibility of the unit just described is shown in the curve by the nearly constant output from 80 to 110 per cent normal load turbine speed and the small variation in part-load fuel flow with wide variation in load-turbine speed.

Fig. 4 shows the variation of plant capability and the corre-

[1] Manager of Engineering, Gas Turbine Engineering Division, Turbine Engineering Divisions, General Electric Company. Mem. ASME.

[2] Section Engineer, Gas Turbine Engineering Division, Turbine Engineering Divisions, General Electric Company. Jun. ASME.

[3] Numbers in parentheses refer to the Bibliography at the end of the paper.

Contributed by the Gas Turbine Power and Power Divisions and presented at the Annual Meeting, Atlantic City, N. J., November 25–30, 1951, of The American Society of Mechanical Engineers.

Note: Statements and opinions advanced in papers are to be understood as individual expressions of their authors and not those of the Society. Manuscript received at ASME Headquarters, September 25, 1951. Paper No. 51—A-113.

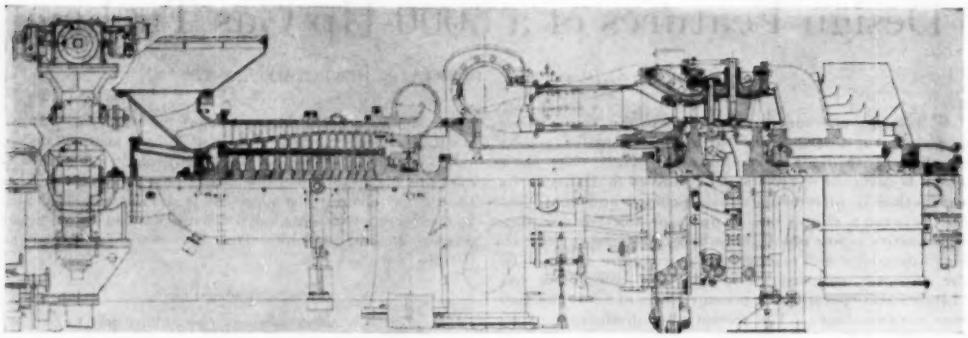

FIG. 2 SEMI CROSS SECTION OF GAS-GENERATOR SET AND LOAD TURBINE OF 5000-HP REGENERATIVE-CYCLE GAS TURBINE

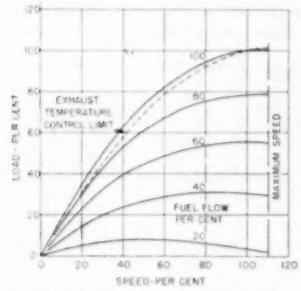

FIG. 3 CALCULATED VARIATION IN CAPABILITY AND FUEL RATES OF 5000-HP REGENERATIVE-CYCLE GAS TURBINE, 1000 FT ALTITUDE, 80 F AMBIENT

(Rated or 100 per cent values are: Load, 5000 hp; speed, 5000 rpm; fuel flow, 50,900,000 Btu per hr—LHV—or 56,400,000 Btu per hr—HHV—when $\frac{LHV}{HHV} = 0.9$.)

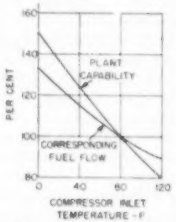

FIG. 4 VARIATIONS IN CAPABILITY AND FUEL FLOW WITH CHANGES IN COMPRESSOR-INLET TEMPERATURE FOR 5000-HP REGENERATIVE-CYCLE GAS TURBINE

sponding variation of fuel flow that occurs as the compressor inlet temperature is changed.

Compressor. The 14-stage 6900-rpm compressor produces a pressure ratio of 5.5 at a flow of 97 lb per sec with inlet conditions of 14.2 psia and 80 F. It is substantially the same compressor as that used on the locomotive power plant but with the last stage left off. All the blades, the wheels, and the forward casing are exactly the same in the two plants.

The four compressor casings are split in a horizontal plane so that their top halves can be removed for inspection of the rotor. The rotor also is assembled in the casings in this way. A silencer is required on the inlet of the compressor to reduce the noise which comes principally from the first three stages and occurs at the blade-passing frequencies of these stages. It is expected that the silencer will reduce the noise resulting from these three frequencies from somewhat over 100 db to approximately 85 db. The aft compressor casing carries an extraction opening at the tenth-stage wheel to provide air for turbine-wheel cooling and for other uses if air is needed. The aft casing also carries the two forward supports for bolting the unit to its foundation.

Turbine. The compressor is driven by the first turbine stage, the rotor of which is bolted to the compressor rotor to form a very simple three-bearing assembly without a flexible coupling and with only one thrust bearing. This simple arrangement is made possible by so proportioning the shaft that it can tolerate a generous amount of misalignment and by limiting the misalignment to this maximum or less. The necessary alignment accuracy is accomplished by a suitably stiff stator structure and supports and by proper manufacturing tolerances. It is insured by making the necessary measurements during the assembly of the unit, which measurements are facilitated by suitable measuring fixtures. The turbine-stator frame is connected to the compressor-exhaust casing by means of a removable ring. When the ring is removed, the compressor and turbine rotors can be disconnected so that the complete turbine can be separated from the compressor at this point and in this way. The removable ring also carries a shim which may be used to adjust the axial clearances of the turbine.

The second stage, or load-turbine rotor, is mounted in a structure which also carries the exhaust hood and the aft supports for bolting the unit to its foundation. The turbine frame and the exhaust hood are connected together by the turbine shell, which also carries the first- and second-stage nozzles and the second-stage diaphragm. Thus the compressor casing (with its forward support) is connected to the exhaust hood (with its aft support) by means of the compressor exhaust casing, the turbine frame, and the turbine shell. This arrangement forms a one-piece rigid supporting structure for the two rotors.

The first-stage nozzle consists of six segments of seven partitions each. The segments are held radially at their outer ring by the turbine shell, which is water-cooled, and axially at their inner ring by a portion of the turbine frame. The partitions are cooled by means of air flowing through them and discharging to the main stream at the nozzle inlet along the inner side wall. The turbine-bucket clearances are maintained by 24 shroud segments held both radially and axially in the water-cooled turbine shell. The nozzle segments and the shroud segments are insulated from the water-cooled shell at all except the necessary locat-

ing surfaces by means of pads formed from thin, dimpled, and laminated strips of stainless steel. These insulators reduce the heat loss and the cooling-water requirements for a given shell temperature and minimize the stresses in the shell and in the segments resulting from temperature gradients.

The effective flow area of the second-stage turbine nozzle can be varied by having its 24 partitions arranged to be rotatable about radial axes. This feature has the following advantages:

1 Overspeeds, which occur on loss of load and under various other contingencies depending upon the application, can be limited to amounts about one half as great with the variable nozzle as without it. This is accomplished by tripping the nozzle wide-open on overspeed.

2 The heat rate can be decreased substantially at light loads by selection of suitable control.

3 The capability at high ambients can be made somewhat greater.

4 Substantial amounts of auxiliary power can be taken out of the gas-generator set, to which it is mechanically more convenient and electrically better to connect an auxiliary generator than to the load shaft. The connections are simpler and the frequency of a driven alternator is more nearly constant for centrifugal-compressor load application.

5 The starting power is reduced.

6 The plant can be run at no load without exceeding the rated speed of the load turbine and without running at excessively high exhaust temperatures. With a fixed nozzle area the exhaust temperature first falls as load is reduced to a minimum at about $\frac{1}{3}$ load. With further reduction of load the speed of the gas-generator set continues to decrease but the exhaust temperature rises rapidly. A specified ceiling on the exhaust temperature requires a corresponding minimum value below which the load cannot go if the rated load speed is not to be exceeded. Furthermore, this minimum load has a higher value, the higher the compressor-inlet temperature and the lower the gas-generator-set efficiency. With movable nozzle partitions, however, the minimum values of any type of load can be met under any reasonable ambients and conditions of machine deterioration.

The disadvantages of the movable nozzle feature are of course the cost and complication.

The partitions are rotated by means of cranks, connected by links to a ring mounted on and fixed to rotate about the turbine shell. The ring is driven by two hydraulic cylinders which are under the influence of the control. The ends of the stainless-steel partitions, which are hardened by nitriding, slide on the spherical-shaped nozzle end walls. These are made in twelve segments and are nitrided also. The end walls are held in contact with the nozzle partitions flexibly. Radial-spring members push the inner end-wall segments outward radially against the ends of the partitions and these in turn press radially outward against the outer side-wall segments. Axial spring members press the inner side-wall segments in a downstream direction against two gas-sealing surfaces on the second-stage diaphragm. Pressurizing air is supplied to the space between these gas-sealing surfaces, which holds the inner side-wall segments against the partitions. In addition, this air prevents deposits from accumulating which might cause the segments to become fixed and not act in a flexible manner.

The hardened stems on the partitions are cooled and prevented from sticking by a flow of water through six axial grooves in the aluminum-bronze bushings.

The turbine wheels are cooled by air streams which flow from the points of introduction at the hubs on both sides of each wheel outward to the rims. This manner of cooling is made effective in spite of pressure variations around the wheel rims by means of three generous ring-shaped equalizing pockets on each side of each wheel.

Combustion System. The combustion chambers and the fuel nozzles now being built are designed to burn natural gas. By changing the fuel nozzles, adding a fuel pump, and making a few other similar modifications liquid fuel can be used, either distillate or residual oil. Air is fed to the six combustion chambers in two groups of three by two three-fingered manifolds connected to the two regenerator return pipes. The fuel gas is supplied to a manifold out of which the six fuel nozzles are fed. The normal or design conditions are as follows:

1 Air flow, $16\frac{1}{2}$ lb per sec per chamber.
2 Preheat temperature, 800 F.
3 Temperature rise, 650 F.
4 Minimum blowout rise, 100 F.
5 Operation pressure, 82 psia.
6 Heat release, 0.7×10^6 Btu per hr per cu ft per atm.

Two retracting spark plugs together with two 15-kw ignition transformers and cross-fire tubes between the chambers are used for ignition. Two thermopiles are used to detect flame and to obtain a signal for the control.

Regenerator. The regenerator is vertical and can be set outdoors as shown in Fig. 5. This arrangement has several advantages. It saves on building volume and on foundation height, and it reduces the heat rejection to the building somewhat. The regenerator forms a convenient base for a stack which is required to carry the exhaust to a height sufficient to prevent recirculation regardless of wind direction. The vertical tubes may collect less deposit from the combustion-gas stream. The disadvantage is that the regenerator insulation has to be weatherproof.

The regenerator weighs 125 tons. It has 5500 tubes $1\frac{1}{4}$ in. diam, which give 46,000 sq ft of surface area. It will return to the air stream 80 per cent of the available heat in the turbine exhaust gases as measured by the temperature difference between the turbine exhaust and the compressor exhaust. The exhaust gases flow inside the tubes, and the compressed air flows on the outside. The sum of the gas-side and the air-side pressure drop is 5 per cent of the absolute pressure.

Lube-Oil System. Lube oil is supplied from a 1000-gal tank located with its top at the operating-floor level. Normally a single vertical water-cooled lube-oil heat exchanger is supplied, but the tank and its associated equipment are so designed that two such oil coolers and a transfer valve also can be supplied when required. The transfer valve is arranged so that the oil flow can be transferred from one cooler to the other, and the tube bundle of the unused cooler can be removed for cleaning while the plant is in operation.

During normal operation when the unit is running, the lube oil is supplied by a positive-displacement pump driven by the gas-generator set through a gearbox called the accessory drive. An auxiliary electrically driven centrifugal pump capable of delivering sufficient lube oil for continuous operation is also furnished. This pump is used for normal starts and stops. It will start up automatically if the lube pressure should drop from the normal value of 25 psig to 12 psig so that it can be used also in place of the unit-driven pump to operate the unit until it is convenient to shut down to determine and fix the fault. A 2-hp centrifugal pump driven by a station battery also is supplied. This can be used for emergency starts when auxiliary power is not available. It will start up automatically, and the plant will be tripped out if the lube pressure drops to 8 psig. Thus it serves to bring the plant to standstill without damage to the bearings in case of loss of the other two pumps.

Starting Assembly. The plant is started by cranking, or driving it by a starting assembly located on the foundation above the

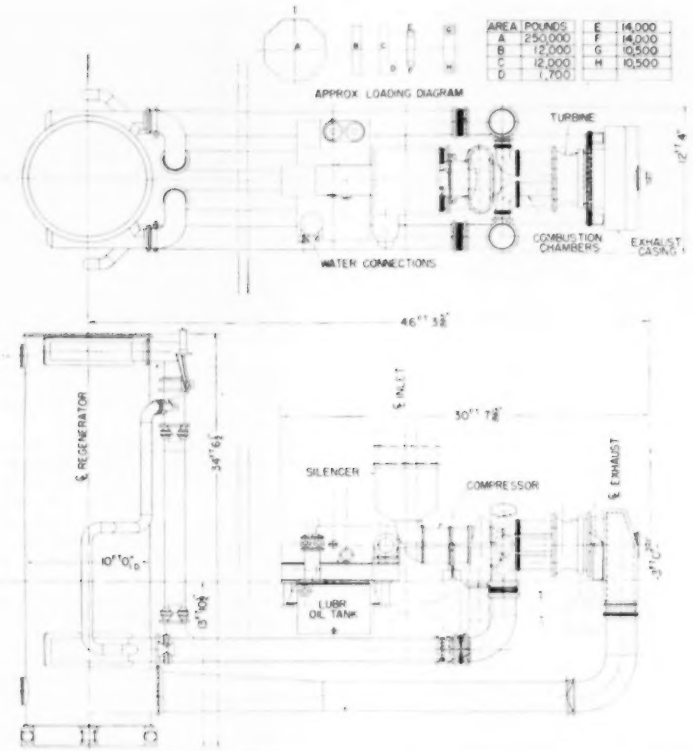

FIG. 5 OUTLINE AND FOUNDATION LOADING DIAGRAM OF 5000-HP REGENERATIVE-CYCLE GAS TURBINE

oil tank but not touching it. Two designs for the starter are available; one is powered by a turbine which can use any available gas, or steam, or air, and the other is powered with an 1800-rpm wound-rotor induction motor. The motor starter is connected through a speed step-up gear to the gas-generator set at the forward end of its compressor shaft. The turbine starter is direct-connected at the same point. Each starter is connected to the gas-generator set by an automatic engaging and disengaging jaw clutch. When starting the plant the clutch is engaged by means of a solenoid. The motion of the engaging member of the clutch operates a switch which starts the induction motor or the turbine as the case may be. When the gas-generator-set speed is sufficiently high the direction of torque through the clutch is reversed. This reversal aided by a spring disengages the starting assembly. An auxiliary generator up to a maximum rating of 125 kw can be mounted on the turbine-driven starting assembly so that it is driven by the gas-generator set in case house power is required.

Control. The unit speed and temperature are controlled as indicated on the block diagram in Fig. 6. A number of the devices indicated on the diagram and used for the control have been described before (10).

The fuel flow to the unit is regulated by a control valve which responds to give flow area about proportional to an oil pressure called "variable control oil pressure" (VCO). This valve, together with the pressure-ratio valve, which maintains at the control valve a fuel pressure that is proportional to the compressor discharge pressure, determines the fuel flow supplied to the unit. Since the plant air flow is roughly proportional to compressor discharge pressure, VCO pressure is roughly proportional to fuel-air ratio.

The VCO pressure and hence the fuel supplied is established by the speed signal from the load-turbine shaft-driven governor generator working through the governor. It is subject to being overridden and set to a lower value, however, as determined by the lowest requirement of either the starting-position solenoids or the thermal unit. The thermal unit using the exhaust-temperature signal establishes a VCO pressure such that a maximum exhaust temperature is not exceeded and also such that the increase in exhaust temperature does not exceed a sudden rise of 175 F (20 psi in VCO) followed by a rate of rise of 15 F per sec. The starting-position solenoids using the signal from the master control panel establish one of four possible VCO pressure limits. These four pressures, established either manually or automatically from the master control panel are selected to set suitable fuel limits during the following four steps when starting and stopping the plant:

1 Shutting down or tripping out the plant.
2 Firing the plant.
3 Accelerating the plant to idle speed, no load.

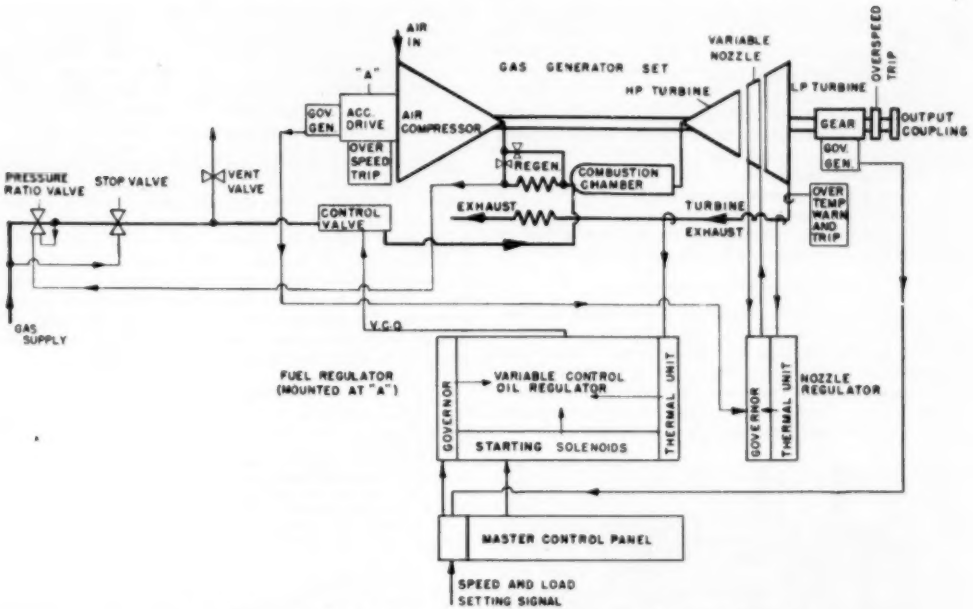

Fig. 6 Schematic Control Diagram of 5000-Hp Regenerative-Cycle Gas Turbine

4 Operating the plant over its normal range of load and speed.

The thermal unit, the governor, and the starting-position solenoids are contained in the fuel regulator in such a way that this device can produce a VCO pressure as described in response to the three signals of load-shaft speed, exhaust temperature, and starting or stopping requirements.

The nozzle regulator sets the turnable second-stage-nozzle partitions to hold substantially constant exhaust temperature in the following manner: The exhaust-temperature signal causes the thermal unit in the nozzle regulator to set a potentiometer in the governor circuit which establishes the proper speed-control point of the gas-generator set, which speed is the one required to hold the selected exhaust temperature. The governor in the nozzle regulator holds this control speed by opening or shutting the second-stage-nozzle partitions with oil pressure supplied to the hydraulic cylinders on the nozzle positioning ring.

The gas-generator-set speed is held by opening or shutting the second-stage nozzle, and the speed to be so held is selected by the thermal unit in the turbine-nozzle regulator. This is done rather than select a position of the nozzle directly from the temperature signal in order to limit the maximum and minimum speed of the gas-generator set by limiting the speed range available to the thermal unit.

At near full load the nozzle-regulator thermal unit reaches the end of its range which is determined by the maximum resistance which it can add to the governor circuit; thus the maximum speed of the gas-generator set is limited. As more load is put on the plant, the exhaust temperature rises until it intersects the control curve of the thermal unit in the fuel regulator. At this point the thermal unit in the fuel regulator prevents the fuel from being increased further. If still more load is added, the speed of the load turbine will fall until the load is reduced to the capability of the plant with this limiting fuel flow.

In starting up and shutting down the plant, whether an emergency or not, the variable-angle nozzle is set at a fixed wide-open position.

In addition to the foregoing normally operating controls and the devices supplied to care for certain abnormal conditions, there are the following emergency controls:

1 Load-turbine overspeed trip.
2 Gas-generator-set overspeed trip.
3 High exhaust-temperature trip.

These controls are entirely independent of the normal regulating controls and servos. They operate to shut down the plant and to indicate the cause when selected values of speed and exhaust temperature are reached.

The master control panel supplied with the plant and shown in Fig. 6 contains all the necessary devices and supervisory instruments to make the plant completely automatic. It should be possible to operate a plant of this kind unattended. When the reliability of these automatic features has been demonstrated and the proper telemetering equipment is added, the plant can be operated remotely in an unattended station.

The necessary signaling devices and relays are in the control panel to crank the unit, fire it, and bring it to speed. The required sequence of events can be controlled manually by means of a multiposition selector switch or the sequencing can be done automatically.

If any of a number of abnormal conditions occurs on starting, either the sequence of events will be interrupted and the machine will be shut down or the sequence will not begin. Examples of such conditions are as follows:

1 Failure to fire.
2 No battery voltage.
3 No voltage on lube-pump supply.

If any of a number of abnormal conditions occurs during oper-

ation, the plant will be automatically shut down. Examples are as follows:

1 Loss of flame.
2 High wheel-space temperature.
3 Low lube-oil pressure.

An annunciator in the master control panel sounds a warning and indicates the cause of any of a number of abnormal conditions existing, such as the following:

1 High bearing temperature.
2 Failure of vibration-recorder amplifier.
3 Auxiliary cooling-water pump not running when required.

The annunciator also indicates why the plant was shut down when it is shut down by any of the abnormal conditions.

Installation Requirements

Fig. 5 shows the outline dimensions, plant weights, and connections for a regenerative plant. Fig. 7 shows an installation of the plant as a drive for a gas pipe-line compressor. Some of the foundation can be seen in this view as well as the stacks on top of the regenerators, the evaporative precoolers, and air washers for the inlet air. The long room between the two units contains the master control panels and some electrical equipment.

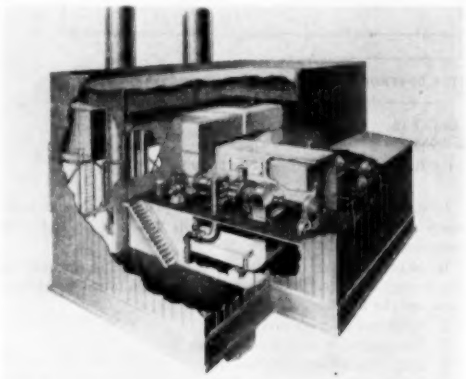

Fig. 7 Artist's Conception of Gas-Pipe-Line Centrifugal-Compressor-Drive Installation With Two 5000-Hp Regenerative-Cycle Gas Turbines

The concrete pilasters under the gas turbine are kept at about the same temperature as those under the gas compressor by blowing from 10,000 to 15,000 cfm of air lengthwise through the foundation spaces with a fan. This insures good line-up of the plant members.

The turbine shell is water-cooled to maintain good turbine clearances and to be able to make the shell of carbon steel. The cooling water is circulated in a closed system so that it can be clean, free from salts, and possibly rust-inhibited. To provide this closed system a small galvanized-steel tank assembled together as one unit with four connections with a heat exchanger and two small pumps is supplied with the plant. The over-all dimensions of this assembly are 26 in. wide × 66 in. long × 65 in. high. It can be located wherever convenient. Two connections are made to the turbine shell, 1¼-in. pipe size to the turbine and a 2-in. return, and two 2-in. pipe connections to external cooling water.

The water requirements for the turbine cooling as well as those for the lube oil are shown in Table 1.

TABLE 1 TURBINE COOLING AND LUBE-OIL REQUIREMENTS

	Water flow, gpm	Heat transfer, Btu per min
Turbine cooling-water heat exchange	100	9100
Lube-oil coolers	250	9400
Total	350	18,500

Acknowledgment

Naturally a great many persons besides the author contributed to the design of this plant. N. E. Starkey and his group, including A. Loft and J. Gatzmeyer, designed the control devices. Dr. C. J. Walker and his group, including C. M. Gardiner and T. N. Hull, designed the buckets and nozzles. C. S. Rice, F. Cummings, R. L. Jackson, G. W. Scheper, T. D. McKone, and many others contributed to the structural design and in other ways. It is sad that Chester Rice did not live to see the plant in operation. The speed and precision with which the design was accomplished is due in large measure to the help and encouragement of G. B. Warren and his staff and to Alan Howard.

BIBLIOGRAPHY

1 "Design Features of a 4800-Hp Locomotive Gas-Turbine Power Plant," by Alan Howard, *Mechanical Engineering*, vol. 70, 1948, pp. 301–306.

2 "Test of a 4800-Hp Gas Turbine Power Plant," by Alan Howard and Bruce Buckland, ASME Paper No. 48—A-98.

3 "Mechanical Investigations of Gas-Turbine Components," by Carl Schabtach, ASME Paper No. 48—A-47.

4 "Combustion System for Burning Bunker C Oil in a Gas Turbine," by Bruce Buckland and Donald Berkey, ASME Paper No. 48—A-109.

5 "A 4500-Hp Gas-Turbine-Electric Locomotive," by Arthur Morey and Robert Williamson, ASME Paper No. 49—A-46.

6 "3500-Kw Gas Turbine Raises Station Capability by 6000 Kw," by J. W. Blake and R. W. Tumy, *Power*, vol. 92, 1948, pp. 518–525.

7 "Huey Gas Turbine Ticks Off 3400 Hours," by J. W. Blake and R. W. Tumy, *Power*, vol. 94, February, 1950, pp. 96–101.

8 "The Combustion Gas Turbine and Its Application as a Prime Mover for Generation of Electric Power and Other Uses," by B. G. Hatch, AIEE Meeting, Dallas, Texas, April, 1949.

9 "A 5000-Kw Gas Turbine for Power Generation," by Alan Howard and C. J. Walker, ASME Paper No. 48—A-83.

10 "Control of Gas Turbines for Power Generation," by N. E. Starkey, D. C. Hoffmann and A. G. Mellor, Trans. AIEE, vol. 69, 1950, part 2, pp. 1637–1641.

Discussion

W. K. Bodger.[4] The authors are to be complimented on their worth-while contribution to the literature on gas turbines. Several of the design features are quite interesting and the writer will look forward to a report on operating experiences.

The expected performance shows clearly the virtue of the use of regeneration. In this design the full-load fuel flow is only about ⅔ of what it would be without heat recovery. It will be interesting to see whether the test performance entirely confirms the expectations. The most striking value of the regenerator, however, is in part-load operation, where 50 per cent load at 100 per cent speed corresponds to about 55 per cent of full-load fuel flow. In other words, at 50 per cent load, the efficiency has dropped only about 10 per cent.

No mention was made of the process of getting the gaseous fuel up to its inlet pressure. In some cases this compression work can be in the neighborhood of 10 per cent of the net power-plant output. In the application to gas-pipe-line pumping or repressurizing oil wells the fuel may be taken from the high-pressure line, but the prorated portion of the work still must be charged against the power plant.

[4] Associate Professor of Mechanical Engineering, Case Institute of Technology, Cleveland, Ohio. Mem. ASME.

Authors' Closure

Mr. Bodger has noted the good part-load performance of this power plant. Gas turbines with regenerators do have much improved part-load performance. In fact, by proper choice of cycle pressure ratio with the two-shaft machine it is possible to have the highest efficiency at reduced load.

Getting the gaseous fuel to the required inlet pressure (150 psig) is no problem for gas-pipe-line pumping units since the gas is already at a higher pressure. If natural gas must be compressed from atmospheric pressure the compression work required would reduce the output and thus increase the fuel rate of the plant about four per cent. With gases of lower Btu content the reduction in plant output is less. For blast-furnace gas, for example, if the required pressure is reduced to 100 psig a net gain in output of about three per cent could be realized. This is due to the extra weight flow that would pass through the turbine. However, the gain in output would be accompanied by about eleven per cent increase in fuel rate.

The authors wish to thank Mr. Bodger for his comments and interesting discussion.

Multistage Radial Turbines

By P. F. MARTINUZZI,[1] HOBOKEN, N. J.

There are many applications of radial-flow turbomachines, but this paper deals particularly with radial turbines for gas-turbine use. The possibility of building a multistage inflow turbine of a type in which all the stages are carried on a single rotor disk is examined.

Nomenclature

The following nomenclature is used in the paper:

A = flow-passage area
F = centrifugal force on blade
F_z = meridian projection of blade area (Zweifel)
G = gas flow, lb per sec
H = pressure head
M = bending moment on blade
R = degree of reaction
R_z = mean radius of blade area (Zweifel)
b = blade width
c = absolute velocity of gas
d = diameter
f = power factor in gas-turbine cycle
f_c = ratio between pressure head developed in rotating diffuser and input head
g = acceleration of gravity
h = blade width (Zweifel)
l = blade chord
p = pressure
r = radius
t = blade pitch
u = peripheral velocity
v = specific volume
w = relative velocity
z = number of blades

Angles:

α_0 — c_0 with u_0
α_1 — c_1 with u_1
α_2 — c_2 with u_2
β_1 — w_1 with u_1
β_2 — w_2 with u_2
δ — w_1 with w_2

Dimensionless coefficients:

$\zeta = \dfrac{\tau_d}{\varphi}$

$\lambda = \dfrac{r_2}{r_1}$ radius ratio of stage

$\Lambda' = \dfrac{r_1'}{r_1}$ radius ratio of successive stage entry to first stage entry

$\Lambda_t = \dfrac{r'_2}{r_1}$ total radius ratio of rotor, exit to entry

$\mu = \dfrac{c_{u2}}{u_0}$ for rotating diffuser

$\xi = \dfrac{u_1}{u_0}$ for rotating diffuser

$\tau_1 = \dfrac{c_{u1}}{u_1}$

$\tau_2 = \dfrac{c_{u2}}{u_2}$

$\tau_s = \tau_1 + \tau_2$
$\tau_d = \tau_1 - \tau_2$

$\varphi = \dfrac{c_m}{u}$

χ = ratio between dimensions of two different rotors
ψ_T = aerodynamic pressure coefficient (Zweifel)
γ = specific gravity
η = turbine efficiency
ω = angular velocity

Usual subscripts:

0 = compressor rotor exit (for rotating diffuser)
1 = stage entry
2 = stage exit
m = meridian (normal) component
u = tangential (peripheral) component
AD = adiabatic

Usual superscripts:

$'$ = second stage
$''$ = third (last) stage

Introduction

Radial-flow turbomachinery has many applications. Centrifugal pumps and centripetal turbines are frequently used in hydraulics; radial outflow steam turbines (Ljungström) are built in standard sizes in Europe. Centrifugal air compressors have many applications in industry, in gas turbines and in jet-propulsion units, while air or gas radial turbines, both of the outflow and of the inflow types, are used particularly for Diesel-engine turbosuperchargers, for cabin-pressurizing units or for other purposes in which the power required is low. This paper will deal more particularly with radial turbines for gas-turbine use.

The qualification "radial" indicates that the fluid passes through the turbine rotor mainly in a radial direction; though often the direction of flow at the low-pressure side is inclined or axial. This paper will refer to radial flow when the flow of the fluid is predominantly radial. While, in practice, radial compressors are always of the outflow (centrifugal) type, radial turbines can be either of the inflow (centripetal) or outflow (centrifugal) type, each having distinctive characteristics, advantages, and disadvantages. Multistage radial compressors are often used for industrial purposes, but they consist of several machines of similar design connected in series, so that they do not constitute a single multistage machine but rather a series of machines. The only well-known example of multistage radial machines is given by the radial steam turbines (Ljungström, Siemens) in which each

[1] Professor of Mechanical Engineering, Stevens Institute of Technology; formerly of Cornell University. Life Member ASME.

Contributed by the Gas Turbine Power Division and presented at the Fall Meeting, Minneapolis, Minn., September 25–28, 1951, of The American Society of Mechanical Engineers.

Note: Statements and opinions advanced in papers are to be understood as individual expressions of their authors and not those of the Society. Manuscript received at ASME Headquarters, July 11, 1951. Paper No. 51—F-15.

rotor actually carries several rows of blades; in the Ljungström type, there are two counter-rotating rotors.

Radial inflow turbines for air or gas are often considered as if they were inverted centrifugal compressors. It is actually possible to use a centrifugal compressor as an inflow turbine by blowing high-pressure air in the volute. Tests made in Europe with jet-engine compressors have shown that, when used as a turbine, they give a better adiabatic efficiency than when employed normally as compressors. Radial inflow turbines of this type are cheap to manufacture and rugged. They are subject to limitations similar to those which beset centrifugal compressors; and these are of two kinds:

(1) The enthalpy drop that can be handled by a given rotor is proportional to the square of the angular velocity; but so are the stresses due to centrifugal force, so that a limit to the enthalpy drop (and, hence, to the pressure head) is set by stress considerations.

(2) There is a severe lack of balance between the flow passage area at the low-pressure side and that at the high-pressure side of the rotor. The area available is much smaller at the inner (low-pressure) than at the outer (high-pressure) side. This is a drawback inherent in the radial design, and it is inconvenient in hydraulic machines in which the fluid has a constant specific volume. In air or gas machinery, the disadvantage is enhanced by the fact that the gas at the low-pressure side, where the available area is small, has a much greater specific volume than at the high-pressure side where the area is large. The pressure-head limitation, due to centrifugal force, is coupled with an inlet-passage area limitation due to variable specific volume. The inflow turbine is actually worse than the centrifugal compressor in this respect; the heating of the fluid, caused by losses in the rotor, increases the specific volume on the low-pressure side in the turbine, making matters worse.

The practical limit set to modern centrifugal compressors is a peripheral speed of about 1500 fps, to which corresponds a theoretical enthalpy rise of about 90 Btu for air. These extreme values are used only in aircraft engines; for industrial machines the maximum peripheral speed is about 1200 fps, corresponding to about 60 Btu for air.

The Multistage Rotor

As the "inverted-compressor-type" radial turbine cannot deal with large enthalpy drops, some new solution must be found. In this paper the possibility of building a multi-stage radial inflow turbine, of the type in which all the stages are carried on a single rotor disk is examined. It is obvious that, for a gas turbine working at high temperatures, only a rotor cast integrally with the blades can be taken into consideration; separate blades working in flexion (as in the Ljungström turbine) are not practical owing to the high heat and centrifugal stresses, while machining the blades out of a forged rotor would be very expensive.

The cast rotor is easy to make; the blades are untwisted and can be given a slight taper, so that getting the pattern out of the mold is quite simple. Casting allows full latitude in the choice of profile and pitch of the blades; and the different stages can have different profiles, chords, and pitches without complicating the operation in any way.

In practice, the last (inner) stage will not be purely radial, the mean meridian axis of the passages will be inclined relative to the radial direction; this inclination, useful to get the gas out of the turbine, must be kept within moderate limits to avoid the necessity of twisting the last blades for good efficiency, as the casting operation would then become very complicated. Modern cast high-temperature steels should be quite satisfactory, using precision casting; the price of this type of rotor should be much cheaper than that of a conventional axial rotor, and should be extremely low for quantity production.

It is now necessary to determine whether such a multistage rotor is feasible. A radial turbine has a great advantage over a compressor; acceleration of fluid can be effected efficiently within a very short length. There is no reason why radial-turbine blading should not give the same deflections as axial-turbine blading, i.e., at least 90 to 100 deg per stage. Actually, the deflection allowable in the radial turbine is greater than that at the mean diameter of an axial turbine; it will correspond to that allowed at the root of an axial blade. By using a suitably small pitch/chord ratio, the effects of the rotation of the gas in the rotor gas passages, so noxious in radial compressors, can be rendered negligible; the more easily because, as will be seen, the angular velocity must be kept low for reasons of stress. The effect of centrifugal force on the boundary layer of such a turbine, in-so-far as is known, has not been analyzed; but common-sense considerations show that it should be much less adverse than in axial turbines.

In general, the radial turbine should not be affected by the three-dimensional effect as much as the axial; there is no force due to rotation which will tend to disturb pressure equilibrium across the flow, except the friction between gas and stator wall, not important when the Reynolds number is high.

Considering the boundary layer in a typical rotor passage, Fig. 1, it will be seen that centrifugal force will have the effect of retarding the boundary layer, which is bad, but it will also tend to make it stick to the suction side of the passage, which is excellent, and unstick on the pressure side. To counteract the retarding action, the flow must be well accelerated in the rotor. For this reason, and also to lower maximum gas velocities and, consequently, obtain high stage efficiencies, velocity diagrams giving a high degree of reaction, near 0.5, will be preferable. The maximum peripheral velocity of this type of rotor is limited by the use of cast material and by the bending stress caused by centrifugal force on the blade root; given a reasonable gas temperature or suitable rotor cooling, the maximum permissible velocity will probably not be greater than 900 fps and would probably be kept smaller.

Fig. 1

The First Stage

If a multistage inflow rotor, of the type proposed, is studied in greater detail, it is necessary to examine what happens in one stage. The first (high-pressure) stage will now be investigated in some detail, and the results found for it can then be adapted to the other stages. If d_1 is the outside diameter of the rotor, it also will be the outside diameter of the first rotor stage; the inner diameter of the first stage will be indicated with d_2; the corresponding outer diameters for the second and third stages will be d'_1 and d''_1, and so on; the subscripts 1 and 2 indicating the inlet and exhaust conditions of each stage, the superscripts $'$ $''$ indicating the second and third stages, respectively (Fig. 2).

Considering now the first stage, the radial extension of the blade is $^1/_2(d_1 - d_2)$ and the blade width at entry is b_1, at the exit b_2. This radial extension is obviously a function of the chord l of

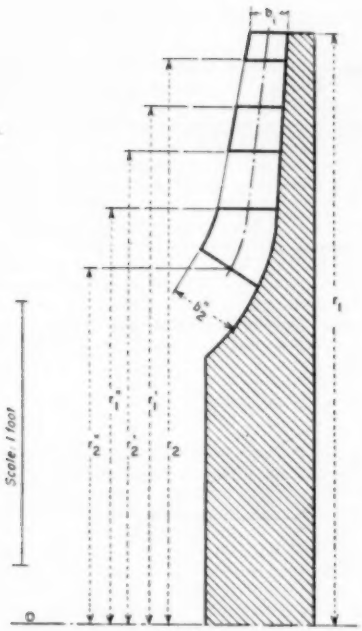

FIG. 2

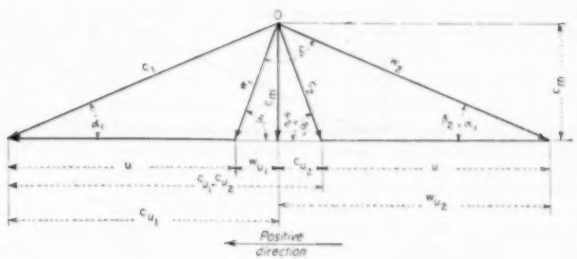

FIG. 3

the profile; and this in its turn depends on the aspect ratio b/l of the blade, and hence on the blade width.

To avoid excessive bending stresses at the blade root, b must be kept as small as possible; it will be shown later that, given the flow of gas G in lb per sec, the radial component of the velocity at entry c_{m1} and the rim peripheral speed u, the bending stress can be reduced at will by increasing d and decreasing b and the angular velocity ω. In practice, b_1 can be as small as possible, provided that the axial clearance between blade tip and stator wall remain small relative to the blade width (from 1 to 2 per cent of b_1). For mediumr or large industrial turbines, this gives the minimum value $b_1 = 1.5$ in. — 1.75 in. Once b_1 is determined, the chord is also determined by the consideration that the aspect ratio b_1/l of the blade should be greater than 1; but not too much greater, because a small chord implies a small moment of inertia at the blade root, and consequently high bending stresses; preferably, b/l should be between 1.2 and 1.5. Given the chord l and the velocity triangles, the radial extension $^1/_2(d_1 - d_2)$ is then determined and, consequently, also the diameter ratio $\lambda = d_2/d_1$. If all the considerations outlined are taken into account, λ for the first stage will very probably come out very near unity (say, $\lambda = 0.95$ or so).

For the reasons given regarding the boundary layer, a good amount of acceleration in the rotor passages is advisable. There is, of course, a wide latitude of choice; but, if it is assumed that the velocity diagram selected corresponds as nearly as possible to a 0.5 reaction axial diagram, then results will certainly be satisfactory, and the calculations will be simplified. In such a diagram, Fig. 3, the absolute velocity of the gas entering the rotor c_1 is symmetrical to the relative velocity leaving the rotor w_2, and the relative velocity entering the rotor w_1 is symmetrical to the absolute velocity leaving the rotor c_2. The deflection angle δ is the angle between w_1 and w_2. As is well known, in any turbine stage, radial or axial, the work done per pound of gas flowing per second is

$$H_{AD} = \frac{1}{g}(c_{u1}u_1 - c_{u2}u_2) \quad \ldots\ldots [1]$$

where u_1 and u_2 are the inlet and exit peripheral velocities, c_{u1} and c_{u2} the tangential components of the absolute velocities c_1 and c_2. In an axial turbine, $u_1 = u_2 = u$ and the work becomes $H = (u^2/g)\tau_d$, where $\tau_d = \tau_1 - \tau_2$ and $\tau_1 = c_{u1}/u$, are the dimensionless whirl coefficients (considered positive if in the direction of u_1). For a given u, the work H (which is equivalent to the adiabatic enthalpy drop) increases with τ_d. The maximum allowable τ_d depends upon the maximum allowable deflection δ (δ varies in general between 70 and 110 deg for a reaction turbine) and on the dimensionless flow coefficient $\varphi = c_m/u$ where c_m is the meridian component of the absolute velocity (axial in an axial turbine; radial in a radial turbine). The deflection is obviously a function of the deflexion coefficient $\zeta = \tau_d/\varphi$. In a radial stage having characteristics as near as possible to those of a 0.5 reaction axial stage, the same absolute velocity angle at entry α_1 can be chosen; but probably the radial component c_m at entry will be smaller than that of the corresponding axial stage, for reasons which will be seen later.

Given d_1 and c_{m1}, the velocity c_1 is determined and, consequently, also w_1, because its peripheral component $w_{u1} = c_{u1} - u_1$. Up to this point, the triangle is geometrically equivalent to that of the axial turbine; but it is impossible to make the other triangle (w_2, c_2) equally equivalent, because u_2 is smaller than u_1, and the condition $c_{u2} = u_2 + w_{u2}$ must be satisfied.

Also, while in an axial turbine stage c_m is generally constant, in a radial turbine it will tend to increase, because the flow-passage area $A = \pi db$ decreases, while the specific volume of the fluid increases. There is consequently again a great latitude of choice; but calculations are considerably simplified, and a satisfactory solution is found, if the assumption is made that the radial component c_m is inversely proportional to the diameter not only in the stage but along the whole turbine rotor

$$c_m d = c_{m1}d_1 = c_{m2}d_2 = \text{const.} \quad \ldots\ldots [2]$$

This assumption implies that, to satisfy the continuity condition, the width of the blades increases proportionally to the specific volume of the gas v, that is

$$\frac{v}{b} = \beta = \text{const.} \quad \ldots\ldots [3]$$

These two assumptions give a reasonable shape to the gas passage along the turbine.

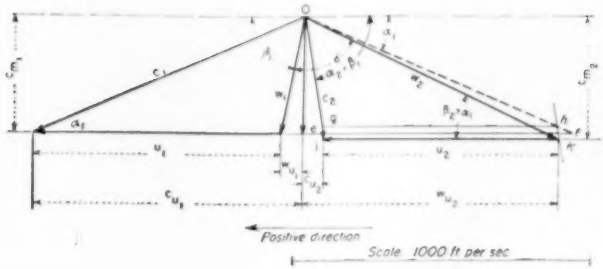

FIG. 4

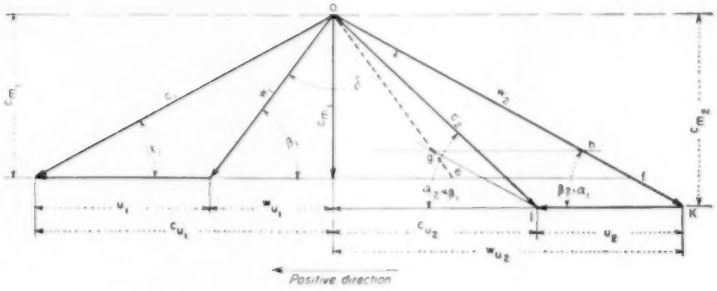

FIG. 5

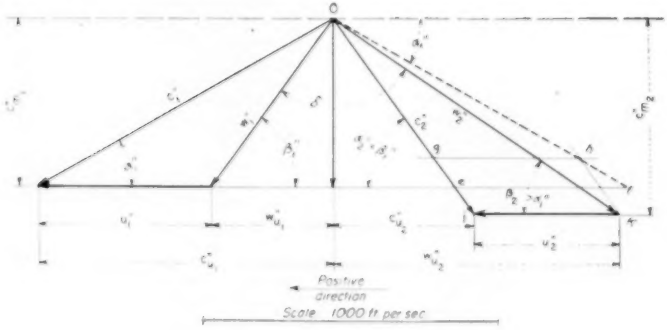

FIG. 6

With these assumptions, $c_{m2} = c_{m1}/\lambda$ and $\varphi_2 = c_{m2}/u_2 = \varphi_1/\lambda^2$. As w_1 and c_2, w_2 and c_1 cannot both be symmetrical, there is the choice of having either w_1 and c_2 symmetrical (that is, $\beta_1 = \alpha_2$) Fig. 4, or w_2 and c_1, that is, $\beta_2 = \alpha_1$, Fig. 5.

In the first case (Figs. 4 and 6), the diagram for the radial turbine can easily be determined graphically from the equivalent axial diagram by tracing c_1, w_1, c_{m1} and c_{m2}; c_2 will be determined by the meeting point of the horizontal from c_{m2} and the line symmetrical to w_1. If an auxiliary horizontal is traced at a distance λc_{m1} from the pole, and segment $ef = u_1$, then obviously segment $gh = \lambda u_1 = u_2$. Tracing from point h a line parallel to c_2, it will cut the horizontal through c_{m2} at a point k, and segment $jk = gh = u_2$. Obviously, then, w_2 will be the vector joining the origin 0 with point k; β_2 will be greater than α_1.

The work is, as usual, given by Equation [1]; but in this case, $u_2 = \lambda u_1$, while Fig. 6 shows that $c_{u2} = c_{u2}^0/\lambda$, where c_{u2}^0 is the tangential component of c_2 in the axial (symmetrical) diagram; consequently

$$H_{AD} = \frac{1}{g}\left(u_1 c_{u1} - \lambda u_1 \frac{c_{u2}^0}{\lambda}\right) = \frac{u_1}{g}(c_{u1} - c_{u2}^0)$$

$$= \frac{u_1^2}{g}(\tau_1 - \tau_2)$$

where τ_1 and τ_2 are those of the axial diagram. τ_1 is the same for the axial and the radial turbine, and, in an axial 0.5 reaction diagram, $\tau_a = \tau_1 + \tau_2 = 1$; hence $\tau_2 = 1 - \tau_1$ and

$$H_{AD} = \frac{u_1^2}{g}(2\tau_1 - 1) = \frac{u_1^2}{g}\tau_d \text{ where } \tau_1 = c_{u1}/u_1 \ldots [4]$$

both for the axial and the radial turbine. Consequently, it will be seen that, if the diagram in Fig. 4 is chosen ($\beta_1 = \alpha_2$), the radial stage gives the same work per pound of fluid as the equivalent axial stage. It will be seen from Fig. 4, $\beta_2 > \alpha_1$, hence the deflection $\delta = (\pi - \beta_1) - \beta_2$ for the radial is smaller (more favorable) than for the corresponding axial. The difference between β_2 and the corresponding value for the symmetrical diagram is small, about 2 to 5 deg.

If the other type of diagram, with $\beta_2 = \alpha_1$, is chosen, Fig. 5, then the deflection is the same both in the symmetrical and in the radial diagram; $\delta = (\pi - \beta_1) - \beta_2$. The unknown is now c_2; as segment gh still represents u_2, if segment gj parallel to segment hk is drawn, c_2 is given by the vector connecting the origin 0 with point j. For the diagram in Fig. 5, $c_{w2} = w_{w2} + u_2$ and it is obvious that $w_{u2} = c_{u1}/\lambda$; it can easily be seen that the Equation [1] becomes

$$H_{AD} = \frac{u_1^2}{g}(2\tau_1 - \lambda^2) \ldots [5]$$

and is slightly greater than the corresponding value in Equation [4]. The deflection in the case of Fig. 5 is the same as that of the symmetrical diagram. The diagrams in Figs. 4 and 5 are about equivalent from the aerodynamical and thermodynamical points of view; other equivalent diagrams could be drawn by making other assumptions. However, the diagram in Fig. 4 has the advantage of being easy to calculate and draw and of permitting an immediate comparison with axial turbines and the "inverted centrifugal-compressor type" (for which $\tau_1 = 1$). Throughout the remainder of this paper, it will be assumed that all multistage inflow diagrams are built according to Fig. 4.

Other Stages

In axial turbomachines it is quite usual to have a certain number of stages with similar diagrams, so that the absolute inlet velocity in the stator of one stage c is equal to the absolute outlet velocity from the rotor of the preceding stage, while c_m remains constant in all the stages of the group. It is manifestly impractical to do the same in a multistage radial turbine; the number of blades in the lower pressure stages must be smaller, as there is less room for them; the blade width increases owing to the increase of specific volume (according to Equation [2] with our assumptions), consequently, the blade chord must also increase, to resist the increased bending moment, as will be seen later. The radial extension will increase in the successive stages while the outer diameter d_1 will decrease; hence the diameter ratio λ will decrease passing from one stage to the other and might become $\lambda = 0.85 \div 0.9$ in the last stage. As will be seen, four stages seem the maximum practical number for any but the largest rotors. In Fig. 1 and the following examples three stages have been chosen.

The outer radius r_1' of the second stage will be equal to the inner radius r_2 of the first stage minus the radial extension of the second stator stage and of the two radial clearances between stator and rotor; in general $r_2 - r_1' > r_1 - r_2$. $\Lambda' = d_1'/d_1$ will show the ratio between the outer diameter of the second stage and the outer diameter of the first stage, $\Lambda'' = d_1''/d_1$, etc. Given the radial extension $r_1' - r_2'$ for the second stage, $\lambda' = d_2'/d_1'$ will give the radial ratio of the second stage, $\lambda'' = d_2''/d_1''$ that of the third stage, etc. In general $\lambda > \lambda' > \lambda''$ and $\Lambda' > \Lambda''$, etc., and also $1 - \Lambda' < 1 - 2\lambda''$, $1 - \Lambda'' < 1 - \Lambda' - 2\lambda''$, etc.

The total rotor diameter ratio between the inner diameter of the last stage and the outer diameter of the first is obviously $\Lambda_2 = \Lambda''\lambda''$ for three stages, $\Lambda_3 = \Lambda'''\lambda'''$ for four stages. Given the ratio Λ and λ for all stages, the peripheral velocities are immediately given by $u_1' = \Lambda' u_1$, etc.

$u_2' = \lambda'\Lambda' u_1$, etc; $c_{m1}' = c_{m1}/\Lambda'$, etc.; $c_{m2}' = c_{m2}/(\Lambda'\lambda')$, etc; $\varphi_1' = \varphi_1/\Lambda'^2$, etc; $\varphi_2' = \varphi_1/(\Lambda'^2\lambda'^2)$, etc.

It is obviously desirable to have each stage give about the same amount of work. From Equation [4] it will be seen that H_{AD} for each stage is proportional to the square of the peripheral velocity at the outer stage diameter; that is, to $\Lambda^2 u_1^2$, where the appropriate Λ is inserted for each stage. This would at first lead one to expect a rather alarming decrease in the work per stage, but in reality it is not so. The decrease in peripheral velocity is compensated by an increase in the tangential whirl component, and it can be seen that constant adiabatic work per stage can be maintained without loading the blades too much. If Λ'' is the diameter ratio for the last (third) stage, to have equal work in all stages according to Equation [4], it must be

$$H_{AD} = H_{AD}'' = \frac{\Lambda''^2 u_1^2}{g}(2\tau_1'' - 1)$$

hence

$$\tau_d'' = 2\tau_1'' - 1 = \frac{2\tau_1 - 1}{\Lambda''^2} = \frac{\tau_d}{\Lambda''^2}$$

and

$$\tau_1'' = \frac{\tau_1}{\Lambda''^2} - \frac{1 - \Lambda''^2}{2\Lambda''^2} < \frac{\tau_1}{\Lambda''^2}$$

But, while τ_d and τ_1 increase, also φ_1 increases, $\varphi_1'' = \varphi_1/\Lambda''^2$ so the deflection coefficient $\zeta'' = \tau_d''/\varphi_1'' = \frac{\tau_d}{\varphi_1}\frac{\Lambda''^2}{\Lambda''^2} = \zeta$ remains constant, and the angle β_2 actually increases as $\beta_2 > \alpha_1$ for this type of diagram and

$$tg\,\alpha_1'' = \frac{\varphi_1''}{\tau_1''} = \frac{\varphi_1}{\tau_1 - \frac{1 - \Lambda''^2}{2}}$$

The actual deflection angle δ'' is in general greater than δ, because β_1 decreases more rapidly than β_2 increases, and $\delta'' = (\pi - \beta_1'') - \beta_2''$. It can easily be shown that

$$\beta_1'' = \frac{\varphi_1}{\tau_1 - \frac{1 + \Lambda''^2}{2}}$$

But the increase in deflection angle is not great, about 15 — 30 deg between first and last stage.

Fig. 6 represents the last-stage diagram for $\Lambda'' = 0.7$, first-stage conditions as in Fig. 4, and equal work per stage. Of course, there is no need to satisfy strictly the equal work per stage condition, or the condition that the degree of reaction should remain 0.5. If an excessive load on the blades of the last stages requires it, the adiabatic work per stage H_{AD}'' can be slightly decreased by decreasing τ_d''; or H_{AD} and τ_d can be kept constant, but the degree of reaction can be increased to cope with the increased loading per blade. But even the simplest solution, as given by Figs. 4 and 6, is perfectly possible without exceeding at the inner stage the maximum deflections usual in axial turbines.

Stresses and Rotor Dimensions

The stresses in the rotor disk are the same as those in a compressor disk and are calculated in the usual way; they are of course proportional to u_1^2; the additional stress in the disk due to the weight of the blades is usually calculated by assuming an

artificial increase in the specific gravity of the disk proportional to the increase in disk weight due to the blades. The permissible maximum peripheral velocity u_1 will then depend on the material chosen, the temperature, the life expected of the rotor, and so forth.

The stresses at the blade root are of two kinds: bending and shear. The force causing these stresses is the centrifugal force applied to the blade

$$F = \frac{\gamma b S u_1^2}{g r_1} = \frac{\gamma b S}{g} \omega^2 r_1 \quad [6]$$

where γ is the specific weight of the material and S is the area of the blade profile (which remains constant along the whole blade); actually, u and r should be intermediate between r_1 and r_2, but taking u_1 and r_1 simplifies calculations and gives a margin of safety. The shear stress is obviously

$$s_c = \frac{F}{S} = \frac{\gamma b}{g} \frac{u_1^2}{r_1} = \frac{\gamma b}{g} \omega^2 r \quad [7]$$

and for a given u_1, is proportional to b_1 and inversely proportional to r_1. The bending moment is

$$M = F \frac{b_1}{2} = \frac{\gamma b_1^2 S u_1^2}{2 g r_1} = \frac{\gamma b_1^2 S}{2g} \omega^2 r_1 \quad [8]$$

proportional to b_1^2 and inversely proportional to r_1.

The maximum bending stress will depend on the section modulus Z of the profile relative to a radial axis. This depends not only on the profile chosen, but on its inclination (stagger) relative to a radial axis. For a given profile, the greater the stagger, the greater obviously will be the maximum stress. It must be noted that the forces exerted by the gas on the blade have a radial component directed toward the center, as may be seen in Fig. 1. This force gives a moment opposed to that due to centrifugal force. But this centripetal component is small in the first stage, which has many small blades working at high speed; so it is better to neglect this compensating moment.

The foregoing considerations refer to any dimension b_1, r_1, etc. For a given turbine, that is, a given power, enthalpy drop, temperature, and so forth, the width of the first-stage blades b_1 is determined by the gas flow G in pounds per second, by the specific volume v_1, by the meridian velocity c_{m1} and by the diameter d_1; then

$$c_{m1} = \frac{G v_1}{\pi d_1 b_1} \quad \text{and} \quad b_1 = \frac{G v_1}{\pi d_1 c_{m1}}$$

The width b_1 is inversely proportional to d_1 when G, v_1, and c_{m1} are constant; but also u_1 is constant (this is one of the fundamental assumptions). In this case, an increase of d_1 to $\chi d_1 (\chi > 1)$ will reduce b_1 to b_1/χ and Equation [6] gives

$$F^* = \frac{\gamma S u_1^2}{g} \frac{b_1}{\chi} \frac{\chi}{r_1} = F$$

and Equation [7] shows that the shear stress is constant; it is generally negligible. From Equation [8], it follows that

$$M^* = \frac{\gamma S u_1^2}{2g} \frac{b_1^2}{\chi^2} \frac{\chi}{r_1} = \frac{M}{\chi} < M^*$$

the bending moment is far from negligible but it is fortunately possible to decrease it at will by increasing the diameter and decreasing the angular velocity ω assuming a constant profile and section modulus. Obviously, the only limit to this increase in diameter is the condition $b_1 \geq 1.5$ in. and $b/l \geq 1$.

For industrial or marine turbines, a large diameter is not a disadvantage, on the contrary, with a given peripheral velocity it gives a low rate of revolutions. For instance, for $u_1 = 850$ fps and $n = 3600$ rpm, $d_1 = 4.5$ ft. A large diameter gives more room for several stages while keeping the total diameter ratio Λ_t between first-stage entry and last-stage exit large, thus allowing plenty of room for the exhaust gas and reducing the leaving loss, as the meridian exit velocity is $c_{m2} = c_{m1}/\Lambda_t$.

Once the conditions for the first stage are determined by choosing b_1 and d_1, the angular velocity $\omega = u_1/r_1$ is determined. The forces F', F'', etc., and the moments M', M'', etc., in the second, third, etc., stages become, from Equation [6] and [8]

$$F' = \frac{\gamma b_1' S'}{g} \omega^2 r_1' = \frac{b_1' S'}{b_1 S} \Lambda' F$$

and

$$M' = \frac{\gamma b_1'^3 S'}{2g} \omega^2 r = \frac{b_1'^3 S'}{b_1^3 S} \Lambda' M$$

It has already been assumed, in Equation [3], that the blade width along the rotor is proportional to the specific volume. The law of variation of the specific volume depends on the thermodynamic expansion in the turbine; v will certainly increase when the diameter decreases, and, as a first rough approximation, it can be assumed that v varies in inverse proportion to the diameter, hence

$$v_1' = \frac{v_1}{\Lambda'}, \text{ etc., and } b_1' = \beta v_1' = \frac{b_1}{\Lambda'}, \text{ etc.}$$

If it is further assumed that the profile area S remains constant it follows that

$$F_1' = \frac{b_1'}{b_1} \Lambda' F = F \quad M' = \frac{b_1'^2}{b_1^2} \Lambda' M = \frac{M}{\Lambda'}$$

With these assumptions, the shear stress remains constant and the bending moment increases from the first to the last stage, although the peripheral velocity decreases in the ratio Λ''; this shows that it is very unsafe to assume that stresses vary with u^2.

In practice, the bending stress can be easily kept constant by using larger chords and thicker profiles, (justified by the greater deflections and aerodynamic loads) with consequent greater moments of inertia. The last stages will have a larger chord and, consequently, a larger pitch; the circumferential space available is smaller, so that there is room for fewer blades. But the work done by all stages is approximately equal, and the radius of the last stages is small. For all these reasons, the aerodynamic resultant acting on each blade of the last stages is far from negligible, and its radial component, directed toward the center, counteracts to a considerable extent the centrifugal bending moment. Also, the last stages work at lower temperatures which allows higher stresses.

The Turbine

It is now possible to examine the design of a multistage turbine calculated according to the foregoing assumptions. Given the power, the total adiabatic enthalpy drop H_{TOT}, the flow G, the state of the gas at entry in the turbine, the presumed adiabatic efficiency of the turbine η, it is possible to determine the state of the gas at the exit of the last stage and hence v_2''.

The exit meridian velocity c_{m2}'' determines the leaving velocity and the leaving losses. If the inflow turbine is used alone, or is followed by a reheater, the leaving velocity c_2'' must be kept small; in that case c_{m2}'' and c_{u2}'' will have to be small, and the power obtainable from the last stage and from the turbine will be reduced. But the inflow turbine can be followed by an axial, running at

higher rpm and driving all or some of the compressors, with a curved stator between the two. This solution, which gives the best combination and the most compact machine, permits higher leaving velocity, c_{m2}'' and c_{u2}'', and high total power. Equal work per stage can easily be obtained. Given c_{m2}'' and the exit specific volume, the width b_2'' of the last stage can be determined, while that of the first stage and the outside diameter d_1 are chosen for stress as seen previously. The ratio $\frac{b_2''}{b_1}$ is the inverse ratio of the entry and exit specific volumes. The radial extension and the different λ and Λ ratios are chosen after considering the profiles and the blade chords desired, the chords being increased from the outer to the inner stages. In practice, the ratio b_2''/b_1 comes out very near Λ_t; it is actually possible to set $b_2''/b_1 = \Lambda_t$, but then Λ_t becomes slightly smaller than it would be otherwise. In this way the main dimensions are defined.

There are no particular difficulties about the stator; this will also be a casting carrying integral radial untwisted blades, and very easy and cheap to make. From the mechanical point of view, the radial turbine has the great advantage that all pieces are symmetrical relatively to the axis of rotation, and so are the joints, hence the risk of deformations due to heating is much reduced.

The first stator stage can, of course, have a much smaller diameter d_0/d_1 than it would have in a centrifugal compressor, which means that the outside diameter will not be excessive. The gas can enter with a certain whirl. If several combustion chambers are used, multiple symmetrical entries are preferable.

In some single-stage radial inflow turbines for Diesel-engine turbosuperchargers, there have been difficulties owing to uneven velocity distributions from the stator, with consequent loss of efficiency. This is undoubtedly due to the fact that, in a turbosupercharger, the different stator sectors are fed by different engine cylinders. All the same, even in pure gas turbines, attention must be paid to even gas pressure and velocity distribution before the stator, by appropriate study of the inlet volute. Attention also must be paid to making the axial clearance between rotor and stator small at all temperatures. Fortunately, both elements being of similar cast material and the hotter blades being the shorter, reasonably constant clearances can be expected.

Efficiency, Pitch, and Reaction

In the foregoing expressions, velocities, pressure heads, work, and so forth, are the theoretical values. They must be corrected for losses, and the losses can be calculated according to the usual methods: pressure-loss coefficients, drag/lift ratios, velocity coefficients, and the like, just as would be done for axial turbines having similar Reynolds and Mach numbers and deflections.

Existing test results can be used; cascade tests particularly should give very reliable indications in radial turbines of this type because, as has been seen already, there is no tri-dimensional effect. Of course, it would be advisable to make special blading tests for this type of turbine. Curved cascades can be used, but much better results should be obtained by means of tests with a rotating model turbine.

The author has studied a simple and cheap special rotating test rig which can give a great variety of data (blade profile, pitch and chord, axial and radial clearance, etc.), under very flexible conditions and with the use of small quantities of air at low pressure. The question of radial clearances is important. Large clearances should be good, as they prevent mutual induction between stator and rotor blades, improve smoothness and evenness of flow, and reduce the danger of vibration (smaller in the radial because the blades are shorter). On the other hand, too-large clearances cause Λ_t to become too small. Also, these clearances influence stage-diagram design.

In an axial turbine, the absolute exit velocity from one row of blades is equal in value and direction to the absolute inlet velocity in the next row whatever the axial clearance. In a radial turbine, this is not true; the absolute velocity leaving one blade differs in value and direction from the absolute velocity at entry of the next row, and the difference increases with increasing radial clearances. This is due to the fact that the fluid, moving toward the center of the rotor, must retain constant angular momentum in the clearance space, where there is free vortex distribution. The entry velocity can be calculated easily from the preceding exit velocity, with methods similar to those employed to find the velocities at entry of the diffuser in centrifugal compressors.

It must also be observed that each centrifugal stage of a centripetal inflow turbine behaves substantially like an inverted centrifugal compressor, in which the transformation of work into pressure in the rotor is due only in part to aerodynamic forces, which are necessarily connected with aerodynamic losses, while the other part is effected directly by the centrifugal field. For all these reasons, the adiabatic efficiency of a well-designed multistage radial inflow turbine should be at least equal, and probably higher, than that of an axial turbine of similar power.

The selection of an appropriate pitch for the different rows of blades and the appropriate pitch/chord ratio t/l can be effected by means of the method given by Zweifel.[9] At the end of his paper, Zweifel gives three expressions for the aerodynamic blade-load coefficient ψ_T for general turbomachine blading; ψ_T is given as function of $S_x = \int R dF = F_x R_x$ (in Zweifel's nomenclature) where F is the meridian projection of the blade surface, and R_x is the distance of the center of gravity of this area to the axis. Also, the number of blades z and the pitch t are given. The first of Zweifel's three expressions, transcribed in the nomenclature and sign convention used in this paper, becomes

$$\psi_T = \frac{4\pi r_2 b_2 c_{m2}}{z S_x w_2^2} (r_1 c_{u1} - r_2 c_{u2}) \quad \ldots\ldots [9]$$

The number of blades z and the pitch t are obviously connected by

$$2\pi r_2 = t_2 z \quad \ldots\ldots [10]$$

For radial inflow bladings of the type discussed in the foregoing, and shown in Figs. 4 and 6, obviously $l_2 = \lambda l_1$; w_2 is very nearly equal to c_1 (the difference is negligible in size, but not in direction) so that

$$w_2^2 = c_1^2 = c_{m1}^2 + c_{u1}^2 = c_{m1}^2 (1 + \cot^2 \alpha_1)$$

with the usual approximate assumption that the specific volumes increase in inverse ratio to the diameters, it is obviously

$$F_x = \frac{b_1 + b_2}{2} (r_1 - r_2) = \frac{b_1 (1 + 1/\lambda)}{2} r_1 (1 - \lambda) = \frac{b_1 r_1}{2\lambda} (1 - \lambda^2) \quad \ldots\ldots [11]$$

and

$$R_x = \frac{r_1 + r_2}{2} = \frac{r_1}{2} (1 + \lambda) \quad \ldots\ldots [12]$$

[9] "The Spacing of Turbo-Machine Blading Especially With Large Angular Deflection," by O. Zweifel, *Brown, Boveri Review*, vol. 32, 1945, pp. 436–444.

so that

$$S_c = \frac{b_1 r_1^2}{4\lambda}(1-\lambda^2)(1+\lambda) \quad [13]$$

Remembering that $r_1 c_{m1} = r_2 c_{m2}$ and that $c_{a1} - c_{a2} = u_1 \tau_d$ and $c_{m1} = u_1 \varphi_1$, it follows from Equations [9], [10], and [13] that

$$\psi_T = \frac{8\lambda l_1 b_1 c_{m1} r_1 (c_{a1} - c_{a2})}{b_1 r_1 g c_{m1}^2 (1 + \cot^2 \alpha_1)(1-\lambda^2)(1+\lambda)}$$

$$= \frac{8 l_1 \tau_d \lambda}{r_1 \varphi_1 (1 + \cot^2 \alpha_1)(1-\lambda^2)(1+\lambda)} \quad [14]$$

and, consequently

$$t = \frac{\psi_T r_1 \varphi_1}{8 \tau_d \lambda}(1 + \cot^2 \alpha_1)(1-\lambda^2)(1+\lambda) \quad [15]$$

where t_1 is given in feet if r_1 is in feet. As Zweifel shows, minimum losses are obtained for $\psi_T = 0.8$. At first it might appear as if Equation [15] gave the pitch t_1 and not the pitch/chord ratio; but of course the radial projection of the chord is given by $r_1(1-\lambda)$. The pitch in radial turbines is constant along the whole blade, while it decreases from tip to hub in axial turbines; the radial is consequently in a better situation in this regard.

The degree of reaction is the ratio between rotor pressure head and stage pressure head. The rotor head is given by the difference in energy between relative entering and leaving velocity plus the work against the centrifugal field, consequently

$$R = \frac{w_2^2 - w_1^2 + u_1^2 - u_2^2}{2(c_{a1} u_1 - c_{a2} u_2)} \quad [16]$$

For the type of blading in Figs. 4 and 6, this becomes

$$R = \frac{c_{m2}^2(1 + \cot^2 \beta_2) - c_{m1}^2(1 + \cot^2 \beta_1) + u_1^2(1-\lambda^2)}{2u_1^2 \tau_d}$$

$$= \frac{\varphi_1^2[1 + \cot^2 \beta_2 - \lambda^2(1 + \cot^2 \beta_1)] + \lambda^2(1-\lambda^2)}{2\tau_d \lambda^2} \quad [17]$$

The symmetrical axial diagram on which Figs. 4 and 6 are based has $R = 0.5$, but the radial diagrams have a slightly higher degree of reaction, $R = 0.515 - 0.65$, owing to the influence of the work against the centrifugal field. This is a function of λ, so R increases from the first to the last stage. An increase in R is favorable.

A Numerical Example

An actual calculation of a multistage radial inflow turbine for a gas turbine shows the advantages of this type. The cycle has a maximum temperature of 1340 F, with a compression ratio of 5.75, a work factor (useful work/total work) of 0.394 and a flow of 89 lb per sec. The radial turbine constitutes the high-pressure stage and is immediately followed by an axial turbine moving at higher rotational speed. Figs. 2, 4, and 6 give (to the scale indicated) the dimensions of the rotor and the velocity diagrams for the first and last stage.

The speed of rotation is 3600 rpm; $d_1 = 4.5$ ft; $u_1 = 850$ fps; $\lambda = 0.953$; $\tau_d = 1.162$; $c_{m1} = 390$ fps; $\delta = 75° 20'$; $\Lambda'' = 0.7$; $d_1'' = 3.15$ ft; $u_1'' = 595$ fps; $\tau_d'' = 2.37$; $\lambda'' = 0.856$; $c_{m1}'' = 650$ fps; $\Lambda_1 = 0.6$; $\delta'' = 93° 30'$.

The exit velocity c_{m2} is only permissible because the leaving energy is fully utilized in the next axial. The deflections are moderate. The first-stage blading has a chord $s = 1.5$ in., a blade length $b = 1.7$ in.; the pitch/chord ratio according to Equation [15] is $t/s = 1.13$; the last stage has a blade length $b'' = 3.05$ in., $s'' = 2.3$ in., and $t''/s'' = 0.96$. The theoretical work per stage according to Equation [4] is $H_{AD} = 33.8$ Btu, so that the total theoretical work is $H_{TOT} = 101.4$ Btu. An "inverted centrifugal" running at the same speed would only give $H_{AD} = u^2/(gJ) = 29$ Btu; so that the multistage turbine gives 3.5 times the work! With an expected turbine efficiency of 88 per cent, the power output 11,200 hp, the useful work of the cycle is 7500 hp, so that 3700 hp are available on the high-pressure shaft to drive part of the compressors (for instance, a high-pressure centrifugal). (The equivalent "inverted centrifugal turbine" would only give one half the useful power.) The low-pressure high-speed axial turbine would drive the low-pressure axial compressors. This example shows that the multistage inflow turbine is eminently suitable for high-power industrial turbines; and it might even be possible to use it for large aircraft turbines.

Rotating Diffuser Compressor

The centrifugal multistage turbine is, of course, represented by the Ljungström and similar types of steam turbines. They are very suitable for steam because the passage areas increase from the high-pressure to the low-pressure stages, and thus follow the large increases of specific volume. The Ljungström turbine is thoroughly well known; also, it seems unlikely that it can find application in gas turbines because of the high temperatures and the small increases in specific volume.

Recently, a very interesting application of the centrifugal multistage turbomachine has arisen: the combination of a compressor stage with a turbine stage, Fig. 7. The machine looks like an ordinary centrifugal compressor, but with a rotating diffuser. Both turn in the same direction, the diffuser at lower rpm; the two shafts are usually independent. The first idea of such a machine and of its applications to the gas turbine seems to be due to Mr. F. A. M. Heppner,[2] but no experimental work seems to have been done by him. The author is grateful to Mr. A. R. Howell of the British NGTE for the first indication, and to Mr. W. E. P. Johnson of Power Jets, Ltd., who, with his usual kindness, provided copies of the specifications. Recently, a Swiss firm of Diesel-engine manufacturers, Saurer of Arbon, has come quite independently and undoubtedly without knowledge of the Heppner patents, on the same idea and has developed some very interesting turbomachines which have given excellent results. These now have been used in a Saurer gas turbine at present under test.

The rotating diffuser compressor (for the machine is essentially a compressor) is based on the following considerations: A centrifugal compressor transforms the input energy into pressure partly in the rotor, mainly due to the centrifugal field, and partly in the diffuser, by slowing down the very high absolute velocity leaving the stator. The compression in the rotor is effected very efficiently while the diffusion process is connected with considerable losses. These are even greater in modern high-speed machines as the absolute velocity leaving the rotor is supersonic, so that the diffuser blade tips work at supersonic or sonic velocity. The losses in the diffuser and exit volute are the main reasons why the centrifugal compressor is not as efficient as it should be. In general, about one half the theoretical pressure rise is in the rotor and half in the stator. In the rotating-diffuser machine, the stator energy, instead of being inefficiently diffused into pressure, is efficiently transformed into mechanical energy. The compression ratio obtained is smaller, but the efficiency of the machine is higher; and, as will be seen, even if the rotor leaving velocity is

[2] British Patents 536,238, of November 6, 1939, and 548,180 of March 26, 1941.

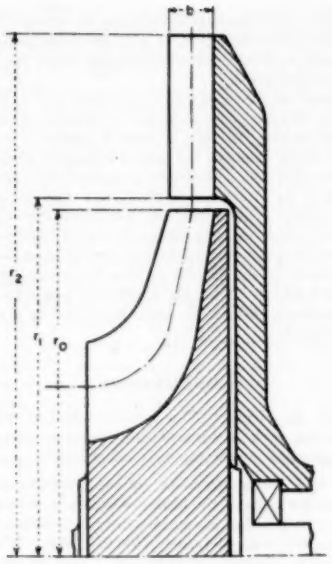

FIG. 7

supersonic, it strikes the diffuser blade tips with subsonic velocity owing to the relative motion.

For simplicity's sake, a rotor of the usual type with radial exit vanes and axial absolute entry velocity will be considered. The radial clearance between rotor and rotating diffuser is considered negligible ($d_0 = d_1$) so that the absolute velocity leaving the rotor c_0 is the same as the absolute velocity entering the stator c_1, Figs. 7 and 8. Only the theoretical pressure heads and velocities will be considered. For this type of rotor

$$u_0 = c_{u0}; \quad c_{m0} = u_0 \tan \alpha_0$$

consequently

$$c_{u1} = c_{u0} = u_0; \quad c_{m1} = c_{m0}; \quad \alpha_1 = \alpha_0$$

The total theoretical energy input in the rotor is

$$H_{IR} = \frac{u_0^2}{g} \quad [18]$$

of which half

$$H_R = \frac{u_0^2}{2g}$$

is transformed into pressure in the rotor, the other half is available in the stator as kinetic energy. If the diffuser rotates (in the same direction as the rotor) with a velocity $u_1 = \xi u_0 < u_0$, the relative inlet velocity w_1 is smaller than c_1; if $\lambda = r_2/r_1 > 1$ is the radius ratio of the rotating diffuser, then $u_2 = \lambda u_1 = \xi\lambda u_0$. For practical reasons, $u_1 < u_0$ as, owing to its shape, the diffuser can resist centrifugal stress less easily than the rotor. Reasonable values are

$$\lambda = 1.3 - 1.7; \quad \xi = 0.6 - 0.3; \quad \lambda\xi = 0.7 - 0.8$$

The theoretical energy converted into work in the diffuser is, as in Equation [1]

$$H_D = \frac{1}{g}(u_1 c_{u1} - u_2 c_{u2}) = \frac{u_0 \xi}{g}(c_{u1} - \lambda c_{u2}) \quad [19]$$

c_{u2} must be small to reduce the energy remaining to be converted into pressure in the stator volute. It is also preferably positive (directed toward the sense of rotation) to decrease deflection in the rotor.

If $c_{u2} = \mu u_0$, with $\mu = 0.1 - 0.5$, and remembering that $c_{u1} = u_0$, then

$$H_D = \frac{u_0^2}{g} \xi(1 - \lambda\mu) \quad [20]$$

The ratio between diffuser energy and total energy input (which is really a power factor) is

$$f_c = \frac{H_D}{H_{IR}} = \xi(1 - \lambda\mu) \quad [21]$$

The theoretical energy convertible into pressure is

$$H_P = (1 - f_c) H_{IR} = \frac{u_0^2}{g}[1 - \xi(1 - \lambda\mu)] \quad [22]$$

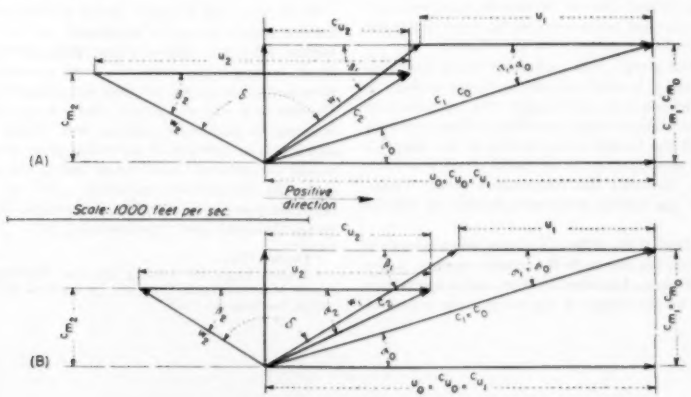

FIG. 8

Equation [21] connects f_a, ξ, λ, and μ; in general f_a and λ are given, and ξ and μ chosen afterward. Usually c_0 and u_0 are supersonic; it is then desirable that w_1 should be subsonic, with a Mach number of 0.8 or smaller.

$$w_1^2 = c_{m1}^2 + (c_{u1} - u_1)^2 = u_0^2 [\tan^2 \alpha_0 + (1 - \xi)^2]$$

hence

$$\frac{w_1}{u_0} = \sqrt{\tan^2 \alpha_0 + (1 - \xi)^2} \quad \ldots\ldots\ldots\ldots [23]$$

permits choosing the diffuser-tip Mach number as a function of ξ. Generally α_0 is small, $\alpha_0 = 15° - 20°$, and $\tan^2 \alpha_0$ can be neglected in the first approximation, so that the reduction is roughly proportional to $1 - \xi$. If it is assumed that the meridian component c_m decreases proportionally to the diameter (i.e., that the width b of the diffuser varies with the specific volume, the variation is very small, because the diffuser transforms kinetic energy and not pressure energy into work, so b can be assumed constant), then $c_{m2} = c_{m1}/\lambda = c_{m0}/\lambda$.

It can easily be seen that, in this case

$$\cot \beta_1 = \tan\left(\frac{\pi}{2} - \beta_1\right) = \frac{1 - \xi}{\tan \alpha_0}$$

and

$$\cot \beta_2 = \tan\left(\frac{\pi}{2} - \beta_2\right) = \frac{\lambda(\xi\lambda - \mu)}{\tan \alpha_0}$$

As $\delta = (\pi/2 - \beta_1) + (\pi/2 - \beta_2)$ is the deflection in the diffuser, it will be seen that this increases with increasing λ and with decreasing α_0 and μ; ξ has little influence. Term δ is generally rather large; attention must be paid that it should not be too large. Figs. 8(*a*) and 8(*b*) shows two diffuser diagrams for the same rotor, with $u_0 = 1300$ fps and $\alpha_0 = 17$ deg; the velocity of sound at the diffuser tip is about 1200 fps. Fig. 8(*a*), with $f_a = 0.3$ and $\lambda = 1.35$, gives $\xi = 0.6$ and $\mu = 0.37$. Fig. 8(*b*) with $f_a = 0.18$ and $\lambda = 1.7$ gives $\xi = 0.5$, $\mu = 0.425$; it will be seen that small differences in the diagram give large differences in the power factor and that w_1 is subsonic in both.

This type of rotating diffuser compressor can be used in a gas turbine to obtain all the useful power from the diffuser, which acts as a rotary torque converter, while all the heat energy of the gases goes from the primary gas turbine to the compressor rotor. In this case f_a is fixed by the cycle conditions and is large, $f_a = 0.28 - 0.4$. But the diffuser also can be made to supply only part of the useful power, the rest being provided by a special gas-turbine stage, mechanically connected with the diffuser.

This second solution gives a higher efficiency but is more complicated. In this case, f_a is small and can be chosen at will. In both types, there are two main advantages; the compressor efficiency is much higher than it would be with an ordinary centrifugal compressor, and the torque characteristic of the engine is excellent, because a slowing down of the useful power shaft, that is, of the diffuser, increases the compression ratio. Consequently, this type of gas turbine seems very suitable for traction purposes.

It must be noted that, if the diffuser is slowed down relative to the rotor, u_2 decreases, but the angle β_2 remains constant, hence, c_{u2} will decrease. When c_{u2} becomes negative, unless special precautions are taken in the design of the volute, the volute efficiency falls rapidly, because the air goes the wrong way round. It can easily be seen that $c_{u2}/u_1 = \mu/\lambda\xi$ gives the maximum percentage range of diffuser velocity variation before the inversion in the volute takes place.

If Equation [20] becomes zero or negative, that is, if $\lambda\mu > 1$, the rotating diffuser gives no power or absorbs power. Both cases are interesting, the first because it permits a decrease in diffuser-tip Mach numbers, the second because it gives a higher compression ratio than an ordinary compressor for a given maximum value of u_0. However, in these cases, the rotary-diffuser machine is purely a compressor, and lies outside the scope of this paper. The counter-rotating diffuser in a centrifugal compressor with high Mach numbers seems to show little promise, because the relative velocity at the diffuser tip becomes greater than in an ordinary compressor. The only application might be for compressing hydrogen, helium, or other gases having a very high velocity of sound.

Discussion

HEINRICH ADENSTEDT.[4] The writer's principal interest is in the materials angle of this problem; therefore, answers to the following questions concerning materials would be appreciated:

1 How high are the maximum stresses due to bending to be expected on the edges of the blades of such a radial-turbine design? In some practical gas-turbine designs of today, we go to gas temperatures of approximately 1400 to 1500 F. It is possible that at these temperatures the permanent bending stresses may involve somewhat of a problem.

2 The writer is greatly interested in the information concerning the rotating diffuser, especially since he happens to know that at the present time in this country work is under way on a similar compressor with a rotating diffuser. Compressor impellers of normal reciprocating engines (materials of aluminum alloy) sometimes show creep on the circumference of the disk or on the shroud, when operated at high circumferential speed (450 m per sec). For the rotating diffuser under certain operating conditions, similar temperatures and maybe higher stresses would be expected. Would aluminum alloys be satisfactory for this part or would steel be necessary, since the stress-temperature level is too high for aluminum? What material was used in Switzerland for this part?

W. T. VON DER NUELL.[5] Stress problems in hot radial-type turbine wheels are most important. It will probably require further extensive studies before these problems, e.g., thermal shock, cooling of the wheel and stress reversals find full answers. However, there seems no need for being more concerned than one was or is with axial type wheels where, as is known, wheel cracking in turbosuperchargers was almost common (maybe still is). Gas turbines of the radial type at AiResearch having passed Government qualification testing and hundreds of starting cycles demonstrated reliability. Due to the very few years that this type has been under development, there are, of course, no ten-thousand-hour runs finished as yet.

[4] Dayton Ohio.

[5] Project Engineer, heading the Gas Turbines Project of AiResearch Manufacturing Company, a division of the Garrett Corporation, Los Angeles, Calif.

Author's Closure

Answering first both discussions as regards stresses in the turbine, there is no doubt that the crucial problem lies in keeping creep and permanent bending stresses low. Very accurate stress analysis is necessary not only for the disk but also for the blades, taking into account the local stresses at the junction between blade and disk, where small fillet radii can often not be avoided. But, particularly for large industrial machines where there are no sharp limitations in radial size, the paper shows that the stresses can be reduced by an increase of diameter. Dr. von der Nuell's experience with high-velocity high-temperature wheels is very encouraging. Although the AiResearch turbines are, of course, single-stage, the shape of the blades is very similar to that of the proposed multistage wheel. In the oral discussion, the figure of 1400 ft/s at 1400 F has been quoted as having proved quite safe under long and repeated tests. This is most satisfactory; the more so, due to the small diameter of the turbines tested, which, as shown in this paper, increases the maximum stresses. In an industrial turbine, 850 to 950 fps at 1400 F degrees would be the maximum required without cooling.

Coming to Dr. Adenstedt's question about rotating diffuser compressors, there is no doubt that this type is raising much interest. To my knowledge, at least two U. S. firms are studying this problem, and there are perhaps more. The creep problem in this type of compressor is, on principle, less serious than in ordinary centrifugal compressors for the reason that, at a given peripheral speed of the rotor, the compression ratio is necessarily smaller with the rotating diffuser, as some of the energy input in the rotor is taken out of the diffuser in the form of mechanical energy; also the adiabatic efficiency is higher, so that the maximum temperature is certainly lower than in an ordinary compressor.

On the other hand, the shape of the rotating diffuser is more awkward than that of the rotor, and care must be taken in its design. But, if the tip peripheral speed of the diffuser is kept not higher than 80 per cent of the rotor tip speed, there should be no essential difficulties as regards stress.

The gas turbine using a rotating diffuser compressor is most interesting and promising, particularly for traction as, if properly designed, it can show most favorable torque characteristics. But there are hidden snags in this cycle, and careful study is necessary if all the advantages of this type of turbine are to be utilized to the full. But this is another story and will have to be told in another place.

Review of Optimum Design of Gas-Turbine Regenerators

By D. ARONSON,[1] HARRISON, N. J.

This paper summarizes design relationships to simplify the design and selection of the most suitable regenerator for a particular gas-turbine application. There are presented the criteria to be applied for the case of shape, volume, weight of surface area being the principal limitation on design. The distinctive features of bare-tube design and of extended-surface design are outlined.

Nomenclature

The following nomenclature is used in the paper:

A = heat transfer area, ft²
a = factor in determining fin effectiveness, $a = (2h/kt)^{0.5}$
b = wetted perimeter, ft
c_p = specific heat at constant pressure, Btu/(lb F)
C = air or gas capacity rate, $C = Wc_p$, Btu/(hr F)
C_5 = constant related to $j(f/2)$, a function of tube spacing for cross flow $C_5 = [j/(f/2)]\,(N_{Re})^{0.2}$
C_7 = constant relating performance inside to outside of tubes for cross flow; the relationship involving C_7 is given in Equation [17]
D_h = equivalent diameter of passage: For flow through rectangular passages

$$D_h = 4r_h = 4S/b = \frac{4(D_1D_2)}{2(D_1 + D_2)} = \frac{2D_1D_2}{D_1 + D_2}$$

For flow parallel to outside of tubes
(square pitch)

$$D_h = D_o\,[(4/\pi)\,(S_T/D_o)^2 - 1]$$

(equilateral triangle pitch)

$$D_h = D_o\left[\left(\frac{2\sqrt{3}}{\pi}\right)(S_T/D_o)^2 - 1\right]$$

D_1 = width of rectangular passage, ft
D_2 = height of rectangular passage, ft
D_i = inside diameter of round tubes, ft
D_o = outside diameter of round tubes, ft
E = friction power (in reference 3 expressed as hp/ft³), ft lb/(hr) (ft³)

$$E = \Delta P'(W/A) = \frac{f\,G^3\,(A/S)\,(W/A)}{2g\rho^2} = \frac{fG^3}{2g\rho^2}$$

F = ratio of design factors, dimensionless (see text)
f = friction factor, see dimensionless groupings
G = mass velocity, lb/(hr ft²) $G = V\rho$ or $= V/v$
G_c = mass velocity at minimum opening between tubes, lb/(hr ft²)
g = proportionality factor, $g = 4.17 \times 10^8$ lb ft/# hr²
h = unit conductance for thermal convection heat transfer, Btu/(hr ft² F)
j = heat-transfer factor, see dimensionless groupings
k = thermal conductivity, Btu/(hr ft² F/ft)
k_1, k_2, k_3 = constants whose values are given in Equations [11], [12], and [13]
L = flow length, ft
L_a = length of passage for flow of air, ft
L_h = length of passage for flow of gas, ft
L_m = length of assembly of passages in no-flow direction for cross flow plate-fin type exchanger, or length in no-flow direction for tubular exchanger, ft
L_n = dimension in direction of stream flowing across outside of tubes, ft
L_t = length of tubes, ft
m = exponent in expression for change of f with N_{Re}
n = exponent in expression for change of j with N_{Re}
N = number of tubes in direction of flow across tubes, dimensionless $N = L_n/S_L$
NTU = number of transfer units, see dimensionless groupings
P = pressure, lb/ft²
$\Delta P'$ = pressure drop, ft of fluid
$(\Delta P/P)$ = pressure-drop ratio, dimensionless
R = gas constant; for air $R = 53.3$ ft #/(lb deg F)
r = exponent in expression for change of h with E, $r = (1 - n)/(3 - m)$
r_h = hydraulic radius, ft
S = free flow area, ft²
S_T/D_o = tube-spacing ratio, center to center, in direction normal to gas flow, dimensionless
S_L/D_o = tube-spacing ratio, center to center, in direction of gas flow, dimensionless
T = temperature, R
t = temperature, F
t = thickness of fin, ft
Δt_{lm} = log mean temperature difference, F

$$\Delta t_{lm} = \frac{[(t_1)_h - (t_2)_c] - [(t_2)_h - (t_1)_c]}{\ln\left[\dfrac{(t_1)_h - (t_2)_c}{(t_2)_h - (t_1)_c}\right]}$$

Δt_m = mean effective temperature difference to be used in determining efficiency for cross flow heat exchangers, F

$$\Delta t_m = Y(\Delta t_{lm})$$
$$\Delta t_m = (\Delta t_m)_h + (\Delta t_m)_c$$

$(\Delta t_m)_c$ = mean effective temperature difference between air and metal wall, F
$(\Delta t_m)_h$ = mean effective temperature difference between gas and metal wall, F

---

[1] Consulting Engineer, Worthington Corporation. Mem. ASME.
Contributed by the Gas Turbine Power and Heat Transfer Divisions and presented at the Annual Meeting, Atlantic City, N. J., November 25–30, 1951, of The American Society of Mechanical Engineers.

Note: Statements and opinions advanced in papers are to be understood as individual expressions of their authors and not those of the Society. Manuscript received at ASME Headquarters, September 18, 1951. Paper No. 51—A-107.

δt = change in temperature of fluid going through regenerator, F

$$\delta t = t_1 - t_2$$

U = unit over-all thermal conductance, Btu/(hr F ft² of A)

V = velocity of fluid, at average air or gas temperature, ft/hr

v = specific volume, at average air or gas temperature, ft³/lb

W = flow rate, lb/hr

x_f = effective length of fin, ft

Y = correction factor to apply to log mean temperature difference to obtain effective temperature difference, dimensionless

$$Y = \Delta t_m / \Delta t_{lm}$$

Values of Y are summarized on p. 147 of ref. 10

δ, Δ = prefixes denoting difference

ϵ = heat-exchanger effectiveness, a function of NTU_c, C_c/C_h and flow arrangement, dimensionless (see Fig. 1)

$$\epsilon = \frac{(t_2)_c - (t_1)_c}{(t_1)_h - (t_1)_c} = X \text{ of McAdams (by definition)}$$

η = combined fin and metal-wall effectiveness, dimensionless

$$\eta = \eta_o \left(\frac{D_2}{D_1 + D_2}\right) + 1.00 \left(\frac{D_1}{D_1 + D_2}\right)$$

η_o = fin effectiveness, dimensionless

$$\eta_o = \frac{\tanh \alpha x_f}{\alpha x_f}$$

μ = absolute viscosity, lb/(hr ft)

ρ = fluid density, lb/ft³

Dimensionless groupings:

A/S = ratio of surface area to net open area. From definition of D_h, A/S is related to length of flow path by

$$A/S = 4L/D_h$$

For flow across outside of tubes

$$A/S = \pi N(S_T/D_o - 1)$$

$f = \dfrac{\Delta P'(\rho)^2}{(G^2/2g)(A/S)}$ = Fanning friction factor. The f versus N_{Re} plot defines friction characteristic of the surface

$j = \left(\dfrac{h}{c_p G}\right)\left(\dfrac{c_p \mu}{k}\right)^{2/3}$ = generalized heat-transfer grouping. This factor, j versus N_{Re}, defines heat-transfer characteristic of surface

$NTU = UA/C_{min}$-number of core "heat-transfer units," a dimensionless expression of "heat-transfer size" of core. Ratio of heat-transfer rate to heat-flow rate is equal to ratio of temperature change of one fluid to temperature difference between the two fluids

$$\frac{UA}{C_{min}} = \frac{\delta t_c}{\Delta t_m} = \frac{\text{temperature change of air}}{\text{over-all mean temperature difference}}$$

NTU_c = this is the NTU for the "cool" air side of core

$$NTU_c = \eta_c h_c A_c / C_c = j_c (N_{Pr})^{-2/3} \eta_c (A/S)_c = \frac{\delta t_c}{(\Delta t_m)_c}$$

NTU_h = this is corresponding NTU for "hot" gas side of core

$$NTU_h = \eta_h h_h A_h / C_h = j_h (N_{Pr})^{-2/3} \eta_h (A/S)_h = \frac{\delta t_h}{(\Delta t_m)_h}$$

$N_{Pr} = (c_p \mu / k)$, Prandtl number, a fluid property modulus

$N_{Re} = (DG/\mu)$, Reynolds number, a flow property modulus characterising "turbulence"

$N_{St} = (h/Gc_p)$, Stanton number, a heat-transfer modulus

Subscripts:

c = cool air side condition

h = hot gas side condition

i = condition on inside of tube

o = condition on outside of tube

1 = fluid condition at entrance to heat exchanger

2 = fluid condition at exit of heat exchanger

Miscellaneous:

lb = pounds mass in distinction to

$\not{\text{}}$ = pounds force

Introduction

The fuel consumption of the gas turbine can be reduced significantly by means of a regenerator to preheat the high-pressure air before it enters the combustion chamber. Thus part of the heat which otherwise would be lost in the turbine discharge gas is returned to the cycle. In the light of the considerable premium associated with obtaining the best design of this regenerator, several papers on this subject have appeared recently. One approach, taken by London and Kays (1)[2] and (2) and by Kays, London, and Johnson (3), is to use compact surfaces having a relatively large surface area per volume of core. While such designs reduce the volume of the heat exchanger, they call for large frontal areas which result in awkward shapes. In order to overcome this difficulty associated with compact surfaces, London and Kays (4) delineated the requirements of a system of heat exchange using a circulated liquid to couple two independent liquid-gas heat exchangers. Then each unit could readily be designed for large frontal areas and short flow paths, and would be similar in construction to conventional radiators used with liquid-cooled internal-combustion engines.

The other approach to the problem of obtaining the most effective regenerator possible within set limits of cost, weight, volume, or shape is to design for the optimum ratio of surface area for the high-pressure fluid to that for the low-pressure fluid, or for the optimum ratio of flow areas. Messinger (5) considers the case of finned tubes, Shepherd (11), Schmidt (6), and Rohsenow, Yoos, and Brady (7) the case of bare tubes in counterflow exchangers. The author (8) has presented the optimum ratios for plate-fin crossflow and bare-tube crossflow arrangements. McAdams[3] outlines the procedure for gas-to-gas heat exchangers of shell-and-tube construction.

Good design involves both the selection of the most suitable surface and the utilization of that surface most effectively. The purpose of this paper is to compare the several types of heat-transfer surfaces or arrangements and to present the optimum relationships applicable to each type.

[2] Numbers in parentheses refer to the Bibliography at the end of the paper.

[3] Reference (10), pp. 363–367.

General Design Relationships

The discussion will be limited to the simplified case, applicable to most gas-turbine cycles, that the mass flow and the specific heat of the fluid on one side of the heat exchanger are essentially equal to the mass flow and specific heat of the fluid on the other side.

The heat-transfer performance of the regenerator will be defined by *NTU*, number of heat-transfer units, which is the term applied to the ratio UA/C_{min} which is related to the temperature conditions by

$$UA/C_{min} = \frac{\text{Temperature change of one fluid}}{\text{Over-all mean temperature difference between one fluid and the other}} \quad [1]$$

Hence

$$NTU = \frac{(t_2)_c - (t_1)_c}{\Delta t_m} \quad [2]$$

The convention is to relate the *NTU* to the temperature change of the fluid having the smaller heat flow so that the value used for *NTU* is the higher one. For the gas-turbine regenerator the mass flow and heat capacity of the cold air are slightly less than those of the hot gas so that the *NTU* will be related to the cold air. However, this distinction is in a sense academic because for the purpose of the present analysis the mass flow and specific heat of the two fluids have been assumed equal.

The relationship between *NTU* and regenerator effectiveness is shown graphically in Fig. 1 for the case of counterflow, single-pass, and multipass crossflow.

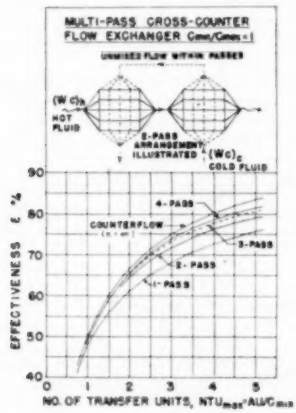

Fig. 1 Plot of *NTU* Versus Exchanger Effectiveness

A similar *NTU* term can be applied to the heat-transfer performance of the hot and cold sides of the regenerator for which the derivation follows:

Over-All Relationships (Combined Effect of Hot and Cold Passages)

The over-all resistance to heat transfer, $1/UA$, is the sum of the individual resistances. For gas-to-gas heat exchangers the significant resistances are the gas films on the two sides so that the expression can be written

$$1/UA = 1/h_hA_h + 1/h_cA_c \quad [3]$$

Dividing the denominator of each term by $Wc_p = (Wc_p)_h = (Wc_p)_c$

$$\frac{1}{UA/Wc_p} = \frac{1}{(hA/Wc_p)_h} + \frac{1}{(hA/Wc_p)_c} \quad [4]$$

which can be expressed in accordance with the original definition as

$$\frac{1}{NTU} = \frac{1}{NTU_h} + \frac{1}{NTU_c} \quad [5]$$

The parasitic losses due to pressure drop in the regenerator have an effect on the cycle proportional to the sum of the individual pressure-drop ratios

$$\Delta P/P = (\Delta P/P)_h + (\Delta P/P)_c \quad [6]$$

or in terms of the total power loss

$$(W)(\Delta P/P) = (W)_h(\Delta P/P)_h + (W)_c(\Delta P/P)_c \quad [7]$$

Individual Relationships (Either Hot Side or Cold Side)

For any surface the individual *NTU* and the individual $\Delta P/P$ terms can be expressed as

$$NTU_h = j_h(A/S)_h(N_{Pr})^{-2/3}(\eta)_h \quad [8]$$

An equation comparable to Equation [8] applies to NTU_c

$$(\Delta P/P)_h = \frac{f_h(G_h)^2(A/S)_h}{2g\,P\rho_h} = \frac{f_h(G_h)^2(A/S)_h}{2g\,RT_h(\rho_h)^2} \quad [9]$$

The relationship between the two terms is obtained by combining Equations [8] and [9]

$$NTU_h = \frac{[j/(f/2)]_h(\Delta P/P)_h\,gRT_h\eta_h(\rho_h)^2}{(G_h)^2(N_{Pr})^{2/3}} \quad [10]$$

The ratio $j/(f/2)$ is from theoretical considerations never greater than unity. Hence Equation [10] with $j/(f/2)$ equal to unity expresses for the ideal regenerator the *maximum NTU* that can be obtained for a *given pressure drop*, assuming that space limitations determine the flow rate of the fluid. Conversely, Equation [10] sets the *minimum cross-sectional area* required to obtain a given *NTU* for a maximum allowable $\Delta P/P$. Where cross-sectional area is not restricted there is no particular advantage to a high value of $j/(f/2)$.

For the *actual* regenerator the ratio of $j/(f/2)$ is less than unity, but its value is reasonably constant for a particular type of surface. Hence Equation [10] is useful for expressing the relationships among *NTU*, $\Delta P/P$, and G for a particular regenerator design.

For a given surface, j and f are functions of N_{Re} and over the range of interest one may express the relationship as

$$j = (k_1)(N_{Re})^{-m} \quad [11]$$

where

$$j = (h/c_pG)(c_p\mu/k)^{2/3}$$

$$f = (k_2)(N_{Re})^{-n} \quad [12]$$

where

$$f = \frac{(\Delta P/P)(RT)(\rho)^2}{(G^2/2g)(A/S)}$$

where the constants k_1 and k_2 and the exponents m and n depend on the type of surface and upon the nature of flow (whether turbulent or laminar).

For a given heat-transfer duty, the surface area required is inversely proportional to h, the local heat-transfer coefficient. The relationship between h and the friction power E expended is obtained from Equations [11] and [12] as

$$h = (k_3)\,(c_p)\,(E)^r\,(\rho)^{2r}\,(2g)^r \quad \ldots\ldots\ldots\ldots\ldots\ldots [13]$$

where

$$E = (\Delta P/P)\,(RT)\,(W/A)$$

$$\text{Exponent } r = (1 - n)/(3 - m)$$

$$\text{Constant } k_3 = \frac{k_1\,(D/\mu)^{(3r-1)}}{(k_2)^r\,(N_{Pr})^{r/3}}$$

The following generalizations applicable to flow in one set of passages may be deduced from Equations [10] and [13], assuming a fixed NTU, fixed $\Delta P/P$, and particular fluid properties:

(*a*) Minimum cross-sectional area is required for the type of surface having the highest value of $j/(f/2)$.

(*b*) Minimum surface area is required for the type of surface having the highest value of h for a given value of E and ρ, hence in general, the highest value of k_3.

Inasmuch as the regenerator has two sets of passages both containing relatively low-density fluids, these generalizations must be modified to allow for differences in density, type of surface, flow area, and surface area for the two fluids. Further, allowance must be made in the design for the effects of the flow arrangement on performance. As shown in Fig. 1, the effectiveness for a given NTU is less for crossflow arrangements than for counterflow.

Since in calculating the design it is seldom possible to arrive at exactly the desired values on the first trial, the following relationships are presented, which apply to a given design:

If the pressure-drop ratio is fixed, and it is desired to change the value of NTU, then the surface area for a given heat-capacity flow is affected as follows

$$A/Wc_p \propto (NTU)^{[1/(1-r)]} \text{ (for constant } \Delta P/P \text{)} \quad \ldots [14a]$$

Conversely, if the NTU is fixed, the relationship between area and pressure drop ratio is

$$A/Wc_p \propto (1/\Delta P/P)^{[r/(1-r)]} \text{ (for constant } NTU \text{)} \quad \ldots [14b]$$

Combining Expressions [14*a*] and [14*b*] and inserting constants, one obtains

$$NTU = k_3\,(A/W)^{1-r}\,[(\Delta P/P)\,(RT)]^r\,(\rho)^{2r}\,(2g)^r \quad \ldots [15]$$

which is essentially just another way of expressing Equation [13] since NTU is by definition $(h)\,(A/Wc_p)$.

These relationships are derived from Equations [11], [12], and [13]. A thermodynamic analysis of the optimum ratio between NTU and $\Delta P/P$ is given by McClintock (12).

Comparison of Surfaces and Arrangements

In order to simplify the comparison of each type of surface and arrangement, the peculiar features of each are summarized.

Shell-and-Tube Construction—Bare Tubes

(*a*) *Counterflow With Both Fluids Flowing Parallel to Tubes:*

Cross-sectional area is smallest for this design because:

1 Ratio of $j/(f/2)$ for flow parallel to smooth surfaces is close to unity.

2 Entire cross-sectional area except for the small space taken by tube walls is available for flow.

Surface area is larger (perhaps double) for flow past smooth surfaces than for flow past interrupted surfaces such as short strip fins or flow across tubes because heat-transfer coefficient for a given friction power is low. For this design the minimum surface area is obtained when the ratio of flow area for the fluid flowing on the outside of the tubes to that for the fluid flowing inside the tubes is

$$\frac{S_o}{S_i} = \frac{G_i}{G_o} = \left(\frac{\mu_o}{\mu_i}\right)^{0.11}\left(\frac{\rho_i}{\rho_o}\right)^{0.56}\left(\frac{T_i}{T_o}\right)^{0.28}\left(\frac{D_o}{D_i}\right)^{0.44} \quad \ldots\ldots [16]$$

for the case of the exponents m and n in Equations [11] and [12] being both equal to 0.2. The ratios given by Equation [16] were derived in similar manner to those for crossflow tubular design presented in reference (8). The values of the ratio obtained by Equation [16] are close to those obtained from the equations of Schmidt (6).

For the high-pressure fluid on the outside of the tubes, Equation [16] gives a flow-area ratio which is difficult to obtain in a practical unit because of the extremely close tube spacing required.

For the high-pressure fluid inside the tubes the optimum flow-area ratio usually can be achieved with a straightforward design. The significance of the optimum for the case of ρ_i/ρ_o equal to 8 is illustrated in Fig. 2. The dashed line shows the tube spacing in terms of tube diameters, assuming the ratio of tube OD to ID of 1.1, and an equilateral-triangle pitch arrangement.

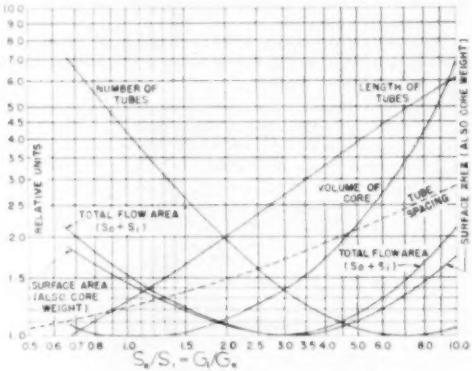

Case of $\rho_i/\rho_o = 8.0$ $T_i/T_o = 1.0$

Fig. 2 Effect of Flow Area Ratio, S_o/S_i, on Regenerator Dimensions

For minimum volume the ratio of S_o/S_i as calculated from the equations of Schmidt (6) is unity or slightly less for the case of the high-pressure fluid inside the tubes. Generally the designer will be limited by the requirement of holding some minimum ligament in the tube sheet.

(*b*) *Crossflow:*

Cross-sectional area is largest for this design because

1 The area for flow on the outside of the tubes is limited by the minimum section between adjacent tubes in each row. Hence a large fraction of the volume on the outside of the tubes is not available for flow.

2 Ratio of $j/(f/2)$ is relatively low except for the case of closely spaced tubes. For closely spaced tubes the area for flow is a small part of the total cross-sectional area so that the first explanation is the more important. The value of $j/(f/2)$ is given by

$$j/(f/2) = C_3/(N_{Re})^{0.37}$$

where C_h is a function of tube spacing. Values of C_h are shown as Figs. 8 and 9 of reference (8).

Surface area is less than for the case of the counterflow arrangement because the heat-transfer coefficient on the outside of tubes for flow across tubes is higher for a given value of E and ρ than for flow parallel to tubes. This is shown in Fig. 5 by the broken line for the case of flow across $^1/_8$-in-OD tubes arranged in line, with spacings of $^1/_{16}$ in. between tubes in the direction of flow and $^1/_4$ in. transverse to flow. The relationship between h and E for flow through the $^1/_8$-in. tube is essentially the same as the curve for the plain fin, 5.3 fins to the inch, PF 5.3.

The advantage of the crossflow arrangement, besides the higher heat-transfer coefficient, is simplicity of ducting. However, as shown in Fig. 1, the effectiveness for a given NTU is appreciably less than for counterflow, unless multipass arrangements are used. In form comparable to Equation [16], the optimum ratio of flow areas for each pass, whether single pass or multipass, is given by

$$\frac{S_c}{S_h} = \frac{G_c}{G_h} = \frac{C_T}{(N_{Re})_c^{0.037}} \left(\frac{\mu_c}{\mu_i}\right)^{0.11} \left(\frac{\rho_i}{\rho_o}\right)^{0.56} \left(\frac{T_i}{T_o}\right)^{0.28} \left(\frac{D_o}{D_i}\right)^{0.44} \quad [17]$$

The values of C_T for different tube configurations are given in reference (8). For flow across in-line tubes or closely spaced staggered tubes C_T may be taken approximately as 3.3. A value of Reynolds number for flow on the outside of tubes must be assumed. However, since it enters only to the 0.037 power a single trial is usually adequate.

With crossflow arrangement the designer can vary the ratio of flow areas without changing the tube spacings, since

$$S_o/S_i = (L_t/L_h)\,(D_o/D_i)^2\,(S_T/D_o - 1)\,(S_L/D_o)\,(4/\pi) \quad [18]$$

For minimum volume of core the tubes are spaced together as closely as possible, minimum value of S_T/D_o and S_L/D_o. Then the ratio of dimensions L_t/L_h is set to give the optimum ratio of S_o and S_i.

The effect of changes in the ratio S_o/S_i on regenerator surface area will be approximately the same as shown in Fig. 2 for the counterflow unit. However, the number of tubes, volume of core, length of tubes, and free-flow area are affected not by the ratio S_o/S_i but instead by the tube spacings, S_T/D_o and S_L/D_o.

Extended Surface—Plate and Fin Construction

(a) Dimensions Set:

The choice of surface determines whether one obtains a unit of low weight or one of high NTU for a given $\Delta P/P$. The relationships for the ideal regenerator to fit into the space defined by L_c, L_h, and L_m have been derived by the author (8). The optimum ratios so derived result in the relationship of maximum NTU attainable to any value of $\Delta P/P$. It is assumed that smooth, continuous fins having a value of $j/(f/2) = 1.0$ are used for both hot and cold passages. The equations given in reference (8) may be modified to the form previously used in this paper

$$\frac{S_h}{S_c} = \frac{G_c}{G_h} = \left(\frac{\rho_c}{\rho_h}\right)^{0.5} \left(\frac{L_c}{L_h}\right)^{0.5} \left(\frac{T_c}{T_h}\right)^{0.25} \quad [19]$$

For counterflow arrangement the values of L_h and L_c are equal.

The values of j and f for flow parallel to smooth surfaces depend on the aspect ratio of the passages. For aspect ratios approaching unity the performance is the same as for flow through tubes. Values of $j/(f/2)$ for several continuous fin arrangements are given in Fig. 3. In the turbulent region exponents m and n may be taken as 0.2 and for this case the over-all relationships among the several terms are given in (8) as

$$\frac{\Delta P/P_c}{\Delta P/P_h} = \frac{NTU_c}{NTU_h} = \frac{(D_e)_h}{(D_e)_c} = \left(\frac{\rho_c}{\rho_h}\right)^{0.5} \left(\frac{L_h}{L_c}\right)^{0.5} \left(\frac{T_c}{T_h}\right)^{0.55} \quad [20]$$

The ratio of surface areas to give the foregoing ratios of $\Delta P/P$ and NTU is

$$A_c/A_h = (G_c/G_h)^{0.5}\,(L_h/L_c) \quad [21]$$

In the actual regenerator in contrast to the ideal regenerator, the values given in Equations [20] and [21] may not be realized because of low fin effectiveness, or because performance of the fin pattern indicated by the design calculations happens to give a value of $j/(f/2)$ much less than unity. For practical reasons the design may not be acceptable because of excessively close fin spacing, or excessive surface area and hence, weight and cost. Therefore one must usually accept a lower NTU or a higher $\Delta P/P$. If friction power is not critical then surface area can be reduced by choosing a fin pattern having a high value of h for a given friction power. If friction power is important, then the selection is made from those fin patterns having relatively high values of $j/(f/2)$. The performance of several compact surfaces is shown in Figs. 3, 4, and 5, giving values of $j/(f/2)$, E and h, for different values of G. The curves have been plotted from data taken from reference (3).

It should be noted that with plate-and-fin construction in contrast to bare-tube design, the ratio of the surface areas A_c/A_h and the ratio of the free-flow areas S_c/S_h can both be varied to meet the desired performance requirements.

(b) Dimensions Not Set:

For minimum volume, without regard to shape, one selects a surface having a large surface area per unit volume and having a high heat-transfer coefficient for a given friction power. Kays, London, and Johnson (3) have plotted the heat transfer per unit volume against friction power for several compact surfaces. With such a plot, selection of a suitable surface is readily made. Then for the particular surface, since the ratio of volume to area is fixed by the core pattern, the optimum ratio of flow areas to give minimum volume is the same as for minimum surface area. The equations are presented in the following paragraph.

The optimum conditions for minimum surface (minimum weight) have been analyzed by Van Le (9). It is assumed that there are no limitations imposed on the shape or volume of the regenerator. For the particular surface pattern selected the following ratios result in the minimum surface area

$$\frac{S_h}{S_c} = \frac{G_c}{G_h} = \left(\frac{D_c/\mu_c}{D_h/\mu_h}\right)^{m/(3-m)} \left(\frac{\rho_c}{\rho_h}\right)^{2/(3-m)} \left(\frac{T_c}{T_h}\right)^{1/(3-m)} \quad [22]$$

and

$$A_c/A_h = F \quad [23]$$

where F is given by

$$F = \left[\frac{(N_{Pr})_c}{(N_{Pr})_h}\right]^{1/3} \left(\frac{D_h/\mu_h}{D_c/\mu_c}\right)^{\frac{2n}{2}-1} \left(\frac{T_h}{T_c}\right)^{\frac{n}{2}} \left(\frac{\rho_h}{\rho_c}\right)^{n} \quad [24]$$

The values of NTU and heat-transfer coefficients are also related by

$$F = NTU_h/NTU_c = (h_h/h_c)^{0.5} \quad [25]$$

The foregoing assumes that values of the exponents m and n are the same for both sides of the regenerator.

The selection of surface to use will be from those having a high value of h for a given value of E.

Extended Surface—Liquid-Coupled Arrangement

The case of designing for minimum volume without regard to shape often results in large frontal areas with short flow paths. For the large flows which obtain on gas turbines this may result in an awkward shape. Hence it is usually necessary to design

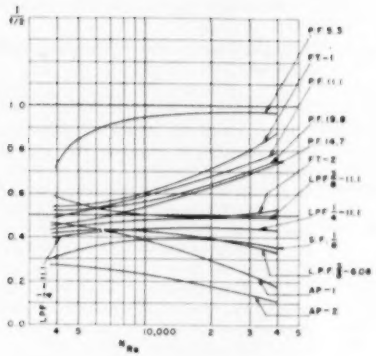

FIG. 3 (*left*) VALUES OF $j/(f/2)$ FOR SEVERAL COMPACT SURFACES
(From reference 3.)

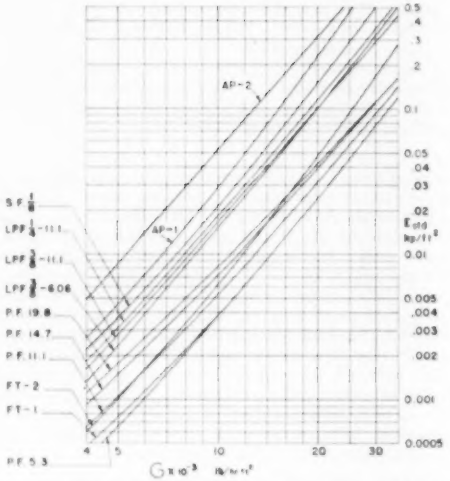

FIG. 4 VALUES OF E FOR DIFFERENT VALUES OF G FOR SEVERAL COMPACT SURFACES FOR AIR AT 500 F, 1 ATM
(From reference 3.)

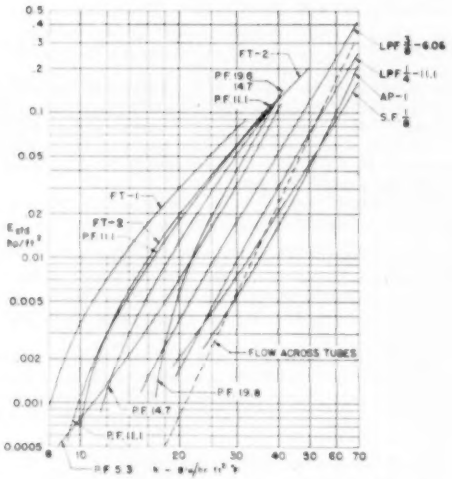

FIG. 5 VALUES OF h FOR DIFFERENT VALUES OF E FOR SEVERAL COMPACT SURFACES FOR AIR AT 500 F, 1 ATM
(From reference 3.)

SUPPLEMENT TO FIGS. 3, 4, AND 5

Description of surfaces							
	Surface, fins/in.	Hydr. radius, ft	Plate spacing, ft	Louver length, in.	Louver gap, in.	Fin thick, in.	Area/volume, sq ft/cu ft
PLAIN PLATE FIN							
	5.3	0.00504	0.0392			0.006	152
	11.1	0.00253	0.0208			0.006	367
	14.77	0.00212	0.0275			0.006	420
	19.86	0.001495	0.0208			0.006	561
LOUVERED PLATE FIN							
5/8	6.06	0.00365	0.0208	0.375	0.055	0.006	256
1/4	11.1	0.00253	0.0208	0.250	0.055	0.006	367
1/8	11.1	0.00253	0.0208	0.375	0.055	0.006	367
STRIP FIN							
1/8	15.2	0.00217	0.0345	0.125	0.031	0.006	417
PIN FIN							
AP-1	8.0	0.00361	0.0200			0.040	188
AP-2	8.33	0.00350	0.0299			0.040	244
Flat tube FT-1 (flow through tube)		0.00358	Tube cross section		0.144 × 0.302		
FT-2 (flow across tube)		0.00358	Tube outside cross section Arranged in staggered pattern Ratio of net opening to tube spacing: 0.095/0.222		0.127 × 0.315		

for the condition that the dimensions are set to some limits. The attractive alternative suggestion has been proposed by London and Kays (4) of using a liquid-coupled system with two heat exchangers, one for the air and one for the gas. The analysis to determine the ratios which give the minimum surface area or the minimum volume are the same as for the previous case of extended surface—dimensions not set. The equations presented are for the case of the exponents m and n being the same for the hot and for the cold passages.

The analysis has not been made for the case of different exponents except for the crossflow tubular arrangement having exponents of

Flow inside tubes $m = 0.2$ $n = 0.2$ $r = (1 - n)/(3 - m) = 0.286$

Flow across tubes $m = 0.13$ $n = 0.4$ $r = (1 - n)/(3 - m) = 0.209$

Since the form of the equation expressing optimum relations for this case is similar to that for the case of exponents being equal, the method of analysis given in reference (8) can be extended readily to apply to other arrangements having different exponents.

Conclusion

From the several types of equations presented one can approximate the relationships to be considered for heat-transfer arrangements differing from those presented.

The author hopes that the material offered will enable the designer to reduce the number of trial-and-error calculations required to arrive at the final design. It is his belief that a knowledge of performance of the ideal regenerator or the optimum design serves as a guidepost, showing the direction and extent to move in order to obtain a desired change.

Acknowledgments

The author wishes to express his indebtedness to Mr. N. Van Le, who developed the optimum relationships for a liquid-coupled regenerator, and to the Elliott Company, which supported this study and agreed to its publication.

BIBLIOGRAPHY

1 "The Gas-Turbine Regenerator—the Use of Compact Heat-Transfer Surfaces," by A. L. London and W. M. Kays, Trans. ASME, vol. 72, 1950, pp. 611–621.

2 "Gas Turbine Regenerator Design Studies," by A. L. London and W. M. Kays, Technical Report No. 8, Navy Contract N6-ONR-251 Task Order 6 (NR-035-104), Department of Mechanical Engineering, Stanford University, Stanford, Calif., December 15, 1949.

3 "Gas-Turbine-Plant Heat Exchangers—Basic Heat-Transfer and Flow-Friction Design Data," by W. M. Kays, A. L. London, and D. W. Johnson, ASME Research Publication, April, 1951.

4 "The Liquid-Coupled Indirect-Transfer Regenerator for Gas-Turbine Plants," by A. L. London and W. M. Kays, Trans. ASME, vol. 73, 1951, pp. 529–542.

5 "Minimum Weight in Heat Exchanger Design," by B. L. Messinger, *Industrial Aviation*, vol. 1, December, 1944, pp. 44–46, 48–49, and 102–103.

6 "The Design of Contra-Flow Heat Exchangers," by E. Schmidt, *Engineers Digest* (American edition), vol. 5, 1948, pp. 55–60.

7 "Optimum Design of Gas-Turbine Regenerators," by W. M. Rohsenow, T. R. Yoos, Jr., and J. F. Brady, ASME Paper No. 50—A-103, presented at the Annual Meeting, New York, N. Y., November 26–December 1, 1950, of The American Society of Mechanical Engineers.

8 "Design of Regenerators for Gas-Turbine Service," by D. Aronson, Trans. ASME, vol. 72, 1950, pp. 967–978.

9 "Design of a Liquid Coupled Regenerator for a Gas Turbine," by N. Van Le, paper to be presented.

10 "Heat Transmission," by W. H. McAdams, second edition, McGraw-Hill Book Company, Inc., New York, N. Y., 1942.

11 "A Design Method for Counterflow Shell-and-Tube Heat Exchangers for Gas Turbines," by D. G. Shepherd, ASME Paper No. 47—A-60, presented at the Annual Meeting, New York, N. Y., 1947, of The American Society of Mechanical Engineers.

12 "The Design of Heat Exchangers for Minimum Irreversibility," by F. A. McClintock, ASME Paper No. 51—A-106, presented at the Annual Meeting, Atlantic City, N. J., November 25–30, 1951, of The American Society of Mechanical Engineers.

Discussion

R. L. Whitelaw.[4] This paper provides a valuable step forward in this field, in that it offers specific methods of designing for various criteria, such as, minimum volume, minimum surface, minimum weight, and so on, as well as for different types of exchangers.

However, one of the most important design criteria appears to be missing in evaluations offered to date, that is, cost—for the best investment is not necessarily synonymous with minimum surface in either type of heat exchanger.

If the gas turbine is to come into general commercial use, the heat exchanger, which for a given power loss and effectiveness is most economical to manufacture and operate, will be favored. In any case it must be designed to meet specified service conditions. This is particularly true for regenerators for locomotives, ships, and other cases where space or weight are at a premium.

In some recent studies made on shell-and-tube-type gas-turbine

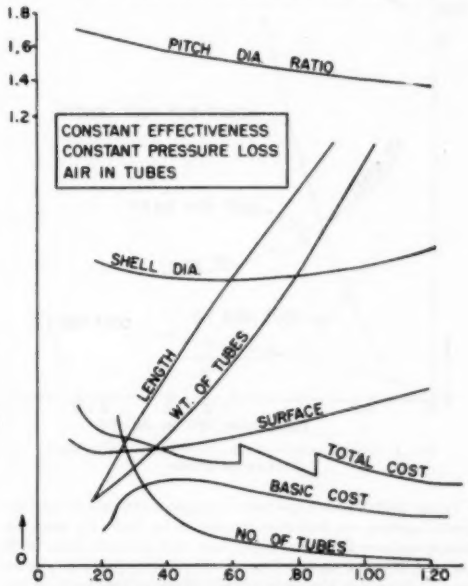

Fig. 6 Typical Characteristics of Shell-and-Tube-Type Counterflow Gas-Turbine Regenerator

regenerators, we adopted the initial approach of assuming that cost was roughly proportional to surface required. For each of several tube diameters, we derived the combination of pitch, number of tubes, and length that would give minimum surface at the design effectiveness and power loss, and plotted these against tube diameter, Fig. 6 of this discussion. Thus each point on

[4] Research and Development Department, The Babcock & Wilcox Company, Alliance, Ohio.

the curves at a given tube diameter is a condition for minimum surface at that diameter, and the curves give us the diameter at which this minimum surface itself becomes a minimum, evidently at about $^1/_8$ in. OD. However, applying known tube costs to this situation, plus costs of rolling-in ends, premium cost of excess lengths, and so on, we get a cost curve as shown, where the minimum is now at about $1^1/_4$ in. or even larger tube diameter. This radical change in design considerations derives from basic economics of tube manufacturing as shown in Fig. 7, herewith, where cost per square foot falls rapidly with increase in diameter. The advent of a radically different and inexpensive method of securing tubes in tube sheets could bring the minimum total cost into the small-tube region, i.e., less than $^1/_4$ in. OD, since in this region the cost of securing tubes by present commercial methods is greater than the cost of the tubes themselves.

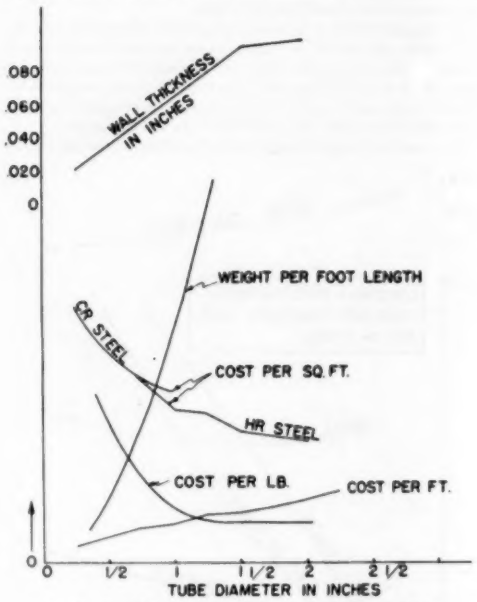

FIG. 7 COST CHARACTERISTICS OF WELDED-STEEL HEAT-EXCHANGER TUBES

In the field of plate-type heat exchangers with and without extended surface, we find the following to be true: By using extended surfaces of various types, each with a fin efficiency of 75 per cent, the total surface (base + extended) required in a plate-type exchanger is almost constant. This in turn leads to the basic economic principle for extended surface that, except where the extended surface can be furnished at the same or less cost as the same area of additional base surface, the extended-surface heat exchanger always will be more expensive than the flat-plate heat exchanger to do the same job. This principle rules out a great many types of extended surfaces being proposed, except for aircraft or other applications where weight or volume is more important than cost. As a result, we have found only one or two types of extended surface currently meeting this requirement, their chief merit being that they can be applied simultaneously and at the same speed as the base surface—tube or sheet—can be manufactured.

With the foregoing principle in mind, we made introductory studies of flat-plate heat exchangers to do the same job at the same effectiveness and power loss as the shell-and-tube design mentioned previously. For each of various assumed total channel widths, we calculated length, flow area, and air-to-gas channel width ratio at which the total surface required is a minimum. Plotting these minimum values against total channel width gave the curves shown in Fig. 8, herewith. We did not go so far as a cost study in this case, although it is apparent that here cost should be more dependent upon surface alone.

An interesting point of comparison between plate-type and shell-and-tube-type heat exchangers arose even from these introductory studies. The minimum basic surface required in each case was practically the same. Now we observe that the minimum total cost of the shell-and-tube-type heat exchanger (i.e., at $1^1/_4$ in. OD or greater) is about twice the cost of the minimum (i.e., $^1/_8$ in. OD) surface for the same duty. Hence it follows that if a plate-type heat exchanger can be built for less than twice the cost of its plate surface reckoned in $^1/_8$ in. OD tubes, it should cost less than a shell-and-tube-type heat exchanger for the same duty.

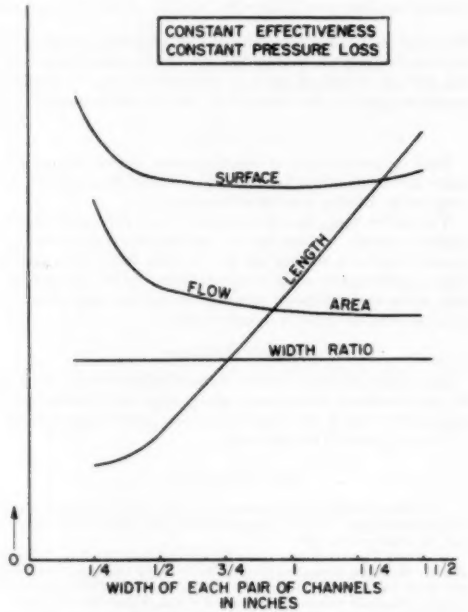

FIG. 8 TYPICAL CHARACTERISTICS OF PLATE-TYPE COUNTERFLOW GAS-TURBINE REGENERATOR

AUTHOR'S CLOSURE

In essence, Mr. Whitelaw's proposition is that the over-all optimum design must include the factor of cost. The author concurs with this view. However, the subject of cost is deserving of a paper in its own right and it is the hope of the author that someone will study a variety of heat-transfer surfaces with respect to cost as Kays, London, and Johnson (3) did with respect to thermal performance.

The present paper is primarily concerned with the most effective use of a given surface. For example, while an analysis such as Mr. Whitelaw's might show that regenerators built with $1^1/_4$-in. diam tubes would have the lowest cost, the most effective use of this surface would be dictated by the analysis given in the present paper.

This analysis guides the designer in establishing the optimum tube spacings, number of tubes, length of tubes, and flow arrangements for the $1^1/_4$-in. diam tubes.

As experience is acquired in the design, construction, and operation of gas-turbine regenerators, more exact data and criteria will become available. In the present paper the author has attempted to summarize and correlate design information currently available.

High-Speed Cascade Testing Techniques

By F. H. KEAST,[1] MALTON, ONTARIO, CANADA

This paper describes a cascade wind tunnel used by the author since 1948. Such auxiliary equipment as an automatic traverse and recording gear and a wedge-shaped probe are described. Some results are presented with a method of analysis for turbine cascades which converts the cascade results into a turbine-performance chart. The existence of a critical load factor results from this analysis.

Introduction

FOR axial-compressor and turbine design the simplest and least costly tool for acquiring basic information is the cascade wind tunnel. In essence this consists of a number of airfoils of constant cross section equally spaced in a rectangular slot which is connected to a supply of air. Traverses are made to determine the drag and turning effect of the airfoil cascade. Although it has its limitations in that it provides information primarily only on the two-dimensional performance of the cascade this does give the essential starting point for a compressor or turbine design and, later, when the complete compressor or turbine is tested, it gives a background of information against which the three-dimensional effects may be assessed as deviations from the two-dimensional performance of the individual blade sections.

Description of Apparatus

The rig described was designed in 1947, and first put into operation in 1948. The air supply immediately available was 15 lb per sec at a pressure of 100 psig. The simplest method of using this supply was to design a blown tunnel similar in principle to the C. A. Parsons No. 2 tunnel.[2] The blown tunnel and sucked tunnel have their advantages and disadvantages. The sucked tunnel has the advantage of giving clean entry conditions to the cascade with negligible turbulence and thin boundary layers on the guide walls. With the blown tunnel many precautions must be taken to achieve this and, in addition, the source of high-pressure air usually contaminates the supply with oil. On the other hand, the blown tunnel discharges from the cascade into the room so that the outlet traverse gear is accessible. For the suction tunnel the exit air from the cascade must be led to the pump inlet. This involves discharging into a large tank or the use of side walls which are undesirable since they influence the air-outlet angle. In either case the outlet transverse gear has to be sealed and is less accessible. With the air supply available and using a blown tunnel, some measure of independent control of Reynolds and Mach numbers is possible by adjustment of the compressor aftercooler. These considerations led to the choice of the blown tunnel.

The pressure was more than adequate to study cascades up to their choking limit. In fact, to simplify the structural design of the tunnel an upper limit of 30 psig was chosen for the inlet pressure. Operating at this pressure and with suitable air temperature, adjustable by the compressor aftercooler, the air supply can choke a hole of approximately 30 sq in. This was then chosen as the outlet area of the tunnel, being 12 in. long and 2.5 in. high. With blades of 0.8-in. chord this gives an aspect ratio over 3 and with a pitch/chord ratio of 1.5 allows 10 blade pitches to be accommodated. This was regarded as the minimum required to avoid end effects due to the wall boundary layer on the end blades of the cascade. In normal operation with turbine cascades with lower pitch/chord ratios about 20 blades are used.

Previous cascade results[3] indicate a critical Reynolds number for compressor sections between 100,000 and 350,000, its actual value being largely dependent on the turbulence factor of the tunnel employed. As the turbulence factor of a blown tunnel is likely to be high[3] the critical value for the tunnel described here probably will be closer to the lower figure quoted. For turbine cascades in blown tunnels the value is approximately 150,000,[4] which for a blade of 0.8-in. chord is attained at a velocity of 350 fps assuming standard density. Above this critical value the effect of further increase of Reynolds number is small. Since the compressor and turbine of a typical jet engine operate in the normal running range above the critical Reynolds number except at extreme altitude, the high-speed range of cascade tests on the tunnel should be directly applicable. Simulation of conditions at extreme altitude and high Mach number is beyond the scope of the present tunnel.

Air enters the rig through filters and a control valve into a 10-in-diam pipe containing two screens and a honeycomb straightener. A transition section with a contraction ratio of 1.8 leads the air to the rectangular section formed by fixed top and bottom plates with movable side walls. A further contraction occurs at the variable side walls of ratio 1.5 when the cascade has zero air-inlet angle and 4.3 when the inlet angle is at its maximum value of 70 deg, all angles being measured from the normal to the plane containing the leading edges. As the side walls move they cause two disks at top and bottom to rotate; the cascade, mounted in end plates fixed to the disks rotates with them. In this way the incidence of the cascade may be varied even with the rig in operation. Fig. 1 shows the outlet end of the rig with its cover plate removed so that the cascade is visible. The transverse probe normally moves in a slot in the cover plate.

Originally, provision was made for boundary-layer suction applied by an ejector through porous metal inserts on the top and bottom plates immediately upstream of the disks holding the cascade. The boundary layers, however, were too thick for suction to be a sufficient remedy, and the suction plates were replaced by slots which permitted high-pressure air taken from the supply upstream of the main control valve to be injected into the boundary layers. Fig. 2 shows the improvement in the entry profile as a result of this. The amount of air injected varies, of course, with different operating conditions. The correct amount is arranged quickly by evening up the total head profile, indicated by a 5-point yaw-insensitive rake placed at the outlet of a blade passage, about halfway between the traversed blades and the

---

[1] Chief Aerodynamicist, Gas Turbine Engineering Division, A. V. Roe Canada Ltd.

[2] "Fluid Dynamics of Axial Compressors," by A. R. Howell, Proceedings of The Institution of Mechanical Engineers, vol. 153, 1945, p. 441.

Contributed by the Gas Turbine Power and Aviation Divisions and presented at the Semi-Annual Meeting, Toronto, Can., June 11–15, 1951, of The American Society of Mechanical Engineers.

Note: Statements and opinions advanced in papers are to be understood as individual expressions of their authors and not those of the Society. Manuscript received at ASME Headquarters, April 18, 1951. Paper No. 51—SA-31.

[3] "The Present Basis of Axial Flow Compressor Design, Part 1," by A. R. Howell, ARC R & M 2095, June, 1942.

[4] "The Performance of Axial Flow Turbines," by D. G. Ainley, Proceedings of The Institution of Mechanical Engineers, vol. 159, 1948, p. 230.

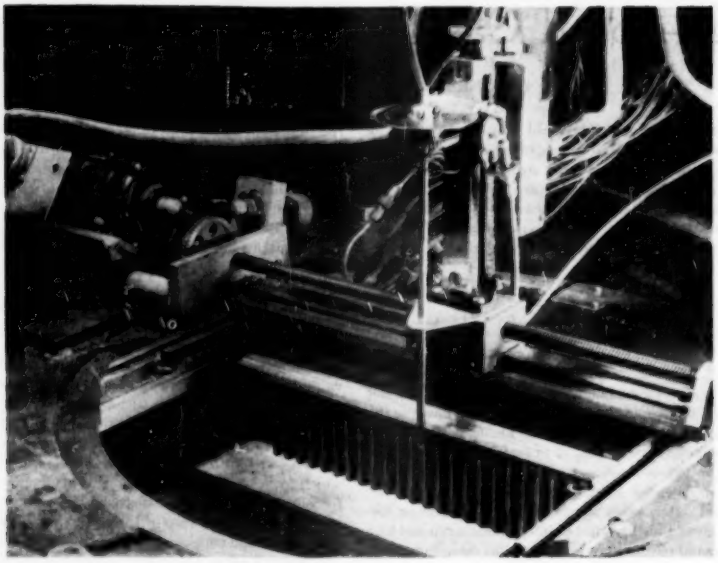

FIG. 1 CASCADE OUTLET WITH COVER PLATE REMOVED

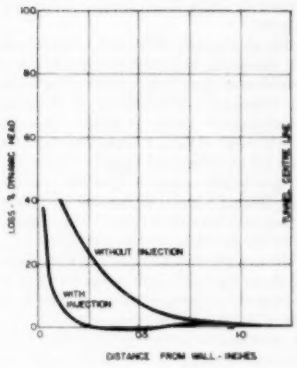

FIG. 2 VERTICAL LOSS PROFILE WITH AND WITHOUT BOUNDARY-LAYER INJECTION

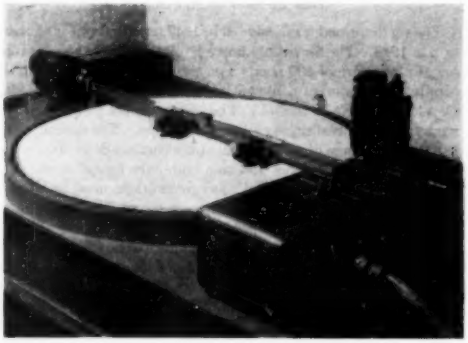

FIG. 3 CASCADE RECORDER

end blade of the cascade. The existence of the wall boundary layer is much more important for compressor cascades than for turbine cascades owing to the adverse pressure gradient with the former. Even the large difference between the inlet profiles shown in Fig. 2 made little difference to the traverse results for turbine cascades with a fairly high degree of reaction.

The entry Mach number is adjusted by means of a simple machmeter operating on the nomogram principle. The nomogram chart is printed on a sheet of paper stretched between two rollers behind two manometer tubes, one of which reads the total head pressure recorded by an upstream probe, the other the average static pressure read from holes on the top rotating plate immediately ahead of the cascade. The paper is moved laterally from one roller to the other by the operator until its zero line coincides with the mercury level of the static-pressure manometer. The Mach number is then read from the paper chart at the mercury level of the total head manometer.

The outlet instrumentation is remotely operated from the observation room, and the readings of total head and yaw are recorded automatically. Fig. 1 shows details of this. It will be seen that the probe is mounted in a motorized traverse gear, its position at any time being indicated by a selsyn motor which transmits to another selsyn acting as driving motor to the circular recording table shown in Fig. 3. The probe shown is of the three-hole yaw type, the pressures of the yaw detection holes being taken to the balance capsule. Any pressure difference between the two holes causes movement of a diaphragm which thereby alters the capacity balance of a bridge circuit. Balance is then

automatically restored by rotation of the probe by a 2-phase 110-volt Dehl motor, driving through a cable. At the same time a selsyn transmits the probe angle to the yaw pen of the recorder, so that radial movement of the pen is proportional to the change in probe angle. Simultaneously, the central hole of the probe transmits the total head pressure to one of the tubes of a recording manometer. The left tube uses mercury for high Mach number traverses while the right tube has Miriam fluid of specific gravity 3 to increase the accuracy for low-speed work. A photoelectric cell with its own light source on the opposite side of the manometer tube is arranged so that it follows the fluid level.

The method chosen for this was to amplify the 60-cycle current emitted by the photocell, resulting from the fluctuating intensity of the lamp which is supplied from the a-c mains through a half-wave rectifier. The amplified current is then mixed with a similar current which is out of phase. The resultant current therefore suffers a phase change between full illumination of the photocell and complete obstruction of the light source. The current is fed to one of the stator windings of another Dehl motor which rotates either clockwise or anticlockwise depending on the phase, and this in turn raises or lowers the photocell until balance—in this case zero current—is achieved. The rotation of this motor is transmitted as before by selsyns to the total head pen of the recorder. Both the yaw and total head pens are equipped with wheels taken from Amsler planimeters and driven by the rotating chart table so that they integrate the readings over the complete blade pitch. Usually three blade pitches are traversed and the mean taken. It has been found that an average traversing rate of 1 ipm is normally possible before inaccuracies due to the response rate of the equipment appear. The operator sees the traverse results being traced on the recorder and may increase the traverse speed in the wake-free distance between blades and reduce it as soon as the pens begin to register a wake.

Fig. 4 shows a typical traverse in which, for the sake of comparison, the yaw trace has been superimposed onto the total head

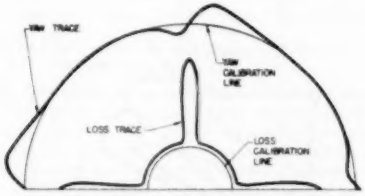

Fig. 4 Typical Traverse Record

trace. Actually, corresponding points are on opposite sides of the center on the same diameter. The use of this traverser and recorder increased the productivity of the tunnel by a factor of about 8. With this rate of accumulation of data the limiting feature then becomes the computing time necessary for its analysis. For this reason the data are transferred to punch cards and all processing, including instrument corrections and final analysis, is done on standard International business machines.

The cylindrical three-hole yaw probe was originally chosen as the standard probe for its robustness. It has the disadvantage, however, that in a flow with a total head gradient it has an error in its yaw indication as it must be turned at an angle to the flow in order to balance the pressures in its yaw holes. This also causes an error in the total head reading. To check this, traverses were made of a two-dimensional jet from a rectangular hole. It was found that the error in total head reading could be accounted for almost exactly by the amount of lateral movement of the total head hole due to the rotation required to balance the yaw holes. This amounts to a distance of $r \sin \theta$, where r is the radius of the probe and θ the angular error. The error in mean yaw indicated is small since the error in entering a wake is opposite in sign to the error in leaving the wake, and, for a symmetrical wake, these cancel each other. However, the error in total head is additive and the effect is to reduce the mean loss indicated. However, this may be reduced to a negligible amount by rotating the probe about an axis through the total head hole. This is not always convenient.

Another disadvantage of this type of probe is that its critical Mach number occurs at about 0.55, making it unsuitable for the measurement of static pressures above this value owing to the large corrections involved. For cascade traversing this is not serious since the static pressure at the outlet is assumed to be atmospheric, but for other applications, such as compressor traversing, this would be more important. This type of probe therefore has been replaced by a wedge-shaped three-hole probe as shown in Fig. 5.

By use of this probe errors in yaw are reduced greatly since the yaw holes are now closer together and the error in total head associated with this is thereby also reduced. The probe also has good characteristics at high Mach numbers and, when calibrated, gives an accurate value of static pressure. The actual position of the holes is not as critical as with the cylindrical probe, so that it is

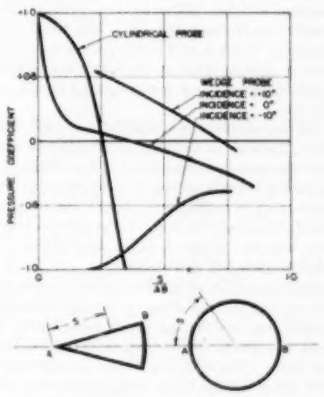

Fig. 5 Characteristics of 30-Deg Wedge-Shaped Probe (Pressure distribution of cylindrical probe shown as comparison.)

possible to manufacture many probes with almost identical calibration.

Fig. 5 shows the pressure distribution around the two types of probe, from which it can be deduced that any error in positioning of the hole designed to read free-stream static pressure causes a difference in pressure about 16 times as great with the cylinder as with the wedge, whereas the sensitivity to yaw is greater in the case of the wedge. Tests have shown that the probe illustrated measures the average static pressure to within 1.5 per cent when used for a wake traverse of a turbine cascade at an outlet Mach number of 0.8 and was even closer at lower Mach numbers.

Analysis of Results

The application of punch-card methods permits the analysis of results to be carried further than normally is considered practical with so large a volume of data. Results, as usually presented, go no further than to show the performance of the cascade. In use

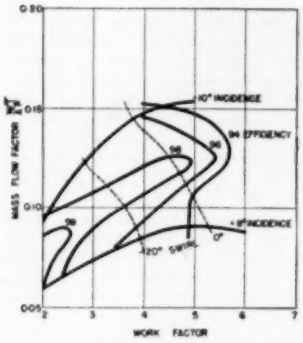

FIG. 6 TURBINE-PERFORMANCE CHART FOR IMPULSE-TYPE SECTION

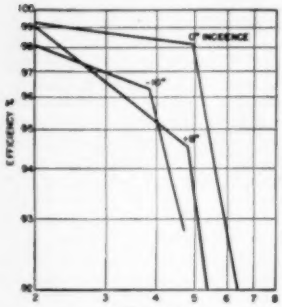

FIG. 7 EFFICIENCY VERSUS WORK FACTOR FOR IMPULSE CASCADE

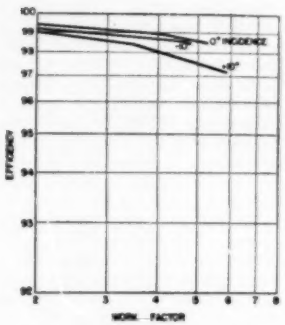

FIG. 8 EFFICIENCY VERSUS WORK FACTOR FOR REACTION CASCADE

in a turbine the value of any cascade depends on a combination of its loss, stagger, incidence range, Mach-number effects, and so on. For instance, the loss itself is not a true measure of the value of a cascade. A cascade with a higher loss also may give a higher lift, so that the loss in proportion to the capacity for doing work is a better measure of value. By an analysis presented in the Appendix, the results can be converted into a form which shows the turbine performance which would result for any given cascade. In the absence of definite data on the three-dimensional effects the only loss considered is the two-dimensional loss as derived from the cascade test.

The nozzle loss also has been omitted, but when sufficient data are available, this may be included, as the analysis does define the required nozzle-operation condition. A loss of complete generality occurs since it is found necessary to fix the ratio of blade speed to the square root of turbine-inlet temperature. However, it is found that this parameter has not too important an effect on the comparison, and its neglect is quite justifiable for the normal range of design operating conditions.

One convenient feature of the use of punch-card methods is that if any new specific turbine design is required having a value of this parameter largely different from the one chosen for the general analysis, all relevant cascade results can be recalculated quickly on the new basis. The most important parameter is the ratio of work to the square of the blade speed, which is used nondimensionally as the abscissa of the plot. Next in importance is the mass flow which unit height of the blade will pass, since, if this is low, a large blade length will be required. This is used, again in nondimensional form, as ordinate.

Fig. 6 is an example of the plot which shows the blade incidence, efficiency contours, and the angle of swirl required at exit. The nozzle-outlet Mach number also may be included on the plot but has been omitted in Fig. 6 to avoid undue complication of the diagram. The angle of swirl is important since there is a limit to this value above which it is found necessary to add an outlet stator to the turbine. In the case of a multistage turbine this restriction applies only to the last stage. If, from these plots, we extract values of efficiency for a given incidence, we find that when plotted on log-log paper in the form illustrated in Figs. 7 and 8, a definite break is found for each cascade section.

Fig. 7 shows such a plot for an impulse type of cascade, which may be compared with Fig. 8 which gives the plot for the same section operated as a reaction cascade. It will be seen that a greater range of incidence at high efficiency is possible with the reaction type of design and that the break when it occurs is much less catastrophic in this case. The lines after the break should not be extrapolated since their end points represent choking of the cascade. The ordinate in this plot is actually the efficiency minus 90 so that efficiencies below 90 cannot be represented, and any efficiency line which closely approaches 90 must have a slope approaching infinity. The fact that the lines below the break value of the work factor show no tendency to fall at the lowest values of the work factor indicates that the test points from which the plot was made did not fall below the critical Reynolds number. Considering Fig. 7, it is obvious that for this particular section a useful gain in efficiency would result for a turbine of work factor 5.5 by making it a two-stage rather than a single-stage turbine, thereby halving the work factor, and that no significant increase of efficiency would result by the use of a three-stage turbine.

Fig. 9 is a comparison of the 98 per cent efficiency curves of

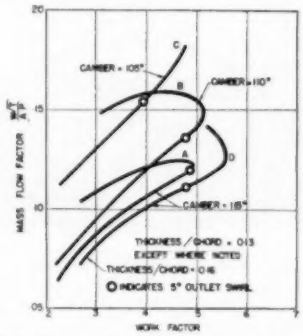

A, Inlet blade angle 60 deg; thickness/chord 0.13
B, Inlet blade angle 55 deg; thickness/chord 0.13
C, Inlet blade angle 50 deg; thickness/chord 0.13
D, Inlet blade angle 60 deg; thickness/chord 0.16

FIG. 9 COMPARISON OF 98 PER CENT EFFICIENCY CONTOURS FOR FOUR T6 AIRFOIL SECTIONS OF FOOTNOTE 4 WITH PARABOLIC CAMBER LINE AND OUTLET BLADE ANGLE 55 DEG

some representative cascades. Curves A, B, and C are for cascades of thickness/chord ratio 0.13, all having a parabolic camber line and the same blade-outlet angle of 55 deg. They differ only in their inlet angles which are 60 deg, 55 deg, and 50 deg, respectively. It will be seen that, for the same work factor, the cascades

pass greater mass flow as the inlet angle is reduced. This means that for given turbine-inlet conditions the lower curves will require a greater blade height. If stresses and blade temperatures are limiting, it is advantageous to use the cascades giving higher values of the mass-flow parameter. However, the smaller blade height has the disadvantage of introducing higher three-dimensional loss and a greater exit velocity, which will result in higher exhaust loss. As soon as reliable data for the prediction of such effects are available they should be used to modify the charts for any specific turbine to present a truer picture. The circled points on the curves indicate where the curve for 5-deg outlet swirl from the turbine cuts the efficiency contours. The parts of the contours to the right of these points therefore must be assessed with this in mind. Curve D is for a cascade similar to that of curve A but having a thickness/chord ratio of 0.16. In this case the thicker profile improves the shape of the passage between adjacent blades so that the 98 per cent efficiency contour extends over a greater range.

Fig. 10 summarizes the results obtained to date on this rig for turbine cascades at an outlet Mach number of 0.90. It will be seen that the main variable influencing loss is the degree of reaction, or the ratio of the outlet flow area to inlet flow area of the cascade. For a given cascade, positive incidence has the effect of increasing this ratio and the resultant increase of loss is shown clearly in Fig. 10. However, the increased incidence permits a higher work factor so that the effect on turbine efficiency is not as great as the effect on the cascade loss and graphs such as Fig. 6 must be used for a proper evaluation of this factor.

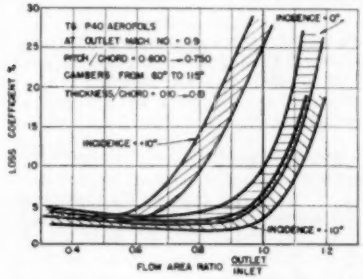

FIG. 10 SUMMARY OF RESULTS FOR OUTLET MACH NUMBER OF 0.90
(Loss coefficient versus blade outlet/blade inlet area ratio.)

CONCLUSIONS

For a full appreciation of the merit of any cascade, it is necessary to make a comparison on the basis of the efficiency which can be achieved by this cascade when operated as a turbine, and for specific turbine designs a satisfactory method has been evolved to make such a comparison. It is essential that methods should be evolved of incorporating the three-dimensional effects into such an analysis to give the true picture. The use of punch-card methods is highly recommended for the type of analysis presented in this paper.

ACKNOWLEDGMENT

The author's thanks are due to A. V. Roe Canada Limited for permission to use the data contained in this paper.

NOMENCLATURE

The following nomenclature is used in the Appendix:

A = turbine annulus area, sq ft
c_p = specific heat of gas at constant pressure, CHU/lb deg C
g = gravitational constant, fps per sec
H_e = turbine work, deg C
J = mechanical equivalent of heat, ft-lb/CHU
M = weight flow through turbine, lb per sec
P_t = total gas pressure, psf
p_s = static gas pressure, psf
R = gas constant $= c_p - c_v$ CHU/lb deg C
T_t = total gas temperature, deg K
t_s = static gas temperature, deg K
U = blade speed, fps
V = gas speed, fps
α = angle relative to rotor or cascade blade, deg
γ = ratio of specific heats $= C_p/C_v$
ρ = gas density, pcf
ψ = outlet swirl angle relative, deg
η_c = cascade profile efficiency (adiabatic)
η_t = equivalent turbine profile efficiency (adiabatic)
θ_u = temperature equivalent of blade speed, deg C
θ_v = temperature equivalent of gas speed, deg C

Subscripts:

r = relative to rotor
1 = rotor inlet plane
2 = rotor outlet plane
A = axial
W = whirl

A METHOD OF PRESENTATION OF TURBINE-CASCADE DATA

Referring to Fig. 11, expansion in cascade is given by line *A-D*.

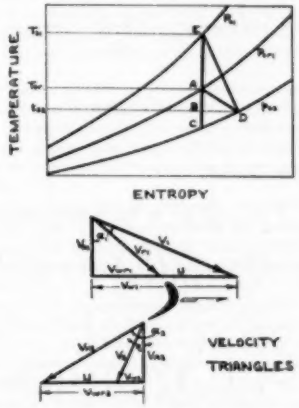

FIG. 11 CASCADE TO TURBINE-CONVERSION DIAGRAMS

Define cascade efficiency

$$\eta_c = \frac{AB}{AC}$$

$$AB = T_{t1} - t_{t2} = \theta_{v2} = \frac{V_{x2}^2}{2gJc_p}$$

As a turbine the expansion is the line E-D, and define turbine efficiency

$$\eta_t = \frac{EB}{EC} = \frac{AB + EA}{AC + EA}$$

$$= \frac{\frac{AB}{AC} + \frac{EA}{AC}}{1 + \frac{EA}{AC}} = \frac{\eta_c + \frac{EA}{AC}}{1 + \frac{EA}{AC}}$$

Now

$$AC = \frac{\theta_{vs}}{\eta_c} = \frac{V_{r1}^2}{K^2\eta_c}$$

where

$$K^2 = 2gJc_p$$

and

$$EA = T_{t1} - T_{s1} = \theta_{t1} - \theta_{s1}$$

$$= \frac{1}{K^2}\left[(U + V_{r1}\sin\alpha_1)^2 - V_{r1}^2\sin^2\alpha_1\right]$$

$$= \frac{1}{K^2}\left(U^2 + 2UV_{r1}\sin\alpha_1\right)$$

$$\therefore \eta_t = \frac{\eta_c\left[1 + \left(\frac{U}{V_{r1}}\right)^2 + 2\left(\frac{U}{V_{r1}}\right)\left(\frac{V_{r1}}{V_{r1}}\right)\sin\alpha_1\right]}{1 + \eta_c\left[\left(\frac{U}{V_{r1}}\right)^2 + 2\left(\frac{U}{V_{r1}}\right)\left(\frac{V_{r1}}{V_{r1}}\right)\sin\alpha_1\right]} \quad \ldots [1]$$

The values of η_c, V_{r2}/V_{r1}, $\sin\alpha_1$ are found from cascade tests. The only unknown is U/V_{r1} and this is found from the cascade Mach number, M_{Nr1}

$$M_{Nr1}^2 = \frac{V_{r1}^2}{n^2 t_{s1}}$$

where

$$n^2 = gJ\gamma R$$

Now

$$t_{s1} = T_{t1} - \theta_{s1}$$

$$= T_{t1} - \frac{1}{K^2}\left[U^2 + V_{r1}^2 + 2UV_{r1}\sin\alpha_1\right]$$

$$\therefore \frac{1}{M_{Nr1}^2} = \frac{n^2T_{t1}}{V_{r1}^2} - \frac{n^2}{K^2}\left[\left(\frac{U^2}{V_{r1}^2}\right) + 1 + 2\left(\frac{U}{V_{r1}}\right)\sin\alpha_1\right]$$

$$= \frac{n^2T_{t1}}{U^2}\frac{U^2}{V_{r1}^2} - \frac{n^2}{K^2}\left[\left(\frac{U^2}{V_{r1}^2}\right) + 1 + 2\left(\frac{U}{V_{r1}}\right)\sin\alpha_1\right]$$

$$= \frac{n^2}{K^2}\left[\left(\frac{U^2}{V_{r1}^2}\right)\left(\frac{T_{t1}}{\theta_{s1}} - 1\right) - 2\left(\frac{U}{V_{r1}}\right)\sin\alpha_1 - 1\right]$$

and

$$\frac{K^2}{n^2} = \frac{2gJc_p}{gJ\gamma R} = \frac{2}{\gamma - 1}$$

$$\therefore \frac{U^2}{V_{r1}^2}\left(\frac{T_{t1}}{\theta_{s1}} - 1\right) - 2\left(\frac{U}{V_{r1}}\right)\sin\alpha_1 - \left[1 + \frac{2}{(\gamma - 1)M_{Nr1}^2}\right] = 0 \quad \ldots [2]$$

From this quadratic a series of values of U/V_{r1} may be found by substituting a series of values of T_{t1}/θ_{s1} equal to that for the turbine design in which the cascade is to be used. Knowing U/V_{r1} and V_{r1}/V_{r2} a value of U/V_{r2} can be calculated and substituted in Equation [1]. A value of $\gamma = 1.4$ is used so that the results refer to a cold-air turbine. However, for the value of T_{t1}/θ_{s1} estimated from the turbine design the value of c_p for hot gas is used.

The two other important values to be calculated are (*a*) the work done and (*b*) the mass flow.

For the work done, H_s deg C, we have

$$H_s = \frac{U(V_{w1} + V_{w2})}{gJc_p}$$

$$= \frac{U(V_{r1}\sin\alpha_1 + V_{r2}\sin\alpha_2)}{gJc_p}$$

$$\frac{H_s}{\theta_{s1}} = 2\left(\frac{V_{r2}}{U}\right)\left(\frac{V_{r1}}{V_{r2}}\sin\alpha_1 + \sin\alpha_2\right) \quad \ldots [3]$$

For the mass flow, M, we have

$$M = \rho A_1 V_{A1} = \frac{1}{RJ}\frac{A_1 p_{s1}}{t_{s1}}V_{r1}\cos\alpha_1$$

Now

$$\frac{M\sqrt{T_{t1}}}{P_{t1}} = \frac{M\sqrt{t_{s1}}}{P_{s1}}\left(\frac{T_{t1}}{t_{s1}}\right)^{\frac{\gamma+1}{2(1-\epsilon)}}$$

and

$$t_{s1} = T_{t1} - \frac{1}{K^2}\left(U^2 + V_{r1}^2 + 2UV_{r1}\sin\alpha_1\right)$$

$$\therefore \frac{t_{s1}}{T_{t1}} = 1 - \frac{\theta_{s1}}{T_{t1}}\left[1 + \frac{V_{r1}^2}{U^2} + 2\left(\frac{V_{r1}}{U}\right)\sin\alpha_1\right]$$

$$\therefore \frac{M\sqrt{T_{t1}}}{A_1P_{t1}} = \frac{n}{RJ}M_{Nr1}\cos\alpha_1$$

$$\left\{1 - \frac{\theta_{s1}}{T_{t1}}\left[1 + \left(\frac{V_{r1}}{U}\right)^2 + 2\left(\frac{V_{r1}}{U}\right)\sin\alpha_1\right]\right\}^{\frac{\gamma+1}{2(\gamma-1)}} \quad \ldots [4]$$

Expressions also may be derived for the outlet swirl angle ψ

$$\tan\psi_2 = \frac{V_{w2}}{V_{A2}} = \tan\alpha_2 - \frac{U}{V_{A2}}$$

$$= \tan\alpha_2 - \left(\frac{U}{V_{r2}}\right)\frac{1}{\cos\alpha_2}$$

$$\therefore \psi_2 = \tan^{-1}\left[\tan\alpha_2 - \left(\frac{U}{V_{r2}}\right)\frac{1}{\cos\alpha_2}\right] \quad \ldots [5]$$

The Mach number at the turbine nozzle outlet may also be evaluated

$$V_1^2 = V_{w1}^2 + V_{A1}^2$$

$$= (U + V_{r1}\sin\alpha_1)^2 + (V_{r1}\cos\alpha_1)^2$$

$$= U^2\left[1 + \left(\frac{V_{r1}}{U}\right)^2 + 2\left(\frac{V_{r1}}{U}\right)\sin\alpha_1\right]$$

and

$$t_{s1} = T_{t1} - \theta_{s1} = T_{t1} - \frac{U^2}{K^2}\left[1 + \left(\frac{V_{r1}}{U}\right)^2 + 2\left(\frac{V_{r1}}{U}\right)\sin\alpha_1\right]$$

but

$$M_{X1}^2 = \frac{V_1^2}{n^2 a_{t1}} = \frac{U^2\left[1 + \left(\frac{V_{r1}}{U}\right)^2 + 2\left(\frac{V_{r1}}{U}\right)\sin\alpha_1\right]}{n^2\left\{T_{t1} - \frac{U^2}{K^2}\left[1 + \left(\frac{V_{r1}}{U}\right)^2 + 2\left(\frac{V_{r1}}{U}\right)\sin\alpha_1\right]\right\}}$$

$$\therefore M_{X1} = \sqrt{\frac{2}{\gamma - 1}\left\{\frac{1 + \left(\frac{V_{r1}}{U}\right)^2 + 2\left(\frac{V_{r1}}{U}\right)\sin\alpha_1}{\left(\frac{T_{t1}}{\theta_n}\right) - \left[1 + \left(\frac{V_{r1}}{U}\right)^2 + 2\left(\frac{V_{r1}}{U}\right)\sin\alpha_1\right]}\right\}} \quad [6]$$

Discussion

W. B. Briggs.[8] *Tunnel Design and Operation.* A cascade-tunnel design having air flow with negligible turbulence is listed as being advantageous and it is in some ways, but it is well to point out that low turbulence has the overpowering disadvantage of delaying transition on the surface of the blades and causing them to perform much differently than they would in a high turbulence machine such as a rotating turbine. A high turbulence level will create a thicker boundary layer on the inlet walls but methods of controlling the boundary layer ahead of the blades, such as sucking or blowing, are available for incorporation in a tunnel design. So, since one is primarily interested in duplicating the performance a blade will give when used in a turbine, the use of highly turbulent air will produce the most natural, two-dimensional boundary-layer behavior.

It is questionable that a tunnel designed with an open jet behind the cascade allows the measurement of the true outlet angle more correctly than will one with side walls. It does afford greater accessibility. However, two-dimensional tunnels customarily employ outlet side walls and, by utilizing adjustable flaps which the operator positions to equalize the static pressure parallel to the cascade axis, they simulate an infinite cascade to obtain the true angle.

The novel feature of the cascade tunnel reported by the author is the control of the side-wall boundary layer by injecting air to energize the low-momentum region near the wall. Blowing is often employed to prevent or delay separation but is seldom thought of as a tool to achieve the thinner boundary layer that is reported in Fig. 2. Suction is most commonly thought of as an effective method for this. It not only requires less power but does not introduce jet boundaries which must intermingle smoothly in a short distance to achieve the uniform inlet-velocity profile desired. An elaboration of this blowing feature would be most interesting. A description of such items as the design and location of the slots, how many slots were used, and the way the uniformity of flow through them is controlled, what per cent of free-stream air was required, and how the quantity varied with free-stream Mach number, how the secondary losses through the cascade are affected by the blowing, and so on, would be most valuable.

Instrumentation. The use of a combination probe for measuring total pressure, static pressure, and yaw in one instrument and the reported automatic recording device are quite ingenious. The claims made for the instrument, however, are far stronger than seem justifiable. To combine the measuring of more than one quantity in a single probe is to compromise the accuracy of measuring each quantity. An error no greater than 1½ per cent in measuring static pressure at 0.8 Mach number would be exceedingly good for a sharp wedge having a very small included angle and measuring static pressure only. The interpretation of Fig. 5 must be that the decreased sensitivity to hole location is concomitant with decreased sensitivity to angle of yaw, hence less accurate angle measurements. The use of a combination instrument in this application seems to decrease unnecessarily the accuracy of measurement because a second probe could be tandem-mounted in phase in the survey slot a blade or two displaced to record one of the quantities on the data table.

The automatic recording device is similar in concept to ones that are commercially available from various companies such as the X-Y Recorder (rectangular co-ordinate) made by Leeds and Northrup.

Proposed Method of Analysis. The author's introduction of "work factor" and "flow factor" makes a good point in that a turbine must be evaluated on the basis of the work it performs, not on the basis of its losses alone. H. Constant, in a discussion of Howell's paper,[9] recorded the degree of advancement of present-day analysis when he stated that it is relatively simple to predict compressor or turbine performance, neglecting losses, from two-dimensional data. However, he says, the most important factor is the behavior of the losses. The analysis presented neglects major losses, which is pointed out. But the claims for the utility of the method seem to be in no way substantiated by the material presented. The assumptions of Fig. 11, used to define cascade and turbine efficiencies, are quite debatable. A different assumption such as both machines having the same polytropic expansion would be as good, but it would give different results. The value and the extent of the applicability of the method can be ascertained only when a comparison of results from a rotating cascade with the predicted values can be made. It will be very valuable if such material can be presented at an early date.

It might be remarked that the behavior shown in the curves of Figs. 7 and 8 is corroborated for impulse and reaction blades in a paper by E. R. G. Eckert.[7] Eckert's conclusion is that the greater range of incidence at high efficiency available with the reaction type of blade is a direct function of the leading-edge radius.

D. G. Traver.[6] The description of the cascade stand is a welcome addition to the literature. Several of the testing techniques are novel. The dimensions of the wedge probe would be of interest since the author states the yaw holes are closer together in his wedge probe than in his cylindrical probe which appears to be about 0.100 in. OD.

Perhaps some of our cascade philosophy would be of interest. We have tested with cascades of blades of the same size as A. V. Roe now uses. This was abandoned in favor of low-speed testing and a new cascade stand was built utilizing larger blades of 3 to 3½ in. chord.

We preserve high Reynolds number but sacrifice high Mach number. We feel that Mach effects are negligible, particularly since our current commercial gas turbines operate below **M** = 0.6. This may have to be revised in the future when the operating Mach number will be higher.

The four times larger blades result in proportionately larger wakes. However, we increased total head-probe size by a factor of 2 (thereby reducing the dynamic response time) and still have one half of the previous probe diameter to wake-width ratio.

[8] National Advisory Committee for Aeronautics, Lewis Laboratory, Cleveland, Ohio

[9] "The Aerodynamics of the Gas Turbine," by A. R. Howell; discussion by H. Constant, *Journal of the Royal Aeronautical Society* London, England, vol. 52, 1948, p. 353.

[7] "Conclusions From Interference Measurements as to the Form to Be Given Turbine Blades," by Ernst R. G. Eckert, from the reports of the Lattice Conference in Braunschweig, Germany, March 27–28, 1944, NACA Rej. TM.

[6] Research and Development Department, Elliott Company, Jeanette, Pa. Jun. ASME.

This probe to wake size effect was the cause of much concern about the validity of our cascade data. In traversing a pressure gradient a total head pressure probe does not read a point pressure, but owing to the finite hole diameter, reads an integrated pressure of the gradient existing over this diameter. The severe wake gradient found at the trailing edge is of course attenuated with distance, and due to the foregoing sources of error we now traverse physically larger wakes at a half chord length downstream.

The blades are large enough to permit extensive instrumentation to obtain the circumferential pressure distribution. This correlates blade performance with pressure distribution, and it is possible to locate regions of adverse gradient and to modify the local blade shape to improve performance further.

Given an inlet and discharge angle, we design a blade shape on a wire flow-net plotting device to give a prescribed pressure distribution. We attempt to realize maximum pressures over as large a percentage of the blade surface as possible and to minimize or prevent separation at the nose and at the vicinity of the trailing edge. We feel that better results are obtained, both on short-term and long-term results, from designing a family of blades on the basis of a previously selected pressure distribution than from designing on the basis of a selected mathematical family of camber lines combined with a blade-thickness schedule.

No mention is made of measuring upstream yaw angles. Owing to the oblique angle of the cascade with reference to the air direction, there may exist a deviation between a geometric inlet angle and the actual air direction. Such a measurement must be made slightly upstream of a cascade to avoid the pronounced local deflections of the air stream at the nose due to circulation. This deflection angle would be of more importance in evaluating compressor cascade results, due to their lower air turning angle than that of turbine cascades.

Author's Closure

The author is in agreement with Mr. Briggs that the turbulence of the blown tunnel may be an advantage. This is illustrated by the tunnel described in the paper, where no disconcerting Reynolds-number effects occur even at the lowest Mach numbers employed, these being around 0.4. Outlet side walls were considered when the tunnel was designed but the extra complication of manipulating them to equalize the outlet static pressure decided us in favor of using more blades instead and accepting the resultant reduction in scale.

Suction of the inlet boundary layer was designed into the rig but reference to Fig. 2 of the paper will show that, with the boundary-layer thickness encountered, the mass of air which would have to be sucked would have been prohibitive. It was decided that it would be easier and more effective to "fill up the hole." Perhaps the closest parallel is the type of ejector where the primary air is introduced at the wall, the so-called annular ejector. The boundary-layer injection slots stretch from wall to wall on top and bottom plates about 1 ft upstream of the cascade. They are curved converging passages discharging from two relatively large plenum chambers, their outlets being flush with the plates and directing the air almost tangentially. The total injected mass flow is roughly 25 per cent of the total flow and is introduced equally at top and bottom. This percentage does not change much with Mach number but varies with the tunnel-angle setting (about 20 per cent at zero angle up to 28 per cent at the 70-deg setting). The most important effect on compressor cascades of improving the inlet profile is to increase the turning angle (by as much as 5 deg in some cases).

The author cannot agree with Mr. Briggs' comments on instrumentation. The measurement of static pressure requires yaw measurement taken simultaneously in order that the probe shall be aligned correctly with the local air flow. It is an extremely doubtful assumption to say that wakes from blades one or two pitches apart are sufficiently similar to allow a yaw measurement in one wake to control the alignment of a probe in another, especially in view of the large rate of change through the wake. The author regrets misinterpretation of his statement on the accuracy of the wedge-type probe. The probe is first calibrated in a wind tunnel to determine a Mach-number correction factor to be applied to the static pressure. After this calibration factor has been applied to the results of a wake traverse, the remaining discrepancy, attributable to the presence of the wakes, is 1.5 per cent at an outlet Mach number of 0.8.

It is believed that Mr. Briggs also has misinterpreted Fig. 5 and an example is given here to clarify any doubts on this score. Take the wedge-shape probe with holes located at $S/AB = 0.25$. Fig. 5 shows that a rotation of the probe through 20 deg, i.e., from +10 to −10 deg incidence, changes the pressure coefficient from +0.5 to −1.0. Tests with the cylindrical probe show that a rotation of 30 deg is required for an equivalent change in pressure coefficient. On the other hand, for probes with the same value of the characteristic dimension (the length of the wedge side for the wedge probe, the diameter for the cylindrical probe), Fig. 5 shows the cylinder to have a much steeper variation of pressure coefficient with the surface distance S from the leading edge.

The choice of a polar plotting table rather than one working in rectangular co-ordinates was to simplify the integration mechanism.

As pointed out in the paper, the analysis is limited in that it is based on two-dimensional losses only, but one thing is fairly certain—that if the charts show that a turbine has a narrow operating range on the basis of the two-dimensional loss alone, it will not be any better with three-dimensional losses included, so that we can weed out, even from these limited charts, the really bad ones. Admittedly, a different definition of turbine efficiency would give different numerical answers, but it is doubtful whether it would alter the relative values of the comparison of two turbines. One refinement which might be added is the inclusion of a fraction of the dynamic head at outlet to represent the loss in the exhaust system. In this way the total-to-static efficiency used here could be converted to a total-to-total efficiency which is the other generally accepted efficiency.

Our tests on turbine cascades, using identical blades but at increased reaction, show the characteristic increase of incidence range even though the leading-edge radius remained unaltered.

Mr. Traver has contributed some interesting points in his discussion. He is fortunate in being able to neglect Mach number in the commercial gas turbines, but this is a difficulty which the designer of aircraft turbines cannot ignore because of the necessity of a compact high-output engine. The author, however, disagrees with a general statement that Mach-number effects below $M = 0.6$ are negligible if this quoted value refers to the inlet Mach number. A reaction blade with a ratio of inlet area to throat area of about 1.2 will choke at an inlet Mach number less than 0.6. In our testing, we recognize that our measured loss values are not the true loss because of probe error in a total pressure gradient but feel that they give, nevertheless, the proper relative results in a comparison of different cascades. Traverses have been made at a series of different distances downstream of the blades and have supported this contention. In particular, it was found that the measured flow angle changed very slightly with distance downstream except in the immediate vicinity of the trailing edge. This is reassuring as the problem of matching stages in a multistage compressor is much more dependent on a knowledge of the direction of exit flow than it is on obtaining a true value of the two-dimensional loss.

The design of blades for a predetermined pressure distribution is fine providing that the time to do this is available, which we usually find is not the case since schedules have to be met. The other prerequisite is that the best form of pressure distribution is known. In the absence of Mach-number effects a uniform pressure over most of the suction surface gives a high lift coefficient and high critical Mach number, but this type of distribution leads to catastrophic deterioration in performance as soon as the critical Mach number is exceeded. A peaked distribution suffers an earlier critical Mach number but the slower rise in loss allows it to be operated to considerably higher Mach numbers. For compressors this avoids marked deterioration in altitude performance.

In answer to the question of probe size, the comparisons were made with probes having the same projected frontal area. The cylindrical was 0.125-in. diam and the 30 deg angle wedge probe fitted within a circumscribing circle 0.250-in. diam. The holes were 0.08 in. apart for the cylindrical and 0.036 in. for the wedge.

Corrections for upstream yaw angles are applied to our cascade results.

The Life of High-Speed Ball Bearings

By A. B. JONES,[1] NEW BRITAIN, CONN.

At high rotational speeds the centrifugal force on the balls increases the probability of failure of the outer race in the case of a radial-type ball bearing under radial load and hence reduces bearing life. In an angular contact bearing operating under thrust load, centrifugal loading of the balls produces a higher operating contact angle for the inner race than the outer, thus affecting the relative probabilities of failure of inner and outer races and hence must be considered in calculating bearing life.

Nomenclature

The following nomenclature is used in the paper:

- n = number of balls
- d = ball diameter, in.
- E = pitch diameter, in.
- N_i = rpm of inner ring
- R = external radial load, lb
- J_o, J_i = radial-load-distribution factors
- T = external thrust load, lb
- P_{max} = load on heaviest loaded ball due to static radial load, lb
- P_φ = load on a ball at co-ordinate φ due to static radial load, lb
- F = ratio defined by Equation [3]
- (CF) = centrifugal force on ball, lb
- P_o = outer race ball load for basic dynamic capacity, lb
- P_i = inner race ball load for basic dynamic capacity, lb
- C_o = capacity of outer race
- C_i = capacity of inner race
- C = capacity of complete bearing, lb
- $_{n\cdot A}$ = subscripts referring, respectively, to centrifugal force and static loading conditions
- L = life
- β' = initial or design contact angle
- β = contact angle under static thrust, T
- β_o = outer race operating contact angle
- β_i = inner race operating contact angle
- δ_o = normal approach of ball to outer race, in.
- δ_i = normal approach of ball to inner race, in.
- K_o, K_i = deflection constants depending on race curvatures and material
- f_o, f_i = outer and inner race curvature factors, respectively = race-curvature radius ÷ ball diameter
- X = relative axial displacement of outer and inner rings, in.
- φ = angular co-ordinate

Introduction

As the result of many years of co-operative effort and research by the ball-bearing industry, the Anti-Friction Bearing Manufacturers' Association published the "Standardized Method for Evaluating the Load Ratings of Annular Ball Bearings" (1)[2] in 1950. This method, which is (1951) the basis for the catalog load ratings of most of the major ball-bearing manufacturers, is built upon the statistical theory of rolling-bearing endurance developed by (2, 3) G. Lundberg and A. Palmgren.

Briefly, the Lundberg-Palmgren theory is based upon (4, 5) Weibull's findings that the strength of a material is dependent on the magnitude of the stressed volume and on a statistical formula for the dispersion in the lives of similar bearings tested under similar conditions. In the Lundberg-Palmgren theory the stress considered decisive in causing fatigue failure is taken as the shear stress amplitude calculated in a plane parallel to the rolling direction and below the surfaces of the rolling elements. The carrying capacity of a complete bearing is shown to be a statistical function of the capacities of the components for a preassigned probability of survival and for a distribution of load among the rolling elements determined from the design configuration and the magnitude and direction of the applied load.

In modern, high-speed ball bearings, such as are used in jet engines, the original premise of the Lundberg-Palmgren theory—that the load distribution is independent of the operating speed—is departed from. In many instances centrifugal forces acting on the balls in a high-speed bearing give rise to load distributions which are appreciably different from those occurring under static loading and which cannot be neglected. Consideration of these forces may result in operating characteristics and bearing lives appreciably different from those calculated by conventional means.

This paper extends the Lundberg-Palmgren theory to include the effect of centrifugal ball loading on the performance and life of high-speed ball bearings. Two particular cases are investigated: (*a*) a radial ball bearing under pure radial load, and (*b*) an angular contact bearing under pure thrust load.

Although exhaustive test series of high-speed bearings for purposes of checking the theories advanced in this paper are not presently available, there are indications from currently classified projects that the predictions of high-speed bearing endurance made in accordance with these theories are substantially correct when satisfactory mounting, lubrication, and cooling are assured.

Theoretical Development

(*a*) *Deep Groove Radial Ball Bearings Under Radial Load.* Fig. 1 illustrates the distribution of ball loads around the pitch circle of the deep groove radial ball bearing under an external, radial load. One half of the pitch circle is under load.

Under static load the load on any ball within the loaded zone is

$$P_\varphi = P_{max}\cos^{1.1}\varphi \quad \text{for} \quad -\frac{\pi}{2} < \varphi < \frac{\pi}{2} \qquad [1]$$

The maximum ball load is related to the external radial load by

$$P_{max} = \frac{R}{nJ_r} \qquad [2]$$

Neglecting a second-order disturbance of the inner-race load distribution, the effect of centrifugal force acting on the balls is to produce additional loading of the outer race.

---

[1] Research Engineer, The Fafnir Bearing Company, New Britain, Conn.; formerly, Director of Research and Development, Marlin-Rockwell Corporation, Jamestown, N. Y.

Contributed by the Aviation Division and presented at the Annual Meeting, Atlantic City, N. J., November 25–30, 1951, of The American Society of Mechanical Engineers.

Note: Statements and opinions advanced in papers are to be understood as individual expressions of their authors and not those of the Society. Manuscript received at ASME Headquarters, August 31, 1951. Paper No. 51—A-69.

[2] Numbers in parentheses refer to Bibliography at end of paper.

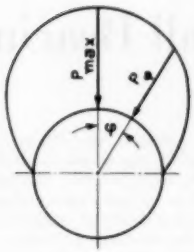

FIG. 1

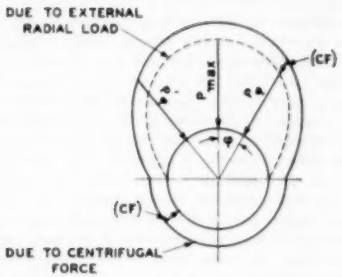

FIG. 2

Then the distribution of ball load around the outer race is as shown in Fig. 2.

The centrifugal force per ball is referred to the maximum ball load through the ratio F, such that

$$(\mathrm{CF}) = FP_{\max} \quad [3]$$

and

$$(\mathrm{CF}) = 5.257 \times 10^{-7}\, d^3 E N_i^2 \left(1 - \frac{d}{E}\right)^2 \quad [4]$$

for steel balls.

Since the outer-race ball load varies with the angular co-ordinate φ, determine the equivalent mean ball load for the outer race such that

$$P_o = \left(\frac{1}{2\pi}\int_{-\pi}^{\pi} P_\varphi'^{10/3}\, d\varphi\right)^{3/10} \quad [5]$$

subject to

$$P_\varphi' = P_{\max}(\cos^{3/2}\varphi + F) \quad \text{for} \quad -\frac{\pi}{2} < \varphi < \frac{\pi}{2} \quad [6]$$

$$P_\varphi' = FP_{\max} \quad \text{for} \quad \frac{\pi}{2} < \varphi < \frac{3\pi}{2} \quad [7]$$

P_o can be related to $P_{\max}$ through J_2 so that

$$P_o = J_2 P_{\max} \quad [8]$$

Values of J_2 are plotted in Fig. 3 as a function of F.

Setting the external radial load equal to the capacity of the outer race, using Equations [2] and [8], the expression for the outer race capacity is written

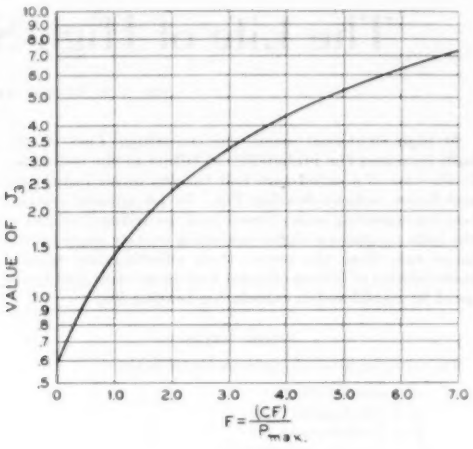

FIG. 3

$$C_o = \frac{P_o n J_r}{J_1} \quad [9]$$

The capacity of the inner race is, in accordance with equation 90 of reference (2)

$$C_i = 0.407\, P_i\, n \quad [10]$$

In accordance with equation 115 of reference (2) the ball load for the basic dynamic capacity is, for outer and inner race contacts, respectively

$$P_o = A\left(\frac{2f_o}{2f_o - 1}\right)^{0.41} \frac{(1+\gamma)^{1.39}}{(1-\gamma)^{1/3}}\, \gamma^{0.3}\, d^{1.8}\, n^{-1/3} \quad [11]$$

$$P_i = A\left(\frac{2f_i}{2f_i - 1}\right)^{0.41} \frac{(1-\gamma)^{1.39}}{(1+\gamma)^{1/3}}\, \gamma^{0.3}\, d^{1.8}\, n^{-1/3} \quad [12]$$

where

A = a constant depending on material
$\gamma = d/E$ for radial bearings

The substitution of Equations [11] and [12] into Equations [9] and [10] using $J_r = 0.2288$ yields

$$\left(\frac{C_i}{C_o}\right) = 1.779\, J_2 \left[\frac{1-\gamma}{1+\gamma}\right]^{1.72} \left[\frac{f_i(2f_o - 1)}{f_o(2f_i - 1)}\right]^{0.41} \quad [13]$$

In accordance with the Lundberg-Palmgren theory the capacity of the complete bearing can be stated in terms of the inner race capacity, through

$$C = g\, C_i \quad [14]$$

where

$$g = \left[1 + \left(\frac{C_i}{C_o}\right)^{10/3}\right]^{-3/10} \quad [15]$$

If centrifugal force is neglected the value of J_2 becomes 0.5875. Consideration of centrifugal force increases the value of J_2. Since the capacity of the bearing is proportional to g it is possible to calculate g with $J_2 = 0.5875$ and again with the value of J_2 as

dictated by the centrifugal-force effect. Call the former g_A and the latter g_B.

Since bearing life is proportional to the cube of the dynamic capacity the life, L_B, when centrifugal force is considered is

$$L_B = L_A \left(\frac{g_B}{g_A}\right)^3 \quad \ldots\ldots [16]$$

where L_A is the bearing life computed by conventional means without consideration of centrifugal force.

(*b*) *Angular Contact Ball Bearings Under Pure Thrust Load.* Assume that the bearing under consideration is maintained in situ solely by an external thrust load and is not prevented from seeking its own axial position of equilibrium. Assume also that the initial or design contact angle of the bearing after mounting is β'. After the application of an axial thrust load T, the static contact angle increases to β due to elastic deformations.

If the inner race of the bearing is driven at high speed, the centrifugal loading of the balls imposes additional forces on the races. In order for equilibrium to exist a relative axial shift of the inner race with respect to the outer must occur. The operating contact angles at inner and outer races are then different as shown in Fig. 4.

Fig. 5 shows the relative position of inner- and outer-race curvature centers when equilibrium is attained under thrust load at high-speed rotation. X is the relative axial shift of inner race with respect to the outer required for equilibrium. This is different than the normal axial deflection encountered under static thrust load and may become negative if thrust load is low and rotational speed high.

In Fig. 5, δ_o and δ_i are the normal approaches of the ball to outer and inner race, respectively, due to elastic deformation at the ball contacts

$$\frac{\delta_o}{d} = \frac{K_o}{d^{1/2}} \left(\frac{T}{n \sin \beta_{1o}}\right)^{2/3} \quad \ldots\ldots [17]$$

$$\frac{\delta_i}{d} = \frac{K_i}{d^{1/2}} \left(\frac{T}{n \sin \beta_{1i}}\right)^{2/3} \quad \ldots\ldots [18]$$

Average values of K_o and K_i for steel balls and races are given in Fig. 6.

Fig. 7 shows the equilibrium of forces acting on a ball. From Figs. 5 and 7 one obtains

$$\cot \beta_{1i} = \cot \beta_{1o} - \frac{(CF)n}{T} \quad \ldots\ldots [19]$$

$$\left(f_o - 0.5 + \frac{\delta_o}{d}\right) \cos \beta_{1o} + \left(f_i - 0.5 + \frac{\delta_i}{d}\right) \cos \beta_{1i} = (f_o + f_i - 1) \cos \beta' \quad \ldots\ldots [20]$$

Combining Equations [19] and [20] and using Equations [17] and [18], one obtains

$$\frac{T}{nd^2} = \frac{1}{K_i^{2/3}} \left\{ \frac{(f_o + f_i - 1) \cos \beta' - (f_o - 0.5) \cos \beta_{1o} - \dfrac{(f_i - 0.5)\left[\cot \beta_{1o} - \dfrac{(CF)n}{T}\right]}{\left[1 + \left(\cot \beta_{1o} - \dfrac{(CF)n}{T}\right)^2\right]^{1/2}}}{\dfrac{K_o \cos \beta_{1o}}{K_i \sin^{1/2} \beta_{1o}} + \dfrac{\left[\cot \beta_{1o} - \dfrac{(CF)n}{T}\right]}{\left[1 + \left(\cot \beta_{1o} - \dfrac{(CF)n}{T}\right)^2\right]^{1/6}}} \right\}^{3/2} \quad \ldots\ldots [21]$$

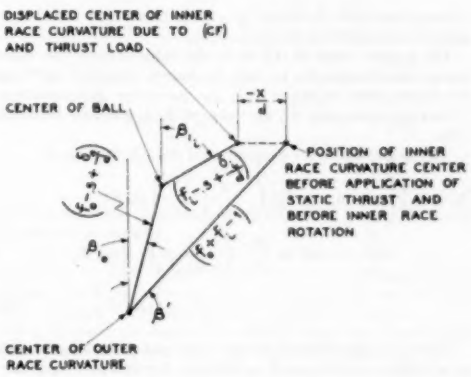

Fig. 5

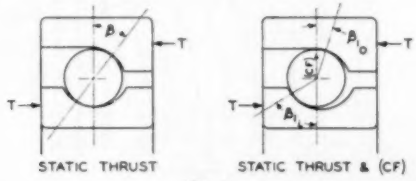

Fig. 4

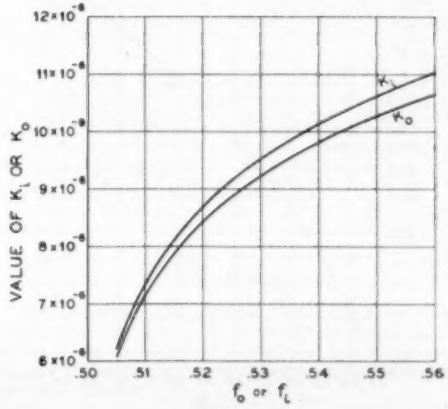

Fig. 6

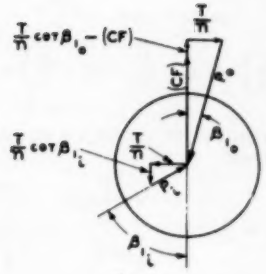

FIG. 7

The centrifugal force per ball is computed from

$$(CF) = 5.257 \times 10^{-7}\, d^3 E N_i^2 \left(1 - \frac{d \cos \beta}{E}\right)^2 \quad [22]$$

β being the angle developed by a static thrust load T and computed in accordance with reference (6).

For a given value of $(CF)n/T$, the value of outer-race operating contact angle, β_{io}, to yield the desired value of $T/(nd^2)$ can be found from Equation [21] by successive approximation.

Having determined β_{io} the value of β_{il} is given by Equation [19].

The magnitude of the dynamic axial shift, X, is given by

$$X = d\left\{\left[f_o - 0.5 + \frac{K_o}{d^{3/2}}\left(\frac{T}{n \sin \beta_{io}}\right)^{2/3}\right]\sin \beta_{io} + \left[f_i - 0.5 + \frac{K_i}{d^{3/2}}\left(\frac{T}{n \sin \beta_{il}}\right)^{2/3}\right]\sin \beta_{il} - (f_o + f_i - 1)\sin \beta'\right\} \quad [23]$$

Most jet-engine thrust bearings in use today are designed with $f_o = 0.52$, $f_i = 0.51$ and $\beta' = 20$ deg. For this particular case, Fig. 8 shows the relation between $T/(nd^2)$ and the static contact angle under thrust, β, and may be used to determine the latter. Also, for this particular case, Fig. 9 enables a rapid solution of Equation [21] and may be used to determine β_{io} directly.

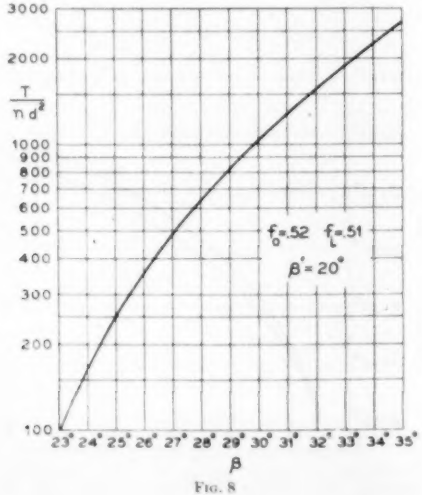

FIG. 8

Having determined the dynamic contact angles the calculation of bearing life is possible.

In accordance with equation 80, reference (2), the thrust capacity of a race is given by

$$C = Pn \sin(\beta, \beta_{io}, \beta_{il}) \quad [24]$$

where the value of P is obtained from Equation [11] or [12] for outer and inner race, respectively.

Assigning the subscript $_B$ to the case where centrifugal force is considered, and the subscript $_A$ to the case where centrifugal force is not considered, one may establish the following ratios

$$\left(\frac{C_i}{C_o}\right)_B = \frac{\sin \beta_{il}}{\sin \beta_{io}}\left[\frac{f_i(2f_o - 1)}{f_o(2f_i - 1)}\right]^{0.41}\left(\frac{1 - \gamma_i}{1 + \gamma_o}\right)^{1.39}\left(\frac{2 - \gamma_o - \gamma_i}{2 + \gamma_o + \gamma_i}\right)^{1/3} \quad [25]$$

$$\left(\frac{C_i}{C_o}\right)_A = \left[\frac{f_i(2f_o - 1)}{f_o(2f_i - 1)}\right]^{0.41}\left(\frac{1 - \gamma}{1 + \gamma}\right)^{1.72} \quad [26]$$

where

$$\gamma_o = \frac{d \cos \beta_{io}}{E} \quad [27]$$

$$\gamma_i = \frac{d \cos \beta_{il}}{E} \quad [28]$$

$$\gamma = \frac{d \cos \beta}{E} \quad [29]$$

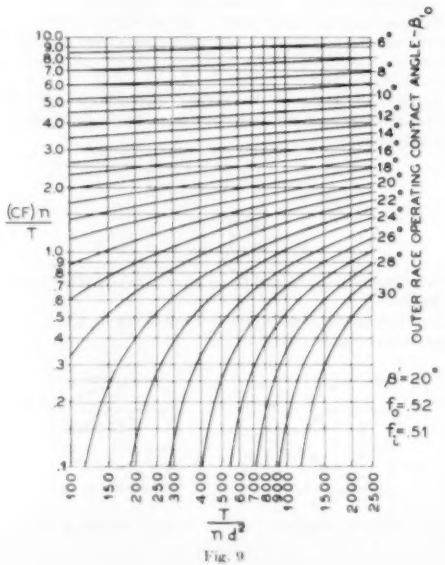

FIG. 9

Then, in accordance with Equations [14] and [15], the capacity for each condition is

$$C_B = C_{iB}\left[1 + \left(\frac{C_i}{C_o}\right)_B^{10/3}\right]^{-3/10} \quad [30]$$

$$C_A = C_{iA}\left[1 + \left(\frac{C_i}{C_o}\right)_A^{10/3}\right]^{-3/10} \quad [31]$$

C_{iB} is related to C_{iA} through

$$C_{iB} = \frac{\sin \beta_{iA}}{\sin \beta}\left(\frac{1-\gamma_i}{1-\gamma}\right)^{1.39}\left(\frac{2+2\gamma}{2+\gamma_o+\gamma_i}\right)^{1/3} C_{iA} \quad [32]$$

Then the life when centrifugal force is considered may be expressed in terms of the life calculated without consideration of centrifugal force by

$$L_B = L_A\left(\frac{C_B}{C_A}\right)^3 \quad [33]$$

or

$$L_B = L_A\left(\frac{\sin \beta_{iA}}{\sin \beta}\right)^3\left(\frac{1-\gamma_i}{1-\gamma}\right)^{4.17}\left(\frac{2+2\gamma}{2+\gamma_o+\gamma_i}\right)\left[\frac{1+\left(\frac{C_i}{C_o}\right)_A^{10/3}}{1+\left(\frac{C_i}{C_o}\right)_B^{10/3}}\right]^{0.9} \quad [34]$$

Some Examples of the Effect of Centrifugal Force on High-Speed-Bearing Endurance

Radial Bearing Under Radial Load. Fig. 10 shows the relation between the life for 10 per cent failure as calculated by conventional means and with consideration of centrifugal force for a 209 size deep groove, radial bearing under 400 lb radial load and at various speeds.

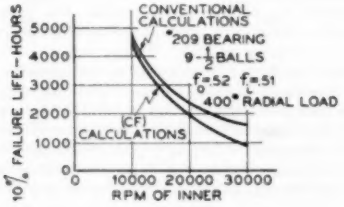

Fig. 10

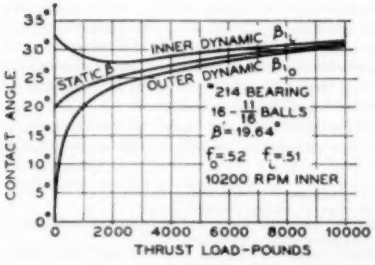

Fig. 11

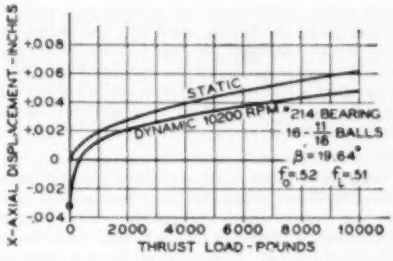

Fig. 12

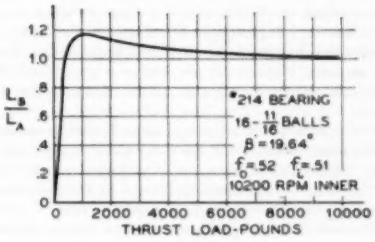

Fig. 13

Angular Contact Bearing Under Pure Thrust Load. Fig. 11 illustrates the effect of centrifugal force on the operating contact angles of outer and inner races of a 214 size angular contact bearing operating at 10,200 rpm under various thrust loads.

Fig. 12 shows the static axial deflection and the dynamic axial deflection at 10,200 rpm under various thrust loads.

Fig. 13 shows the relation between 10 per cent failure life as calculated by conventional means and with consideration of centrifugal force.

BIBLIOGRAPHY

1 "Method of Evaluating Load Ratings of Annular Ball Bearings," AFBMA Standards, The Anti-Friction Bearing Manufacturers' Association, Incorporated, New York, N. Y., 1950.

2 "Dynamic Capacity of Rolling Bearings," by G. Lundberg and A. Palmgren, *Acta Polytechnica*, Mechanical Engineering Series, vol. 1, no. 3, Stockholm, Sweden, 1947.

3 "Dynamic Capacity of Rolling Bearings," by G. Lundberg and A. Palmgren, *Journal of Applied Mechanics*, Trans. ASME, vol. 71, 1949, p. 165. This is a condensation of reference (2).

4 "A Statistical Theory of the Strength of Materials," by W. Weibull, IVA Handlingar, No. 151, Stockholm, Sweden, 1939.

5 "The Phenomena of Rupture in Solids," by W. Weibull, IVA Handlingar, No. 153, Stockholm, Sweden, 1939.

6 "Analysis of Stresses and Deflections," by A. B. Jones, New Departure Division, GMC, Bristol, Conn., vols. 1 and 2, 1946.

Discussion

Thomas Barish.[3] This thorough technical analysis of the effect of centrifugal force on the life of high-speed bearings constitutes a complete solution of an important facet of this problem, now becoming of great interest because of the demands for gas-turbine bearings.

[3] Consulting Engineer, Cleveland, Ohio. Mem. ASME.

This is a long advance from the rule-of-thumb method used about 1925, giving the limiting speed of a ball bearing as that point where the centrifugal force per ball was 50 lb regardless of size. The author has stated the complete theory for calculating the effect of this centrifugal force per ball on bearing performance but has carefully avoided the resulting conclusions and practical considerations in ball-bearing usage. They deserve discussion:

1 Using the author's example and Fig. 10 of the paper, we take the 209 size at 30,000 rpm, near its maximum allowable speed. The current limit is supposed to be $DN = 1{,}500{,}000$, which would give 33,300 rpm. Even at that speed, the bearing capacity is reduced only 15 per cent by the centrifugal force of the balls.

2 Next is the effect of the author's theory on the constantly arising question of whether to use the heavier series with larger balls for the very highest speeds. Compare the medium series size 309 which has the same shaft but larger balls. The theoretical capacity is about 50 per cent over that of the 209, and hence is still preferable even after taking off the effect of centrifugal force.

This is especially so if the larger series permits a smaller shaft size with much reduced ball speed for these extreme speed conditions. Shafts should be as small as possible at the bearings.

3 The effect of the centrifugal force at the balls is not the only consideration that limits high-speed performance. It is only a small part of the total problem. For example, at 30,000 rpm, an eccentricity of only 0.0002 in. would give a radial load of 5 times the weight; especially bad when operating over the first critical because then the resulting vibration is not so noticeable, and the outer-race eccentricity and looseness contribute.

4 The author's Fig. 13 indicates that for thrust load, the centrifugal force on the ball increases the bearing capacity for all but the very lightest loads. No doubt this conclusion results from the fact that the contact angle on the inner race is increased. This is a startling observation and infers that the bearings should have had higher contact angles for the lower speeds.

5 Actually, pure thrust load rarely exists. Even a small radial load or radial displacement plays havoc with high-speed bearings owing to a further development of the condition outlined by the author. The contact angle on the inner race, angle B_{14} in Fig. 7, changes a relatively large amount from the top to the bottom of the bearing. This induces large changes in ball speed, and in extreme cases, makes the ball ride over the edge of the inner ring. Rapid failure results, and for that reason even smaller angles of contact are desirable for these very high speeds.

6 This condition becomes critical on the idle row of a pair of duplex ball bearings mounted opposed, as indicated by the very low life shown in Fig. 13 for loads near zero. In fact, this condition has caused definite failures and makes such a combination impractical with certain increased axial loosenesses. The geometry for solving this problem was reported in a recent paper.[4]

7 The author's theory indicates certain possible changes in the internal bearing design to make them better for extreme speeds; for example, closer curvatures at the outer-ring contact would reduce the harmful effect of the centrifugal force on the bearing life. Here again practical considerations point oppositely. Flatter curvatures would show less heat and less sensitivity to change in contact angle.

The author should be encouraged to continue this valuable type of work in improving the performance of high-speed turbine ball bearings, and in understanding how they act.

[4] "Ball Bearing Geometry," by Roy Krouse, *Machine Design*, February, 1951.

F. J. Garbarino.[5] This paper presents an interesting and useful extension of the principles of bearing fatigue based on the Weibull theory of statistical strength of materials as adapted to ball bearings in a paper by G. Lundberg and A. Palmgren.[6] These principles are now finding wide acceptance and use in the ball-bearing industry. However, the constants derived in the original paper, on the basis of experiments on bearings made of Swedish steel, and accepted for use in the present paper, differ somewhat from those derived from similar tests run on bearings made of domestic steels.

The B-10 life of bearings, that is, the life at which 10 per cent of the bearings in a test lot have failed, is generally taken as 20 per cent of the average life. If this figure is accepted, and there is considerable test evidence confirming it, the exponent of the life-distribution curve should be $^{4}/_{3}$ rather than the $^{10}/_{9}$ accepted in the present paper. Similarly, a summary of load-life tests on a large number of domestic bearings indicates that the life varies inversely with the fourth power of the load rather than inversely with the third power as assumed in this paper. These domestic tests imply considerable changes in many of the equations of the paper. For example, the exponents of Equation [5] would become $^{10}/_{3}$ and $^{3}/_{10}$ rather than $^{10}/_{9}$ and $^{2}/_{10}$, respectively.

The paper gives a method for computing expected life when the bearing operates either under pure radial or pure thrust load. It is to be hoped that the author ultimately will be able to modify this method to include the more general case of combined load.

Arthur S. Irwin.[7] This paper constitutes a tangible, workable summary of one of the factors which will contribute to, or prevent, satisfactory life in high-speed bearings. The problems to which this theory is applicable are increasing in number and severity with the development of aircraft gas-turbine power plants. Frankly, the requirements which we are required to meet are becoming so increasingly severe that without such theoretical data as included in this paper, we will soon be lost. Another factor which makes this work of extreme importance is the customer interest shown in the design factors which control bearing performance and which factors were formerly the responsibility and prerogative of the bearing manufacturers. Our customers are becoming increasingly inquisitive and critical regarding the methods used in designing bearings. This is, indeed, a healthy condition, since the further development of this inquisitive attitude can lead to closer co-operation between the bearing manufacturers and their customers. We all know that the bearing engineers, in the past, have been hampered by lack of information from the equipment designers. The presentation of such theoretical work as is here represented can arouse further interest on the part of users of ball bearings in the theory on which their bearings are based.

The treatment of the subject matter is practically identical to a paper[8] prepared by the author while with the writer's company. The formulas for calculation of life (with consideration of centrifugal loading) are identical in the original work and in the present paper. We have been using this theory for over 2 years, and have checked critical high-speed bearings by this theory. It is too early to evaluate the results or the limitations of this theory as reflected in practical experience.

The incorporation of this theory in the design of a bearing affects race curvatures, shoulder heights, and initial contact

[5] Chief Engineer, New Departure, Bristol, Conn.

[6] Reference (3), author's bibliography.

[7] Assistant Chief Engineer, Aircraft and Special Projects, Marlin-Rockwell Corporation, Jamestown, N. Y.

[8] "The Dynamics of High Speed Ball and Roller Bearings," by A. B. Jones, Jr.

angle. The bearings which we have designed, and subsequently checked by means of this theory, have not failed because of the increase in contact angle on the inner race and decrease of contact angle on the outer race. It is difficult to evaluate the effect of this theory on bearing life because, invariably, high-speed bearings, in which the centrifugal-force effect is a critical factor, are very difficult to lubricate, and usually the life of the bearing is prejudiced by the lubrication, or lack thereof.

Mr. Lundquist, in working with this theory, has found certain variables to be of importance. We have found that it is possible to select race curvatures and initial contact angles to control the result to be obtained by this theory in such a manner as to obtain optimum bearing configuration and performance.

The operational characteristics which determine the influence to be exerted by this theory on bearing design are speed and thrust load, and initial contact angle. Fig. 14 of this discussion demonstrates the results of varying speed on a 214 size bearing, subjected to thrust loads of 1000 lb and 6000 lb. It will be noted that under heavier loads the centrifugal-force effect increases the calculated life, while at reduced thrust loads, the increased speed

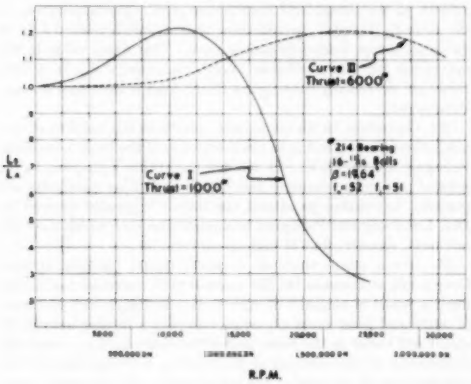

FIG. 14

seriously reduces the theoretical life to be calculated for high *DN*-values. The reason for an increase in theoretical life is found in the reduction of loading on the inner race, which is usually the more highly loaded bearing element. Therefore the centrifugal force will increase the calculated life until the endurance factors of the two races are equal. Beyond this point the life will be decreased, owing to the lowered endurance of the outer race, while that of the inner race continues to increase.

In summary, the theory here presented is a valuable, usable contribution to the bearing art. In some cases, consideration of the theory reduces the life originally calculated for the bearing, and in other cases, it increases the life calculated.

It is difficult to evaluate this theory because of the other factors which prejudice the life of high-speed bearings in the types of application in which they are being increasingly used. We have started the application of the theory and expect that time will produce operational experience data which will permit us better to evaluate the validity of the theory.

G. LUNDBERG[9] AND A. PALMGREN.[10] The theory worked out by us, and on which the author has based his deduction, is valid at such rotational speeds where centrifugal forces and gyratory moments are negligible. The applicability of our theory at extreme speeds has not been discussed by the author.

The main effect of the centrifugal force without doubt is an increase of the loading on the balls but there are also other effects.

At radial loads on deep groove ball bearings, the motion of the bearing elements is not changed essentially by the centrifugal force. But on account of elastic deformation, at higher speeds, there will be a diminution of the loaded zone of the circumference of the inner ring. As the author's theory does not take this fact into consideration, there is to be expected in reality a somewhat greater reduction in life on account of the centrifugal force than he shows.

At thrust loads on angular contact ball bearings the centrifugal force also will influence the rolling conditions. The cage speed and thus the number of repeated stresses will be influenced to some extent.

No regard has been given to the gyratory moments appearing at high speed when the contact angle of the balls β is not zero. These moments raise frictional forces which, to a certain extent, will influence stresses as well as the equilibrium conditions. Extra friction also may develop if the spin of the balls (around an axis normal to the contact surface) in some way or other is different from that at low speed. Even for angular contact ball bearings there is thus to be expected a shorter life than that calculated by the author.

Combined thrust and radial load has not been treated.

The approximations introduced are perhaps, at least in part, not to be avoided at the present level of the science. Especially regarding the gyratory forces, however, these approximations may be of such a magnitude that they should have been mentioned.

With this formal reservation we consider the author's deduction correct and of great merit, and also well adapted to deepen our knowledge about the performance of high-speed ball bearings.

A. R. SPICACCI.[11] The author discusses the effect of centrifugal forces of balls in a ball bearing running at the higher speeds. He evaluates this effect both on the bearing load carrying capacity and on the contact angles of an angular contact bearing.

In regard to the effect on capacity, the writer feels that this is secondary in importance. To quote Boyd and Eklund:[12] "In none of these first tests was there any indication that fatigue of the balls and races, the factor which limits life, was present but that life was being determined by cage wear, ball wear, race wear, etc." A paper by Macks, Nemeth, and Anderson[13] as well as one by Phillips[14] seem to be well in accord with that statement. As a matter of fact, practically all investigators have come to the conclusion that the critical factors at the higher speeds are (*a*) cage failure, (*b*) heat dissipation, (*c*) lubrication.

Conceive a bearing at these higher speeds in which the balls

[9] Professor, Chalmers Institute of Technology, Gothenburg, Sweden.

[10] Doctor of Engineering, SKF, Gothenburg, Sweden.

[11] Vice-President, Bearings Company of America, Lancaster, Pa. Mem. ASME.

[12] "Some Performance Characteristics of Ball and Roller Bearings for Aviation Gas Turbines," by John Boyd and P. R. Eklund, presented at the Annual Meeting, Atlantic City, N. J., November 25–30, 1951, of THE AMERICAN SOCIETY OF MECHANICAL ENGINEERS. Paper No. 51—A-78.

[13] "Operating Characteristics of Cylindrical Roller Bearings at High Speeds," by E. F. Macks, Z. N. Nemeth, and W. J. Anderson, published in this issue, pp. 705–714.

[14] "Some Lubrication and Bearing Problems in Aircraft Gas Turbines," by E. M. Phillips, presented at the Annual Meeting, Atlantic City, N. J., November 25–30, 1951, of THE AMERICAN SOCIETY OF MECHANICAL ENGINEERS. Paper No. 51—A-58.

move at uniform speed. It is obvious that the cage would have very little work to do. It follows that heat dissipation and lubrication would not be as exacting as present experience indicates. Something happens that throws the balls out of equilibrium. Consequently, they jam against the cage pockets causing excessive heat.

The lubricant is then called upon to cope with these conditions. It is true that at the higher speeds, the lubricant itself creates problems. Its churning action and its viscosity generate heat and consume power; its propagations to the locations needed becomes extremely difficult because of windage and turbulence. The frictional forces of the bearing and lubrication form a vicious circle from which the investigator seeks the best compromise. It must be agreed that as the frictional forces operating in a bearing are diminished, the lesser the difficulty with lubrication.

It appears to the writer that no investigator, so far, has attempted to get at the root of the trouble—the disturbance of the ball motion. The author calls our attention to the change of contact angle by centrifugal forces of the balls. Consider the kinematic results as shown in Fig. 15, herewith. It is obvious from

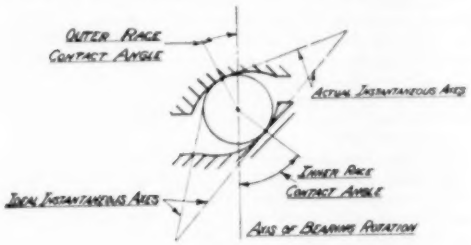

Fig. 15

the position of the instantaneous axes of rotation of the balls that the bearing must operate with undue friction at the contact areas. Furthermore, the two normal forces at these contact areas can only be held in equilibrium by friction at these areas. Since frictional forces are always unstable, the balls tend to shift from their regular path. The question is not just of spinning but of improper location of the instantaneous axes. At ordinary speeds these considerations are of no consequence. At the higher speeds their effects are considerably magnified.

There is another factor which produces similar results, namely, the curvature of the races. Test results on a No. 208 bearing illustrate the point as shown in Table 1 of this discussion.

TABLE 1 TEST RESULTS ON NO. 208 BEARING

—Race curvatures, per cent—		—Contact angles, deg—	
Outer race	Inner race	Outer race	Inner race
80	51	18°	28°
51	80	30°	21°
54	54	27°	27°

Notes: Race curvatures are given in percentage of the ball diameter. Thrust load, 100 lb; speed 1200 rpm. The effect of centrifugal force of the balls—negligible.

The race curvatures are exaggerated purposely to bring out clearly the effect. Here again, it may be seen that the instantaneous axes of rotation of the balls are not located for pure rolling and that the balls are unstably held in position by friction at the contact areas of the races.

If we were to venture into the realm of speculation, we would say that the race curvatures should be something other than circular to achieve more stability of the balls in the higher speed range.

The problem is not an easy one. Consideration must be given to practical means of reproducing such noncircular races. For circular races the best compromise is to achieve equal contact angles for both inner and outer races with consideration of the effect of centrifugal forces.

The author should be complimented for his excellent paper. He alluded to one of the disturbing influences of the ball motion. The writer has indicated another. There are many others which cannot be discussed adequately here. It is hoped that these comments will stimulate more efforts along the lines of these comments.

Author's Closure

Regarding Mr. Barish's comments, it is not possible to state a hard and fast rule as to whether or not the heavier series bearings are preferable to the lighter series bearings when operating speeds are high. The choice depends on the load as well as the speed and each application must be considered separately.

Fig. 13 in the paper plots the *ratio* L_B/L_A against thrust load for a particular speed. Conventional calculations without consideration of centrifugal force would indicate that L_A tends to infinity as the thrust load approaches zero. The application of the ratio L_B/L_A to L_A would show that L_B tends toward a finite value as thrust load approaches zero. This finite value is the maximum for the particular speed concerned. L_B is a continuously decreasing function as thrust load is increased at constant speed.

Mr. Garbarino, in his comments, questions the validity of certain exponents appearing in the derivation of the basic Lundberg-Palmgren theory (2, 3). It was not the author's purpose, in the present paper, to examine the validity of these particular exponents, but rather to extend the theory originally derived by Drs. Lundberg and Palmgren to a particular case which they did not treat, namely, that of high-speed rotation.

Mr. Irwin states that, at constant thrust load, centrifugal force tends to increase the life calculated by conventional means until a speed is attained at which the endurance factors (lives) of outer and inner races are equal and that a further increase in speed will result in the reduction of the ratio L_B/L_A. Since the probability of the survival of the bearing is the product of the probabilities of survival of the components, the maximum value of L_B/L_A will occur when the product of the probabilities of survival of outer and inner races are a maximum. It does not necessarily follow that the lives of the components are equal at that time.

The comments by the authors of the basic theory, Drs. Lundberg and Palmgren, are especially appreciated. The author felt that it was inadvisable to attempt to evaluate the effect of gyroscopic moments since very little is known regarding the effect of tangential stresses at the pressure surface on fatigue life. Similarly, the case of combined radial and axial load was not considered because of the difficulties in evaluating the effect of widely varying ball transational velocities on separator performance.

Mr. Spicacci's comments regarding cage failure, heat dissipation, and lubrication are well taken. Theoretical life resulting from computation can only be attained if mounting and lubrication are adequate and operating temperature is satisfactorily controlled.

Mr. Spicacci's measurements of contact angles in a 208 bearing under 100 lb thrust load at 1200 rpm are interesting. Mr. Spicacci has since told the author that the bearings in question were run dry for purposes of developing visible paths in raceways.

The differences in contact angles between outer and inner races undoubtedly result from friction forces developed at the pres-

sure surfaces due to sliding and spin. When the inner race has a very close curvature and the outer race a very wide curvature, all the spinning occurs at the outer-race contact. As the balls roll around the outer race, spinning about the normal to the outer-race contact at the same time, a frictional force at right angles to the direction of rolling is induced tending to reduce the outer-race contact angle. The reaction at the inner race tends to increase the contact angle on this member although no spinning occurs here. If the curvatures are interchanged the reverse occurs. If the outer and inner-race curvatures are nearly the same, the difference in the torques required to spin the ball on outer and inner races is greatly reduced and the forces on the ball at right angles to the rolling direction are correspondingly reduced. The lack of lubrication and the very low thrust employed in Mr. Spicacci's experiments greatly exaggerate this effect. The author does not believe it to be of great importance where lubrication is good and loads are heavier as is the case in most applications.

Operating Characteristics of Cylindrical Roller Bearings at High Speeds

By E. F. MACKS,[1] Z. N. NEMETH,[2] and W. J. ANDERSON,[2] CLEVELAND, OHIO

The significance of bearing operating temperature is discussed with regard to bearing operating limitations. The extent of the effects of various operating variables upon the bearing inner-race and outer-race temperatures is shown. Test-rig results as well as turbojet-engine data have been generalized by means of a cooling correlation analysis so that the designer may predict either the inner-race or the outer-race bearing temperature from a single curve, regardless of whether bearing speed, bearing load, oil flow, oil-inlet temperature, oil-inlet viscosity or oil-inlet velocity vary over wide ranges.

Introduction

THERE is a distinct need for research information on high-speed bearings inasmuch as turbojet-rotor shafts are presently equipped with bearing systems designed from extrapolated bearing knowledge. This fact has accounted for numerous turbojet-engine bearing failures. Other high-speed bearing systems are designed just to operate—there is little factor of safety. To make things more interesting, the operating conditions of turbojet-rotor bearings are being extended rapidly to higher surface speeds and higher temperatures to permit the design of more efficient engines.

The rolling-contact bearing is used in present-day turbojet engines because it has certain advantages over the hydrodynamic bearing for this application. These advantages are, primarily, its lower starting torque and its comparative insensitivity to oil interruptions.

The region of bearing knowledge with respect to bearing surface speed for both the rolling-contact and the hydrodynamic bearing types is shown in Fig. 1. The present maximum turbojet service is at about 220 fps. The maximum service under consideration by designers is at about 500 fps. The dotted line on the left indicates the surface speed of an automobile-wheel bearing when the car is traveling at 80 mph.

The region of present knowledge of the rolling-contact bearing is to about 120 fps. It is evident that extrapolation of present knowledge has been required to design current engine bearings. The NACA research on roller bearings, which is nearing completion, is to 290 fps, well beyond present maximum turbojet service. The NACA is now extending its research to the region above 300 fps.

The region of present knowledge for the hydrodynamic bearing extends to a point at about 210 fps. The NACA is conducting research in the region above 210 fps. In addition, we are attacking the previously mentioned disadvantages of the hydrodynamic

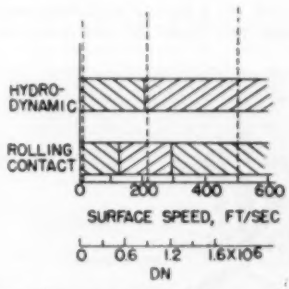

Fig. 1 Bearing Knowledge With Respect to Bearing-Pitch Surface Speed

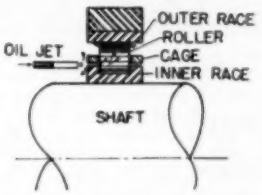

Fig. 2 A Particular High-Speed Roller Bearing

bearings. Just how far into these regions the NACA can obtain research information successfully, and thereby extend the operating limits of bearings, depends entirely upon ingenuity and resourcefulness in employing all the concepts of friction, hydrodynamics, and heat transfer.

The turbine wheel of a turbojet engine is supported generally on a roller bearing to allow for thermal expansion of the shaft in the axial direction. Fig. 2 shows a particular design of high-speed roller bearing. In order for any bearing to function, it must operate at an equilibrium temperature below the tempering temperature of the bearing steel and below the breakdown temperature of the lubricant. Therefore a safe balance must be maintained between the heat input and the heat removed. Therefore the operating temperature of the bearing has been chosen as the over-all criterion of bearing operation.

Heat is generated within the bearing by friction at the bearing surfaces which are in sliding and rolling contact as well as by churning of the oil by the moving parts. Heat also enters the bearing by conduction through the shaft, by conduction through the housing, and by radiation and convection from the surrounding environment.

To maintain a safe equilibrium bearing operating temperature this "bearing heat" must be removed. For high-speed bearings the lubricant removes a major part of this heat. Thus the function of the lubricant has been extended to include cooling, as well as lubricating. In the research to be discussed the study has been limited to lubricating and cooling conventional types of roller

[1] Research Staff, NACA, Lewis Flight Propulsion Laboratory, Cleveland Airport. Jun. ASME.

[2] Research Staff, NACA, Lewis Flight Propulsion Laboratory, Cleveland Airport.

Contributed by the Aviation Division and presented at the Annual Meeting, Atlantic City, N. J., November 25–30, 1951, of The American Society of Mechanical Engineers.

Note: Statements and opinions advanced in papers are to be understood as individual expressions of their authors and not those of the Society. Manuscript received at ASME Headquarters, August 28, 1951. Paper No. 51—A-66.

bearings in which the heating of the bearing occurs only by the friction and churning within the bearing.

Bearing speed, bearing load, and cage design have been investigated as these variables affect the heat generation within the bearing. Oil flow, oil-inlet temperature, oil-inlet velocity, oil-inlet viscosity, and oil-inlet distribution also have been investigated as these variables affect the heat removal from the bearing.

Test Equipment and Procedure

The bearing rig, Fig. 3, used for this investigation is described fully in reference (1).[2] Briefly, the test bearing was mounted on

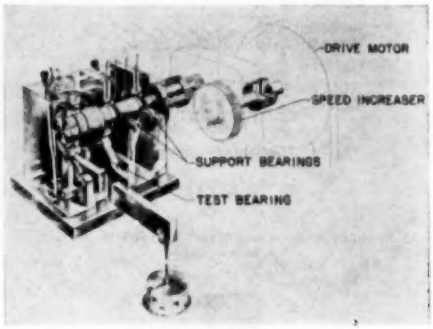

Fig. 3 Bearing Test Rig

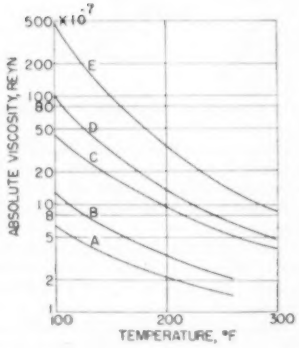

Fig. 4 Absolute Viscosity of Five Oils

one end of the test shaft, which was supported in cantilever fashion so that component parts of the bearing and the lubricant flow could be observed during operation. Radial load was applied to the test bearing by means of a lever and dead-weight system in such a manner that the outer race of the test bearing was essentially unaffected by small shaft deflections or by small shaft and load-arm misalignments.

The test bearings were 75-mm-bore 130-mm-OD cylindrical roller bearings (size 215) of the type used currently as the turbine roller bearing of turbojet engines. The bearings were equipped with one-piece inner-race-riding bronze cages.

[2] Numbers in parentheses refer to the Bibliography at the end of the paper.

Five oils of widely different viscosities were used in the investigation. The viscosity-temperature characteristics of each of these oils are given in Fig. 4. The majority of the data to be presented were obtained with oil C.

So as not to complicate the situation, the data to be presented have been selected to show the effect of a single operating variable upon the bearing operating temperature—all other operating variables remaining constant.

Experimental Results

Effect of Variables. The bearing operating temperature that is shown plotted against the operating variable in the following figures is that temperature (either the inner or outer race) which we feel best illustrates the effect of the variable under discussion.

Speed. The effect of speed on bearing operating temperature is shown in Fig. 5 where bearing operating temperature is plotted against bearing surface speed. It is seen that the bearing temperature increases approximately linearly with an increase in speed over the operable range of bearing speeds. If the bearing speed is increased beyond a critical value, indicated by the dotted line, the bearing will not reach an equilibrium operating temperature. This indicates an incipient bearing failure. We have found that these high-speed failures usually occur as surface damage at the cage locating surface in presently designed high-speed roller bearings.

Load. The effect of load on bearing operating temperature for both an inner-race-riding and a roller-riding cage-type bearing is shown in Fig. 6 where bearing operating temperature is plotted against bearing load. It is seen that there is little change in bearing temperature with a decrease in load down to about 300 lb.

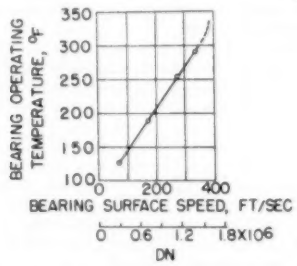

Fig. 5 Effect of Speed on Outer-Race-Bearing Operating Temperature, All Other Operating Conditions Remaining Constant

(Load, 1613 lb; oil flow, 8 lb per min; jet diameter, 0.180 in.; oil-inlet temperature, 100 F.)

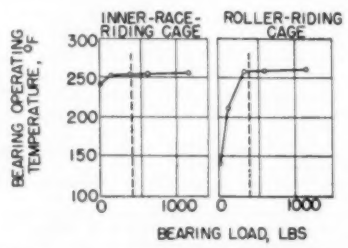

Fig. 6 Effect of Load on Bearing Outer-Race Operating Temperature

(Oil flow, 2.75 lb per min; oil-jet diameter, 0.089 in.; oil-inlet temperature 100 F; DN, 1.2×10^6 [surface speed, 290 fps].)

Also, there is little difference in the operating temperature of each bearing type in this load range. Below 300 lb load, however, the temperature of the roller-riding cage-type bearing, (RRCTB will be used hereafter), decreases rapidly as contrasted to the temperature decrease of the inner-race-riding cage-type bearing (IRRCTB will be used hereafter). It is to be noted that these data are given for very high speeds. The difference in the operating characteristics between the cage-type bearings investigated can be explained on the basis of the different amounts of heat generation at the cage-contacting surfaces as influenced by the roller slip between the rollers and inner race. This roller slip was discovered in the course of the investigation.

The dotted line indicates the gravity load acting on the turbine roller bearings in a conventional turbojet engine. Aircraft manœuvers increase the loads to the region above 400 lb. This low-load region is of interest since the shaft-stiffening bearings of certain turbojet engines operate at very light loads and high speeds. Considerable service trouble at this bearing location has occurred owing to raceway scuffing. While this trouble has been encountered with both bearing types, the RRCTB is seen to have inherent advantages for this particular operating condition due to its lower operating temperature. The RRCTB therefore better lends itself to development for the solution of this particular bearing problem. It is of interest to note that the outer-race-riding cage-type bearing (ORRCTB) also will show a reduction of heat generated at the cage-locating surface as slip increases.

Roller slip as influenced by speed, load, and cage type is shown in Fig. 7. The curves in Fig. 7 are for relatively new bearings.

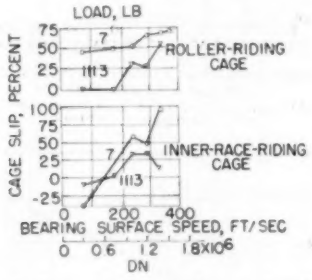

FIG. 7 EFFECT OF SPEED AND LOAD ON CAGE SLIP
(Load, 7 and 1113 lb; oil flow, 2.75 lb per min; oil-jet diameter, 0.080 in.; oil-inlet temperature, 100 F.)

It has been found that the cage speed is not readily reproducible, particularly at the higher *DN*-values. The general trend of these curves, however, indicates an increase in slip with increase in speed, and a decrease in slip with increase in load. Under certain operating conditions (low *DN*-values) the cage speed of an IRRCTB is greater than the theoretical cage speed indicating that friction at the cage-locating surface is the cage driving force which overcomes the roller friction between the inner race and rollers. This result was not observed for an equivalent bearing having a roller-riding cage.

Fig. 8 serves to explain the difference in the amount of heat generated in each of the cage-type bearings investigated when roller slip occurs. A roller-riding cage-type bearing and an inner-race-riding cage-type bearing are shown each with no roller slip and each with 50 per cent roller slip. In a bearing having a roller-riding cage only one source of cage friction exists, and that is between the cage pockets and rollers. In a bearing having an inner-race-riding cage, however, sliding friction occurs at the surfaces between the cage and the inner race, as well as in the roller pockets. For this illustrative purpose round numbers will be used. The case when no roller slip occurs will be discussed first. For each bearing type, when the shaft speed is 20 rpm, the roller speeds about their respective axes will be about 80 rpm, and the cage speeds will be about 10 rpm. In the case of the RRCTB, the cage frictional heat is proportional to the load in the cage pockets times the relative speed between the surfaces of the roller and the surface of the cage pocket.

In the case of the inner-race-riding cage, the same relative speed occurs in the cage pockets as for the roller-riding-cage, but,

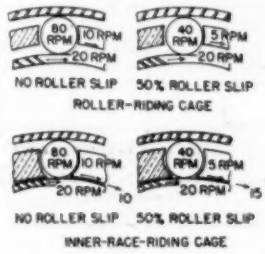

FIG. 8 EFFECT OF ROLLER SLIP ON HEAT GENERATED WITHIN TWO CAGE-TYPE BEARINGS

in addition, a relative speed of 10 rpm occurs at the cage-locating surface. The loads at the cage pockets are not known. However, these two bearing types have about the same operating temperatures under certain equivalent operating conditions (see Fig. 6). This indicates that the heat generated in the cage pockets of the RRCTB is about equal to the sum of the heat generated in the cage pockets and at the cage-locating surfaces of the IRRCTB.

This apparent paradox is due to the fact that the loads in the cage pockets of the RRCTB are greater than are the loads in the cage pockets of the IRRCTB, since the cage of the RRCTB not only spaces the rollers but also supports itself at these surfaces. However, in the case of the IRRCTB, the cage only spaces the rollers in the roller pockets, while supporting itself on the inner-race flanges.

The case where 50 per cent slip occurs will now be discussed. For each bearing type the same amount of roller slip occurs between the rollers and the inner race. Also, for each bearing type, the roller speeds about their respective axes will be the same, that is, about 40 rpm, and the cage speeds will be about the same, that is, about 5 rpm. For each bearing, then, the cage-supporting load has decreased about the same amount, and the relative speed in the cage pockets also has decreased by the same amount. In the IRRCTB, however, there is the additional heat generated at the cage-locating surface—for with roller slip the relative speed increases at this surface since the shaft speed remains constant while the cage speed decreases. It is believed that this source of cage frictional heat accounts for the major part of the difference in the operating temperature of these two bearing types in the low-load, high-speed region of operation.

Oil Flow. The effect of oil flow on bearing inner-race operating temperature is shown in Fig. 9. These data were obtained with the bearing lubricated with a solid jet of oil from a single oil jet as shown. The bearing operating temperatures were found to be minimum when the oil jet was directed perpendicular to the bearing face, that is, not at an angle into or with the direction of shaft rotation (2). The bearing temperatures also were found to

be minimum when the oil was directed at the cage-locating surface rather than at the cage or at the space between the cage and the outer race (2).

It is seen that there is an appreciable decrease in bearing temperature with an increase in oil flow. A similar curve was ob-

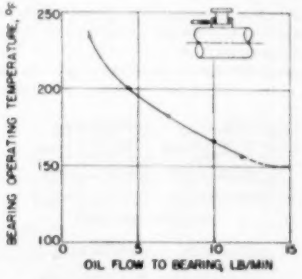

FIG. 9 EFFECT OF OIL FLOW ON BEARING INNER-RACE OPERATING TEMPERATURE

(*DN*, 1.2×10^6 [surface speed, 290 fps]; load, 368 lb; oil-jet diameter, 0.080 in.; oil-inlet temperature, 100 F.)

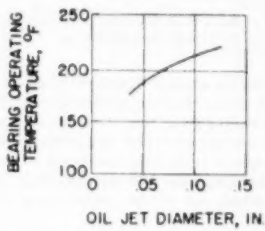

FIG. 10 EFFECT OF OIL-JET DIAMETER ON BEARING INNER-RACE OPERATING TEMPERATURE

(Load, 368 lb; *DN*, 1.2×10^6 [surface speed, 290 fps]; oil flow, 4 lb per min; oil-inlet temperature, 100 F.)

tained by Dawson (3) for ball bearings operating at high speed. This decrease in bearing temperature results so long as complete oil scavenging is maintained—the oil must not be allowed to collect around the bearing and churn into a froth. Over the flow range where churning is allowed to occur without immediate removal of the churned oil—for example, as indicated by the dotted curve—there may be an increase in bearing temperature with an increase in flow. This is a concept not entirely appreciated by many users of high-speed bearings.

Oil Velocity. The effect of oil-jet diameter upon bearing operating temperature is shown in Fig. 10 where bearing operating temperature is plotted against oil-jet diameter. These data are for a constant oil flow of 4 lb per min. It is seen that there is a decrease in bearing inner-race temperature with a decrease in oil-jet diameter. This effect is due to the increase in oil-inlet velocity associated with the decrease in oil-jet diameter at a given oil flow. This increased oil-stream velocity results in an increase in the film coefficient of heat transfer due both to the velocity effect and to the fact that the higher-velocity oil stream is better able to penetrate the windage barrier set up by the high-speed bearing components.

Oil-Inlet Temperature. The effect of oil-inlet temperature on bearing inner-race temperature is shown in Fig. 11 where bearing operating temperature is plotted against oil-inlet temperature. It is seen that bearing operating temperature decreases

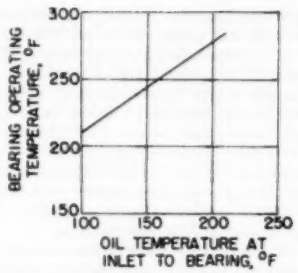

FIG. 11 EFFECT OF OIL-INLET TEMPERATURE ON BEARING INNER-RACE TEMPERATURE AT HIGH SPEED

(*DN*, 1.2×10^6 [surface speed, 290 fps]; load, 368 lb; oil-jet diameter, 0.050 in.; oil flow, 4 lb per min.)

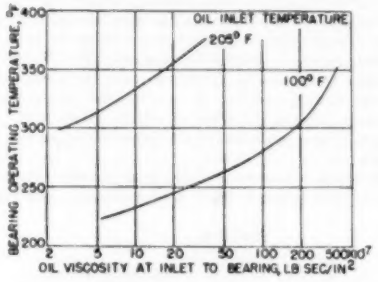

FIG. 12 EFFECT OF OIL-INLET VISCOSITY ON BEARING OUTER-RACE MAXIMUM TEMPERATURE

(*DN*, 1.2×10^6 [surface speed, 290 fps]; load, 368 lb; oil flow, 3.1 lb per min; oil-jet diameter, 0.050 in.)

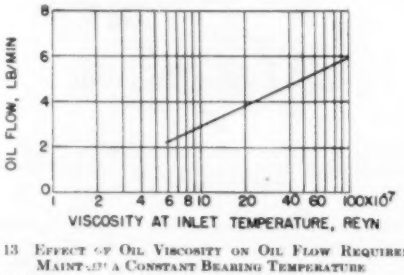

FIG. 13 EFFECT OF OIL VISCOSITY ON OIL FLOW REQUIRED TO MAINTAIN A CONSTANT BEARING TEMPERATURE

(Load, 368 lb; *DN*, 1.2×10^6; oil-inlet temperature, 100 F; bearing outer-race maximum temperature, 240 F.)

approximately linearly with a decrease in oil-inlet temperature. This reduction in bearing operating temperature is appreciable. For example, for each 1 F decrease in oil-inlet temperature, the bearing temperature decreases 0.5 F to 1 F, depending upon the operating condition.

Oil-Inlet Viscosity. The effect of oil viscosity upon the bearing outer-race operating temperature is shown in Fig. 12 for oil-inlet temperatures of 100 F and 205 F. The oils having the properties shown in Fig. 4 were used for the investigation. The bearing operating temperature is seen to be higher for a higher-viscosity oil at constant flow; therefore a higher flow of a higher-viscosity oil is required to maintain a constant bearing tempera-

ture. This is shown in Fig. 13 for a bearing outer-race-maximum temperature of 240 F with an oil-inlet temperature of 100 F. Data for oils A, B, C, and D were employed since the use of data for oil E would require the extrapolation of curves. To maintain a constant bearing temperature, the oil flow is approximately a linear function of the oil-inlet viscosity at the inlet temperature over the range of viscosities investigated when the data are plotted on semilog paper.

Oil-Inlet Distribution

The number of the oil jets, as well as their location, influence the distribution of oil to the bearing and, therefore, serve also to control the bearing operating temperature.

It has been found that no appreciable difference in maximum bearing operating temperature occurs when a single jet is indexed circumferentially with respect to a unidirectional load acting on the bearing (4). The loads investigated were 368 and 1120 lb. Furthermore, it has been found that the region of outer-race maximum temperature always occurs 60 to 120 deg before the oil-jet location in the direction of shaft rotation, and the region of minimum outer-race maximum temperature always occurs 60 to 120 deg after the oil-jet location in the direction of shaft rotation, regardless of the relative location of the oil jet with respect to the load vector.

An evaluation was made of the cooling efficiency of various oil-introduction techniques. A comparison between a single oil jet, a radial hole in the outer race, and 12 jets is shown in Fig. 14.

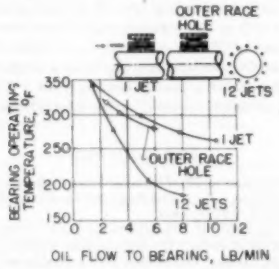

Fig. 14 Effect of Oil-Inlet Distribution on Bearing Operating Temperature

(DN, 1.2×10^6 (surface speed, 290 fps); load, 368 lb; oil-inlet temperature, 100 F.)

The 12 jets were spaced circumferentially about one side of the bearing. It is seen that for a given oil flow the 12-jet system resulted in appreciably lower bearing inner-race temperatures than did the other systems. Also, as one might expect, the temperature variation about the outer race is much less for the 12-jet system. This circumferential variation was found to be but 5 F for the 12-jet system, compared to 93 F for the outer-race hole and 35 F for the single jet. An outer-race circumferential temperature variation may cause an out-of-round of the outer race which might influence adversely the bearing performance and its reliability.

A tremendous amount of test work is required to determine all of the effects of each variable. As one can appreciate, only a very small part of the total experimental work is included herein. Furthermore, in spite of all the testing anyone might do, the chances are small that any specific operating condition, which a designer may be interested in, will have been investigated. Therefore it is necessary to generalize the results so as to allow one to predict the bearing-temperature rise at any operating condition.

Theory

Dimensional analysis was employed to generalize the foregoing results. The general form of the solution and application of the results are given herein. Further details of the analysis are given in reference (4).

The general equation relating all of the variables is

$$\frac{\Delta T C}{(DN)^a} = \Omega\left[\frac{\rho D(DN)}{\mu}, \frac{k}{\mu C}, \frac{d}{D}, \frac{v}{DN}, \frac{W}{\mu D(DN)}, \frac{x}{D}, \frac{y}{D}, \frac{z}{D}, n\right] \quad \ldots\ldots [1]$$

where

$\frac{\Delta T C}{(DN)^a}$ is some function Ω of the several nondimensional quantities

ΔT = temperature rise of bearing above oil-inlet temperature
C = specific heat of oil at oil-inlet temperature
D = bearing bore
N = shaft speed
ρ = mass density of oil at oil-inlet temperature
μ = viscosity of oil at oil-inlet temperature
k = thermal conductivity of oil at oil-inlet temperature
d = oil-jet diameter
v = oil-inlet velocity (v is proportional to M/d^2, where M is mass flow of oil)
W = bearing load
x, y, z = space co-ordinates in temperature field
n = number of oil jets

As an approximation, the function Ω in Equation [1] is assumed to be the product of the independent nondimensional groups each raised to an empirically determined power. When written as a power function for a specific point on a specific bearing and for a specific lubrication arrangement, Equation [1] may be simplified to

$$\frac{\Delta T C}{(DN)^a} = A\left[\frac{\rho D(DN)}{\mu}\right]^q \left(\frac{k}{\mu C}\right)^r \left(\frac{M}{d^2 DN}\right)^s \left(\frac{d}{D}\right)^t \quad \ldots [2]$$

where A, q, r, s, and t are constants that may be determined empirically. The term containing W has been omitted from Equation [2] because experimental results showed only a small effect of W on ΔT for the range of loads of interest, that is, about 300 to 1100 lb (1).

For the oils used and for the range of oil-inlet temperatures investigated herein, the effects of specific heat, density, and thermal conductivity of the oils are small with respect to the effect of a change of viscosity. In addition, for a given bearing, the quantity D is fixed. For oil-inlet temperatures in the range 100 to 205 F, and for a given bearing, Equation [2] may be simplified to

$$\frac{\Delta T}{(DN)^a} = B\left(\mu^b \frac{d^c}{M}\right)^f \quad \ldots\ldots [3]$$

where B, a, b, e, and f are constants that may be determined empirically for a specific bearing system.

Equation [3] is applicable in the determination of the rise above oil-inlet temperature of either the inner- or outer-race temperatures of any bearing system having jet lubrication.

Application of Theory

In order to apply Equation [3] to a specific bearing system, the inner or outer-race bearing temperatures for a number of representative bearing-operating conditions must be determined experimentally.

Outer-Race Cooling Correlation. The method of determining

the exponents of Equation [3] for the outer-race cooling correlation is given in reference (4).

The cooling-correlation curve for the outer-race temperature is shown in Fig. 15. The slope of the solid straight line in Fig. 15 is the constant B of Equation [3]. The significance of the scatter is illustrated by the broken lines on either side of the cooling-correlation curve. The dotted lines shown indicate a deviation of ±5 F from the cooling curve at a DN-value of 0.735×10^6. This ± 5 F spread decreases with an increase in DN.

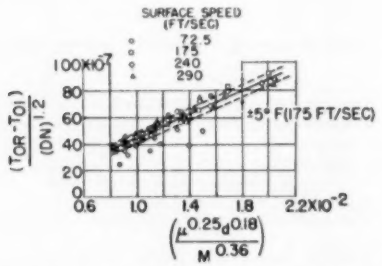

FIG. 15 TEST-RIG COOLING-CORRELATION CURVE FOR OUTER-RACE TEMPERATURE RISE ABOVE OIL-INLET TEMPERATURE

(Surface speeds, 175 to 290 fps; oil flow, 1 to 8 lb per min; oil-inlet temperature, 100 to 205 F; load, 300 to 1100 lb; jet diameter, 0.023 to 0.129 in.)

The estimated range of applicability of the cooling- correlation curve, Fig. 15, is as follows: DN, 0.3×10^6 to 1.2×10^6 (surface speeds 72.5 to 290 fps); load, 300 to 1100 lb; oil flow, 2 to 10 lb per min; oil-inlet temperature, 100 to 205 F; oil-inlet viscosity, 2×10^{-7} to 470×10^{-7} reyns; oil-jet diameter, 0.023 to 0.129 in. (The oil-inlet velocity must be in the range 10 to 150 fps, as determined from $V = 0.0574\ [M/d^2]$ in order to stay within the range of oil-inlet pressures from 5 to 400 psi.)

A similar cooling curve has been obtained for the bearing inner-race temperature rise above oil-inlet temperature (4).

COMPARISON WITH ENGINE DATA

A series of tests were completed with the rear turbine bearing of a turbojet engine instrumented to determine if the foregoing correlation also applied to engine-bearing data. Inner-race temperatures as well as outer-race temperatures were obtained. The outer-race cooling-correlation curve for a turbojet-engine bearing using the same exponents as were used for the test-rig bearing is shown in Fig. 16 along with the test-rig correlation previously presented. The engine correlation is seen to be fair.

The cooling curve for the engine data lies slightly above the cooling curve for the test-rig data and has a slope of 3.66×10^{-4} compared to a slope of 4.42×10^{-4} for the test-rig data. The differences in level and slope of the outer-race cooling curves for the engine and test-rig data are due to the different heat-flow paths to and from the engine and test-rig bearings, and particularly to the external heat associated with engine operation.

The ranges of variables for which the engine-cooling correlation curve was determined are as follows: Surface speeds, 108 to 210 fps, oil-inlet temperatures, 100 to 210 F, oil flows, $^3/_4$ to 2 lb per min, oil-inlet viscosities from 2×10^{-7} to 53×10^{-7} reyns.

A similar cooling curve has been obtained for the engine-bearing inner-race temperature rise above oil-inlet temperature (5).

SUMMARY

The high-speed aspect of bearings in general has been discussed so as to establish a perspective of where the problem stands with respect to present and future service requirements. The significance of the bearing operating temperature was discussed with regard to bearing operating limitations. The extent of the effects of speed, load, oil flow, oil-inlet temperature, oil-inlet velocity, and oil viscosity upon the bearing inner and outer-race temperatures was shown. It was shown that roller slip occurred in high-speed roller bearings, and that there is a fundamental difference in the operating characteristics of certain types of high-speed bearings heretofore considered to be essentially equivalent. Oil-inlet distribution also was found to be a significant factor regarding the control of bearing operating temperature. The test-rig results as well as the turbojet-engine data have been generalized by means of dimensional analysis to allow the designer to predict the bearing-temperature rise from a single curve regardless of whether bearing speed, bearing load, oil flow, oil-inlet temperature, oil-inlet velocity, or oil-inlet viscosity vary over wide ranges.

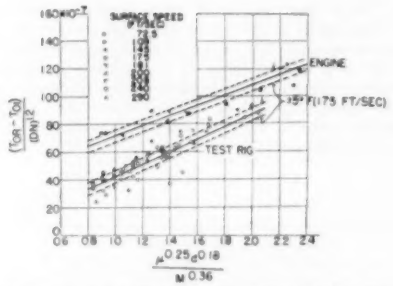

FIG. 16 COMPARISON OF TEST-RIG AND ENGINE-COOLING CORRELATION CURVES FOR OUTER-RACE TEMPERATURE

BIBLIOGRAPHY

1 "Investigation of 75-Millimeter-Bore Cylindrical Roller Bearings at High Speeds. I—Initial Studies," by E. F. Macks and Z. N. Nemeth, NACA TN 2128, 1950.

2 "Investigation of 75-Millimeter-Bore Cylindrical Roller Bearings at High Speeds. II—Lubrication Studies—Effect of Oil-Inlet Location, Angle, and Velocity for Single-Jet Lubrication," by E. F. Macks and Z. N. Nemeth, NACA TN 2216, 1950.

3 "Lubricating Problems of the Gas Turbine Engine," by J. G. Dawson, *Shell Aviation News*, vol. 133, July, 1949, p. 14.

4 "Investigation of 75-Millimeter-Bore Cylindrical Roller Bearings at High Speeds. III—Lubrication and Cooling Studies—Oil-Inlet Distribution, Oil-Inlet Temperature, and Generalized Single-Oil-Jet Cooling—Correlation Analysis," by E. F. Macks and Z. N. Nemeth, NACA TN 2420, 1951.

5 "Comparison of High Speed Operating Characteristics of Size 215 Cylindrical Roller Bearings as Determined in a Turbojet Engine and in a Laboratory Test Rig," by E. F. Macks and Z. N. Nemeth, NACA TN 1951.

6 "Experiments on Ball and Roller Bearings Under Conditions of High Speed and Small Oil Supply," by Günter Getzlaff, NACA TM 945, 1940.

7 "Improved High-Speed Roller Bearings," by D. F. Wilcock and F. C. Jones, *Lubrication Engineering*, vol. 5, 1949, pp. 129–133; discussion, vol. 5, August, 1949, p. 184.

8 "Eine hydrodynamische Theorie der Flüssigkeitsreibung in Rollenlagern," by Walter Büche, *Forschung*, vol. 5, September/October, 1934, pp. 237–244.

9 "Lubrication Characteristics of Involute Spur Gears," by E. K. Gatcombe, Trans. ASME, vol. 67, 1945, pp. 177–185; discussion, pp. 185–188.

10 "Heat Transfer," by Max Jakob, John Wiley & Sons, Inc., New York, N. Y., vol. 1, 1949, pp. 543–566.

11 "On Physically Similar Systems; Illustrations of the Use of Dimensional Equations," by E. Buckingham, *Physical Review*, vol. 4, 2nd series, October, 1914, pp. 345–376.

12 "Methods for Connection to Revolving Thermocouples," by P. R. Tarr, NACA RM E50J23a, January, 1951.

Discussion

ARTHUR S. IRWIN.[4] This paper represents an interim report of the continuing work being done by the NACA, Lewis Flight Propulsion Laboratory, which work is being followed closely by our organization. We feel that the fine laboratory technique applied by the NACA to all such problems can only result in a major advancement in our mutual knowledge of the solutions to the specific problems applying to aircraft gas-turbine work.

The authors point out that the retainer guiding surface is one of the more critical points in such high-speed bearings. Their work on oil viscosity as related to bearing temperature and heat rejection must be considered on this basis. We must not select a bearing lubricant solely on the basis of ease of design of lubrication-system components, adjusting the quantities and viscosities to suit this design convenience without realizing that the type and amount of lubricant is critical in determining whether the plain-bearing surface, represented by the retainer contact against its guiding surfaces, may be prejudiced by this selection.

In fact, consideration of oil additives should be made primarily on the basis of improving the lubrication conditions at the rubbing contact of the retainer and its guiding land. Contemporary experience indicates that the performance of a plain bearing, or a pair of mating gears, can be improved drastically by the use of oil additives. On the other hand, the present types of oils are apparently satisfactory for lubricating and cooling the rolling elements of antifriction bearings.

We appreciate the complications involved in introducing into a test program of this nature, a variable such as that represented by retainer guiding-surface lubrication. It may be that a separate program or approach may be desirable in order to investigate the effect of various oils on retainer performance, but it is surely worth while in view of the authors' statements regarding the critical nature of the retainer-guidance problem.

R. W. MORAN.[5] While the results of this paper are based on oil-flow jet lubrication for roller bearings, it might be interesting to know, with reference to Fig. 5, where bearing operating temperature is plotted against bearing surface speed, somewhat parallel test results are being obtained with grease-lubricated ball bearings on high-speed spindles. However, our testing has been limited to a bearing surface speed of 160 fps.

Our test of bearing temperature as a function of bearing-cage speed in feet per second, shows a curve which is linear and closely parallels the authors' results, but shows approximately a 15 F increase in the bearing operating temperature. For the ranges we have tested, the lower operating temperatures shown in Fig. 5 point out the importance of controlled oil flow.

It is far too early to attempt to correlate fully the data obtained with grease lubrication. We merely wish to point out that the authors of this paper, in our opinion, have covered thoroughly the many factors which influence bearing operating temperatures. Our limited investigation indicates an agreement of the theory advanced by the authors for predicting bearing operating temperatures.

E. M. PHILLIPS.[6] Too little information concerning the limitations of the rolling contact bearing is available for engineering design. Because of the many advantages of these bearings in high-speed aircraft gas turbines, it is desirable that the designer have a good knowledge of the limitations of their use and a good understanding as to the best means of lubrication and the effects of the design modifications and other factors on temperature rise, on friction losses, and on life. While it cannot be expected that the gas-turbine designer will ever be relieved of the need for final testing of the adequacy of his bearings selections, an increase in available research data will eliminate some of the present estimating as to possible safe extension of his knowledge and some of the preliminary testing now necessary in connection with any extended design. Such extension may be expected to become more difficult with the increase in design requirements for future aircraft gas turbines.

The data reported in the paper can be obtained only from research testing made in special laboratory test equipment. They cannot be obtained from engine testing. Furthermore, successful bearing applications in engines come far short of giving satisfactory information as to limitations since no knowledge of further extension in use is made available. Because of the many added factors present in the completed engine, it is not possible sufficiently to control conditions that are necessary for obtaining accurate test data. Also, because of the difficulties in making modifications, it becomes difficult to obtain any large amount of data in a reasonable time on actual gas turbines.

The authors furnish much data on the effects of operating conditions, design, and lubrication on temperature rise in a roller bearing. Much of this is an extended application field needed for present and future design. For this information the designer is very grateful. He will find it not only directly applicable but also of considerable aid in his analysis as to probable effects on life. It is to be hoped that these investigations reported will be extended and that much further research will be undertaken and reported so as to increase the fund of information available to the designer. The field is very large, and the gains to be expected from these investigations are very great. Furthermore, the improvements in bearings resulting from them should prove valuable in other applications of rolling contact bearings and may well result in an extension of applications.

H. R. ROCK.[7] We cannot help but feel that some of the data presented in the paper should have been based on more than the one run apiece which we have been given to understand was the case.

Having run large numbers of bearings of all types over long periods of time, we feel it can be, in some cases, dangerously misleading to draw conclusions on the basis of one or two tests.

Aside from this criticism, which we hope has by now been rendered null by further test work, we have the following comments:

1 The fact that NACA found the roller-riding cage superior to land-riding is most interesting in the light of general experience in the high-speed field where roller-riding cages are usually, with good cause, considered unsatisfactory. The point would be very worthy of additional work.

2 In Fig. 7 of the paper the extremely high cage slippages indicated are unbelievable. Under no conditions have we been able to measure slippage of anywhere near that magnitude.

3 The nondimensional analysis of bearing data to predict operating temperatures, and so forth, is very interesting, but it would seem that the validity of any one analysis would be limited to the particular type and size of bearing upon which it was based, as well as to the various operating conditions. Based upon this premise, the value of the method appears somewhat doubtful.

4 The use of many jets instead of one or two is admittedly desirable from the thermal viewpoint, but in order to keep down

[4] Assistant Chief Engineer, Aircraft and Special Projects, Marlin-Rockwell Corporation, Jamestown, N. Y.

[5] Application Engineer, The Fafnir Bearing Company, New Britain, Conn.

[6] Aircraft Gas Turbine Engineering Department, General Electric Company, West Lynn, Mass. Mem. ASME.

[7] Analytical Design Engineer, Pratt & Whitney Aircraft, East Hartford, Conn.

the total oil flow, the jets would usually be of a size to create a clogging problem.

5 It would appear that the direction of the jet, i.e., perpendicular to bearing or pointed with or against direction of rotation, should depend upon the range of speed involved.

In conclusion, let us express the hope that more and more test work will be done on many different types of bearings.

V. M. Zwicker.[8] The authors have covered well the characteristics of two types of roller bearings, namely, the RRCTB (roller-riding cage-type bearing) and the IRRCTB (inner-race-riding cage-type bearing), but they have omitted the third conventional type which is the ORRCTB (outer-race-riding cage-type bearing). Possibly the fact that the two types discussed are, for various reasons, generally used in turbo jet-engine designs may have placed the latter in a third order of importance with respect to these investigations.

The ORRCTB has several advantages over the other two types. The greatest of these is the application and efficient use of the lubricant. Oil applied by means of a single jet to the relatively wide space between the outside diameter of the inner ring and the inside diameter of the cage is considerably less difficult from the standpoint of targeting, particularly in comparison with the IRRCTB where the space may vary from the diametral piloting clearance to a completely closed position depending upon the instantaneous cage-locating point on the inner ring land. Generally, the diametral piloting clearance of the IRRCTB is less than the orifice diameter so that under no condition can the entire oil flow pass through the bearing. That which does not pass through reduces the temperature of the entering side of the bearing and causes a temperature differential between the two sides. This, together with the 35 F temperature differential around the circumference of the outer ring, may cause additional distortion.

The path of the oil which enters the bearing is well illustrated in the authors' Fig 2. It is noted that no oil is shown passing through the pilot clearance space on the side opposite the oil nozzle. The cage-piloting surface is one of the most critical in bearings of the race-riding type and frequently the point of incipient failure can be located on these surfaces, particularly on the surface receiving the lesser quantity of oil.

As pointed out previously, the oil has much less difficulty entering the ORRCTB and after it has entered it tends to flow radially outward between the outer ring bore and the cage outer surface on both sides, and thus the most critical surfaces are lubricated adequately. This applies to both ball and roller bearings. Tests indicate that the cage surface as well as the ring land is in better condition than equivalent surfaces in the IRRCTB operating under similar environment.

One of the principal objections raised against the ORRCTB is that the path of escape for the oil offers greater resistance to flow, resulting in higher bearing temperatures. The oil becomes trapped, as it were, in the channel formed by the two-flanged outer ring, and is further confined by the small distance of the cage from the outer ring lands.

This claim may have some support in extremely high-speed applications, but for speeds on the order of present-day turbine-engine applications, and with proper flow and scavenging, temperatures do not become excessive. For the extremely high-speed applications some design modifications can be made if found necessary. Without any modifications in the conventional design, the greater resistance to flow of oil out of the bearing may even create a slight pressure at the entrance of the orifice which may be thought of as the space between the outer ring ID and the cage OD. Pressure oil to these plain-bearing surfaces is beneficial, but certainly must not be obtained at the cost of the disadvantages incurred by flooding the bearing.

The authors have discussed three methods of applying oil to the bearing—single jet, multiple jets, and a radial hole through the center of the outer ring. The first method is the most simple design, and therefore is used in the majority of applications, but as shown in the authors' Fig. 14, it is not as good as the other two. A fourth method is a single jet on either side, applied at the pilot surface, which probably could be classified as second in order of simplicity, and may well bring the temperature down below the bearing lubricated with the outer ring hole. Here again the ORRCTB lends itself to a more simply designed application since the single jet will provide adequate lubrication.

Other desirable features of the ORRCTB are that the rubbing speed at the critical piloting surfaces is less and the contact area is greater. For a typical roller bearing similar to the one on which the authors tested the cage rubbing speed, neglecting slip, is 14.3 per cent less if the cage is piloted on the outer-ring ID and the projected area of contact is 26.8 per cent greater. Following the illustrations in Fig. 8, an ORRCTB would have lower rubbing speeds with higher slip. Using the authors' value of 50 per cent slip, the relative speed between outer ring and cage is 5 rpm, but 15 rpm between the inner ring and cage ID. With any degree of slip, conditions are less severe at the critical surfaces.

Based on all the advantages pointed out for the ORRCTB it is hoped that the NACA can arrange to test this bearing under the same conditions that applied to the other two. The results of such tests will be of great value to engine builders.

Authors' Closure

In reply to Mr. Irwin we wish to state that we are in agreement with his viewpoint that an investigation of oil additives upon cage performance is a much-needed research program.

We also have conducted research on a large number of bearings of all types and are in agreement with Mr. Rock that reproducibility of results is of paramount importance. In this regard the authors developed a "severity factor," reference (1) of the paper, so that we might gain an insight into the effect of both the particular bearing tested and its running time upon reproducibility of test results of several bearings. At the extreme speeds of the subject tests we have found that small differences of bearing geometry and running time are both significant regarding reproducibility of results. Having gained the foregoing background, we have conducted the research reported in the present paper with great care so as to avoid the possibility of drawing conclusions from too few data.

The authors do not state that the roller-riding cage is superior to the land-riding cage. In fact, we reported exactly the opposite, reference (1) of the paper. We do, however, state that in the specific region of low load and high speed the roller-riding cage, if developed further, might prove to be superior to the inner-race-riding cage. We also state in the paper that this same improvement is to be expected with the outer-race-riding cage.

As has been mentioned in the paper, cage slip is not reproducible. We feel that it depends to a great extent upon (*a*) operating internal-bearing clearances, (*b*) extent of roller skewing as caused by shaft deflection, runout, and so on, (*c*) vibration and damping characteristics of the shaft and bearing housing, and (*d*) surface finish. To substantiate our data we refer to the data[9] of Messrs. Boyd and Eklund of Westinghouse Research Laboratories, who have found cage slippages of over 70 per cent

[8] Allison Division, General Motors Corporation, Indianapolis, Ind.

[9] "Some Performance Characteristics of Ball and Roller Bearings for Aviation Gas Turbines," by John Boyd and P. R. Eklund. Presented at the Annual Meeting of The American Society of Mechanical Engineers, Atlantic City, N. J., Nov. 25-30, 1951. Paper No. 51—A-78.

at DN values as low as 0.9×10^6. If these dataare extrapolated to DN values in the neighborhood of 1.5×10^6 it is evident that cage slippages close to 90 per cent would be expected.

We are pleased that the usefulness of the cooling correlation was questioned as there are probably many others in the field who are not familiar enough with dimensional analysis to realize the extent of its usefulness as well as the limitations of this powerful research tool. We would like to answer Mr. Rock's question by summarizing the range of usefulness of dimensional analysis as applied to the subject case.

Dimensional analysis tells the research worker and designer how to group the various variables entering the problem so that he is able to correlate results with a minimum of test data. Of utmost importance in deriving the dimensionless equation is to include *all* of the significant variables entering the problem. If the technique is employed correctly a correlation curve may be expected for the case considered over the range of variables encountered. Obviously, for another case the same correlation curve cannot be used. The important things to realize are: (*a*) that a correlation curve *is possible* with a problem as vastly complicated as a jet-lubricated roller bearing operating at ultra-high speeds in a jet engine; (*b*) what the significant variables are and how to group these variables so that for the present and as well as for entirely different applications the operating temperature may be estimated over a wide range of operating variables with a minimum number of tests.

Some readers may be concerned over the fact that they do not feel justified in using either the test-rig correlation curves or the engine correlation curves of the paper to design the bearings for their new engines or other applications. They are correct—they should not use the authors' curves quantitatively—but the curves may be used qualitatively. Naturally, any designer would like to be able to predict exactly the bearing temperatures for a new engine which is in the development stage. In this respect, the designer has a very real problem. To get an answer, however, the designer or his colleagues must also do some testing. All we have done is to point the way. We have tried to anticipate the designer's problem and have tried to present him with an approach which we felt was far better than what has been heretofore available. For the designer to use the correlation analysis presented herein most effectively we recommend the following procedure for a specific hypothetical problem which we state as follows.

Problem:

To choose the oil, oil flow, oil-inlet temperature, and oil-jet diameter which will give a safe operating temperature of 325 F in a new high-power turbojet engine which is in the design state and which has a maximum bearing design DN of 1.5×10^6. The engine is equipped with three roller bearings of essentially the same bore. Single-jet lubrication is desired since it is less costly and requires minimum assembly difficulties and maintenance.

Solution:

Step 1. The oil is chosen on the basis of military specification, say, for the present case, AN-0-9 grade 1010 oil. The oil flow is chosen at first at 2 lb per min on the premise that the smaller the flow the less will be the cooler requirements which are critical in jet engines. The oil-inlet temperature is chosen at 200 F based on cooler and oil-stability requirements. The jet diameter is chosen at 0.050 in. based upon available pump pressure to give the desired flow.

Step 2. The engine is built and a trial run is made at bearing DN values of 0.7×10^6, 0.9×10^6, and 1.1×10^6. The bearing temperatures are measured and Fig. 17 is plotted for, say, the outer-race maximum temperatures for each bearing (inner-race temperatures also if data are available).

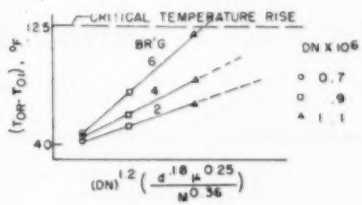

FIG. 17

The curves in Fig. 17 are plotted as soon as the data are obtained. It is evident for the subject case that the temperature of bearing 6 will exceed 325 F if the engine is operated at bearing DN values much in excess of 1.1×10^6. Bearings 2 and 4, however, may still be expected to lie in the safe region of operation at the higher DN values. The slopes of the curves are different due to the different amounts of engine heat at the various bearing locations.

Step 3. After a thorough study of the situation the project engineer concludes for the particular case that the expedient procedure is to make but a single change, that is, to increase the flow to bearing 6 by increasing the oil-jet diameter. This involves no major changes in cooler design, military lubrication specification, or pump design as pumps usually have extra capacity. From the cooling correlation equation for the outer-race bearing temperature rise

$$(T_{OR} - T_{OI}) = B(DN)^{1.2}\left(\frac{d^{1.8}\,\mu^{0.25}}{M^{0.36}}\right)$$

where B is the slope of the correlation curve for bearing 6, the required flow is at once estimated. Based upon engine oil pressure the jet diameter for this flow is chosen, and the flow corrected based upon the effect of $d^{1.8}$ upon $(T_{OR} - T_{OI})$. Of course, any combination of T_{OI}, d, μ, and M could have been varied to give the desired results.

The versatility of the cooling correlation analysis has thus been illustrated. Without it the designer would not have realized all the variables and their interaction upon one another, he would not have realized that a straight line would be expected with engine data using the same exponents as were obtained from test-rig data, and he would not have known what values of the exponents to assume. There are numerous ramifications of the foregoing applications, but we hope that by the single illustration we have shown the designer how he can save his company much time and effort by intelligent use of the cooling correlation presented herein.

In reply to the question that the use of several jets would present a jet-clogging problem we believe that clogging would only be a problem in those engines not having filtered oil.

Regarding the direction of the jet relative to the bearing we call attention to reference (2) of the paper where this point is thoroughly covered.

In reply to Mr. Zwicker, we state that we are in agreement with his viewpoints on the ORRCTB. We have not placed this type in a third order of importance, but rather we are presently engaged in an extensive program to evaluate this cage-type bearing.

With regard to the single opposed jets we call attention to reference (3) of the paper where this mode of lubrication is thoroughly covered.

Regarding the fact that with any degree of slip the conditions are less severe at the critical surface of an ORRCTB than for an IRRCTB, we refer to the paper where this point is covered.

The authors wish to thank the discussers sincerely for their time and effort taken to submit comments and criticisms. The remarks are valuable and are most welcome.

Angles for Machining

By M. F. SPOTTS,[1] EVANSTON, ILL.

For a machining operation, trial and error is ordinarily used to orient an inclined plane of a workpiece into the proper position on a machine tool. This process is wasteful of time and often results in spoiled work. This article attempts to correct the situation by describing in detail some simple mathematical methods for calculating the angles required to rotate the inclined plane into the horizontal. Numerical examples accompany all the mathematical developments.

THIS paper deals with the machining of a plane surface that is part of a workpiece of irregular shape. By rotations through what are commonly called compound angles, the surface under consideration can be oriented into position for machining. If the Cartesian co-ordinates for any three noncolinear points of the surface are known, its location in space is determined. Although the surface may be bounded by a figure of any shape, consideration need only be given to the triangle $P_1P_2P_3$ determined by the positions of the three known points. Such a plane $P_1P_2P_3$, as a part of a larger workpiece, is shown in Fig. 1.

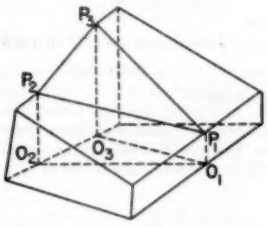

FIG. 1 WORKPIECE WITH SURFACE $P_1P_2P_3$ TO BE MACHINED

As an additional requirement, suppose that surrounding material obstructs any overrun of the cutting tool or grinding wheel across line P_1-P_2. Not only must $P_1P_2P_3$ be rotated into the horizontal, but line P_1-P_2 must be made parallel to the ways of the machine tool.

Since the locations of P_1, P_2, and P_3 are known, the locations of projections O_1, O_2, and O_3 upon the horizontal are also known. It is therefore necessary to deal only with the solid $P_1P_2P_3O_1O_2O_3$ in Fig. 1.

Milling Machine or Planer

Suppose the work is to be done on a milling machine or planer equipped with an adjustable angle plate. Fig. 2 shows the workpiece in position with plane $P_1P_2P_3$ horizontal, and line P_1-P_2 parallel to the ways of the machine. This figure shows that it is necessary to determine the values of the following angles:

φ = angle between direction of hinge of angle plate and direction of ways of machine
θ = inclination of angle plate
ψ = angle between hinge and side O_1-O_2 of workpiece

Without loss of generality, the co-ordinates for P_1, P_2, P_3 can be taken so that P_1 lies in the x, y-plane, P_3 lies in the y, z-plane, and P_2 lies in the z, x-plane. In addition, side O_1-O_2 is taken parallel to the z-axis. Plane $P_1P_2P_3$, when so located, is shown in Fig. 3.

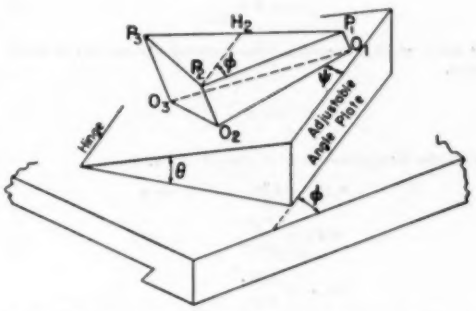

FIG. 2 WORKPIECE MOUNTED ON MILLING MACHINE PREPARATORY TO MACHINING

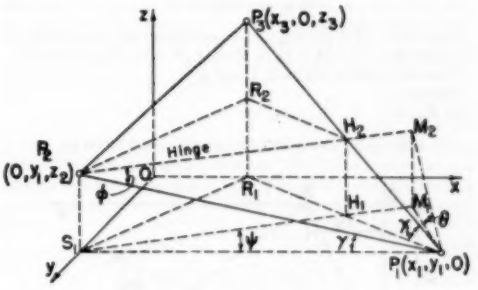

FIG. 3 GEOMETRIC RELATIONSHIPS

Some of the co-ordinates will be zero, as shown, and simplifications of the algebra will result.

Line P_2-H_2 is the intersection of a horizontal plane at elevation z_2 with plane $P_1P_2P_3$. Rotation about P_2-H_2 will bring $P_1P_2P_3$ into the horizontal; line P_2-H_2 therefore must be parallel to the hinge of the angle plate and accordingly is marked "hinge" in Fig. 3.

Line S_1-H_1 in Fig. 3 is the projection of P_2-H_2 upon the x, y-plane. P_1-M_1 is a perpendicular drawn from P_1 to S_1-H_1 extended. Point M_2 lies directly above M_1 on the extension of P_2-H_2.

The three angles φ, θ, and ψ of Fig. 2 will appear at the locations shown in Fig. 3. Angle φ is the angle between P_2-H_2 and

[1] Professor of Machine Design, Technological Institute, Northwestern University. Mem. ASME.

Contributed by the Production Engineering Division and presented at the Fall Meeting, Minneapolis Minn., September 25–28, 1951, of THE AMERICAN SOCIETY OF MECHANICAL ENGINEERS.

NOTE: Statements and opinions advanced in papers are to be understood as individual expressions of their authors and not those of the Society. Manuscript received at ASME Headquarters, July 13, 1951. Paper No. 51—F-19.

P_1-P_3, since, after rotation of the plane, these lines are respectively parallel to the hinge and to the ways. Angle $M_2P_2M_1$ or θ is the angle required to bring $P_1P_2P_3$ into the horizontal; hence it is equal to the inclination of the angle plate. Angle ψ is the angle between P_1-S_1, or side O_1-O_2, and the direction of the hinge.

(*a*) *Solution by Use of a Tetrahedron.* Fig. 4 shows the x, y-plane in Fig. 3. Since the locations of points P_1, S_1, and R_1 are known, the various lengths on this figure can be computed easily by trigonometry. Angle ψ can be found from the following equation

$$\tan \psi = \frac{N_1H_1}{N_1S_1} \quad \ldots\ldots [1]$$

From Fig. 3 the following equation can be written for finding θ

$$\tan \theta = \frac{z_2}{M_1P_1} \quad \ldots\ldots [2]$$

Angle γ which is needed in subsequent calculations can be found from

$$\tan \gamma = \frac{z_2}{x_1} \quad \ldots\ldots [3]$$

Consider tetrahedron $P_1 - P_2M_2M_1S_1$ in Fig. 3

$$P_2M_2 = S_1M_1 = P_1S_1 \cos \psi$$

$$P_2P_1 = \frac{P_1S_1}{\cos \gamma}$$

$$\cos \varphi = \frac{P_2M_2}{P_2P_1}$$

When the first two of the foregoing equations are substituted in the third, the following equation for finding φ is obtained

$$\cos \varphi = \cos \psi \cos \gamma \quad \ldots\ldots [4]$$

Example 1. Let the x, y, and z-co-ordinates for the three points be as follows: $P_1(7.78, 4.32, 0)$, $P_2(0, 4.32, 1.65)$, $P_3(1.97, 0, 3.36)$. Find the values of angles φ, θ, and ψ.

Solution:

In Fig. 3

$$P_1R_1 = [(7.78 - 1.97)^2 + 4.32^2]^{1/2} = 7.24006 \text{ in.}$$

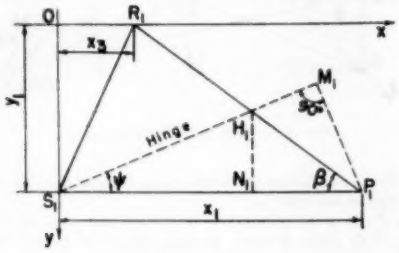

FIG. 4 GEOMETRIC RELATIONSHIPS

In Fig. 4

$$\tan \beta = \frac{4.32}{7.78 - 1.97} = 0.7435456$$

$$\beta = 36.6325°$$

$$\sin \beta = 0.596\,6802$$

$$\cos \beta = 0.802\,4792$$

In Fig. 3 consider the similar triangles $P_1H_1H_2$ and $P_1R_1P_3$. The following proportion can be written:

$$\frac{P_1H_1}{H_1H_2} = \frac{P_1R_1}{R_1P_3}$$

or

$$P_1H_1 = \frac{H_1H_2 \times P_1R_1}{R_1P_3} = \frac{1.65 \times 7.24006}{3.36} = 3.55539$$

$$N_1H_1 = P_1H_1 \sin \beta = 3.55539 \times 0.596\,6802 = 2.12143$$

$$N_1P_1 = P_1H_1 \cos \beta = 3.55539 \times 0.8024792 = 2.85312$$

$$S_1N_1 = 7.78 - 2.85312 = 4.92688$$

In Equation [1]

$$\tan \psi = \frac{N_1H_1}{S_1N_1} = \frac{2.12143}{4.92688} = 0.4305837$$

$$\psi = 23.2959°$$

$$M_1P_1 = x_1 \sin \psi = 7.78 \times 0.3954798 = 3.07683$$

In Equation [2]

$$\tan \theta \frac{z_2}{M_1P_1} = \frac{1.65}{3.07683} = 0.5362662$$

$$\theta = 28.2031°$$

In Equation [3]

$$\tan \gamma = \frac{z_2}{x_1} = \frac{1.65}{7.78} = 0.2120823$$

$$\gamma = 11.9740°$$

In Equation [4]

$$\cos \varphi = \cos \psi \cos \gamma = 0.918\,4747 \times 0.978\,2418$$

$$= 0.898\,4903$$

$$\varphi = 26.0397°$$

Additional tetrahedron equations are given elsewhere.[1]

(*b*) *Solution by Analytical Geometry.* Any equation of the first degree in x, y, and z represents a plane. Thus, if A, B, and C are not all zero

$$Ax + By + Cz + D = 0 \quad \ldots\ldots [5]$$

represents a plane.

Assume the plane is determined by the three points $P_1(x_1, y_1, z_1)$, $P_2(x_2, y_2, z_2)$, and $P_3(x_3, y_3, z_3)$. The coefficients A, B, C, and D can be found by substituting the co-ordinates of P_1, P_2, P_3 in Equation [5]. Three equations in A, B, C, and D will be obtained which may be solved for A, B, and C in terms of D. When these are substituted in Equation [5], D will cancel out and the equation of the plane will result.

Angle θ, which measures the inclination of plane $P_1P_2P_3$ with the x, y-plane, can be found from the following equation

$$\cos \theta = \frac{C}{\pm \sqrt{A^2 + B^2 + C^2}} \quad \ldots\ldots [6]$$

The sign of the denominator should be chosen so as to give a positive quotient since θ is an acute angle.

Line P_2-H_2 in Fig. 3 is the intersection of plane $P_1P_2P_3$ and plane $z = z_2$. The equation for line S_1-H_1 can be found from Equation [5] for $P_1P_2P_3$ by making the substitution $z = z_2$. Division by the absolute term will put the equation in the following form

$$\frac{x}{a} + \frac{y}{b} = 1 \quad \ldots\ldots [7]$$

[1] "Practical Shop Mathematics," by J. H. Wolfe and E. R. Phelps, McGraw-Hill Book Company, Inc., New York, N. Y., vol. 2, 1939.

Here a is the intercept on the x-axis and b is the intercept on the y-axis. Hence

$$\tan \psi = \frac{b}{a} \quad [8]$$

Values for γ and φ can be found by Equations [3] and [4], respectively.

Example 2. Use the data of Example 1 to solve for the angles by the method of analytical geometry.

Solution: The co-ordinates of the three points, when substituted into Equation [5], will give the following equations

$$\begin{aligned} 7.78A + 4.32B + D &= 0 \\ 4.32B + 1.65C + D &= 0 \\ 1.97A + 3.36C + D &= 0 \end{aligned}$$

These equations can be solved for A, B, and C as follows

$$\begin{aligned} A &= -0.056\,139D \\ B &= -0.130\,379D \\ C &= -0.264\,704D \end{aligned}$$

When these are substituted into Equation [5] the following equation will result

$$x + 2.322433y + 4.715151z - 17.812910 = 0$$

Substitution into Equation [6] gives

$$\cos \theta = \frac{4.715\,151}{\sqrt{1 + 2.322433^2 + 4.715151^2}} = 0.8812775$$

$$\theta = 28.2031°$$

The substitution of $z = 1.65$ should now be made in the equation for the plane to give the equation for line S_1-H_1 in Fig. 4. The result can be written in the following form

$$\frac{x}{10.03291} + \frac{y}{4.32} = 1$$

In Equation [8]

$$\tan \psi = \frac{b}{a} = \frac{4.32}{10.03291} = 0.4305830$$

$$\psi = 23.2959°$$

Angle φ is found by Equations [3] and [4] as in Example 1.

Application of either of the foregoing methods necessitates some preliminary calculations. The tetrahedron method requires the computation of certain lengths by trigonometry. The use of analytical geometry requires the solution of three simultaneous equations. It would be highly desirable to have a procedure by which angles φ, θ, and ψ can be found by direct substitution of the co-ordinates of the three known points. Such a method can be obtained by use of Euler's angles as follows:

(*c*) *Solution by Euler's Angles.* In Fig. 5 (*a*) let axes x and y be fixed in space, and let axes x_1 and y_1 be attached to the body. Point P in the body has co-ordinates x_1 and y_1 with respect to axes x_1 and y_1.

Fig. 5 (*b*) illustrates the situation after the body, together with axes x_1 and y_1, has been rotated counterclockwise through angle φ. The relationship between new co-ordinates x and y and the old co-ordinates x_1 and y_1 is given by the following equations

$$x = x_1 \cos \varphi - y_1 \sin \varphi \quad [9]$$

$$y = x_1 \sin \varphi + y_1 \cos \varphi \quad [10]$$

Fig. 6 illustrates similar operations of rotations of axes when

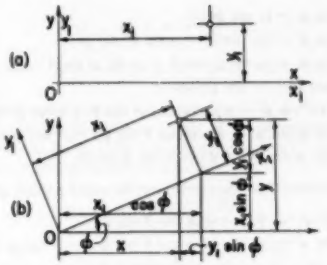

Fig. 5 Rotation of Axes—Two Dimensions

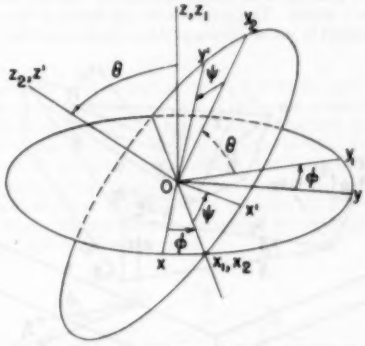

Fig. 6 Rotation of Axes—Three Dimensions

conducted for three-dimensional space. As a first operation, axis z is held, and the system is rotated through angle φ into $x_1y_1z_1$. The relationships between new co-ordinates x, y, and z and old co-ordinates x_1, y_1, and z_1 is given by Equations [9] and [10] plus the following equation

$$z = z_1 \quad [11]$$

The second rotation consists of keeping Ox_1 fixed and rotating the system through angle θ into $x_2y_2z_2$. For this rotation, the new co-ordinates will be x_1, y_1, and z_1, and the old co-ordinates will be x_2, y_2, and z_2. They are connected through the following equations

$$x_1 = x_2 \quad [12]$$

$$y_1 = y_2 \cos \theta - z_2 \sin \theta \quad [13]$$

$$z_1 = y_2 \sin \theta + z_2 \cos \theta \quad [14]$$

For the third and last rotation, Oz_2 is held fixed and the system is rotated through angle ψ into $x'y'z'$. New co-ordinates x_3, y_3, and z_3 will be connected to old co-ordinates x', y', and z' by the following equations

$$x_2 = x' \cos \psi - y' \sin \psi \quad [15]$$

$$x_3 = x' \sin \psi + y' \cos \psi \quad [16]$$

$$z_3 = z' \quad [17]$$

It is now necessary to express the new co-ordinate x in terms of the original co-ordinates x', y', and z'. This can be done easily by taking Equation [9] and substituting previous equations as follows

$$x = x_1 \cos \varphi - y_1 \sin \varphi$$
$$= x_2 \cos \varphi - (y_2 \cos \theta - z_2 \sin \theta) \sin \varphi$$
$$= x_3 \cos \varphi - y_2 \sin \varphi \cos \theta + z_2 \sin \varphi \sin \theta$$
$$= (x' \cos \psi - y' \sin \psi) \cos \varphi$$
$$-(x' \sin \psi + y' \cos \psi) \sin \varphi \cos \theta + z' \sin \varphi \sin \theta$$
$$= x'(\cos \varphi \cos \psi - \sin \varphi \cos \theta \sin \psi) - y'(\cos \varphi \sin \psi$$
$$+ \sin \varphi \cos \theta \cos \psi) + z' \sin \varphi \sin \theta \ldots\ldots\ldots\ldots [18]$$

Similar substitutions are carried out for y and z which give

$$y = x'(\sin \varphi \cos \psi + \cos \varphi \cos \theta \sin \psi)$$
$$+ y'(-\sin \varphi \sin \psi + \cos \varphi \cos \theta \cos \psi) - z' \cos \varphi \sin \theta \ldots [19]$$

$$z = x' \sin \theta \sin \psi + y' \sin \theta \cos \psi + z' \cos \theta \ldots\ldots\ldots\ldots [20]$$

Angles φ, θ, and ψ of Equations [18], [19], and [20] are known as Euler's angles. The various axes and angles as they appear when applied to the machining problem are shown in Fig. 7.

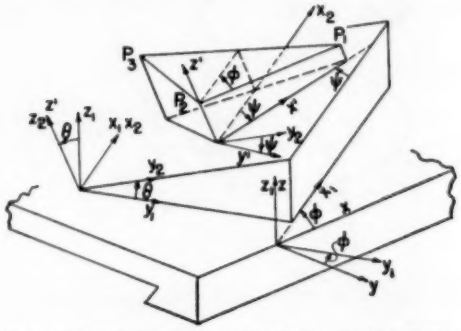

FIG. 7 CO-ORDINATE AXES FOR USE WITH EULER'S EQUATIONS

The co-ordinates x, y, and z of points P_1, P_2, and P_3 should be substituted into Equations [18], [19], and [20] and the resulting equations solved simultaneously for angles φ, θ, and ψ. However, in general, it will be found more convenient to use the following explicit equations for these angles:

When the body is located as in Fig. 3, the co-ordinates of the points will be $P_1(x_1, y_1, 0)$, $P_2(0, y_1, z_2)$ and $P_3(x_3, 0, z_3)$. After rotation of surface $P_1P_2P_3$ into the horizontal, the z-co-ordinates for all three points will be equal. Substitution into Equation [20] will give

$$z = x_1 \sin \theta \sin \psi + y_1 \sin \theta \cos \psi \ldots\ldots [21]$$

$$z = y_1 \sin \theta \cos \psi + z_2 \cos \theta \ldots\ldots\ldots\ldots [22]$$

$$z = x_3 \sin \theta \sin \psi + z_3 \cos \theta \ldots\ldots\ldots\ldots [23]$$

After the rotation that makes P_1-P_2 parallel to the ways, the y-co-ordinates for P_1 and P_2 will be equal. Substitution into Equation [19] will give

$$y = x_1(\sin \varphi \cos \psi + \cos \varphi \cos \theta \sin \psi)$$
$$+ y_1(-\sin \varphi \sin \psi + \cos \varphi \cos \theta \cos \psi) \ldots\ldots [24]$$

$$y = y_1(-\sin \varphi \sin \psi + \cos \varphi \cos \theta \cos \psi)$$
$$-z_2 \cos \varphi \sin \theta \ldots\ldots\ldots\ldots [25]$$

Subtract Equation [22] from Equation [21]

$$x_1 \sin \theta \sin \psi - z_2 \cos \theta = 0 \ldots\ldots\ldots\ldots [26]$$

Subtract Equation [22] from Equation [23]

$$x_3 \sin \theta \sin \psi - y_1 \sin \theta \cos \psi + (z_3 - z_2) \cos \theta = 0 \ldots [27]$$

Equations [26] and [27] should now be combined so as to eliminate the last terms. The following equation results

$$[x_1(z_3 - z_2) + x_3 z_2] \sin \theta \sin \psi - y_1 z_2 \sin \theta \cos \psi = 0 \ldots [28]$$

or

$$\tan \psi = \frac{y_1 z_2}{x_1(z_3 - z_2) + x_3 z_2} \ldots\ldots\ldots\ldots [29]$$

Equation [26] can be rearranged as follows

$$\tan \theta = \frac{z_2}{x_1 \sin \psi} \ldots\ldots\ldots\ldots [30]$$

Equation [25] should now be subtracted from Equation [24] to give

$$x_1(\sin \varphi \cos \psi + \cos \varphi \cos \theta \sin \psi) + z_2 \cos \varphi \sin \theta = 0 \ldots [31]$$

or

$$\tan \varphi = -\frac{x_1 \cos \theta \sin \psi + z_2 \sin \theta}{x_1 \cos \psi} \ldots\ldots [32]$$

Example 3. Apply the foregoing equations to the data of Example 1 and solve for angles φ, θ, and ψ.

Solution: The co-ordinates of the points will be $P_1(7.78, 4.32, 0)$, $P_2(0, 4.32, 1.65)$, and $P_3(1.97, 0, 3.36)$.

Substitution in Equation [29] will give

$$\tan \psi = \frac{4.32 \times 1.65}{7.78(3.36 - 1.65) + 1.97 \times 1.65} = 0.4305830$$
$$\psi = 23.2959°$$
$$\sin \psi = 0.3954798$$
$$\cos \psi = 0.9184748$$

Substitution in Equation [30] will give

$$\tan \theta = \frac{1.65}{7.78 \times 0.3954798} = 0.5362657$$
$$\theta = 28.2031°$$
$$\sin \theta = 0.4725984$$
$$\cos \theta = 0.8812776$$

Substitution in Equation [32] will give

$$\tan \varphi = -\frac{7.78 \times 0.8812776 \times 0.3954798 + 1.65 \times 0.4725984}{7.78 \times 0.9184748}$$
$$= -0.4885896$$
$$\varphi = -26.0397°$$

Fig. 6 from which Equations [18], [19], and [20] were derived, shows a right-hand system of axes. The equations are equally applicable for left-hand systems. The axes in Fig. 7 are left-hand and on this basis ψ and θ are positive and φ is negative as indicated by the results given in the equations of the foregoing example.

A slight modification of the foregoing procedure must be made if, instead of P_1-P_2, line P_1-P_3 is to be made parallel to the ways of the machine. Let the body in Fig. 3 be rotated so that P_1 is on the x-axis; P_2 remains in the y, z-plane, and P_3 remains in the z, x-plane. Angle θ, as before, can be found by Equation [2]. Angle ψ_1, between the hinge and side O_1-O_b, can be found from the following equation

$$\tan \psi_1 = \frac{M_1 P_1}{M_1 H_1} \ldots\ldots\ldots\ldots [33]$$

Angle γ_1 can be found from the following equation

$$\tan \gamma_1 = \frac{z_2}{H_1P_1} \quad \ldots\ldots\ldots\ldots\ldots\ldots [34]$$

Also from Fig. 3

$$M_1H_1 = P_1H_1 \cos \psi$$

$$H_2P_1 = \frac{P_1H_1}{\cos \gamma_1}$$

$$\cos \varphi_1 = \frac{H_2M_2}{H_2P_1} = \frac{M_1H_1}{H_2P_1}$$

The first two of the foregoing equations should be substituted into the third equation to give

$$\cos \varphi_1 = \cos \psi_1 \cos \gamma_1 \ldots\ldots\ldots\ldots\ldots [35]$$

Angle φ_1 is the angle between the hinge and the ways.

The Euler equations can be applied to the case where P_1-P_3 is to be parallel to the ways of the machine. The co-ordinates, when the body is located as described previously, will be P_1 $(x_1, 0, 0)$, $P_2(0, y_2, z_2)$, and $P_3(x_3, 0, z_3)$. The Euler equations are manipulated by exactly the same steps as previously used, and the following results will be obtained

$$\tan \psi = \frac{y_2z_3}{x_1z_3 - z_2(x_1 - x_3)} \quad \ldots\ldots\ldots\ldots [36]$$

$$\tan \theta = \frac{z_3}{(x_1 - x_3) \sin \psi} \quad \ldots\ldots\ldots\ldots [37]$$

$$\tan \varphi = -\frac{(x_1 - x_3) \sin \psi \cos \theta + z_3 \sin \theta}{(x_1 - x_3) \cos \psi} \quad \ldots\ldots [38]$$

A third possibility to be considered is the case in which line P_2-P_3 is to be parallel to the ways. Fig. 8 shows the body located so

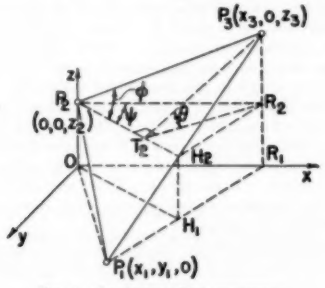

FIG. 8 GEOMETRIC RELATIONSHIPS

that P_1 is in the x, y-plane, P_3 is on the z-axis, and P_2 is located in the z, x-plane. Hinge P_2-H_2 can be located by passing a horizontal plane through P_2. Draw plane $P_2R_2T_2$ perpendicular to P_2-H_2. Angle θ will be the rotation about the hinge. Angle ψ is the angle between hinge and side O_2O_3 of the body, and φ is the angle between the hinge and the ways.

Consider tetrahedron $P_2T_2R_2P_3$

$$P_2T_2 = \frac{R_2T_2}{\cos \theta}$$

$$P_2T_2 = \frac{R_2T_2}{\tan \psi}$$

The foregoing equations can be combined to give

$$\tan \varphi = \frac{\tan \psi}{\cos \theta} \quad \ldots\ldots\ldots\ldots\ldots [39]$$

The solution by analytical geometry is similar to the first case considered.

The Euler equations can be applied equally well when P_2-P_3 is made parallel to the ways. In Fig. 8 the co-ordinates of the points are $P_1(x_1, y_1, 0)$, $P_2(0, 0, z_2)$, and $P_3(x_3, 0, z_3)$. Elimination by the same steps previously used will give

$$\tan \psi = \frac{y_1(z_2 - z_3)}{x_2z_3 - x_1(z_2 - z_3)} \quad \ldots\ldots\ldots\ldots [40]$$

$$\tan \theta = \frac{z_2 - z_3}{x_2 \sin \psi} \quad \ldots\ldots\ldots\ldots [41]$$

$$\tan \varphi = -\frac{x_2 \sin \psi \cos \theta + (z_2 - z_3) \sin \theta}{x_2 \cos \psi} \quad \ldots\ldots [42]$$

SHAPER

Suppose the work on surface $P_1P_2P_3$ is to be done on a shaper instead of a milling machine. Fig. 9 shows the workpiece properly mounted to make the surface horizontal and line P_1-P_2 parallel to the ways of the machine. With the table horizontal, $(\lambda = \gamma = 0)$, the body is first located so that line O_1-O_3 is parallel to the ways. Plane $O_1O_2P_3P_1$ will then be vertical. Rotation of the rocker through a suitable angle γ will make line P_1-P_2 parallel to the ways. The box table is now rotated through angle λ until surface $P_1P_2P_3$ becomes horizontal.

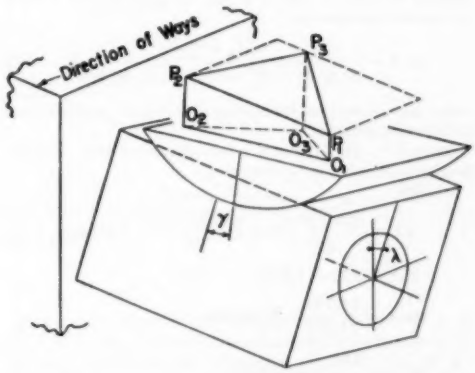

FIG. 9 WORKPIECE MOUNTED ON SHAPER PREPARATORY TO MACHINING

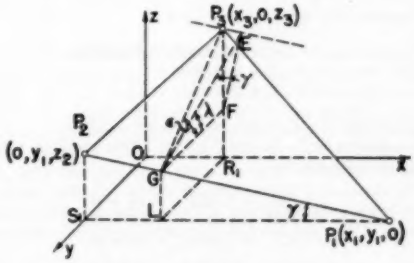

FIG. 10 GEOMETRIC RELATIONSHIPS

The values of γ and λ can be found by reference to Fig. 10 where the co-ordinates for P_1, P_2, and P_3 are taken as in Fig. 3. Pass plane P_2R_1LG parallel to the y, z-plane and draw line FG parallel to the x, y-plane. Draw plane EFG perpendicular to P_1-P_3. Let P_1-E be the trace of plane $P_1P_2P_3$ in the z, x-plane. It is parallel to line P_1-P_2. Line E-F will be located at angle γ with P_2-F.

Angle γ can be found by Equation [3]. Length P_2-F is easily found by trigonometry. The following equations can be written for tetrahedron P_2EFG

$$EF = P_2F \cos \gamma$$

$$y_1 = FG = \frac{P_2F}{\tan \epsilon}$$

$$\tan \lambda = \frac{EF}{FG}$$

The first two of these equations should be substituted into the third one to give

$$\tan \lambda = \cos \gamma \tan \epsilon \quad \ldots\ldots\ldots\ldots\ldots [43]$$

Another equation for finding angle λ can be had from analytical geometry. Pass a plane through line P_1-P_3 and FG. The equation for this plane will have the form

$$A_2x + B_2y + C_2z + D_2 = 0 \quad \ldots\ldots\ldots\ldots [44]$$

The coefficients can be found by the method previously explained. Coefficient B_2 will come out equal to zero. Angle λ, which lies between the plane of Equation [44] and plane $P_1P_2P_3$, is given by the following equation

$$\cos \lambda = \frac{AA_2 + CC_2}{\pm \sqrt{A^2 + B^2 + C^2} \times \pm \sqrt{A_2^2 + C_2^2}} \quad \ldots\ldots [45]$$

In the denominator, use the sign for each radical opposite to that of the corresponding D.

Example 4. Find values of λ and γ for the shaper. Data for the plane is the same as for Example 1.

Solution:

$$GL = \frac{(LP_1)\,(P_2S_1)}{S_1P_1} = \frac{5.81 \times 1.65}{7.78} = 1.23220 \text{ in.}$$

$$P_2F = 3.36 - 1.23220 = 2.12780$$

$$\tan \epsilon = \frac{2.12780}{4.32} = 0.4925463$$

$$\tan \gamma = \frac{1.65}{7.78} = 0.2120823$$

$$\gamma = 11.9740°$$

In Equation [43] $\tan \lambda = \cos \gamma \tan \epsilon$

$$= 0.9782418 \times 0.4925463$$
$$= 0.4818294$$
$$\lambda = 25.7261°$$

To solve for λ by Equation [45], proceed as follows:

Co-ordinates for P_1, P_2, and $F(1.97, 0, 1.2322)$ should be substituted into Equation [44]

$$\begin{aligned} 7.78A_2 + 4.32B_2 \quad + D_2 &= 0 \\ 4.32B_2 + 1.65C_2 \quad + D_2 &= 0 \\ 1.97A_2 + 1.2322C_2 + D_2 &= 0 \end{aligned}$$

These equations are now solved for the coefficients

$$A_2 = -0.1285345D_2$$
$$B_2 = 0$$
$$C_2 = -0.6060598D_2$$

When the values for A_2, B_2, and C_2 are substituted into Equation [44], the resulting equation for plane P_1P_2F can be written as

$$x + 4.715152z - 7.78 = 0$$

The equation for plane $P_1P_2P_3$ as found in Example 2 is

$$x + 2.322433y + 4.715152z - 17.812910 = 0$$

Substitution should now be made in Equation [45]. The value for the first radical of the denominator is the same as in Example 2

$$\cos \lambda = \frac{1 + 4.715152 \times 4.715152}{5.350\,359 \sqrt{1^2 + 4.715152^2}} = 0.900\,8791$$

$$\lambda = 25.7262°$$

Conclusion

The paper shows that the application of simple algebra and trigonometry will give a direct solution to the problem of determining the machining angles for an arbitrarily located inclined plane.

Discussion

R. A. Kliphardt.[1] This paper presents two interesting and useful problems that well illustrate the directness and brevity of "Descriptive Geometry" in completing solutions of three-dimensional problems. We recognize that no matter what type of solution is undertaken, we first must represent the spatial situation graphically. The author does this very adequately. If in terms of descriptive geometry we make a vertical X, Z projection and a horizontal X, Y projection, we are in line with his orientation of the workpiece and have a representation which is readily drawn, easily understood, and reveals the desired angles ϕ, θ, ψ, γ, λ with a few additional constructions. These will be described.

With the desirable speed and lessened labor of the graphical solution, there is loss in the accuracy of the result. However, many engineering problems do not require accuracy in excess of that obtainable by graphical solution. In those problems where precision is demanded in the results, Descriptive Geometry offers a quick method of obtaining a good first approximation or check on the calculations. In all space problems Descriptive Geometry provides an orderly analysis and representation to serve as a guide to the numerical calculations.

Milling-Machine Solution. Let the X, Y and X, Z projections of A-B represent the line of the ways of the machine, Fig. 11, herewith.

Locate projections of P_1, P_2, and P_3 in the given position so that

1 The three points have the given relative Z position (elevation).

2 The three points have the given relative X position (along the direction of the ways).

3 P_1P_2 bears along the direction of the ways.

4 The three points have the given relative Y position (horizontal and normal to the ways).

Line S is a horizontal line (parallel to X, Y) in the surface of $P_1P_2P_3$ and is always parallel to the hinge line.

In the final position of the block, P_1-P_2 is parallel to the ways. Thus the angle ϕ is the angle between P_1-P_2 and S. As S and P_1-

[1] Assistant Professor of Civil Engineering, Northwestern University, Evanston, Ill.

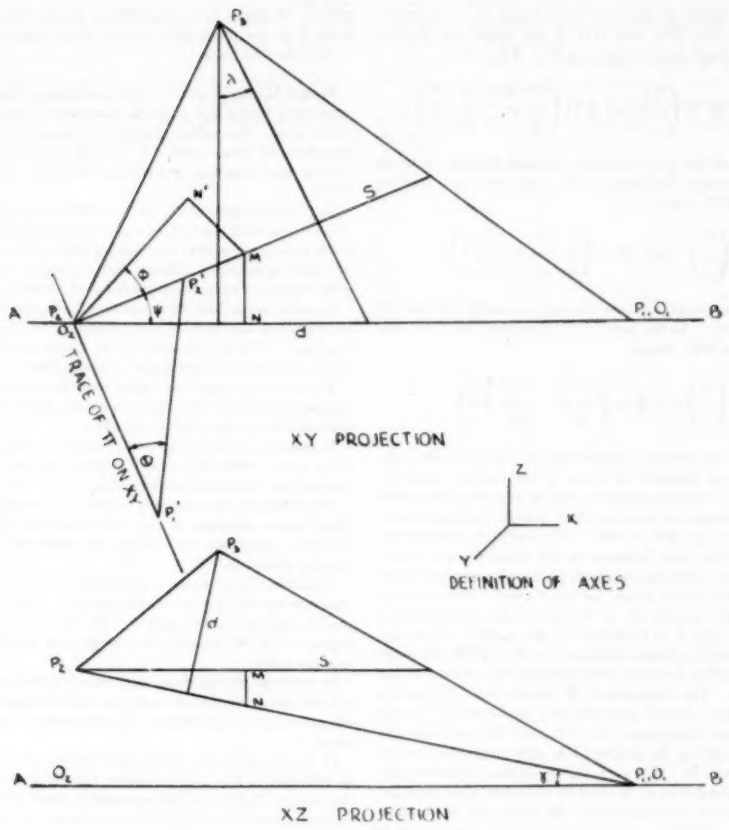

FIG. 11

P_2 are coplanar, the angle between them in the given position is the same as the angle between them in the final position. The angle ϕ between S and P_1-P_2 was found by constructing the true size and shape of triangle P_3MN. It is MP_3N'.

A projection of surface $P_1P_2P_3$ on a plane, π, perpendicular to S is a line labeled P_1', P_3'. The angle between P_1'-P_2' and the trace of π on X-Y reveals the angle θ.

The hinge line (parallel to S) and O_1-O_2 are coplanar, and thus the angle between them is the same in the given position as in the final position. We recall that S is always horizontal and that O_1-O_2 is horizontal in the given position. Thus the angle ψ is revealed between the given X, Y, projections of S and O_1-O_2.

Shaper Solution. As line P_1, P_2 is parallel to the X, Z-plane, we read the angle γ in that projection as angle $P_2P_1O_2$.

If the projections are changed to accomplish a revolution of surface $P_1P_2P_3$ through the angle γ about the Y axis, the Y, Z-projection becomes a straight line connecting the coinciding Y, Z-projections of P_1 and P_2 with the Y, Z projection of P_3. Such a Y, Z projection shows the relative Y and relative Z position of points P_1, P_2, and P_3. It is constructed on the X, Y projection as follows: The relative Y position of P_1-P_2 and P_3 is still the distance already shown as the distance from P_3 to P_1-P_2 in the X, Y-projection, and the relative Z-position of P_1-P_2 and P_3 after revolution is shown as the distance from P_3 to P_1-P_2 in the X, Z projection before revolution and is labelled d. The Y, Z projection gives us angle λ. (This process is often called "counter-revolution" and is so simple that the drawing details have been abbreviated.)

E. L. BUELL:[4] Some of the derivations stated in this paper may be regarded from other mathematical viewpoints. For example, the basic problem treated here is a transformation of coordinates, realized physically on the milling machine as a sequence of planar rotations interspersed with arbitrary translations. However, the translations may be neglected in this problem, since translations of the piece to be machined present no handling difficulty to the operator. Such a sequence of pure planar rotations, each succeeding one taking place about an axis perpendicular to that of the preceding rotation, may be expressed

[4] Aerial Measurements Laboratory, Northwestern University, Evanston, Ill.

conveniently in terms of matrices, as is shown in many texts.[6] Thus Equations [9], [10], and [11] of the paper may be condensed into the single matrix equation $\mathbf{X} = \Phi\mathbf{X}_1$, where

$$\mathbf{X} = \begin{pmatrix} x \\ y \\ z \end{pmatrix}, \mathbf{X}_1 = \begin{pmatrix} x_1 \\ y_1 \\ z_1 \end{pmatrix}, \text{ and } \Phi = \begin{pmatrix} \cos\varphi & -\sin\varphi & 0 \\ \sin\varphi & \cos\varphi & 0 \\ 0 & 0 & 1 \end{pmatrix}$$

Φ is the matrix of the planar rotation through the angle φ about the z-axis. Similarly, Equations [12], [13], and [14] may be written as $\mathbf{X}_1 = \Theta\mathbf{X}_2$, where

$$\mathbf{X}_2 = \begin{pmatrix} x_2 \\ y_2 \\ z_2 \end{pmatrix} \quad \text{and} \quad \Theta = \begin{pmatrix} 1 & 0 & 0 \\ 0 & \cos\theta & -\sin\theta \\ 0 & \sin\theta & \cos\theta \end{pmatrix}$$

the matrix of the planar rotation through the angle θ about the new x-(i.e., x_1) axis. In the same way Equations [15], [16], and [17] become $\mathbf{X}_2 = \Psi\mathbf{X}'$, where

$$\mathbf{X}' = \begin{pmatrix} x' \\ y' \\ z' \end{pmatrix} \text{ and } \Psi = \begin{pmatrix} \cos\psi & -\sin\psi & 0 \\ \sin\psi & \cos\psi & 0 \\ 0 & 0 & 1 \end{pmatrix}$$

The substitution expressed by Equations [18], [19], and [20] may now be carried out formally in terms of the matrix equations. Thus $\mathbf{X} = \Phi\Theta\Psi\mathbf{X}'$, where care must be taken to preserve the order in which the matrices are written, since matrix multiplication is not commutative, i.e., $\Phi\Theta \neq \Theta\Phi$. (Physically this means that a rotation about the z-axis followed by one about the new x-axis, in general, does not yield the same orientation as a rotation about the x-axis followed by one about the new z-axis.) This equation indicates that the matrix $\mathbf{R}$, of the resultant transformation which carries $\mathbf{X}'$ into $\mathbf{X}$ is expressed by the product of the matrices of the successive planar rotations, i.e., $\mathbf{R} = \Phi\Theta\Psi$, the order being the same as that in which these rotations are realized on the milling machine. The elements of $\mathbf{R}$ can be found by merely applying the rules of matrix multiplication to expand the formal product $\Phi\Theta\Psi$, and Equations [18], [19], and [20] may then be obtained by expanding the product $\mathbf{RX}'$ and comparing its elements with those of $\mathbf{X}$. However, for the present purposes only the second and third rows of $\mathbf{R}$ need be obtained, since only the y and z-co-ordinates are compared in the derivation of formulas for φ, θ, and ψ. (This is equivalent to the fact that no use is made of Equation [18].)

Equations [4], [35], and [43] also may be derived from spherical trigonometry. If in Fig. 3 of the paper a sphere of arbitrary radius is drawn with its center at P_2, the lines P_2-H_2, P_2-P_1, and a line through P_2 parallel to S_1-P_1 will intersect the sphere in three points which form the vertexes of a right spherical triangle. Its hypotenuse will be φ and its legs will be γ and ψ. Equation [4] of the paper is the known relation between these three parts of the right spherical triangle.[6] The derivation of Equation [4] in this paper is essentially the standard method of establishing the relation in spherical trigonometry. Equation [35] is obtained in the same manner as Equation [4].

To derive Equation [43] of the paper draw a sphere of arbitrary radius with its center at G in Fig. 10 of the paper. The lines G-F, G-E, and G-P_3 will intersect this sphere in three points which also form the vertexes of a right spherical triangle. Its hypotenuse will be ϵ, one leg will be λ, and the included angle will be γ. Equation [43] is the known relation between these three parts.[7] It also may be regarded as the formula for rotating an angle ϵ, in one plane into another plane making a known angle γ, with the first plane.[8]

MARIO MARTELLOTTI.[9] The machining of surfaces located at compound angles is a problem encountered frequently in a machine shop. The author should be congratulated for calling the attention of those interested in this problem by showing the various mathematical procedures which are available for its solution.

Typical examples of surfaces inclined at compound angles are those which form the cutting end of single-point cutting tools, and those surfaces provided for locating inserted teeth in the body of face-milling cutters. Many other examples can be found in a large variety of component parts for all kinds of machinery.

In order to machine these surfaces it is necessary to place them in a machine tool parallel to the direction of the path of the cutting tool. This is accomplished by tilting the part or workpiece in two directions at right angles to each other.

The values of these two angles are determined in relation to the manner in which the workpiece is placed and held on the machine selected for the machining operation.

In general, no distinction is necessary regarding the kind of machine used. Whether it be a milling machine, a planer, or a shaper, the calculation of the angles of tilt is the same for all.

Attachments incorporating means for tilting the workpiece either in one direction or two directions mutually perpendicular are often employed for holding the workpiece during the machining operation.

Consideration of rigidity of support and size of the workpiece may rule against the use of attachments. The workpiece is then placed directly on the table of the machine, and the required angles of tilt are obtained by wedging or propping the piece at selected points.

In any case, the mathematical calculations for the angles of tilt will be either simple or complex, depending upon the relative placement of the attachment and the workpiece or the workpiece alone.

If, for example, the attachment and the workpiece are located as indicated in Fig. 2 of the paper, the required angles for setting the surface $P_1P_2P_3$ on the horizontal plane will be three. The various methods of calculations are shown by the author. This requirement is the same, regardless of the type of machine used and as long as the piece and the angle plate are located as shown in Fig. 2.

However, a considerable simplification will result, and with improved accuracy of setting, by considering the advantage of placing the hinge of the angle plate parallel to the table's ways, and by subsequently setting the line P_1-P_2 on the workpiece at right angles to the hinge.

By tilting the angle plate to the angle made by the line P_1-P_2 with the base line O_1-O_2 (which angle is usually given) the line P_1-P_2 will be rotated into the horizontal position. This is followed by tilting the base of the angle plate (by wedging) at right angles to the line P_1-P_2, at an angle which is the resultant of the angle θ at which the plate was tilted previously, and the angle which the side P_2-P_3 makes with the base line O_2-O_1. If the line P_2-P_3 is perpendicular to P_1-P_2 no calculations are necessary, since in this case the angle of tilt for the base of the angle plate is the same as the angle between P_2-P_3 and O_2-O_1.

---

[6] See, for example, "Classical Mechanics," by Herbert Goldstein, Addison-Wesley Press, Cambridge, Mass., 1950, pp. 99–100 and 107–109.

[6] See any text on spherical trigonometry; for example, "Elements of Trigonometry With Applications," by D. R. Curtiss and E. J. Moulton, D. C. Heath & Company, 1942, p. 111, art. 66, equation [9].

[7] Ibid., Equation [6] or [8].

[8] See, for example, "Aircraft Analytical Geometry," by J. J. Apalategui and L. J. Adams, McGraw-Hill Book Company, Inc., New York, N. Y., 1944, p. 16.

[9] Development Engineer, Cincinnati Milling Machine Company, Cincinnati, Ohio. Mem. ASME.

Generally, P_2-P_3 is not perpendicular to P_1-P_3. In this case the angle of tilt is different from the angle between P_2-P_3 and O_2-O_1. The calculation of the angle of tilt can be performed by using Equation [43] of the paper

The same procedure is used if the workpiece is placed on an attachment similar to that indicated by the author in Fig. 9, which permits tilting in two perpendicular directions by means provided for this purpose in the attachment.

This illustrates the point that to locate horizontally a surface inclined at compound angles the procedure is the same regardless of the kind of machine used.

The author makes an interesting analysis of the mathematical methods for the solution of this problem. It is, however, necessary to point out that for shop use a more satisfactory approach is the simpler procedure exemplified by Equation [43] of the paper.

Hydraulics Applied to Molten Aluminum

By D. S. RICHINS[1] and W. O. WETMORE,[2] PASADENA, CALIF.

It has long been recognized in foundry practice that visual agitation or riling of molten metals susceptible to dross formation or gas absorption may affect casting quality adversely. Accordingly, flow systems are continually being sought which permit the flow of quiet nonriled metal at controlled delivery rates. Some of the more common fluid-dynamic properties of a molten aluminum alloy when flowing in sand ducts are reported in this paper. These were evaluated in the initial phase of an investigation to determine the effects of various configurations of casting flow systems upon casting quality.

Nomenclature

The following nomenclature is used in the paper:

μ = absolute viscosity
ρ = density
A = cross-sectional area of duct
V = velocity
P = pressure
h_s = elevation change between reference sections
H = total head available to system
w = specific weight, molten alloy
W = flow rate
K_e = loss coefficient, entrance
K_b = loss coefficient, bend
f = loss coefficient, friction
D = diameter or equivalent diameter of noncircular section
L = length of passage

Introduction

A casting flow system for use in founding must (*a*) permit easy transfer of metal from the ladle; (*b*) carry the metal to the mold cavity in the desired manner; and (*c*) be economically feasible. Such flow systems are divided for convenience into several distinct components as follows:

1 A reservoir to receive metal from the ladle, the pouring basin.

2 A vertical duct to transport the metal to the lowest level of the flow system, the downsprue.

3 A horizontal duct, the runner, to transport metal to the various points of entry, the gates, to the mold cavity.

Although these components can be found in any flow system, the wide variety of cast shapes require many odd modifications in order to introduce metal into the mold cavity correctly, Fig. 1. For experimental analysis and the evaluation of flow properties, a simple system was selected. This system consisted of a pouring basin and single downsprue, termed the vertical component, and a single horizontal runner, termed the horizontal component, Fig. 2. Studies of more complex systems, while of foundry value, did not add to the basic metal-flow data and consequently are not discussed herein.

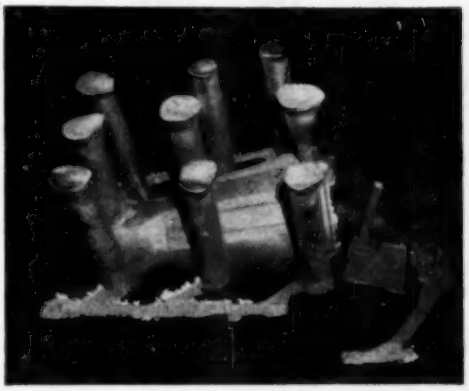

Fig. 1 A Complete Casting

Fig. 2 Simplified System Used in Flow Tests

Theoretical Considerations

It is generally accepted that molten metals are viscous fluids, and within limitations, behave as the more common viscous fluids. Certain properties such as viscosity, density, temperature, surface tension, presence of solid and gaseous inclusions, chemical reactivity, surface contact angles, and so on, are common with other fluids, but vary in degree. In some cases these properties conceivably could alter the observable flow phenomena, and consequently must be considered in the development work.

If an acceptance of the ideal or perfect-fluid concept is made with molten metals, as is common with water in hydraulic analysis, the simplified equations of motion may be applied to the flow of the metal. It is known that the kinematic viscosities of molten metals at pouring temperatures are generally less than those of water, and thus the metals may be considered as frictionless fluids. Values for aluminum are given in Table 1. Then for adiabatic and isothermal flow conditions

$$\rho AV = \text{const} \quad [1]$$

$$\frac{V^2}{2} + \frac{P}{\rho} + gh_s = \text{const} \quad [2]$$

[1] Metallurgist, Metallurgy Branch, Naval Ordnance Test Station.
[2] Head, Metallurgy Branch, Naval Ordnance Test Station.

Contributed by the Hydraulic Division and presented at the Heat Transfer and Fluid Mechanics Institute, Stanford, Calif., June 21–22, 1951, of The American Society of Mechanical Engineers.

Note: Statements and opinions advanced in papers are to be understood as individual expressions of their authors and not those of the Society. Manuscript received at ASME Headquarters, January 21, 1952.

TABLE 1 VISCOSITIES OF MOLTEN ALUMINUM

Temperature, deg F	Kinematic viscosity, stokes	Absolute viscosity, centipoises	Reference
1350	0.009*	2.3	Flow data
1290	0.0105	2.5	Ref. (8)
1238	0.0262*	6.555	
1292	0.0116*	2.890	
1346	0.0084*	2.195	Ref. (4)
1409	0.0075*	1.865	
1472	0.0057*	1.418	

* Calculated from absolute viscosity and density of molten aluminum.

For the specific application, these equations may be developed to show that

$$w\,AV = W \quad \ldots\ldots [3]$$

$$\frac{V^2}{2g} + \frac{P}{w} + h_s + k_e \frac{V_e^2}{2g} + f \frac{L}{D} \frac{V_f^2}{2g} + K_b \frac{V_b^2}{2g} + h_{minor} = H \quad \ldots [4]$$

For this analysis, the minor losses may be neglected since experimental accuracy does not permit their evaluation.

If the system be divided such that the flow losses can be measured and assigned to pertinent terms of the equations, it is possible to evaluate a numerical value for the flow coefficients. Comparison of such data with similar data for more common fluids, water, for example, will determine the accuracy of the method as well as reveal some concepts of the mechanism of metal flow. Further use of such coefficients may be to predict metal-flow data for other systems.

Experimental Procedure

It was decided initially to confine all testing procedures to those reproducible with careful foundry techniques. Consequently, dimensional tolerances were greater than those common to rigorous laboratory practice, and experimental accuracy accordingly reduced. Such tests, however, offer a more direct solution to the foundry problems which motivated the investigation. Generally, experimental shapes and sizes of the various components were held to those in keeping with foundry practice. Some shapes of special theoretical interest, admittably of questionable foundry value, were used. Changes in shapes and lengths of the system were required to isolate certain variables for equating to the loss expressions and the tests were conducted accordingly.

A normal test is conducted as follows:

1 The dimensions of the pertinent parts are determined.

2 Wooden patterns are constructed.

3 The parts are molded with as exacting techniques as are practical.

4 Prior to final assembly of the mold, sand dimensions are recorded.

5 The camera, thermocouples, receiving flask, and any special equipment are located as required, the metal poured through the system, and necessary data recorded.

6 A casting of the system is preserved for further observations and final dimensions.

For each test, the weight flow rate, pertinent areas and lengths, metal-pouring temperatures, and photographs of metal flowing from the various systems are recorded. In addition, special tests were made to determine static pressures, metal and sand temperatures throughout various systems, and velocity heads with a modified Pitot tube.

All testing was done with 356 aluminum alloy (7 per cent Si, 0.3 per cent Mg, remainder Al). The flow systems were molded in a synthetic molding sand having an AFS fineness of 57 and containing 5.5 per cent southern bentonite and 3.2 per cent water. The pouring temperature was held to a constant value of 1350 F for all tests.

The various parts of the flow system were studied individually and collectively. At least two tests were made of each part in the system to check reproducibility of results. The recorded data were averaged and analyzed in accordance with accepted hydraulic practice.

Determination of Fluid Properties

Velocities. The average or flow-rate velocities were calculated for all tests from the measured area of the system, the flow rate, and the specific weight of the molten metal. This value was used for further calculations and for design purposes wherever the delivery of a specified quantity of metal was desired. These values are recorded in the various tables.

Some energy transformations and loss considerations necessitate a more exact knowledge of maximum velocities as compared with average. For measuring these velocities a modified Pitot tube, Fig. 3, was devised and located at the exit of a 40-in-long runner system where the static pressure approached zero. Velocities by

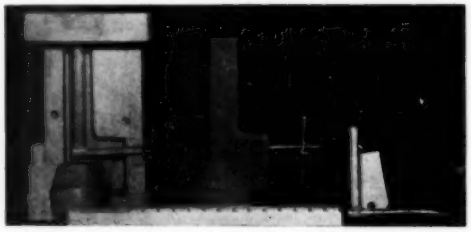

Fig. 3 Details of Pitot-Tube Assembly

this method are shown in Fig. 4 where the observed values are compared with those of water at the same Reynolds number. The velocities are expressed in this figure as the ratios of point velocities to average velocities for the same runs. The symbol α is commonly used to express this ratio.

Additional velocity determinations were made from the trajectory of the metal stream as it exited from a horizontal system in jet form. While this method is not accurate for the systems tested, primarily because of the changing stream configuration, it offered a maximum and minimum velocity figure which could be compared with average velocities. This method was used on two of the systems for verification of other data. In the case of very smooth flow, the data taken by this method show an α of 1.1 to 1.0, which indicated little velocity profile was developed in that system. The particular system had a 4-in. horizontal runner.

Viscosity. An approximate determination of the viscosity of molten aluminum may be made by a comparison of the flow of the metal with the flow of water from the experiments conducted to evaluate an entrance-loss coefficient. The metal in this instance was allowed to flow from a reservoir wherein the head was held constant. The outlet was located in the bottom of the reservoir and was well rounded for best entrance conditions. The experiment with water was conducted in an identical system except that the materials were changed from sand to plaster and lucite. The apparatus may be likened to an unrefined Saybolt viscosimeter. Such a comparison gives a value of 2.3 centipoises for the viscosity of aluminum at 1350 F. Since the values of N_R approach 30,000 for this system, the results cannot be considered valid as the flow is turbulent. However, the results are in good agreement with those given in the literature, Table 1.

Reynolds Number. Reynolds number, as calculated from the relationship $N_R = \rho VD/\mu$, varies from 11,000 to 48,000 at different portions of the systems. As used herein, D consists of the diameter of the circular section or 4 times the hydraulic radius of a noncircular section.

Pressure Measurements. To obtain quantitative values of high and low pressures, small-diameter risers, open to the atmosphere, were molded into the system such that the lower end was in contact with the metal stream. The diameters of these risers were varied until a size was found that permitted the metal to reach equilibrium under the static forces prior to solidification. The metal in the riser could be checked while liquid, during the pour, and recovered after solidification for verification. Such a technique will not measure negative pressures. Data thus recorded were employed in the computation of friction factors and in the comparison of the various systems.

Flow Losses. The flow-loss factors were found for each system by determining the total loss and the number of sources of loss. By starting at the pouring basin and sprue entrance, finding their losses and then adding separate increments to the system, it was possible to evaluate the losses in each portion.

The entrance-loss coefficient K_e was determined by evaluation of the efficiency of a square cross section vertical outlet from the pouring basin. The area of the pouring basin at this section was a minimum of 30 times the outlet area. The data are plotted in Fig. 5 which shows the discharge coefficient for various radii of curvature of the outlet. At the optimum point, 1¼ in. radius, the discharge coefficient is 0.86. This represents a head loss of

$$0.35 \frac{V^2}{2g} \text{ or } K_e = 0.35$$

For the sharp entrance, the head loss equals

$$1.23 \frac{V^2}{2g} \text{ or } K_e = 1.23$$

For the latter case the coefficient of discharge = 0.67. Daugherty (1)[3] lists a coefficient of discharge for water in a similar system of 0.622.

The addition of a downsprue to the pouring basin adds additional losses to the system, the primary one being a frictional loss. This loss may be evaluated by measuring the flow retardation

[3] Numbers in parentheses refer to the Bibliography at the end of the paper.

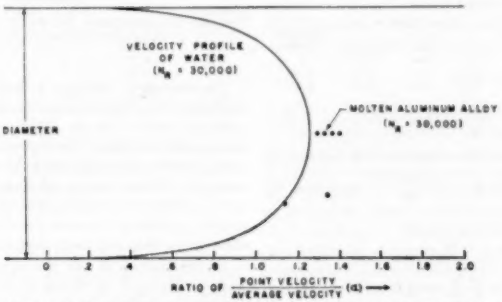

FIG. 4 COMPARISON OF ALUMINUM POINT VELOCITIES WITH THOSE OF WATER

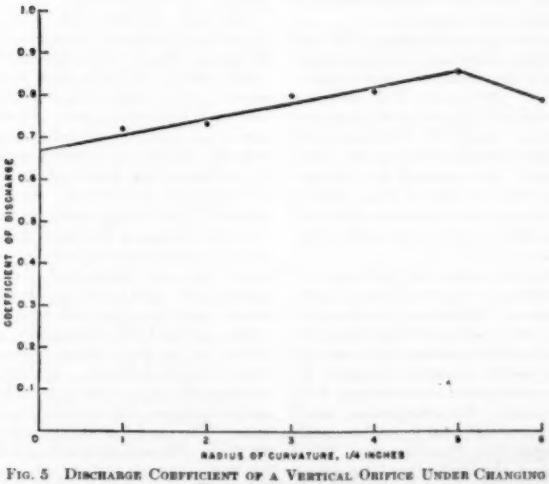

FIG. 5 DISCHARGE COEFFICIENT OF A VERTICAL ORIFICE UNDER CHANGING ENTRANCE CURVATURE

caused by the addition. Frictional resistance to flow is proportional to surface area, other factors remaining constant. Accordingly, sprues of different cross-sectional shapes, but with equal heights and exit areas, were used in the flow tests. For each of the common shapes, circular, square, rectangular, and slot type, flow rates were measured, and friction factors were calculated where possible.

Two general types of sprues were used in the various shapes. One of these types is tapered according to the acceleration of the metal and the other is the constant-area sprue of extreme foundry popularity. From Equations [1] and [2] it can be shown that by allowing for the increasing velocity of the metal, that is diminishing the area toward the exit, the sprue can be kept full, will flow quieter, and will exert a positive pressure upon the sprue walls. In this type of sprue, wherein sand-metal contact exists throughout the entire length, a valid friction factor can be determined. These factors are tabulated in Table 2 for the previously mentioned shapes. Data are not included for the constant-area sprues. In this type of sprue the metal breaks away from the sprue walls and falls as a free stream from some undetermined

TABLE 2 FRICTION FACTORS FOR DOWNSPRUES

(Tapered sprues, rounded entrance)

Shape	Areas,[a] sq in. Ent.	Exit	Velocity,[b] ips Exit	Head losses,[c] in. Al. Total	Ent. loss	Friction loss	Friction[d] factor, f
Round	0.83	0.40	106	3.5	1.2	2.3	0.02
Square (1:1)	0.90	0.42	91	7.3	0.8	6.5	0.06
Rectangular (5.3:1)	0.74	0.38	87	8.2	0.9	7.3	0.06
Slot (21.4:1)	0.79	0.37	70	11.7	0.5	11.2	0.07

[a] Areas: Measured from patterns.

[b] Velocities at exit: Calculated from measured flow rate, area, and density of molten metal.

[c] Head losses: Total loss is equal to $H - \frac{(Ax \text{ exit } V)^2}{2g}$, where H = 18 in. of aluminum in all cases.

$$\text{Entrance loss} = 0.35 \frac{(Ax \text{ entrance } V)^2}{2g}$$

$$\text{Friction loss} = (\text{head loss}) - (\text{entrance loss})$$

[d] Friction factor = f = friction loss $\times \frac{D}{13} \frac{2g}{V^2}$ where D and V are averaged over sprue length L.

point below the sprue entrance. Thus, for the greater portion of the length of the sprue, no frictional resistance exists.

Flow-rate data are presented for the various shapes of the two type sprues in Fig. 6. A coefficient of discharge, or ratio of actual to theoretical flow rate, is used as the ordinate to eliminate small-area discrepancies in the models. The abscissa is the total surface area of the sprue. Generally, with tapered sprues of angular cross section, the discharge varies linearly and in proportion to the surface area. The circular sprue deviates from the linear relationship and is more efficient. It is apparent that the constant-area sprues are less dependent on surface area. This is readily explainable since the entrance area controls the flow rate of this type of sprue and the effective head is the depth of the pouring basin, 5 in. for all tests.

Photographic evidence verified the supposition indicated previously that the flow characteristics in a tapered sprue are superior to those of a constant-area sprue. Additional information relative to the behavior of metal in these two types of sprues was obtained from static-pressures and sand-temperature measurements. The tapered sprue registered positive pressures throughout its length while the constant-area one required severe choking at its base to maintain positive pressures. Sand-temperature measurements around the tapered sprue indicated a positive metal-sand contact because of the regular rate of heat transfer. When the constant-area sprue was used, the contact was intermittent as indicated by a low and irregular rate of transfer.

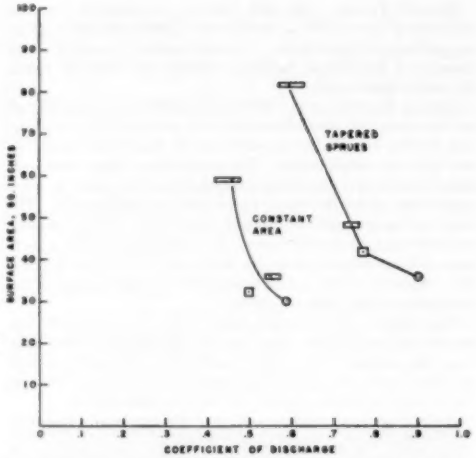

FIG. 6 RELATIONSHIP BETWEEN COEFFICIENT OF DISCHARGE OF VARIOUS DOWNSPRUES AND SURFACE AREA

The increased efficiency in flow of the round sections can be explained by a temperature traverse of the channels. A temperature drop of about 100 F was recorded in the corners of the angular sections. At the pouring temperature, such a decrease means a tripling of the viscosity. Additionally, recovered castings indicated some solidification had occurred during the pour, partially obstructing the corners. The total effect is of the proper magnitude to cause the observed decrease of flow rate in the angular channels when compared with circular.

At the bottom of the downsprue the direction of metal flow must be changed by 90 deg in order to flow into the horizontal components. Such a bend can produce considerable riling in the stream and so several types of bends which could be made in molding sand were evaluated.

Two types of bends used in the aluminum study that lend themselves more readily to analysis and comparison are the sharp 90-deg and the smooth radius bends. The former is a simple vertical 90-deg, effected in green sand by molding the downsprue normal to the runner and in contact with it, while the latter is a core insert fitted to the sprue and runner. The radius of curvature of this bend was selected to give a minimum critical length with the velocity and diameter required from flow-rate criteria. In addition to these bends, others of foundry interest, which can be considered intermediate, were tested. Of the additional bends, the large or surge sump warrants additional comment.

Observed losses in the sharp 90-deg and smooth radius bends may be used to evaluate the bend-loss coefficient K_b. The head loss in the sharp 90-deg bend is equal to 1.8 $V^2/2g$ and in the smooth radius bend, 0.4 $V^2/2g$. Hydraulic systems (2, 3) show that similar bends have loss coefficients of 1.8 and 0.6 to 0.9, respectively. Losses in the surge sump are comparable to those observed for the sharp 90-deg system; however, flow from this bend is smooth and quiet. Analysis of the bend reveals an exit loss from the sprue to the sump, although its magnitude is small, and an entrance loss into the runner which is of more importance. The head loss in this latter case could be as great as 0.5 $V^2/2g$. The over-all bend-loss factor then should be high. The loss factors for this and the other bends tested are reported in Table 3.

TABLE 3 BEND-LOSS COEFFICIENTS "K_b"

Description	Total[a] head, (h, Al	Runner[b] exit velocity, ips	Sprue[c] entrance velocity, ips	Sprue[d] exit velocity, ips	Head distribution[e] — Sprue — Ent. (1)	Sprue — Friction (2)	Runner — Friction (3)	Runner — Velocity (4)	Bend (5)	Bend[f] loss coefficient, K_b
Sharp 90 deg	18	63	40	63	2.5	1.0	1.2	4.0	9.3	1.8
Surge sump	18	70	44	70	3.0	1.3	1.5	6.3	7.9	1.2
Rect. sump	18	68	43	68	2.8	1.2	1.4	6.0	6.6	1.1
Single curved	18	77	49	77	3.7	1.6	1.8	7.7	3.2	0.5
Double curved	18	77	49	77	3.7	1.6	1.8	7.7	3.2	0.5
Radius bend	20	82	52	82	4.2	1.8	2.0	8.7	3.3	0.4

[a] Measures from top of runner to height of metal in pouring basin.
[b] Calculated from measured area, flow rate, and density of molten metal.
[c, d] Calculated from measured area and law of continuity.
[e] Head is distributed as follows:

1 Lost at sharp sprue entrance = $1.2 \frac{V^2}{2g}$ (V = average entrance velocity).

2 Lost in sprue friction = $0.02 \frac{13}{0.9} \frac{V^2}{2g}$ (V^2 = average of entrance and exit velocities squared).

3 Lost in runner friction = $0.04 \frac{4}{0.7} \frac{(V^2)}{2g}$ (V = velocity in runner).

4 Velocity head = $1.0 \frac{V^2}{2g}$ (V = velocity at exit).

5 Found by difference from available head.

[f] Calculated from head lost = $K_b \frac{V^2}{2g}$ (V = velocity at bend).

TABLE 4 FRICTION FACTORS / DETERMINED FROM PRESSURE GRADIENT IN HORIZONTAL RUNNER

Shape	Area,[a] sq in.	Velocity,[b] Δc, ips	$\frac{\Delta P}{L}$[c] in. Al / in.	D or $4R$[d]	Friction factor,[e] f
Round	0.67	64	0.13	0.91	0.02
Trapezoidal	0.67	51	0.15	0.83	0.04
Trapezoidal	1.00	43	0.10	0.95	0.04
Rectangular (4:1)	1.00	40	0.10	0.80	0.04
Slot (8:1)	0.54	37	0.21	0.48	0.06
Slot (16:1)	1.03	36	0.14	0.48	0.04

[a] Areas: Measured from castings of systems.
[b] Velocities at exit: Calculated from measured flow rate, area, and density of molten metal.
[c] Pressure gradient: Calculated from measured static pressures in runner and length of runner.
[d] Equivalent diameters: $4 \frac{\text{(cross-sectional area)}}{\text{perimeter}}$.
[e] $f = \frac{\Delta P}{L} \frac{2gD}{V^2}$.

The runner friction-loss coefficient was evaluated from the observed pressure drop in horizontal runners, varying in length between 40 and 65 in. Runners of various cross-sectional shapes were used. The factors, which were evaluated, varied from 0.06 for a slot-type runner to 0.02 for a round and are tabulated in Table 4. The over-all average for all systems was approximately 0.04. From these values, estimates of the effective surface roughness may be made for comparison with hydraulic systems at the same Reynolds numbers. Reference (2) shows that the relative roughness[4] of circular pipe containing water flowing with similar friction factors and Reynolds numbers varies from 0.00001 to 0.03. These values range from those found for very smooth pipe to riveted and concrete pipe. Since flow above an N_R of about 10,000 is considered in the "rough zone," wherein the friction factor becomes a function of surface roughness, a better agreement of friction factors would be expected. However, some factors that occur under the test conditions conceivably contribute to the observed scatter. Among the most important are runner length, bend effect, and the solidification of the surface layer of molten aluminum.

By design necessity, the test work was conducted with runners wherein bend-induced flow distortions existed, resulting in pressure fluctuations, varying with the type of bend used. Runners of sufficient length to quiet this disturbance and still permit measurement of the pressure gradient are impractical in a foundry application and would not reproduce the conditions which were under investigation. Additionally, the surface of the ducts could vary from the roughness of the molding sand to a very smooth tube of solidified aluminum. The reported friction factors are indicative of observed flow losses under the desired conditions.

[4] A parameter expressing the geometry of pipe and surface.

Heat Losses

The general energy equation as used herein was developed for adiabatic and isothermal conditions. Obviously, when molten metal is poured through wet sand at room temperature, some heat will be transferred to the walls of the ducts. This will result in a lowering of the temperature of the moving fluid, with accompanying changes in its energy content. The heat loss of the metal during the pouring period was experimentally determined to amount to approximately 2000 Btu or 1 per cent of the heat content of the melt. This value was obtained by recording entrance and exit temperatures while pouring approximately 250 lb of metal through the system, Fig. 7.

As a verification of the heat-loss figures, the heat gain by the sand was measured. Thermocouples were placed at varying distances from the sand-metal interface. Generally, it was found that the temperature at the metal-sand interface was 1000 to 1100 F, and decreased nonlinearly from the surface. The first

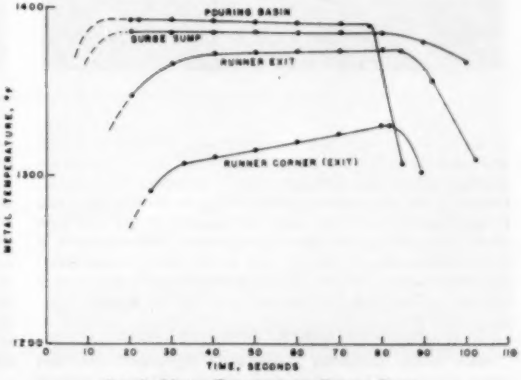

FIG. 7 METAL TEMPERATURE DURING POUR

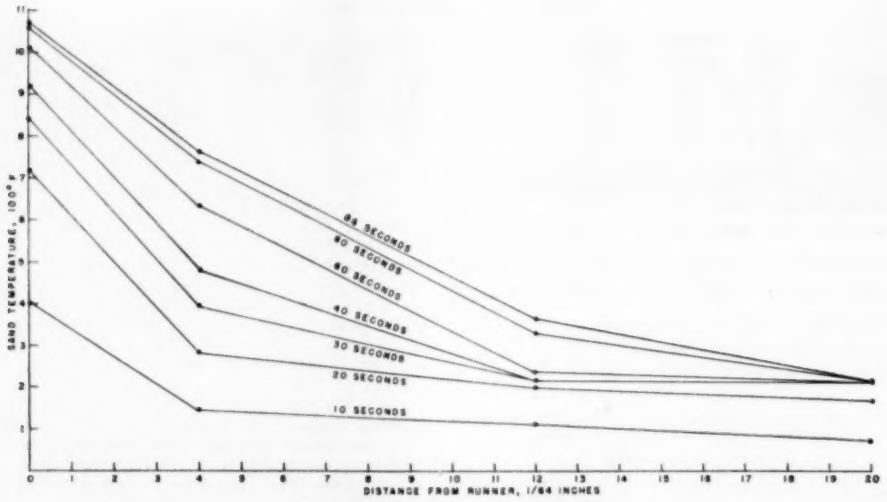

FIG. 8 SAND TEMPERATURE DURING POUR

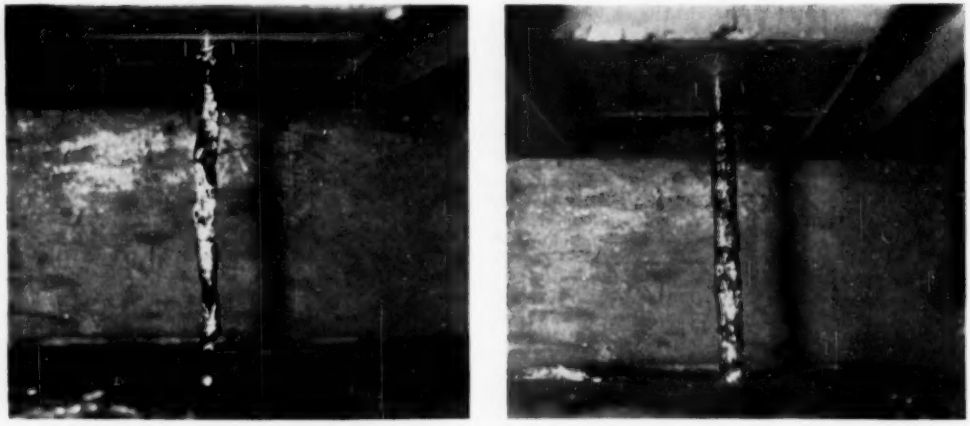

FIG. 9 FLOW APPEARANCE FROM TWO TYPES OF VERTICAL SYSTEMS; STEADY FLOW

$^1/_8$ in. of sand shows a rather steep temperature gradient with a gradual shallowing to 212 F at $^5/_{16}$ in., Fig. 8. At $^1/_2$ in. from the interface, only a slight rise above room temperature was recorded, indicating the steam which passed the $^5/_{16}$-in. thermocouple had recondensed in the cooler sand. Integration of the heat gain of the sand and moisture gave approximately 2000 Btu which is in close agreement with the heat lost by the metal. Accordingly, since the flow-rate data can only be reproduced with an accuracy of about ±5 per cent, the 1 per cent heat loss was ignored.

INTERPRETATION OF PHOTOGRAPHIC DATA

Since molten aluminum is opaque in appearance, dyes and other aids cannot be used to study stream patterns or internal riling. Transparent containers are not practical so the metal cannot be observed in the sprues and runners used to transport it. Accordingly, the photographic studies are limited to the observation of one or more free surfaces.

Photographic exposures were usually 50 microsec in duration. This exposure was varied only for special purposes. The short exposure was necessary to arrest all details of motion of the stream. From the configuration of the free surface, conclusions can be made regarding relative degrees of agitation resulting from the flow system being examined. Photographs were taken at various portions of the system by opening or cutting into the mold.

Fig. 9 illustrates two cases of flow from the vertical systems.

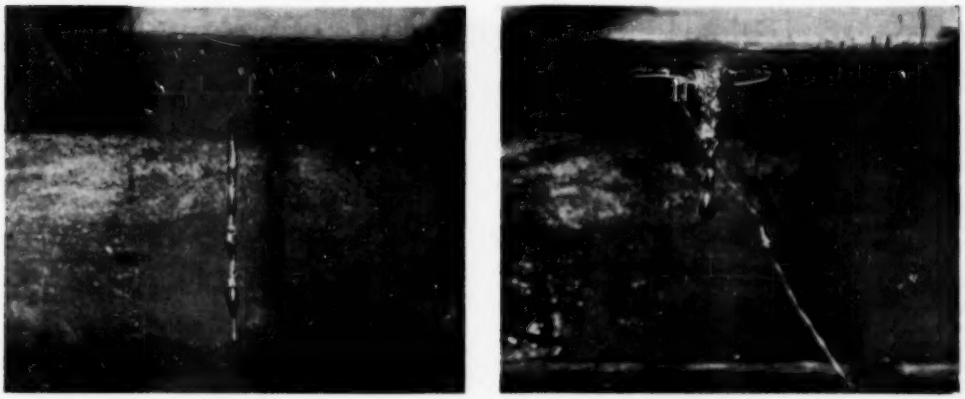

FIG. 10 APPEARANCE OF INITIAL METAL FROM TWO TYPES OF VERTICAL SYSTEMS

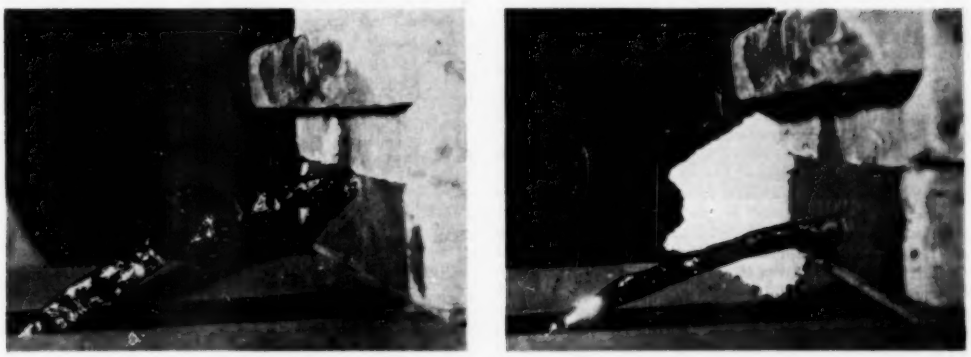

FIG. 11 APPEARANCE OF FLOW FROM EXTREME 90-DEG BENDS

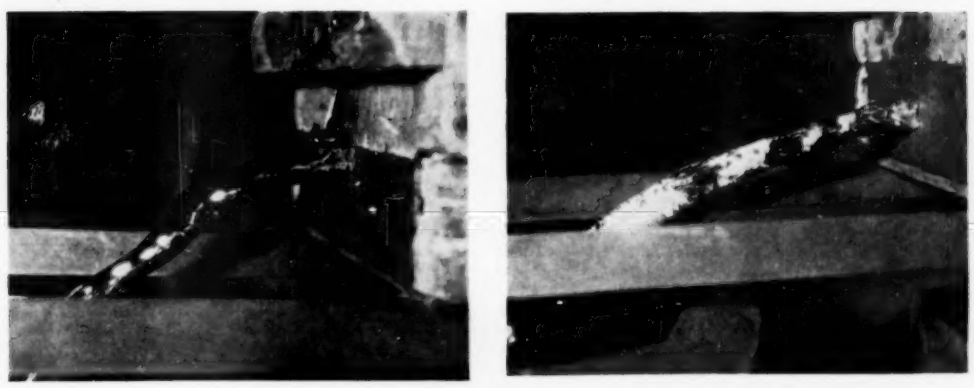

FIG. 12 EFFECT OF 2× ENLARGEMENT OF HORIZONTAL SEGMENT OF BEND

The flow from the tapered sprue is smooth with the sprue running full. The flow from the constant-area sprue shows the agitation of free fall and is not in contact with the walls of the sprue. Additional information relative to the two types of sprue is revealed in Fig. 10 which shows the first metal through the sprues. The tapered sprue flows continuously from the first instance, while the constant-area one is interrupted.

The appearance of the metal after adding two types of vertical 90-deg bends to the tapered sprue is shown in Fig. 11. The sharp 90 deg (left) has a head loss of $1.8\ V^2/2g$. The smooth 90-deg bend has a head loss of $0.4V^2/2g$. The greater head loss in the former case is shown as agitation revealed by surface high lights.

The effect of enlarging the horizontal segment of the system is shown in Fig. 12. Here an area enlargement of 1 to 2 from the vertical to horizontal was made. The flow in one case fails to fill the enlarged portion of the system and in the other is very riled. Extreme degrees of riling are caused by some configurations of the vertical sprue-runner bend. It was not possible with techniques used to evaluate rational loss coefficients for these enlarged bends.

Application

These data may be used by the foundry metallurgist or engineer to effect more precise control in the rate and mechanism of filling a casting. Generally, the engineer will be required to select a pouring basin, downsprue, runner, and gating network according to the requirements of the casting.

It was found in the study of the vertical system that if it were designed according to Equation [3] where $V = \sqrt{2gh_s}$, quieter and more uniform flow resulted. Free fall and its accompanying agitation were eliminated and gas absorption was minimized because of positive static pressure. This equation sets a minimum size for the pouring basin related to the required flow rate. Under actual conditions, a basin designed exactly according to the equation proved too small for proper operator control, so in practice a much larger one is resorted to. Since shape has little effect, the selection of a basin is relatively simple. More careful consideration must be given to the sprue. The exit area is determined from Equation [3] using the required delivery rate and the available head. The entrance area is determined similarly excepting the head existing in the pouring basin is used. If small highly efficient sprues are required, the round or square shapes would be selected. If the vertical section is great, and high metal velocities with sand washout are anticipated, a sprue with a high friction loss such as the slot type would be selected.

The selection of the runner and gates can be made from the tables and casting requirements. Excessively large runners result in agitation while small ones retard the flow and cause high metal velocities with mold cavity riling. The use of special shapes, slot type, and so on, are justified in some applications.

The joining of the vertical and horizontal sections can be accomplished with any of the bends studied. The flow losses can be anticipated from the loss coefficients. To insure freedom from metal agitation, the use of the smooth bend or surge sump is recommended.

Conclusions

Data obtained from the flow of molten aluminum alloy in foundry sand has shown that many common hydraulic flow coefficients may be used to interpret and predict the flow of molten metals with but little error. Thermal and other factors peculiar to the molten metals require some consideration in the interpretation of the flow data and resulting design factors. Basically, however, flow mechanism and properties are the same.

Accordingly, the foundry metallurgist or engineer may borrow a vast backlog of working knowledge from the science of hydraulics and apply such information to the solution of his metal-flow problems.

BIBLIOGRAPHY

1 "Hydraulics," by R. L. Daugherty, McGraw-Hill Book Company, Inc., New York, N. Y., fourth edition, 1937.

2 "Fluid Mechanics," by R. C. Binder, Prentice Hall, Inc., New York, N. Y., second edition, 1949.

3 "Engineering Applications of Fluid Mechanics," by J. C. Hunsaker and B. G. Rightmire, McGraw-Hill Book Company, Inc., New York, N. Y., 1947.

4 "Metals Reference Book," by C. S. Smithells, New York Interscience Publishers, Inc., New York, N. Y., 1949, p. 415.

5 "Fluidity of Metals," by C. W. Briggs, Metals Handbook, ASM, 1948, p. 199.

6 "A Study of Factors Affecting Pouring Rates of Castings," by H. E. Elliot and J. G. Mezoff, Trans. AFS, vol. 56, 1948, p. 279.

7 "Effect of Gating Design on Metal Flow Conditions in the Casting of Magnesium Alloys," by H. E. Elliot and J. G. Mezoff, Trans. AFS, vol. 56, 1948, p. 223.

8 "A Study of the Principles of Gating," by R. W. Swift, J. H. Jackson, and L. W. Eastwood, Trans. AFS, vol. 57, 1949, p. 76.

9 "A Study of the Principles of Gating," by K. Grube and L. W. Eastwood, Trans. AFS, vol. 58, 1950, p. 76.

10 "Conditions of Flow in Bronze Castings," by J. T. Robertson and R. G. Hardy, Trans. AFA, vol. 54, 1946, p. 732.

Measurement of Hydraulic-Turbine Vibration

By JOHN PARMAKIAN[1] and R. S. JACOBSON,[2] DENVER, COLO.

This paper describes a test program used to measure and eliminate the vibration which had produced extensive cracking in the blading of a slow-speed, 40,000-hp hydraulic turbine. Strains, accelerations, and pressures were measured at various locations on the turbine runner while the unit was in operation. The instruments used for these measurements were of the resistance type. Instrument signals were transmitted through collector rings and brushes to direct-writing oscillographs. The vibration was eliminated successfully by an inexpensive modification of the runner blading which is described in the paper.

Introduction

PARKER Power Plant is located on the Colorado River downstream from Hoover and Davis dams. It is essentially a run-of-the-river plant and consists of four 30,000-kva generators, each of which is coupled to a 40,000-hp hydraulic turbine. These turbines are designed to operate at a speed of 94.7 rpm under an effective head of 80 ft. The turbine runners, shown in Fig. 1, are of the Francis type and have 15 blades. These runners are 14 ft in diameter and weigh about 60 tons each.

Operating History

The generating units of this power plant were placed in operation during late 1942 to early 1943, and for the next three years they contributed greatly to the war effort. During this operating period, considerable vibration of the units was felt especially at the higher gate positions, but this condition was not considered to be too serious at the time. In 1946 a thorough inspection of the units revealed the runner blades were cracking badly. The length and location of the cracks varied somewhat among the four units, but the cracking appeared to be greatest in unit No. 1 at the junction of the blades and the crown. Some of these cracks are shown in Figs. 2, 3, and 4.

On unit No. 1, the cracks were repaired by welding in May, 1946. In October, 1947, an inspection of this unit revealed that the blades had cracked again, in and near the welded regions. This runner was repaired again in November, 1947, and from then until the middle of 1949 various methods were tried to eliminate the periodic runner vibration and cracking of the runner blades. For example, compressed air was forced into the unit at the lower seal chamber, upper seal chamber, and even mixed with the water in the scroll case upstream from the stay vanes. In addition, the leading edges of the runner blades were sharpened, and alternate pairs of blades were braced with struts near the mid-length of the blades. However, these measures were not effective in eliminating the vibration and progressive cracking of the runner blades.

A spare runner was not available at the plant until November, 1950. Therefore, in order to minimize the danger of a possible complete failure of the runners during the interim period, the maximum turbine-gate openings were restricted to 0.80.

Fig. 1 Parker Power-Plant Turbine Runners

Development of Instruments

In order to measure the pressure changes on the surfaces of the runner blades and streamlined water passages, it was necessary to develop a button-type pressure cell which could be recessed into the surfaces of the water passages as shown in Fig. 5. The design of this pressure cell was improved constantly as deficiencies showed up during the testing. The final design, shown in Figs. 6 and 7, consisted essentially of a thin diaphragm on which the pressure acted. Pressure changes on the diaphragm were then sensed as bending strains by SR-4 type strain gages located inside the pressure cell. Calibration and frequency-response curves for one of these pressure cells are shown in Figs. 8 and 9, respectively.

Changes in strain on the surfaces of the runner blades were measured directly with SR-4 strain gages which were cemented to the runner blades. In order to protect these strain gages from the action of the water, they were waterproofed with a tar compound and then sealed with a brass receptacle placed over the strain gage.

One of the most difficult problems associated with these tests was that of obtaining data from the rotating runner. For the instruments located on the rotating runner, the gage leads were drawn through copper tubing on the back face of the blading to the fairing cone and then upward through the center of the turbine shaft and out of a hole in the shaft to the turbine pit. In order to transmit the instrument signals from the rotating runner

---

[1] Engineer, Design and Construction, U. S. Bureau of Reclamation. Mem. ASME.

[2] Engineer, U. S. Bureau of Reclamation.

Contributed by the Hyraulic Division and presented at the Annual Meeting, Atlantic City, N. J., November 25–30, 1951, of The American Society of Mechanical Engineers.

Note: Statements and opinions advanced in papers are to be understood as individual expressions of their authors and not those of the Society. Manuscript received at ASME Headquarters, September 4, 1951. Paper No. 51—A-88.

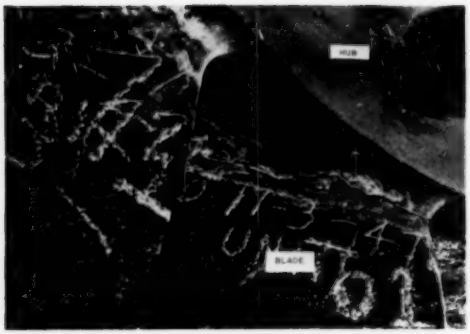

FIG. 2 CRACKING OF RUNNER BLADES NEAR RUNNER CROWN

FIG. 3 CRACKING OF RUNNER BLADES NEAR RUNNER CROWN

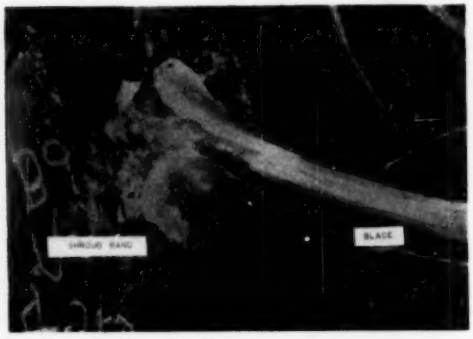

FIG. 4 CRACKING OF RUNNER BLADES NEAR RUNNER SHROUD BAND

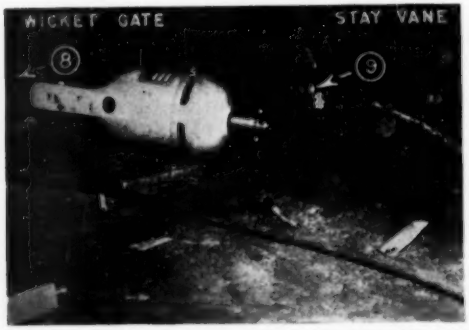

FIG. 5 BUTTON-TYPE PRESSURE CELLS RECESSED INTO STAY VANE AND WICKET GATE

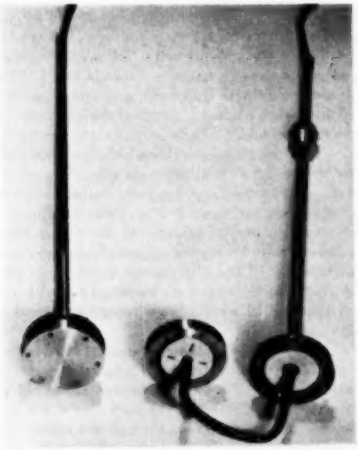

FIG. 6 BUTTON-TYPE PRESSURE-CELL ASSEMBLY

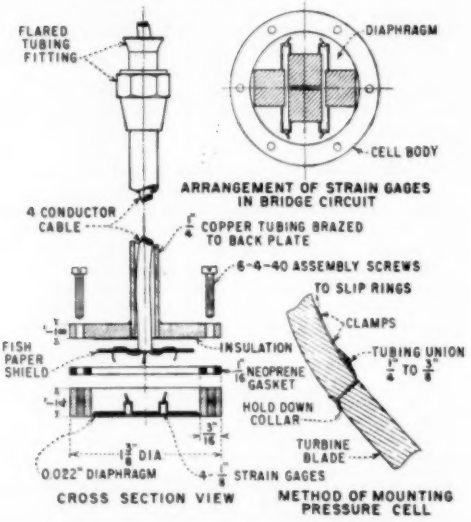

FIG. 7 STAINLESS-STEEL BUTTON-TYPE PRESSURE CELL

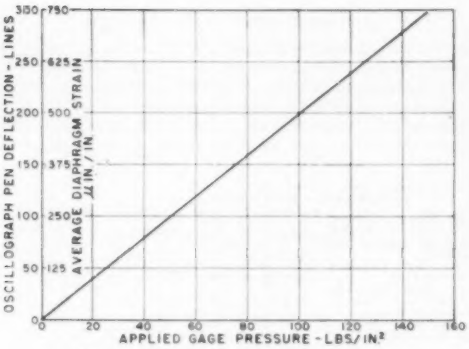

FIG. 8 TYPICAL STATIC CALIBRATION CURVE
(Button-type pressure cell; design pressure, 100 lb per sq in.)

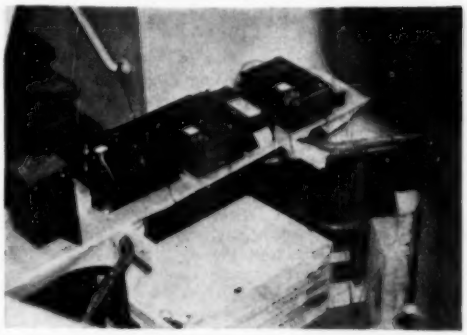

FIG. 11 DIRECT-WRITING RECORDING APPARATUS

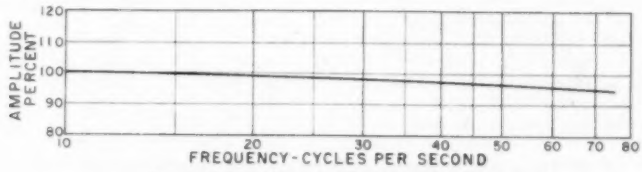

FIG. 9 TYPICAL OVER-ALL FREQUENCY RESPONSE
(Button-type pressure cell and Brush strain analyzer and oscillograph.)

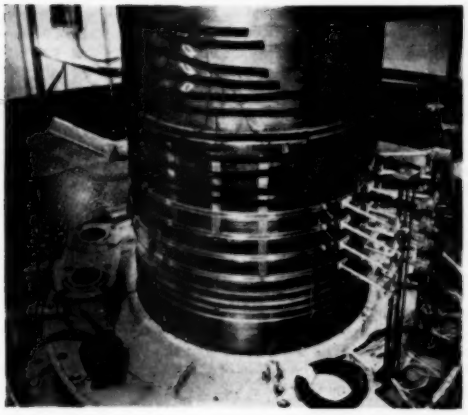

FIG. 10 SLIP RING AND BRUSH ASSEMBLY

shaft to the recording oscillographs, a slip-ring brush assembly was developed as shown in Fig. 10. The rings consisted of silver-plated copper strips which were insulated from the turbine shaft by layers of cellulose acetate. Four silver graphite brushes per ring were connected in parallel in the brush assembly to minimize the effect of contact-resistance changes when the runner shaft was rotating. The recording apparatus, which is shown in Fig. 11, consisted of strain amplifiers and direct-writing oscillographs, manufactured by the Brush Development Company. The gage leads from instruments located on nonrotating members passed through tubing and were connected directly to recording oscillographs on the outside of the unit.

FIRST FIELD-TESTING PROGRAM

In the spring of 1950 it was decided that unit No. 1 of this plant could be spared for approximately 50 hr over one week end. During this period a series of vibration tests were performed to determine the source of the runner vibration. The measurements taken consisted of oscillograph records of the changes in pressure and strain at various locations inside the unit. The location of instruments is shown in Fig. 12. Instruments were located at the turbine inlet, stay vanes, wicket gate, various locations on the turbine runner, upper and lower seal chambers, and in the draft tube.

A summary of the significant results of the analysis of the first field tests is as follows:

(*a*) For the pressure-cell locations at the leading edge of the runner blades, periodic impulse excitation due to the action of the streams (formed by the guide vanes and wicket gates) striking the blades could not be detected.

(*b*) For the pressure-cell location at the trailing edge of the runner, large pressure changes of the impulse type were recorded at the higher gate positions. The amplitudes and frequencies of the indicated pressure varied somewhat with the gate position, but there was a significant indication of periodicity of these pressure changes (see Fig. 13).

(*c*) For the other pressure-cell locations on the unit there were no significant differences in the records as the gate openings were varied.

ANALYSIS OF TEST RESULTS

The theoretical considerations involving impulse excitation of turbine runners are usually associated with the pressure impulses exerted on each turbine blade by the action of each of the partial

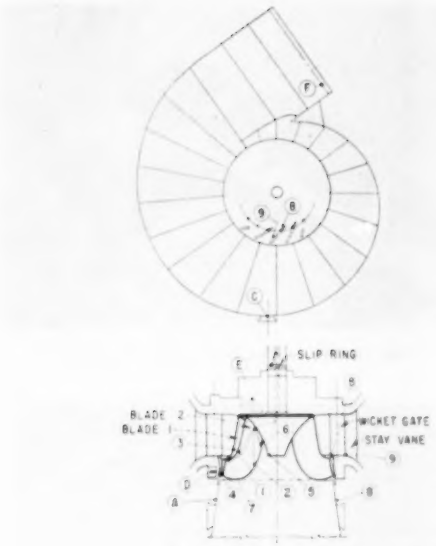

NUMBERS 6 AND 7 ARE STRAIN GAGES
ALL OTHERS ARE PRESSURE CELLS

A—Draft Tube—Left Side
B—Draft Tube—Right Side
C—Centerline of Scroll Case Mandoor
D—Lower Seal Chamber Shroud Ring
E—Upper Seal Chamber Below Head Cover
F—Penstock Piezometer
1—Leading Edge—Blade 2
2—Trailing Edge—Blade 2
3—Leading Edge—Blade 1
4—Shroud Ring Midway Between Blades
5—Fairing Cone Midway Between Blades
6—Trailing Edge—Blade 2 Near Crown
7—Leading Edge—Blade 2 Near Shroud Ring
8—Trailing Edge—Wicket Gate (See Plan)
9—Trailing Edge—Stay Vane (See Plan)

FIG. 12 LOCATION OF INSTRUMENTS FOR PARKER DAM TURBINE VIBRATION TESTS

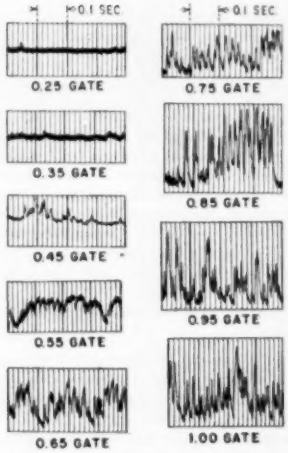

FIG. 13 PRESSURE CHANGES AT TRAILING EDGE UNIT NO. 1—BLADE NO. 2

streams which are formed by the space between the wicket gates. Prior to passing the leading edge of the turbine runner, these partial streams are conducted into the moving ring of water downstream from the wicket gates and tend to rejoin within this region. The oscillograph records of the pressure changes at the leading edge of the runner blades indicated that periodic impulse excitation due to these partial streams was not present. Hence the annular water ring between the wicket gates and the sharp leading edges of the runner blades is sufficient to break up the pressure-impulse effect of the partial streams.

The most probable source of excitation of the runner at the higher gate positions appeared to be associated with the shock-type pressure changes which were recorded at the trailing edge of a runner blade. The phenomena producing these pressure changes are not fully understood at present as there is difficulty in distinguishing between cause and effect. However, exciting forces acting on the runner blades which can produce pressure changes of this type may result from either or both of two causes, namely, vibration of the runner blades due to vortex formation near the trailing edges of the blades or vibration of the runner blades resulting from high-velocity flow and an inadequate torsional rigidity of the blades.

The first type of self-induced vibration might be described in the following manner: The trailing edges of the runner blades are not streamlined but end abruptly at a thickness of 1 to $1^1/_2$ in. There is a minimum velocity of water through the runner associated with the shape of the blades below which periodic vortexes are not produced. However, when this critical velocity is exceeded, the streamlines no longer hug the blades, and vortexes form in the wake. The action of the vortexes imposes periodic transverse forces on the runner blades and causes them to vibrate across the streamlines.

In explaining the second type of self-induced vibration for high-velocity flow the effect of turbulence is considered to be negligible. For a given position of a runner blade with respect to the velocity of flow, a hydrodynamic force and a twisting moment are exerted on the face of the blade. If the torsional rigidity of the blade is low, the blade will twist appreciably, and the twisting moment and hydrodynamic force acting on the face of the blade will change, increasing for one direction of motion and decreasing for the other direction of motion of the blade. Energy is thus supplied from the flow of water to sustain the vibration of each blade.

As a result of these studies and tests, it was recommended that when field conditions permitted, alterations be made at the trailing edges on one of the existing runners.

Second Field-Testing Program

During the period from October 4 to October 24, 1950, when field conditions permitted, additional vibration tests of various types were conducted on unit No. 1. During this period accelerations, strains, and pressures were measured on turbine blade No. 2 which was the only uncracked blade in the unit. The locations of the instruments are shown in Fig. 14. The accelerometer used during these tests was of the unbonded strain-element type, manufactured by Statham Laboratories Inc., Beverly Hills, Calif. It was enclosed in a waterproofed brass case and attached to the blade.

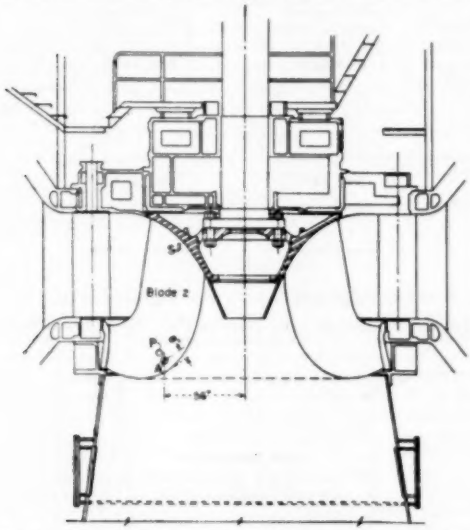

Fig. 14 Location of Instruments on Negative Pressure Face Unit No. 1

(A, accelerometer, P, pressure cell, S, strain gage.)

The instrument records are shown in Figs. 15, 16, and 17, and the results of the measurements as plotted against gate opening are shown in Fig. 18. The accelerometer and strain-gage records indicate the same general pattern with the principal component of vibration of 55–57 cycles per sec reached near the 0.80 gate position. The pressure-cell record indicated a small component of 55–57 cycles per sec near 0.80 gate.

From October 25 to November 5 the trailing edges of all 15 runner blades were chipped and ground along their entire length. The original and final cross sections of a typical blade at the trailing edge are shown in Fig. 19.

Accelerometer readings were again taken at blade No. 2 when the unit was placed back in operation. These records are shown in Fig. 20. A comparison of the acceleration records of blade No. 2 before and after the modifications for all gate positions is shown in Fig. 21. It is apparent that the vibration of the blading has been drastically reduced.

A summary of the conclusions drawn from the second field tests is as follows:

(*a*) The modifications at the trailing edge of the runner eliminated the periodicity of the turbine-blade vibrations and reduced the vibration accelerations of the blading to small fractions of their previous values.

(*b*) The modifications also increased the power output of the unit for all gate positions with an increase of 6.5 per cent in the maximum output of the turbine unit.

Modification of Other Units

Turbine-runner modifications on the remaining three units were started on January 9, 1951, by government forces and completed on February 16. These modifications were effective in eliminating the periodic vibrations of all turbines. An inspection

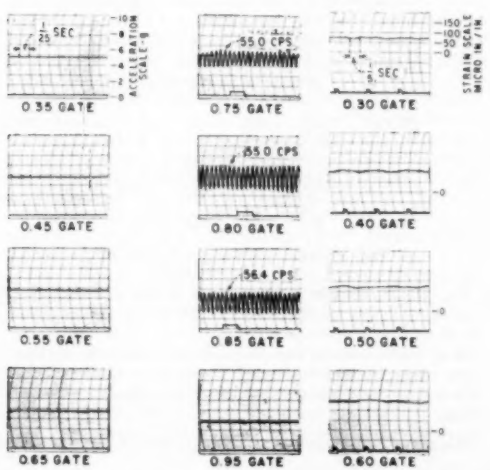

Fig. 15 Transverse Accelerations Unit No. 1—Blade No. 2 Before Modifications

Fig. 16 Strain Records Unit No. 1—Blade No. 2 Before Modifications

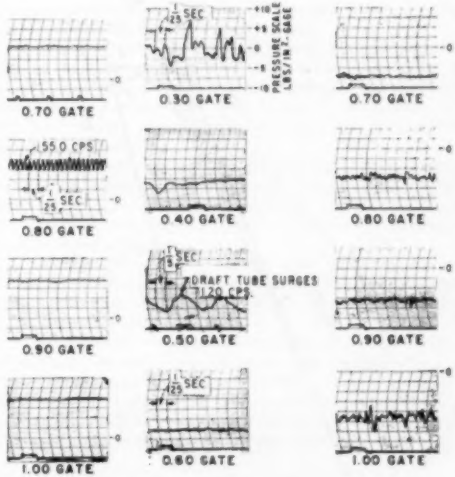

Fig. 17 Pressure Records Unit No. 1—Blade No. 2 Before Modifications

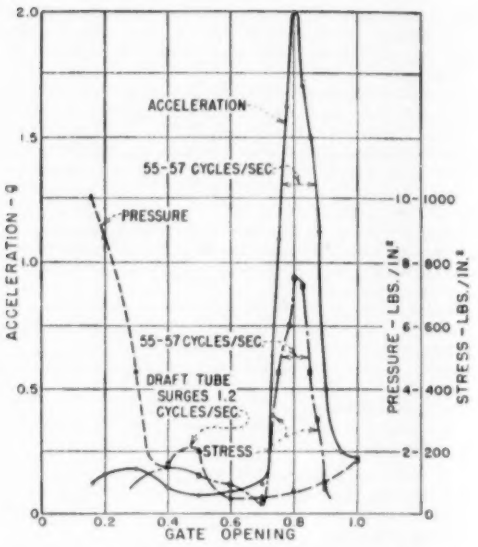

FIG. 18 AMPLITUDE OF DYNAMIC COMPONENT OF INSTRUMENTS RECORDS BEFORE MODIFICATION—BLADE 2

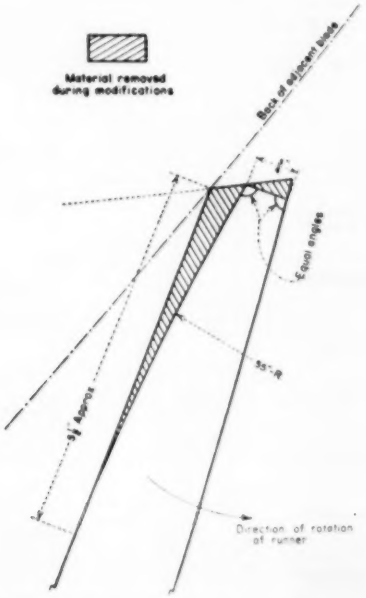

FIG. 19 CROSS SECTION OF TRAILING EDGE AND MODIFICATION OF TURBINE BLADE

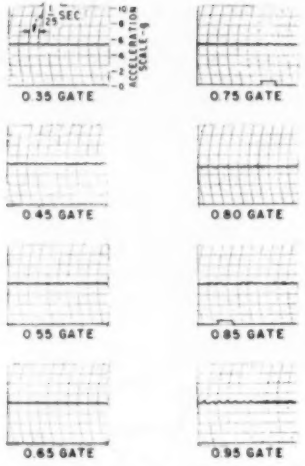

FIG. 20 TRANSVERSE ACCELERATIONS UNIT NO. 1—BLADE NO. 2 AFTER MODIFICATIONS

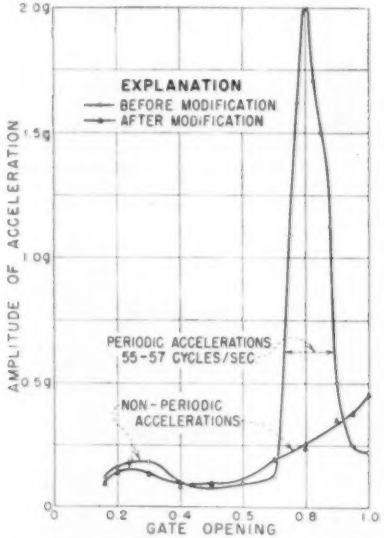

FIG. 21 TRANSVERSE ACCELERATIONS OF BLADE 2 BEFORE AND AFTER MODIFICATION

of all four runners in May indicated that no further cracking of the runner blades had occurred during the 5-month period and that there was a negligible increase in the cavitation of the blading.

EFFECT OF TAIL-WATER SURFACE ELEVATION ON TURBINE VIBRATION

At Parker Power Plant the tail-water elevation is relatively constant and is about 3 to 5 ft below the horizontal center line of

the unit. Subsequent tests at Keswick Power Plant with a comparable turbine unit indicate that the periodic vibration of the turbine blades appears to vary with the tailwater elevation. At this plant severe periodic turbine vibration was measured when the tail-water elevation was about 3 ft below the horizontal center line of the unit, but this vibration was reduced to about one fourth of its previous values when the tail-water elevation was 10 ft lower.

ACKNOWLEDGMENTS

The authors wish to acknowledge the assistance of I. A. Winter, Head of the Hydraulic Machinery Division, under whose direction these tests were conducted, and to G. C. Rouse and F. W. Taylor who assisted in the preparation of the instruments and in the field testing.

BIBLIOGRAPHY

1 "Measurement of Vibration in a Large Slow-Speed Hydraulic Turbine," by J. Parmakian and R. S. Jacobson, a paper presented at the ASME meeting in Kansas City, April 17, 1951.

2 "Mechanical Vibrations," by J. P. Den Hartog, McGraw-Hill Book Company, third edition, 1947.

Discussion

F. E. JASKI.[3] The writer has had experience with several cases of runner-blade vibration both with Francis runners as well as with propeller runners which were corrected in a similar manner and which may be of interest. The first of these was at Norris Dam, Tennessee Valley Authority. The two runners had the discharge edge of the blades sharpened rather abruptly on the back side about 5 to 6 in. from the edge and rounded on the edge to about a $^{3}/_{8}$-in. radius. When first put in operation they developed a singing note which was quite loud. The noise was traced to the runner, and the first step was to put temporary wooden wedges between the blades at the spoon of the blade on the trailing edge. This quieted the runner and indicated that the noise was caused by blade vibration. (This work was done by the late Mr. R. V. Terry who was then Hydraulic Engineer for the Newport News Shipbuilding and Dry Dock Company.) Permanent steel struts were then placed between all of the blades and welded to them. The struts were streamline shape about $1^{1}/_{2} \times {}^{3}/_{4}$ in. thick and 3 in. wide, long enough to reach from the back of one blade to the face of the next blade. They were located on the mean flow line about midway of the width of the blade. These struts have been very satisfactory and in so far as the writer knows, have not had to be replaced.

Later, this same runner was used at Hiwassee TVA plant under a higher head. For this application the design was changed slightly by making the blades $^{1}/_{2}$ in. thicker at the connection with the crown and tapered to the original thickness at the center line of the guide case. The discharge edge was given a more gradual change in thickness and left square about $^{3}/_{4}$ in. thick.

This modified design also was used when the same runner was installed for the Flathead Development of the Phoenix Utility Company. The specific speed of this runner is about 48.

The next case was with a runner of about 68 specific speed, at the Appalachian Electric Power Company Claytor Dam.

Here the vibration occurred at about 62 per cent gate. In this case the blades were sharpened on the discharge edge by chipping back from the edge on the face to reduce the thickness gradually from about $1\ ^{1}/_{8}$ in. to about $^{11}/_{16}$ in. While the chipping was in progress it was necessary to put the unit on the line because of a flood on the New River, July, 1940. Although only 12 of the 16 blades were chipped, and no grinding had yet been done, the unit ran very smoothly at all gate openings. The work was completed on all the blades after the flood subsided.

The next case was a 5-blade fixed propeller of specific speed about 140, at Drop 4 Powerhouse Imperial Irrigation District, about 1942. This runner had vibration periods at 28, 42, and 63 per cent gate openings. The remedy used here again was to sharpen the discharge edge of the blades from about $1^{1}/_{4}$ to $^{3}/_{4}$ in. from the periphery about $^{2}/_{3}$ of the length of the edge. The chipping was done on the face of the blade and carried up the blade far enough to maintain a gradual taper.

The last instance was at Grand Coulee Dam with the first three runners of specific speed 34 in units L1, L2, and L3. These runners also had a vibration period between 60 and 65 per cent gate opening. Here again the discharge edge was sharpened from about $1^{3}/_{16}$ to $^{11}/_{16}$ in. and all the way from the band to about 15 in. from the crown. The chipping was done on the face of the blade and far enough to obtain a gradual taper. A slight increase in output also was obtained both at Claytor Dam and at Grand Coulee, as expected, because the discharge vents were increased by this chipping.

W. B. RHEINGANS.[4] The use of modern instruments to locate and measure hydraulic-turbine vibration is interesting and instructive.

The writer was faced with a somewhat similar situation in 1930, on two Francis units for the Upper Notch Power Plant, Power Corporation of Canada. Each unit was rated 6500 hp at 48-ft head 125 rpm. There was a distinct loud hum or singing noise in each unit at 65 per cent gate which disappeared at 70 per cent gate, but reappeared again at 75 per cent gate, and disappeared completely at 80 per cent gate. A slight increase of vibration of the unit accompanied the noise. However, no cracks were found in the runner.

Since the modern instruments for measuring vibrations which were used by the author were not available at that time and place, the pitch of the hum was determined by comparing it to the notes of a violin. This indicated that the frequency of the hum at 65 per cent gate was 326 cps and at 75 per cent gate 391 cps. This frequency did not correspond to any combinations of speed, number of wicket gates, or number of runner buckets. As was the case with the turbines described by the author, admission of air to the runner or draft tube had no effect on the hum.

An interesting observation with these units was that when the head on the turbine was lowered the hum and noise shifted to higher gate openings, corresponding to approximately equal discharge for the various heads. This seemed to indicate that the hum was a function of quantity of water or of the water velocity through the runner.

In trying to locate the source of the noise, the turbine was unwatered and various portions were struck with a hammer. It was found that the discharge edge of the runner buckets gave about the same pitch noise (as checked by the violin) as the objectionable hum during operation.

It was then decided to try placing some temporary wooden blocks between all of the runner buckets near the discharge edge. These blocks eliminated all of the noise and hum during operation of the unit and reduced the vibration.

Although no apparent damage was produced by the vibration of the runner buckets, it was felt that it might produce cracks in the buckets at some future time. Therefore permanent streamlined steel struts were installed between the runner buckets about halfway between the runner band and crown. These struts were $1^{1}/_{4}$ in. at their maximum thickness and 6 in. long. Since this

[3] Assistant Chief Engineer, Hydraulic Section, Power Department, Allis-Chalmers Manufacturing Company, Milwaukee, Wis.

[4] Manager, Hydraulics Section, Power Department, Allis-Chalmers Manufacturing Company, Milwaukee, Wis. Mem. ASME.

was a cast-iron runner, the struts were held in place by means of two $^3/_4$-in. patch bolts at each end.

These struts have now been in place for over 20 years. During this time they have shown no tendency to produce cavitation and pitting. The runners themselves also have shown no signs of cracking or other failure. Therefore it can be said that the installation of the struts on these units was a successful solution of the vibration problem.

It is interesting to speculate whether the vibration could also have been stopped by thinning down the discharge edges of the runner buckets similar to what was done on the Parker Dam units.

R. E. B. SHARP.[b] Consider the authors' second type of self-induced vibration resulting from the possibility of the torsional rigidity of the blades being low, causing a torsional vibration of runner with respect to the shaft and runner crown: This design of runner has been used in some 45 separate installations. The majority of such installations comprise plate-steel blades with relative strength to resist bending and torsion decidedly lower than at Parker. This, I think, indicates that the Parker vibrations are not due to this cause.

The first type of self-induced vibration involves in effect the von Kármán vortex trail. This phenomenon exists to some extent in all turbine installations, and undoubtedly in all of the 45 installations involving the Parker runner model. However, at Parker the vibrating tendency set up by the von Kármán trail seems to have been in resonance with the natural frequency of the blades.

As pointed out by the authors, the thinning down of the trailing edges not only eliminated the difficulty but increased the power output in the most effective manner as was indicated by model tests. With the frequency of vibrations, or I think we can say, with the natural frequency of the blades in water well established, how does this check with the probable frequency caused by the von Kármán trails?

Fig. 22(*a*) of this discussion shows the relations determined by

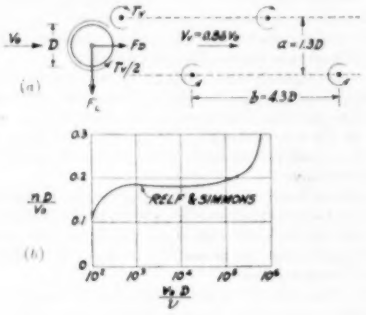

FIG. 22

von Kármán wherein water at a velocity v_0 flows past an immersed cylinder of diameter D. The net result is an oscillating side thrust F_L away from the last vortex. The frequency of oscillation n may be expressed in terms of the Strouhal number nD/v_0 which varies with the Reynolds number as shown.

At Parker Dam the authors determined n to be 55 to 57 cycles per sec (cps) at the critical gate opening of 0.8.

[b] Consultant, S. Morgan Smith Company, York, Pa. Fellow ASME.

It will be noted that the accelerometer, authors' Fig. 14, my Fig. 23, is located almost at the bottom of the runner, at a radius of 56 in. Our object being to determine the average value of v_0 causing this vibration, it seems logical to consider the portion of the blade nearer the crown as being the location of the greatest amplitude of vibration. This was found to be the case in the 20,000 hp turbine at the Holtwood plant of the Pennsylvania Water and Power Company where vibrational stress tests were made. Point A is almost in the curved or "spoon" portion of the blades. Instead of A I have therefore assumed that at B at a radius of 36 in. n would be the same as at A, but with greater amplitude. At a radius of 36 in. the peripheral velocity of the blade for 94.7 rpm is 30 fps.

A Pitot-tube traverse made in the laboratory across the draft tube immediately below this runner model showed, at that proportional radius and at conditions corresponding with 0.8 gate opening and 75-ft head on the prototype, a whirl of about 20 deg

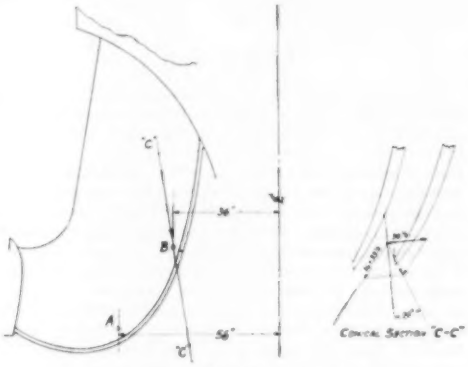

FIG. 23

with the meridian. The resulting velocity relative to the blades is 33 fps as shown in Fig. 23, herewith.

The Reynolds number being based on the cylinder diameter in the von Kármán relation, Fig. 22(*a*), at Parker, it would be based on the blade thickness, and would be for an average blade thickness of 1.25 in.

$$\text{Re} = \frac{1.25 \times 33}{12 \times 10^{-5}} = \frac{1.25 \times 33 \times 100{,}000}{12} = 344{,}000$$

For this value of R the Strouhal number = + 0.205, according to experiments by Relf and Simmons, Fig. 22(*b*), herewith. Then the frequency of the vibrating force, caused by the von Kármán trail, would be equal to

$$\frac{0.205\, v_0}{D} = \frac{0.205 \times 33 \times 12}{1.25} = 65 \text{ cps}$$

as compared with the measured value of 55 to 57 cps.

The radius of 36 in. must be considered as subject to a fairly wide range of probable values and this applies to the foregoing calculated value of 65 cps. Nevertheless, the von Kármán relation seems to apply fairly well, and this I think points up the importance of avoiding excessive thickness at the trailing edges of large Francis runners for comparable requirements. On the basis of the foregoing relation the reduction in the value of D to $^3/_4$ in. as in the authors' Fig. 19, apparently so increased n as to take that

value sufficiently above the natural frequency of the blades as to be harmless.

In several instances blade vibration has been eliminated by the provision of struts between all of the blades. It is my belief that this method would have been successful at Parker had struts been provided between all blades rather than between alternate pairs. The latter method provides insufficient support. For example, at Norris Dam (TVA) struts were entirely successful. This also is the case at the Holtwood Plant of the Pennsylvania Water and Power Company as well as Denison Dam in Texas. In that case some pitting due to cavitation appeared just downstream from the struts, requiring relocation. These struts can be made so small relatively that the effects on efficiency and power are negligible.

At Denison Dam, with the von Kármán trail phenomenon in mind, strips were welded to the discharge edges of the blades from the crown down to some location between *A* and *B*, Fig. 23 of this discussion. These strips had a thickness at the discharge edge of about $^{3}/_{4}$ in. and had the effect of increasing the length of the blades by about 3 in. In this case these extensions actually aggravated the trouble and were removed. The greatest improvement was experienced by what amounted to sharpening the blades at the entrance edges. On the second Denison runner the operating engineers decided to weld a continuous ring to the discharge edges of the blades about at location *B*. This was considerably easier to install than the struts on the first runner, and so far has been effective.

It is hoped that when finally published the paper will contain descriptions of as many as possible of the instances of resonant vibration and their cures, since this seems to be a most appropriate place for all of such valuable information as may be available.

Authors' Closure

The authors wish to thank Messrs. Jaski, Rheingans, and Sharp for their discussions. Mr. Jaski's discussion includes several examples of the successful elimination of blade vibration by sharpening the trailing edges in the manner described in this paper and one instance in which the blade vibration was reduced by the use of struts. Mr. Rheingans' discussion includes an interesting description of the elimination of blade vibration by the use of struts. Mr. Sharp's discussion of the vortex trail phenomena adds to the value of the paper. His description of the use of struts between the blades at other turbine installations is also of interest.

It appears to the authors that wherever possible it is better to eliminate the source of blade vibration than to contain it with struts. The type of blade vibration described in this paper is easily eliminated by avoiding excessive thicknesses at the trailing edges.

Apparently none of the examples of blade vibration indicated in the discussions included actual cracking of the blades as at Parker Power Plant. At this plant the use of struts increased the rate of cracking and had to be removed. Mr. Sharpe believes that the vibration at Parker Power Plant might have been eliminated by the use of struts between all the blades rather than between alternate pairs. This was recently tried out on a comparable unmodified turbine runner at Keswick Power Plant where blade cracking was also present and was not successful with high-tailwater operation.

A possible explanation of the effect of the tail water on the blade vibration is that as the tail water is lowered, the flow conditions near the trailing edge approach the cavitation limit and the vortex trails are broken up.

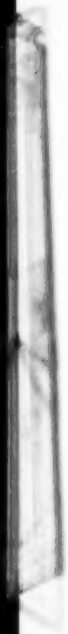

Design of Flat-Wound Tension Springs

By R. M. CONKLIN[1] and D. R. FORRY,[2] COLUMBUS, OHIO

The design of spring-actuated mechanisms often can be improved by the use of a flat-wound spring. Over-center snap-action and similar devices, where it is advantageous to keep the line of action of the spring as close to the bearings as possible, can be made appreciably more compact because of the narrow width of the spring. Equations for the deflection and stress of flat-wound springs are developed. A nomogram, which can be used to solve the stress and deflection equations simultaneously for square and round wire springs, is presented. Experimental results which support the theoretical analysis have been obtained and are discussed in detail.

Nomenclature

The following nomenclature is used in the paper:

- A = area of wire cross section, sq in.
- d = diameter of round wire, or side of square wire, in.
- E = modulus of elasticity of wire material, psi
- I = moment of inertia of wire cross section, in.^{4}
- K = ratio of width of spring to radius of bend, in. per in.
- M = instantaneous moment, in-lb
- M_0 = bending moment on plane a-b, in-lb
- M_1 = instantaneous moment over interval 1, in-lb
- M_2 = instantaneous moment over interval 2, in-lb
- M_3 = instantaneous moment over interval 3, in-lb
- M_M = maximum bending moment, in-lb
- P = total load on spring, lb
- q = distance measured along neutral fiber of spring, in.
- R = mean radius of bend of spring, in.
- R_1 = inner radius of spring, in.
- C = distance to outer fibers from neutral fiber, in.
- s = bending stress, psi
- S = maximum bending stress, psi
- S_t = tension stress, psi
- S_1 = bending stress at inner fiber, psi
- S_{TM} = total maximum stress, psi
- U = total internal energy, in-lb
- W = width of spring, center to center of bend radius, in.
- y = deflection per coil, in.
- Q = total length of neutral fiber in free body under consideration, in.
- α = initial angle of spring bend (constant), radian

Introduction

Anyone associated with the machine-design field at one time or another in his experience has been confronted with the problem of securing sufficient space for a spring of the required properties. It is more or less common practice to postpone until the end of a design problem the detailed computations of the necessary springs. In fact, many designers are guilty of ignoring spring calculations and merely marking the spring location with a note "spring to suit." Many times this procedure has resulted in the unfortunate shopman undertaking to provide a satisfactory spring in a wholly inadequate space. This paper is intended to present a solution to some of these spring problems which has not been thoroughly explored in the past.

Fig. 1 illustrates the physical appearance of flat-wound springs. This type of spring permits its utilization in many places where

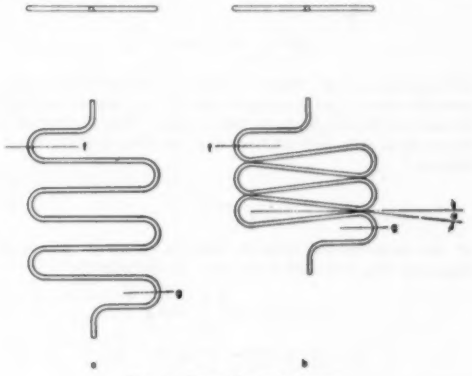

Fig. 1 Flat-Wound Springs

the conventional helical spring would be difficult to apply. In many mechanisms, the narrow cross section of the flat-wound spring will result in a considerably more compact design. In addition, it will permit the line of action of the spring to be located as close as possible to the bearings, thus reducing the cantilever load on the mechanism. This is especially true in certain over-center snap-action devices.

The objective of this paper is to provide the machine or tool designer with easily applied formulas and a nomogram which will quickly and easily permit him to determine the applicability of the flat-wound spring to a design problem.

While a flat-wound spring of the type shown in Fig. 1(a), may be used in compression, it is susceptible to buckling in the plane of the spring. Because of this instability, it is therefore desirable to guide the moving end and to restrain the sides of the spring when used in compression.

Derivation of Deflection Equation

The deflection equation is most easily derived by making use of the Castigliano theorem[3] in conjunction with the strain-energy equation. In order to simplify the problem further, the cross-sectional dimension of the wire perpendicular to the plane about which bending occurs is assumed to be small compared to the radius of curvature R of the spring.

[1] Supervisor, Mechanical Engineering Division, Battelle Memorial Institute. Mem. ASME.

[2] Professional Engineer in Training, Mechanical Engineering Division, Battelle Memorial Institute.

Contributed by the Machine Design Division and presented at the Annual Meeting, Atlantic City, N. J., November 25–30, 1951, of The American Society of Mechanical Engineers.

Note: Statements and opinions advanced in papers are to be understood as individual expressions of their authors and not those of the Society. Manuscript received at ASME Headquarters, August 27, 1951. Paper No. 51—A-59.

[3] "Strength of Materials," by J. E. Boyd and S. B. Folk, McGraw-Hill Book Company, Inc., New York, N. Y., fifth edition, 1950, p. 341, article 169.

The total strain energy of bending contained in the free body of Fig. 2 is expressed by the equation[4]

$$U = \int_0^Q \frac{M^2\,dq}{2EI} \quad \ldots\ldots [1]$$

where the length q is measured along the neutral axis of the free body, and the integration is extended throughout the total length

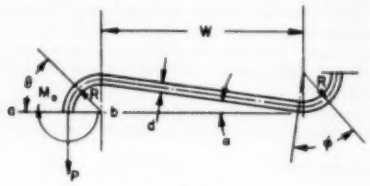

FIG. 2 FREE BODY

of the neutral axis Q. Further, it may be established by inspection that there are no shearing stresses on the plane ab, and that the plane ab does not rotate during bending. Thus the deflection due to M_0 must be zero and, therefore, according to Castigliano's theorem

$$\frac{dU}{dM_0} = 0 \quad \ldots\ldots [2]$$

M, the instantaneous moment, must be expressed by several equations along the length of the wire. In the interval

$$0 \leqslant q \leqslant R\left(\frac{\pi}{2} + \alpha\right)$$

$$M = M_1 = P(R - R\cos\theta) - M_0 \quad \ldots\ldots [3]$$

In the interval

$$R\left(\frac{\pi}{2} + \alpha\right) \leqslant q \leqslant R\left(\frac{\pi}{2} + \alpha\right) + \left(\frac{W - 2R\sin\alpha}{\cos\alpha}\right)$$

$$M = M_2 = P\left\{R + R\sin\alpha + \cos\alpha\left[q - R\left(\frac{\pi}{2} + \alpha\right)\right]\right\} - M_0 \quad \ldots\ldots [4]$$

and in the interval

$$R\left(\frac{\pi}{2} + \alpha\right) + \left(\frac{W - 2R\sin\alpha}{\cos\alpha}\right) \leqslant q \leqslant 2R\left(\frac{\pi}{2} + \alpha\right) + \left(\frac{W - 2R\sin\alpha}{\cos\alpha}\right)$$

$$M = M_3 = P[R + W + R\sin(\phi - \alpha)] - M_0 \quad \ldots\ldots [5]$$

Also

$$\frac{dM_1}{dM_0} = \frac{dM_2}{dM_0} = \frac{dM_3}{dM_0} = -1 \quad \ldots\ldots [6]$$

Substituting the value of U from Equation [1] in Equation [2]

$$\frac{dU}{dM_0} = 0 = \frac{d}{dM_0}\int_0^Q \frac{M^2 dq}{2EI} = \frac{1}{EI}\int_0^Q M\,\frac{dM}{dM_0}\,dq$$

and substituting the expression for M obtained in Equations [3], [4], [5], and [6]

$$0 = \frac{1}{EI}\left[\int_0^{R\left(\frac{\pi}{2}+\alpha\right)} M_1\frac{dM_1}{dM_0}\,dq + \int_{R\left(\frac{\pi}{2}+\alpha\right)}^{R\left(\frac{\pi}{2}+\alpha\right)+\left(\frac{W-2R\sin\alpha}{\cos\alpha}\right)} M_2\frac{dM_2}{dM_0}\,dq + \int_{R\left(\frac{\pi}{2}+\alpha\right)+\left(\frac{W-2R\sin\alpha}{\cos\alpha}\right)}^{2R\left(\frac{\pi}{2}+\alpha\right)+\left(\frac{W-2R\sin\alpha}{\cos\alpha}\right)} M_3\frac{dM_3}{dM_0}\,dq\right]$$

or, using the actual value of M, the following expression is obtained

$$0 = -\left\{\int_0^{R\left(\frac{\pi}{2}+\alpha\right)} [P(R - R\cos\theta) - M_0]\,dq + \int_{R\left(\frac{\pi}{2}+\alpha\right)}^{R\left(\frac{\pi}{2}+\alpha\right)+\left(\frac{W-2R\sin\alpha}{\cos\alpha}\right)} \left\{P\left[R + R\sin\alpha + \cos\alpha\left(q - R\left[\frac{\pi}{2} + \alpha\right]\right)\right] - M_0\right\} dq + \int_{R\left(\frac{\pi}{2}+\alpha\right)+\left(\frac{W-2R\sin\alpha}{\cos\alpha}\right)}^{2R\left(\frac{\pi}{2}+\alpha\right)+\left(\frac{W-2R\sin\alpha}{\cos\alpha}\right)} \{P[R + W + R\sin(\phi - \alpha)] - M_0\}\,dq\right\}$$

In order to simplify the integration, it will be necessary to change the integrator and the limits of integration of the first and third terms, as follows:

In the interval

$$0 \leqslant q \leqslant R\left(\frac{\pi}{2} + \alpha\right), \quad dq = Rd\theta,$$

and in the interval

$$R\left(\frac{\pi}{2} + \alpha\right) + \left(\frac{W - 2R\sin\alpha}{\cos\alpha}\right) \leqslant q \leqslant 2R\left(\frac{\pi}{2} + \alpha\right) + \left(\frac{W - 2R\sin\alpha}{\cos\alpha}\right), \quad dq = Rd\phi$$

and now

$$0 = -\left[\int_0^{\left(\frac{\pi}{2}+\alpha\right)} [PR(R - R\cos\theta) - M_0R]\,d\theta + \int_{R\left(\frac{\pi}{2}+\alpha\right)}^{R\left(\frac{\pi}{2}+\alpha\right)+\left(\frac{W-2R\sin\alpha}{\cos\alpha}\right)} \left\{P\left[R + R\sin\alpha + \cos\alpha\left(q - R\left[\frac{\pi}{2} + \alpha\right]\right)\right] - M_0\right\} dq + \int_0^{\frac{\pi}{2}+\alpha} \{PR[R + W + R\sin(\phi - \alpha)] - M_0R\}\,d\phi\right]$$

[4] "Strength of Materials," equation 163.4, p. 334. See footnote 3.

Performing the integration and solving for M_0

$$M_0 = P\left(R + \frac{W}{2}\right) \quad [7]$$

Substituting the value of M_0 in Equations [3], [4], and [5]

$$M_1 = -P\left(\frac{W}{2} + R\cos\theta\right) \quad [8]$$

$$M_2 = -P\left[\frac{W}{2} + R\left(\frac{\pi}{2} + \alpha\right)\cos\alpha - R\sin\alpha - q\cos\alpha\right] \quad [9]$$

$$M_3 = P\left[\frac{W}{2} + R\sin(\phi - \alpha)\right] \quad [10]$$

$$\frac{dM_1}{dP} = -\left(\frac{W}{2} + R\cos\theta\right) \quad [11]$$

$$\frac{dM_2}{dP} = -\left[\frac{W}{2} + R\left(\frac{\pi}{2} + \alpha\right)\cos\alpha - R\sin\alpha - q\cos\alpha\right] \quad [12]$$

$$\frac{dM_3}{dP} = \left[\frac{W}{2} + R\sin(\phi - \alpha)\right] \quad [13]$$

The Castigliano theorem expresses the deflection of the point of application of a load P, in the direction of P, as

$$y = \frac{\partial U}{\partial P} \quad [14]$$

Substituting the actual value of M in Equations [1] and [14]

$$y = \frac{d}{dP}\int_0^Q \frac{M^2\,dq}{2EI} = \frac{1}{EI}\left[\int_0^{R\left(\frac{\pi}{2}+\alpha\right)} M_1\frac{dM_1}{dP}\,dq + \int_{R\left(\frac{\pi}{2}+\alpha\right)}^{R\left(\frac{\pi}{2}+\alpha\right)+\left(\frac{W-2R\sin\alpha}{\cos\alpha}\right)} M_2\frac{dM_2}{dP}\,dq + \int_{R\left(\frac{\pi}{2}+\alpha\right)+\left(\frac{W-2R\sin\alpha}{\cos\alpha}\right)}^{2R\left(\frac{\pi}{2}+\alpha\right)+\left(\frac{W-2R\sin\alpha}{\cos\alpha}\right)} M_3\frac{dM_3}{dP}\,dq\right]$$

Changing the integrator and limits of integration

$$y = \frac{1}{EI}\left[\int_0^{\frac{\pi}{2}+\alpha} RM_1\frac{dM_1}{dP}\,d\theta + \int_{R\left(\frac{\pi}{2}+\alpha\right)}^{R\left(\frac{\pi}{2}+\alpha\right)+\left(\frac{W-2R\sin\alpha}{\cos\alpha}\right)} M_2\frac{dM_2}{dP}\,dq + \int_0^{\frac{\pi}{2}+\alpha} RM_3\frac{dM_3}{dP}\,d\phi\right]$$

Substituting the values of the moments and their derivatives from Equations [8], [9], [10], [11], [12], and [13], and integrating

$$y = \frac{P}{12\,EI}\left[\frac{W^3}{\cos\alpha} + 3W^2R\,(\pi + 2\alpha - 2\tan\alpha) + 12\,WR^2(\sin\alpha\tan\alpha + 2\cos\alpha) + 6R^3\left(\pi + 2\alpha - 2\sin\alpha\cos\alpha - \frac{4}{3}\sin^3\alpha\tan\alpha\right)\right]$$

and letting $K = \frac{W}{R}$

$$y = \frac{PR^3}{12\,EI}\left[\frac{K^3}{\cos\alpha} + 3K^2(\pi + 2\alpha - 2\tan\alpha) + 12K\,(\sin\alpha\tan\alpha + 2\cos\alpha) + 6\left(\pi + 2\alpha - 2\sin\alpha\cos\alpha - \frac{4}{3}\sin^3\alpha\tan\alpha\right)\right] \quad [15]$$

Derivation of Stress Equation

The maximum stress occurs at the point of the maximum moment. Referring to the free body in Fig. 2, it is seen that maximum moment occurs at two places, one where θ is zero, and the other where ϕ is $\frac{\pi}{2} + \alpha$ radians. In both cases the absolute value of the maximum moment is

$$M_M = P\left(R + \frac{W}{2}\right)$$

Now

$$s = \frac{Mc}{I} \quad \text{and} \quad S = \frac{M_M c}{I}$$

Substituting the value of M_M

$$S = \frac{P\left(R + \frac{W}{2}\right)\frac{d}{2}}{I}$$

Again, letting $W/R = K$

$$S = \frac{PR\left(1 + \frac{K}{2}\right)d}{2\,I} \text{ (tension or compression)}$$

Owing to the curvature of the spring, the neutral axis of the section is caused to shift toward the center of curvature. This results in higher tension stresses at the inner surface, and lower compression stresses at the outer surface. The change is inversely proportional to the ratio of the mean radius of curvature to the depth of section R/d. The change in stresses is also determined by the shape of the wire cross section. For round wire, the stress at the inner (tension) surface is approximated by the formula[5]

$$S_i = S\left(1 + 0.3\,\frac{d}{R_i}\right)$$

where $R_i = R - (d/2)$; therefore

$$S_i = \left[\frac{PR\left(1 + \frac{K}{2}\right)d}{2\,I}\right]\left[1 + \frac{1}{\frac{10}{3}\frac{R}{d} - \frac{5}{3}}\right] \quad [16]$$

For square or rectangular wire, the tensile stress at the inner surface is approximated by the formula[6]

$$S_i = S\left(1 + 0.25\,\frac{h}{R_i}\right)$$

where $h = d$ and $R_i = R - (d/2)$; therefore

[5] "Strength of Materials," equation 185.15, p. 375. See footnote 3.
[6] Ibid., equation 181.4, p. 367.

$$S_b = \left[\frac{PR\left(1 + \frac{K}{2}\right)d}{2I}\right]\left[1 + \frac{1}{4\frac{R}{d} - 2}\right] \quad \ldots\ldots [17]$$

To the maximum tension stress resulting from bending, a straight tension stress, S_t, must be added

$$S_t = \frac{P}{A}$$

The total maximum stress S_{TM}, which occurs on the inside surface of the bend, where $\theta = 0$, is expressed by

$$S_{TM} = S_b + S_t = P\left\{\left[\frac{R\left(1 + \frac{K}{2}\right)d}{2I}\right]\left[1 + \frac{1}{10\frac{R}{d} - 5}\right] + \frac{1}{A}\right\} \quad \ldots\ldots [18]$$

for round wire, and

$$S_{TM} = P\left\{\left[\frac{R\left(1 + \frac{K}{2}\right)d}{2I}\right]\left[1 + \frac{1}{4\frac{R}{d} - 2}\right] + \frac{1}{A}\right\} \quad \ldots [19]$$

for square wire.

To construct an effective nomogram for the solution of the stress and deflection equations of flat-wound springs requires simplification and rearrangement of Equations [15], [18], and [19] in the following manner:

From Equation [15], if $\alpha = 0$, see Fig. 1(*a*)

$$y = \frac{PR^2}{12\,EI}(K^2 + 9.43\,K^2 + 24\,K + 18.85) \quad \ldots\ldots [20]$$

(For values of α less than 20 deg, the error in making this assumption is less than 3 per cent.) Representing the bracketed quantity by the term $f(K) \times 12$

$$y = PR^2 \times f(K) \div EI \quad \ldots\ldots [21]$$

Now, assuming $R = 2d$

$$y = 8Pd^2 \times f(K) \div EI \quad \ldots\ldots [22]$$

Since $I = \pi d^4/64$ for round wire, and E is 30,000,000 for steel

$$y = \frac{P}{d} \times \frac{1}{184,078} f(K) \quad \ldots\ldots [23]$$

From Equation [18]

$$S_{TM} = P\left\{\left[\frac{R\left(1 + \frac{K}{2}\right)d}{2I}\right]\left[1 + \frac{1}{10\frac{R}{d} - 5}\right] + \frac{1}{A}\right\}$$

Again, assuming $R = 2d$, and letting $I = \pi d^4/64$, and $A = \pi d^2/4$, and $E = 30,000,000$ for steel, then

$$S_{TM} = P\left(\frac{25.720 + 12.223\,K}{d^2}\right)$$

from which

$$d = \sqrt{\frac{P}{S_{TM}}}\sqrt{25.720 + 12.223\,K} \quad \ldots\ldots [24]$$

Since the right-hand term is a function of K and the ratio R/d, the quantity $\sqrt{25.720 + 12.223\,K}$ may be replaced by $f(K, R/d)$. Then

$$d = \sqrt{\frac{P}{S_{TM}}} \times f\left(K, \frac{R}{d}\right) \quad \ldots\ldots [25]$$

Substituting the value of d from Equation [25] in Equation [23]

$$y = \frac{P}{\sqrt{\frac{P}{S_{TM}}}} \frac{1}{184,078} \times \frac{f(K)}{f\left(K, \frac{R}{d}\right)}$$

or

$$\frac{y \times 184,078}{\sqrt{PS_{TM}}} = \frac{f(K)}{f\left(K, \frac{R}{d}\right)} \quad \ldots\ldots [26]$$

Since $R = 2d$

$$\frac{y \times 184,078}{\sqrt{PS_{TM}}} = \frac{f(K)}{f\left(K, \frac{R}{d}\right)} = \frac{K^2 + 9.43\,K^2 + 24\,K + 18.85}{12\sqrt{25.720 + 12.223\,K}} \quad \ldots\ldots [27]$$

Equations [25] and [26] are of the general form used for construction of the nomogram. From Equation [26] the function of K (and, therefore, K), may be determined by assuming a value of R/d, $P \times S_{TM}$, and y. Knowing K, R/d, and P/S_{TM}, the deflection per coil may then be found. Equations [24] and [27] are the specific solutions of Equations [25] and [26] when $R/d = 2$.

Equations for use with square wire are developed in a similar manner, and are used to determine the values shown for square wire in the nomogram.

The nomogram is shown in Fig. 3.

Use of Nomogram[7]

To find the diameter d, of wire required for a flat-wound spring, having y inches deflection per coil, with an allowable stress S_{TM}, under a load of p pounds, use the following procedure:

On the $P \times S_{TM}$ scale, locate the value of $P \times S_{TM}$ (e.g., $P = 20$ lb, and $S_{TM} = 50,000$ psi, then $P \times S_{TM} = 1,000,000$). On the y-scale, locate the required value of the deflection per coil in inches (e.g., $y = 0.01$ in.). Connecting these two points with a straight line, locate the intersection of this line and the Q-scale. From this intersection, project horizontally to intercept one of the curves of the upper group. The choice of this curve will depend upon the ratio of the bend radius to the diameter of wire which is assumed and whether square or round wire is to be used (e.g., if round wire with $R = 2d$ is selected, use curve 6). At this point, the W/R ratio may be read on the horizontal W/R scale (e.g., $W/R = 2.7$). From the point of intersection on the upper curve, project vertically to a lower curve having the same letter and the subscript A (e.g., curve 6A). From this point, project horizontally until once again at the Q-scale. Now, locate the computed value of P/S_{TM} (e.g., $P/S_{TM} = 4 \times 10^{-4}$) and connect this point and the last intersection on the Q-scale with a straight line.

The intersection of this line and the d-scale gives the required

[7] This example is constructed on the nomogram, the procedure being consecutively numbered 1 through 8.

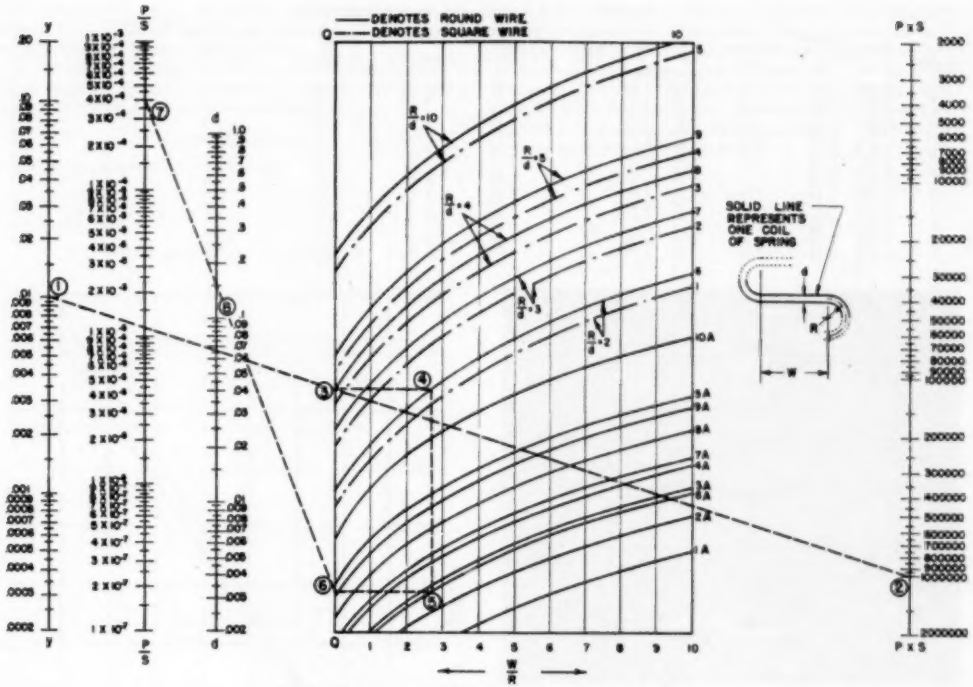

FIG. 3 NOMOGRAM FOR DETERMINING FLAT-WOUND SPRING

value of d (e.g., $d = 0.15$ in.). In the case of square wire, d = distance across flats.

Any of the scales of the nomogram may be expanded in the following manner: The $P \times S_{TM}$ scale may be multiplied (or divided) by 100 if, at the same time, the y-scale is multiplied (or divided) by 10. Similarly, the P/S_{TM} scale may be multiplied (or divided) by 100 if the d-scale is multiplied (or divided) by 10. Note that while the $P \times S_{TM}$ and y-scales must be expanded simultaneously, and the P/S_{TM} and d-scales must be expanded simultaneously, it is not necessary to expand all four scales at once.

The nomogram is constructed for steel ($E = 30{,}000{,}000$); however, it may be modified for other materials by dividing the values on the y-scale by the modulus of elasticity of the material, and multiplying by 30,000,000.

Example 1: Suppose $P = 40$ lb and $S_{TM} = 100{,}000$ psi ($P \times S_{TM} = 4{,}000{,}000$), and $y = 0.06$ in. Expand the $P \times S_{TM}$ scale by multiplying by 100, at the same time expanding the y-scale by multiplying by 10. It is not necessary to expand the P/S_{TM} and d-scales.

Example 2: Suppose $P = 0.001$ lb and $S_{TM} = 200{,}000$ psi ($P/S_{TM} = 5 \times 10^{-9}$). Expand the P/S_{TM} scale by dividing by 100 and, at the same time, divide the d-scale by 10. Note that the $P \times S_{TM}$ and y-scales need not be changed.

Example 3: Suppose $P = 500$ lb and $S_{TM} = 200{,}000$ psi ($P \times S_{TM} = 100{,}000{,}000$; and $P/S_{TM} = 2.5 \times 10^{-3}$), $y = 0.9$ in., and $R = 5d$. Expand the $P \times S_{TM}$ scale by multiplying by 100, and the y-scale by multiplying by 10. Locate 0.9 on the expanded y-scale and 100,000,000 on the expanded $P \times S_{TM}$ scale. Also, it is necessary to expand the P/S_{TM} scale by multiplying by 100, at the same time multiplying the d-scale by 10. Now, locating 2.5×10^{-3} on the P/S_{TM} scale and using the foregoing method of solution, it is found that $W/R = 2.1$ and that $d = 0.55$ in. on the expanded d-scale. In this particular example, it was found necessary to expand all four scales.

Note that when interpolating for values of R/d, other than those given on the nomogram, interpolate between successively numbered curves for the particular cross section in question (round or square). This applies to both the upper and lower sets of curves on the nomogram.

EXPERIMENTAL RESULTS

The derived formulas indicate that flat-wound springs have a constant spring rate, and the experimental results confirm this condition. Since K changes slightly during the deflection of the spring, there is theoretically a slight variation in spring rate which may be neglected in the majority of applications, it being less than the experimental error.

The deflection equation was verified by measuring the deflections of a number of flat-wound springs of varying wire sizes and dimensions. Table 1 gives the physical dimensions of these springs, their observed spring rate in pounds per inch, the calculated spring rate, the spring rate obtained by use of the nomogram, and the percentage error in each case. All of the springs tested were made from oil-tempered spring wire.

Fig. 4 shows a photoelastic model which was used to determine the stress distribution in the spring. The model was made of photoelastic plastic having the following dimensions: Depth of

TABLE 1 FLAT-WOUND SPRING DEFLECTIONS

Spring	Diam., in.	R-mean radius, in.	W-width, in.	$\frac{W}{R}$ ratio	$\frac{R}{d}$ ratio	No. active coils	Spring rate, lb per in. Observed	Computed	By nomogram	Error, per cent: Computed versus observed	Nomogram versus observed	Angle alpha deg
1	0.064	0.28	0.50	1.78	4.40	9	16.62	15.32	15.00	−7.8	−9.7	0.0
2	0.064	0.28	1.00	3.56	4.40	9	5.71	5.59	5.42	−2.1	−5.1	0.0
3	0.064	0.28	1.50	5.33	4.40	9	2.70	2.61	2.72	−3.3	+0.8	0.0
4	0.064	0.28	2.00	7.12	4.40	9	1.52	1.45	1.36	−4.6	−10.5	0.0
5	0.055	0.56	3.00	5.33	10.10	11	0.13	0.14	0.14	+7.7	+7.7	0.0
6	0.055	0.56	3.00	5.33	10.10	11	0.13	0.14	0.14	+7.7	+7.7	0.0
7	0.055	0.56	2.00	3.56	10.10	11	0.28	0.30	0.29	+7.1	+3.6	0.0
8	0.055	0.56	2.00	3.56	10.10	11	0.28	0.30	0.29	+7.1	+3.6	0.0
9	0.125	0.56	3.00	5.33	4.45	11	3.92	3.89	4.21	−0.8	+7.6	0.0
10	0.125	0.56	3.00	5.33	4.45	11	4.22	3.89	4.21	+7.8	−0.2	0.0
11	0.125	0.56	2.00	3.56	4.45	11	7.50	8.24	8.05	+9.9	+7.3	9.0
12	0.125	0.56	2.00	3.56	4.45	11	7.56	8.24	8.05	+8.9	+6.4	0.0
13	0.063	0.28	2.00	7.12	4.40	10	1.17	1.22	1.23	+4.3	+5.1	8.0
14	0.063	0.28	1.50	5.33	4.40	11	1.80	2.00	2.12	+5.8	+12.1	9.5
15	0.063	0.28	1.00	3.56	4.40	11	5.00	4.56	4.46	−8.8	−10.8	15.0
									Avg	6.3	6.5	

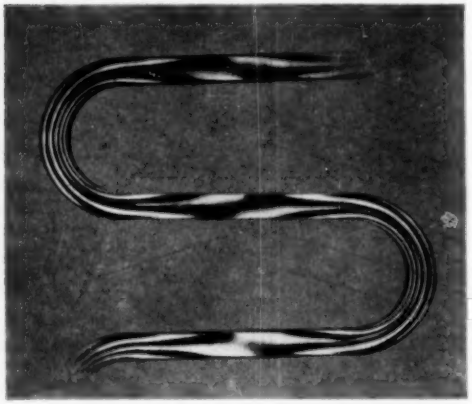

FIG. 4 PHOTOELASTIC MODEL SHOWING STRESS DISTRIBUTION IN A FLAT-WOUND SPRING

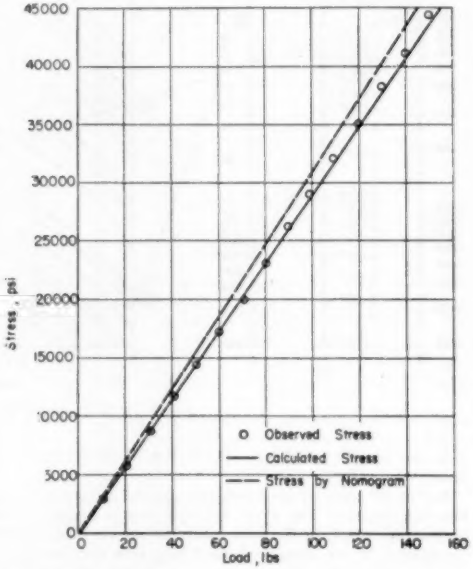

FIG. 5 STRESS AS FUNCTION OF LOAD ON A FLAT-WOUND SPRING

section, 0.500 in.; width of section, 0.500 in.; W/R ratio, 3.2; R/d ratio, 2.5; and R, 1.25 in. A 5-lb load on the model produced a deflection of 0.345 in. with the stress pattern shown in Fig. 4. The illustration shows a greater line density and, therefore, a higher stress level near the inner radius of the bend than at the outer radius. This is the result of two factors. One is the shift in the neutral axis due to the curved-beam effect. The other is the straight tension stress, which adds to the bending stress on the inner surface, and subtracts from the bending stress on the outside surface.

In order to determine the validity of the stress equations, a large flat-wound spring of rectangular cross section was made from hot-rolled steel having the following dimensions: Depth of section, 0.500 in.; width of section, 0.555 in.; W/R ratio, 6; R/d ratio, 3; and R, 1.5 in. On the spring were mounted three Baldwin type A-8 SR-4 strain gages which were used to measure stresses produced by various loads. The graph in Fig. 5 shows the observed stress, and the calculated stress at three points along the bend of the spring where maximum stress occurs. Due to the shift in neutral axis, these stresses are 10 per cent higher than those calculated without the correction factor of

$$1 + \frac{1}{4\frac{R}{d} - 2}$$

It was found that for most flat-wound spring applications the spring ends could be considered inactive for purposes of calculation without serious error. Thus, for all practical purposes, the number of coils may be determined by counting the number of full free bodies between the points marked F and g in Fig. 1. Where necessary, the formulas presented in the paper may be used to calculate the deflection and maximum stress in the spring ends. For ends, as shown in Fig. 1, the maximum stress will always occur in the spring proper rather than the ends.

CONCLUSIONS

1 The flat-wound spring has, for all practical purposes, a constant spring rate and, therefore, can be used in much the same way as a helical spring.

2 The list of formulas derived in this paper may be used to solve mathematically the stress and deflection values for flat-wound springs.

3 Fig. 3 illustrates a nomogram by which flat-wound spring characteristics can be determined easily.

4 The formulas and nomogram have been checked experimentally and found to be correct within 6 per cent.

5 The value of alpha, the original angle of spring bend, has little effect on deflection, and the use of the simplified expression for deflection may be used with small error.

6 Consideration of the use of flat-wound springs should be given where spring space limitations are severe or where spring forces result in excessive cantilever loads on bearings.

List of Formulas

Actual equation for deflection per coil

$$y = \frac{PR^3}{12\,EI}\left[\frac{K^3}{\cos\alpha} + 3K^2(\pi + 2\alpha - 2\tan\alpha) + 12K(\sin\alpha\tan\alpha + 2\cos\alpha) + 6\left(\pi + 2\alpha - 2\sin\alpha\cos\alpha - \frac{4}{3}\sin^2\alpha\tan\alpha\right)\right]$$

Simplified equation for deflection per coil, assuming $\alpha = 0$

$$y = \frac{PR^3}{12\,EI}(K^3 + 9.43\,K^2 + 24\,K + 18.85)$$

Actual equation for maximum stress in round wire

$$S_{TM} = P\left\{\left[\frac{R\left(1 + \frac{K}{2}\right)d}{2\,I}\right]\left[1 + \frac{1}{\frac{10}{3}\frac{R}{d} - \frac{5}{3}}\right] + \frac{1}{A}\right\}$$

or

$$S_{TM} = P\left[\frac{\left(10.19\frac{R}{d} + 5.09\,K\frac{R}{d}\right)\left(1 + \frac{1}{\frac{10}{3}\frac{R}{d} - \frac{5}{3}}\right) + 1.28}{d^3}\right]$$

Actual equation for maximum stress in square wire

$$S_{TM} = P\left\{\left[\frac{R\left(1 + \frac{K}{2}\right)d}{2\,I}\right]\left[1 + \frac{1}{4\frac{R}{d} - 2}\right] + \frac{1}{A}\right\}$$

or

$$S_{TM} = P\left[\frac{\left(6\frac{R}{d} + 3\,K\frac{R}{d}\right)\left(1 + \frac{1}{4\frac{R}{d} - 2}\right) + 1}{d^3}\right]$$

Discussion

J. E. Brock.[5] The authors have made an interesting contribution, especially in presenting their nomographic solution which should prove of value to those who have frequent occasion to design springs of this nature.

While the authors have nowhere explicitly described the precise nature of the loading to which their calculations refer, it is easily inferred that the coils are to be considered subjected to equal, opposite, and collinear forces applied at the ends of the coils. It may be of interest to consider the relation between more general force systems applied to coils of this nature and the deflections they produce. In the following, subscripts 1, 2, 3 refer to "forces" or "translations" in the positive x, y, z-directions, respectively, while subscripts 4, 5, 6 refer to "moments" or "rotations" about the x, y, z-directions, respectively, the positive sense being given by the right-hand rule. We consider only the case where the authors' angle α is zero. Let the coil be fixed at one end, as shown in the accompanying Fig. 6, and otherwise free. Let the x-direction be from free end to fixed end as shown, the y-direction in the direction of the first return bend counting from the free end, and the z-direction so as to form a right-handed triad. (In Fig. 6 the z-axis is directed toward the reader.)

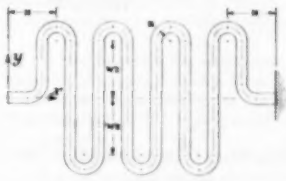

Fig. 6

We define influence coefficients as follows:

C_{ij} = i-deflection due to application of a *unit* j-force ($i, j = 1, \ldots, 6$)

Here, of course, "deflection" means translation or rotation and "force" means force or moment. Forces are applied and deflections are measured at the free end.

It is not difficult to calculate the values of C_{ij} presented in Table 2 of this discussion. The nomenclature is as follows:

EI = flexural rigidity of straight bar
m = Poisson's ratio
N = number of return bends (180-deg bends) in coil
p = $(-1)^N$
K = W/R
h = H/R
k = flexibility factor, unity for solid cross section and = $(u + 10)/(u + 1)$ for hollow circular cross section
u = $192t^2R^2/(D - t)^4$
t = wall thickness of circular tube
D = outside diameter of circular tube

Only the customary assumptions are involved (small deflections, D small compared to R, direct axial and cross shearing deformations neglected, etc.). These assumptions are implicit in the paper. (The correction for increased flexibility for "in-plane" bending of hollow circular sections follows the old and well-known von Kármán-Hovgaard analysis although it would be easy to make use of the analyses of Beskin or Vigness; the results exhibited in the tabulation, of course, would be altered.)

Cofficient C_{11} of Table 2 is comparable to the authors' Equation [15] if in the latter we take $\alpha = 0$ and multiply by N to account for the total number of "loops." A comparison indicates that the authors' formula should be multiplied by the factor

$$M = 1 + F/N$$

where

$$F = (K^3 + 18\pi - 48)/(K^3 + 3K^2\pi + 24K + 6\pi)$$

to account for end effects. Values of F are shown in the accompanying Fig. 7 for various values of K. (F approaches unity as K becomes large.) As might be expected, the correction is small if N is large. However, for a small number of loops, the correction may become significant. It is interesting to note also the effect of an odd or even value of N on the value of C_{15}, C_{24}, and C_{33}. One also should observe that N, the number of return

[5] Director of Research, The Midwest Piping and Supply Company, Inc., St. Louis, Mo. Mem. ASME.

TABLE 2

$$
\begin{aligned}
12EIC_{11}/R^3 &= 3k(2\pi N + 6\pi - 16 + \pi K^2 N + 8KN) \\
&\quad + (N+1)K^2 \\
8EIC_{12}/R^2 &= 2k(\pi K + 4)[2pN - (h-1)(1-p)] \\
&\quad + 8k(h-3) - 8pk(h + 2N + 1) \\
&\quad - (K^2 - 4)[h - 1 - p(h - 1 + 2N)] \\
&\quad - 4\pi k[h - 2 - p(h + 2N)] \\
8EIC_{14}/R^2 &= (1-p)(2\pi kK + K^2 + 4\pi k - 4) \\
12EIC_{22}/R^2 &= 5(h-2)^2 + 4(k\pi N + KN - K) \\
&\quad [3h^2 + 6h(N-1) + 2(N-1)(2N-1)] \\
&\quad + 6k\pi[N + 1 + (h-2)^2 + (h + 2N)^2] \\
&\quad + 3(h-2)(3h - 2 + 2N)^2 \\
&\quad + 6(K-2)[(h-1)^2 + (h - 1 + 2N)^2] \\
&\quad - 4K(N-1)(2N-1) - 48k(N+1) \\
-EIC_{25}/R^2 &= (h + N - 1)(k\pi N + KN + 2k + \pi k - 6)
\end{aligned}
$$

$$
\begin{aligned}
12EIC_{33}/R^3 &= (1+m)\{4K[6N + (N-1)(3h^2 + 6hN - 6h + 4N^2 - 8N + 3)] - 12(4N + 8 - N\pi - \pi) \\
&\quad + 6(K-2)[(h-1)^2 + (h - 1 + 2N)^2]\} + \pi(1 + m/2)\{6[(h-2)^2 + (h + 2N)^2 + 2] \\
&\quad + 3(N-1)K^2 + 4N[3h^2 + 6h(N-1) + 2(N-1)(2N-1)]\} + 5(h-2)^2 \\
&\quad + 3(h-2)(3h - 2 + 2N)^2 + 24m(N+1) + (K-2)^2 + (N-1)K^2 \\
-8EIC_{34}/R^2 &= (1-p)[(2\pi + K)(2+m) \\
&\quad + 4m(h + 2N) + K^2 - 4] \\
&\quad - 8m(h + N - 1) \\
2EIC_{35}/R^2 &= (h + N - 1)[\pi(N+1)(2+m) \\
&\quad + 2(N + K - 3)(1+m) + 4(h-2)] \\
2EIC_{44}/R &= \pi(N+1)(2+m) + 4(h-2)(1+m) + 2NK \\
&\quad - 4 \\
2EIC_{45}/R &= m(1+p) \\
2EIC_{55}/R &= \pi(N+1)(2+m) + 4h + 2NK - 12 \\
EIC_{66}/R &= k\pi(N+1) + NK + 2h - 6
\end{aligned}
$$

$C_{21} = C_{12}$; $C_{31} = C_{13}$; $C_{32} = C_{23}$; $C_{41} = C_{14}$; $C_{42} = C_{24}$; $C_{43} = C_{34}$; $C_{51} = C_{15}$; $C_{52} = C_{25}$; $C_{53} = C_{35}$; $C_{54} = C_{45}$

All other C_{ij} are zero

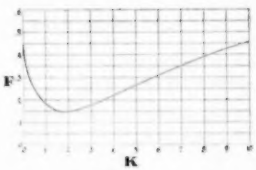

FIG. 7

bends, is one larger than the number of active coils as determined by the rule given by the authors.

A remark is called for concerning the authors' first conclusion. One might reasonably assert a priori that the spring rate for a spring of this nature is essentially constant for "all practical purposes." This "conclusion" is a consequence of the assumptions involved (implicitly or explicitly) in any reasonably simple analysis of such a spring, including the analyses of the authors and of the writer. If more than this is implied, it must be based on experiments which are not reported in sufficient detail to support the conclusion.

The authors' fourth conclusion is puzzling. In the first place, the meaning of the word "correct" in this context is not at all clear. Since experiment involves error and analysis involves approximation, no absolute standard is available by which to gage correctness. Furthermore, the source of the figure of 6 per cent is not evident, since 18 out of 30 values of per cent error listed in the authors' Table 1 have magnitudes greater than 6 per cent. The fact that the per cent error for "nomogram versus observed" does not coincide with that for "computed versus observed" reflects merely slight inaccuracies in constructing and reading the nomogram. The per cent error for computed versus observed is hardly significant. It seems to indicate fairly good experimental technique more than anything else. An error of only 0.001 in. in measuring the diameter of the wire for springs 1 through 8 and 13 through 15 would account for 5 per cent error in the computed result. The writer wonders what the authors were seeking in their experimental program. Since evidently the end effect corrections are negligible, such experiments measure experimental technique rather than anything else.

The authors' fifth conclusion is interesting and important. That the variation due to α is indeed small may be seen from the following form of the authors' Equation [15].

$$
\begin{aligned}
12EIy &= PR^3[K^3(1 + \alpha^2/2 \ldots) + K^2(3\pi - 2\alpha^2 \ldots) \\
&\quad + K(24 + 3\alpha^4 \ldots) + (6\pi - 8\alpha^2/5 \ldots)]
\end{aligned}
$$

S. B. FOLK.[9] While the paper indicates that the springs are to be used in tension there is no reason why compression springs, if properly restrained, cannot be analyzed by the formulas presented.

The writer finds that the analysis used is somewhat long and cumbersome. He has checked the derivation of the deflection for one loop by taking advantage of symmetry and doubling the energy equation for one bend. To this is added the energy in the straight portion with translation of the origin to the junction of the bend with the straight portion. Substitution in Equation [14] of the paper then gives

[9] Professor of Mechanics. The Ohio State University, Columbus, Ohio.

$$y = \frac{1}{EI}\left[2\int RM_1 \frac{dM_1}{dP}\,d\theta + \int M_2 \frac{dM_2}{dP}\,dq\right]$$

where the limits on the first integral are from 0 to $R(\pi/2 + \alpha)$ and on the second, from 0 to $(W - 2R\sin\alpha)/\cos\alpha$. In this solution M_0 is given by Equation [7] which, incidentally, can be obtained directly by statics from the free body; M_1 is given by Equation [8]; and in the foregoing equation

$$M_2 = P(W/2 - R\sin\alpha - q\cos\alpha).$$

Utilizing the approximate formulas (just above and below Equation [16]) for the maximum stresses in the curved portions of the springs, materially shortens the calculations and gives quite accurate results providing the ratio d/R is less than 3 which is certainly true of the cases analyzed. One very interesting observation of the authors is the very small error introduced by neglecting α for values up to 20 deg. This greatly simplifies the calculations.

The writer regrets that the nomograph is not reproduced to a larger scale. While he has not checked the construction of it, he believes the errors reported in Table 1 of the paper may be due to the reduced scales. The photoelastic model provides a check which instills confidence in the work of the investigators.

Authors' Closure

Mr. Brock has presented an interesting discussion, although much of it deals with subjects outside the intended scope of the paper. A significant contribution is the correction factor to account for end effects. The graph of end-correction factor F versus the L/R ratio, K, shows that minimum values of F occur at the most commonly used values of K, i.e., $K = 1/2$ to $K = 4$. For values of K in this range, and for a spring containing four or more coils, the deflection as computed by Equation [15] will vary less than 6 per cent from the deflection computed using Mr. Brock's end-correction factor.

Mr. Brock's trigonometric expansion of Equation [15] clearly shows the validity of conclusion (5). The assumption that the effect of the original spring angle, α, may be neglected, greatly simplifies computation, since the nomogram may then be used.

Professor Folk's use of symmetry in the derivations of the equations for deflection do, of course, simplify these calculations. The use of statics to obtain the expression for M_0, as suggested by Professor Folk, was presented by the authors during the 1951 ASME Annual Meeting session.

As Professor Folk has observed, the accuracy of a nomographic solution depends to a great extent upon the physical scale of the nomogram. It is felt, however, that the nomogram as reproduced in the paper will give adequate accuracy if sufficient care is exercised in constructing a solution. Twice-size copies of the nomogram may be obtained, however, upon request to either of the authors.

It is interesting to note that both Mr. Brock and Professor Folk have been able to confirm the derivation of the deflection equation by somewhat different methods.

The authors would like to take this opportunity to thank Professor Folk and Mr. Brock for their contributions and their interest in the work represented by this paper.

Hysteresis of Shaft Materials in Torsion

By W. P. WELCH[1] and B. CAMETTI[2]

Static determinations of hysteresis of typical shaft materials in torsion show that the values are low for high-quality materials in unidirectional loading after several cycles of loading up to a shear-stress amplitude of 24,000 psi. For reversed loading, the hysteresis becomes several times larger and may be of significance in accurate torque-weighing devices. The measured hysteresis in a tubular specimen had values 3 to 4 times that for a solid specimen. Two nonmagnetic materials displayed very low values of hysteresis. The apparatus developed for this investigation had sensitivity sufficient to measure displacement changes of 0.002 per cent of the full-load deflection, and was designed to eliminate errors due to temperature changes, extraneous loads, and external vibration.

Introduction

The term "elastic hysteresis" is now the well-accepted term describing inelastic effects at stresses below the conventional elastic limit. In the design of torque-weighing devices, an important practical problem is the selection of a shaft material having very low hysteresis and creep. It is for applications of this category that the tests to be described were performed. Inasmuch as the specific developments involved required large-diameter shafts, the hysteresis tests have been limited to those shaft materials that could be supplied in large diameters. Moreover, since solid shafts are usually employed in these applications, the tests were conducted on solid specimens, except that one tubular specimen was included for the purpose of comparison.

Elastic Hysteresis

The inelastic behavior of metals has been the subject of many investigations since the publication in 1865 of Lord Kelvin's paper entitled "On the Elasticity and Viscosity of Metals." The term elastic hysteresis was first applied by Hopkinson and Williams (1912), to the noncoincidence of the loading and unloading phases of a stress-strain diagram.

In a torque-weighing system, whereas hysteresis is a primary cause of error in all cases, "creep" at the ambient temperature may be sufficiently large so as to introduce errors, especially for long-time measurements of torque. Recognizing that some part of hysteresis must also be creep, the two effects are illustrated in an exaggerated manner by the curves in Fig. 1. It should be noted that in this paper the actual width of the nonreversible stress-deflection diagram is employed as the quantity which describes hysteresis. This width may be measured at one or several stress levels, and, in general, in the vicinity of the greatest width of the hysteresis loop.

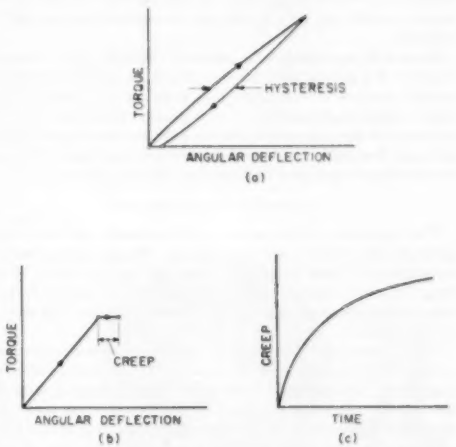

Fig. 1 Load-Deflection Diagrams Illustrating Hysteresis and Creep

(a, Hysteresis; b, creep; c, typical creep-time relationship.)

In 1914 Rowett (1)[3] published the results of static hysteresis tests on thin-walled tubular specimens in torsion, whereas Dorey (1932) made similar static measurements on solid specimens of typical crankshaft steels (2). Other than these limited experiments there appears to be no specific information on the subject of the static hysteresis of shafting materials.

An extensive amount of work has been done in the field of "internal damping" of materials. Almost all of this information has been determined by dynamic methods which evaluated either directly or indirectly the energy loss per cycle of stress or strain. For a comprehensive review of this closely related field, the reader is referred to references (3 and 4) with their accompanying bibliographies.

In the field of spring materials, Sayre has published several papers which include hysteresis data on both steel tensile specimens and helical springs (5, 6, 7). On nonferrous spring materials, especially beryllium-copper, Carson has conducted several investigations (8) and has developed specialized apparatus for testing hysteresis effects in springs. Carson proposed the use of the term "elastic drift" to describe the combined result of hysteresis and creep in spring materials.

As to the magnitude of hysteresis and creep effects in helical-spring materials, Sayre and deForest succeeded in developing a modified elinvar alloy for precision spring scales, to which alloy they gave the name "Iso-elastic" (9). Springs made of this material not only displayed a very small thermoelastic coefficient, but also the hysteresis did not exceed 0.04 per cent of the full-load deflection, and the creep at room temperature was even less, 0.02 per cent, these data being for working stresses up to 60,000 psi.

[1] Transportation Engineering Department, Westinghouse Electric Corporation, East Pittsburgh, Pa. Jun. ASME.

[2] Atomic Power Division, Westinghouse Electric Corporation, Pittsburgh, Pa.

Contributed by the Machine Design Division and presented at the Annual Meeting, Atlantic City, N. J., November 25–30, 1951, of The American Society of Mechanical Engineers.

Note: Statements and opinions advanced in papers are to be understood as individual expressions of their authors and not those of the Society. Manuscript received at ASME Headquarters, August 7, 1951. Paper No. 51—A-64.

[3] Numbers in parentheses refer to the Bibliography at the end of the paper.

The composition of Iso-elastic alloy is 36 per cent nickel, 8 per cent chromium, and the balance iron except for small additions, and the finished material has been given a very high degree of cold work. Because large-diameter shafts could not be supplied in this material, it was not included in the present investigation.

Materials of low hysteresis and creep also have been developed for proving rings used for calibrating materials testing machines. In fact, the ASTM specification for proving rings requires an accuracy of ±0.1 per cent of full load throughout the range 0.2 to full load.

Despite the apparently large amount of data that have been collected in this general field, we were unable to obtain data for the specific problem of evaluating the errors due to hysteresis in a large torque-weighing shaft. Consequently, the apparatus to be described in the next section was designed and constructed, and a series of hysteresis and room-temperature creep tests were conducted on several typical high-strength shafting materials.

Description of Apparatus

The apparatus for conducting static-hysteresis and room-temperature creep tests is shown in Fig. 2. The specimen tested is comparatively large, being 1 in. diam and approximately 26 in. long. A pure torque loading is achieved by means of dead weights, the maximum load giving a shearing stress of 24,000 psi in the specimen.

It was considered necessary to evaluate with engineering accuracy hysteresis effects of the order of 0.1 per cent of full-load deflection. This required a sensitivity of approximately 0.01 per cent in the measuring system. As will be described later, the sensitivity achieved in the design was considerably better than 0.01 per cent, the actual sensitivity being 0.002 per cent of full-load deflection.

Specimen. Fig. 3 is a dimensional sketch of the finished specimen. A finished diameter of 1 in. and an effective length of 26 in. was considered a representative size for the test. The diameter was consistent with initial stress and load requirements, and the free length sufficient for the necessary sensitivity. However, in its final form the cost of machining a number of solid specimens in that shape would have been prohibitive. To overcome this, a method of shrinking the end flanges on the specimen proper was used. Fig. 4 shows the specimen and end flanges prior to the shrinking operation. The finished specimen is shown in Fig. 5. The s-shaped end flange is considered the built-in end of the specimen whereas the conventional flange at the opposite end is the free or rotating end.

Since the apparatus would not distinguish between joint slippage and hysteresis, a preliminary investigation of shrink-fit assemblies was made. The tests were patterned around information obtained from a similar investigation by R. Russell in Eng-

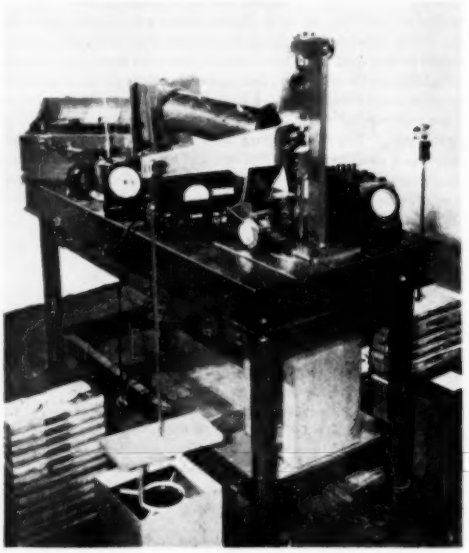

Fig. 2 General View of Apparatus

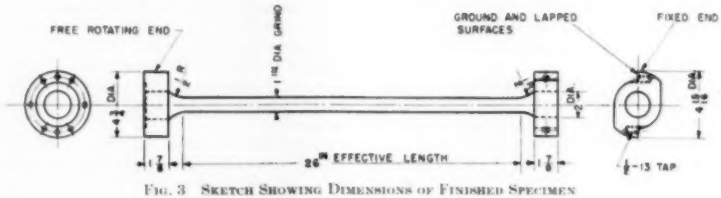

Fig. 3 Sketch Showing Dimensions of Finished Specimen

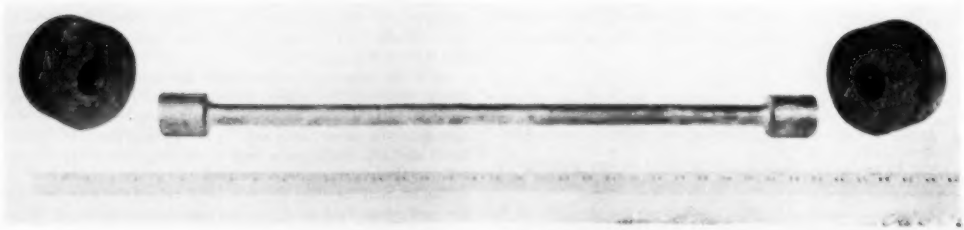

Fig. 4 Specimen Prior to Shrinking Operation

FIG. 5 FINISHED SPECIMEN

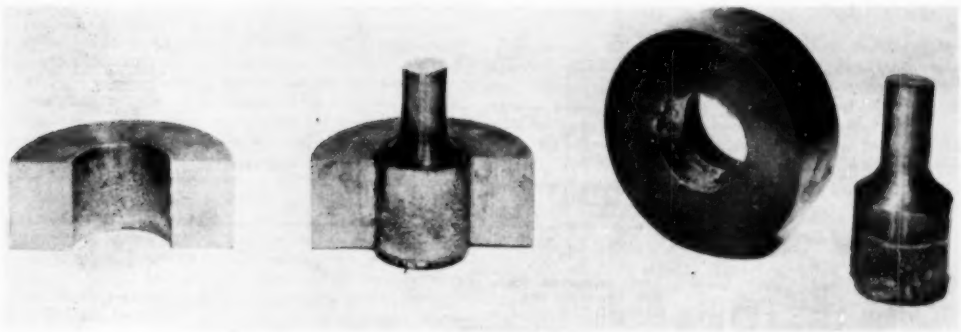

(a) (b)

FIG. 6 SHRINK-FIT TEST PIECES

land (10). Fig. 6 (*a*) and (*b*) shows the results of some of these tests. An interference of 0.006 in. on a 2-in-diam shaft was used, with a resulting tensile stress of 90,000 psi in the flange bore. The pieces were carefully ground to size and thoroughly cleaned and rinsed three times using hot water and soap. The flange was heated to 800 F and the shaft was kept at room temperature. The specimen shown in Fig. 6(*b*) had entered the flange two thirds of the way and froze in this position. An axial load of 187,000 lb was required to press the shaft back out, this corresponding to a computed coefficient of friction of 0.76. Specimen shown in Fig. 6(*a*), required 650,000 lb to cause initial slippage of $^1/_{16}$ in. Seizure occurred after this and it was impossible to produce further slippage. As a final check a specimen with integral flanges was machined and then tested for hysteresis. These results were compared with those from tests on a similar specimen with shrink-on flanges. No appreciable difference in the behavior of the two specimens could be detected. These tests are described later.

Measuring Device. Referring to Figs. 7 and 8, the measuring system comprises two stationary micrometer screws mounted to a rigid reference column. The screws engage insulated contacts which are mounted on the rotating measuring arm. The arms are securely bolted to the free rotating end of the specimen. The contacts are mounted 10 in. from the center of the specimen twisting axis. A connection from the high side of a 1000-megohm d-c amplifier is made to the contacts in series with a $1^1/_2$-volt dry-cell battery. The grounded input terminal of the amplifier is connected to the micrometer screws. Contact closure is indicated by an upward deflection of the horizontal sweep line on a cathode-ray oscilloscope connected in the circuit. The high input impedance of the d-c amplifier eliminates contact pitting because the interrupted current is very minute. A positive deflection of the oscilloscope trace represents a motion of 0.00002 in. of the micrometer screws. The full-load deflection, measured by the micrometer screws, is approximately 1 in.—thus the sensitivity of the measuring apparatus is 0.002 per cent of the full-load deflection. This corresponds to a change in stress of 0.56 psi on the specimen.

This sensitivity could not be realized without suitable damping devices to absorb the transient and steady-state vibrations of the apparatus. To minimize the steady-state vibrations, the apparatus was erected on the ground floor far removed from any rotating apparatus. Special large vane-type oil-filled dampers were used to damp out the transient vibrations induced in the system during the loading cycles. The effectiveness of these dampers enabled one to take readings 5 sec after a load change had been made.

The measuring system was checked for errors resulting from temperature changes by subjecting the entire apparatus to a 20 F temperature rise. The errors were found to be of negligible magnitude.

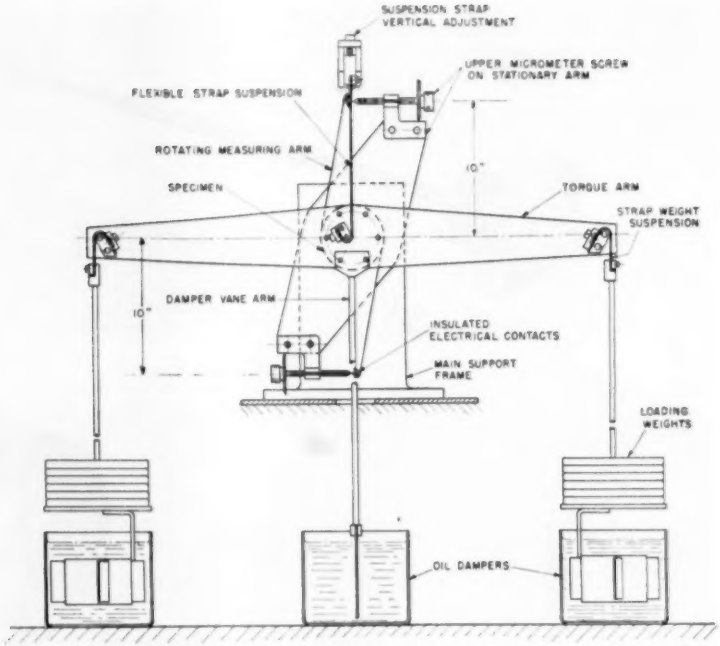

FIG. 7 SCHEMATIC SKETCH OF APPARATUS SHOWING FRONT ELEVATION

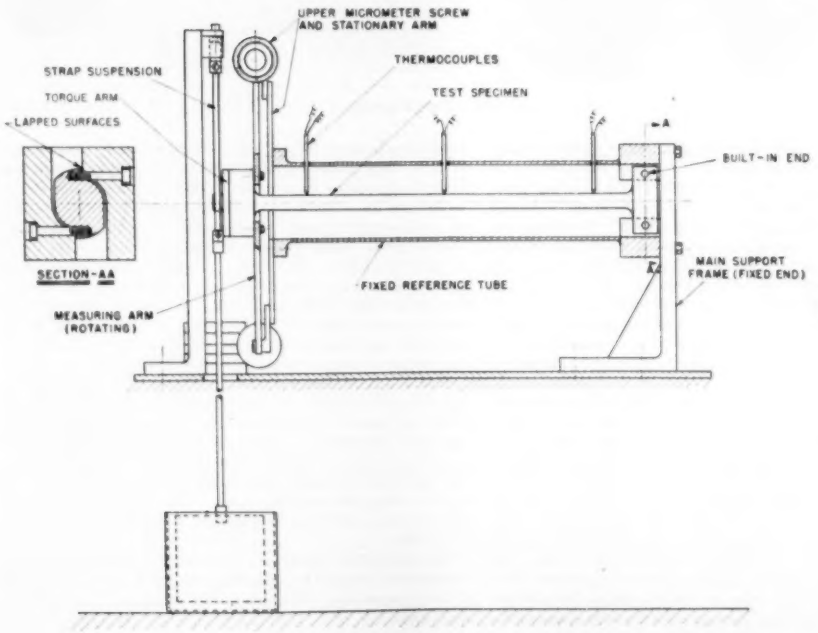

FIG. 8 SCHEMATIC SKETCH OF APPARATUS SHOWING SIDE ELEVATION

Loading Device. Torque is applied to the specimen by means of loading weights. These weights are placed on a pan suspended from a flexible hanger fastened to the torque arm. The length of the loading arm is so chosen that the following relation applies:

$$\tau = 100\ W$$

where τ is the maximum shearing stress (psi) in a 1-in-diam specimen, and W is the weight on the pan (lb). The torque arm is bolted to the front flange of the specimen, and was made symmetrical to permit reversed loading. The flexible suspension strap which is fastened at the center of rotation of the specimen takes the vertical reaction of the loading weights and permits pure rotation of the specimen without any horizontal restraint. The strap which is made from clock-spring steel 0.008 in. thick and $^3/_4$ in. wide is provided with vertical adjustment at the built-in end to insure proper vertical alignment.

It should be noted that the entire support and loading system is designed to be completely frictionless, this being accomplished by the use of the elastic hinge straps previously described.

The opposite built-in end of the specimen is bolted to a massive block by means of tangential clamping bolts shown in Fig. 8, section A-A. All mating surfaces were ground and lapped to insure maximum area of contact, thus eliminating any small angular displacements during loading. As a further check on this, a special dummy specimen having a section modulus 50 times greater than the standard specimen was employed for a series of hysteresis tests. Since the maximum stress in this dummy specimen was low, even for the greatest load, the expected hysteresis should be low, unless there was some inelastic action at the built-in end. The actual measured hysteresis was so low as to be almost below the sensitivity of the apparatus, thereby confirming the adequacy of the end construction employed.

Temperature Measurements. Because the deflection changes due to variations in the modulus of rigidity with normal room temperature were of the same order compared to the deflections due to creep, it was necessary during the creep tests to measure the specimen temperature and make the corrections. Three thermocouples made from 0.007-in-diam chromel-alumel wire were spaced axially along this specimen as indicated in Fig. 8. The reference junction was carefully insulated and its temperature was measured to 0.1 C. Readings were taken on a precision potentiometer.

A determination of the temperature coefficient of the modulus of rigidity was made, and the correction factor applied to the readings. The modulus factor was obtained by comparing deflection readings taken at different loads at a room temperature of 81 F to similar readings taken at a room temperature elevated to 101 F. The value of the thermoelastic coefficient over the temperature range tested gave $\Delta G/G$ as 0.000161 per F for SAE 4140 steel. This value agrees very closely with the value given in reference (11).

Test Procedure. Referring to Table 1, the tabulation of a complete hysteresis cycle at 24,000 psi maximum unidirectional loading is shown. The data are recorded in the sequence at which they were taken. The load increments were 80 lb with a maximum load of 240 lb giving a stress of 24,000 psi. After each load change, a reading at each upper and lower micrometer screw was taken. An average of these readings was made to determine the hysteresis at any one load. In the example shown, the maximum average deflection is given as 27.2547 mm. The per cent hysteresis based upon this maximum deflection is given for $^3/_4$, $^1/_2$, and zero loading as 0.161 per cent, 0.164 per cent, and 0.128 per cent, respectively. The third cycle is also given in Table 1 to show how the hysteresis has been reduced.

Extreme care was exercised during each load change to avoid excessive stresses due to impact. The average time required to complete the cycle was usually 13 min.

After a sufficient number of complete cycles at a given stress were completed, a creep test was run using the maximum load for the previous cycle. All creep tests were conducted at room temperature, and the readings corrected for modulus changes referred to the temperature at the start of the test.

Materials Tested

This investigation was limited to high-strength shafting materials that could be supplied in large diameters. Heat-treatments were chosen as typical of those producing the best attainable properties in large-diameter shafts. Low-carbon steel was included in the test program merely for comparative purposes.

The list of materials tested, with their physical properties, is given in Table 2. Tables 3 and 4 give the compositions and the heat-treatments of the specimens.

TABLE 2 PHYSICAL PROPERTIES OF SPECIMENS TESTED

		Physical properties in tension					
Specimen	Material	Elastic limit	Yield stress, 1000 psi	Ult. stress	Elong., per cent	Red. of area, per cent	Bhn
A	SAE 4140	128	132	146	18.4	61.3	
B	SAE 4140	128	132	146	18.4	61.3	
C	SAE 1015	34.4	34.8	50.5	44.3	70.9	65.9
D	K Monel	102	120	156	25.7	38.1	304
E	Inconel X	...	153	191	15.0	...	39*
F	Same as A						

* Rockwell C.

The chrome-molybdenum alloy steel, specimens A and B, conforms to the SAE steel No. 4140, as well as to the AISI steel No. 8742. This is a high-strength shafting steel quite generally used by the authors' company, and is identified as Westinghouse P.D. Spec. 7940 or P.D. Spec. 8368. As may be seen from Table 2, a yield stress of 132,000 psi is realized in this material by the heat-treatment employed.

The low-carbon steel (specimen C) is fully normalized and possesses a yield strength of 34,800 psi, which is only 26 per cent of the yield stress for specimens A and B.

K Monel and Inconel X were included in the investigation on

TABLE 1 TABULATION OF A TYPICAL HYSTERESIS TEST TO 24,000 PSI (MAXIMUM)

Cycle	Time elapsed, min	Room temp, deg F	Load, lb	Upper screw reading	Lower screw reading	Upper screw diff	Lower screw diff	Average diff, or hysteresis	Hysteresis, per cent
First		80.0	0	50.9450	51.3048				
First	0		80	41.9393	42.2225				
First	2		160	32.9358	33.0705				
First	5		240	23.9112	23.9192	(27.0338)*	(27.4756)*	(27.2547)*	
First	8		160	32.8905	33.0282	.0453	.0423	.0438	0.161
First	10		80	41.8942	42.1785	.0453	.0440	.0446	0.164
First	13	80.5	0	50.9095	51.3605	.0355	.0343	.0349	0.128
Third		78.2	0	50.9060	51.3590				
Third	0		80	41.9035	42.1805				
Third	2		160	32.9025	33.0412				
Third	5		240	23.9165	23.9252				
Third	8		160	32.8925	33.0325	.0100	.0087	.0094	0.035
Third	10		80	41.892	42.1765	.0110	.0110	.0110	0.040
Third	13	78.5	0	50.9025	51.3555	.0035	.0035	.0035	0.013

* Figures in parentheses are values of maximum deflection in mm.

TABLE 3 CHEMICAL COMPOSITION OF SPECIMENS

Specimen	Material	C	Mn	Fe	S	Si	Cu	Ni	Cr	Al	Mo	P	Ti	Cb
A	SAE 4140	0.4	0.75	97.7					0.95		0.2			
B	SAE 4140	0.4	0.75	97.7					0.95		0.2			
C	SAE 1015	0.13	0.47	Bal	0.026	0.04						0.016		
D	K Monel	0.14	0.58	0.86	0.005	0.14	28.82	66.36		2.60				
E	Inconel X	0.04	0.35	6.64	0.007	0.39	0.02	73.40	14.85	0.94			2.32	1.02

TABLE 4 HEAT-TREATMENT OF SPECIMENS

Specimen	Material	
A	SAE 4140	Quenched at 1550 F in oil Tempered at 1320 F in furnace
B	SAE 4140	Same as above
C	SAE 1015	Normalized from 915 C
D	K Monel	Heat-treated—1100 F for 16 hr and 1000 F for 6 hr
E	Inconel X	Aged at 1300 F for 20 hr

account of their nonmagnetic property. They were considered to be the most appropriate alloys for large-diameter nonmagnetic shafts. Generally speaking, as shown by Table 2, K Monel and Inconel X have approximately the same physical properties as the SAE 4140 alloy with the heat-treatments employed.

Results

Method of Presentation of Results. It is evident from the description of the experimental procedure described that one hysteresis cycle yields only three numbers which relate to the hysteresis. Each of these numbers is merely the difference between the deflection reading of the loading phase and that of the unloading phase of the cycle, for the same load. In the case of reversed loading, five numbers instead of three are thus obtained.

Rather than present the data in tabular form, the graphical means shown in Figs. 10 to 19 is employed. The "surface shearing stress" is plotted on the vertical scale, and the hysteresis in terms of "per cent of full-load deflection" (for the specific test in question) is plotted on the horizontal axis. Thus the definition of hysteresis used throughout the paper is as follows:

$$\text{Per cent hysteresis} = \frac{100\,(\text{Deflection during unloading cycle} - \text{Deflection during loading cycle})}{(\text{Maximum deflection during cycle})}$$

Thus, referring to Fig. 10(*a*), the hysteresis for a 6000-psi cycle is 0.018 per cent at 4000 psi, 0.027 per cent at 2000 psi, and 0.027 per cent at zero stress, the latter figure being the "failure to return to zero." The curve groups are presented in the order in which the tests were made, and the small figures on the individual curves in a group refer to the order within the group, e.g., Fig. 10(*c*).

Because of the small number of points determined for each cycle, no attempt is made to fair a curve through the points. They are merely connected by straight lines, except that for stresses above the $^3/_4$ loading point, no curve at all is drawn, since the amount of hysteresis (or creep) at full load is not evaluated. However, this amount may be considered to be very small, probably almost zero.

For the tests on specimens C and D, many hysteresis loops were run during which only the hysteresis at the $^1/_2$ point and the no-load point were determined. This was justified because the overall purpose of the program was to determine maximum values, and test experience had shown that the maximum value almost invariably occurs at the $^1/_2$ point or at the no-load point. For examples of this procedure, see Figs. 14 and 16.

Specimen A: SAE 4140 Alloy Steel. The sequence of tests conducted on this specimen is shown by the bar chart, Fig. 9. The single lines represent hysteresis cycles, while the rectangular areas represent creep tests, all at room temperature.

An important feature of specimen A is that the flanges are integral with the test shaft, there being no shrink fits. The specimen was forged down from a 9-in-square billet, to the approximate final shape, rough-machined, heat-treated, and then finish-machined.

Fig. 10 presents the results of the unidirectional hysteresis cycles on specimen A. At 6000 psi stress amplitude (*a*), the hysteresis was so low that only one cycle was run. At 12,000 psi, data from 5 cycles are shown in (*b*). Note the larger hysteresis for the first cycle.

At 18,000 psi stress amplitude, a value of hysteresis of 0.144 per cent is recorded on the first cycle. Thereafter, the hysteresis is below 0.05 per cent, finally stabilizing at 0.03 per cent maximum.

At the highest stress amplitude, 24,000 psi, the value for the first cycle is appreciable, 0.164 per cent, but after 3 cycles the hysteresis is down to 0.03 per cent, Fig. 10(*d*). Thus it is seen that the strain history has a marked effect on the hysteresis in this material. However, after 3 or 4 cycles of unidirectional loading, the hysteresis appears to have assumed a stable value, which, in all cases, is small, approximately 0.03 per cent.[4]

[4] The reader should remember that these percentage figures are taken with respect to the full-load deflection for the cycle in question. Thus an 0.03 per cent hysteresis on the 12,000 psi cycle is only one half the absolute value (in deflection units) of a 0.03 per cent hysteresis on the 24,000 psi cycle.

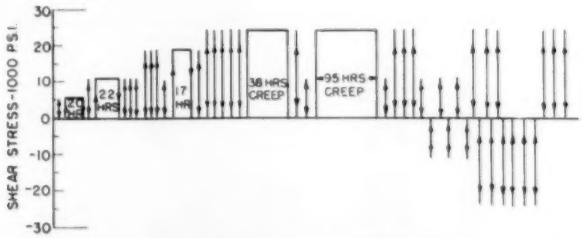

FIG. 9 HISTORY OF SPECIMEN A

It should be noted that in almost every case the maximum value occurs at the 1/4 load level.

Figs. 11, 12, and 13 present the data for the two-directional (or reversed) loading cycles on specimen A. In Fig. 11, curve 1 displays low values since it was the initial positive half cycle following the cycles, the results of which are presented in Fig. 10. Conversely, the initial negative half cycle 2, produces very large values of hysteresis. Thereafter, the hysteresis becomes stabilized, and it is seen that the maximum value occurs when the stress passes through zero. This stabilized value of the hysteresis is 0.12 per cent for the ±12,000-psi cycle, or 4 times the value for unidirectional loading.

In Fig. 12 a similar pattern is presented for the ±24,000-psi cycle, except that the stabilized hysteresis value here is 0.42 per cent of the maximum deflection. This is 13 times the corresponding value of 0.032 per cent for the unidirectional 24,000-psi cycle.

Upon completion of the reversed-loading cycles in Fig. 12 the specimen was subjected to three —24,000-psi cycles followed by three +24,000-psi cycles. The results, shown in Fig. 13, indicate that the hysteresis quickly assumes a low value even after repeated reversed loadings.

A summary of the results of the room-temperature creep tests is presented in Table 5. The values of creep are low, 0.03 per cent for the higher stress, which are approximately the same as the hysteresis values for single-direction loading.

TABLE 5 ROOM-TEMPERATURE CREEP

Specimen	Maximum stress, psi	Elapsed time, hr	Creep—per cent of deflection at maximum stress
A	6000	18	0.01
	12000	18	0.02
	18000	17	0.03
	24000	38	0.03
	24000	95	0.03*
B	6000	24	0.03
	12000	26	0.01
	18000	23	0.03
	24000	24	0.02
	24000	236	0.04*
C	10000	28	0.16
D	18000	75	0.01
E	18000	336	0.01
F	25200	243	0.06

* Separate test.

Specimen B: SAE 4140 Alloy Steel. Specimen B is identical to specimen A except that B has the standard design of flanges fitted to the specimen proper with heavy shrink fits. To insure identity of material, the two specimens were forged from the same billet of steel. These two specimens were made to be identical

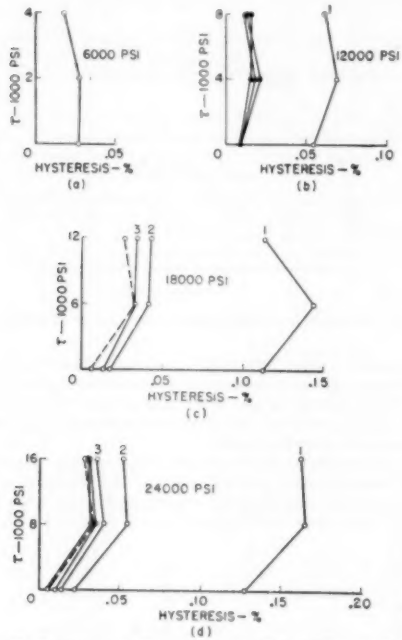

FIG. 10 SPECIMEN A—HYSTERESIS FOR UNIDIRECTIONAL LOADING CYCLES OF STRESS AMPLITUDE SHOWN

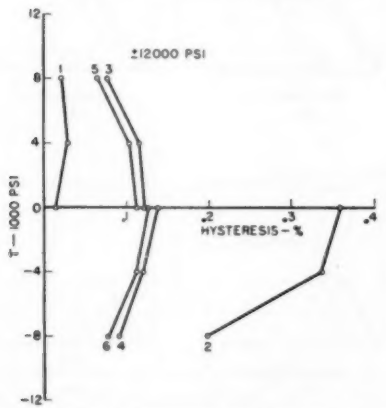

FIG. 11 SPECIMEN A—HYSTERESIS FOR REVERSED LOADING AT 12,000-PSI STRESS AMPLITUDE

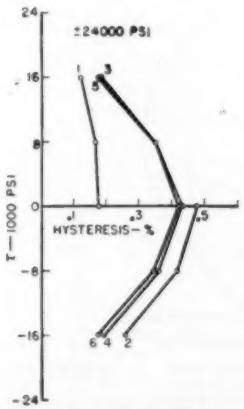

FIG. 12 SPECIMEN A—HYSTERESIS FOR REVERSED LOADING AT 24,000-PSI STRESS AMPLITUDE

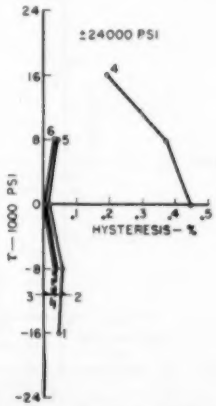

FIG. 13 SPECIMEN A—HYSTERESIS FOR UNIDIRECTIONAL LOADING CYCLES FOLLOWING REVERSED CYCLES IN FIG. 12

(except for the flange construction) for the purpose of proving the efficacy of the shrink-fit flange construction.

Specimen B was subjected to exactly the same sequence of hysteresis and creep-test cycles as was specimen A, up to the reversal cycles, this history being shown in Fig. 9. The tabulation of hysteresis and creep values for the two specimens[4] shows a remarkable identity in results, even better than would be expected for two specimens having no variation even in construction. As a consequence, one can state with confidence that the shrink fits do not affect the results of either the hysteresis or the creep tests.

During the course of tests on specimen B, a 24,000-psi hysteresis loop was run with readings taken every 2000 psi. The data from this test are given in Table 6 and on the curve in Fig. 14. In column 5 are given the deviations of the deflections of column 4 with respect to a straight line that passes through the points 0, 0 and 120, 13.540. The larger deviations, which begin at the 160-lb load, are probably due to the geometry of the measuring apparatus. From the deflection at 120 lb the modulus of rigidity is calculated to be 11,800,000 psi.

Fig. 14 shows the shape of the hysteresis curve in some detail. Here it is seen that the maximum value occurs at 1/4 load, although this does not seem to be entirely representative of the other hysteresis tests inasmuch as the 1/2 and 3/4-load values are almost the same, and this is usually not the case.

TABLE 6 SPECIMEN B—24,000 PSI HYSTERESIS CYCLE; TEMP = 18 C

(1) Load	(2) Hysteresis, mm	(3) Hysteresis, per cent	(4) Deflection, mm	(5) Deviation, mm	(6) Elapsed time, min Up	(6) Elapsed time, min Down
0	0.0030	0.011	0	0	0	29
20	40	14	2.259	+0.003	3	28
40	53	19	4.415	+0.002	4	27
60	70	25	6.773	+0.003	6	26
80	70	25	9.030	+0.004	7	25
100	75	27	11.286	+0.003	8	24
120	76	27	13.540	0	9	23
140	74	26	15.792	−0.004	10	22
160	60	21	18.043	−0.010	12	21
180	60	21	20.291	−0.019	13	20
200	38	14	22.539	−0.027	14	19
220	15	0.005	24.784	−0.038	15	18
240	0	0	27.025	−0.054	16	

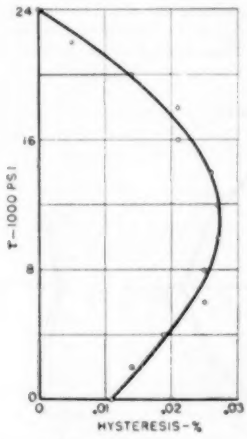

FIG. 14 SPECIMEN B—HYSTERESIS LOOP FOR 24,000-PSI UNIDIRECTIONAL LOADING (Elapsed time = 29 min.)

[4] This tabulation is omitted, the data being almost identical for the two specimens, and therefore the table would add little to the paper.

Fig. 15 is a plot of data from a room-temperature creep test on specimen B. Because of variations in ambient temperature affecting the deflection, these data are not as accurate as the hysteresis data. Table 5 is a comparison of maximum room-temperature creep values for several specimens and stress levels. It is seen that the creep is low and of the same order and usually less than the unidirectional hysteresis values.

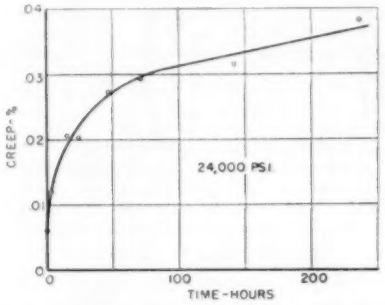

FIG. 15 SPECIMEN B—ROOM-TEMPERATURE CREEP AT 24,000 PSI

Specimen C: Low-Carbon Steel. As shown in Table 2, the tensile-yield strength of the low-carbon steel specimen is only 34,800 psi. This is only 26 per cent of the yield strength of the chrome-molybdenum specimens. This fact must be borne in mind while examining the following results:

Fig. 16 presents the data for unidirectional loading. Since the yield stress in torsion is 17,400 psi (one half the tensile yield stress), the stress amplitudes were chosen considerably lower than for prior tests. In some of the cycles shown, the simple 0, 1/3, 2/3,

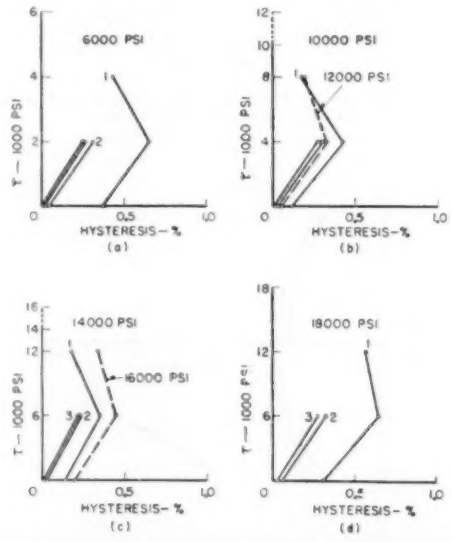

FIG. 16 SPECIMEN C—HYSTERESIS FOR UNIDIRECTIONAL LOADING CYCLES OF STRESS AMPLITUDES SHOWN

and full-load increments were not maintained, but these cycles are evident upon inspecting Fig. 16. Moreover, in many of the cycles only the no-load and $^1/_2$ (approximately) values of hysteresis were taken e.g., cycles 2 and 3 in Fig. 16(*d*).

Fig. 16 shows that the hysteresis values for low-carbon steel are very high, approximately 0.25 per cent for the several stress amplitudes tested, even after three or four repetitive cycles. This is true even for 6000-psi amplitude, which amplitude is comparable to a 24,000-psi amplitude for specimens A and B with their higher yield strength.

The stabilizing effect of repetitive cycles is also prominent but also less pronounced in low-carbon steel. Note that the 18,000-psi stress is slightly above the yield point as determined from a tensile specimen.

For reversed loading, Fig. 17, at 10,000-psi amplitude, hysteresis of 1.15 per cent is obtained. For 18,000-psi amplitude, the hysteresis increases to 2.05 per cent. These values are 4.1 times and 7.6 times the single-direction values.

The results of a creep test on specimen C are given in Fig. 18, the amount of creep at 28.5 hr being 0.16 per cent.

Specimen D: K Monel. Referring to Tables 2, 3, 4 for data on K Monel, we see that it is similar in physical properties to SAE 4140 alloy steel. Unlike the steels, however, K Monel is nonmagnetic. Also, the modulus of rigidity is lower, being 9,500,000 compared with 11,800,000 for SAE 4140.

The results of the hysteresis tests on K Monel are presented in Figs. 19 and 20. The hysteresis values are remarkably low, approximately 0.01 per cent, even on the first cycle of loading and even for reversed loading. In view of the data presented in Figs. 19 and 20, no discussion is required to show that K Monel is superior in respect to hysteresis to any of the materials previously described.

As for creep at room temperature, the experimental data could not be corrected for temperature variation because of the unavailability of the thermoelastic coefficient for K Monel. By interpolation of the creep-test data we estimate that the creep in 75 hr is 0.005 mm at 24,000 psi on a total deflection of 30.6 mm. This is only 0.01 per cent.

Specimen E: Inconel X. The physical properties of Inconel X are appreciably higher than those of either SAE 4140 or K Monel as shown in Table 2. The modulus of rigidity is lower, being approximately 11,000,000, as compared to 11,800,000 for SAE 4140. Also Inconel X like K Monel is nonmagnetic.

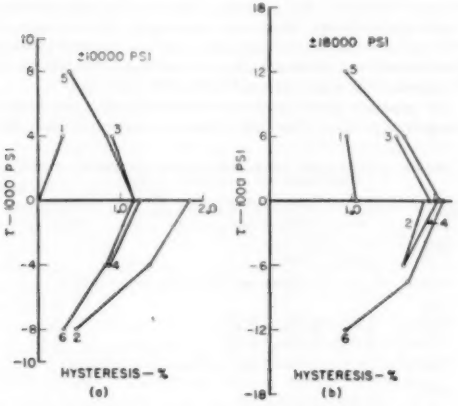

FIG. 17 SPECIMEN C—HYSTERESIS FOR REVERSED LOADING AT 10,000-PSI AND 18,000-PSI STRESS AMPLITUDES

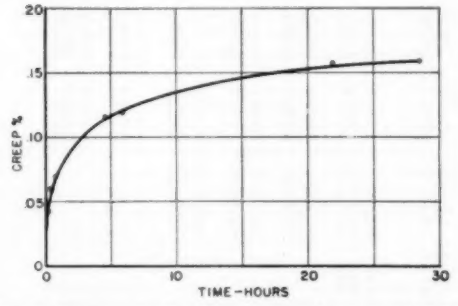

FIG. 18 SPECIMEN C—ROOM-TEMPERATURE CREEP AT 10,000 PSI

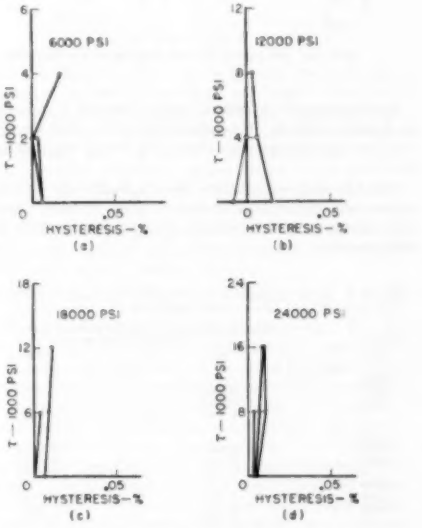

FIG. 19 SPECIMEN D—HYSTERESIS FOR UNIDIRECTIONAL LOADING CYCLES OF STRESS AMPLITUDES SHOWN

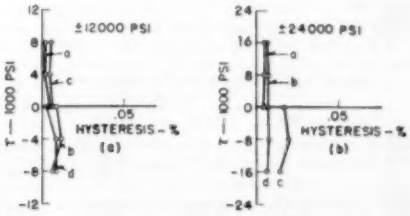

FIG. 20 SPECIMEN D—HYSTERESIS FOR REVERSED LOADING CYCLES

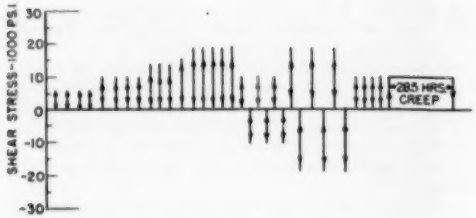

FIG. 21 SPECIMEN C—HISTORY

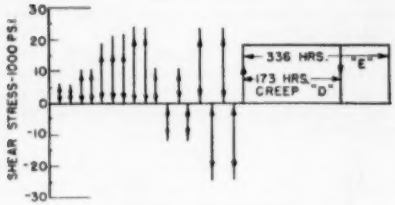

FIG. 22 SPECIMEN D AND SPECIMEN E—HISTORY

The results of the hysteresis tests on Inconel X appear in tabular form in Table 7. It is interesting to note that the values are very low and compare with those of K Monel tested as specimen D.

Creep at room temperature, like the K Monel specimen, could not be corrected for temperature variation because of insufficient data; however, by interpolation the estimated creep for 336 hr is 0.01 per cent.

TABLE 7 HYSTERESIS AND CREEP OF SOLID INCONEL X, SPECIMEN E

Stress, psi	Hysteresis in per cent of full-load deflection, cycle of loading 1st	2nd
6000	...	...
4000	0.069	0
2000	0.083	0
0	0.090	0
12000	...	...
8000	0.022	0.0075
4000	0.026	0.0037
0	0.022	0.0037
18000	...	...
12000	0.025	0.005
6000	0.020	0.005
0	0.022	0.005
22000	...	...
16000	0.022	...
8000	0.010	...
0	0.018	...
24000	...	...
16000	0.013	0.008
8000	0.004	0.004
0	0.010	0.002

PER CENT HYSTERESIS FOR REVERSE LOADING

Stress, psi	Cycle of loading 1st CW	1st CCW	2nd CW	2nd CCW
12000	...	...	...	...
8000	0.0075	0.0075	0.0075	0.0037
4000	0	0.0075	0.019	0.015
0	0	...	0.0075	0.010
24000	...	...	...	...
16000	0.0074	0.048	0.0095	0.013
8000	0.018	0.052	0.013	0.024
0	0.0074	0.05	0.0074	0.017
18000	Creep test: 0.01 per cent in 336 hr			

Specimen F: Tubular Specimen of SAE 4140 Alloy Steel. This specimen is from the same billet, and was forged and heat-treated at the same time as specimen A. Also, both specimen A and specimen F have integral flanges. The only difference is that specimen F was bored and honed throughout its length to a 0.847-in. diam, and thereby we produced a tubular specimen 0.847 ID × 1.000 OD with an effective length of 26 in. The wall thickness is seen to be 0.0765 in. or approximately $^5/_{64}$ in.

The stress ranges at which the tubular specimen was tested were chosen to be approximately the same as for the solid specimen (specimen A), although exact duplication of stress range was not possible on account of the different section modulus of the two specimens. Thus a reasonably good comparison of the hysteresis of a solid versus tubular specimen was obtained. The data on the latter are of course the more interesting to the investigator of the behavior of materials, on account of the almost constant shearing stress in the tubular specimen. Because of the possible scientific value of these data, they are reproduced in full in Table 8.

The entries in the table are in the order of test, as follows: Each series of tests shown between two horizontal lines in the table were run in sequence from left to right. The series were run in the order from top to bottom. A word of explanation of the entries in the stress column is in order. The first entry is the maximum stress of the cycle. The successive entries are the stress levels at which the hysteresis values were determined. For example, in the next to the last entry in the table, the test comprised loading the specimen to a maximum stress of 16,800 and determining the hysteresis at the stress levels of 12,600, 8400, and zero.

An inspection of the results presented in Table 8 reveals that the general pattern of the data follows the results previously pre-

TABLE 8 HYSTERESIS AND CREEP OF SPECIMEN F—TUBULAR SPECIMEN OF SAE 4140 STEEL

Stress, psi	Hysteresis in per cent of full-load deflection, cycle of loading 1st	2nd	3rd	4th	5th	6th	7th
4200	...	...					
0	0.032	0.000					
4200	Creep test: 0.093 per cent in 10 hr						
6300	...	...					
4200	0.031	0.024	0.017				
2100	0.029	0.004	0.007				
0	0.043	0.004	0.007				
6300	Creep test: 0.014 per cent in 600 hr						
8400	...	...					
0	0.038	0.013					
	0.008	0.016					
12600	...	...	...	...	...	...	...
8400	0.107	0.054	0.036	0.039	0.039	0.032	0.039
4200	0.114	0.047	0.044	0.047	0.043	0.037	0.027
0	0.093	0.021	0.032	0.021	0.025	0.009	0.007
16800	...	...	...	...	...	...	
12600	0.214	0.078	0.060	0.060	0.070	0.062	
8400	0.206	0.084	0.064	0.071	0.082	0.068	
4200	0.190	0.071	0.063	0.057	0.072	0.059	
0	0.186	0.029	0.009	0.030	0.036	0.008	
21000	...	...	...	...	...	...	
16800	0.266	0.092	0.087	0.067	0.061	0.054	
12600	0.292	0.123	0.114	0.091	0.087	0.085	
8400	0.271	0.107	0.117	0.091	0.086	0.090	
4200	0.252	0.100	0.082	0.069	0.052	0.056	
0	0.197	0.049	0.047	0.024	0.057	0.017	
25200	...	...	...	...			
21000	0.254	0.057	0.081	0.081			
16800	0.308	0.135	0.115	0.114			
12600	0.312	0.137	0.123	0.122			
8400	0.287	0.137	0.115	0.113			
4200	0.262	0.099	0.084	0.078			
0	0.239	0.051	0.028	0.033			
16800	...	...					
12600	0.054						
8400	0.074						
0	0.013						
25200	Creep test: 0.080 per cent in 243 hr						

sented for the identical solid specimen (specimen A), with one important difference: Whereas the hysteresis for the solid specimen was 0.03 per cent, approximately, at 24,000 psi, after several cycles of loading, for this tubular specimen the following peak values were obtained on the last cycles of loading:

Stress amplitude	Hysteresis, per cent
21000	0.090
25200	0.122

these values being 3 × and 4 × the value for the solid specimen, respectively. Thus we observe the important but expected fact that the hysteresis in a thin-walled tubular specimen in torsion is several times that of a solid cylindrical specimen. The logical explanation is that in the solid specimen the lower-stressed material in the core acts as a more perfectly elastic spring (as confirmed by our experiments at lower stress levels) in parallel with the spring composed of the highly stressed material in the outer shell of the specimen. This combination quite evidently should be more elastic than a simple tubular specimen. From both the experimental and analytical points of view, a solid cross section for a torque-weighing bar is superior to a tubular cross section.

Discussion

As a result of the torsional hysteresis and creep tests on the several materials, a number of conclusions may be stated. These are of considerable interest and importance in those applications employing the twist of a shaft as a measure of torque.

For stresses up to 24,000 psi in chrome-molybdenum steel (SAE 4140), hysteresis and creep are low in magnitude, 0.03 per cent, for unidirectional loading. For reversed loading, however, the hysteresis is many times greater, being 0.12 per cent for 12,000-psi stress amplitude, and 0.42 per cent for 24,000-psi amplitude. These latter values are sufficiently large to be objectionable in torque measuring systems.

The hysteresis values in torsion for a thin-walled tubular specimen proved to be large compared with the values for a similar solid specimen. For an SAE 4140 steel tubular specimen, the stabilized values were 0.090 per cent and 0.122 per cent for unidirectional loading to stress amplitudes of 21,000 and 25,200 psi, respectively.

Low-carbon steel, as would be expected, displays large hysteresis for all the test conditions imposed, even for the single-direction loading to 6000 psi. The smallest observed values were 0.25 per cent, whereas some cycles showed almost 10 times this amount.

For both steels tested, strain history was an important factor in the results. In all cases, however, the hysteresis apparently had reached a stable value in from 3 to 4 cycles of loading. On the first cycle the hysteresis was as much as 5 times the stabilized value obtained after several cycles of loading.

The nonmagnetic alloys, K Monel and Inconel X proved to have exceptionally low hysteresis and creep for shearing stresses up to 24,000 psi. Both hysteresis and creep values were only 0.01 per cent, even for reversed loading.

Acknowledgments

The authors desire to thank the Westinghouse Materials Engineering Department for recommending and supplying the materials for these tests, and Mr. G. O. Sankey of the Westinghouse Research Laboratories for his assistance. This investigation was conducted while the authors were on the staff of the Westinghouse Research Laboratories.

BIBLIOGRAPHY

1 "Elastic Hysteresis in Steel," by F. E. Rowett, Proceedings of the Royal Society of London, series A, vol. 89, 1914, pp. 528–543.

2 "Elastic Hysteresis in Crankshaft Steels," by S. F. Dorey, Proceedings of The Institution of Mechanical Engineers, vol. 123, 1932, pp. 479–535.

3 "Internal Friction in Engineering Materials," by J. M. Robertson and A. J. Yorgiadis, *Journal of Applied Mechanics*, Trans. ASME, vol. 68, 1946, p. A-173.

4 "Vibration Problems—Friction and Damping in Vibrations," by A. L. Kimball, *Journal of Applied Mechanics* (Design Data), Trans. ASME, vol. 63, 1941, part 4, pp. A-37–A-41; part 5, pp. A-135–A-140.

5 "Elastic and Inelastic Behavior in Spring Materials," by M. F. Sayre, Trans. ASME, vol. 52, 1930, paper APM-52-9.

6 "Elastic and Inelastic Behavior in Spring Materials," by M. F. Sayre, Trans. ASME, vol. 53, 1931, paper APM-53-8, pp. 99–105.

7 "Laws of Elastic Behavior in Metals," by M. F. Sayre, Trans. ASME, vol. 56, 1934, pp. 555–558 and 559–561.

8 "Measuring Elastic Drift," by R. W. Carson, Proceedings of the ASTM, vol. 37, 1937, pp. 661–674.

9 "New Spring Formulas and New Materials in Precision Spring Scale Design," by M. F. Sayre and A. V. deForest, Trans. ASME, vol. 58, 1936, pp. 379–387.

10 "Factors Affecting the Grip in Force, Shrink, and Expansion Fits," by R. Russell, Proceedings of The Institution of Mechanical Engineers, vol. 125, 1933, pp. 493–535.

11 "Temperature Coefficients of the Moduli of Metals and Alloys Used as Elastic Elements," by G. H. Keulegan and M. R. Houseman, Research Paper No. 531, Bureau of Standards, *Journal of Research*, vol. 10, 1933, pp. 289–320.

Discussion

J. F. Downie Smith.[6] Many years ago the study of alternating current in electrical engineering was largely devoted to 60-cycle frequency, since that was the principal frequency used at that particular time. Later, however, as the science of high-frequency currents was developed, a broader concept of a-c theory was produced, and these broader concepts included 60-cycle frequency as a special case, whereas formerly the high frequency was the special case. It also was found that the more general theories involving high frequency enabled us to predict certain things with regard to other frequencies not at all evident in the study of the more specialized 60-cycle.

It has occurred to the writer that possibly we may be going through the same type of change in mechanical engineering that formerly was experienced with electrical engineering. For example, the principal structural and engineering materials used at the present time are metals—and for metallic materials, many assumptions are made which are perfectly valid within the limits used in engineering. For example, in the determination of strain, it is a matter of little consequence, generally, whether we define this in terms of the angle, or the tangent of the angle, and both have been used extensively. But we also have a relatively new material for certain types of engineering applications which does not follow the same restricted rules as steel, namely, the use of rubber as a spring, where it is not satisfactory to make the same assumptions as were made for steel. For example, the angles of deflection in shear for a rubber mount are frequently such that the tangent of the angle, and the angle, are widely different. Nevertheless, it is possible to develop theories for the deflections of rubber which obey experiment quite closely. In general, it is found that deflections are calculated from an infinite series, the first term of which frequently gives the deflections for steel. Several terms occasionally may be required to get the proper answer for rubber.

Thus it occurs to the writer that possibly a more careful study of the solutions obtained for deflections of rubberlike materials would yield results of a more general nature than would be the case in studying metallic materials alone. In addition, several years of test data have been obtained in the field of rubber

[6] Dean of Engineering, Iowa State College, Ames, Iowa. Fellow ASME.

and plastics on creep and other factors. It is possible that the exaggerated characteristics obtained on those materials might be an indication of what conceivably could be expected in a minor way in the metallic materials.

Hence it is suggested to the authors, and to others who might be interested, that perhaps a more careful study of the literature in the field of rubber and plastics might yield great benefits to those who have specialized in the metallic materials. Thus, particularly in connection with machine design, closer co-operation with the Rubber and Plastics Division is advisable. From such close co-operation it is believed both divisions would benefit materially.

A Time-Temperature Relationship for Rupture and Creep Stresses

By F. R. LARSON[1] and JAMES MILLER[2]

A relation which evaluates the relative effects of time and temperature on the tempering of steels has been developed by previous investigators. In this paper this relation has been adapted to rupture and creep behavior and applied to existing data on several widely different alloys with outstanding results. Methods are described by which short-time tests can be used to determine long-time properties.

Introduction

IN the field of high-temperature testing, considerable effort has been expended to discover a relationship between short- and long-time tests. Such efforts are considered worth while because elevated-temperature tests which simulate actual operating times are extremely costly and time-consuming. Present methods of extrapolation of a log-log plot of stress versus rupture time are often inaccurate and misleading. These extrapolations frequently lead to high values of strength since increases in slope cannot be anticipated.

It has been shown by many investigators that creep (1, 2, 3, 4),[3] tempering (5, 6), and diffusion (7) appear to obey rate-process theories, and the rates are expressible by an equation of the form

$$\dot{\epsilon} = Ae^{-Q(S)/RT} \quad [1]$$

where $\dot{\epsilon}$ is the rate, A is a constant, $Q(S)$ is the activation energy for the process under the conditions considered, R is the gas constant, and T is the absolute temperature. Holloman and Jaffe (5) have shown that the relation between tempering time and temperature for a given hardness, derived from Equation [1], is expressed by the following equation

$$T(C + \log t) = \text{const} \quad [2]$$

where T is the absolute temperature, C is a material constant, and t is the time. Since both tempering and creep seem to obey the rate-process theories, it was believed that this concept should be directly applicable in creep and rupture testing for the purpose of shortening the test time.

Discussion of Results

Materials Investigated. Although the authors and their associates have analyzed a large amount of rupture data to determine the degree to which it complies with the time-temperature parameter $T(C + \log t)$, the quantity of data which can be presented here is of course limited. In selecting the data to be presented, an effort was made to include representative cases rather than only cases which showed the best agreement. The alloys presented are listed in Table 1, together with the source of data and chemical composition. These alloys were selected on the following basis:

1 Test results available over a wide range of temperature and time.

2 Typical alloys covering a wide variety of compositions.

3 Test data reliable and free from discrepancies.

It is obviously difficult to satisfy these conditions completely, but it is felt that the alloys listed will serve our purpose.

Master Rupture Curves. The proposed relation as applied to rupture strength states that for a given stress the time to rupture is related to temperature by the equation

$$T(20 + \log t) = \text{const} \quad [3]$$

T being the absolute temperature (deg R), and t the rupture time in hours. A value of 20 has been substituted for C in Equation [2]. The method by which this value was arrived at is discussed later.

According to Equation [3], if rupture stress is plotted as a function of the parameter $T(20 + \log t)$, all the points should fall on a single curve, regardless of the temperature at which the tests were conducted. Such a plot will be called a master rupture curve since it is actually a superposition of rupture curves at different temperatures, the parameter performing the function of modifying the times so that the various curves fall on a single line.

In Figs. 1 to 8, inclusive, master rupture curves have been plotted for the eight alloys using all the actual test points availa-

TABLE 1 LIST OF ALLOYS INVESTIGATED, TOGETHER WITH SOURCE OF DATA AND CHEMICAL ANALYSIS

Alloy no.	Alloy	Form	Source of data	Chemical composition, per cent C	Si	Mn	Cr	Ni	Co	Fe	Mo	W	Ti	Others
1	Low-carbon steel.....	Hot-rolled	*Timken Digest* (8)	0.15	0.28	0.46	..	..	..	Bal	..	..	..	...
2	Carbon-moly steel....	Hot-rolled	*Timken Digest* (8)	0.13	0.25	0.49	..	..	..	Bal	0.52	..	..	...
3	Cr-Mo-Ti-B steel.....	Sheet	Wright Field (9)	0.05	0.49	0.61	3.04	..	..	Bal	0.95	..	0.59	B-0.04
4	18-8 stainless steel....	Hot-rolled	*Timken Digest* (8)	0.06	0.61	0.50	17.75	9.25	..	Bal	..	..	..	...
5	18-8-Mo stainless steel	Hot-rolled	*Timken Digest* (8)	0.08	0.45	1.40	16.42	13.44	..	Bal	2.81	..	..	...
6[a]	S-590 alloy.....	Forged	ASM Trans. (10) and Allegheny-Ludlum (15)	0.4	0.4	1.5	20	20	20	Bal	4	4	..	Cb-4
7[a]	Haynes Stellite No. 34	Cast	General Electric, Thomson Laboratory	0.4	0.5	0.5	27	2.5	Bal	1	5.5	..	..	...
8[a]	Titanium D9.....	Forged	General Electric, Thomson Laboratory	..	..	1	..	..	..	1	..	..	Bal	Al-1, Cu-1 0-0.3

[a] Nominal analysis.

[1] Physical Metallurgist, Watertown Arsenal, Watertown, Mass.; formerly of Thomson Laboratory, General Electric Company.

[2] Metallurgical Engineer, Thomson Laboratory, General Electric Company, River Works, West Lynn, Mass.

[3] Numbers in parentheses refer to Bibliography at end of paper.

Contributed by the Metals Engineering Division and the Joint ASTM-ASME Committee on Effect of Temperature on Properties of Metals and presented at the Annual Meeting, Atlantic City, N. J., November 25-30, 1951, of The American Society of Mechanical Engineers.

Note: Statements and opinions advanced in papers are to be understood as individual expressions of their authors and not those of the Society. Manuscript received at ASME Headquarters, August 10, 1951. Paper No. 51—A-36.

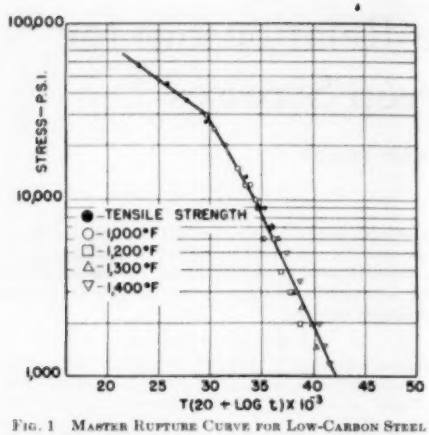

FIG. 1 MASTER RUPTURE CURVE FOR LOW-CARBON STEEL
(*T*, temperature in deg R, *t*, rupture time in hours.)

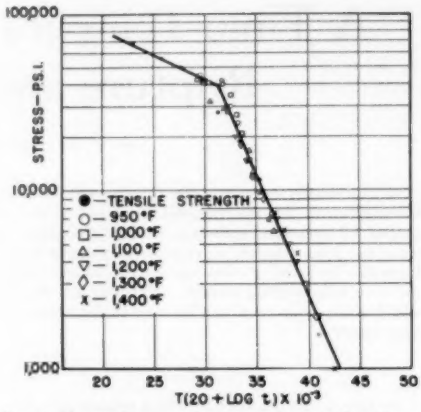

FIG. 2 MASTER RUPTURE CURVE FOR CARBON-MOLY STEEL
(*T*, temperature in deg R, *t*, rupture time in hours.)

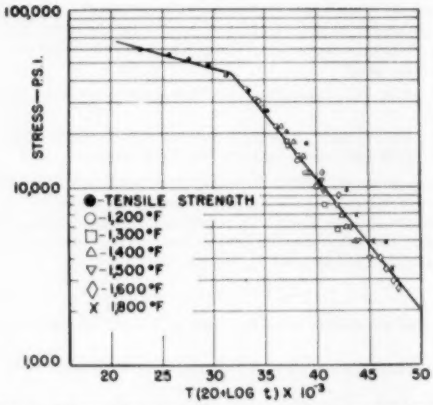

FIG. 3 MASTER RUPTURE CURVE FOR 18-8 STAINLESS STEEL
(*T*, temperature in deg R, *t*, rupture time in hours.)

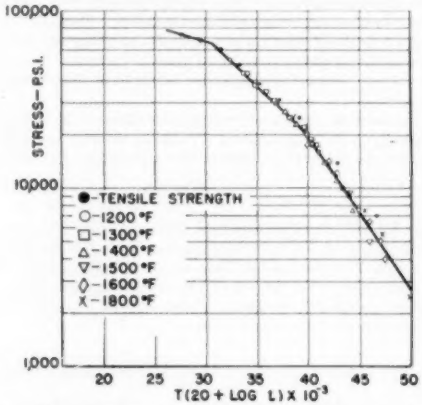

FIG. 4 MASTER RUPTURE CURVE FOR 18-8 MO STAINLESS STEEL
(*T*, temperature in deg R, *t*, rupture time in hours.)

ble. Examination of these curves reveals that the deviation of points from a single curve is small and is felt to be due to experimental error. Considering the wide range of materials, times, and temperatures, a remarkable correlation exists. Hot tensile strength where data were available was plotted on the same curves using 0.10 hr as the time factor. Although more variables are involved in a tensile test, the data show good agreement.

In addition to the data presented in this paper, the authors and their associates have applied the proposed relation to over 40 alloys. Although occasional larger deviations appeared, the majority of data conformed within ±10 per cent of stress.

The implications of this concept are of great practical significance since a complete master curve may be constructed from short-time rupture data over a range of temperatures. Once this curve is obtained, long-time data within the limits of the parameter values covered may be calculated immediately. It also becomes possible to compare the complete rupture characteristics of various alloys on a single graph. A comparison of this type is shown in Fig. 9 for the eight alloys considered.

In order to eliminate mathematical calculations, a graph relating time and temperature to the parameter $T(20 + \log t)$ has been constructed and is shown in Fig. 10.

Comparison of Rupture and Tempering Curves. Since the original work on this parameter was concerned with the tempering of steel, it was felt that it might be interesting to compare a master rupture and a master tempering curve using the same parameter equation. In order to make any relation that might exist more evident, a material whose tempering curve was already known to have sharp changes was selected. These two curves are plotted in Fig. 8 for a Cr-Mo-Ti-B steel and show a striking similarity, for when sharp changes occur in hardness on the tempering curve, sharp changes also appear in the rupture strength at the same parameter value.

Master Creep Curves. Although creep data covering a wide enough range of variables to check compliance with the proposed theory are scarce, existing data indicate that creep follows the same relation. Master creep curves may be constructed in either of two ways, as follows:

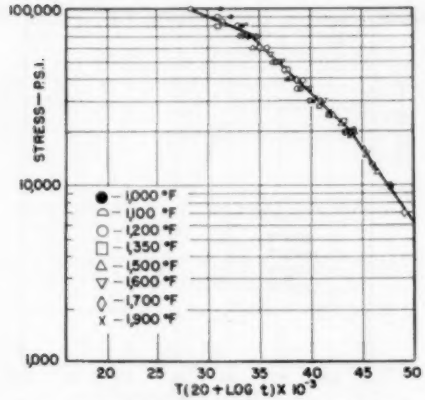

FIG. 5 MASTER RUPTURE CURVE FOR S-590 ALLOY
(*T*, temperature in deg R, *t*, rupture time in hours.)

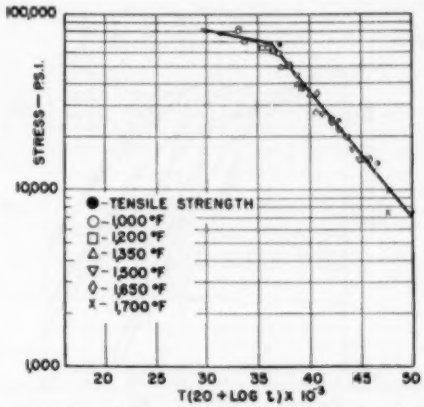

FIG. 6 MASTER RUPTURE CURVE FOR HAYNES STELLITE NO. 34
(*T*, temperature in deg R, *t*, rupture time in hours.)

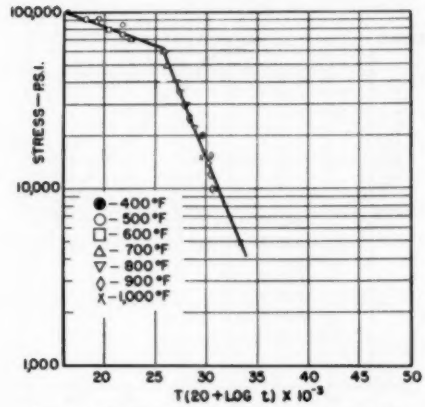

FIG. 7 MASTER RUPTURE CURVE FOR TITANIUM D9
(*T*, temperature in deg R, *t*, rupture time in hours.)

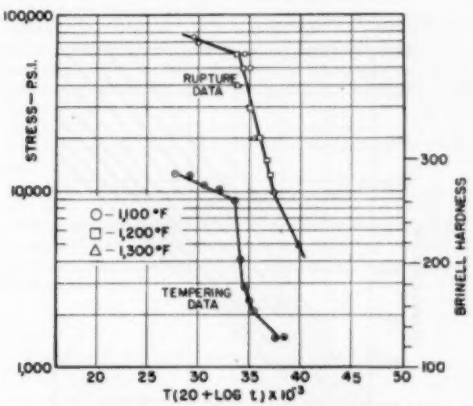

FIG. 8 MASTER RUPTURE AND TEMPERING CURVES FOR CR-MO-TI-B STEEL
(*T*, temperature in deg R, *t*, time in hours.)

1 Where the time for a given elongation is considered, the parameter used is the same as for rupture except that *t* is now the time to a given elongation.

2 If minimum creep rate is considered the parameter becomes $T\ (20 - \log r)$, where r is the creep rate.

Master creep curves for minimum creep rate are plotted for carbon-molybdenum steel and S-590 alloy in Figs. 11 and 12. A complete analysis of creep data has not yet been made, and a value of 20 may not be the best value to use in considering creep rates.

Predicting Specific Data. A relationship between time and temperature, such as is suggested in this paper, can be put to a variety of uses. One of the most important is the determination of specific long-time data from comparatively short tests at a higher temperature.

The data presented in the plots of stress versus $T\ (20 + \log t)$ indicate that for a constant stress the following equation is true

$$T_1\ (20 + \log t_1) = T_2\ (20 + \log t_2) \ldots\ldots\ldots [4]$$

It now becomes possible to calculate a short-time combination of temperature and time which is equivalent to any desired operating conditions. For example, substitution in Equation [4] shows that the following combinations should have equivalent rupture stresses:

	Operating conditions	Test conditions
1	10000 hr at 1000 F	= 13 hr at 1200 F
2	1000 hr at 1200 F	= 12 hr at 1350 F
3	1000 hr at 1350 F	= 17 hr at 1500 F
4	1000 hr at 300 F	= 1.1 hr at 400 F

Lists of rupture strengths for these equivalent combinations of temperatures and time have been prepared and are shown in Tables 2 to 4. Table 2 lists all the ferritic steels for which data were available for both 10,000 hr at 1000 F and 13 hr at 1200 F (8). Table 3 lists high-temperature alloys for which adequate data were available, and Table 4 some aluminum alloys. The correlation between the long-time rupture strengths obtained by established methods and that predicted by the short-time values is

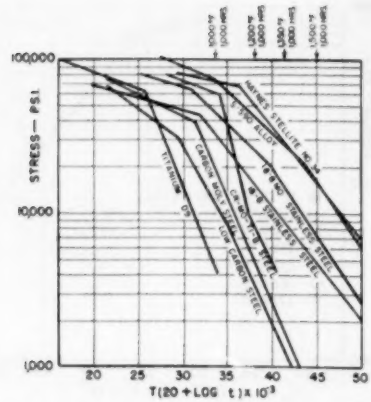

FIG. 9 MASTER RUPTURE CURVES FOR SEVERAL ALLOYS
(*T*, temperature in deg R, *t*, rupture time in hours.)

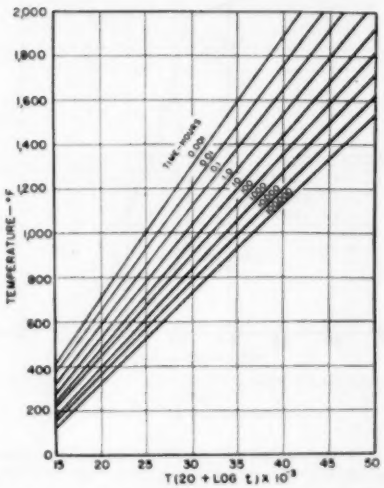

FIG. 10 TEMPERATURE VERSUS PARAMETER T (20 + LOG t) FOR VARIOUS TIMES
(T, temperature in deg R, t, time in hours.)

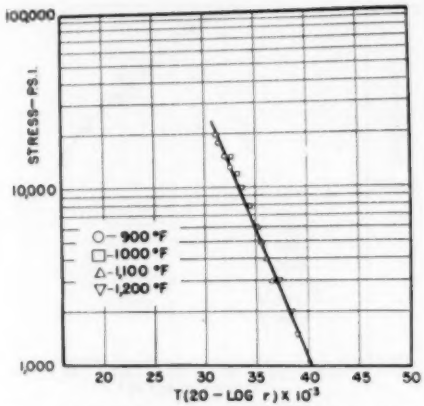

FIG. 11 MASTER CREEP CURVE FOR CARBON-MOLY STEEL
(T, temperature in deg R, r, creep rate in per cent per hour.)

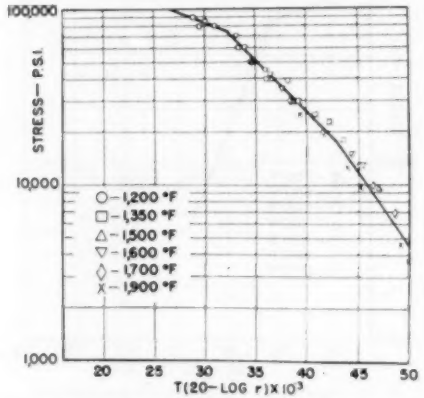

FIG. 12 MASTER CREEP CURVE FOR S-590 ALLOY
(T, temperature in deg R, r, creep rate in per cent per hour.)

impressive. In Table 5 similar comparisons are shown for stresses to produce 1 per cent creep in several austenitic sheet materials, in both the annealed and cold-rolled condition. Here again there is close agreement between the long-time data and that predicted by the short-time data.

Deviations Encountered. In order to determine the validity of the proposed relation between temperature and time to rupture, it has been applied to as wide a range of materials, temperatures, and times as available data permitted. It is the authors' belief that if over a very wide range of variables only minor deviations are encountered, these deviations may reflect normal variation in test data rather than a fallacy in the theory. With this in mind a closer examination of the plots of stress versus T (20 + log t) and of the tabulated values is of importance.

It is found that the average scatter of points about the mean value is approximately ±10 per cent in stress, which is not an excessive amount on an ordinary stress-rupture curve. In some cases, particularly at low parameter values, deviations up to 25 per cent of the mean stress are found; but it must be admitted that errors of this magnitude sometimes appear in rupture data. It is felt that a large amount of careful testing is required to establish the cause of the variations within these limits.

Value of the Constant C. Upon first consideration it is surprising that the value of 20 for C in the parameter T (C + log t) works so well for such a variety of materials. The method for determining the constant for any particular material is discussed under theoretical considerations, and a list of the values obtained for several different materials is given in Table 6. The values vary from 15 to 23, and the average is 19.3. While it is certainly possible that C actually does vary from material to material, the value

TABLE 2 COMPARISON OF 10,000-HR RUPTURE STRENGTH AT 1000 F WITH 13-HR RUPTURE STRENGTH AT 1200 F FOR LOW-ALLOY STEELS

Steel	Stress for rupture in 10,000 hr at 1000 F, psi	Stress for rupture in 13 hr at 1200 F, psi
C-Steel	7000	8000
C-Mo	12000	12000
Sicromo-58	13000	12000
Sicromo-3	15000	13000
Sicromo-2	15000	14000
2 Cr-Mo	15000	14000
5 Cr-Mo	17000	13000
2¼ Cr-1 Mo	19000	17000
DM-2	22000	18000
DM	23000	17000

NOTE: Source of data—*Timken Digest* stress-rupture curves (8).

TABLE 3 COMPARISON OF 1000-HR RUPTURE STRENGTH AT 1350 F WITH 17-HR RUPTURE STRENGTH AT 1500 F FOR HIGH-TEMPERATURE ALLOYS

Alloy	Stress for rupture in 1000 hr at 1350 F, psi	Stress for rupture in 17 hr at 1500 F, psi
Inconel	8000	9000
Timken	19000	20000
Hastelloy B	19000	22000
N-155	24000	25000
S-590	25000	26000
H.S.-34	29000	28000
H.S.-88	30000	30000
S-816	30000	30000
X-40	34000	32000
Inconel X	41000	39000

NOTE: Source of data—average values from General Electric, Thomson Laboratory files.

TABLE 4 COMPARISON OF 1000-HR RUPTURE STRENGTH AT 300 F WITH 1.1-HR RUPTURE STRENGTH AT 400 F FOR ALUMINUM ALLOYS

Alloy	Stress for rupture in 1000 hr at 300 F, psi	Stress for rupture in 1.1 hr at 400 F, psi
99.6% Al-H12	6000	6000
99.6% Al-H18	6000	8000
2S-H12	6000	7000
3S-H12	11500	10000
3S-H18	13500	12000
52S-H38	12500	17000
61S-T6	28000	27000
24S-T3	40000	43000

NOTE: Source of data—Dorn, Tietz, and Sherby (11, 12).

TABLE 5 COMPARISON OF 1000-HR CREEP STRENGTH AT 1200 F WITH 12-HR CREEP STRENGTH AT 1350 F FOR STAINLESS SHEET ALLOYS

Type	Stress for 1 per cent creep in 1000 hr at 1200 F	Stress for 1 per cent creep in 12 hr at 1350 F
321-CR*	3000	3600
Inconel-A†	9000	10000
347-CR	10500	11500
321-A	13000	15500
Inconel-CR	17000	19000
347-A	18000	17500
316-A	19000	16000
Timken-CR	26000	28500
316-CR	29000	27500
Inconel-X	52000	56000

* CR = cold-rolled.
† A = annealed.
NOTE: Source of data—General Electric, Thomson Laboratory creep tests on sheet alloys.

of 20 has been used in all cases in this paper for four reasons.

1 The scatter of points on the parameter curves is insensitive to changes in C.

2 Since the variation in C between materials of widely different compositions is no greater than that found between materials of relatively similar composition, it is felt that the variation may not be real.

3 The use of one value of C makes possible the comparison of master curves of various alloys on one graph.

4 Nehrenberg (6) has found 20 to be the best value for the tempering of steels.

If there is actually a variation in C, by the following equation the error in time, introduced by using the wrong value, can be determined by differentiating $\log t$ with respect to C, holding T_1, T_2, and t_2 constant

TABLE 6 VALUE OF C IN PARAMETER T (C + LOG t) FOR SEVERAL ALLOYS

Alloy	Value of C (for t in hours, and T in deg R)
Low-carbon steel	18
Carbon-moly steel	19
2¼ Cr — 1 Mo steel	23
Cr-Mo-Ti-B steel	22
18-8 stainless steel	18
18-8 Mo stainless steel	17
25-20 stainless steel	15
S-590 alloy	20
Haynes Stellite No. 34	20
Titanium D9	20

$$T_1 (C + \log t_1) = T_2 (C + \log t_2) \quad [5]$$

This results in the following expression

$$\frac{d(\log t_1)}{dC} = \frac{T_2 - T_1}{T_1} \quad [6]$$

From this it is evident that if the value of C used is not correct, the error in $\log t_1$ will be proportional to the difference in temperatures considered. Substitution of actual values shows that for small changes in C the error is negligible if the temperatures are not too widely separated.

Metallurgical Changes. It is believed that the relationship in question will be invalidated if major phase changes are encountered. However, other metallurgical changes involving diffusion, such as tempering or overaging, have previously been shown to follow this relation (5, 6) and consequently are accounted for. It is logical to assume that oxidation, if it is a significant factor, also may follow the same time-temperature relation.

Theoretical Considerations

The proposed time-temperature relation is based in part on the well-known theory of rate processes, which states that the rate at which certain processes progress is related to temperature by the following equation

$$r = Ae^{-Q/RT} \quad [7]$$

where

r = rate
A = constant
e = natural logarithm base
Q = activation energy for process
R = gas constant
T = absolute temperature

Several investigators (7, 13, 14) have demonstrated that for a constant stress, creep-rate data fit Equation [7] providing the rate taken is either the minimum rate or the rate at a constant strain. Since the time to rupture depends upon the summation of creep rates out to rupture, Equation [7] may be written

$$\frac{1}{t} = Ae^{-Q/RT} \text{ (for constant stress)} \quad [8]$$

where t equals time to rupture. Equation [8] is easily reduced to the following form

$$T (C + \log t) = \frac{Q}{2.3R} = \text{const (for constant stress)} \quad [9]$$

where $C = \log A$.

This is seen to be the parameter against which values of stress were plotted in the master curves. Equation [9], however, implies that C is constant only for constant stress, whereas the rela-

tion stated in this paper asserts that C is independent of stress and possibly of material.

A graphical presentation is the easiest way to demonstrate the fact that C actually is independent of stress. According to Equation [9], if log t is plotted against the reciprocal of the absolute temperature for constant stress, the result should be a straight line. Moreover, when $1/T = 0$, the value for log t equals $-C$. In Figs. 13 and 14 the rupture data on carbon-moly steel and S-590 alloy have been plotted in this manner. It will be noted that regardless of stress the value of log t at $1/T = 0$ is the same. Values of C for the two materials are therefore 19 and 20, respectively. As pointed out earlier, an analysis of widely different materials indicates that a value for C of 20 may be used in each case with satisfactory results.

From the foregoing it is seen that C is theoretically the log time to rupture at $1/T = 0$, that is, at an infinite temperature. Therefore the following calculation of C may be made. This calculation is intended as a matter of interest only; whether or not it has any significance is not known. Assuming that at infinite temperature the creep rate would be the fastest rate physically possible, it would be a creep rate at which adjacent atoms were separating at the speed of light, that is

$$r = \frac{c}{\delta} \quad \ldots\ldots [10]$$

where c is the speed of light (3×10^{10} cm per sec), and δ is the interatomic spacing (3×10^{-8} cm approximately). For an elongation (ϵ) of 1 cm per cm, the corresponding rupture time would be

$$t = \frac{\epsilon}{r} = \frac{\epsilon\delta}{c} \quad \ldots\ldots [11]$$

Substituting values in the foregoing equation gives

$$t = 10^{-19} \text{ sec} = 2.8\ 10^{-22} \text{ hr}$$

Since $C = -\log t$, a value of 21.5 is obtained for C.

Other interesting observations may be made from an examination of the shape of typical master rupture curves, Fig. 9. It will be noted that all the curves are made up of two comparatively straight-line portions separated by a sudden change in slope.

Furthermore, it is seen that the lines at higher parameter values if extended to a parameter of zero (i.e., 0 deg abs) appear to converge in the vicinity of the theoretical breaking strength of metals. This suggests the idea that in the low parameter region, stress concentrations reduce the strength below the theoretical value, whereas at higher parameter values these stress concentrations are relieved.

Conclusions

The time-temperature relation expressed by the parameter $T(C + \log t)$ has been applied to rupture and creep data on a variety of alloys with the following results:

1 All the data analyzed complied with the foregoing relation within limits which could be attributed to experimental deviations.

2 A value for C of 20 was found to be satisfactory for all the alloys considered.

3 Application of this relation allows the use of short-time tests to determine long-time data with remarkable accuracy.

4 It also allows the presentation of the complete rupture characteristics of an alloy on a single master curve which facilitates comparison with other alloys.

Acknowledgments

The authors wish to express their gratitude to the following organizations for their kind permission to make use of their rupture and creep data: Timken Roller Bearing Company; American Society for Metals; Allegheny-Ludlum Steel Corporation; Wright Air Development Center; General Electric Company.

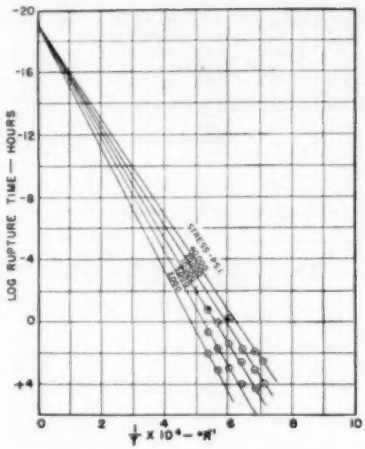

Fig. 13 Log Rupture Time Versus Reciprocal Absolute Temperature for Carbon-Moly Steel

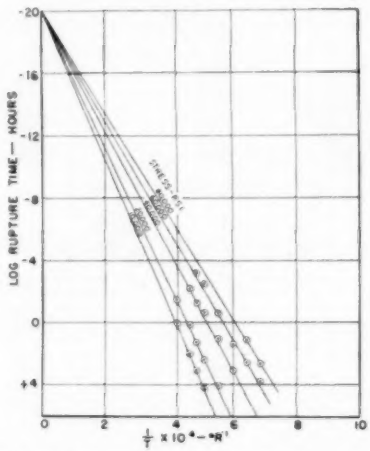

Fig. 14 Log Rupture Time Versus Reciprocal Absolute Temperature for S-590 Alloy

Bibliography

1 "Tension Tests at Constant True Strain Rate," by J. C. Fisher and C. W. MacGregor, *Journal of Applied Mechanics*, Trans. ASME, vol. 67, 1945, p. A-824.

2 "A Velocity-Modified Temperature for the Plastic Flow of Metals," by J. C. Fisher and C. W. MacGregor, *Journal of Applied Mechanics*, Trans. ASME, vol. 68, 1946, p. A-11.

3 "The Flow of Metals at Elevated Temperatures," by J. H. Holloman and J. D. Lubahn, part 1, *General Electric Review*, vol. 50, February, 1947, pp. 28, 32; April, 1947, pp. 44–50.

4 "Problems in Non-Elastic Deformation of Metal," by J. H. Holloman and C. Zener, *Journal of Applied Physics*, vol. 17, February, 1946, pp. 69–82.

5 "Time-Temperature Relations in Tempering Steel," by J. H. Holloman and L. C. Jaffe, Trans. AIME, Iron and Steel Division, vol. 162, 1945, pp. 223–249.

6 "Master Curves Simplify Stainless Tempering," by A. E. Nehrenberg, *Steel*, vol. 127, October 23, 1950, pp. 72–74.

7 "Cohesion and Atomic Structure," by Saul Dushman, Proceedings of the ASTM, vol. 29, 1929, pp. 7–64.

8 "Digest of Steels for High Temperature Service," Timken Roller Bearing Company, Steel and Tube Division, fifth edition, 1946.

9 "Utilization of Low Alloy Materials for High Temperature Applications," by P. K. Porter, L. W. Smith, and J. Miller, AF Technical Report No. 6221, Air Materiel Command, Wright-Patterson Air Force Base, fig. 28.

10 "On the Extrapolation of Short Time Stress Rupture Data," by N. J. Grant and A. G. Bucklin, Trans. ASM, vol. 42, 1950, pp. 720–751.

11 "Effect of Cold Rolling on the Creep Properties of Several Aluminum Alloys," by O. D. Sherby and J. E. Dorn, Trans. ASM, vol. 43, 1951, pp. 611–634.

12 "Aluminum Sheet Alloys," by J. E. Dorn and T. D. Tietz, Proceedings of the ASTM, vol. 49, 1949, p. 815.

13 "Physics of Metals," by Frederick Seitz, McGraw-Hill Book Company, Inc., New York, N. Y., 1943, pp. 137–142.

14 "Short-Time High Temperature Deformation Characteristics of Several Sheet Alloys," by G. Guarnieri and J. Miller, Trans. ASM, vol. 41, 1949, pp. 167–188.

15 Allegheny-Ludlum unpublished data supplied by Dr. Gunther Mohling.

Discussion

J. C. Fisher[4] and J. H. Hollomon.[5] It is quite probable that the authors have shown the way toward significantly shortening the time required for the rupture testing of alloys. Use of the parameter $T\ (C + \log t)$ may reduce this time as much as tenfold, leading to important savings in all laboratories where rupture testing is employed. As described in the authors' first six references, the parameter $T\ (C + \log t)$ or its equivalent has been used to represent the combined influence of time and temperature upon the tempering process and upon creep rates. Its use in rupture testing is a logical although not obvious extension to another important group of tests, for which the authors are to be commended.

Application of the parameter $T\ (C + \log t)$ to rupture testing is an important step forward, but it is desirable to discover the limitations, if any, upon its use. It seems probable that the success of the parameter depends upon two things: (*a*) In much rupture testing, failure is due to local necking in the specimen, after which rapid elongation and fracture quickly follow; the necking strain is about the same from specimen to specimen and, therefore, the reciprocal of the time to fracture is a measure of the average strain rate throughout the test. (*b*) The stress is related to temperature and average creep rate through the parameter $T\ (C - \log \dot{\epsilon})$. When a brittle alloy is tested, for which the reciprocal rupture time may not be a measure of the average creep rate, there is a possibility that the rupture stress will not depend upon $T\ (C + \log t)$ alone.

As the authors state, use of the value 20 for C is justified at this time only for those classes of metals for which experience has shown it to be satisfactory. The values of C in reference (2) of the paper vary by a factor of 5, suggesting that $C = 20$, while valid for certain classes of high-temperature alloys, is not a universal constant.

It is our opinion that the parameter $T\ (C + \log t)$ should find wide and satisfactory application to rupture and creep testing.

[4] Research Associate, Research Laboratory, General Electric Company, Schenectady, N. Y. Jun. ASME.

[5] Research Associate, Research Laboratory, General Electric Company.

N. J. Grant.[6] The writer has found this paper to be an extremely interesting one and definitely suggestive of a reasonable short cut in evaluating material behavior as a function of time and temperature.

It suffers, unfortunately, in certain respects from an effort to include all of the possible instabilities of an alloy in the one expression $T\ (20 + \log t) = \text{const}$. This is, of course, asking a lot of any equation. Most reactions in metals are strain sensitive; for example, the transformation of martensite in steel, or the precipitation of carbide or sigma in stainless steels is accelerated by the superimposition of tensile strain. On the other hand, although oxidation of metals and decarburization of metals are time-temperature controlled, they are not measurably strain sensitive. Yet both of these instabilities have a large effect on the long-time creep or stress-rupture performance of metals at elevated temperatures. It is not expected that the same T–t expression would fit both strain-affected reactions as well as strain-unaffected ones.

For example, in examining stress-rupture data for Monel over a wide temperature-rupture time range of values, we have found a severe deviation from linearity in the log stress versus log rupture time plot due to oxidation. We find that this deviation is not anticipated by the authors' Equation [3] because oxidation is not a strain-affected behavior. A plot of log stress versus the term $T\ (20 + \log t)$ is given in Fig. 15, herewith, and shows a progressively wider spread of data at the lower stresses (higher temperatures and longer test times) where oxidation is more severe. In the same way all the reactions occurring during creep testing which are not strain sensitive will result in deviations from a curve based on short-time data as shown in Fig. 15.

[6] Department of Metallurgy, Massachusetts Institute of Technology, Cambridge, Mass.

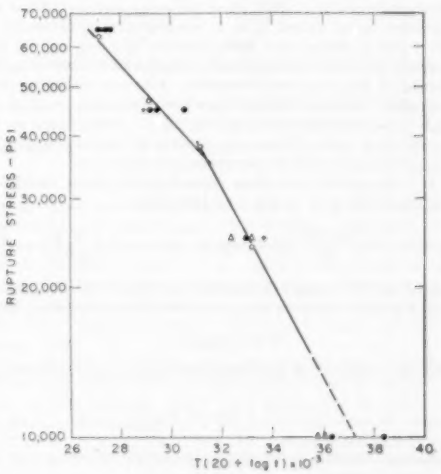

Monel

Test temperatures from 700–1700 F
Test times from 0.01 to 2000 hr

o—o Experimental curve based on 1 hr rupture life
+ Transcrystalline low-temperature-type fracture
● Intercrystalline high-temperature-type fracture
Δ High-temperature points—oxidation factor

Fig. 15 Log Stress Versus Term $T\ (20 + \text{Log } t)$

TABLE 7 COMPARISON OF EXPERIMENTAL VERSUS PREDICTED RUPTURE LIVES USING METHOD OF LARSON AND MILLER

Test temp, deg F	At 20,000 psi: Rupture life, hr	
	Predicted	Experimental
1100	80	48
1200	4	3.6
	At 10,000 psi	
1100	13,000	840
1200	400	52
1500	0.16	0.4

Table 7 of this discussion shows the differences in rupture life between predicted values and the experimental values. Note that the differences are greater at longer times.

This is not entirely bad since such deviations call attention to important material instabilities which result in poorer performance. It does mean, however, that an accurate knowledge of the instabilities which may be encountered during the life of a material application must be anticipated to utilize the data available from the use of this analysis, otherwise large errors may ensue.

For those materials which are quite stable or which do not have instabilities which are insensitive to strain, there is every reason to believe that the authors' analysis is extremely useful and should find important application.

J. J. KANTER.[7] The parameter $T\,(C + \log t)$ as applied to rupture and creep data by the authors, seems to promise considerable usefulness and to be worthy of further careful discussion. They have chosen to plot their parameter against the logarithm of stress and as so plotted their curves generally show a sharp break at the higher stress values. In the cases of the data for 18-8 Mo and S590 alloys where two breaks are shown, a smooth curve might better be passed among the points. While it is recognized that plotting log stress does conveniently expand the stress scale at low values, there are some interpretational advantages to be gained from a consideration of parameter $T\,(C + \log t)$ plotted as a linear function of stress, and for this purpose the writer has replotted a number of the curves in this manner in Fig. 16 of this discussion. It is seen that linear plotting gives reasonably straight lines free of the sharp break at the high stress values shown by the log plots. Furthermore, on the straight-line plots, it becomes possible to consider unique intercept values on both the parameter and stress axes.

If it be granted that stress approximates a linear function of the parameter $T\,(C + \log t)$ we may write

$$S/S_0 = 1 - \frac{2.3\,RT}{Q}\,(C + \log_{10} t) \quad \text{or} \quad t = t_0\, e^{\frac{Q}{RT}\left(1 - \frac{S}{S_0}\right)}$$

where S_0 is the stress axis intercept, a value of the magnitude of the short-time breaking strength or "true stress" rupture, where

$$C = -\log_{10} t_0$$

and the intercept of the parameter axis is determined where

$$T\,(C + \log_{10} t) = \frac{Q}{2.3R}$$

affording a method for computing the activation energy Q for the unstressed system.

It is also of interest to note that the magnitude of constant C may be accounted for by an alternative argument to the speed-of-light calculation offered by the authors. If it be supposed that under activation Q a time for dislocation obtains comparable to the thermal-vibration period, an argument may be used similar

[7] Directing Engineer, Engineering Laboratories, Crane Co., Chicago, Ill. Mem. ASME.

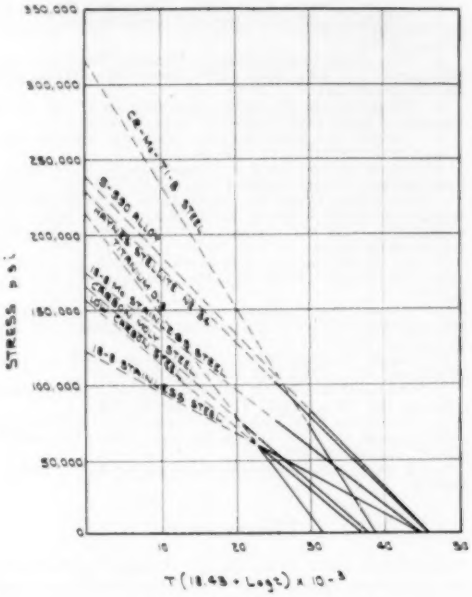

FIG. 16

to the one proposed by Dushman and Langmuir in discussion of the solid-diffusion process. They supposed that the time per atomic jump could be approximated by

$$t = \frac{N_e h}{jQ}$$

where

N_e = Avogadro's number = 6.061×10^{23} atoms per gram atom
h = Planck's constant of action, 6.554×10^{-27} erg sec
j = mechanical equivalent of heat, 4.185×10^{7} ergs per cal
Q = activation energy, cal per gram atom

It was suggested by the present discusser[8] that the same argument might be applied in considering the creep process. Since the creep strain would on the average be directed along the planes of maximum shear, the time for unit strain would be increased by a factor $\sqrt{2}$ and since the values of Q are of the order of 10^5, we find

$$t_0 = \frac{\sqrt{2}\,N_e h}{Q \times 3.6 \times 10^3} = \frac{1.414 \times 6.061 \times 10^{23} \times 6.554 \times 10^{-27}}{4.185 \times 10^7 \times 10^5 \times 3.6 \times 10^3}$$

$$= 3.75 \times 10^{-19}$$

or

$$C = -\log_{10} t_0 = 18.43$$

which is a fair median value for the range 15 to 23 reported by the authors.

The range of Q-values for the materials covered by the authors appears to be about 82,000 to 116,000 cal per gram atom, which corresponds to a range in values for constant C of 18.49 to 18.34.

[8] "The Problems of the Temperature Coefficient of Tensile Creep Rate," by J. J. Kanter, Trans. AIME, vol. 131, 1938, pp. 385–418.

TABLE 8

Alloy no.	Alloy	Q, cal/gram atom	S_0, psi
1	Low-carbon steel	94000	160000
2	Carbon-moly steel	96000	170000
3	Cr-Mo-Ti-B steel	100000	320000
4	18-8 stainless steel	112000	125000
5	18-8 Mo stainless steel	114000	175000
6	S-590 alloy	116000	240000
7	Haynes Stellite No. 34	116000	230000
8	Titanium D9	82000	220000

If the curves are replotted linearly using a value of 18.43 for the parameter constant instead of 20, the fit of the points to a straight line is improved. The shift to the left of the higher parameter values is 2 to 3 times as great as that at the lower values and, therefore, the apparent downward concavity of the right side end of the curves, found when using the value 20, is corrected for. The values for Q and S_0 of Table 8, herewith, are derived using 18.43 as the value of $-\log t_0$. Quite astonishingly, the Q-values so derived place the alloys in exactly their commonly accepted order of high-temperature strength.

D. L. Newhouse[9] and J. L. Van Ullen.[9] For many years designers of high-temperature equipment for long-time service have been faced with the problem of predicting creep and rupture strength on the basis of expensive and time-consuming creep and rupture tests. When an equipment life of 10 to 40 years is demanded, extrapolations are required in the best of these tests. By permitting the rapid evaluation of high-temperature design strength, the authors' procedure would appear to circumvent this difficulty. Realistic acceptance tests can be devised using the parameter principles, and the development of new materials can be facilitated.

A fundamental principle of the parameter procedure described is that time and temperature may be equated by employing the constant C. Thus the correctness of the method is predicated on an accurate value of the constant. Although the authors have shown some variation in constant, its effect on scatter was minor and they conclude that "since the variation in C between materials of widely different compositions is no greater than that found between materials of relatively similar composition, it is felt that the variation may not be real."

While we agree that many materials can be represented by 20, there are enough exceptions of a significant degree to warrant consideration of other constants. Twelve per cent Cr steels with constants of around 25, and many austenitic steels with constants of less than 20, are some exceptions. This difference in behavior was first observed several years ago while developing a suitable acceptance test for high-temperature steels. It was found that a controlled strain-rate tensile test at 1400 F gave strength values numerically equivalent to the 1000 F, 100,000-hr rupture strength for medium-alloy steels as shown in Fig. 17 of this discussion. For the conditions of the test, this temperature is close to that predicted by the authors' parameter, using a constant of 20. However, Fig. 17 also shows a different equivalence between tensile and rupture strength for some 12 per cent chrome steels. It was found necessary to use a 1300 F tensile test to obtain numerical equivalence between tensile strength and rupture strength for the 12 per cent chrome steels which is comparable to a constant of about 25.

Examination of the data on austenitic steels[10] quoted by the authors indicates that the constant varies with composition and in an apparently consistent pattern with stress level as shown in Fig. 18, herewith. Are such variations of constant significant? It is true, as the authors have pointed out, that scattering is not influenced markedly by moderate variations of constant. Nevertheless, the greatest scattering may occur where one wishes to run a short-time test to assess the long-time strength at a lower temperature. For instance, in the authors' Fig. 3, the use of 20 for 18-8 material, when 16 or 17 would be more accurate at a stress of 10,000 psi or less, results in a greater scattering in which short-time high-temperature points will be on one side, and long-time lower-temperature points will be on the other side, of the scatter band.

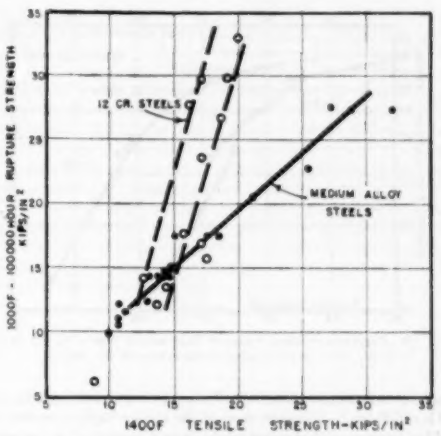

Fig. 17 Plot Showing 1000 F—100,000-Hr Rupture Strength Versus 1400 F Tensile Strength

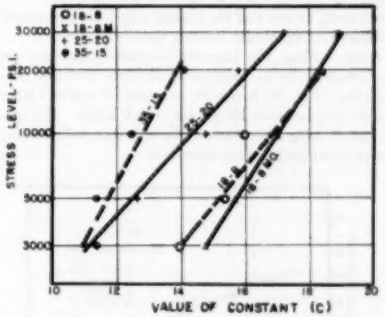

Fig. 18 Plot Showing Variation of Constant With Stress Level

Fig. 19 of this discussion shows stress-parameter curves for a 12 per cent Cr-Co-W-V steel using constants of 20 and 25. A bar tested at 1200 F at 35,000 psi would, according to test, fail in 60 hr. With a constant of 20, this is equivalent to 1400 hr at 1100 F. Actually the 1100 F test at this stress lasted 3500 hr and an error of 2 to 1 in time, and 20 per cent in strength, exists. With the use of a constant of 25, the error in time is reduced to $1/_3$ and the error in stress to about 3 per cent. If one assumes a constant of 20 for this material when the constant is actually 25, a 100-hr test at 1200 F would be assumed to be 100,000 hr at 1000 F, whereas it is actually equivalent to 100,000 hr at 1035 F.

Since variations in constant apparently do exist, and are significant, it would seem advisable to minimize this error, even if the

[9] Steam Turbine Engineering Division, General Electric Company, Schenectady, N. Y.

[10] Reference (8), authors' bibliography.

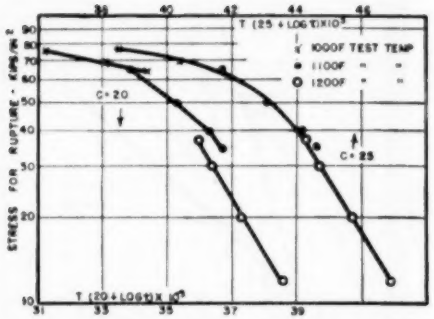

FIG. 19 RUPTURE STRESS VERSUS PARAMETER FOR A 12 CR, 5 CO, 3 W, 1/4 V STEEL USING CONSTANTS OF 20 AND 25

ready comparison of materials afforded by a universal constant of 20 is sacrificed. Although most of the master rupture curves are said to be composed of two straight lines, it appears that a smooth curve can be drawn through most of the points equally well. A smooth-curve representation on a parameter plot would lead one to doubt the straight-line sections of log-log rupture curves as conventionally drawn and the abrupt transition point from transcrystalline to intergranular fracture usually shown.

In creep testing, the time-temperature parameter has been applied successfully to residual-stress data at 0.002 in. per in. total strain. Fig. 20, herewith, is a plot of residual stress for a 1 per cent Cr 1 per cent Mo 1/4 per cent V steel. The agreement is quite good using a constant of 30, although values as low as 20 have been observed for some materials.

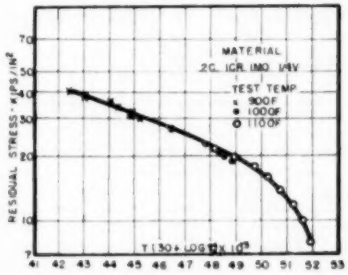

FIG. 20 RESIDUAL STRESS AT 0.002 IN/IN TOTAL STRAIN VERSUS TIME-TEMPERATURE PARAMETER

In conclusion, we feel that the authors' time-temperature parameter should prove a boon to designers and an aid in understanding the behavior of high-temperature materials.

ERNEST L. ROBINSON.[11] The authors are to be credited with the vision to see how a well-known relationship which physical chemists have used to describe the effect of temperature on behavior may be applied to modern stress-rupture test results over a much wider range of stresses, lives, and temperatures than heretofore had been thought possible. Just how far we can go with this new technique of test analysis is still to be found out. The narrowness of the spread in the test data presented by the authors is most noteworthy and encouraging. In the interest of perfecting our understanding, the writer would ask the following questions:

1 There seems to be no question about the ability to "trade time for temperature" (in the language of R. W. Bailey) as long as the "master rupture curve" runs straight on the semilog plot. But it is hard to see how there can be any algebraic continuity around the sharp corners put in these curves by the authors. The writer suggests that maybe it would be better to fillet these corners with curves.

2 The consequence of being able to trade time for temperature on one set of rules below the "knee" and another above it is to place the knee of the log-log stress-time rupture line always at the same stress level regardless of time and temperature whereas we have commonly regarded this knee as occurring somewhere along a "northeast" "southwest" line—that is, at moderate temperatures rather late at a high stress but at higher temperatures much earlier and at much lower stresses. It is possible we have been drawing the lines wrongly with too slavish a regard for the test points but the writer wonders if the use of some curves instead of corners in the master lines might not result in still better agreement with test points.

For predicting behavior with moderate variations of stress or temperature, or both, the writer suggests relationships described in his paper,[12] in which he uses two descriptive coefficients k and m which, respectively, are the per cent change of strength per degree change of temperature and the per cent increase in rate of life expenditure per per cent increase in stress. Their product km, which is the per cent increase in rate of life expenditure per degree, may be determined directly from the parameter by means of the authors' Equations [8] and [9] and the writer's Equation [3]. Thus, letting the parameter $T\,(C + \log t) = P$

$$Q/R = 2.3\,P \text{ and } km = 100\,Q/RT^2 = 230\,P/T^2$$

or similarly

$$Q/R = km\,T^2/100 \text{ and } P = km\,T^2/230$$

AUTHORS' CLOSURE

The authors are indeed grateful to the discussers for their interest and valuable comments.

Messrs. Fisher and Hollomon point out that in very brittle materials the rupture stress may not depend upon $T(C + \log t)$ alone. We have not at the present time sufficient data to check this point although scattered data on brittle cermets indicate that their rupture strength may be a function of $T(C + \log t)$ alone.

Mr. Grant's data on Monel plotted as a function of $T(20 + \log t)$ is of considerable interest. He notes deviations from the theory at the high temperatures and long times and attributes these to oxidation effects. It is quite possible that severe oxidation effects would not conform to the same parameter as rupture stress; however, rupture stress is usually of interest only at times and temperatures where oxidation is not severe enough to effect rupture stress. As Mr. Grant suggests, deviations such as these would call attention to instabilities which might otherwise go unnoticed.

The authors are indebted to Mr. Kanter for his theoretical calculation of the constant C in the parameter $T(C + \log t)$ based on atomic vibrations and jump distance. This calculation supports the idea that the value of C is actually a constant independent of material. Whether a value of 20 or 18.43 is used

[11] Structural Engineer, Turbine Division, General Electric Company, Schenectady, N. Y. Fellow ASME.

[12] "Effect of Temperature Variation on the Long-Time Rupture Strength of Steels," by Ernest L. Robinson, published in this issue pp. 777-781.

would have only a minor effect on the results obtained. Mr. Kanter also suggests that if stress is plotted as a linear function of the parameter instead of a logarithmic function, a straight-line relation will be obtained. We cannot agree with him on this point since in a linear plot the values approach zero stress asymptotically rather than intersecting at a finite value as he has shown. His calculations of activation energies at zero stress are therefore open to some doubt.

Messrs. Newhouse and Van Ullen feel that certain materials require the use of a constant other than 20 (e.g., 25 for 12 per cent Cr steels). Our experience has indicated that in the vast majority of alloys (from nonferrous to ferritic and austenitic) a constant of 20 works very well. We suspect that in cases where it differs appreciably from 20 there may be other factors involved such as a phase change. It is true that the prediction of long-time data from extremely short tests (less than an hour) requires an accurate value of the constant. However, if tests of at least 10 to 100 hr duration are used the value of the constant is less critical. Further work on this subject should be fruitful.

In answer to Mr. Robinson we agree that in some cases a curved line might show better agreement with the data than the straight lines with breaks. It is believed by the authors, however, that in many cases these breaks denote an important change in the flow and fracture process. Examples would be the change from transgranular to intergranular fracture and the attainment of a time-temperature combination which causes a sharp drop in hardness. His application of the parameter to his calculations on the effect of varying temperature and stress should be useful providing as he points out the formulas are applied only to moderate variations.

Effect of Temperature Variation on the Long-Time Rupture Strength of Steels

By ERNEST L. ROBINSON,[1] SCHENECTADY, N. Y.

This paper presents a method of computing the factor of safety of a structural member with reference to a stated life, when operating under stress at high temperature when the temperature varies or when the stress varies moderately according to some definite pattern. The formulas presented herein are based on the supposition that the expenditure of each particular fraction of the life span at elevated temperature is independent of and without influence upon the expenditure of all other fractions of the life to rupture. The author makes no claim that this assumption is wholly true. The suggested procedure is offered simply to provide a means for making engineering estimates with some greater validity than always to assume that the worst conditions are present all the time. The desirability of taking account of certain additional influences which may differ from one material to another is recognized.

Introduction

IN 1937 the author worked out a series of formulas for computing the effect of moderate temperature variation on the creep strength of steels at high temperature.[2] Those formulas were based on the straight-line semilog plot of creep rate or creep strength against temperature and, as in this paper, made no attempt to consider transient effects which may be of importance in the case of extremely rapid swings. More specifically, it was shown that steady-state test results may be well presented, often over a range of several hundred degrees F, by a linear relationship between the logarithm of the creep rate or creep strength and the temperature.

In the discussion of that article the author was criticized for not plotting rates and strengths against the reciprocal of the absolute temperature instead of the temperature itself. In defense of his procedure, the author pointed out its convenience, the minor character of the error, and the fact that his assumption was conservative as compared with the more precise technique.

In what follows, the author proposes to make the same assumptions again, reiterating that no claim is made that the theory is widely descriptive of the behavior of metals. This is no more than a way to compute what a machine is good for under an ordinary range of variation in the operating conditions.[3]

Test Relationships

The long-time rupture test shows a straight-line plot on log-log paper of life-to-rupture versus applied stress such that

$$\frac{L}{L_0} = \frac{S_T^m}{S^m} \quad \ldots\ldots [1]$$

where L = life in hr at stress S, psi
S_T = nominal strength, psi, at temperature T, deg F, for a particular stated life L_0 in hr
m = slope of the line on the log-log plot, which is the ratio of the per cent increase in the rate of life expenditure to the per cent increase of stress. (See Fig. 1 and also Appendix.)

Having found by test a number of values of the nominal strength S_T for the same life L_0 at various temperatures, a plot of these on semilog paper is represented by a straight line such that

$$\frac{S_T}{S_0} = e^{-k\,\Delta T/100} \quad \ldots\ldots [2]$$

where S_0 is the nominal strength in psi for a stated normal temperature, and ΔT is the departure from that normal temperature, e is the base of the natural logarithms, and k is the per cent change of strength per degree change of temperature. The author's previous paper explains the similarity between this rule and the rules for compound interest and explains the manner of plotting to determine suitable values of k. (See Fig. 2 and also Appendix.)

Expenditure of Life

As explained at the beginning, it is assumed that each fractional expenditure of life is independent of all others except as each contributes to the total exhaustion and eventual rupture of the material. In order to facilitate calculation of this quantity, it may be designated as E where $E = t/L$, t being the time in hours of sojourn at any particular condition of stress and temperature. A formula for E may be written based on Equations [1] and [2] as follows

$$E = \frac{t\,S^m}{L_0\,S_0^m}\,e^{km\,\Delta T/100} \quad \ldots\ldots [3]$$

This expression is convenient for evaluating the life expenditure in any particular cycle of stresses and temperatures.

Case 1. For instance, suppose the temperature runs hot by an amount ΔT. The life expenditure E_1 relative to E_T at normal temperature is

$$\frac{E_1}{E_T} = e^{km\,\Delta T/100} \quad \ldots\ldots [4]$$

Case 2. If the temperature runs hot by an amount ΔT for half the time, and cold by the same amount for the other half of the time, as in a "square wave," the life expenditure, E_2, relative to E_T at normal temperature, is

$$\frac{E_2}{E_T} = \cosh\, km\,\Delta T/100 \quad \ldots\ldots [5]$$

[1] Structural Engineer, Turbine Engineering Divisions, General Electric Company. Fellow ASME.

[2] "Effect of Temperature Variation on the Creep Strength of Steels," by Ernest L. Robinson, Trans. ASME, vol. 60, 1938, pp. 253–259; Discussion, Trans. ASME, vol. 61, 1939, pp. 49–53.

[3] For a relationship descriptive of behavior over a wide range of conditions, see "A Time-Temperature Relationship for Rupture and Creep Stresses," by Frank R. Larson and James Miller, published in this issue, pp. 765–775.

Contributed by the Metals Engineering Division and the Joint ASTM-ASME Committee on the Effect of Temperature on the Properties of Metals and presented at the Annual Meeting, Atlantic City, N. J., November 25–30, 1951, of The American Society of Mechanical Engineers.

Note: Statements and opinions advanced in papers are to be understood as individual expressions of their authors and not those of the Society. Manuscript received at ASME Headquarters, July 13, 1951. Paper No. 51—A-33.

Case 3. If the temperature fluctuates in a sawtooth wave an amount ΔT above and below normal in a uniform manner so that an equal fraction of the cycle is spent at each intermediate temperature between $+\Delta T$ and $-\Delta T$, then an integrated average life expenditure, E_3, for the whole cycle relative to E_T at normal temperature is given by

$$\frac{E_3}{E_T} = \frac{\sinh km\ \Delta T/100}{km\ \Delta T/100} \quad [6]$$

Effective Strength

In each of the three cases one may find an effective strength S_1, S_2, S_3, in psi relative to the nominal strength S_T at normal temperature by taking the reciprocal of the mth root of the expression for relative expenditures of life thus

$$\frac{S_1}{S_T} = \left[e^{km\ \Delta T/100}\right]^{-\frac{1}{m}} \quad [7]$$

$$\frac{S_2}{S_T} = \left[\cosh km\Delta T/100\right]^{-\frac{1}{m}} \quad [8]$$

$$\frac{S_3}{S_T} = \left[\frac{\sinh km\Delta T/100}{km\Delta T/100}\right]^{-\frac{1}{m}} \quad [9]$$

Table 1 summarizes these various formulas for easy reference. They are identical in form with the expressions given in the author's previous paper on creep behavior. However, the symbols bear a different significance in the present application.

TABLE 1 FORMULAS FOR RELATIVE LIFE EXPENDITURE AND EQUIVALENT STRENGTH FOR SIMPLE MODES OF VARIATION FROM STEADY TEMPERATURE CONDITIONS

CASE	TYPE OF VARIATION	RELATIVE LIFE EXPENDITURE	EQUIVALENT STRENGTH
1		$\frac{E_1}{E} = e^{Km\Delta T/100}$	$\frac{S_1}{S} = \left[e^{Km\Delta T/100}\right]^{\frac{1}{m}}$
2		$\frac{E_2}{E} = \cosh km\ \Delta T/100$	$\frac{S_2}{S} = \left[\cosh km\Delta T/100\right]^{\frac{1}{m}}$
3		$\frac{E_3}{E} = \frac{\sinh km\Delta T/100}{km\ \Delta T/100}$	$\frac{S_3}{S} = \left[\frac{\sinh km\Delta T/100}{Km\ \Delta T/100}\right]^{\frac{1}{m}}$

Note: *Case 1.* The temperature stays above normal all the time by an amount ΔT (or below by $-\Delta T$).

Case 2. The temperature stays above normal for half the time by an amount ΔT and below normal an equal amount for the other half of the time.

Case 3. The temperature fluctuates uniformly with time between a level ΔT above normal and an equal amount below normal so that an equal fraction of the time is spent at each temperature within this range.

(In each case the temperature variations are assumed to be slow enough to obviate any need to take account of thermal strains.)

There is not enough information in existence at present to say just how good these rules are. Claims have been made that strength at high temperature is reduced by temperature fluctuation and so these rules show. Engineers have to make designs and when they run tests and obtain a set of properties characteristic of a material at various temperatures, it is natural to accept these as cardinal properties independent of past history and without effect on the future. Indeed, without any better data to go by, such an assumption protected by a suitable factor of safety has to be made in order to use the data.

It is, of course, always wise to use care in the evaluation of data and not to go beyond reasonable limits in applying test results. The relationships here used to portray test results are often good for several hundred degrees of temperature variation. But this is not always so. At moderate temperatures the rate of increase of strength is much less and for a wide range above room temperature it used to be common practice to disregard any effect. Not only does temperature affect the strength but it is also likely to affect the relationship between stress and life characterized by the exponent "m."

In applying the foregoing easy rules, the values of k, m, and S_0 should be chosen for the region of maximum stress and temperature. Inaccuracies at lower stress and temperatures are not likely to affect the result seriously. However, for wide fluctuations it may be reassuring to make an actual integrated analysis of the cycle.

Example

The example given in the following is intended to illustrate the application of these formulas.

Fig. 1 shows the long-time rupture strength of 16-25-6 "Timken" material such as might be used as a wheel or bucket material in a high-temperature turbine. The slope of the lines indicates that the per cent expenditure of life m per per cent increase in stress, is 7.0, while the strength, S_0, for a life of 10,000 hr at 1200 F, is 24,000 psi.

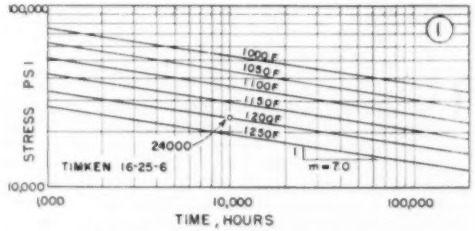

Fig. 1 Long-Time Rupture Strength of Timken 16-25-6 as Determined by Test

[(The strength for a life of 10,000 hr at 1200 F is 24,000 psi. This is a log-log plot and the slope of the lines is $m = 7.0$.) Usually there is a "knee" in the rupture line between 100 and 1000 hr and, for short-lived service, values of k and m corresponding to the other branch of the curve should be used.]

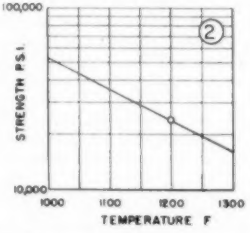

Fig. 2 Relation Between Nominal Strength for a Life of 10,000 Hr and Temperature

(From the slope of the line on this semilog plot the per cent loss in strength k per degree rise in temperature is determined. It is the reciprocal of the number of degrees corresponding to a strength ratio $e = 2.718$.)

Fig. 2 is obtained by cross-plotting from Fig. 1. As explained in the author's previous paper, the per cent change in strength k per deg F may be found by dividing 100 by the number of degrees corresponding to a strength ratio $e = 2.718$. Thus, in this case, $k = 100/250 = 0.40$, and $km/100 = 0.028$.

It is now possible to write Equation [3] for this particular material

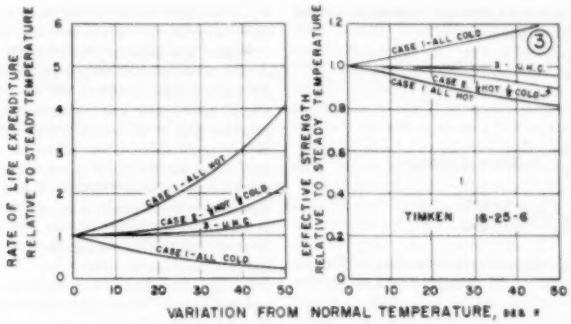

FIG. 3 EFFECT OF TEMPERATURE VARIATION ON RATE OF LIFE EXPENDITURE AND ON EFFECTIVE STRENGTH OF TIMKEN 16-25-6 STEEL FOR WHICH $k = 0.4$, $m = 7.0$, $km = 2.8$

(Case 1 shows the behavior when the member is too hot, or too cold, all the time; Case 2 when it is hot half the time and cold half the time; and Case 3, when the member varies uniformly from hot to cold spending an equal fraction of the time at each temperature.)

$$E = \frac{t}{10{,}000}\left[\frac{S}{24{,}000}\right]^{7} e^{0.028\,\Delta T}$$

Fig. 3 illustrates the effect of temperature variation on the life expenditure and effective strength of the material under simple cycles.

A proposed application is to operate on a stress and temperature cycle described for 1000 hr in Table 2. The temperature variations in this cycle are illustrated in Fig. 4. At each of the several temperature levels there is a fluctuation through a range of 100 F ranging from 50 F below to 50 F above average in the manner described by Case 3.

TABLE 2

Phase	Temperature, deg F	Fluctuation, deg F	Stress, psi	Duration, hr
A	1200	±50	20,000	100
B	1180	±50	18,000	100
C	1160	±50	16,500	100
D	1140	±50	15,000	100
E	1120	±50	13,500	100
F	1100	±50	12,000	500

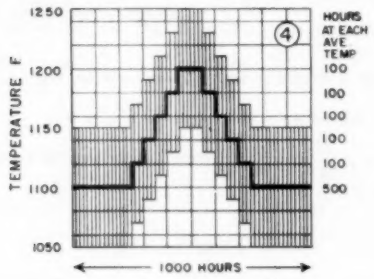

FIG. 4 SERVICE TEMPERATURE CYCLE

(Half the time is spent at an average temperature level of 1100 F with swings to 50 deg above and below. The other half is divided equally among the five other levels up to 1200 F. At each level the variation is 50 deg above and below.)

An operating life of 20,000 hr is desired and a factor of safety of 1.5 is required to take care of the possibility that the actual effective strength may be less than calculated. With a complex cycle of this nature, the procedure is to compute the fraction of life expended in each phase of the cycle and thus for the complete cycle. See Table 3.

TABLE 3

Phase	$\frac{t}{10{,}000}$	$\left[\frac{S}{24{,}000}\right]^{7}$	$e^{0.028\,\Delta T}$	Case 3	E
A	0.01	0.279	1.00	1.36	0.00380
B	0.01	0.134	0.575	1.36	0.00104
C	0.01	0.073	0.325	1.36	0.00063
D	0.01	0.037	0.185	1.36	0.00010
E	0.01	0.018	0.105	1.36	0.00003
F	0.05	0.008	0.061	1.36	0.00003
				Total	0.00533

Each column of this table corresponds to a term in the formula. The next to last column is the effect of the variation from average at each of the several levels. The total fractional life expenditure in the 1000-hr cycle is, thus, 0.00533, from which the life to rupture may be determined as $\frac{1000}{0.00533} = 187{,}000$ hr.

EQUIVALENT STRESS OR TEMPERATURE

For convenience, the stress which would lead to rupture in the same time at the nominal temperature of 1200 F, may be determined from Equation [1] and called the "equivalent stress" at 1200 F. This is

$$S = \left[\frac{L_0}{L}\right]^{\frac{1}{m}} S_T = \left[\frac{10{,}000}{187{,}000}\right]^{\frac{1}{7}} 24{,}000 = 15{,}800 \text{ psi}$$

Or from Equation [3] and the nominal maximum stress of 20,000 psi, one may determine an "equivalent temperature" which would lead to the same life

$$e^{km\,\Delta T/100} = \frac{L_0}{t}\left[\frac{S_0}{S}\right]^{m}$$

$$e^{0.028\,\Delta T} = \frac{10{,}000}{187{,}000}\left[\frac{24{,}000}{20{,}000}\right]^{7} = 0.192$$

$$0.028\Delta T = \log_e 0.192 = -1.652$$

$$\Delta T = -59 \text{ F}$$

$$T = 1200 - 59 = 1141 \text{ F}$$

FACTOR OF SAFETY

From either of these "equivalent" figures, one may determine the effective factor of safety with reference to a desired life of 20,000 hr as follows:

At 1200 F the equivalent stress is 15,800 psi whereas, according to Equation [1], the material is good for

$$S = \left[\frac{L_0}{L}\right]^{\frac{1}{m}} S_T$$

$$S = \left[\frac{10{,}000}{20{,}000}\right]^{\frac{1}{7}} 24{,}000 = 21{,}800 \text{ psi}$$

Therefore the factor of safety is $\frac{21{,}800}{15{,}800} = 1.375$.

At 20,000 psi stress and an equivalent temperature of 1141 F, the material according to Equation [3], making $E = 1$, is good for

$$S = \left[\frac{L_0}{t}\right]^{\frac{1}{m}} S_0\, e^{-k\,\Delta T/100}$$

$$S = \left[\frac{10{,}000}{20{,}000}\right]^{\frac{1}{7}} 24{,}000\, e^{0.239} = 27{,}500 \text{ psi}$$

Therefore the factor of safety determined in this manner is $\frac{27{,}500}{20{,}000} = 1.375$.

Thus it appears that the proposed design must have its stresses reduced by 9 per cent in order to have the desired factor of safety. Since the strength of the material is improved 0.4 per cent per deg, the same result could be secured by revising operating temperatures 22 F downward. Having made either one of these design revisions, the calculation may be repeated for assurance that the required figure of 1.5 has been attained.

The "Factor of Safety" for a stated life may be defined as what the material is good for divided by the equivalent stress applied in the cycle of stresses and temperatures encountered in operation. If the expected life under a proposed cycle of conditions has been determined as in Table 3 as L_c, the equivalent stress S_e for the cycle in question is

$$S_e = \left[\frac{L_0}{L_c}\right]^{\frac{1}{m}} S_T$$

The effective strength of the material for the required life L_r is $S_r = \left[\frac{L_0}{L_r}\right]^{\frac{1}{m}} S_T$ from which the Factor of Safety F_c may be written

$$F_c = \frac{S_r}{S_e} = \frac{\left[\frac{L_0}{L_r}\right]^{\frac{1}{m}} S_T}{\left[\frac{L_0}{L_c}\right]^{\frac{1}{m}} S_T} = \left[\frac{L_c}{L_r}\right]^{\frac{1}{m}}$$

At this point it may be noted that where a complete test plot in the form of Fig. 1 is available, it is possible to scale the total life for each stress and temperature and thus to compute directly the fractional expenditure in each phase of a cycle. When the temperature range is so great that there is a variation in the slope m it may be desirable to base cycle analysis on the actual test lines. However, an analysis based on the formulas is not likely to be very far off if the value of m corresponds to the highest temperatures in the cycle.

There remains a need to come back to the possible uncertainty in the procedure outlined which was mentioned at the start since any such uncertainty would have to be covered along with all other uncertainties by the over-all factor of safety.

Wilkes, in a paper presented at the fifty-third annual meeting of the American Society for Testing Materials, June, 1950,[4] gives the results of 100 to 500-hr tests on a number of "super-alloys" both in air and combustion gases both at constant temperature and with hourly cycles between 500 F and 1500 F. Wilkes finds most of the materials somewhat stronger when a part of the time is spent at low temperature than when the temperature is at a steady 1500 F. When the cycling is in an oxidizing atmosphere the strength may even be less than the strength in air at the top of the cycle. Under such severe cycles it is difficult to be sure that any credit can be given for the fraction of time at less than top temperature.

On the other hand, in more recent tests on Timken 16-25-6 material in hourly cycles between 1000 F and 1200 F, the 1000-hr strength appears to agree with what would be arrived at by calculation on the basis of the assumptions used here.

The author's conclusion is that one should not expect strength under cyclic conditions in excess of what these simple formulas indicate and that under severe conditions of temperature elevation or variation, or both, additional margins of safety may need to be provided.

Appendix

If one has a "Master Rupture Curve" of rupture strength versus the parameter $T(C + \log t)$ prepared as described in the Larson-Miller paper on "A Time-Temperature Relationship for Rupture and Creep Stresses," the values of k and m for use in evaluating the factor of safety under cyclic conditions may be found as follows:

Note the values of the parameter corresponding to two values of stress in the operating range. Let these be P_1 and S_1 and P_2 and S_2 respectively. Then the change of strength with temperature, k, expressed in per cent per deg F is

$$k = \frac{100\,(20 + \log t)\,(\log S_1 - \log S_2)}{\log e\,(P_2 - P_1)}$$

$$= 230\,(20 + \log t)\,\frac{\log S_1 - \log S_2}{P_2 - P_1}$$

for a life of 100,000 hr, $\log t = 5$ and $k = 5750\,\frac{\log S_1 - \log S_2}{P_2 - P_1}$

The slope of the time-stress rupture line, m, is

$m = \frac{(P_2 - P_1)}{T(\log S_1 - \log S_2)}$ where T is the absolute temperature in deg F.

Discussion

W. B. Hoyt.[5] The author points out that mechanical tests on stress-rupture specimens which have been tested for time periods approximately one half of their anticipated life fail to show any marked changes in the properties of the material. Are there any test data which show definite deterioration in the properties of materials which are approaching failure, that is, which have spent 90 or 95 per cent of their available life?

[4] "Stress-Corrosion Tests on Turbosupercharger Materials in the Products of Combustion of Leaded Gasoline," by G. B. Wilkes, Jr., ASTM Special Technical Publication No. 108, pp. 11–25.

[5] The M. W. Kellogg Company, Jersey City, N. J.

L. F. Kooistra.[6] The author has performed a real service for the designing and operating engineer of high-temperature turbines in developing a method of predicting the useful life of such equipment under varying operating conditions from the standpoint of stress and temperature. This development in essence is a mathematical accounting system in which operating hours at various stress and temperature levels can be evaluated on the basis of existing creep data, under the assumption that changes from one operating level to another, or rest periods during which the machine returns to no-load or room-temperature conditions, have no effect on creep behavior.

Very few published data seem to be available on the subject of creep performance of high-temperature materials under periodically interrupted or changing load conditions. H. J. Tapsell, P. G. Forrest, and G. R. Tremain[7] have reported on experiments, which, however, were of short duration (100–300 hr) and high frequency (2000 cpm) and, therefore, do not apply directly to varying turbine-load problems.

Some work was done under project "Squid"[8] on Armco iron and comparatively fast cycles. The results indicate that there is a substantial increase in creep rate for the slow cycle and that this effect is increasing when the interval of the cycle increases.

The method developed could be used with considerably more confidence and assurance if a series of simple creep tests, under various predetermined load changes could be conducted, which would determine the correctness of the assumption on which it is based. Any information the author may have on the effect of such load and temperature variations would be very much appreciated.

Author's Closure

Mr. Hoyt asks a rather exacting question. The author would be surprised if a group of specimens supposed to be identical should break with no more spread in life than 5 or 10 per cent. Roughly speaking, one might expect as much as 25 or 50 per cent variation in life for 5 per cent variation in strength.

So far as the author knows, there are few test data on the short-time properties of materials approaching long-time failure and such tests as are available show the opposite of what Mr. Hoyt's question anticipates. The author's impression is that the material maintains good short-time strength until it is so near to the end of its long-time life that failure at a minor fraction of its short-time strength is to be expected. Under such circumstances it would seem as if the impending failure at low stress is a matter of much graver concern than whether or not the short-time properties are still fully capable of being realized.

For instance, a low-alloy steel, whose composition is not important for this illustration, has a short-time tensile strength at 1000 F of 69,000 psi. Its 10,000 hour strength at the same temperature is 38,000 psi. A bar which had been in test for 7595 hours at 1000 F under a stress of 38,000 when loaded to failure at temperature broke at 68,000 psi.

Miller, Smith, and Kehl[9] concluded that "under slow rates of straining at elevated temperature the normal mode of failure of a metal is through the grain boundaries, and that intergranular failure of a metal is through the grain boundaries, and that intergranular failure does not necessarily indicate deterioration of the metal or lack of plasticity preceding fracture. It should be emphasized that even though considerable intergranular cracking may have occurred, the remaining sound metal may be no less ductile than it was originally, and may still withstand considerable bending or other rapid deformation."

Mr. Kooistra has very neatly epitomized what the author has attempted to do. The author concurs with Mr. Kooistra as to the desirability of conducting of some comparative series of tests under steady and cyclic conditions whereby the correctness of the assumptions might be verified. As the author pointed out, some work has been done but more would be welcome. However, it must be kept in mind that the conduct of such tests would displace still more fundamental tests on the evaluation of newer and better materials, whereas the evaluation of the differences due to cyclic conditions has always seemed to the author a matter of secondary importance even though by no means negligible. For this reason he has offered a means of calculating the effects in order to facilitate consideration without pressing the matter of test results. These will come in due time.

---

[6] Superintendent, Materials Division, Research and Development Department, The Babcock & Wilcox Company, Alliance, Ohio.

[7] "Creep Due to Fluctuating Stresses at Elevated Temperatures," by H. J. Tapsell, P. G. Forrest, and G. R. Tremain, *Engineering*, vol. 170, August 25, 1950, pp. 189–191.

[8] "Squid," Quarterly report of July, 1950.

[9] "Influence of Strain Rate on Strength and Type of Failure of Carbon-Molybdenum Steel at 850, 1000 and 1100 Degrees Fahr.," by R. F. Miller, G. V. Smith, and G. L. Kehl, Trans. American Society of Metals, vol. 31, 1943, p. 844.

High-Temperature Stress-Rupture Testing of Tubular Specimens

By L. F. KOOISTRA,[1] R .U. BLASER,[2] AND J. T. TUCKER, JR.[3]

A large percentage of the high-temperature alloys is used in tubular form but most of the high-temperature strength data for these materials are based on simple tension bar specimens. Testing these materials in the shape and condition in which they are used eliminates many of the discrepancies between test specimen and actual service. A method has been developed in which a tubular specimen under internal steam pressure and at a controlled temperature is tested in stress rupture. This method closely simulates actual service conditions, except for the external flue-gas atmosphere and the temperature gradient through the tube wall existing in heat-transfer service. A suitable environment can, however, be provided when service conditions are known. The test apparatus is described and a number of the test results are discussed in relation to similar data obtained on simple tension specimens. Failures obtained under test conditions are compared with similar failures suffered by tubes in actual service.

Introduction

CREEP and stress-rupture tests are generally performed on round-bar specimens under uniaxial tension. The results of such tests are, in most cases, used as a basis for design on structures for high-temperature application and to predict the useful life span of such structures (1).[4] In very few of these applications is the state of stress as simple as it is in the stress-rupture tensile specimen, and it is therefore almost always necessary for the designer to analyze a complex stress system before the uniaxial creep or stress-rupture data can be applied to the problem. The process of translation from simple tension to a complex plastic-state stress system is quite often complicated and in many cases involves factors of uncertainty. Considerable work has been done on the theoretical analysis to formulate the plastic stress-strain relationship in a tube under internal pressure (2).

Since rupture is seldom caused by stress only, considerations based purely on stress cannot give the whole answer. In order to simplify the task of interpretation between test data and application to design, it is of practical importance to test the materials of construction under loading conditions as closely analogous to actual service conditions as possible. It is equally important to have the material of the test specimen in the same metallurgical condition as that of the structure being used in service. It is therefore preferable that the metal of the specimen have the same steelmaking and fabricating history as that of the service structure. In the case of high-temperature tubes, all these requirements are very difficult, if not impossible, to fulfill simultaneously. In a simple tension test, for instance, the stress-rupture specimen generally requires a section of the material of sufficient dimension to accommodate a $^{3}/_{8}$-in-diam bar. The tube wall, however, is usually not of sufficient thickness to supply anything more than a subsize specimen which is too small to yield representative data. Also, the grain structure of the alloy may be quite different in a tube wall as compared to that of a bar, as a result of manufacturing operations.

In many of the stabilized austenitic materials nonmetallic compounds, such as carbides and nitrides, are formed in the interior of the metal. During the fabrication process these inclusions are aligned in the form of stringers in a longitudinal or axial direction. In a tension bar these stringers, as discontinuities, are parallel to the direction of stress but in a tube they are transverse to the direction of the principal stress.

With the great number of variables involved in the testing of high-temperature alloys, it is therefore imperative to eliminate as many dissimilarities as possible between the test specimen and the actual service structure. Since a large percentage of the materials of construction in the power and the process industry is used in tubular form, it appears of definite advantage to test them in this same form. To this end, tubular specimens made from full-sized superheater tubing have been tested in controlled-temperature electric furnaces with the stresses in the tube wall maintained by internal steam pressure. This method of testing produces the same stress pattern and the same internal atmosphere in the tube as in actual superheater service.

Future tests are contemplated in which the atmosphere surrounding the specimen will also be controlled.

History

Tubular stress-rupture testing is not new. Tests on full-sized superheater tubes were conducted by The Babcock & Wilcox Tube Company under the direction of H. D. Newell around 1931. The metals tested were carbon steel, 4-6 Cr plus tungsten, 18-8, and 18-8 Si. The results on these tests, however, were discouraging, in that the furnace used for bringing the specimens up to temperature was destroyed repeatedly by the explosive force of the rupture. Due to these and other experimental difficulties, tubular stress-rupture testing was discontinued at that period.

Some unpublished experimental data exist on room-temperature creep tests conducted on lead tubes in The Babcock & Wilcox laboratory at the Barberton Works about 1935.

Experimental work was conducted on 4-in-OD carbon-moly and 4-6 chrome-moly tubes (3) in 1938–1942, under the auspices of the Joint (ASTM-ASME) Committee on Effect of Temperature on the Properties of Metals, by Norton (3, 4, 6). Theoretical

[1] Superintendent, Materials Division, Babcock & Wilcox Company, Research and Development Department, Alliance, Ohio. Mem. ASME.

[2] Assistant Superintendent, Materials Division, Babcock & Wilcox Company, Research and Development Department, Alliance, Ohio.

[3] Supervisor, Stress Analysis Group, The Babcock & Wilcox Company, Research and Development Department, Alliance, Ohio.

[4] Numbers in parentheses refer to Bibliography at end of paper.

Contributed by the Metals Engineering Division and the Joint ASTM-ASME Committee on Effect of Temperature on the Properties of Materials and presented at the Annual Meeting, Atlantic City, N. J., November 25–30, 1951, of THE AMERICAN SOCIETY OF MECHANICAL ENGINEERS.

NOTE: Statements and opinions advanced in papers are to be understood as individual expressions of their authors and not those of the Society. Manuscript received at ASME Headquarters, August 1, 1951. Paper No. 51—A-44.

relationships in a tubular member under plastic conditions were developed by Soderberg in 1941 (5) and 1942 (6).

The stress levels in these specimens were designed to produce elongations of relatively small magnitude, and the instrumentation was such that creep measurements could be taken to determine axial and circumferential elongations. Although rupture was not contemplated, it did occur on one of the hemispherical ends.

In connection with the design of high-temperature low-pressure superheaters, considerable work was done in the Babcock & Wilcox laboratory on different alloy tubes at 1600 F in 1943 and 1944. These tubes were placed in a common furnace and were pressurized by small electric boilers. The furnace was fired with natural gas under semiautomatic control. Neither gas nor specimen temperatures could be controlled very accurately.

The data obtained were more of a practical and operating nature. With both internal steam and external flue-gas atmospheres present, valuable data on hydrogen formation, steam dissociation, and metal oxidation and corrosion were obtained. Several stress-rupture failures occurred, but the value of these data as far as strength at elevated temperatures is concerned is rather insignificant.

The metals included in these tests were steel (849), Croloy 3M, Croloy 9, Croloy 12, 16-13-3, 18-8, 18-8 Cb, and 18-8 Si. Experience gained during these tests concerning operational troubles in the testing of tubular specimens under internal pressure was of considerable value in the development of the experimental technique described in this paper.

Description of Apparatus

Tubular stress-rupture or tubular creep tests up until a few years ago have been too costly: first, because the tubular specimens used were too expensive; and second, because quite regularly the electric furnace used for heating the specimens was either damaged or destroyed when a specimen ruptured. In designing the present apparatus an attempt was made to eliminate the troubles encountered on former experiments.

For the sake of safety in the present setup, as well as for better room-temperature control, a group of six furnaces were placed in a steel-plate enclosure. An exterior view of this enclosure is shown in Fig. 1. The individual units, however, are independent in so far as pressurizing equipment and furnace temperature control are concerned. Each unit consists of a specimen, an electric furnace, a temperature control, and a pressurizing system. The arrangement of the component parts is shown in Fig. 2.

Based on previous experience, the requirements of a test unit are as follows:

1 The specimen must be representative of actual tubes in service.

2 The specimen must be maintained at the testing temperature within close temperature limits.

3 The explosion force released at rupture of the specimen should be reduced to a minimum.

4 The furnace must have considerable strength to withstand the specimen explosive force.

5 The pressurizing system must be capable of delivering a nearly constant pressure up to about 10,000 psi.

6 The pressurizing system must allow for sufficient volume expansion to take care of the increase in volume of the specimen during the test.

7 If testing superheater tubing materials, the internal atmosphere should be high-pressure steam.

8 The external atmosphere should be representative of contemplated service conditions.

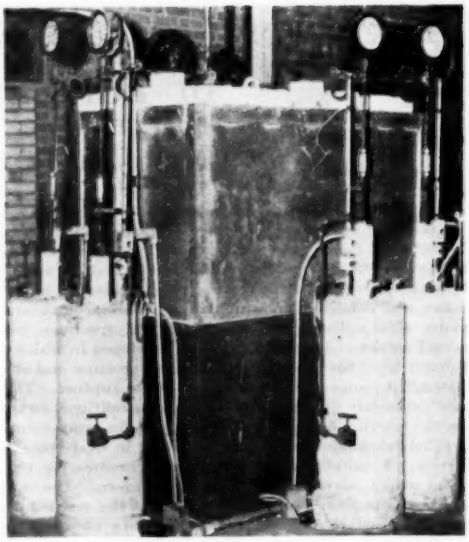

Fig. 1 Exterior View of Tubular Stress-Rupture Setup Showing Plate Enclosure and Pressure-Supply Reservoirs

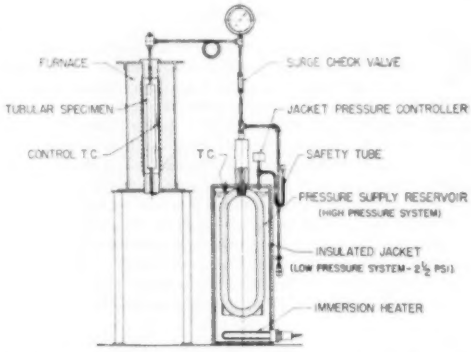

Fig. 2 Diagrammatic Arrangement of Tubular Stress-Rupture Unit

All requirements from 1 to 7 have been satisfied to a large degree in the present apparatus. Item 8 will be included in future tests when the external environment is defined.

A brief description of each component part will serve to give the characteristics of the test setup.

The Specimen

The construction details of the specimen are shown in Fig. 3. In order to minimize the explosive force during rupture, the internal volume of the tubular specimen has been reduced as much as is practicable. This was done by inserting a close-fitting solid core taking up nearly all of the internal volume. The specimen is about 10 diam long and is closed on the ends by means of round plugs welded into the tube. One plug is provided with a small

tube connection to the pressurizing system. The tube and the small dummy pipe on the bottom are the only metallic parts conducting heat through the furnace walls so that heat losses can be reduced to a minimum. Regular superheater tubing is used "as received" from stock without machining or any other refinement or preparation.

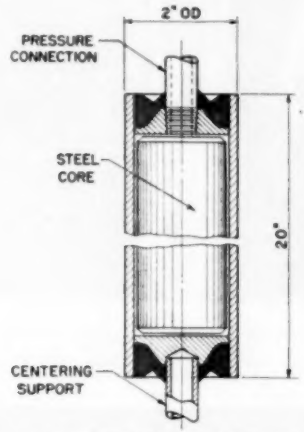

FIG. 3 DESIGN OF TUBULAR SPECIMEN

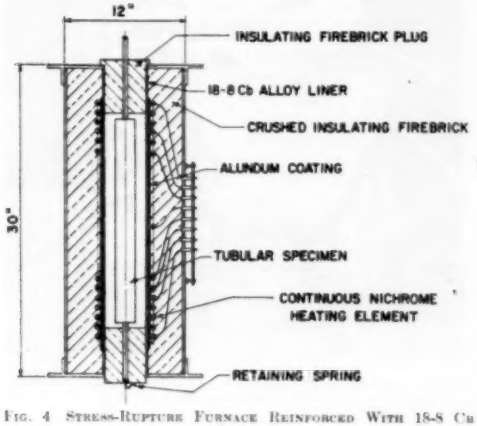

FIG. 4 STRESS-RUPTURE FURNACE REINFORCED WITH 18-8 Cb LINER

THE FURNACE

The furnace construction is shown in Fig. 4. In so far as the electric-resistance heating coils are concerned, this furnace can be treated the same as any other creep or stress-rupture furnace. The sectional winding is tailored to provide an even temperature over the central portion (10 in.) of the specimen. A typical temperature gradient is shown in Fig. 5.

The distinguishing feature is that this furnace is reinforced on the inside wall by means of a $4^1/_8$-in-OD × 0.095-in-wall 18-8 Cb tube. Except on the short-time high-pressure tests, this lining has withstood the explosive force of the tube rupture very well.

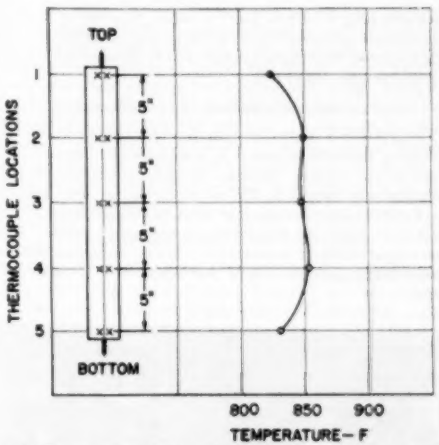

FIG. 5 TEMPERATURE GRADIENT AT 850 F ON TUBULAR STRESS-RUPTURE SPECIMEN

FIG. 6 VIEW SHOWING SPECIMEN ASSEMBLY BEING PLACED IN FURNACE

For the present low-temperature operation this liner runs the full length of the furnace, but for high-temperature operation it should be about 2 in. shorter on each end to reduce metallically conducted heat losses.

The furnace casing is 12 in. in diam × 30 in. long, and is reinforced top and bottom with heavy steel caps. The insulating filler is crushed K-23 insulating firebrick.

The force of the explosion is prevented from going upward by the strongback shown above the specimen in Fig. 6. The lower

refractory plug is held in place vertically by a spring wire connected to the centering pipe on the bottom of the specimen. This plug is ejected when rupture occurs, and the force of the explosion is thus expended downward.

Temperature Control and Measurement

Temperature is controlled by means of a Leeds and Northrup indicating controller actuated by a thermocouple located at the center of the furnace. Specimen temperatures are measured by thermocouples peened in the specimen wall at 5-in. intervals. Fig. 6 shows a complete specimen assembly being lowered into the furnace on which the thermocouples are clearly visible. Specimen temperatures are measured by a Brown multipoint electronic temperature indicator. Fig. 7 shows a view of the instrument board.

Fig. 7 View of Instrument Board

The Pressurizing System

Pressure is supplied to the top of the specimen through the stainless-steel connecting tube from a high-pressure water reservoir, Fig. 8. This reservoir, which is made to safely withstand internal pressures up to 10,000 psi, is placed in a constant-temperature water jacket. The water in the jacket is kept at constant temperature by means of an immersion-type heater operated from a diaphragm-type pressure switch. By maintaining the pressure in the jacket constant at $2^1/_2$ psig, the temperature is held at 220 F. A mercury-filled U-tube, which is designed to blow out at 4 psig, is connected to the jacket as a safety feature. In a constant-temperature room or laboratory the jacket is not necessary.

The highly pressurized water in the reservoir has considerable compressibility so that it can serve as a steady high-pressure source. When the internal volume of the specimen increases due to plastic deformation, the pressure would drop proportionately. This drop in pressure allows the water in the pressure reservoir to expand slightly and deliver a minute quantity of water to the specimen. At the high testing temperature this water will immediately flash to steam and become superheated. The volume

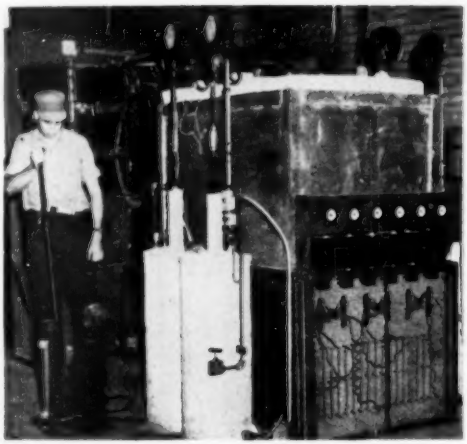

Fig. 8 View Showing Specimen Being Pressurized by Means of 30,000-Psi Hand Pump

(Small instrument panel containing timers, relays, switches, and shunts is visible on near side of enclosure.)

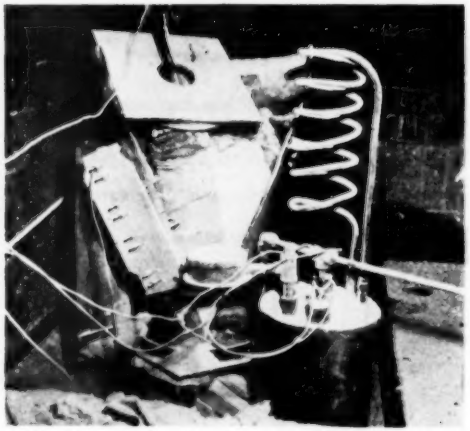

Fig. 9 View Showing Damage to Furnace Caused by Short-Time Rupture Test

of the high-pressure reservoir (5 gal) is such that only a very small drop in water pressure results over long periods of time. Usually a weekly correction of system pressure is more than adequate to maintain virtually constant load on the specimens. Pressure corrections are made by means of a small hand-operated 30,000-psi pump. This operation is illustrated in Fig. 8. The two white cylinders in the foreground are jacketed pressure reservoirs.

A surge-check valve is placed in the line between the pressure reservoir and the specimen. Immediately after rupture occurs this valve closes automatically and prevents the expanding volume of water from being discharged rapidly into the hot furnace.

A microswitch is mounted in the housing of the gage in such

manner that the linkage of the gage trips off the furnace relay and the timer when the pressure drops below a fixed amount after rupture.

In addition to the six-unit battery, one test unit was designed for obtaining "short-time-tensile" values. These tests are usually conducted at comparatively high pressures and the rupture occurs in a more violent manner. It was therefore deemed advisable to place this unit in a pit for safe operation. Fig. 9 shows that this was a justifiable precaution.

Test Procedure

Sections of regular superheater tubing are cut to the specimen length of 20 in. and measured for initial dimensions. Outside diameters are taken at 90-deg points at $2^1/_2$-in. intervals along the specimen length. In all cases, these measurements have been so near to the nominal diameter that this value can be used throughout in the stress calculations. Wall-thickness measurements are taken at 45-deg points at each end previous to welding the end plugs into the specimen. The wall thickness used for calculation purposes is defined as the average of the minimum values measured on each end of the tube. Measured differences are relatively small.

After the specimen is assembled, 22-gage chromel-alumel thermocouples are peened into the wall at 5-in. longitudinal intervals. The K-23 furnace closure plugs are then fastened to the pressure pipe at the top and the centering pipe at the bottom. The lower closure plug makes a snug fit with the liner as the specimen is placed in the furnace from the top and thus effects a tight seal. In addition, the upper closure plug is sealed with high-temperature mortar, and after the strongback has been placed on top of the specimen, the space between the strongback and the top of the furnace is further insulated with insulating blocks. The complete assembly of specimens with thermocouples, sealing plugs, and strongback, is shown ready for insertion into the furnace in Fig. 6.

The top outlet of the T-fitting located above the specimen serves as a vent at the highest point of the pressure system. After all the air is vented from the system through this connection, a room-temperature hydrostatic test of 1000 psi pressure is applied to check for leakage. Absolute tightness of the system is imperative because with the combination of relatively small volume and long duration of test, even the minutest leak would cause an objectionable drop in operating pressure. When the system has been found pressuretight, the pressure is brought back to zero. The specimen and the pressure-supply reservoir are then brought up to their respective temperature levels.

After operating temperature has been reached, the system is brought up to test pressure slowly by means of adding distilled water with the 30,000-psi hand pump as shown in Fig. 8. This pressure is maintained throughout the life of the specimen by making slight water additions in the same manner during the periodic checks.

A series of tests on a particular tube size and material is started with short-time high-temperature tensile tests on duplicate specimens. This information is used to decide upon the stress and pressure levels for the first few specimens of relatively short-life tests. These tests in turn will furnish information for the succeeding tests of increasingly longer life. Stress levels for the final test are aimed at a 10,000-hr life which is considered sufficiently long for further extrapolation. A progressive stepwise procedure of estimating the loading for the next-longer rupture time from the previous test is fair assurance against loading a specimen too low, which would extend its rupture life to an unreasonably long period.

Accuracy of Measurements and Controls

The maximum temperature gradient over the central 10-in. length of the specimen was ±10 F. Temperature variations on any one point within the test length were controlled within ±3 F.

Internal pressure on the specimens was maintained within ±25 psi. The frequency of pressure correction depends on many factors, such as stress level, testing temperature, ratio between pressure-system volume and specimen dilation, and micro leakage and diffusion through the tube wall. However, on the average weekly pressure corrections were sufficient for maintaining system pressures at testing level.

Dimensional measurements of diameter and wall thickness were obtained on a simple statistical basis with an ordinary micrometer and without establishing index points or datum references. No special machinery of any kind was used.

Discussion of Results

In developing a method of testing materials, the first questions that have to be answered are the following:

1 How does it compare with existing methods?
2 What significant differences exist?
3 What effect do these differences have on present design values?

On the present development these questions, of course, could best be answered by conducting tubular stress-rupture tests on a material on which considerable conventional data were available or on which conventional tests were currently being conducted. At the time the preliminary tests of the tubular stress-rupture apparatus entered the state of dependable operation, a program on stress-rupture testing of SA-210 steel was being started, and it therefore appeared timely to conduct a parallel tubular stress-rupture program on the same type of material for comparison.

Two sources of steel were used for the tubular stress-rupture tests and one for the tensile bar test. The chemical analysis, heat-treatment, and oxidation practice are given in Table 1.

The original physical properties at room temperature as well as those required by ASTM standard specifications are given in Table 3.

TABLE 1 SA-210 MATERIALS TESTED

	Specimen type	Chemical analysis, per cent							Heat-Treatment
		C	Mn	P	S	Si	N	Al*	
Steel A	Tube	0.22	0.54	0.009	0.035	0.12	0.003	0.030	H. F. no heat-treatment
Steel B	Tube	0.35	0.48	0.010	0.036	0.15	0.003	0.025	1650 F normalized
Steel C	Bar	0.23	0.55	0.01	0.02	0.14		0.02	$^1/_2$ hr, 1300 F, furnace-cooled
Standard specifications ASTM A-210-46		0.35 Max	0.80 Max	0.040 Max	0.045 Max	0.10 Min			Annealed at 1300 F min for H. F. tubes

Note: Deoxidation Practice:
Steel A 2.72 lb. 50 per cent FeSi per ton + 1.50 lb Al per ton
Steel B 5.49 lb. 50 per cent FeSi per ton + 1.37 lb Al per ton
Steel C 6.10 lb. 50 per cent FeSi per ton + 1.60 lb Al per ton
* Metallic aluminum

TABLE 2 SUMMARY OF RESULTS

	Specimen Type Note (a)	Temp. °F	Min. Wall inches Note (b)	Internal Press., psi	Stress, psi Note (c)	Rupture Time Hours	Elong. %	Red. of Area %
Steel A	Tube	850	0.156	9600	51,900	short time	4.1	
			0.168	6800	33,700	36.1	2.7	
			0.167	5800	28,900	112.4	3.2	
			0.161	4800	25,000	744.2	8.3	
			0.168	4000	19,800	2969.8	10.4	
			0.167	3600	18,000	5682.0	6.5	
			0.159	3100	16,400	10591.0	8.6	
Steel A	Tube	950	0.159	8000	42,300	short time	8.8	
			0.157	5000	26,800	8.0	8.1	
			0.163	4410	22,600	28.0	12.3	
			0.161	3700	19,300	98.8	5.4	
			0.166	3150	15,800	327.7	8.3	
			0.170	2750	13,400	711.9	9.4	
			0.161	2100	10,900	2404.0	11.4	
			0.161	1700	8,900	6661.3	11.5	
Steel B	Tube	850	0.152	5400	30,100	13.2	14.9	
			0.152	4400	24,500	64.8	11.6	
			0.149	3700	21,100	399.4	14.9	
			0.156	2850	15,400	2851.2	25.4	
Steel B	Tube	950	0.156	5000	27,100	1.4	14.0	
			0.157	2500	13,400	197.8	21.8	
			0.157	2000	10,800	483.6	14.3	
			0.154	1650	9,100	1287.2	14.0	
			0.154	1500	8,200	2951.3	19.1	
Steel C	Bar	850			27,000	144.8	38.0	57.5
					25,000	203.8	41.2	52.2
					23,000	449.8	29.6	38.9
					21,600	793.8	43.2	42.9
					18,000	2566.5	31.0	38.3
					16,500	8930.7	37.6	22.1
					15,000	still running		
					13,500	still running		
Steel C	Bar	950			20,000	20.4	29.5	43.2
					18,000	87.3	31.6	37.3
					16,800	235.6	27.2	35.4
					12,800	983.1	26.4	31.9
					10,500	2384.0	22.0	26.8
					8,500	8261.0	21.5	22.3
					7,500	still running		

NOTE:
a Tubes were 2 in. OD × 0.150 in. min wall. Bars were 0.505-in-diam standard specimens.
b Min wall = average of the minimum wall thicknesses measured at both ends of specimen.
c Tube stresses were calculated using formula

$$\text{Stress} = \frac{\text{Pressure} \times \text{ID}}{2 \times \text{min wall thickness}}$$

Elongation is circumferential for tubular specimens and axial for bar specimens.

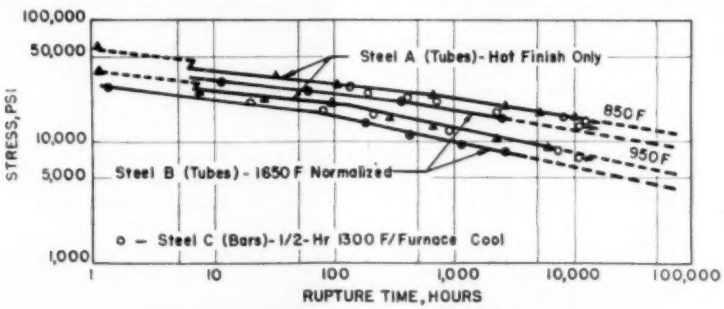

FIG. 10 STRESS-RUPTURE CURVES FOR SA-210 TUBES AND BARS

TABLE 3

	Ultimate strength	Yield point	Elongation % in 2 in.	Hardness Rockwell B
Steel A	79400	60800	50	70–79
Steel B	71800	51000	50	71–83
Steel C[a] bar	61000	32500	69.8	70.5
3-inch OD tube	72600	49550	35.5	75–77.5
1-inch OD tube	80400	50800	38	71–73
ASTM SPEC's. A-210-46	60000	37000	25	79 max.

[a] Physical properties on steel C were determined on 0.505-in. standard test bars and on longitudinal sections of a 1-in and a 3-in-diam tube. There appears to be a noticeable increase in room-temperature properties with an increase in the "working" of the material.

The stress-rupture data for tubular as well as bar specimens are given in Table 2 and are plotted in Fig. 10. Although steels A and B have substantially the same chemical analysis, a consistent difference in stress-rupture life was obtained on them. The metallurgical characteristics that may be involved in this difference will be discussed separately.

The plotted data show good consistency for each heat by itself with very little scatter from the straight-line logarithmic plot. Steel SA-210, similar to many other steels and alloys, shows a distinct difference between various heats within the specification range, again indicating the advisability of reporting stress-rupture values as a band rather than a single curve. Although the two curves shown are not necessarily the extreme boundaries of the band for SA-210 steel, the points obtained on the bar specimens fall within the band indicated by steels A and B. Within the limits of the presented data the tubular stress-rupture tests do not show any striking difference from the uniaxial tests. A great deal more work, however, has to be done before any definite conclusions can be drawn on these relationships. Tests on other steels and particularly austenitic alloys are contemplated.

Metallurgical Considerations

Metallurgical investigation of the test ruptures brought out that all these failures had been initiated by longitudinal oxide notches in the outside surface. Shallow transcrystalline oxide notches were present in the outside surface of both steels A and B prior to the test, as a result of their fabrication history. On the high stress loading, leading to short-time rupture (one hour), failure is entirely transcrystalline at 850 F as well as at 950 F and is accompanied by severe plastic crystal deformation in the vicinity of the rupture.

With increasing test duration, intercrystalline oxide notches are formed in the external surface. Under loads producing failure in about 700 hr, ruptures are already partly intercrystalline; and with a stress-rupture life of over 1000 hr, fracture is entirely intercrystalline. Plastic crystal deformation in the immediate vicinity of the rupture was evident in almost all cases but in decreasing degree with increasing rupture life.

At the internal surface, oxide notch formation is considerably less pronounced than at the outside surface. With increasing test duration, the oxide formed on the internal tube surface gradually advances in rootlike penetrations along the grain boundaries. Occasionally a somewhat deeper V-shaped penetration was observed; but, in general, the depth of oxide penetration was shallow and did not extend beyond the first layer of crystals. Carbide spheroidization in situ was almost complete after a rupture time of about 750 hr at 850 F and less than one-half hour at 950 F. Near the surface and in the plastically deformed metal adjacent to the rupture the carbide also showed considerable coalescence. After 700 hr at the two testing temperatures carbide agglomeration increased progressively with increasing test duration.

Steel A displayed a somewhat larger grain size in its initial condition than steel B. This larger grain size is believed to be at least partly responsible for the slightly higher stress-rupture strength displayed by steel A. It is interesting to note that steel A, displaying the higher stress-rupture strength was appreciably lower in carbon and had a higher metallic aluminum content. Steel B showed a slightly higher degree of banding than steel A which may have had some adverse effect upon the stress-rupture strength of this material.

Steel B formed graphite nodules at 950 F after some 1300 testing hours while steel A was free of graphite after 2400 testing hours at the same temperature and under a higher stress. The metallic-aluminum content is the dominant factor for increasing the tendency toward graphitization and since it is higher in steel A than in steel B, the observed results are in conflict with this criterion. Although steel B has a higher carbon content than steel A, this fact alone would not be a satisfactory explanation. The chemical analysis therefore offers no explanation for this difference in susceptibility to graphitization. It is beyond the scope of this paper to determine the metallurgical reasons for the difference in results obtained on the two steels. However, it might be well to mention here the possibility that submicroscopic nonhomogeneity is responsible for the observed difference in the graphitization behavior and at least to some extent for the lower stress-rupture strength of steel B.

Mode of Failure

The magnitude and mode of failure changes considerably with increasing rupture time as indicated in Fig. 11 by the series of test failures at 950 F. It is evident that violent or explosive rupture

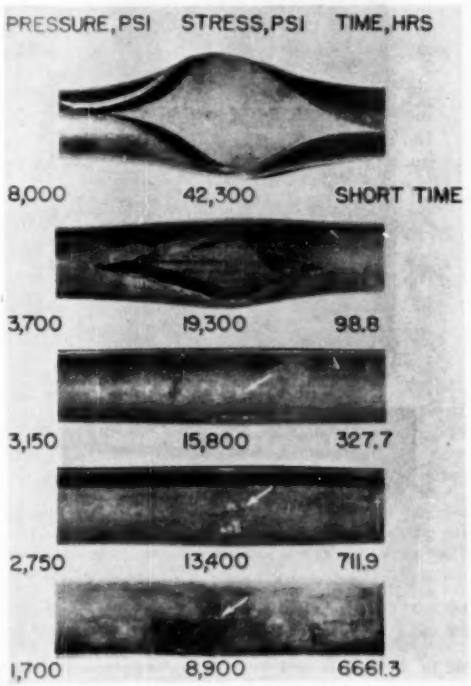

Fig. 11 Mode of Failure With Varying Stress-Rupture Life in SA-210 Tubing at 950 F

becomes less likely for the longer-life specimens. This is to be expected because these specimens are under lower pressure and stress, and the rupture defects develop in a more gradual manner.

In order to determine whether or not the mode of failure produced during the stress-rupture test is representative of failure suffered by tubes in actual high-temperature service, a comparison was made with several service failures which have been investigated in the past. One such comparison is shown in Fig.12. The service failure is shown on the left in photographs *a* and *b* and the stress-rupture failures on the right in photographs *c* and *d*.

The service failure is a superheater tube operated at a metal temperature of 985 F and generally shows the results of 17,500 hr of exposure to flue gas and its constituents. The service tube has a rougher-appearing surface due to the greater degree of general scaling as a result of so much longer exposure and somewhat higher temperature.

As a further result of longer exposure to a higher temperature, the service tube displayed complete carbide spheroidization and carbide coalescence whereas the carbide in the stress-rupture tube was only spheroidized in situ and did not display diffusion and agglomeration.

The mode of failure, however, is very much alike for the two ruptures. It is initiated as a number of parallel longitudinal oxidation notches on the outside surface of the tube. The bottoms of these notches progress inwardly by way of intercrystalline oxidation. When they advance beyond mere surface defects and measurably begin to reduce the effective tube-wall thickness, the bottoms of the notches begin to suffer the effects of stress concentration in a gradually increasing degree. This in turn accelerates the oxidation progress and so on until ultimate failure occurs.

Comparison of the various tubular stress-rupture failures to a considerable number of service failures, investigated during the past several years, furnishes definite evidence that the ruptures produced in the test described in this paper are similar to actual service failures and conversely that most service failures are stress-rupture failures.

Conclusions

1 An experimental technique for testing materials in tubular form has been developed.

2 The data obtained on tubular stress rupture with this apparatus are consistent with existing data. Test points plotted on logarithmic co-ordinates satisfy the straight-line function with very little scatter. These results are obtained by means of generally available control methods.

3 The mode of failure obtained with the tubular stress-rupture method of testing is similar to failures on tubes in actual high-

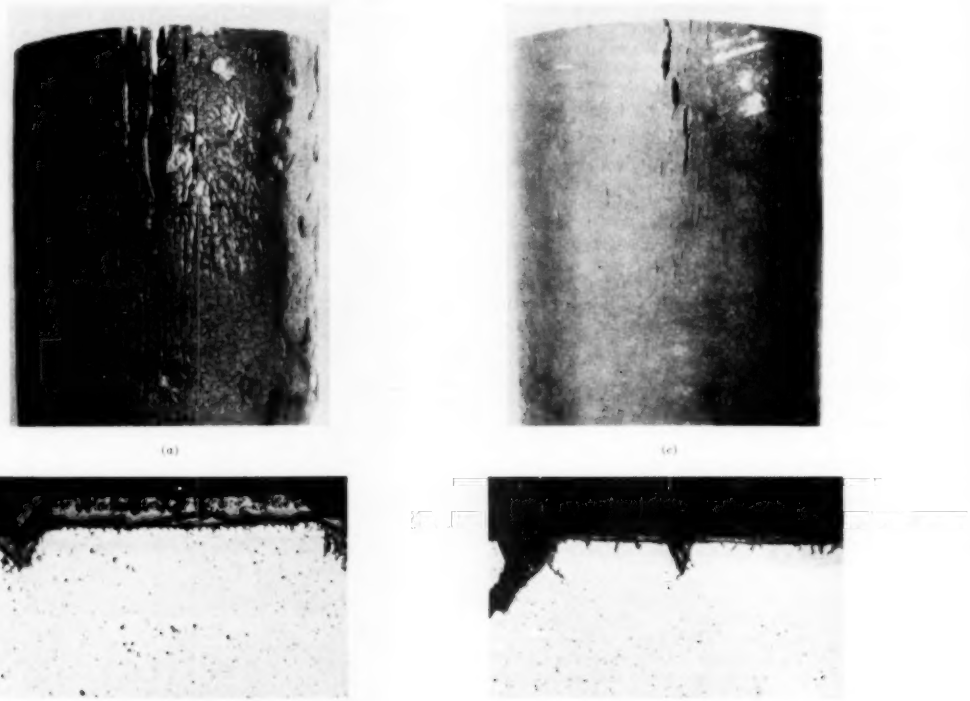

Fig. 12 Comparison of a Tubular Stress-Rupture Failure With a Superheater Tube Which Failed in High-Temperature Service

(*a*, External appearance of rupture, ×1½; *b*, microstructure and external tube surface, ×50. Service failure—tube temperature 985 F [measured with thermocouple]. Failure occurred after 17,500 hr. Analysis of steel, C 0.29, Mn 0.41, Si 0.18, metallic Al 0.035; *c*, external appearance of rupture, ×1; *d*, microstructure and external tube surface, ×50. Tubular stress-rupture failure—950 F, stress 14,830 psi, 711.9 hr to rupture, 9.4 per cent elongation.)

temperature service. The method is therefore closely representative of actual practice.

4 Stress-rupture results obtained on standard 0.505-in-diam tensile coupons of a representative SA-210 material fall within the boundaries of the tubular data band. This fact supports the tentative conclusion that tubular stress-rupture results for SA-210 material do not indicate any serious fundamental discrepancies in the use of existing uniaxial results.

5 Tubular stress-rupture test data obtained on two heats of SA-210 steel exhibit a consistent difference in high-temperature strength of about 20 per cent. This is not unusual, since a spread of high-temperature values within specification limits has been found on many steels and alloys. These results only r' rate the validity of representing such values with a band rather an a single line plot.

6 The demand for accuracy of measurements is quite modest and does not require more than ordinary tools available in any laboratory.

Remarks

Tubular stress-rupture testing is in its infancy and the data presented here are a good indication of its possibilities. The apparatus described can be simplified considerably. Tests on subsize specimens have been started in an attempt to reduce space and electric power requirements. Expectations are that a more advanced development of the apparatus will take up less floor space and will require less load on a laboratory air-conditioning system than conventional machines. This in turn will make possible a greater number of units and an increase in data-producing capacity which is urgently needed by the industry. The method and the apparatus in its present trend of development is of a practical economic nature and rather avoids academic exactitude.

In the course of developing the method various materials were spot-tested. Much more work, particularly on austenitic alloys, is required. Data on elongation at rupture proved to be very useful as a criterion in the investigation that led to the adoption of the new ASME formula for calculating allowable tube wall thicknesses.

Another method of testing high-temperature tubular materials almost entirely simulating high-temperature superheater conditions has been under development for some time by the authors' company. In this apparatus steam is flowing inside the tube specimen and heat is flowing through the tube wall establishing an actual and representative temperature gradient through the wall. The rate of elongation for these tests is contemplated to fall in the creep range. Some data on "tubular-creep" may be available in another year.

Acknowledgment

The authors want to express their appreciation for the help and active co-operation rendered by their fellow workers; and in particular to Messrs. D. E. Price and C. R. Culp for carrying out the tests, and to Dr. F. Eberle and V. E. Stanton, Jr., for making the metallurgical investigations.

BIBLIOGRAPHY

1 "The Creep and Stress-Rupture Testing of Steam-Boiler Materials," by J. B. Romer and H. D. Newell, presented at the Annual Meeting of ASME, 1950.

2 "Utilization of Creep Test Data in Engineering Design," by R. W. Bailey, Proceedings of The Institution of Mechanical Engineers, London, England, vol. 131, 1935, pp. 131–269.

3 "Creep in Tubular Pressure Vessels," by F. H. Norton, Trans. ASME, vol. 61, 1939, pp. 239–245.

4 "Progress Report on Tubular Creep Tests," by F. H. Norton, Trans. ASME, vol. 63, 1941, pp. 735–736.

5 "Interpretation of Creep Tests on Tubes," by C. R. Soderberg, Trans. ASME, vol. 63, 1941, pp. 737–748.

6 "Report on Tubular Creep Tests," by F. H. Norton and C. R. Soderberg, Trans. ASME, vol. 64, 1942, pp. 769–777.

7 "The Creep of Lead and Lead Alloys Used for Lead Sheathing," by H. F. Moore and N. J. Alleman, University of Illinois Bulletin No. 243, 1932.

Discussion

S. B. Black.[8] This paper is timely and furnishes a partial answer to the ever-recurring question regarding the applicability of unidirectional high-temperature rupture tests to actual design problems involving multidirectional stresses.

In the present instance, the effect of a longitudinal stress equal to one half of the tangential hoop stress does not appear to affect rupture strength as indicated by comparison with rupture tension-test bars.

Within the limited range of these tests, it appears that the practice of designing for elevated-temperature service upon the basis of maximum stress is vindicated. More tests of this type are needed to prove conclusively the validity of this assumption.

The excellent quality of the tests can be demonstrated by plotting the log of rupture stress against the parameter $T(20 + \log t)\ 10^{-3}$, Fig. 13, where T = absolute temperature

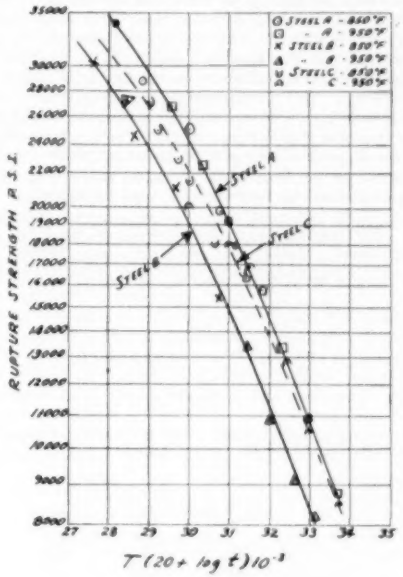

Fig. 13

(F deg), and T = hr to rupture. The use of this parameter enables tests for different temperatures to be compared by causing test points of any one material to fall on a single master curve.

C. L. Clark.[9] A need has long existed for rupture test data on tubular specimens for comparison with similar results from

[8] Mechanical Design Section, Turbine Engineering Division, General Electric Company, West Lynn, Mass.

[9] Metallurgical Engineer, Special Steel Development, Steel and Tube Division, The Timken Roller Bearing Company, Canton, Ohio. Mem. ASME.

bar specimens tested in tension, and it is gratifying to find that the authors are investigating this problem so thoroughly with their very extended-time tests.

In 1925 the writer undertook similar type tests on Grade A and B pipe of ASTM Specification A106 and Enduro metal (18 per cent Cr steel). The findings were presented before this Society[7] as well as before the American Society for Metals.[8] The refinements of our testing procedures or the duration of the tests were not comparable to those of the authors but the results were in agreement with respect to the effect of time on the type fracture and the fact that a plotting of stress and fracture time resulted in straight-line relationships.

We are not in complete agreement with the authors' statement that subsize specimens taken from the tube wall are too small to yield representative results. This may be true for the thinner-wall superheater tubes but we have conducted a great number of rupture tests on specimens taken from walls of 0.300 to 0.400 in. thickness and have found the results to be comparable to those from the 0.505-in-diam specimens.

Likewise with respect to the authors' statement that tubes may show entirely different properties in the transverse, as compared to the longitudinal direction, we have conducted many rupture tests, particularly on tubes after service, in which the specimens were taken in both directions. The steels involved include carbon, 0.50 Mo, 5 Cr Mo, and 18-8 stainless. In every case not only was close agreement obtained in the times required for fracture under the same stresses, but also in the total ductility to fracture. As a specific example, 5 longitudinal and 5 transverse specimens were taken completely around the circumference of an 18-8 tube that had been in 1200 F service for 60,000 hr. All were subjected to a stress of 20,000 psi at 1200 F. The fracture times for the longitudinal specimens ranged from 155 to 210 hr, and those for the transverse, from 140 to 190 hr. The corresponding ranges in total elongation to fracture were 38 to 50, and 34 to 41 per cent, respectively.

It is hoped that the authors will continue this work and cover a sufficiently wide range of analyses so that definite relationships can be established between the results from the two types of tests. If this is done it is further hoped that the additional results will show the same relationship as the present ones as it is obviously easier to conduct rupture tests on bar specimens than on tubes.

[7] "Properties of Ferrous Metals at Elevated Temperatures as Determined by Short-Time Tensile and Expansion Tests," by C. L. Clark. Trans. ASME, vol. 50, 1928, pp. 263–280.

[8] "The Stability of Metals at Elevated Temperatures," by C. L. Clark and A. E. White. Trans ASM, vol. 15, 1929, pp. 670–714.

Authors' Closure

The authors would like to thank the discussers for their interest in the paper and for the various points that were brought out. These discussions have emphasized the authors' contention that a comprehensive test program is needed to verify the use of uniaxial stress-rupture data in design problems with multiaxial stresses.

Mr. Black's correlation of the tubular stress-rupture test data against the parameter $T\ (20 + \log t)\ 10^{-3}$ is not unexpected since several checks which have been conducted in the authors' laboratory on ferritic materials against this parameter also checked very closely. Since the tubular stress-rupture experiments were conducted on ferritic tubes the good correlation demonstrated is within expectations.

The authors regret the omission of Mr. Clark's early work on tubular specimens which was reported in his evaluation of high-temperature metal stability in 1928 and 1929.[7,8] These two references are a valuable addition to our bibliography. The authors agree with Mr. Clark on his statement that representative data can be obtained on relatively heavy wall tubes by means of uniaxial specimens, particularly in a longitudinal direction. There are also several cases on record where good data have been obtained on such tubes in a circumferential direction. The materials investigated so far have been largely of the ferritic type. The newer materials, particularly those of the stabilized austenitic variety, have exhibited directional effects which may noticeably affect the testing results and should be further investigated.

Rupture and Creep Characteristics of Titanium-Stabilized Stainless Steel at 1100 to 1300 F

By J. W. FREEMAN,[1] G. F. COMSTOCK,[2] and A. E. WHITE[3]

Rupture and creep strengths were established at 1100, 1200, and 1300 F for 18–8 + Ti steel heat-treated at 1900 and 2050 F. Several Ti/C ratios were included as a variable. Creep and rupture strengths were higher for the higher-temperature heat-treatment. The lower Ti/C ratio steel had the higher strengths for a given heat-treatment, although this effect was somewhat less than that of temperature of heat-treatment. Limited tests indicated that water-quenching prior to testing slightly improves strength at 1100 F and reduces it at 1300 F. The steels varied in susceptibility to sigma-phase development during testing. The lower Ti/C ratio steels were less susceptible than the higher. In the commercial steels tested, those steels which developed sigma phase had abnormal creep characteristics, with first-stage creep virtually absent and increasing creep rates at short-time periods and low creep rates. This indication of premature third-degree creep was false in that prolonged testing established a true secondary creep rate as predicted by the rupture tests. Use of the minimum creep rates of short duration for establishing the usual creep strengths led to values estimated to be 1000 to 3000 psi high. The creep and rupture strengths of 18–8 + Ti and 18–8 + Cb steels probably have about the same range in strengths at high temperatures. Under present specifications it is entirely possible to have very low or very high strengths for both steels.

THE good strength and general corrosion resistance of the "18–8" types of austenitic steels at high temperatures is well known. Unless stabilized with titanium or columbium, these steels may, however, be made sensitive to intergranular corrosion by exposure to temperatures in the range from 800 to 1500 F. Because equipment made of 18–8 steel is often heated to the sensitization temperature range both during fabrication and during service, it is often considered desirable to stabilize these steels. This is generally accomplished by adding titanium or columbium in amounts sufficient to combine chemically with the carbon present in the steel.

Relatively little has been published on the rupture and creep characteristics of titanium-stabilized 18 Cr - 8 Ni steel. This paper contributes data of this type, together with information on metallurgical properties of such steels at elevated temperatures.

Review of the Literature

Prior to 1949 the only published data for stress-rupture tests for 18–8 + Ti steel were presented in 1933 (1).[4] These showed that titanium-bearing 18–8 steel required over 47 hr for failure under 8000 psi at 1500 F, whereas plain 18–8 steel failed in 12–15 hr. In 1949 stress-rupture curves for a single heat of 18–8 + Ti steel were published (2) which showed that the stresses for rupture in 1000 hr at 1100 and 1300 F were slightly higher than for plain 18–8 steel, and considerably below those of columbium-bearing steel. At 1500 F all three were about the same.

Creep data were published in 1944 (3), indicating the following ranges in stress for a creep rate of 0.0001 per cent per hr at 1100 F:

18–8 + Ti	10,000 to 15,000 psi
18–8	13,000 to 15,000 psi
18–8 + Cb	15,000 to 25,000 psi

These data were accepted generally as evidence that 18–8 + Cb steel had superior strength, and that the titanium-bearing grade was no stronger than plain 18–8 steel.

An earlier publication (4) had suggested that 18–8 + Ti steel was stronger than 18–8 steel. Stresses for a creep rate of 0.001 per cent per hr at 1200 F for 18–8 + Ti were given as nearly twice those for the plain stainless steel. However, this creep rate was much higher than is usually employed in this country for evaluating steels.

Differences in creep resistance that may be expected between individual heats was pointed out by the 1949 paper (2). That same paper also indicated that the relative strengths of the various alloys would be dependent upon the temperature, because one of the heats of 18–8 + Ti steel had superior creep resistance at the highest test temperature, as is shown in Table 1.

TABLE 1 SUMMARY OF RELATIVE STRENGTHS OF VARIOUS ALLOYS

Type steel	Ti/C or Cb/C	Grain size	—Stress for creep rate of 0.0001 per hr— 1100 F	1200 F	1300 F
18–8 + Ti	3.8	5–8	21000	7800	2700
18–8 + Ti	8.4	6–8	16000	4600	850
18–8	...	3–5	13000	5200	2100
18–8 + Cb	13 and 8.6	6–8	27000	8000	1800

The authors concluded that their data were inadequate to determine whether the Ti/C ratio was a controlling factor or if other unknown variables were responsible for the differences between the two heats of 18–8 + Ti steel and between the 18–8 + Ti and the other steels.

[1] Research Engineer, Engineering Research Institute, University of Michigan, Ann Arbor, Mich.

[2] Assistant Director of Research, Titanium Alloy Manufacturing Division, National Lead Company, Niagara Falls, N. Y.

[3] Director, Engineering Research Institute, University of Michigan, Ann Arbor, Mich. Fellow ASME.

Contributed by the Metals Engineering Division and the Joint ASTM-ASME Committee on Effect of Temperature on the Properties of Metals and presented at the Annual Meeting, Atlantic City, N. J., November 25–30, 1951, of The American Society of Mechanical Engineers.

Note: Statements and opinions advanced in papers are to be understood as individual expressions of their authors and not those of the Society. Manuscript received at ASME Headquarters, September 10, 1951. Paper No. 51—A-46.

[4] Numbers in parentheses refer to the Bibliography at the end of the paper.

In 1951 another publication (5) presented rupture and creep data for 18–8 + Ti steel which indicated that 18–8 + Ti and 18–8 + Cb were interchangeable at any given grain size for high-temperature applications.

Procedure and Materials

The investigation was planned to determine the influence on properties at high temperatures of heat-treatment and of variation in the ratio of titanium to carbon within the usual ranges for AISI type 321 steel. Bar stock from commercial heats with the compositions listed in Table 2 and heat-treated as described in Table 3 were tested for rupture and creep properties at 1100, 1200, and 1300 F. The main investigation was based on specimens air-cooled after solution treatment. Only a very few tests were made on water-quenched specimens, to investigate the possibility that cooling rate might be a factor in the observed creep properties. A minor study of the effect of aluminum was carried out on split heats from a laboratory induction furnace. Subsequent to testing, many of the specimens were examined microscopically to determine structural changes and were tested for changes in room-temperature mechanical properties.

TABLE 2 CHEMICAL COMPOSITION OF 18 8 + Ti STEELS INVESTIGATED

Steel	Ti/C ratio	C	Mn	Si	S	P	Cr	Ni	Ti	Al
C	5.3	0.07[a]	1.40	0.53	...	...	17.06	9.52	0.36–0.38[a]	..
D	9.5	0.06[a]	0.59	0.53	...	...	17.74	10.64	0.57[a]	..
E	9.4	0.07[a]	1.45	0.40	0.010	0.019	17.47	10.40	0.66[a]	..
F	11.2	0.08[a]	1.31	0.52	0.006	0.015	18.54	12.80	0.56[a]	..
1225-1	12.2	0.055	1.36	0.44	...	...	18.27	11.98	0.67	<0.01
1225-2	10.3	0.057	1.37	0.45	...	...	18.27	11.98	0.59	0.32
1305-1	7.9	0.057	1.29	0.43	...	...	17.92	10.65	0.45	0.01
1305-2	9.6	0.055	1.29	0.43	...	...	17.92	10.65	0.53	0.22

[a] Analyses made by the Titanium Alloy Manufacturing Division, National Lead Company; the remainder reported from the heat analysis by the steel manufacturer.

TABLE 3 SUMMARY OF TEST MATERIALS

Steel	Ti/C ratio	Source of material	Heat-treatments	Testing temperature (deg F) Rupture	Testing temperature (deg F) Creep	ASTM grain size
C	5.3	Hot-rolled 1-in. round bars from commercial heat	1900 F, 1 hr, air-cooled	1100, 1200	1100, 1200	7–8
C	5.3	Hot-rolled 1-in. round bars from commercial heat	1900 F, 1 hr, water-quenched	.. ..	1100	7–8
C	5.3	Hot-rolled 1-in. round bars from commercial heat	2050 F, 1 hr, air-cooled	1200, 1300	1200, 1300	2–5; 6–7
C	5.3	Hot-rolled 1-in. round bars from commercial heat	2050 F, 1 hr, water-quenched	.. ..	1200, 1300	2–4
D	9.5	Hot-rolled 1-in. round bars from commercial heat	1900 F, 1 hr, air-cooled	.. ..	1100, 1200	7–8
D	9.5	Hot-rolled 1-in. round bars from commercial heat	2050 F, 1 hr, air-cooled	.. ..	1200, 1300	1 and 6–7
D	9.5	Hot-rolled 1-in. round bars from commercial heat	2050 F, 1 hr, water-quenched	.. ..	1300	1 and 6–7
E	9.4	Hot-rolled 1-in. round bars from commercial heat	1900 F, 1 hr, air-cooled	1100, 1200	1100, 1200	4 or 5–7; (3–4)
E	9.4	Hot-rolled 1-in. round bars from commercial heat	2050 F, 1 hr, air-cooled	1200, 1300		4 or 5–7
F	11.2	Hot-rolled 1-in. round bars from commercial heat	1900 F, 1 hr, air-cooled	.. ..	1100, 1200	5–7
1225-1	12.2	⅞-in. round bars forged from induction heat	1900 F, 1 hr, air-cooled	.. ..	1200	4
1225-2	10.3	⅞-in. round bars forged from induction heat	1900 F, 1 hr, air-cooled	.. ..	1200	4
1305-1	7.9	⅞-in. round bars forged from induction heat	1900 F, 1 hr, air-cooled	.. ..	1200	6
1305-2	9.6	⅞-in. round bars forged from induction heat	1900 F, 1 hr, air-cooled	.. ..	1200	6

The grain sizes resulting from the heat-treatments are listed in Table 3. The grain sizes after a 1900 F solution treatment ranged from 4 to 8 in the various steels. Only one exception was observed to a uniform grain size in each material—the specimen of steel E rupture-tested at 1200 F under 21,000 psi had a 3–4 grain size whereas all other specimens were 4 or 5 to 7. After the steels were heat-treated at 2050 F, considerably more variation in grain size developed. Apparently this was related to variations along the length of the original bar stock. The steel C specimens used for creep tests were all uniformly 6–7 in grain size. The rupture specimens, however, varied from predominantly 2 to predominantly 5 grain size. Steel D had a mixed 1 and 6–7 grain size resulting from a variation in grain growth along the length and across the section of the original bar.

Stress-Rupture Properties

On the basis of the data obtained from stress-rupture tests (see Figs. 1 through 3 and Table 4), increasing the temperature of heat-treatment from 1900 to 2050 F substantially increased the rupture strength of the two steels tested. The steel with a Ti/C ratio of 5.3 was slightly stronger than that having a ratio 9.4. At 1200 F, however, the difference was less than that due to variation in temperature of heat-treating.

The rupture strengths reported in Table 4 for 10,000 and 100,000 hr are based on the usual extrapolations. In all but one case the test of longest duration for each material was over 1000 hr. In several cases the longest tests exceeded 2000 hr, and in one instance was 6084 hr.

The elongations of the fractured specimens were generally high. At 1200 F the specimens which had the larger grains tended to have lower elongation. No explanation could be found for the erratic rupture times from steel E at 1100 F. Grain-size variation was not the cause. The stress-rupture time curve for steel E at 1100 F was drawn consistent with the curves for the other steels. The stress-rupture - time curves for steel C (air-cooled from 2050 F) are more representative of material with a 2–5 grain size rather than a 6–7 grain size.

Creep Properties

The stresses for creep rates of 0.0001 and 0.00001 per cent per hr resulting from creep tests of 1000 to 1600 hr duration are summarized in Table 5. The values reported, however, are subject to limitations due to abnormal creep behavior in part of the tests. The abnormality consisted of a false second-stage creep rate of short duration followed by the apparent onset of third-stage creep at abnormally short-time periods and low creep rates.

The usual stress-creep rate curves are shown in Figs. 4 and 5, respectively, for steel C (Ti/C = 5.3) and steel D (Ti/C = 9.5). It is indicated on these figures that abnormal creep was encountered in the following cases:

Steel	Ti/C ratio	Heat-treatment	Test temperature, deg F
C	5.3	Air-cooled 2050 F	1300
D	9.5	Air-cooled 1900 F	1100, 1200
D	9.5	Air-cooled 2050 F	1300

Similar abnormal creep behavior was exhibited by the other high Ti/C ratio steels E and F for which data are shown in Fig. 6.

The apparent early onset of third-stage creep suggested that fracture ought to take place relatively soon in those materials. This was not, however, borne out by the rupture strengths. It appeared that prolonging the testing time should show a second decrease in creep rate to a true secondary creep rate. To verify this a test prolonged to 7600 hr was made on steel E (air-cooled

TABLE 4 RUPTURE STRENGTH OF 18-8 + Ti STEELS AT 1100, 1200, AND 1300 F

Steel	Ti/C ratio	Grain size	Testing temperature, deg F	Rupture strength, psi — 100 hr	1000 hr	10,000 hr	100,000 hr
			Solution-treated 1 hr at 1900 F and air-cooled				
C	5.3	7–8	1100	42,000	34,000	27,000	22,000
E	9.4	4 or 5–7	1100	42,000	31,000	22,500	16,000
C	5.3	7–8	1200	29,500	21,000	13,000	8,000
E	9.4	4 or 5–7	1200	28,000	20,500	12,000	7,400
			Solution-treated 1 hr at 2050 F and air-cooled				
C	5.3	2–5	1200	32,500	24,000	18,000	13,000
E	9.4	4 or 5–7	1200	31,500	21,500	14,500	10,000
C	5.3	2–5	1300	21,000	14,500	9,200	5,500
E	9.4	4 or 5–7	1300	18,500	12,500	7,700	4,600

TABLE 5 CREEP STRENGTH OF 18-8 + Ti STEELS AT 1100, 1200, AND 1300 F

Steel	Ti/C ratio	Heat-treatment, deg F	Grain size	Testing temperature, deg F	Stress, psi, for second-stage creep rate of— 0.00001 per cent per hr	0.0001 per cent per hr
C	5.3	1900 A.C.	7–8	1100	10,500	16,500
D	9.5	1900 A.C.	7–8	1100	(12,000)[a]	(20,500)[a]
E	9.4	1900 A.C.	5–7	1100	(12,000)[a]	
F	11.2	1900 A.C.	5–7	1100	(10,000)[b]	(23,000)[a, b]
C	5.3	1900 A.C.	7–8	1200	7,000	10,900
D	9.5	1900 A.C.	7–8	1200	(5,700)[a]	(10,500)[a]
E	9.4	1900 A.C.	5–7	1200	(5,800)[a]	(9,000)[a]
C	5.3	2050 A.C.	6–7	1200	8,600	12,500
D	9.5	2050 A.C.	1 and 6–7	1200	6,600	12,000
C	5.3	2050 A.C.	6–7	1300	(4,000)[a, b]	(10,000)[a]
D	9.5	2050 A.C.	1 and 6–7	1300	(3,300)[a]	(7,400)[a]

NOTES: [a] Values questionable because of irregular creep and no tests longer than 1000 hr. [b] Insufficient tests for accurate value. [c] Based on a prolonged test in which true secondary creep was attained.

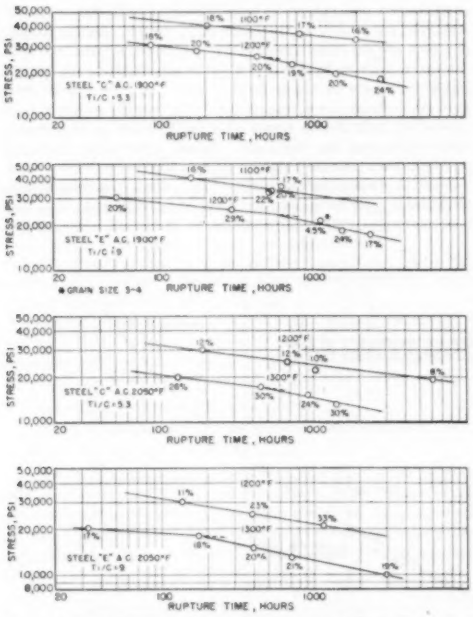

FIG. 1 STRESS-RUPTURE TIME CURVES FOR 18-8 + Ti STEELS (Numbers on curves indicate elongation of fractured specimen.)

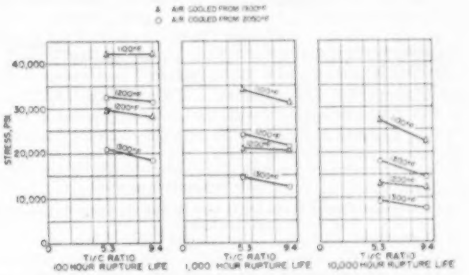

FIG. 2 EFFECTS OF Ti/C RATIO ON STRESS-RUPTURE STRENGTHS AT 1100, 1200, AND 1300 F OF 18-8 + Ti STEELS IN AIR-COOLED CONDITION

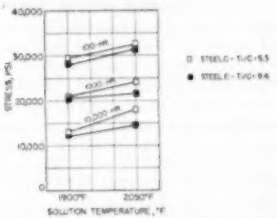

FIG. 3 EFFECT OF SOLUTION TEMPERATURE ON STRESS-RUPTURE STRENGTHS AT 1200 F OF 18-8 + Ti STEELS

from 1900 F) at 1200 F under a stress of 11,000 psi. This test, Fig. 7, showed that true secondary creep was attained after 2000 hr and persisted to 4500 hr. The start of third-stage creep at 4500 hr was consistent with the true second-stage rate of 0.18 per cent per 1000 hr.

The abnormal creep characteristics apparently were caused by structural instability as discussed in a subsequent section. The reliance which can be placed on the creep strengths of Table 5 should, however, be considered at this time. The possibility of establishing true secondary creep rates by prolonged testing did not seem feasible without excessive testing times. The rupture test on steel E (air-cooled from 1900 F) under 17,000 psi at 1200 F attained true secondary creep in 500 hr. The prolonged creep test at 11,000 psi required 2000 hr even though the rate was above 0.0001 per cent per hr. Assuming this to be sufficient evidence of stress dependency of the time required to reach true secondary creep rates, tests would have to be of many thousands of hours in duration to establish true secondary creep rates in the range from 0.00001 to 0.0001 per cent per hr.

An estimate of the degree of error in the creep strengths of

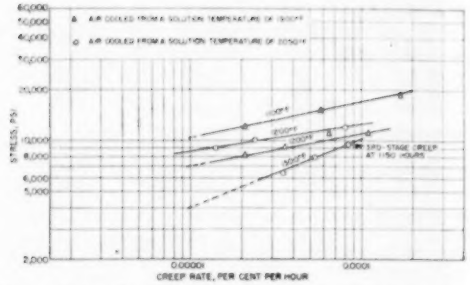

FIG. 4 STRESS-CREEP RATE DATA FOR 18-8 + Ti STEEL C AT 1100, 1200, and 1300 F; Ti/C = 5.3

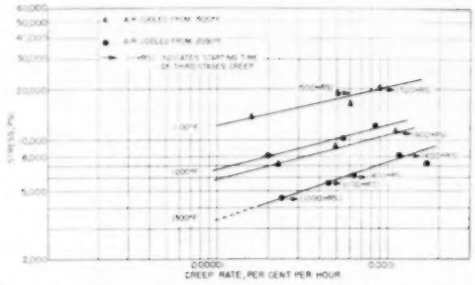

FIG. 5 STRESS-CREEP RATE DATA FOR 18-8 + Ti STEEL D AT 1100, 1200, and 1300 F; Ti/C = 9.5

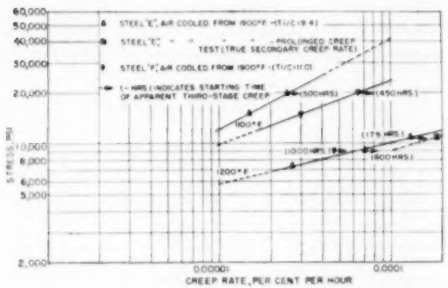

FIG. 6 STRESS-CREEP RATE DATA FOR 18-8 + Ti STEEL E AND F AT 1100 and 1200 F

Table 5 can be made. The prolonged creep test on steel E at 1200 F indicated that the 0.0001 per cent per hr strength of Table 5 was high by about 1000 psi (see Fig. 6). For the other materials tested, advantage can be taken of the ratios of creep strengths to rupture strengths. For ductile materials, the ratio of the 0.0001 per cent per hr creep strengths to 10,000-hr rupture strengths are usually of the order of 0.7 to 0.8; for the 0.00001 per cent per hr creep strength to 100,000-hr rupture strength, the ratios are usually 0.4 to 0.6. The actual ratios set forth in Table 6 indicate that only steel C tested at 1100 F gave creep strengths reliable for extrapolation. The steel C samples, heat-treated at 2050 F and tested at 1200 F, gave creep strengths only slightly on the high side. In all other cases the creep strengths were probably high by 1000 to 3000 psi.

Effect of Aluminum Content on Creep. Two induction-furnace heats were split to make two ingots from each heat, one with and one without aluminum addition. Titanium was added to

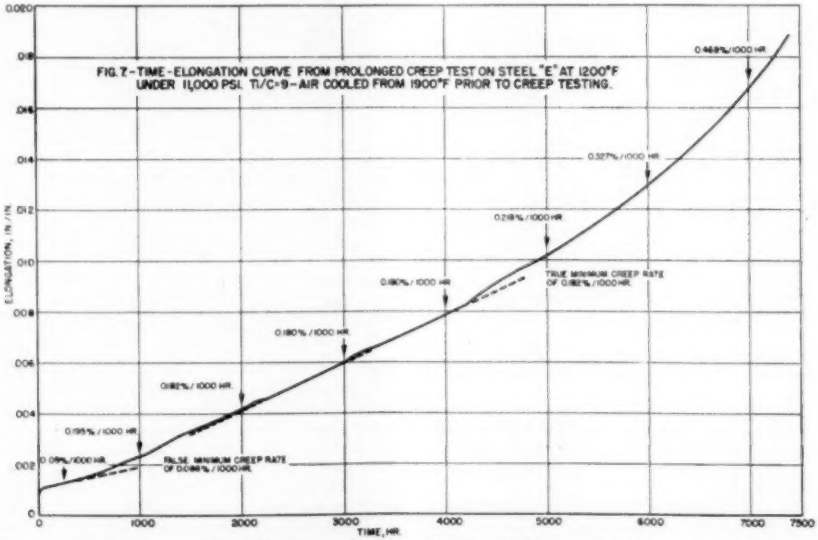

FIG. 7 TIME-ELONGATION CURVE FROM PROLONGED CREEP TEST AT 1200 F AND 11,000 PSI, FOR STEEL E, AIR-COOLED FROM 1900 F PRIOR TO TESTING; Ti/C = 9.4

TABLE 6 RATIO OF CREEP TO RUPTURE STRENGTHS

Steel	Ti/C ratio	Heat-treatment	Test temp., deg F	Creep strengths: 0.0001 per cent per hr, psi	Creep strengths: 0.00001 per cent per hr, psi	Extrapolated Rupture strengths: 10,000 hr, psi	Extrapolated Rupture strengths: 100,000 hr, psi	Ratio creep to rupture strengths: 0.0001 per cent per hr, 10,000 hr	Ratio creep to rupture strengths: 0.00001 per cent per hr, 100,000 hr
C	5.3	A.C. 1900 F	1100	16,500	10,500	27,000	22,000	0.61	0.45
D	9.5	A.C. 1900 F	1100	20,500[a]	(12,000)[a]	....	....	(0.9)[c]	(0.73)[c]
E	9.4	A.C. 1900 F	1100	....	(12,000)[a]	22,500	16,500	....	0.73
C	5.3	A.C. 1900 F	1200	10,900	7,000	13,000	8,000	.84	.87
D	9.5	A.C. 1900 F	1200	(10,500)[a]	(5,700)[a]	....	....	(.87)[c]	(.88)[c]
E	9.4	A.C. 1900 F	1200	(10,000)[a]	(5,800)[a]	12,000	7,400	.83	.78
E	9.4	A.C. 1900 F	1200	9,000[b]	....	12,000	7,400	.75	....
C	5.3	A.C. 2050 F	1200	12,500	8,600	18,000	13,000	.70	.66
D	9.5	A.C. 2050 F	1200	12,000	6,600	....	....	(.83)[c]	(.66)[c]
E	9.4	A.C. 2050 F	1200	....	....	14,500	10,000	....	....
C	5.3	A.C. 2050 F	1300	(10,000)[a]	(4,000)[a]	9,200	5,500	1.08	0.73
D	9.5	A.C. 2050 F	1300	(7,400)[a]	(3,300)[a]	....	....	(.96)[c]	(.68)[c]
E	9.4	A.C. 2050 F	1300	....	....	7,700	4,600	....	....

NOTES: [a] Based on false second-stage creep rates. [b] Based on true second-stage creep rate from one prolonged test. [c] Ratio of creep strength of steel D to rupture strength of steel E.

the heat as metallic Ti, one ingot was poured and then aluminum was added and the other ingot poured. The stresses for a creep rate of 0.0001 per cent per hr at 1200 F, approximated from a limited number of tests on specimens air-cooled from 1900 F, are given in Table 7.

TABLE 7 STRESSES FOR CREEP RATE OF 0.0001 PER CENT PER HR AT 1200 F

Heat number	Al added, per cent	Ti/C ratio	Grain size	Approximate stress for 0.0001 per cent/hr creep rate, psi
1225–1	0	12.2	4	13000
1225–2	0.32	10.3	4	14000
1305–1	0	7.9	6	13500
1305–2	0.22	9.6	6	12000

The effect of aluminum was slight and reversed in each heat. In each heat the ingot with the lower Ti/C ratio had the higher creep resistance. Ti/C ratio, however, was not the only factor. Heat 1305 ingots tended to be slightly weaker than those from heat 1225 even though the former had the lower ratio. Likewise, the induction heats had higher creep strengths than the lower Ti/C ratio commercial heats previously discussed.

There was no evidence of premature third-stage creep. The amount of first-stage creep was normal for heat 1225 specimens while it was quite small for heat 1305.

Effect on Creep of Air-Cooling Versus Water-Quenching. A limited number of creep tests were made on specimens water-quenched after solution-treating. The results summarized in Table 8 indicate that water-quenching

1 Increased creep resistance at 1100 F.

2 Reduced creep resistance and induced false third-stage creep in shorter time periods at 1300 F.

While it is recognized that these data are too few for definite conclusions, they do indicate that cooling rate is a factor in the measured creep resistance. The good check for duplicate tests on steel C at 1100 F lends substantiation to the indication that the observed differences between air-cooled and water-quenched specimens are outside the normal scatter of data.

Structural Changes During Testing

Those specimens which had normal creep curves developed the usual precipitates during testing, mainly at the grain boundaries. Small separate grains of a new easily etched phase formed in the grain boundaries of those materials which underwent an increase in creep rate at abnormally low creep rates and short time periods. The development of this phase was accelerated by stress so that it was present to a larger extent in the rupture than in the creep specimens. For instance, while it was absent in the creep specimens of steel C tested at 1200 F, it was present in the rupture specimens. These general characteristics are shown in Figs. 8 and 9 for steels C and E, respectively.

The new phase was similar to the unknown phase originally reported for 18–8 + Cb and 25–20 steels (6) and subsequently identified as sigma phase (7). Subsequently the presence of this form of sigma phase has been reported for these two types of steel by several investigators and for 18–8 + Ti (2, 5). Therefore it is assumed that the new phase in the steels showing abnormal creep characteristics was sigma phase.

The rate and extent of formation of sigma phase was subject to several variables, as follows:

1 The lowest Ti/C ratio steel C was more resistant to its formation than the higher Ti/C ratio steels. It could not be identified in any of the 1100 or 1200 F creep specimens of steel C whereas it was present in recognizable amounts even in the creep specimens tested at 1100 F of steels D and E, solution-treated at 1900 F. A similar effect of Ti/C ratio has been noted before (2).

2 Increasing the solution temperature reduced the tendency for sigma phase to form during testing. There was no evidence of it in the creep specimens of steel D tested at 1200 F after the higher-temperature treatment, even though it was recognizable in both the 1100 and 1200 F specimens when heat-treated at 1900 F. The amount present in the specimens tested at 1300 F was less in the specimens heat-treated at the higher temperature.

3 The rate and extent of sigma-phase formation increased markedly with increased temperature of testing. Thus the specimens tested at 1300 F had more sigma phase than those tested at 1200 F which in turn had more than those tested at 1100 F. All of the materials tested developed sigma phase at 1300 F, although as noted previously, certain of the materials did not at 1100 and 1200 F.

4 The amount of sigma phase was less in the samples showing

TABLE 8 EFFECT ON CREEP STRENGTH OF WATER-QUENCHING VERSUS AIR-COOLING AFTER SOLUTION HEAT-TREATMENT OF 18-8 + Ti STEELS

Steel	Ti/C ratio	Heat-treatment, deg F	Method of cooling	Grain size	Creep Test: Testing temp, deg F	Applied stress, psi	Time, hr	Minimum rate of creep, per cent per hr	Start of 3rd-stage creep, hr
C	5.3	1900	A.C.	7–8	1100	15,000	1000	0.000058	*
C	5.3	1900	A.C.	7–8	1100	15,000	1170	0.000056	*
C	5.3	1900	W.Q.	7–8	1100	15,000	1150	0.000023	*
C	5.3	2050	A.C.	6–7	1300	8,000	1110	0.000053	*
C	5.3	2050	W.Q.	6–7	1300	8,000	1365	0.000170	500
D	9.5	2050	A.C.	1 and 6–7	1300	8,000	1110	0.000118	400
D	9.5	2050	W.Q.	1 and 6–7	1300	8,000	1460	0.000450	300

* The creep rate shown is for a second-stage creep which probably would not undergo an increase for very long-time periods.

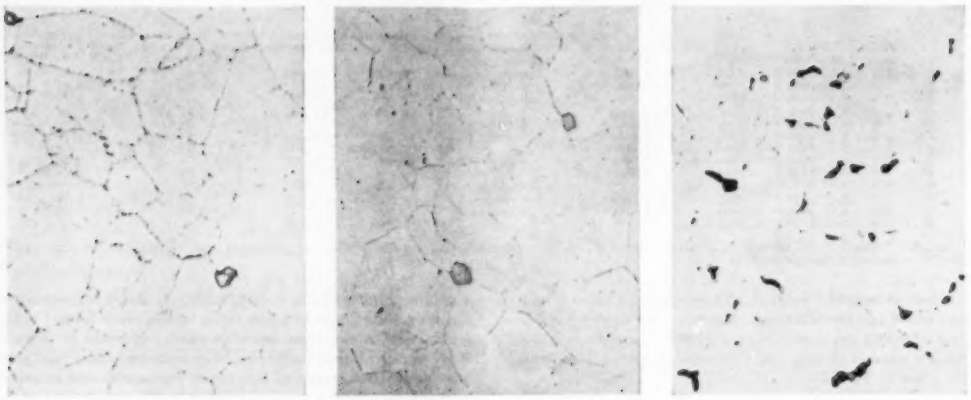

(a) Structure as air-cooled from 1900 F (b) Same steel after creep-testing 1176 hr at 1200 F and 10,000 hr (c) Same steel after rupture in 2823 hr at 1200 F and 17,500 psi

FIG. 8 DEVELOPMENT OF A SEPARATE PHASE DURING TESTING OF 18-8 + Ti STEEL C, Ti/C = 5.3; ×1000

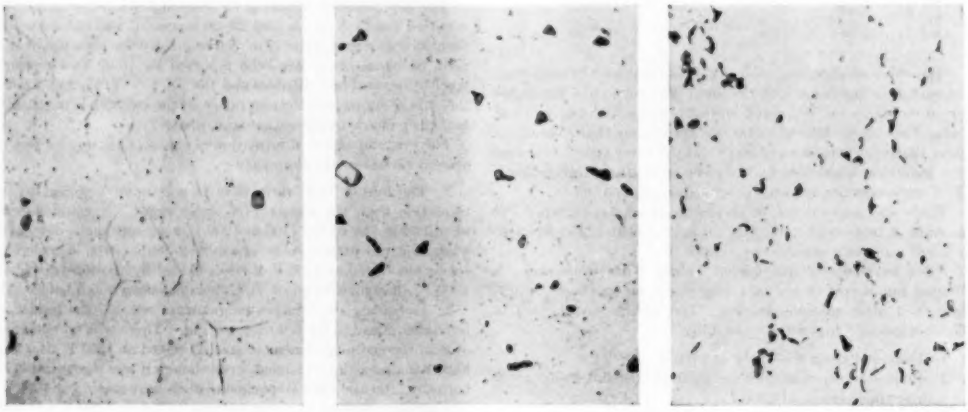

(a) Structure as air-cooled from 1900 F (b) Same steel after creep-testing 1078 hr at 1200 F and 11,000 psi (c) Same steel after rupture in 1522 hr at 1200 F and 18,000 psi

FIG. 9 DEVELOPMENT OF A SEPARATE PHASE DURING TESTING OF 18-8 + Ti STEEL E, Ti/C = 9.4; ×1000

larger grains. This was most apparent in the induction heats used for the study of aluminum additions. Heat 1305 with a grain size of 6 had the most sigma phase after testing. The samples with mixed grain size showed sigma phase segregated to the fine grains. The coarse-grained rupture specimen of steel E and the larger-grained rupture specimens of steel C were nearly free of recognizable sigma phase.

5 The water-quenched specimens creep-tested at 1300 F appeared to have more sigma phase than the corresponding air-cooled specimens.

PHYSICAL PROPERTIES AFTER CREEP-TESTING

The physical properties at room temperature of specimens after creep-testing, Table 9, were measured to determine the effect of structural changes during exposure to temperature and stress. All of the specimens had normal properties and there was remarkably little difference after testing at the various temperatures. There was no evidence of embrittlement from the sigma phase, a characteristic which seems to be typical of this phase when it forms as small separate grains. The data indicate that 18-8 + Ti steel of the proper composition retains excellent properties at room temperature after exposure to high temperature under stress.

ABNORMAL CREEP

The reason for the increase in creep rates at abnormally short time periods and low creep rates in some of the tests is uncertain. It was accompanied by the appearance of recognizable sigma-phase particles in the specimens after testing. Apparently, however, sigma phase alone is not the only possible cause of such behavior inasmuch as similar behavior was reported in reference (2) for 18-8 steel which is not susceptible to the sigma-phase reaction.

TABLE 9 ROOM-TEMPERATURE, TENSILE, IMPACT, AND HARDNESS PROPERTIES OF COMPLETED CREEP TEST SPECIMENS OF 18–8 + Ti STEELS

Steel	Ti/C ratio	Heat-treatment, deg F	Creep, test conditions: Temp, deg F	Stress, psi	Time, hr	Tensile strength, psi	Yield strength, psi: 0.1 per cent offset	Yield strength, psi: 0.2 per cent offset	Elongation, per cent in 2 in.	Reduction of area, per cent
Tensile tests										
C	5.3	A.C. 1900 F	1100	15,000	1007	88,300	34,000	34,900	52.5	71.5
D	9.5	A.C. 1900 F		13,500	1295	84,800	31,400	33,800	52.0	71.8
E	9.4	A.C. 1900 F		15,000	1083	86,250	30,500	33,250	55.0	76.8
F	11.2	A.C. 1900 F		15,000	1074	83,400	31,800	32,500	60.0	73.6
C	5.3	A.C. 1900 F	1200	9,000	1031	84,800	30,600	33,300	51.5	71.8
C	5.3	A.C. 2050 F		9,000	1623	85,300	30,800	32,000	56.5	72.5
D	9.5	A.C. 1900 F		9,000	1063	85,700	28,700	31,200	55.0	73.0
D	9.5	A.C. 2050 F		10,000	1111	84,750	31,250	32,700	62.0	76.0
E	9.4	A.C. 1900 F		9,000	1086	86,250	28,500	30,500	59.0	71.9
C	5.3	A.C. 2050 F	1300	6,500	1291	86,750	30,500	32,300	60.0	74.2
D	9.5	A.C. 2050 F		4,500	1623	85,000	28,750	30,200	62.0	64.0

Steel	Ti/C ratio	Heat-treatment, deg F	Creep, test conditions: Temp, deg F	Stress, psi	Time, hr	Brinell hardness number	Izod impact[a] (ft-lb)
Hardness and impact tests							
C	5.3	A.C. 2050 F		original		146	86
C	5.3	A.C. 1900 F	1100	18,500	1295	160	92
D	9.5	A.C. 1900 F		original		144	
D	9.5	A.C. 1900 F	1100	20,000	1365	154	90
E	9.4	A.C. 1900 F	1100	20,000	1079	...	89
F	11.2	A.C. 1900 F	1100	20,000	1082	...	84
C	5.3	A.C. 1900 F	1200	11,000	1010	157	88
C	5.3	A.C. 2050 F	1200	10,000	1176	...	80
D	9.5	A.C. 1900 F	1200	11,000	1128	150	87
D	9.5	A.C. 2050 F	1200	12,000	1620	...	83
E	9.4	A.C. 1900 F	1200	11,000	1078	...	82
F	11.2	A.C. 1900 F	1200	9,000	1895	...	79
C	5.3	A.C. 2050 F	1300	9,500	1625	...	82
D	9.5	A.C. 2050 F	1300	8,000	1110	...	80

[a] Impact specimen 0.395 inch square with a 0.080-inch V-notch

Likewise, the induction heats 1225 and 1305 developed sigma phase but did not undergo the abnormal creep found for the commercial steels. The amount of sigma phase developed in the steel tested for reference (5) was more than in the steels tested for this investigation, although the creep curves were not abnormal.

The small amount or absence of first-stage creep, together with the low creep rate followed by increasing creep rate at relatively short-time periods was very suggestive of strengthening by a precipitation reaction, followed by overaging. There was however, insufficient evidence of the precipitation hardening which should have been present to account for such a mechanism. The hardness and the other physical properties of the specimens after testing did not support this type of mechanism. The only evidence supporting the possibility of strengthening by precipitation was the abnormally high yield strengths of the material tested for reference (5).

The more probable explanation is that the main strengthening against creep is associated with odd-size atoms in solid solution. If these atoms precipitate rapidly from solid solution, the creep resistance is rapidly reduced and the creep rate increases with time of testing. The small amount of first-stage creep and the low creep rates initially encountered would be due to a combination of initial high creep resistance and the volume decrease accompanying the precipitation reaction. When a sample of steel E (air-cooled from 1900 F) was held for 300 hr at 1200 F without stress in a thermal-expansion unit, the length decreased steadily for a total of 0.0002 in. per in. After the precipitation reaction had progressed far enough for appreciable reduction of creep resistance, the volume decrease no longer would offset creep, and an increase in creep rate would result; or, the reaction may reach completion so that the volume decrease would cease entirely. The tests could then proceed in normal creep and finally establish true secondary creep typical of the altered structure, as was found in the prolonged test on steel E.

The apparent extreme stress dependency of the rate of reaction appears to be a weakness of either the precipitation-hardening theory or that based on solid-solution depletion. It was pointed out earlier that there appeared to be strong stress dependency on the time to reach true minimum creep. Likewise there was no question that the amount of sigma phase was greater in the rupture than in the creep specimens. Usually, however, such precipitation reactions are not found to be nearly so stress-dependent as seems to be indicated. Also the amount of volume decrease accompanying the removal of odd-size atoms from solution is rather small.

The reporting of the same type of abnormal creep behavior for 18–8 (2) which does not develop sigma phase, and the occurrence of sigma phase without abnormal creep, raise doubts as to whether sigma phase is actually responsible for abnormal creep. It is entirely possible that sigma phase is a structural change which happens to accompany abnormal creep in some cases and not in others. Inasmuch as precipitates no longer affect creep resistance when they are large enough to be resolved under the light microscope, many possibilities exist. The most that can be said is that there probably are variations in prior history which affect both the amount of strengthening atoms taken into solid solution during heat-treatment and the rate of precipitation from solid solution during testing. For a given heat-treatment, particularly at 1900 to 2000 F, it might be expected that hot-working conditions and probably melting practice would affect the amount of solution of carbides and nitrides and their subsequent precipitation characteristics.

A wider range in properties has been reported for the steels susceptible to the sigma-phase reaction than for the plain 18–8 steel. Therefore it seems probable that the sigma-phase reaction does participate in the structural reactions controlling strength. This is supported by the fact that a high solution temperature, while coarsening the grains, suppresses sigma-phase development (6), yielding high creep strength. Such steels are, however, brittle in the rupture test.

Comparative Creep and Rupture Properties of 18–8 + Ti, 18–8 + Cb, and 18–8 Steels

Tables 10 and 11 compare the creep and rupture strengths obtained for 18–8 + Ti with other values reported in the literature. In addition, the ranges in strengths for 18–8 + Cb and 18–8 steels as reported in the Miller-Heger (8) compilation of data have been included for comparative purposes. A number of interpretations can be placed on these data. The more important are as follows:

1 A wide range in either creep or rupture strengths is possible for all three grades of steel. Under present applicable specifications there would seem to be little to differentiate between the

TABLE 10 COMPARATIVE CREEP STRENGTHS OF 18-8 + Ti, 18-8 + Cb, AND 18-8 STEELS

Type steel	Ti/C ratio	Heat-treatment	Grain size	Stress for creep rate of 0.00001 per cent per hr, psi	Stress for creep rate of 0.0001 per cent per hr, psi	Reference
Testing temperature 1100 F						
18-8	Range reported			7,000–10,000	9,500–15,000	8
18-8 + Cb	Range reported			12,000–22,000	13,500–27,000	8
18-8 + Ti	Range reported			...	12,000–14,000	8
18-8 + Ti	5.3	A.C. 1900 F	7–8	10,500	16,500	Table 5
18-8 + Ti	8.4	A.C. 1900 F	8	12,500	16,000	2
18-8 + Ti	8.8	A.C. 1900 F	...	...	13,600	3
18-8 + Ti	9.5	A.C. 1900 F	7–8	(12,000)[a]	(20,500)[a]	Table 5
18-8 + Ti	10.9	W.Q. 1900 F	7–8	6,300	14,000	5
Testing temperature 1200 F						
18-8	Range reported			4,000–4,500	6,000–9,000	8
18-8 + Cb	Range reported			1,800–11,500	5,000–16,000	8
18-8 + Ti	Range reported			...	7,000–8,000	8
18-8 + Ti	5.2	A.C. 1900 F	7–8	7,000	10,900	Table 5
18-8 + Ti	9.4	A.C. 1900 F	5–7	(5,800)[a]	9,000	Table 6
18-8 + Ti	9.5	A.C. 1900 F	7–8	(5,700)[a]	(10,000)[a]	Table 5
18-8 + Ti	5.3	A.C. 2050 F	6–7	8,000	12,500	Table 5
18-8 + Ti	9.5	A.C. 2050 F	1 and 6–7	6,600	12,000	Table 5
18-8 + Ti	10.9	W.Q. 1900 F	7–8	2,700	9,200	5
Testing temperature 1300 F						
18-8	Range reported			1,500–4,000	3,000–5,500	8
18-8 + Cb	Range reported			600–7,000	2,000–15,000	8
18-8 + Ti	Range reported			...	4,000–5,000	8
18-8 + Ti	8.4	A.C. 1900 F	8	3,200	4,600	2
18-8 + Ti	5.3	A.C. 2050 F	6–7	(4,000)[a]	(10,000)[a]	Table 5
18-8 + Ti	9.5	A.C. 2050 F	1 and 6–7	(3,300)[a]	(7,400)[a]	Table 5
18-8 + Ti	3.8	W.Q. 1950 F	5–8	5,200	7,800	2
18-8 + Ti	10.9	W.Q. 1900 F	7–8	1,450	3,700	5

[a] Values somewhat high due to abnormal creep curves; see discussion of Table 6.

TABLE 11 COMPARATIVE RUPTURE STRENGTHS FOR 18-8 + Ti, 18-8 + Cb, AND 18-8 STEELS

Type steel	Ti/C ratio	Heat-treatment	Grain size	Rupture strengths 100-hr, psi	Rupture strengths 1000-hr, psi	Rupture strengths 10,000-hr, psi	Estimated elongation after rupture in 1000 hr, per cent	Reference
Testing temperature 1100 F								
18-8	Range reported			...	22,000	17,000	..	8
18-8 + Cb	Range reported			...	29,000–36,000	20,000–28,000	..	8
18-8 + Ti	5.3	A.C. 1900 F	7–8	42,000	34,000	27,000	17	Table 4
18-8 + Ti	9.4	A.C. 1900 F	8	35,000	26,000	16,000	30	2
18-8 + Ti	9.4	A.C. 1900 F	4 or 5–7	42,000	31,000	22,500	20	Table 4
18-8 + Ti	10.9	W.Q. 1900 F	7–8	42,000	34,000	27,000	15	5
Testing temperature 1200 F								
18-8	Range reported			...	12,000–17,000	8,000–13,500	..	8
18-8 + Cb	Range reported			...	16,000–23,000	10,000–11,000	..	8
18-8 + Ti	5.3	A.C. 1900 F	7–8	29,500	21,000	13,000	20	Table 4
18-8 + Ti	9.4	A.C. 1900 F	4 or 5–7	28,000	20,500	12,000	24	Table 4
18-8 + Ti	5.3	A.C. 2050 F	2–5	32,500	24,000	18,000	10	Table 4
18-8 + Ti	9.4	A.C. 2050 F	4 or 5–7	31,500	21,500	14,500	30	Table 4
18-8 + Ti	10.9	W.Q. 1900 F	7–8	32,000	21,000	11,000	15	5
Testing temperature 1300 F								
18-8	Range reported			...	8,500–10,000	5,500–6,500	..	8
18-8 + Cb	Range reported			...	9,000–19,000	4,500–9,000	..	8
18-8 + Ti	8.4	A.C. 1900 F	8	19,000	10,000	6,000	80	2
18-8 + Ti	5.3	A.C. 2050 F	2–5	21,000	14,500	9,200	25	Table 4
18-8 + Ti	9.4	A.C. 2050 F	4 or 5–7	18,500	12,500	7,700	20	Table 4
18-8 + Ti	10.9	W.Q. 1900 F	7–8	26,000	13,500	7,300	20	5

18-8 + Ti and 18-8 + Cb steel. The strengths of 18-8 + Ti and 18-8 + Cb tend to average higher than 18-8, although some values are lower than those for 18-8.

2 The low strengths for 18-8 + Ti and 18-8 + Cb steels at temperatures of 1200 F and higher have been associated with fine grain size and the development of sigma phase; the high strengths with solution treatments which resulted in coarsening of the grains. In all probability, if tests were made with higher solution temperatures than those reported, values would be obtained for 18-8 + Ti as high as have been reported for 18-8 + Cb steel.

3 Study of the individual tests which have been reported for both 18-8 + Ti and 18-8 + Cb steel indicate that the properties obtained are not predictable from heat-treatment or grain size alone, at least where grain sizes are finer than No. 4. Considerable study of the phenomena suggests that the properties are certainly affected by hot-working conditions and probably by melting practice. Because a given grain size can be obtained by various prior treatments, it is probable that specification of grain size, Ti/C ratio and heat-treatments would not entirely insure closely reproducible properties.

4 Some of the data reported in the literature indicate that heat-treatment at 1900 to 2000 F produces the best all-round properties in 18-8 + Ti or 18-8 + Cb steel. Both Tables 10 and 11 show that properties on the low side of the range can result from heat-treating 18-8 + Ti steel at 1900 F. Because the low properties are associated with sigma-phase formation and because 18-8 + Cb is also susceptible to the same reaction, it would seem possible that 18-8 + Cb might also have low strengths with such treatments.

5 Although the fine-grained 18-8 + Ti and 18-8 + Cb steels have quite good comparative strengths at 1100 F, one exception is found in the 0.00001 per cent per hr creep strength reported in reference (5) for 18-8 + Ti. Thus it does not appear safe to generalize that a fine-grained material will always have good comparative strength at 1100 F.

6 In general, 18-8 steel data do not show as high or as low values as have been reported for 18-8 + Ti or 18-8 + Cb steel. In so far as the authors have been able to determine, 18-8 steel is not subject to the sigma-phase reaction. The somewhat narrower range for the unstabilized steel is probably associated with the absence of the sigma-phase reaction.

7 The data in the literature seem generally to bear out the findings of the present tests that strength at high temperatures in 18-8 + Ti steel is a function of Ti/C ratio. The 3.8 Ti/C ratio steel of reference (2) had high strengths, and the 10.9 Ti/C ratio steel of reference (5) had low strength.

BIBLIOGRAPHY

1 "Titanium in Steel," by G. F. Comstock, S. F. Urban, and M. Cohen," Pitman Publishing Company, New York, N. Y., 1949, p. 251, table 11.3.

2 "Creep and Rupture of Several Chromium-Nickel Austenitic Stainless Steels," by G. V. Smith, E. J. Dulis, and E. G. Houston, Trans. ASM, vol. 42, 1950, pp. 935–980.

3 "Creep Strength, Stability of Microstructure, and Oxidation Resistance of Cr-Mo and 18 Cr-8 Ni Steels," by R. F. Miller, W. G. Benz, and M. J. Day, Trans. ASM, vol. 32, 1944, pp. 381–407.

4 "Creep Strength, of 18–8 + Ti," by A. M. Portevin, *Metal Progress*, vol. 41, 1942, p. 88.

5 "Resumé of High Temperature Investigations Conducted During 1948–50," Timken Roller Bearing Company, Steel and Tube Division, Canton, Ohio, 1950, pp. 51–60.

6 "The Apparent Influence of Grain Size on the High Temperature Properties of Austenitic Steels," by C. L. Clark and J. W. Freeman, Trans. ASM, vol. 38, 1947, pp. 148–179. (Some unpublished data used for this paper were also referred to.)

7 "X-Ray Identification of Sigma Phase in 25–20 Cr-Ni Stainless," by W. J. Barnett and A. R. Troiano, *Metal Progress*, vol. 53, 1948, pp. 366–367.

8 "Report on the Strength of Wrought Steels at Elevated Temperatures," by R. F. Miller and J. J. Heger, ASTM Special Technical Publication No. 100.

Discussion

W. L. Fleischmann.[5] The authors are to be congratulated on this study of the high-temperature behavior of the titanium-stabilized austenitic steels which are replacing the niobium-stabilized steels in many applications. The data the authors offer show that an increase of the Ti/C ratio from 5.3 to 9.4 lowers the rupture strength, Fig. 2. Furthermore, one reference (2) is quoted by the authors which indicates a likelihood that a low Ti/C ratio, in that case 3.8/1, will exhibit high-temperature properties superior to the 5.3 and 9.4 Ti/C ratios investigated by them. Though in the reference quoted the increase in the high-temperature strength is not considered as proved to be caused by the lower Ti/C ratio than usually specified, it appears to the writer to be of technical importance to study this lead in detail.

Therefore it is hoped that the authors will continue the investigation of the effect of the Ti/C ratio upon the high-temperature strength without regard for the fact that an alloy with a lower Ti/C ratio will not possess the high resistance of a "stabilized" stainless steel to some corrosive media.

This latter characteristic, corrosion resistance, is rarely the determining factor in the choice of material for high-temperature applications and no reason exists why austenitic steels intended for that service should be purchased to a specification including the necessity of withstanding the Strauss or boiling nitric-acid test. As a matter of fact, it would be desirable to have an austenitic steel which has the properties, specifically the high strain to fracture of an 18-8 steel, with better creep resistance which seems to be indicated in the one titanium-stabilized austenitic steel with the 3.8 Ti/C ratio.

[5] Engineer, Metallurgy Section, Knolls Atomic Power Laboratory, General Electric Co., Schenectady, N. Y. Member ASME.

Authors' Closure

Mr. Fleischmann's comments are appreciated. The authors are, in general, in agreement with what he had to say.

Experimental Superheater for Steam at 2000 Psi and 1250 F—Progress Report of Field Operation

By F. G. ELY[1] and F. EBERLE,[2] ALLIANCE, OHIO

To investigate the properties of new superstrength alloys for high-temperature steam superheater service a test element constructed of 2-in-OD alloy tubes was installed in an operating boiler at Twin Branch Plant and supplied with steam at 2000 psig 950 F, which was heated to 1250 F. Operating conditions, and results of the first 5000 service-hours are described in this paper. The test is being continued for thorough evaluation of the materials.

Introduction

In the use of steam for power generation, there has been a steady increase in operating pressures and temperatures, with the objective of improving cycle efficiency and producing more electrical energy per pound of fuel burned. Limitations upon this trend are imposed chiefly by the characteristics of the currently available materials of construction, and, as new developments are made in improving those materials, advances can be made in the design of power-plant equipment.

Under the sponsorship of the ASME Research Committee on High-Temperature Steam Generation, Knowlton and Hartwell (1)[3] have published a study of the theoretical possibilities of the regenerative steam cycle at temperatures up to 1600 F, from which the curves in Figs. 1 and 2 have been reproduced to indicate the trend of maximum throttle steam temperature as used in power-plant practice during the past 45-year period, and to indicate the percentage of reduction in heat rate that might be expected in a practical cycle if steam temperature were to be increased above the present ceiling of 1050 F.

For the steam-generating phase of the cycle, it is well recognized that the critical limitations on the use of higher steam temperature lie in the materials of which the final stages of the superheater are constructed. The duty on these pressure parts requires that they be resistant to oxidation, or to other forms of corrosive attack, by steam or by the products of combustion at elevated temperatures, and that they possess sufficient strength and related physical properties at these temperatures to withstand the stresses due to internal pressure, heat transfer, and structural loading encountered in normal operating service. Furthermore, as a matter of foremost consideration, they must be capable of being produced commercially in the form of tubes, and must have welding characteristics suitable for dependable fabrication.

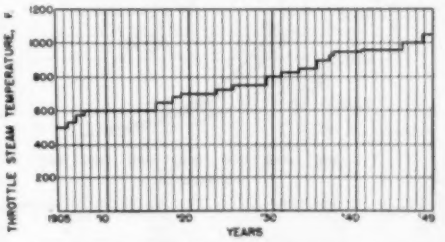

Fig. 1 Maximum Throttle Steam Temperatures for the Past 45-Year Period (1)

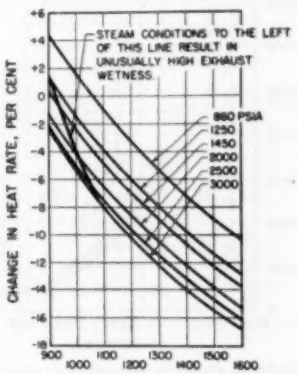

Fig. 2 Heat Rate Versus Throttle Temperature (1) Per Cent Change in Practical Cycle
(Base condition 1250 psia—950 F, 1 in. Hg absolute exhaust pressure.)

They must also be of such availability and cost as to justify their use economically in commercial practice.

Certain new alloys developed during the war period were found to have characteristics which appeared promising for steam-superheater service at temperatures well in advance of present-day practice. Laboratory tests made with these materials indicated considerably better high-temperature load-carrying ability than that of austenitic alloys in present use, and similar good resistance to high-temperature corrosion attack. Examples of the creep and stress-rupture properties of the superstrength alloys are shown in Figs. 3 and 4 in comparison with carbon steel and alloys now commonly employed. Because of limited experience in their use, and owing to the inadequacy of laboratory tests for complete demonstration of their suitability, it was considered wise to obtain practical experience with these materials under ex-

---

[1] Consultant, Research and Development Department, The Babcock & Wilcox Company. Mem. ASME.

[2] Chief Metallurgical Engineer, Research and Development Department, The Babcock & Wilcox Company.

[3] Numbers in parentheses refer to Bibliography at end of paper.

Contributed by the High-Temperature Steam Generation Research Committee, the Joint ASTM-ASME Committee on Effect of Temperature on the Properties of Metals, and the Power Division and presented at the Annual Meeting, Atlantic City, N. J., November 25–30, 1951, of The American Society of Mechanical Engineers.

Note: Statements and opinions advanced in papers are to be understood as individual expressions of their authors and not those of the Society. Manuscript received at ASME Headquarters, August 20, 1951. Paper No. 51—A-37.

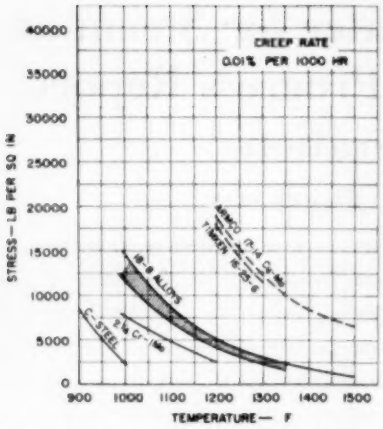

FIG. 3 CREEP STRENGTH OF VARIOUS ALLOY MATERIALS

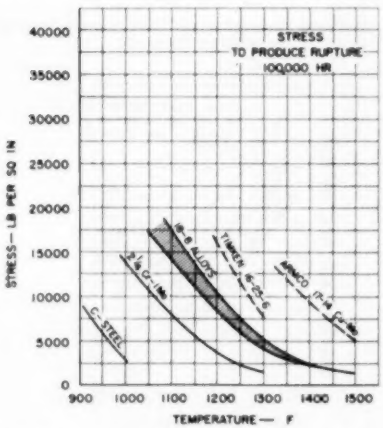

FIG. 4 RUPTURE STRENGTH OF VARIOUS ALLOY MATERIALS

pected conditions of actual superheater duty in field operation.

With the wholehearted co-operation of the American Gas & Electric Service Corporation and its affiliate the Indiana and Michigan Electric Company, the authors' company constructed and installed a field-test superheater element in an operating boiler unit at Twin Branch plant during 1950, where steam pressure of 2000 psi was available from existing boilers. The element was designed to receive steam at 950 F to 1000 F from the superheater outlet of these units, and to increase its temperature to 1200 F or 1250 F, under conditions in which the test element should function exactly as would be expected of a commercial unit, having complete exposure of the tube materials to the action of flue gases from pulverized-coal firing, to normal heat-transfer rates, and three-dimensional stresses, corresponding to realistic operation, and also to the internal action of highly superheated steam at established rates of mass flow within the tubes.

The unit was first placed in service in March, 1950. To date, approximately 5000 hr of operating service time have been accumulated, of which approximately one third has been with steam-outlet temperatures in excess of 1200 F, another third in the temperature range from 1100 to 1200 F, and the remainder of the time at temperatures below 1100 F. It is planned to continue this operation for an indefinite time, for thorough study of the endurance of these materials in this range of high-temperature high-pressure duty

DESCRIPTION OF EQUIPMENT

The test element was constructed of 2-in-OD alloy tubes, in the form of four parallel hairpin loops, connected in series, for semiportable insertion through the rear wall of boiler No. 42 at the Twin Branch plant. Field location of the test element is shown in Fig. 5. In this location it is swept by the gas stream approaching the superheater at temperatures in the range of 2000 F, and is exposed to the action of a type IK sootblower operated on normal schedule. Steam from the main superheater outlet is supplied to the inlet of the test element and flows through the four consecutive loops to a final outlet for disposal. Appearance of the element in the boiler setting is shown in Fig. 6.

General arrangement of the test element is shown schematically in Fig. 7 which also indicates the type of materials employed. Details of their composition and heat-treatment, as well as design factors and welding schedules are included in Tables 1 and 2. It will be observed that increasing alloy compositions were used in successive parts of the assembly, with the final outlet leg comprising an 18-in. length of Timken 16-25-6 alloy, and a similar exposed length of Armco 17-14 Cu-Mo (Gt-45). Satisfactory weldability of the superalloys had been established by preliminary

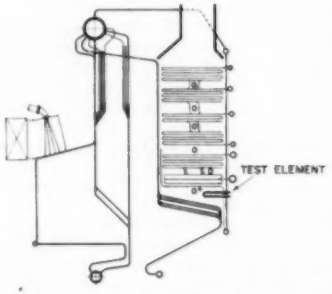

FIG. 5 LOCATION OF SUPERHEATER TEST ELEMENT IN OPERATING BOILER

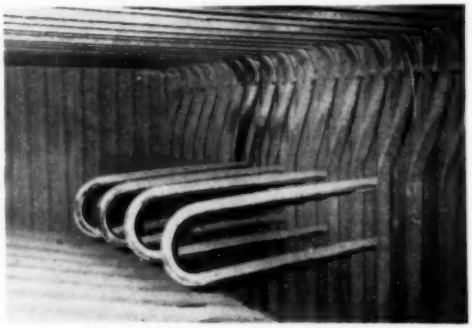

FIG. 6 SUPERHEATER TEST ELEMENT IN BOILER SETTING

TABLE 1 COMPOSITION AND HEAT-TREATMENT OF ALLOYS USED

Leg no.	Alloy	Heat no.	Chemical composition C	Mn	Si	Cr	Ni	Mo	Other elements	Heat-treatment	Electrode
1	Croloy 2¼	27772	0.11	0.45	0.27	2.45	...	0.99	...	Isothermally annealed	Croloy 2¼
2	Croloy 2¼	27772	0.11	0.45	0.27	2.45	...	0.99	...	Isothermally annealed	19-9Cb
3	Type 304	28104	0.066	1.61	0.35	18.86	10.18	...	...	1950 F, water quench	19-9Cb
4	Type 347	15806	0.064	1.55	0.39	17.68	12.42	...	0.80 Cb	1950 F, water quench	19-9Cb
5	Type 321	18251	0.050	1.78	0.60	18.07	12.22	...	0.48 Ti	2000 F, water quench	19-9Cb
6	Type 316	28081	0.077	1.66	0.45	16.32	13.42	2.36	...	2050 F, water quench	18-13-3
7	Type 318	26383	0.07	1.62	0.51	17.17	14.96	2.03	0.72 Cb	2050 F, water quench	Armco 17-14 Cu-Mo
8(a)	Timken 16-25-6	14999	0.075	1.64	0.45	16.18	26.42	6.40	0.167 N	2150 F, water quench	Armco 17-14 Cu-Mo
8(b)	Armco 17-14 Cu-Mo	B-54a	0.11	0.99	0.45	15.50	13.48	2.18	3.15 Cu 0.45 Cb 0.30 Ti	.225 F water quench[a] +5 hr 1350 F, air cool	

[a] Experimental heat.

TABLE 2 TUBE DATA AND METAL-TEMPERATURE CONDITIONS

Leg no.	Alloy	Tube dimensions, in. OD	ID	Minimum wall thickness	Stress at 2000 psig, Lamé	ASME proposed formula (1951)	Metal temperature corresponding to 1250 F outlet steam: Outer surface (Fig. 15)	Inner surface	Average
1	Croloy 2¼[a]	2.00	1.156	0.411	4120	2860	1175	1147	1161
2	Croloy 2¼[a]	2.00	1.156	0.411	4120	2860	1250	1222	1236
3	Type 304	2.00	0.974	0.512	3250	1905	1300	1258	1279
4	Type 347	2.00	1.188	0.396	4275	3025	1285	1255	1270
5	Type 321	2.00	0.952	0.521	3190	1836	1335	1292	1314
6	Type 316	2.00	0.982	0.504	3300	1970	1350	1288	1309
7	Type 318	2.00	0.966	0.509	3270	1930	1355	1326	1340
8(a)*	Timken 16-25-6	2.00	1.446	0.273	6490	5320	1350	1332	1341
8(b)	Armco 17-14 Cu-Mo	2.00	1.446	0.268	6650	5460	1350	1332	1341

[a] Replaced by Type 304 after operating period No. 1.

*8(a) Test section bored from solid billet.

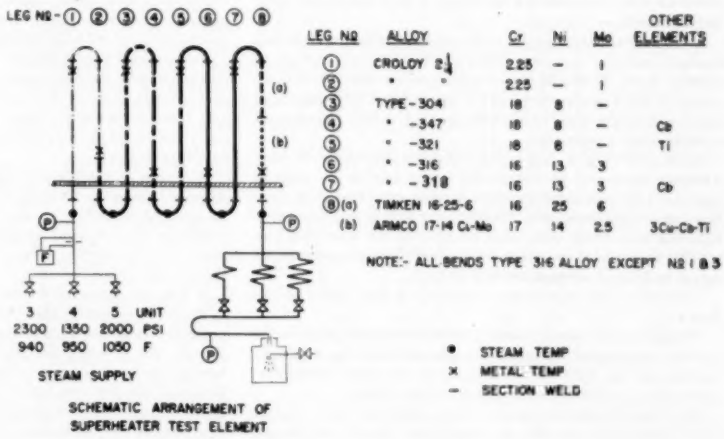

SCHEMATIC ARRANGEMENT OF SUPERHEATER TEST ELEMENT

FIG. 7 SCHEMATIC ARRANGEMENT OF SUPERHEATER TEST ELEMENT

tests. The chosen arrangement assured evaluation of the field performance, not only of the wrought tube materials, but also of the section weldments.

As indicated in Fig. 7, steam may be supplied from either of three sources, at various pressure and temperature conditions. This will be described later. Provisions were made for metering and recording the rate of flow of inlet steam. Rate of flow may be adjusted by manual selection of appropriate flow-control resistors in the outlet circuit. There are three resistors, comprising different lengths of small-bore tubing, wound in helical form, and connected in parallel at the outlet manifold. Virtually all of the pressure drop of the system occurs in the resistor section, so that the test element proper is maintained at full operating pressure. Outlet steam is discharged to a small direct-contact condenser, using service water, and is drained to waste.

While a general endurance field test of this nature might of itself be considered worth while, it was felt to be important to include actual measurement of the tube-metal temperatures and to obtain the recorded temperature history of each material in so far as it might be practical to do so. Accordingly, considerable effort was made to install thermocouples of a durable type, located at the hotter portion of each of the test alloys in the construction.

The method of installing thermocouples is shown in detail in Fig. 8. In this design the thermocouple hot-junction was formed by peening separately the chromel and alumel wires into chisel notches cut at the surface of the tube, and the lead wires from this junction were passed through holes, drilled as chords in the tube wall, which communicated with a small conduit tube ex-

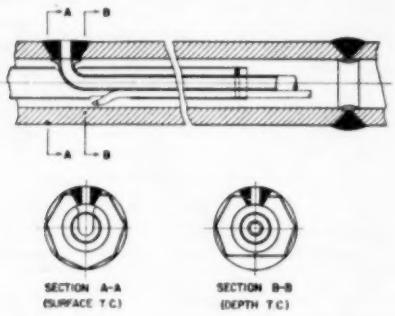

FIG. 8 DETAIL OF THERMOCOUPLE INSTALLATION IN SUPERHEATER TUBE

tended through the steam space to a suitable point of emergence outside of the boiler setting. By this arrangement a maximum of protection was afforded to the thermocouple leads to provide maximum durability. Many difficulties were encountered in making such an installation because of physical and metallurgical problems, and the procedure introduced a local mutilation of the element itself.

A companion thermocouple with welded-bead hot junction was similarly installed, at a measured depth from the tube surface, to provide direct reading of temperature gradient through the material. A third couple was placed in a closed-end tube, positioned in the steam-flow space at the same general locality for measurement of steam temperature.

As shown in Fig. 8, core tubes of suitable diameter were used, wherever necessary, to restrict the steam flow to the annular space between core and superheater tube, in order that steam mass flow rates of approximately 230,000 lb per sq ft hr might be maintained in accordance with usual practice, at the same time permitting moderate steam usage and desired steam-temperature increase in passage through the test element.

A detail of the tube-section weldment is also shown in this figure.

Measurement of steam temperatures at successive points in the system, as indicated in Fig. 7, were obtained from thermocouples peened into the tube surface external to the boiler, which were thoroughly insulated from heat-conduction effects.

The most significant couples were connected to a 16-point L&N Speedomax recorder for continuous record, and supplementary temperature readings were taken by portable potentiometer.

OPERATING NARRATIVE

It was planned initially to install the test element, in boiler No. 3 at the Twin Branch plant, which is operated at nominal base load, producing steam at 2300 psi and 940 F. Certain physical interferences, as well as restrictions on outage time of this unit for making such an installation, led to the decision to install the element in an adjacent boiler of unit No. 4, which is of similar open-pass type, but is designed for 1350 psi with 950 F final temperature. Constructional features of the rear wall of boiler No. 42 and general accessibility afforded a much simpler problem for the physical installation. It was considered that gas temperature and composition in the two units would be comparable.

The operating schedule of unit No. 4 included some variation of load, with outages each night and over week ends, which presented a very different situation for test conditions as compared to the nominal base load on boiler No. 3. It was felt, however, that such load variations would, if anything, offer a more severe test of the materials and, therefore, would be desirable to accelerate the investigation. The periodic outages, furthermore, would provide opportunity for interim inspection, which might not be available on the base-loaded unit. Therefore the test was started with the element inserted in the setting of boiler No. 42, using high-pressure steam supplied from adjacent boiler No. 3.

Coincident with the completion of the test element, the new high-pressure installation of unit No. 5 was completed at the Twin Branch plant and afforded an additional source of high-pressure steam at 2000 psi and 1050 F. Provision was made to deliver steam from this source to the test element.

A graphic record of the entire test operation is shown in Fig. 9. Because of heat loss from the connecting lines and low rate of steam flow, a considerable drop in temperature occurred between the superheater outlet and the test-element inlet. With an initial insertion of the element to 3 ft 6 in. distance and with steam taken from boiler No. 3, it was found impractical to develop the desired final outlet temperature. During the first test period of March and April, 1950, using the lowest flow resistor and with boiler No. 42 operating at full load, the outlet steam temperature rarely exceeded 1200 F.

In the course of operation a considerable amount of metal-temperature data were procured, but eventual failure of the thermocouples occurred, apparently resulting from deterioration of the chromel and alumel wires at their points of maximum exposure in the chord-hole cavities.

Preparations were made for inserting the element to a greater exposed length, but during progress of the work it was discovered that internal elements of the spray condenser had been damaged, and, because immediate repair could not be made, the test element was removed from the setting before boiler No. 42 was returned to service.

Opportunity was taken at this point to return the element to Alliance Laboratory for three primary purposes, viz., (*a*) for careful external inspection of alloy materials and welds, (*b*) for reinstallation of tube-metal-temperature thermocouples, and (*c*) for removal of the ferritic material and dissimilar weld occurring in the first loop of the element.

It had been observed during the initial run that temperatures in the first loop were higher than expected, and would exceed acceptable strength and oxidation limits for the ferritic material by 100 to 150 F when the final outlet-steam temperature was brought up to the desired range. Inasmuch as the principal objective of the test was to investigate the materials at the high-temperature end of the element, it was felt unwise to jeopardize this purpose by retaining the ferritic material and weldment under the prevailing excessive operating conditions at the low-temperature section. Accordingly, the complete first loop was removed during this intermission, replacing the Croloy $2^1/_4$ alloy by 18Cr-8Ni (Type 304). Laboratory examination revealed that none of the materials had suffered damage from the previous operation.

Upon returning the test element to service in August, 1950, installation was made with 4-ft insertion length, providing slightly more exposure for heat absorption, but it was found that the steam temperature obtained from boiler No. 3 still did not produce outlet steam as high as was desired in the program. For later operation it was decided to utilize steam from boiler No. 5, at a

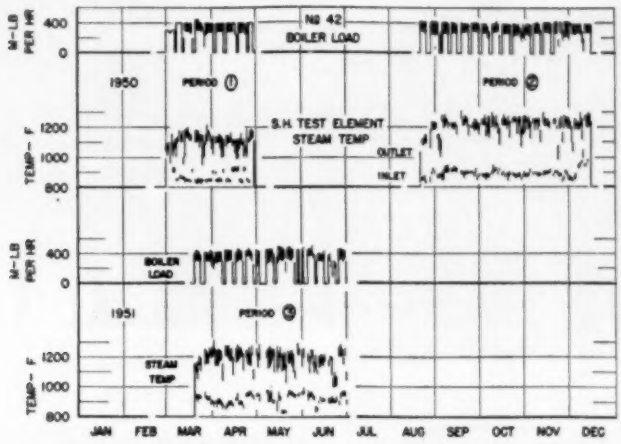

FIG. 9 GRAPHIC LOG OF TEST ELEMENT OPERATION 1950–1951

slight sacrifice of internal pressure but with higher initial temperature, in order that superheating could be developed at the higher range of outlet-steam temperature.

Some risk is involved in depending upon steam from a source external to the unit in which the test element is installed. It was found advisable in a number of instances to operate this element with steam supply from boiler No. 42, as, for example, over unattended week ends, or in the case of outage of the high-pressure units. Under these circumstances steam-flow rates were adjusted to maintain desired outlet temperatures; however, the operating stress in the test materials was reduced to a lower value. Provision was also made for protection of the test element, in case of steam failure from the high-pressure source, by automatic cut-in of supply from boiler No. 42.

With the initial arrangement, the rate of steam flow through the test element could be changed in stepwise increments by suitable choice of the resistors used in the circuit. The valves were employed as selectors, for complete-open or complete-closed duty, and were not used for throttling control of flow. This method of adjustment resulted in some variation of outlet temperature when operating conditions were varied on boiler No. 42. In consequence, a comparatively large portion of the accumulated service time occurred at temperatures below the desired range of 1200 to 1250 F. Steps are now being taken to install a control valve at the resistor outlet for closer regulation of steam flow to maintain the higher temperatures over a greater percentage of the time.

During the second operating period, from August 28 to December 16, 1950, outlet-steam temperatures in the desired range above 1200 F were generally attained by the use of supply steam from boiler No. 5. Typical operating conditions are illustrated in the graphical weekly plot in Fig. 10. This record indicates the nature of the load carried on boiler No. 42, with overnight banking periods, and with customary outage on the week end. Steam-flow and pressure conditions in the test element are graphically indicated, and show response to the different sources of steam supply, as well as the effect of using various flow resistors during the calibration tests which were run on August 28 and 29, 1950.

Steam-temperature values for each section are plotted, and it will be seen that temperature gains were made in successive loops, with the final outlet temperature being held nominally in the range of 1200 to 1250 F. During the nightly banking periods,

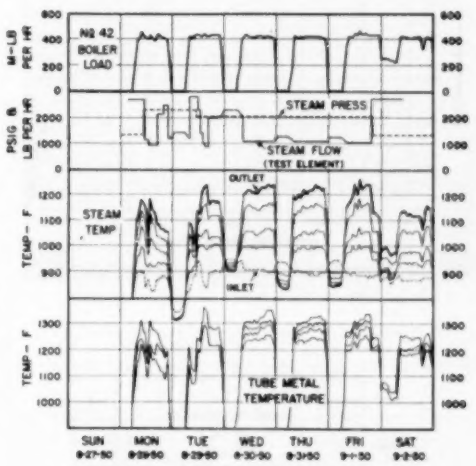

FIG. 10 WEEKLY LOG OF TEST-ELEMENT OPERATION

steam flow was maintained without manual readjustment, and cooling of the steam occurred in the test element instead of heating. For the longer week-end outages the steam supply was shut off and the element cooled to temperatures below saturation.

In the lower portion of the figure the record of metal temperatures is shown as obtained from the newly restored thermocouples. In subsequent weeks, failure of these thermocouples again occurred from the same cause of deterioration of the wires.

During the final week of this operating period, on December 13, 1950, it was observed that a small but definitely increasing rate of excess steam flow was occurring in the system, and it was suspected that a leak had developed, although no other evidence could be detected. Arrangements were made for a week-end shutdown of the boiler, and upon inspection it was found that a crack had developed in the outlet leg, adjacent to the rear wall of

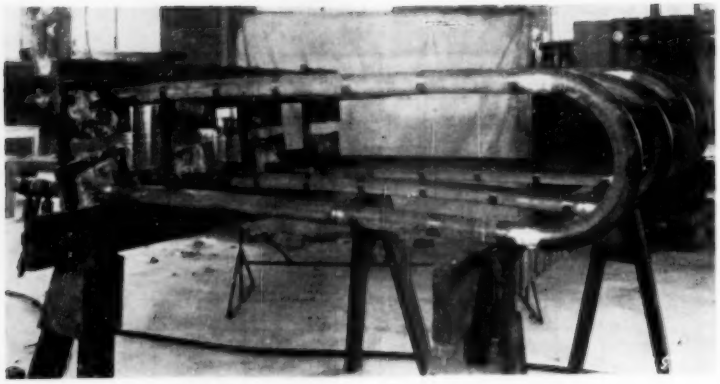

FIG. 11 TEST ELEMENT AFTER OPERATING PERIOD NO. 2

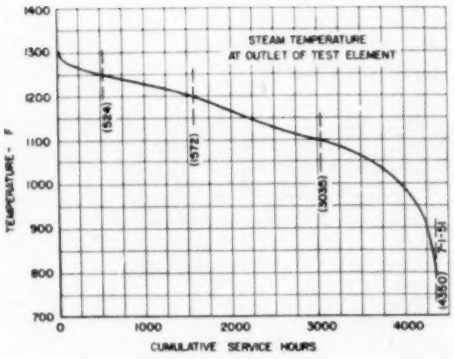

FIG. 12 OUTLET-STEAM-TEMPERATURE DURATION CURVE TO JULY 1, 1951

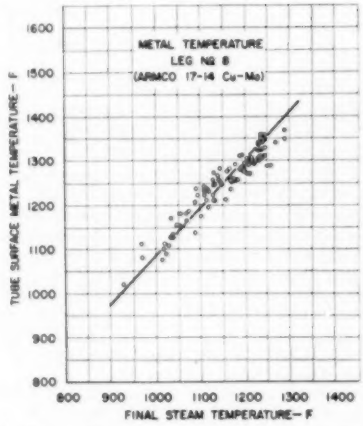

FIG. 14 METAL TEMPERATURE AS RELATED TO OUTLET-STEAM TEMPERATURE, LEG NO. 8 ARMCO 17-14 CU-MO

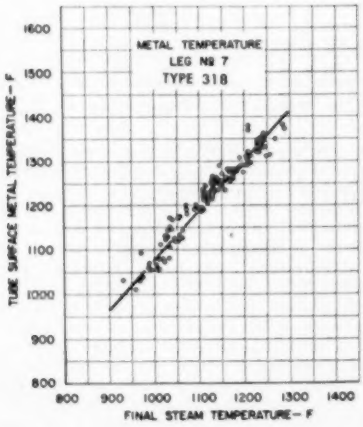

FIG. 13 METAL TEMPERATURE AS RELATED TO OUTLET-STEAM TEMPERATURE, LEG NO. 7 TYPE 318 ALLOY

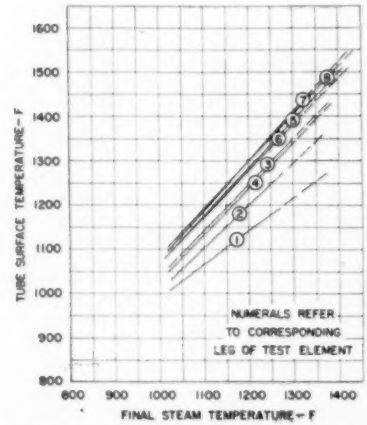

FIG. 15 SUMMARY OF METAL TEMPERATURE VERSUS FINAL STEAM TEMPERATURE FOR VARIOUS TUBE SECTIONS IN TEST ELEMENT

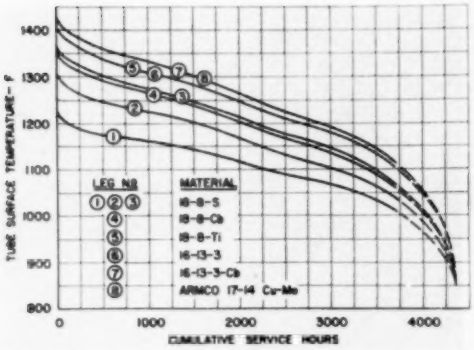

FIG. 16 SUMMARY OF METAL TEMPERATURE VERSUS TIME FOR VARIOUS ALLOYS IN TEST ELEMENT TO JULY 1, 1951
(Derived from Fig. 12 and Fig. 15.)

(a)

(b)

FIG. 17 INTERNAL SURFACE CONDITION AND MICROSTRUCTURE OF 18CR-8NI, TYPE 304, ALLOY TUBE
(a, Top view of inside surface; × 10. b, Section through internal surface; aqua regia—glycerin etch; ×500.)

(a)

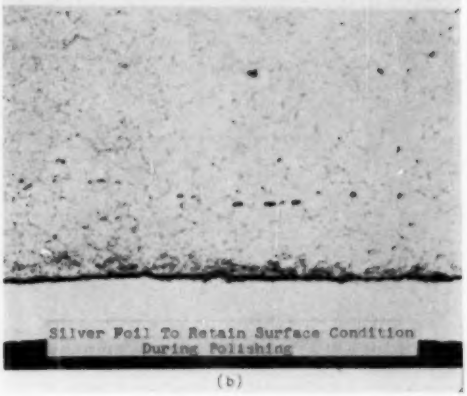

(b)

FIG. 18 INTERNAL SURFACE CONDITION AND MICROSTRUCTURE OF 18CR-8NI-CB, TYPE 347, ALLOY TUBE
(a, Top view of inside surface; ×10. b, Section through internal surface; aqua regia—glycerin etch; ×500.)

the boiler, at the location where the chord-hole type of thermocouple had been installed in the Armco 17-14 Cu-Mo material. The test element thereupon was removed from the setting and returned to the laboratory for further inspection and repair.

INSPECTION OF RETURNED ELEMENT

Visual examination of the returned element indicated that, in general, all materials were in satisfactory condition. The external surfaces were smooth and displayed an unexpectedly small degree of oxidation. The appearance of the element at this time is shown in Fig. 11. A major crack existed at the thermocouple weld of the outlet leg and inspection revealed incipient or minor cracks in three other thermocouple welds. These cracks undoubtedly resulted from the adverse effect of the chord holes and the weakening of the plug welds by the unavoidable notch which was formed on the inner tube surface at the junction with the internal thermocouple conduit tube. A small amount of warping was present in the third loop, showing a maximum deflection of $1^1/_2$ in. in the Type 321 material of leg No. 5.

Since a considerable amount of metal-temperature data had

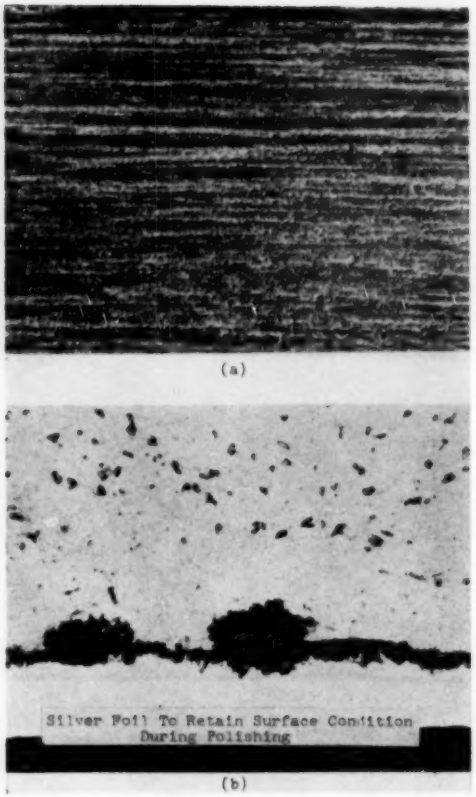

(a)

(b)

FIG. 19 INTERNAL SURFACE CONDITION AND MICROSTRUCTURE OF 18CR-8NI-TI, TYPE 321, ALLOY TUBE

(a, Top view of inside surface; ×10. b, Section through internal surface; aqua regia—glycerin etch; ×500.)

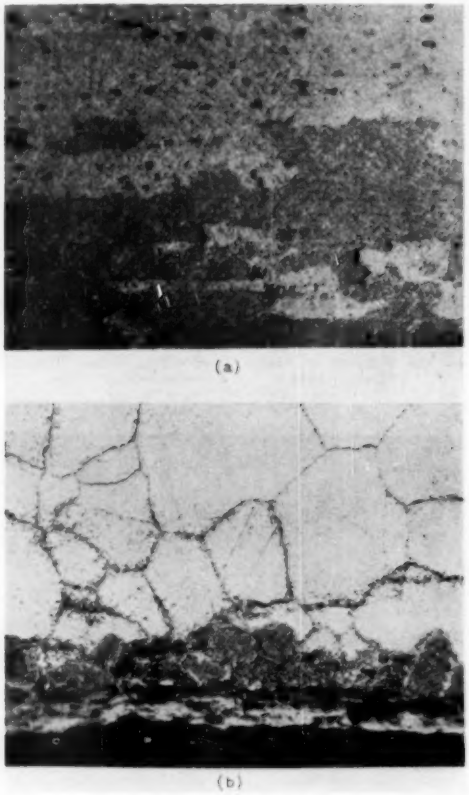

(a)

(b)

FIG. 20 INTERNAL SURFACE CONDITION AND MICROSTRUCTURE OF 16CR-13NI-3MO, TYPE 316, ALLOY TUBE

(a, Top view of inside surface; ×10. b, Section through internal surface; aqua regia—glycerin etch; ×500.)

already been procured, it was decided to remove all thermocouple weldments by cutting out 2-in-long sections and rejoining the cut ends by regular ring welds.

The removed sections containing the thermocouple junctions were subsequently subjected to a metallurgical examination. No significant surface deterioration was found in any of the materials. However, certain differences were noted on the steam side of some of the materials. For example, Armco 17-14 Cu-Mo and Type 316 tubes appeared to be attacked by steam to a slightly greater extent than alloys Types 304, 321, 347, and 318. This was indicated by the miscroscopically determined internal scale thicknesses which were as follows:

Armco 17-14 Cu-Mo	0.002 in.
Type 316	0.002 in.
Type 318	0.0002–.0005 in.
Type 347	0.00012 in.
Type 321	0.0002–.0005 in.
Type 304	0.0012 in.

It was also noted that the internal scale of the Armco 17-14 Cu-Mo and the Type 316 tubes was loosely adhering and leafy. However, there appears to be no reason to assume that these conditions, which are illustrated in Figs. 17 to 22, are indicative of inadequate surface stability under the given testing conditions. Likewise, there were no signs of significant microstructural changes. The nonstabilized alloys Types 304 and 316, as well as Armco 17-14 Cu-Mo, displayed an intercrystalline precipitate but no indications of intercrystalline attack. Type 321 contained scattered sigma-phase particles, and traces of sigma phase were also noted in the grain boundaries of Type 318 alloy. Timken 16-25-6 alloy was not included in this examination since it contained no thermocouple weld and was, therefore, not sampled. Summarily, it may be said that the examined alloys appeared to stand up very well under the given field conditions.

Measurements of tube diameter at this time indicated no perceptible amount of enlargement.

SUMMARY AND CONCLUSIONS

Since all materials and section welds were found to be in satisfactory condition, the repaired test element was again placed in service on March 19, 1951, continuing to the present date.

As a summary of the entire period to July 1, 1951, a temperature-duration curve, as shown in Fig. 12, has been drawn to indi-

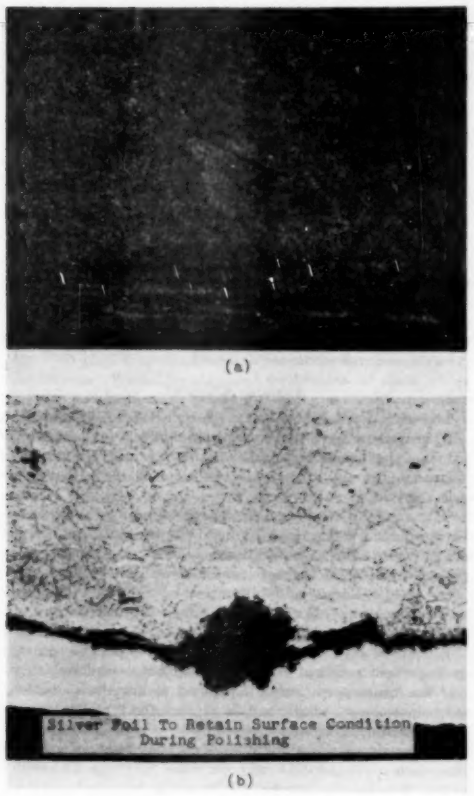

FIG. 21 INTERNAL SURFACE CONDITION AND MICROSTRUCTURE OF 16CR-13NI-3MO + CB, TYPE 318, ALLOY TUBE
(a, Top view of inside surface; ×10. b, Section through internal surface; aqua regia—glycerin etch; ×500.)

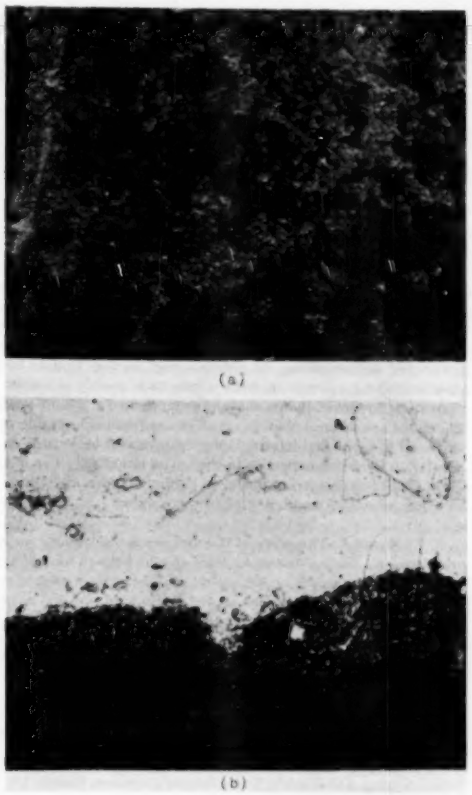

FIG. 22 INTERNAL SURFACE CONDITION AND MICROSTRUCTURE OF ARMCO 17-14 CU-MO ALLOY TUBE
(a, Top view of inside surface; ×10 b, Section through internal surface; aqua regia—glycerin etch; ×500.)

cate the extent of time in which the element has actually produced steam at the various temperature ranges detailed in the figure.

Statistical data on metal temperatures for the various alloys are limited to the periods of endurance of the special thermocouples. A great many metal-temperature readings were obtained during the initial several weeks of operation in periods 1 and 2. Relationships have been drawn between these metal temperatures and the associated steam temperatures which make it possible to approximate the temperature history of the materials under test. Examples of this metal-to-steam-temperature relationship are shown in Fig. 13 to Fig. 15, and a corresponding time versus temperature plot is indicated in Fig. 16.

Field and laboratory inspection of the test element has shown that all materials are in generally good condition for continued service. However, subsequent periodic measurements of the tube diameters indicate the development of a small rate of creep at the hotter end of the 18-8 Ti (Type 321) material amounting to approximately $^3/_4$ per cent of tube diameter enlargement.

It is planned to continue the test program for an indefinite period in substantially the same manner as it is now being operated, and to make ultimately a more detailed comparison between the material removed from service and coupons of the original tubes which were retained at the time of fabrication.

While it is much too soon to draw definite conclusions from this experience, the evidence on the whole gives favorable indications for the practical construction of commercial steam superheaters for operation in the range of 2000 psi and 1200 F final temperature, considering the possibility that service life may be limited but justifiable on the basis of economic replacement.

ACKNOWLEDGMENTS

The authors wish to acknowledge, with appreciation, the progressive and co-operative assistance extended by The American Gas & Electric Service Corporation and The Indiana & Michigan Electric Company in their accommodation of the test program, and the services of Mr. J. A. Dillon of The Babcock & Wilcox Company, who carried out the field supervision of the project.

BIBLIOGRAPHY

1 "Possibilities of the Regenerative Steam Cycle at Temperatures up to 1600 F," by P. H. Knowlton and R. W. Hartwell, Trans. ASME, vol. 72, 1950, pp. 1017-1022.

2 "Report on the Strength of Wrought Steels at Elevated Temperatures," prepared by R. F. Miller and J. J. Heger, ASTM Special Technical Publication No. 100, March, 1950.

3 "The Creep and Stress-Rupture Testing of Steam-Boiler Materials," by J. B. Romer and H. D. Newell, Trans. ASME, vol. 74, 1952, pp. 157–174.

4 "Proposed Revisions and Addenda to Boiler Construction Code," *Mechanical Engineering*, August, 1951, pp. 672–676.

5 "Product Data Bulletin," Armco Steel Corp., Jan. 3,1950.

6 "Influence of Extended Time on Creep and Rupture Strength of 16-25-6 Alloy," by C. L. Clark, M. Fleischmann, and J. W. Freeman, ASM Fall Meeting, 1951.

Discussion

S. N. Fiala.[4] The need for advanced information on the behavior of various superheater-tube materials at high temperatures and under operating conditions is of vital interest to the power-generation field. The authors' company is to be commended on sponsoring a program of this type, and the authors are to be congratulated on presenting the program and findings to date in a concise manner which makes the information readily available.

As hosts to the field portion of the program in our Twin Branch Plant, we are pleased that the studies are producing usable results and that the findings are being made available through this paper and subsequent reports to the entire industry. The work in the plant has progressed in a most cordial manner, attributable to the organization and handling of the program.

C. L. Clark.[5] This work of the authors is most timely for as additional results are obtained they should help to answer the question as to whether or not stabilized austenitic steels are required for superheater service at metal temperatures of 1100 to 1300 F. We always have believed the standard 18-8 to be the most foolproof, and its properties least affected by possible variations in grain size and structure, and if the authors' findings show 304 to be suitable for this type of service, it will be a notable contribution.

[4] Head of Mechanical Engineering Division, American Gas and Electric Service Corporation, New York, N. Y. Mem. ASME.

[5] Metallurgical Engineer, Special Steel Developments, Steel and Tube Division, The Timken Roller Bearing Company, Canton, Ohio. Mem. ASME.

The values given in Table 2 of the paper show that for their particular tube size an appreciable variation exists in the tube-wall stress depending on the formula used. In Table 3, herewith, are listed these values, together with the average metal temperature, and the new allowable Code stresses taken from Table UHA-23.

TABLE 3 TUBE DATA

Alloy	Stress in tube wall, Lamé	Stress in tube wall, ASME	Average temp	Allowable stress, psi	Ratio of allowable stress to Lamé	Ratio of allowable stress to ASME
304	3250	1905	1279	2700	0.83	1.42
347	4275	3025	1270	3200	0.75	1.06
321	3190	1836	1314	2250	0.70	1.23
316	3300	1970	1309	3700	1.12	1.90

There is no constant relationship for the various steels between the stress, as determined by either of the formulas, and the maximum allowable stress and we are wondering if a constant relationship should not exist for the proper evaluation of the behavior of the steels. Also, in this connection, which of these two formulas gives the more correct tube-wall stress?

Authors' Closure

The comparisons drawn by Dr. Clark in Table 3 are pertinent, and the authors agree that a more constant relation between the values of the ratio of actual to allowable stress, for the individual components of the superheater test element, would have been desirable.

Part of the discrepancy may be accounted for by differences between actual and anticipated metal temperatures, and by small deviations in tube wall thickness compared to design specifications. Further discrepancy results from the fact that the present code values of allowable stress, on which the comparison is based, were not available at the time the test element was constructed.

In spite of this we believe that the test experience provides an important practical evaluation of materials and weldments, and for future operation it is planned to introduce additional new superstrength alloys, and to advance the type 304 material to a higher-duty position in the assembly.

We are particularly grateful for Mr. Fiala's remarks, and trust that future relationships will continue to be as satisfactory as they have been in the past.

Behavior of Superheater Tubing Materials in Contact With Combustion Atmospheres at 1350 F

By H. A. BLANK,[1] A. M. HALL,[2] AND J. H. JACKSON,[3] COLUMBUS, OHIO

With steam temperature of central-station boiler plants advancing to 1050 F in new installations today, and with indications that steam temperatures of 1200 F are not too far in the future, selection of suitable materials for superheater and reheater tubing requires special consideration. Alloys having good service characteristics in the range of 1100 F to 1350 F are required to meet the foregoing steam conditions. While mechanical properties of such alloys are not too serious a problem, the matter of corrosion resistance is a critical one. The ASME Special Research Committee on High-Temperature Steam Generation, recognizing the importance and the complexity of the corrosion problems, undertook sponsorship of a comprehensive program to evaluate commercially available alloys for suitability as superheater and reheater tubing at metal temperatures up to 1350 F. (The program is divided into two broad parts.) One is concerned with the reaction of high-pressure high-temperature steam on such materials. The other deals with corrosion by flue gases and slag-forming ash on the external surface of the tubing, and is divided in turn into two phases. The specific objective of one phase is the evaluation of the alloys with respect to resistance toward corrosion by the combustion products of the various fuels used for boilers, under actual field conditions. The objective of the other phase, carried out in the laboratory, is the investigation of the effect of certain components of a combustion atmosphere on the rate of corrosion of the same alloys. This paper is concerned with the field-test phase of the program which was carried out at Battelle. The laboratory work done at Battelle will be the subject of a future paper.

Introduction

As a result of the constant demand for increased station efficiency, steam temperature in central-station boiler plants has increased markedly in the past few years. Whereas a steam temperature of 950 F was considered a satisfactory maximum 4 or 5 years ago, today numerous installations are in operation or are being built in which the steam temperature is as high as 1050 F, and one installation for 1100 F steam is under construction. There are many indications that steam temperatures up to at least 1200 F will be used in the not too distant future.

To permit these increases in operating temperatures, considerable attention must be given to the selection of suitable materials for superheater and reheater tubing. As the temperature of these heat-receiving surfaces will range from 50 to 150 F higher than the steam temperature, it is apparent that alloys having good service characteristics in the range of 1100 F to 1350 F must be used. The alloys must have the necessary mechanical properties, must be sufficiently resistant to reaction with steam on internal surfaces, and must withstand the action of hot flue gases and slag deposits on external surfaces.

The strength requirements, while very important, do not appear to present so serious a problem as do the corrosion requirements. Certain problems relating to corrosion on external surfaces have been the subject of previous investigations, among which should be mentioned those by Schläpfer, Amgwerd, and Preis (1),[4] C. T. Evans (2, 3), Engel (4), Skinner and Kozlik (5), O. L. Wood (6), C. F. Tibbetts (7), V. F. Estcourt (8), and D. Douglass (9). Particular attention has been paid to the corrosion problems produced by the use of certain residual fuel oils, and it has been reported that vanadium, especially in combination with sulphur and alkali metals, increases tremendously the corrosiveness of the oil ash. Furthermore, to date no metallic material satisfactorily resistant to attack by the products of combustion of high-vanadium, high-sulphur residual oils at temperatures above 1200 F has been reported. There are indications, however, that chromium as an alloying element increases while molybdenum reduces resistance to this type of attack.

The ASME Special Research Committee on High-Temperature Steam Generation, recognizing the importance and the complexity of the corrosion problems, undertook sponsorship of a comprehensive program to evaluate commercially available alloys for suitability as superheater and reheater tubing at metal temperatures up to 1350 F. The program is divided into two broad parts. One is concerned with the reaction of high-pressure high-temperature steam on such materials. The other deals with corrosion by flue gases and slag-forming ash on the external surface of the tubing, and is divided in turn into two phases. The specific objective of one phase is the evaluation of the alloys with respect to resistance toward corrosion by the combustion products of the various fuels used for boilers, under actual field conditions. The objective of the other phase, carried out in the laboratory, is the investigation of the effect of certain components of a combustion atmosphere on the rate of corrosion of the same alloys.

This paper is concerned with the field-test phase of the program which was carried out at Battelle. The laboratory work done at Battelle will be the subject of a future paper.

[1] Principal Metallurgist, Battelle Memorial Institute.
[2] Assistant Supervisor, Battelle Memorial Institute.
[3] Supervisor of Physical Metallurgy, Battelle Memorial Institute.

Contributed by the High-Temperature Steam Generation Research Committee the Joint ASTM-ASME Committee on Effect of Temperature on the Properties of Metals, and the Power Division and presented at the Annual Meeting, Atlantic City, N. J., November 25–30, 1951, of The American Society of Mechanical Engineers.

Note: Statements and opinions advanced in papers are to be understood as individual expressions of their authors and not those of the Society. Manuscript received at ASME Headquarters, August 20, 1951. Paper No. 51—A-42.

[4] Numbers in parentheses refer to the Bibliography at the end of the paper.

TABLE 1 TEST MATERIALS

Material	Composition, per cent Fe	Ni	Cr	C	Mn	Si	P	S	Mo	Other elements
16-25-6	Balance	24.8	16.3	0.08	1.7	0.34	0.017	0.012	5.95	0.146 N_2
AISI 3098	Balance	13.8	23.7	0.09	1.4	0.58	0.020	0.012	0.03	0.132 N_2
AISI 310	Balance	20.3	25.2	0.08	1.7	0.75	0.013	0.015	0.02	...
AISI 347	Balance	11.1	17.2	0.06	1.6	0.58	0.013	0.017	0.02	0.73 Cb
AISI 308	Balance	10.0	20.8	0.06	2.0	0.38	0.025	0.008	0.24	...
AISI 309	Balance	14.54	23.12	0.13	2.0	0.40	0.026	0.008	0.15	...
AISI 314	Balance	21.45	24.56	0.09	1.3	2.20	0.024	0.011	0.13	...
AISI 321	Balance	10.36	17.72	0.07	1.4	0.47	0.026	0.010	0.15	0.45 Ti
AISI 304	Balance	8–11	18–20	0.08 max	2.0 max	1.0 max	0.04 max	0.03 max	...	...
AISI 316	Balance	10–14	16–18	0.10 max	2.0 max	1.0 max	0.04 max	0.03 max	2.0–3.0	...
17-14 Cu-Mo	Balance	13–15	15.5–17.5	0.151	1.0	1.0	0.04	0.03	1.75–3.0	0.15–0.45 Ti 0.35–0.65 Cb 2.5 –4.0 Cu
Inconel	10 max	70 min	11–15	0.15 max	1.0 max	0.5 max	...	...	...	...
Illium G	6.0	58	22	...	1.2	0.4	...	...	6.0	6.0 Cu
Aluminized mild steel	Aluminum-coated samples of cold-rolled steel									

Procedure

Test Materials. Fourteen commercially available alloys were selected by the ASME Special Research Committee on High-Temperature Steam Generation for evaluation of their resistance to corrosion by flue gases and furnace slags. The designations and compositions of these materials are listed in Table 1. The group consists of austenitic stainless steels, nickel-base alloys, and an aluminized cold-rolled steel.

The alloys were obtained in the form of 1-in-diam round bars. The austenitic iron base alloys were solution-heat-treated by water quenching after heating 2 hr at 2050 F. The other alloys were tested as hot-rolled. Field-test specimens, with dimensions as shown in Fig. 1, were machined from the bars. The form of the specimens was dependent upon the design of the specimen rack discussed in the following section.

FIG. 1 SKETCH OF FIELD-TEST SPECIMENS

Specimen Rack. Since this phase of the program called for evaluation of the selected alloys under actual field conditions, it was necessary to place specimens of these materials in the gas stream. Wherever possible, it was desirable to place specimens where they would attain an average temperature of about 1350 F. This meant a location at some point in the superheater section. In addition, the actual installation of the specimens had to be arranged to avoid inconvenience to boiler operation. To expedite the program it was necessary to install each set of specimens in a unit while it was in operation, thus avoiding any long delay until a shutdown period.

Thus it is evident that the manner of installing the specimens was of considerable importance. Of major concern was the development of a suitable specimen rack. After several preliminary designs were tested in different types of steam-generating units at the Picway Station of the Columbus and Southern Ohio Electric Company, a specimen rack of simple design was developed which was generally satisfactory for the installations made in this program. The rack consisted of a $^3/_8$-in-thick plate of AISI 310 stainless steel formed as shown in the perspective view given in Fig. 2. The over-all dimensions of the rack were $6^1/_4$ in. $\times$ 6 in. $\times$ $11^3/_4$ in. It contained 14 holes, each $^3/_8$-in. diam, on $1^1/_8$-in. centers. A specimen was dropped into each hole, the head machined on it preventing it from falling through the hole. The rack could be equipped with AISI 310 hooks for installation in a superheater having vertical tubes, or it could be inverted and set upright on horizontal tubes.

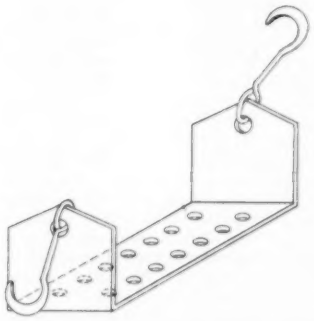

FIG. 2 PERSPECTIVE VIEW OF TEST RACK AND HOOKS

Field-Test Installations. Racks of field-test specimens were located in steam-generating units of ten companies. Included among these were the boilers of seven public utilities, a steel company, an oil company, and a merchant ship. The selection of installations was made by representatives of the manufacturers of steam-generating units who are members of the ASME Research Committee on High-Temperature Steam Generation. The installations were chosen to include those fired by various types of coal and by various methods of burning coal as well as those fired by gas and oil. An effort was made to cover the entire range of the types of combustion products which might be encountered in commercial service. The locations of the installations are given in Table 2, together with the duration of the tests, the type of furnace and fuel, and the approximate specimen temperature.

Before a rack of test specimens was installed in a unit, temperature measurements were made with a probing thermocouple to locate a zone in the gas stream where an average metal temperature of approximately 1350 F would prevail. To be sure that the proper metal temperature was obtained, the thermocouple hot junction was peened into a metal slug $^3/_4$ in. diam $\times$ 1 in. long, i.e., a section equivalent to that of a test specimen.

In some steam-generating units, the location of the access doors made it impossible to insert the rack in the desired temperature zone. In these units the rack was installed where metal temperature was as close to the desired value as was practical. In selecting a location for a specimen rack, account was taken of the effect on temperature of fluctuations in the load on the unit.

Because metal temperature varied with the thickness of the scale and the amount of soot and ash deposited on the tubes as well as with the load on the unit, an effort was made to record the metal temperature during the test. A chromel-alumel thermocouple was peened into the specimen rack before it was placed in

TABLE 2 FIELD-TEST INSTALLATIONS

Company	Station	Unit no.	Location	Length of test, days	Type of unit	Fuel	Approximate average specimen temp, deg F
Philadelphia Electric Company	Richmond	64	Philadelphia, Pa.	...	C. E.[a] radiant pulverized-coal, dry-bottom	Central Pa. coal	1300–1375
Moore-McCormack Lines	*S. S. Mormactide*	..	Merchant ship	148	F. W.[b], Type D	Bunker-C fuel oil	[e]
Public Service Electric & Gas Company of New Jersey	Sewaren	1	Sewaren, N. J.	93.5	C. E.[a] radiant	No. 6 fuel oil	1350
Commonwealth Edison Company	Fisk	17	Chicago, Ill.	[d]	B. & W.[c] cyclone	Illinois No. 6 coal	1200–1375
Bethlehem Steel Company	Penwood	2	Sparrows Point, Md.	120	C. E.[a] stoker-fired, dry-bottom	Coke and blast-furnace gas	1250
Pacific Gas & Electric Company	Oleum	..	San Francisco, Calif.	...	F. W.[b]	High-sulphur, high-vanadium, petroleum coke and gas	...
Gulf States Utilities Company	Baton Rouge	8	Baton Rouge, La.	109	B. & W.[c]	Natural gas	1250
Pennsylvania Power & Light Company	Sunbury	1A	Sunbury, Pa.	156.5	F. W.[b] pulverized-coal, dry-bottom	Anthracite	1350
Standard Oil Development Company	Bayway Refinery	1	Linden, N. J.	160	Riley	82% oil (2% S) 18% gas (4–20% S)	1200–1400
Union Electric Company of Missouri	Venice No. 2	7	St. Louis, Mo.	120	B. & W.[c] radiant dry-bottom	Illinois coal and natural gas	1250–1300

[a] Combustion Engineering-Superheater, Inc.
[b] Foster Wheeler Corporation.
[c] The Babcock & Wilcox Company
[d] Specimens were not recovered.
[e] Average temperature not known. Specimens installed in cold furnace at a location where it was estimated the desired temperature would be attained.

the unit. However, the couple failed after several hours of exposure to the furnace gases. Consequently, the metal temperatures shown in the table are approximate values. The thermocouple readings were usually sufficient to give an indication of the probable fluctuations in temperature the specimens would experience. In particular, these data gave information on the relation between specimen temperature and the load on the unit, on the basis of which average specimen temperature was estimated.

Originally it was planned to leave all specimens, except those installed at Sewaren, on test for a period of about 6 months. The conditions at Sewaren were known to be extremely corrosive. Consequently, it was deemed advisable to remove these specimens after a period of only 3 months. The rack of specimens that had been installed at Penwood was returned for evaluation after 4 months on test. Considerably more corrosion was observed on these two sets of specimens than was originally anticipated. Consequently, it was decided to request return of all the remaining test racks as soon as possible, even though they were on test for periods of less than 6 months.

Evaluation of Specimens. After being returned to Battelle, a $^3/_4$-in-thick disk was cut from the shank of each specimen for metallographic examination to determine the character and depth of any subsurface corrosive attack. The disks were mounted in Bakelite in transverse section and examined both as-polished and as-etched.

Attempts were then made to descale the remaining part of each specimen by electrolytic pickling in various acid solutions and by the sodium hydroxide–sodium hydride process. None of these methods attacked the scale. An auxiliary experiment was then performed to determine whether the scale could be removed satisfactorily by buffing with a wire wheel. It was found that this could be done, and the loss of metal involved in the operation would be negligible. Buffing an unscaled specimen for 5 min caused a weight loss of only 0.014 per cent.

When the specimens were suspended in the rack, approximately $^3/_8$ in. of the shank just below the head was partially protected from the atmosphere by the rack. Consequently, this portion of each specimen was not attacked so severely as the unprotected part. In order to prevent any inaccuracy in results because of this circumstance, a section 4.5 in. long was taken from the unprotected portion of each specimen for weight-loss determinations. The original weight of each section was calculated from the density, and the change in weight was determined by direct measurement. From the weight-loss data and the density the loss in diameter was calculated.

Results of Tests

The corrosion data obtained on the alloys installed in the various steam-generating units are given in Table 3. The specimen rack installed at the Fisk Station was lost, while the tests at the Richmond and Oleum Stations were not completed in time for inclusion in the paper.

Corrosion rate is given both in terms of grams lost per square inch per month and as inches lost from the diameter per month. The extent of corrosion penetrating below the surface of the specimens (specifically, below the scale to metal interface), as determined metallographically, is also indicated in the tables. The figure given is the maximum depth of subsurface attack observed in the microsection. For better visualization the results are also shown in graphical form in Figs. 3 and 4.

Figs. 5 through 8 are illustrative of the appearance of the specimens after removal from the various steam-generating units. Figs. 5 and 6 show the specimens which were removed from the Sewaren Station after 93.5 days of exposure to the combustion products formed from the burning of a high-sulphur, high-vanadium bunker C fuel oil. The condition of these specimens is representative of severe corrosion. Figs. 7 and 8 show specimens which were removed from the Baton Rouge Station after 109 days of exposure to an atmosphere produced by burning sulphur-free natural gas. This is typical of a mild corrosion attack.

Discussion

In examining the results, account must be taken of the fact that each set of specimens underwent a somewhat different cycle of temperature fluctuations during its test. This cycle, of course, was directly related to boiler operations which inevitably varied from plant to plant. It is considered, however, that the testing time was long enough to have equalized the effects of the cycles to a considerable extent.

Probably of greater importance is the spread in the average temperature attained by the different sets of specimens. The data in Table 2 indicate that this amounted to at least 100 F. As mentioned earlier, in some steam-generating units the location of the access doors made it impossible to insert the rack of specimens in the zone having the desired average temperature. It was necessary in these cases to use the next best location. In

TABLE CORROSION DATA FOR MATERIAL EXPOSED TO VARIOUS COMBUSTION ATMOSPHERES

Alloy	High-sulphur, high-vanadium fuel oil — Weight loss, g./in.²/mo	Decrease in diam, ipm[a]	Max depth subsurface attack, in.	High-alkali content coke and blast-furnace gas — Weight loss g./in.²/mo	Decrease in diam, ipm[a]	Max depth subsurface attack, in.
	Sewaren Station			Penwood Station		
Aluminized steel	1.451	[d]	None	2.535	[d]	0.008
Illium G[b]	0.835	0.0062	0.002	1.290	0.0093	0.036
Inconel	0.455	0.0032	0.009	1.762	0.0134	0.035
17-14 Cu-Mo	[c]	[c]	[c]	1.808	0.0139	0.010
AISI 316	2.029	0.0156	0.006	0.785	0.006[e]	0.008
AISI 308	0.543	0.0042	0.001	0.618	0.0048	0.001
AISI 321	3.452	0.0266	0.002	0.945	0.0075	0.005
AISI 314	0.867	0.0068	None	0.078[e]	0.0006	None
AISI 309	0.681	0.0052	None	0.493	0.0038	0.002
AISI 304	1.439	0.0110	None	0.783	0.0061	0.005
AISI 347	1.492	0.0114	0.001	0.643	0.0049	0.003
AISI 310	0.310	0.0023	None	0.048[e]	0.0004	0.005
AISI 309S	0.183	0.0013	None	0.210[e]	0.0016	0.001
16-25-6	[c]	[c]	[c]	0.810	0.0062	0.008
	Natural gas and Illinois coal — Venice No. 2 Station			High-sulphur oil and gas — Bayway Refinery		
Aluminized steel	0.099	[d]	None	0.724	[d]	None
Illium G[b]	...	...	...	...	...	...
Inconel	0.210	0.0015	None	1.860	0.0134	None
17-14 Cu-Mo	0.098	0.0008	None	[c]	[c]	[c]
AISI 316	0.007	0.0001	None	1.216	0.0094	None
AISI 308	0.098	0.0008	None	0.063	0.0005	0.004
AISI 321	0.068	0.0005	None	0.896	0.0070	0.013
AISI 314	0.048	0.0004	None	0.607	0.0048	0.003
AISI 309	0.203	0.0015	None	0.127	0.0010	0.005
AISI 304	0.195	0.0015	None	0.544	0.0042	0.013
AISI 347	0.128	0.0010	0.001	0.141	0.0011	0.003
AISI 310	0.000	0.0000	None	0.171	0.0013	0.001
AISI 309S	0.100	0.0007	None	0.067	0.0005	0.003
16-25-6	0.000	0.0000	None	[c]	[c]	[c]
	Low-sulphur anthracite coal — Sunbury Station			Sulphur-free natural gas — Baton Rouge Station		
Aluminized steel	0.62	[d]	None	0.565	[d]	None
Illium G[b]	...	...	...	...	...	...
Inconel	0.0000	0.0000	None	0.0008	0.0001	None
17-14 Cu-Mo	0.0000	0.0000	None	0.0279	0.0002	None
AISI 316	0.0000	0.0000	None	0.1508	0.0012	None
AISI 308	0.0000	0.0000	None	0.0307	0.0002	None
AISI 321	0.0000	0.0000	None	0.2520	0.0020	0.001
AISI 314	0.0084	0.0001	None	0.0195	0.0002	None
AISI 309	0.0000	0.0000	None	0.0923	0.0007	None
AISI 304	0.0218	0.0002	None	0.0279	0.0002	None
AISI 347	0.0082	0.0001	None	0.0307	0.0002	None
AISI 310	0.0000	0.0000	None	0.0081	0.0001	None
AISI 309S	0.0000	0.0000	None	0.0106	0.0001	None
16-26-5	0.0455	0.0003	None	0.0162	0.0001	None

[a] ipm = inches per month.
[b] No specimens available for 4 of 6 stations.
[c] Specimens completely corroded away.
[d] Due to uncertainty of density figure required in calculation, conversion to inches of radius lost per month could not be accomplished.
[e] Slight pitting occurred.

one case, that of the steamship *Mormactide*, circumstances dictated that the rack of specimens be installed when the boiler was cold and a guess had to be made as to the location where the specimens would attain the desired average temperature. The results of this test indicated very strongly that the average metal temperature was considerably lower than desired and the data obtained had to be discarded.

Taking these limitations into consideration, it is evident, nevertheless, that wide differences occurred in the corrosiveness of the various combustion atmospheres toward most of the alloys under study. As would be expected from the results of other investigations (1 to 11), the products of combustion of the high-sulphur, high-vanadium residual oil (Sewaren Station) were extremely corrosive. In all probability, the ash formed contributed largely to this corrosiveness. Schläpfer, Amgwerd, and Preis (1) postulate that vanadium compounds prevent the formation of, or destroy, the protective scale on heat-resisting steels. According to these authors, vanadates are formed which act as carriers of oxygen to the surface of the metal.

The high-alkali coke and blast-furnace gas used at Penwood, and the high-sulphur oil and gas burned at the Bayway Refinery, also produced highly corrosive atmospheres. The latter observations are not unexpected. Schläpfer, Amgwerd, and Preis (1), in their study of oil-ash corrosion, found that the extent of attack on metal was related to the alkali content of the oil ash. Moore, Richmond, and Harrison (10), in a study of the effect of contact with numerous substances on the oxidation of certain high-temperature alloys, found the extent of attack increased by alkalies, alkaline earths, and lead compounds. Sulphur in the fuel is a well-known accelerator of corrosion in combustion atmospheres, probably through the formation of sulphates.

On the other hand, the low-sulphur anthracite (Sunbury Station) and the sulphur-free natural gas (Baton Rouge Station) produced atmospheres that caused very little corrosion. This also is in line with expectations.

Examination of Table 3 and Figs. 3 and 4, for the performance of the individual alloys under test, shows that when the general corrosiveness of the combustion products was mild, all of the materials showed good corrosion resistance, with respect to both general corrosion and subsurface attack, with the exception of the aluminized mild steel. It was rather surprising to observe that this material usually had a substantially higher weight loss than the others.

When corrosion conditions were severe, some differences in resistance to attack occurred among the test materials. At Sewaren, AISI steels 308, 309, 309S, and 310, Inconel, and Illium G showed better resistance to general corrosion than the others. AISI steels 309S and 310 were the best under these conditions. The Inconel had a fairly low weight loss but suffered considerable subsurface attack. The 17-14 Cu-Mo steel and the 16-25-6 alloy

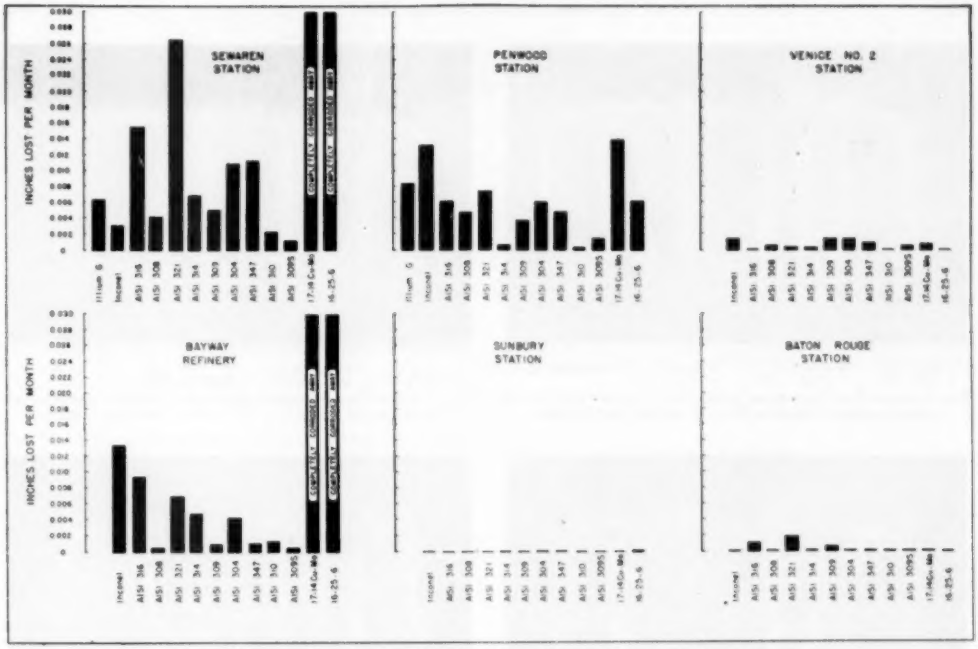

FIG. 3 GENERAL CORROSION OF TEST METALS IN VARIOUS COMBUSTION ATMOSPHERES

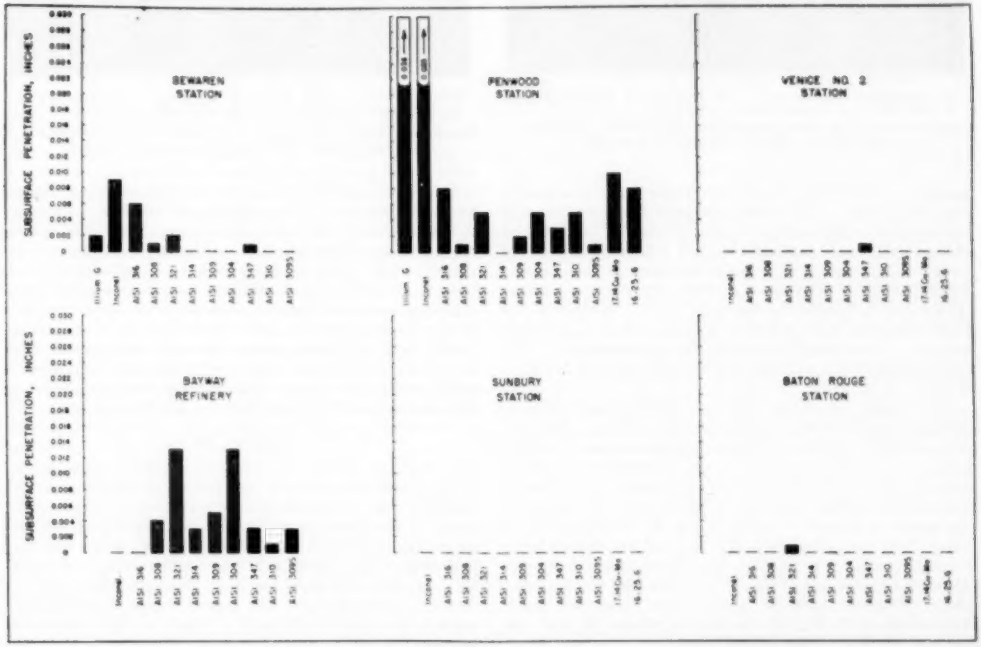

FIG. 4 SUBSURFACE ATTACK ON TEST MATERIALS IN VARIOUS COMBUSTION ATMOSPHERES

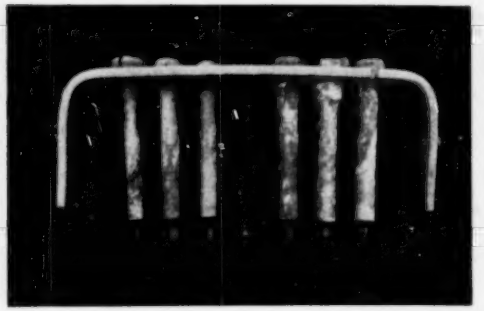

1 AISI 321 3 AISI 316 5 Inconel 7 Aluminized steel
2 AISI 308 4 17-14 Cu-Mo 6 Illium G

FIG. 5 FIELD-TEST SPECIMENS AFTER 93.5 DAYS OF EXPOSURE AT APPROXIMATELY 1350 F IN NO. 1 UNIT, SEWAREN STATION

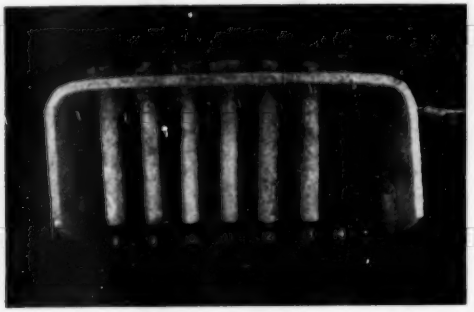

8 AISI 314 10 AISI 304 12 AISI 310 14 16-25-6
9 AISI 309 11 AISI 347 13 AISI 309S

FIG. 6 FIELD-TEST SPECIMENS AFTER 93.5 DAYS OF EXPOSURE AT APPROXIMATELY 1350 F IN NO. 1 UNIT, SEWAREN STATION

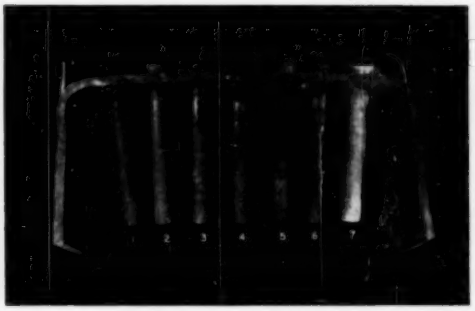

1 AISI 321 3 AISI 316 5 Inconel 7 Aluminized steel
2 AISI 308 4 17-14 Cu-Mo 6 Illium G

FIG. 7 FIELD-TEST SPECIMENS AFTER 109 DAYS OF EXPOSURE AT APPROXIMATELY 1250 F IN BATON ROUGE STATION

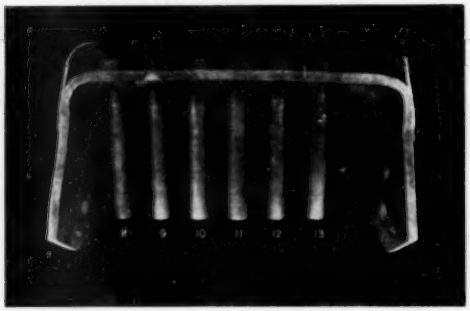

8 16-25-6 10 AISI 310 12 AISI 304 14 AISI 314
9 AISI 309S 11 AISI 347 13 AISI 309

FIG. 8 FIELD-TEST SPECIMENS AFTER 109 DAYS OF EXPOSURE AT APPROXIMATELY 1250 F IN BATON ROUGE STATION

specimens were missing from the test rack when it was removed from the furnace. It is a safe assumption that these materials had completely disintegrated during the test, or had corroded through at the shank just below the rack. Both alloys contained comparatively large percentages of molybdenum and, as such, would be subject to very severe oxidation which is accelerated by the presence of vanadium compounds (1, 11). In addition, it is known that stagnant atmospheric conditions, such as were likely to have prevailed immediately below the rack, accelerate greatly the oxidation of alloys containing substantial amounts of molybdenum.

At Penwood, less marked differences developed among the alloys regarding their resistance to general corrosion. However, more extensive subsurface attack was usually observed on all materials except AISI 314 (this alloy showed no subsurface attack at either Sewaren or Penwood). The high-nickel alloys, Illium G and Inconel, suffered severe subsurface attack. The nature of this attack on Illium G is shown in Fig. 9. Among the alloys tested, AISI steels 309, 309S, 310, 314, and 347 showed better over-all resistance toward their environment than did the rest. Among the latter group, AISI 310, 314, and 309S were the better alloys. However, AISI 310 suffered some subsurface attack. This is illustrated in Fig. 10. In addition, alloys AISI 309S, 310, and 314 showed some slight pitting attack.

The specimens of 17-14 Cu-Mo and 16-25-6 were again missing from the rack removed from the Bayway Refinery. Evidently they had disintegrated or corroded through at the shank during the test as they had at Sewaren. At the Bayway Refinery, if account is taken of both general corrosion and subsurface attack, there appeared to be less variation in the resistance of the alloys than at Sewaren or Penwood. The 17-14 Cu-Mo and 16-25-6 alloys, of course, were very poor. In addition, Inconel and AISI steels 316, 321, and 304 could be considered inferior in these tests to other materials. Noteworthy was the absence of subsurface attack on nickel-base alloys. Little difference was observed among sets of alloys tested at Venice, Sunbury, and Baton Rouge.

CONCLUSIONS

1 The data confirm the fact that wide differences in general corrosiveness occur among the atmospheres produced by the combustion of the various kinds of fuel used for steam-generating units. In the tests reported in the paper, low-sulphur coal and gas produce combustion products which are only mildly corrosive. High-sulphur, high-alkali, and high-vanadium fuels, on the other hand, produce combustion products which are often extremely corrosive toward metals. The general degree of corrosiveness seems to be related to the sulphur, vanadium, and alkali metal content of the fuel.

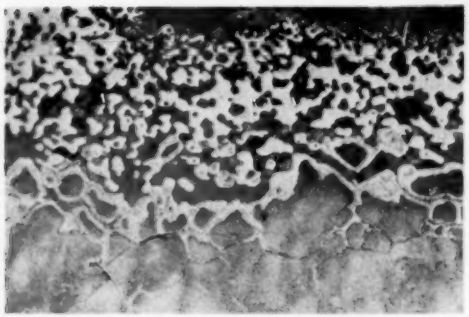

FIG. 9 PHOTOMICROGRAPH SHOWING EXTENSIVE SUBSURFACE ATTACK SUFFERED BY ILLIUM G TESTED AT PENWOOD STATION; ×50

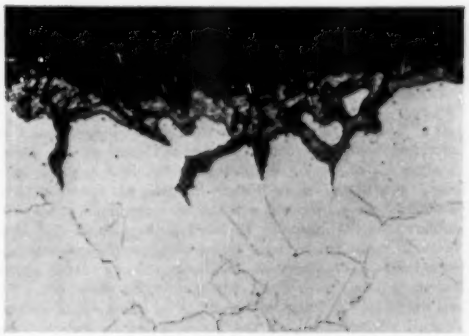

FIG. 10 PHOTOMICROGRAPH SHOWING SUBSURFACE CORROSION OF ALLOY AISI 310 TESTED AT PENWOOD STATION; ×250

2 Excluding considerations of strength and resistance toward internal corrosion, it may be said that under mild corrosion conditions, a variety of alloys is available for superheater tubing to operate at metal temperatures up to 1350 F without appreciable external attack. Under very corrosive conditions, all the alloys tested were corroded. Among them, however, AISI 309S, 310, and 314 usually showed the better resistance to both general corrosion and subsurface attack.

ACKNOWLEDGMENT

The authors wish to thank the ASME Special Research Committee on High-Temperature Steam Generation for permission to publish this paper. In particular, they wish to thank Prof. H. L. Solberg and Dr. C. L. Clark for their helpful suggestions.

The authors wish to acknowledge the co-operation of the following companies for their generosity in supplying test materials: Timken Roller Bearing Company; Republic Steel Corporation; Carnegie-Illinois Steel Corporation; Armco Steel Corporation; International Nickel Company; The Illium Corporation.

They also wish to acknowledge the interest and co-operation shown by the following companies which permitted racks of test specimens to be installed in their steam-generating units: Philadelphia Electric Company; Moore-McCormack Lines; Public Service Electric and Gas Company of New Jersey; Commonwealth Edison Company; Bethlehem Steel Company; Pacific Gas and Electric Company; Gulf States Utilities Company; Pennsylvania Power and Light Company; Standard Oil Development Company; Union Electric Company of Missouri.

Special mention must be made of the generosity of the Columbus and Southern Ohio Electric Company in providing facilities at the Picway Station for development of the test rack. Mr. D. H. Vogel and his staff were particularly co-operative.

Grateful acknowledgment is also due the Babcock & Wilcox Company, Foster-Wheeler Corporation, and Combustion Engineering-Superheater, Incorporated, for their assistance in the installation of the racks of specimens.

BIBLIOGRAPHY

1 "The Attack of Vanadium-Bearing Oil Ash on Heat-Resistant Steel," by P. Schläpfer, P. Amgwerd, and H. Preis, *Schweizer Archiv für angewandte Wissenschaft und Technik; Annales, Suisses*, vol. 15 1949, pp. 292–299.

2 "Coal-Ash Corrosion of Metals at Elevated Temperatures," by C. T. Evans, ASTM, Special Technical Publication No. 108, 1951, pp. 3–8.

3 "Oil-Ash Corrosion of Metals at Elevated Temperatures," by C. T. Evans, ASTM, Special Technical Publication No. 108, 1951, pp. 59–105.

4 "Erosion and Corrosion of Damage From Heavy Fuel Oils Used as a Motor, Boiler or Gas-Turbine Fuel," by B. Engel, *Erdoel und Kohle*, vol. 3, 1950, pp. 321–327.

5 "Corrosion of Alloys at High Temperatures With Special Reference to Attack by Vanadium Pentoxide," by E. N. Skinner and R. A. Koslik, unpublished report.

6 "Problems Encountered in Burning Heavy Fuel Oil as Related to Attack of Metals at High and Low Temperatures and the Fouling of Tube Banks," by O. L. Wood, Panel Discussion, presented at the Annual Meeting, New York, N. Y., November 26–December 1, 1950, of THE AMERICAN SOCIETY OF MECHANICAL ENGINEERS.

7 "Problems Encountered in Burning Heavy Fuel Oil as Related to Attack of Metals at High and Low Temperatures and the Fouling of Tube Banks," by C. F. Tibbetts, Panel Discussion, presented at the Annual Meeting, New York, N. Y., November 26–December 1, 1950, of THE AMERICAN SOCIETY OF MECHANICAL ENGINEERS.

8 "Problems Encountered in Burning Heavy Fuel Oil as Related to Attack of Metals at High and Low Temperatures and the Fouling of Tube Banks," by V. F. Estcourt, Panel Discussion, presented at the Annual Meeting, New York, N. Y., November 26–December 1, 1950, of THE AMERICAN SOCIETY OF MECHANICAL ENGINEERS.

9 "Problems Encountered in Burning Heavy Fuel Oil as Related to Attack of Metals at High and Low Temperatures and the Fouling of Tube Banks," by D. Douglass, Panel Discussion, presented at the Annual Meeting, New York, N. Y., November 26–December 1, 1950, of THE AMERICAN SOCIETY OF MECHANICAL ENGINEERS.

10 "High-Temperature Attack of Various Compounds on Four Heat-Resisting Alloys," by D. C. Moore, J. C. Richmond, and W. N. Harrison, Technical Note No. 1731 NACA, October, 1948.

11 "Mechanism of the Rapid Oxidation of High-Temperature, High-Strength Alloys Containing Molybdenum," by W. C. Leslie and M. G. Fontana, Trans. ASM, vol. 41, 1949, pp. 1213–1243.

Determination of Principal Plastic Strains[1]

By W. E. COOPER,[2] WEST LAFAYETTE, IND.

Techniques are presented whereby the grid method of plastic-strain determination may be extended to include the determination of strain at a point, rather than over a finite gage length, and the determination of the principal strain, magnitude, and direction, when these directions are not necessarily in alignment with the original grid. Measurement may be made in terms of either the tensor or logarithmic definitions of finite strain.

Introduction

EXPERIMENTAL studies in the field of plasticity necessitate the measurement of finite strains. One of the strain-indicating devices for this purpose is known as photogrid and consists of a grid applied photographically to the surface of the specimen. This method is particularly well adapted to cases in which it is impractical to use a strain-indicating device which projects from the surface. Also, the grid is resistant to forming lubricants up to approximately 600 F and, if lubricated, will withstand many of the common forming processes. The range of strain which may be measured has been given as 275 per cent but is often established by such metallurgical factors as "orange-peel" effect rather than the failure of the grid itself. It is not the purpose of this paper to discuss the techniques of applying photogrid to the specimen since this information is well covered in the literature (1).[3]

In all cases found in the literature in which the grid method was used for strain determination, the principal strain directions were known and the grid was applied in alignment with these directions. Also, a finite gage length was used in the determination of the strain. It is the purpose of this paper to make the photogrid process more useful by developing the techniques whereby the strain may be determined at a point, rather than the average strain over a finite gage length; and the techniques for the determination of the principal surface strains and their directions when the grid is not necessarily aligned with the principal strain directions are presented. It is believed that the method is particularly valuable in studying problems with regard to the forming of sheets and plates.

Before the experimental techniques may be studied it is necessary to establish the finite strain definitions which are to be used. Since the restriction on a finite strain definition is that it reduces to the classical definition of the theory of elasticity for small strains, many definitions of finite strain have been proposed.

Strain Definitions

As only the surface strains may be measured, consider that the x and y-axes lie in the surface with the z-axis normal to the surface. If the surface considered is a free surface, one of the three principal strain directions will be normal to the surface, since the axes of the principal strain increment and the principal stress are in alignment. In this case the third principal surface strain may be determined from the condition that the volume remains essentially constant during plastic deformation (2). According to the usual conventions, designate the displacement of a point in the direction of the x-axis by u and that in the direction of the y-axis by v. It will be assumed that either the elastic strains are negligible or that the unloaded condition is being considered.

Two of the finite-strain definitions which have been proposed will be used in this paper. The first of these is the tensor definition of strain which has been proposed by a number of authors (3). As is implied by the designation, this strain definition is a tensor quantity, and therefore has a number of mathematical advantages. It may be regarded as an extension of the nominal-strain definition, that is, the usual definition of mechanics of materials, and has the same disadvantage in that the strain obtained by an n-fold repetition of the same elongation dl is different from that resulting from the elongation ndl imposed in one operation (4). It is, however, the most common definition used in the mathematical theory of plasticity.

The components of tensor strain are

$$\left.\begin{aligned} \epsilon_x &= \frac{\partial u}{\partial x} + \frac{1}{2}\left[\left(\frac{\partial u}{\partial x}\right)^2 + \left(\frac{\partial v}{\partial x}\right)^2\right] \\ \epsilon_y &= \frac{\partial v}{\partial y} + \frac{1}{2}\left[\left(\frac{\partial u}{\partial y}\right)^2 + \left(\frac{\partial v}{\partial y}\right)^2\right] \\ \gamma_{xy} &= \frac{1}{2}\left[\frac{\partial u}{\partial y} + \frac{\partial v}{\partial x} + \frac{\partial u}{\partial x}\frac{\partial u}{\partial y} + \frac{\partial v}{\partial x}\frac{\partial v}{\partial y}\right] \end{aligned}\right\} \quad \ldots\ldots[1]$$

If we designate the principal components of the tensor strain as ϵ_1, ϵ_2, and ϵ_3, the condition of constant volume for large strains may be written as (5)

$$(1 + 2\,\epsilon_1)(1 + 2\,\epsilon_2)(1 + 2\,\epsilon_3) = 1 \quad \ldots\ldots[2]$$

The second definition of strain which will be considered is an extension of the true (or natural, or logarithmic) strain concept. The true-strain concept, which has been variously attributed to Roentgen, Ludwik, and Hencky, was devised to overcome the objection, previously cited, against the nominal-strain definition (4). The extension to the general case is due to Jelinek, et al. (6). Although the logarithmic definition is not presented in terms of the displacements they may be shown to be (7)

$$\left.\begin{aligned} \bar{\epsilon}_x &= \frac{1}{2}\ln\left[1 + 2\frac{\partial u}{\partial x} + \left(\frac{\partial u}{\partial x}\right)^2 + \left(\frac{\partial v}{\partial x}\right)^2\right] \\ \bar{\epsilon}_y &= \frac{1}{2}\ln\left[1 + 2\frac{\partial v}{\partial y} + \left(\frac{\partial u}{\partial y}\right)^2 + \left(\frac{\partial v}{\partial y}\right)^2\right] \\ \bar{\gamma}_{xy} &= \left[\frac{\partial u}{\partial y} + \frac{\partial v}{\partial x} + \frac{\partial u}{\partial x}\frac{\partial u}{\partial y} + \frac{\partial v}{\partial x}\frac{\partial v}{\partial y}\right] e^{-(\bar{\epsilon}_x + \bar{\epsilon}_y)} \end{aligned}\right\} \quad \ldots[3]$$

If the principal components of the logarithmic strain are designated as $\bar{\epsilon}_1$, $\bar{\epsilon}_2$, and $\bar{\epsilon}_3$, the condition of constant volume may be written as (8)

---

[1] Excerpt from a thesis submitted in partial fulfillment of the requirements for the degree of Doctor of Philosophy at Purdue University, August, 1951.

[2] Instructor in Engineering Mechanics, Purdue University. Jun. ASME.

[3] Numbers in parentheses refer to the Bibliography at the end of the paper.

Contributed by the Metals Engineering and Applied Mechanics Divisions and presented at the Annual Meeting, Atlantic City, N. J., November 25–30, 1951, of The American Society of Mechanical Engineers.

Note: Statements and opinions advanced in papers are to be understood as individual expressions of their authors and not those of the Society. Manuscript received at ASME Headquarters, October 16, 1951. Paper No. 51—A-128.

$$\bar{\epsilon}_1 + \bar{\epsilon}_2 + \bar{\epsilon}_3 = 0 \quad \ldots\ldots [4]$$

Although the form of the equation for constancy of volume is simpler with this definition than with the tensor definition, the logarithmic definition, in general, is mathematically awkward as compared to a tensor quantity. Physically, however, it is more easily described, particularly the shear-strain concept. This definition may prove the most valuable in experimental plasticity.

A relationship may be obtained between the two definitions by comparison of Equations [1] and [3]. These relationships are

$$\left.\begin{aligned} \bar{\epsilon}_x &= \frac{1}{2}\ln(1 + 2\,\epsilon_x) \\ \bar{\epsilon}_y &= \frac{1}{2}\ln(1 + 2\,\epsilon_y) \\ \bar{\gamma}_{xy} &= 2\,\gamma_{xy}\,e^{-(\bar{\epsilon}_x + \bar{\epsilon}_y)} \end{aligned}\right\} \quad \ldots\ldots [5]$$

Determination of Displacements

In order to designate the grid points the following technique will be adopted. The point in which we are interested in determining the strain will be designated as P_{00}. Adjacent points will be designated as illustrated in Table 1. The displacements will be designated as shown in Fig. 1.

TABLE 1 DESIGNATION OF GRID POINTS

$P_{\bar{3}3}$	$P_{\bar{2}3}$	$P_{\bar{1}3}$	P_{03}	P_{13}	P_{23}	P_{33}
$P_{\bar{3}2}$	$P_{\bar{2}2}$	$P_{\bar{1}2}$	P_{02}	P_{12}	P_{22}	P_{32}
$P_{\bar{3}1}$	$P_{\bar{2}1}$	$P_{\bar{1}1}$	P_{01}	P_{11}	P_{21}	P_{31}
$P_{\bar{3}0}$	$P_{\bar{2}0}$	$P_{\bar{1}0}$	P_{00}	P_{10}	P_{20}	P_{30}
$P_{\bar{3}\bar{1}}$	$P_{\bar{2}\bar{1}}$	$P_{\bar{1}\bar{1}}$	$P_{0\bar{1}}$	$P_{1\bar{1}}$	$P_{2\bar{1}}$	$P_{3\bar{1}}$
$P_{\bar{3}\bar{2}}$	$P_{\bar{2}\bar{2}}$	$P_{\bar{1}\bar{2}}$	$P_{0\bar{2}}$	$P_{1\bar{2}}$	$P_{2\bar{2}}$	$P_{3\bar{2}}$
$P_{\bar{3}\bar{3}}$	$P_{\bar{2}\bar{3}}$	$P_{\bar{1}\bar{3}}$	$P_{0\bar{3}}$	$P_{1\bar{3}}$	$P_{2\bar{3}}$	$P_{3\bar{3}}$

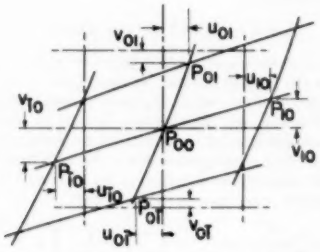

FIG. 1 DESIGNATION OF DISPLACEMENTS

The strain magnitude does not depend upon the absolute displacement but upon the rate of change of the displacement with respect to the distance along the axis considered. Also, since the major problem is the determination of the principal strains, the direction of the axes of the superimposed grid is unimportant. The effect of the rigid-body rotation of the superimposed grid is rejected by the strain definitions. The problem of determining the displacements then consists of mapping the points of grid intersection after deformation and superimposing upon this map the original grid to the same magnification. From this map, tabular or graphical, the displacements in the axis directions may then be determined.

For the determination of the strain values at a particular point the values of u_{i0}, u_{0i}, v_{i0}, and v_{0i}, where $-n < i < n$ and n is chosen large enough so that a sufficient number of points is considered, are necessary. The value of n will depend upon the strain gradient at the point considered and the curvature of the deformed grid.

Determination of the Partial Derivatives

In order to evaluate the partial derivatives, $\partial u/\partial x$, $\partial u/\partial y$, $\partial v/\partial x$, and $\partial v/\partial y$, a numerical differentiation technique will be used. Since the original points will be equally spaced and the known values will be arranged symmetrically about the point, differentiation of Stirling's central difference equation may be used to determine the necessary derivatives (9). In order to express the technique in a general form let us write the relationship in terms of new variables as

$$S = F(r) \quad \ldots\ldots [6]$$

Then the determined pairs are of the form (r_{0i}, S_{0i}) and (r_{i0}, S_{i0}).

The next step is to adopt a form for the symbolism of the diagonal difference table as illustrated in Table 2; this symbolism

TABLE 2 DIAGONAL DIFFERENCE TABLE

$r_{0\bar{3}}$	$S_{0\bar{3}}$						
		ΔS_{-3}					
$r_{0\bar{2}}$	$S_{0\bar{2}}$		$\Delta^2 S_{-3}$				
		ΔS_{-2}		$\Delta^3 S_{-3}$			
$r_{0\bar{1}}$	$S_{0\bar{1}}$		$\Delta^2 S_{-2}$		$\Delta^4 S_{-3}$		
		$\underline{\Delta S_{-1}}$		$\underline{\Delta^3 S_{-2}}$		$\underline{\Delta^5 S_{-3}}$	
r_{00}	S_{00}		$\Delta^2 S_{-1}$		$\Delta^4 S_{-2}$		$\Delta^6 S_{-3}$
		ΔS_0		$\underline{\Delta^3 S_{-1}}$		$\underline{\Delta^5 S_{-2}}$	
r_{01}	S_{01}		$\Delta^2 S_0$		$\Delta^4 S_{-1}$		
		ΔS_1		$\Delta^3 S_0$			
r_{02}	S_{02}		$\Delta^2 S_1$				
		ΔS_2					
r_{03}	S_{03}						

is that of Scarborough. The terms needed in the differentiation equation, Equation [7], are underlined.

Since the value is desired at the point at which $r = r_{00}$, the following equation is valid for the derivative of S with respect to r (10)

$$\left(\frac{dS}{dr}\right)_{P(00)} = \frac{1}{r_{01} - r_{00}}\left(\frac{\Delta S_{-1} + \Delta S_0}{2} - \frac{1}{3!}\,\frac{\Delta^3 S_{-2} + \Delta^3 S_{-1}}{2} + \frac{4}{5!}\,\frac{\Delta^5 S_{-3} + \Delta^5 S_{-2}}{2} + \ldots\right) \quad \ldots [7]$$

Equation [7] is for $n = 3$. Similar equations may be developed for any value of n by use of the equations given in the reference. In the use of finite differences the ideal situation is to have enough differences so that the values in the last vertical difference column used become equal. This ideal condition is seldom attained in experimental work since the experimental errors magnify as we go to the right in the difference table. In no case should differences be formed beyond the point where they begin to show signs of fluctuating irregularity (11). The effect of magnitude of error is discussed in both references cited. Note that in the case of a constant-strain region only the first difference appears.

Determination of Magnitude and Direction of Principal Strains

From the derivatives determined in the manner outlined in the preceding section the components of the tensor definition of strain ϵ_x, ϵ_y, and γ_{xy} may be calculated from Equations [1]. The method of determining the principal strains will now be developed.

The principal-strain magnitudes, and their directions, may be found by consideration of the characteristic equation of the tensor (12). In this case the characteristic equations are

$$\left.\begin{aligned}(\epsilon_x - \lambda)\, n_x + \gamma_{xy}\, n_y &= 0\\ \gamma_{xy}\, n_x + (\epsilon_y - \lambda)\, n_y &= 0\end{aligned}\right\} \quad \ldots\ldots [8]$$

where n_x and n_y are the vector components along the X and Y-axes, respectively, of the principal-strain direction. The condition for a nontrivial solution is that

$$\begin{vmatrix}\epsilon_x - \lambda & \gamma_{xy}\\ \gamma_{xy} & \epsilon_y - \lambda\end{vmatrix} = 0 \quad \ldots\ldots [9]$$

Note that this equation has two roots for λ which are the principal strains ϵ_1 and ϵ_2. Corresponding to each of these roots there is a nonzero solution to Equations [8] which will be designated as n_{x1}, n_{y1}, n_{x2}, and n_{y2}. Expansion of Equation [9] gives

$$\lambda^2 - (\epsilon_x + \epsilon_y)\,\lambda - \gamma^2_{xy} + \epsilon_x\,\epsilon_y = 0 \quad \ldots\ldots [10]$$

and the principal strains become

$$\epsilon_{1,2} = \frac{\epsilon_x + \epsilon_y}{2} \pm \left[\left(\frac{\epsilon_x - \epsilon_y}{2}\right)^2 + \gamma_{xy}{}^2\right]^{1/2} \quad \ldots\ldots [11]$$

Substitution for the strain components in terms of the displacement leads to a complicated expression.

It is now possible to solve Equations [8] for one of the components of the principal-strain direction vector in terms of the other (13). We find

$$\frac{n_{x1}}{n_{y1}} = \frac{-\gamma_{xy}}{\epsilon_x - \epsilon_1} \quad \ldots\ldots [12]$$

The principal logarithmic strains are then

$$\left.\begin{aligned}\bar{\epsilon}_1 &= \frac{1}{2}\ln(1 + 2\,\epsilon_1)\\ \bar{\epsilon}_2 &= \frac{1}{2}\ln(1 + 2\,\epsilon_2)\end{aligned}\right\} \quad \ldots\ldots [13]$$

If the surface is not loaded, the third principal strain may be found from consideration of the conditions of plastic deformation as an isovolumetric condition, Equation [2] or [4].

The equation for the angle between the superimposed grid and the original grid may be determined, if desired for some reason such as a check on the accuracy, from the equation for a rigid body rotation

$$\text{Rotation} = \frac{1}{2}\left(\frac{\partial u}{\partial y} - \frac{\partial v}{\partial x}\right) \quad \ldots\ldots [14]$$

The angle of the rigid-body rotation will be obtained in radian measure.

Accuracy of Method

The accuracy of the method is primarily dependent upon the ability of the operator to measure the grid accurately. This accuracy is dependent upon the uniformity and sharpness of the grid, and the measuring device used. The best comparator for this purpose is a toolmaker's microscope. The accuracy to which the grid may be read provides a lower limit for the grid spacing, since it affects the number of reliable terms in the difference table. It is desirable to have a very fine grid in locations of high strain gradient but a coarser grid may be used where the gradient is not large. The particular grid-microscope combination used in verifying the theory could be read with an accuracy of ±200 microinches and a grid spacing of 20 lines per in. was used. Photogrid was applied to a tapered tensile specimen in which the strains varied from elastic to failure in an original length of 2¼ in. Strains obtained from measurements of the photogrid were compared to the strains obtained by measuring the cross-sectional areas before and after deformation. These strains obtained from the photogrid were on the axis of the specimen and the maximum error in 40 determinations, with various orientations of original grid and superimposed grid, was less than 10 per cent.

Illustration of Method

As an illustration of the method in a complex strain region let us consider a point off the center line of the tensile specimen and in the necked area. The material was 28-O aluminum and the original cross-sectional area was ½ in. × ½ in. The grid was applied to the specimen at an angle of approximately 51 deg to the longitudinal axis of the specimen. Previous test had shown that within the accuracy of the grid-microscope combination the grid spacing could be considered as uniform and the average of a large number of determinations was 0.049263 in. In the calculations nonsignificant figures were carried in accordance with usual practice. The specimen was deformed and the grid intersections

TABLE 3

Point	X (co-ordinate, in.)	w (in.)	Δw (in.)	$\Delta^2 w$ (in.)	$\Delta^3 w$ (in.)
P_{20}	−0.117215	0.018689			
			0.007062		
P_{10}	−0.060890	0.011627		0.004565	
			0.011627		0.000934
P_{00}	0	0		0.005519	
			0.017148		0.009279
P'_{10}	0.066411	0.017148		0.014798	
			0.031946		
P'_{20}	0.147620	0.049094			

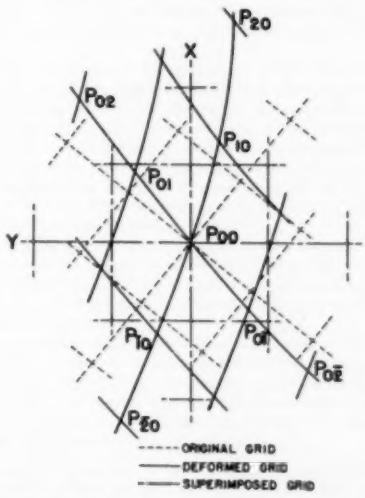

Fig. 2 Schematic Diagram of Grids

mapped with respect to axes parallel and perpendicular to the longitudinal axis of the specimen.

A schematic diagram of the grid systems is shown in Fig. 2 where X and Y are the longitudinal and transverse axes. The values of the displacements, and the difference tables, necessary for the determination of $\partial u/\partial x$, are given in Table 3. From these and similar values, and Equation [7], the partial derivatives were evaluated as

$$\frac{\partial u}{\partial x} = 0.274745 \qquad \frac{\partial v}{\partial x} = -0.476898$$

$$\frac{\partial u}{\partial y} = 0.923329 \qquad \frac{\partial v}{\partial y} = -0.263727$$

These values may then be substituted into Equations [1] to give the components of the tensor definition in the direction of the original grid as

$$\epsilon_x = 0.426198 \qquad \epsilon_y = 0.197317 \qquad \gamma_{xy} = 0.412939$$

That this is the case may be shown by evaluating the rigid-body rotation from Equation [14] which yields a rotation of 50 deg; this compares favorably with the known angle of 51 deg.

The principal strains may then be found from Equation [11] as

$$\epsilon_1 = 0.740 \qquad \epsilon_2 = -0.117$$

and the direction from Equation [12] as 45 deg. This indicates that the principal-strain direction at the time of fracture has inclined 6 deg toward the center of the specimen from an axis parallel to the longitudinal axis of the specimen, in much the same manner that the theoretical stress distribution in the necked zone would predict.

The third principal strain or the logarithmic strain components could then be determined from the appropriate equations.

Conclusions

A method has been presented whereby the principal plastic strains, and their directions, may be determined from photogrid data in the case when the grid is not necessarily in alignment with the principal-strain directions. The accuracy of the method is dependent upon the ability to measure accurately the spacing of the grid. For many purposes it will be possible to design the specimen and grid to suit available comparators and provide the desired accuracy. For certain tests the method provides a usable technique for cases in which no other method is available. One such case would be the forming of sheet material when the direction of the principal strains could not be predicted.

BIBLIOGRAPHY

1 "An Introduction to Experimental Stress Analysis," by G. H. Lee, John Wiley and Sons, Inc., New York, N. Y., 1950, p. 262.
2 "The Mathematical Theory of Plasticity," by R. Hill, Oxford University Press, London, England, 1950, p. 27.
3 "Mathematical Theory of Elasticity," by I. S. Sokolnikoff, McGraw-Hill Book Co., Inc., New York, N. Y., 1946, p. 30.
4 "The Inelastic Behavior of Engineering Materials and Structures," by A. M. Freudenthal, John Wiley and Sons, Inc., New York, N. Y., 1950, p. 182.
5 "Theory of Plasticity," by W. Prager, mimeographed notes, Brown University, Providence, R. I., 1942, p. 4, 24.
6 "Plastic Flow in Metals," by J. J. Jelinek, A. J. Latter, E. G. Thomsen, and J. E. Dorn, O. P. R. D. Project Report W-200, Project NRC-548, WPB-128, 1945, p. 70.
7 Unpublished thesis for Doctor of Philosophy degree at Purdue University, by W. E. Cooper, 1951, p. 26.
8 Reference (6), p. 93.
9 "Numerical Mathematical Analysis," by J. B. Scarborough, The Johns Hopkins Press, Baltimore, Md., 1930, p. 114.
10 Reference (9), p. 115.
11 "Numerical Calculus," by W. E. Milne, Princeton University Press, Princeton, N. J., 1949, p. 156.
12 Reference (5), p. 8.
13 Reference (11), p. 12.

Discharge Measurements by Means of Cylindrical Nozzles

By A. L. JORISSEN[1] and H. T. NEWTON[2]

Cylindrical nozzles maintain a constant coefficient of discharge at Reynolds numbers lower than standard pressure-difference devices of flow measurement. Tests on nozzles of various opening ratios have indicated the optimum proportions for each ratio.

Nomenclature

The following nomenclature is used in the paper:

L = length of test section
D = pipe diameter
$A_1 = \frac{\pi D^2}{4}$ = area of pipe cross section
d = throat diameter
$A_2 = \frac{\pi d^2}{4}$ = area of throat cross section
$\beta = \frac{d}{D}$ = diameter ratio
$m = \beta^2 = \left(\frac{d}{D}\right)^2 = \frac{A_2}{A_1}$ = opening ratio (used in Europe, preferably to β)
z = nozzle length
z/d = length ratio
Q = volumetric rate of flow
v = volume of volumetric tank
l = depth of water in volumetric tank
$V_1 = Q/A_1$ = mean pipe velocity
γ = specific weight of fluid
ρ = fluid density
g = acceleration of gravity
μ = coefficient of absolute viscosity of fluid
ν = coefficient of kinematic viscosity of fluid
$N_R = (V_1 D\rho)/\mu = V_1 D/\nu$ = Reynolds number
$(N_R)_c$ = value of Reynolds number for which the coefficient of discharge can be maintained within 0.5 per cent of its constant value
p_1 = pressure at upstream corner tap
p_2 = pressure at downstream corner tap
$\Delta h = (p_1 - p_2)/\gamma$ = differential pressure head
C = coefficient of discharge
C_c = constant value of coefficient of discharge
$\Delta' h$ = differential pressure head between piezometer rings P_3 and P_4
f = friction factor of test section
Δh_L = nonrecoverable head loss
K = head-loss coefficient
λ = head-loss ratio
K' = value of head-loss coefficient at high Reynolds numbers[3]
λ' = value of head-loss ratio at high Reynolds numbers

Introduction

It is well known that the curves of coefficient of discharge in function of Reynolds number for standard pressure-difference devices of flow measurement such as orifices, nozzles, and Venturi tubes, exhibit a variation of the coefficient when the Reynolds number falls below a certain value, called "limit of constancy" (1, 2).[3]

For example, the coefficient of discharge of Herschel-type Venturi tubes decreases by about 0.5 per cent of its constant value at a Reynolds number of 100,000,[4] 1.5 per cent at a Reynolds number of 50,000 and 2.5 per cent at a Reynolds number of 20,000 (6).

This variable trend of the coefficient of discharge not only causes difficulties both in the calculation and in the use of the devices with registering mechanisms, but it must also be observed that tolerances and errors are considerably larger in the nonconstancy range. This explains why a large number of investigations have been devoted to the study of new types of devices which are expected to maintain a constant coefficient down to Reynolds numbers much lower than standard devices (5, 11).

These types are numerous: standard ISA nozzles without cylindrical throat, double-bevel orifices, round-edge orifices, orifices in series, cylindrical nozzles, cylindrical nozzles with rounded entrance edge, and so forth.

The ISO/TC/30 Committee, which is the standing committee of the International Organization for Standardization dealing with problems of flow measurement, has so far retained for discussion the double-bevel and the round-edge orifices only, judging that insufficient information was still available about the other types (11).

Recently, the Research Committee on Fluid Meters of the Society has appointed a new subcommittee (Subcommittee No. 7) to study the problem of discharge measurements at low Reynolds numbers. One of the first tasks of this subcommittee is the preparation of a report in which will be presented the information available on the behavior of standard devices at Reynolds numbers below the limit of constancy, and on the characteristics of other types of devices, more suitable for discharge measurements at low Reynolds numbers.

One of these devices, the cylindrical nozzle, appears of particular interest, not only because it is of simple manufacture, but also because an extensive series of tests conducted by Koennecke (7, 8, 9, 10) has indicated an excellent behavior in the range of low Reynolds numbers.

Another possible advantage would be that, by the addition of a conical diffuser, the over-all pressure loss of this device could be considerably reduced. The cylindrical nozzle could thus be transformed into a Venturi tube of simple construction, expected to have a constant coefficient even at relatively low Reynolds numbers and a small permanent head loss.

---

[1] Head, Department of Hydraulics and Hydraulic Engineering, School of Civil Engineering, Cornell University, Ithaca, N. Y. Mem. ASME.

[2] Instructor in Civil Engineering, The Pennsylvania State College, State College, Pa.

Contributed by the Fluid Meters Research Committee and presented at the Annual Meeting, Atlantic City, N. J., November 25–30, 1951, of The American Society of Mechanical Engineers.

Note: Statements and opinions advanced in papers are to be understood as individual expressions of their authors and not those of the Society. Manuscript received at ASME Headquarters, September 12, 1951. Paper No. 51—A-63.

[3] Numbers in parentheses refer to Bibliography at end of paper.

[4] Reynolds numbers are here expressed, according to standard practice, in function of the pipe diameter.

Some preliminary tests in which the senior author participated gave promise that such could be the case and induced him to undertake a more extensive research program.

The first phase of this program has been conducted in the Hydraulics Laboratory, Department of Civil Engineering, The Pennsylvania State College, under the sponsorship of Builders-Providence, Inc. It consists of the calibration and study of cylindrical nozzles of various proportions in view not only of checking Koennecke's results but also of determining the best proportions for the nozzles.

Description of Installation

Cylindrical Nozzles. Five cylindrical nozzles of various dimensions have been studied in a 4-in. pipe line. Both the nozzles and the test sections in which they were installed were of brass. The nozzles are shown in Fig. 1 and a typical nozzle installation is represented in Fig. 2.

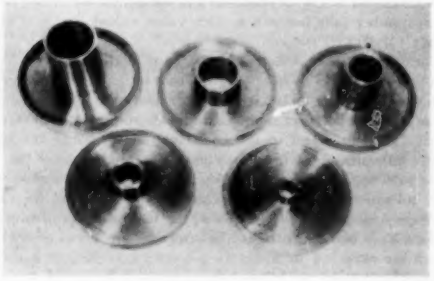

Fig. 1 Cylindrical Nozzles

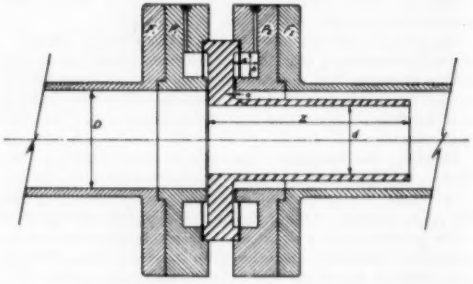

Fig. 2 Nozzle Installation

As noted, a nozzle had a throat section of diameter d and length z and was inserted in a pipe line of diameter D. The ratio $\beta = d/D$ is called diameter ratio; the ratio z/d is the length ratio.

The upstream face of each nozzle is perfectly smooth and the entrance or leading edge is sharp and machined according to the same specifications as those given for standard ISA orifices. These specifications are as follows (3): "On the upstream side, the edge must be perfectly sharp. The sharpness of the edge will be judged sufficient when a ray of light falling on the edge is not visibly reflected. Generally this will be obtained by a very fine final pass of the tool, starting from the orifice radially outward on the upstream face of the device. An edge obtained by planing the face first and then boring the hole is not fine enough."

The centering of the nozzle was insured by the piezometer rings P_1 and P_2 (see Fig. 2).

The upstream and downstream sections of pipe, the piezometer rings, and the cylindrical nozzles were also machined according to strict specifications.

The inside diameter d of each nozzle was measured by means of inside micrometers reading to 0.0001 in. Four diameters at 45 deg were measured in various sections, and the mean diameter was obtained. No individual measurement differed from the mean by more than ± 0.0003 in.

The exact machining of the upstream and downstream pipe sections, which were 6 ft long, offered difficulties. It was not possible to maintain for these sections of pipe the same rigid specifications as for the nozzles. The pipes were somewhat out-of-round and bent. However, the worst bend amounted to only $^{1}/_{32}$ in. in the total length of pipe. Precautions had been taken to choose the pipe ends at flanges F_1 and F_2 (see Fig. 2) as regular as possible. It may be estimated that the mean inside diameter of the pipe corresponded with the mean diameter of the piezometer rings P_1 and P_2 within ± 0.001 in. No individual diameter differed from the mean by more than ± 0.005 in.

Each nozzle was first studied with a maximum value of z. The nozzle was then shortened to obtain different values of the length ratio.

Table 1 gives the principal dimensions and proportions of the nozzles studied.

TABLE 1 DIMENSIONS AND PROPORTIONS OF CYLINDRICAL NOZZLES

Over-all mean pipe diameter: $D = 4.043$ in.

d, in.	$\beta = \frac{d}{D}$	$m = \left(\frac{d}{D}\right)^2$	z, in.	$\frac{z}{d}$
0.8990	0.2224	0.0495	1.391	1.547
			1.250	1.389
			1.125	1.251
1.4995	0.3709	0.1376	2.625	1.750
			2.500	1.667
			2.375	1.581
1.9990	0.4944	0.2444	4.297	2.150
			4.063	2.032
			3.797	1.899
2.3992	0.5934	0.8521	5.641	2.350
			5.141	2.140
			4.625	1.927
			4.125	1.720
			3.625	1.515
			3.109	1.296
			2.609	1.088
2.8008	0.6928	0.4800	7.992	2.854
			7.500	2.678
			7.250	2.589
			6.750	2.410
			6.266	2.237
			5.766	2.059
			5.250	1.874
			4.734	1.690
			4.250	1.517
			3.734	1.333
			3.250	1.157
			2.750	0.982

Pipe-Line Installation. Fig. 3 is a sketch of the pipe-line installation. As shown, water was supplied to the experimental pipe by a constant-level tank which was alimented by the laboratory pumps. A 6-in-ID vertical steel pipe line led to a 6-in. valve, a 90-deg bend, and a horizontal reducer changing the inside diameter to 4 in.

The test assembly was preceded by a 24-ft length of 4-in. aluminum piping, in 2 sections and consisted of the following:

Section of 4-in. brass pipe, 4 ft long.
Piezometer ring P_3.
Section of 4-in. brass pipe, 6 ft long.
Piezometer ring P_1.
Cylindrical nozzle being tested.
Piezometer ring P_2.
Section of 4-in. brass pipe, 6 ft long.
Piezometer ring P_4.
Section of 4-in. brass pipe, 4 ft long.

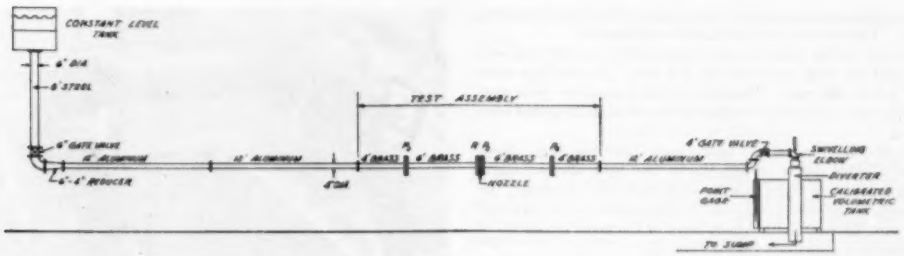

FIG. 3 GENERAL INSTALLATION

The test assembly was then followed by a straight 12-ft length of 4-in. aluminum piping, two vertical 90-deg bends, a valve, a short section of cast-iron piping leading to a swiveling elbow and diverter.

Thus the nozzle being tested was preceded by a straight pipe section of 102 pipe diameters and followed by a straight pipe section of 66 pipe diameters.

Differential-Pressure Measurements. The calibration of each cylindrical nozzle called for the measurement of the differential pressure across the nozzle (corner taps at piezometer rings P_1 and P_2, Fig. 3) at various rates of flow. The differential pressure was also measured between piezometer rings P_3 and P_4, situated at a distance of 6 ft upstream and downstream from the nozzle, respectively.

As shown in Fig. 2, the connection between the inside of the pipe and a pressure chamber was through a slot, the width of this slot being determined by the dimensions of the piezometer ring and the thickness of the gaskets. The latter was of the order of 0.035 in. A constant slot thickness $e = 0.08$ in. was maintained. Since the dimensions of the cross section of the pressure chamber were $a = 1$ in., and $b = 1$ in., the condition

$$\pi De = ab$$

was exactly verified. In other words, the cross-sectional area of the pressure chamber was equal to the area of the slot. Thus it was felt that a satisfactory equalization of pressure in the pressure chamber would be obtained (4).

Connection between the pressure chambers and the manometers was by conduits of $^1/_8$ in. diam through the piezometer rings and saran tubing of 0.2 in. ID.

Each differential pressure could be measured by means of either a water-mercury manometer, an air-water manometer, or a point-gage differential manometer, or any combination of these three manometers. A system of valves and tubing provided the necessary connections. Fig. 4 shows the arrangement of the manometers.

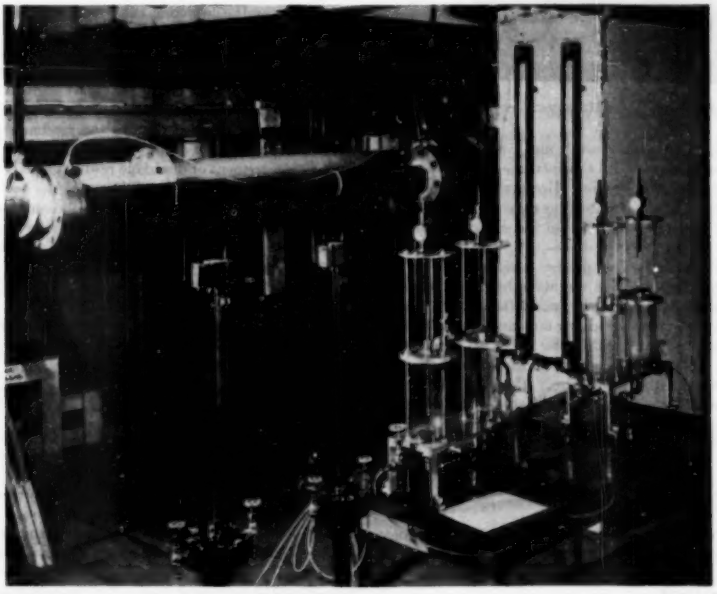

FIG. 4 MANOMETER ARRANGEMENT

The water-mercury and air-water manometers were of standard design. Their scales were graduated in millimeters.

The scale of the water-mercury manometer was 560 mm long and could be read accurately to 0.5 mm. No readings were taken below 100 mm. Readings at this manometer were consistently very steady after a sufficient time of adjustment had been allowed.

The air-water manometer had a scale 1280 mm long. Even after a suitable period of adjustment had been allowed, slight fluctuations of the water column were detected. However, the maximum deviation of a series of 10 observations never exceeded 1 per cent, the root-mean-square error of the mean of a series of readings being always less than 0.2 per cent.

The point-gage micromanometer is represented in Fig. 5. The scale of the gages, which were 260 mm long, could be read

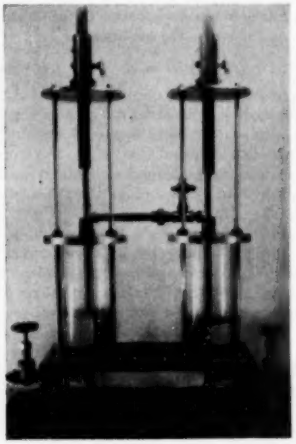

FIG. 5 POINT-GAGE MICROMANOMETER

by means of verniers to within ±0.1 mm. Small differential pressures only were measured with this instrument, and the readings generally were very consistent. However, no differential pressure smaller than 15 mm of water was measured, since it was felt that for lower values the precision of the readings would be unsatisfactory.

Discharge Measurements. The precise measurement of the rate of flow through the pipe line was done by the volumetric method into a tank 5 ft long, 4 ft wide, and 4 ft deep. The calibration of the tank was made by adding increments of volume of 5 cu ft. This capacity was obtained by accurate weighing, a suitable correction taking into account the variation of the specific weight of the water with temperature. The level of the water in the tank was read by a point gage situated in a connected well. The point gage gave the water elevation in the tank to within ± 0.0005 ft. Repeated calibrations produced a straight-line calibration curve, the equation of which could be written as

$$\Delta v = 20.110\ \Delta l$$

Δv being the difference in volume in the tank (cu ft) for a change in water-surface elevation Δl(ft). A statistical analysis of the data indicated that the root-mean-square error on the coefficient 20.110 was ±0.10 per cent.

The measurement of discharge was made by the switching

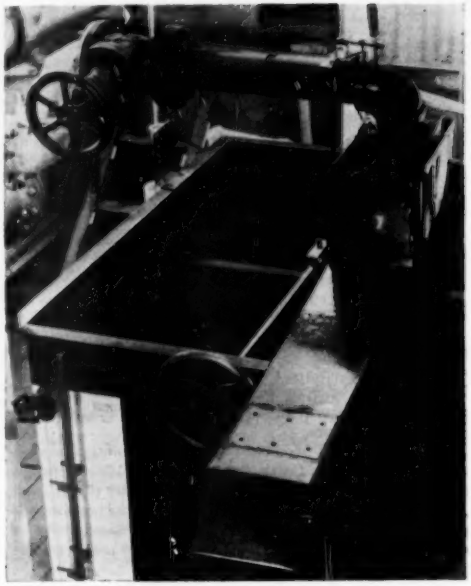

FIG. 6 VOLUMETRIC TANK

method, using a swiveling elbow and pivoted chute represented in Fig. 6.

An index on the swiveling elbow actuated an electric timer on which time intervals could be read to the $^1/_{100}$ sec. The accuracy of the timer was checked over long periods of time by radio signals. Since electrical contact was made and broken at the same extremity of the swiveling movement, a time correction was computed to make allowance for the discharge of water into the tank during the operation of the mechanism. This correction was of the order of magnitude of 0.20 sec.

The measurement of discharge resulted from a measurement of volume and a measurement of time. It has been estimated that the root-mean-square error on volume measurement was 0.10 per cent, and the root-mean-square error on time measurement 0.01 per cent. Therefore the root-mean-square error on the discharge was 0.10 per cent.

TEST PROCEDURE

The relation between rate of flow and differential pressure at the nozzle is given by the equation

$$Q = \frac{CA_2}{\sqrt{1-\beta^4}}\sqrt{2g\frac{p_1 - p_2}{\gamma}} = \frac{CA_2}{\sqrt{1-\beta^4}}\sqrt{2g\Delta h}$$

The value of the coefficient of discharge C is thus dependent upon the dimensions and proportions of the nozzle, the volumetric rate of flow, and the differential pressure through the nozzle. The methods followed in the measurement of these various quantities have been explained previously.

For each nozzle from 10 to 25 tests were run at various rates of flow, each test being repeated several times, and no reading being taken until a suitable period of time had been allowed for the adjustment of the rate of flow and of the manometric columns.

Furthermore, to insure against any possible defect in the in-

stallation, each series of tests was repeated after disassembling and reassembling the installation completely. No discrepancy in the results was noticed.

The coefficient of discharge was computed for each test. Since the value of this coefficient depends on the dimensions of the nozzle tested, on the rate of flow, and on the differential pressure, the root-mean-square error on C could be computed. This root-mean-square error was always smaller than 0.2 per cent in the constancy range.

The values of C were plotted in function of the Reynolds number

$$N_R = \frac{V_1 D}{\nu} = \frac{4Q}{\pi D \nu}$$

The temperature of the water was measured in each test and the coefficient of kinematic viscosity ν read from a standard table (2).

The nonrecoverable pressure loss of each nozzle was determined in the following manner:

Measurements were taken of the differential pressure head, $\Delta' h$ between the piezometer connections P_3 and P_4. It was assumed that the nonrecoverable pressure head of the nozzle was equal to this value minus the friction head lost between P_3 and P_4.

Preliminary tests were run to obtain an accurate value of the friction factor of the experimental pipe line. A plot of friction factor against Reynolds number is shown in Fig. 7. Values of the friction factor slightly larger than those of smooth pipes were obtained, due probably to the existence of several joints in the test section. Thus the friction loss could be computed exactly by Darcy Weisbach equation

$$h_f = f \frac{L}{D} \frac{V_1^2}{2g}$$

and the nonrecoverable head loss was

$$\Delta h_L = \Delta' h - h_f$$

The nonrecoverable head loss of each nozzle has been expressed in two different manners, first by computing the coefficient K in

$$\Delta h_L = K \frac{V_1^2}{2g}$$

then by figuring the ratio λ of Δh_L to the nozzle differential-head reading

$$\lambda = \frac{\Delta h_L}{\Delta h}$$

Discussion of Results

Values of the coefficient of discharge C, of the pressure-loss coefficient K, and of the pressure-loss ratio λ are plotted, in function of Reynolds number, in Figs. 8, 9, and 10, respectively.

For each nozzle, the first series of tests were made with the length ratio indicated by Koennecke as being optimum. A comparison of Koennecke's results with our own is given in Table 2. The coefficient of discharge α indicated by Koennecke (7, 8, 9, 10) can be converted easily into our coefficient C by the equation

$$C = \alpha \sqrt{1 - \beta^4}$$

As seen from Table 2, a very good check of Koennecke's results was obtained for all values of β, except for $\beta = 0.6928$. The larger difference (approximately 1.0 per cent) will be discussed later.

TABLE 2 COMPARISON OF KOENNECKE'S AND THE AUTHORS RESULTS

	Koennecke			Authors' results	
z/d	m	β	C	β	C
1.547	0.0506	0.2249	0.8000	0.2224	0.798
1.750	0.1408	0.3752	0.8029	0.3709	0.803
2.150	0.25	0.50	0.8075	0.4944	0.812
2.350	0.36	0.60	0.8117	0.5934	0.811
2.854	0.49	0.70	0.8037	0.6928	0.812

Our tests could not be carried to Reynolds numbers as low as those attained by Koennecke owing to the fact that water only was used in our experiments.

It was then sought if, by cutting the nozzles, shorter devices could be obtained, still maintaining satisfactory constancy of the coefficient of discharge at low Reynolds numbers. The results obtained have been summarized in Table 3. This table gives, for each value of β and z/d:

(*a*) The constant value of the coefficient of discharge, C_c. This is the mean value of the coefficient of discharge C in the constancy range. The root-mean-square error on C_c was smaller than 0.1 per cent.

(*b*) The minimum value $(N_R)_c$ of Reynolds number for which the coefficient of discharge could be maintained within 0.5 per

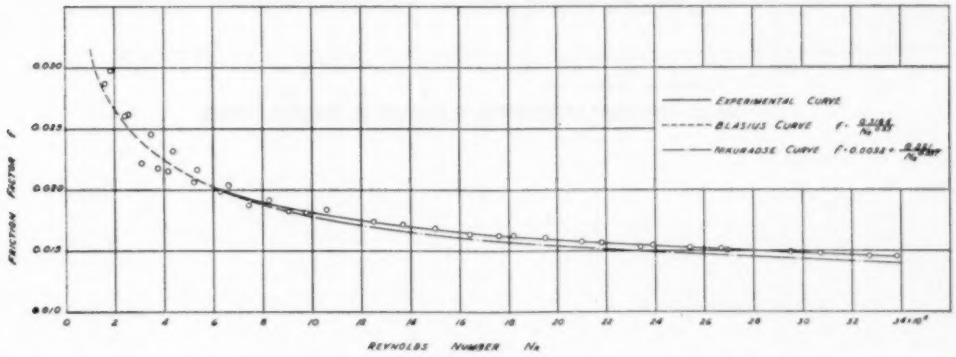

Fig. 7 Friction Factor in Function of Reynolds Number for Experimental Pipe Line

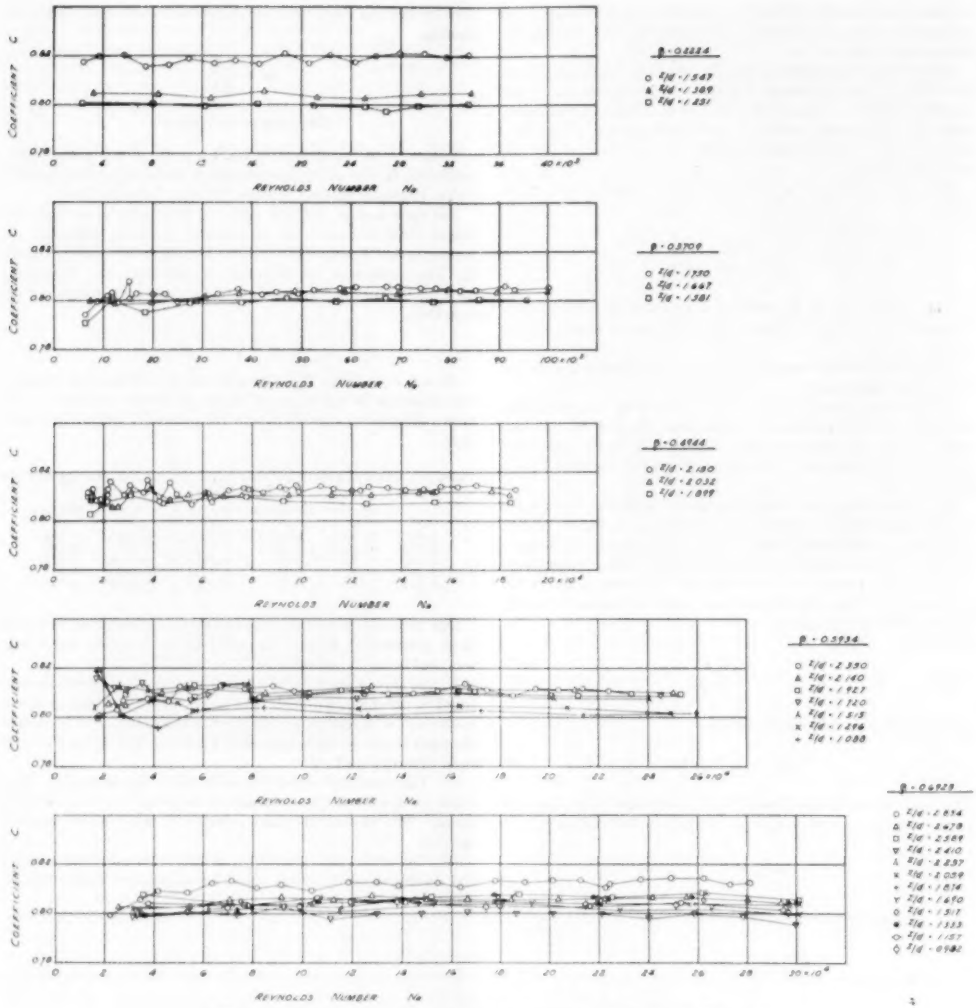

FIG. 8 COEFFICIENT OF DISCHARGE IN FUNCTION OF REYNOLDS NUMBER

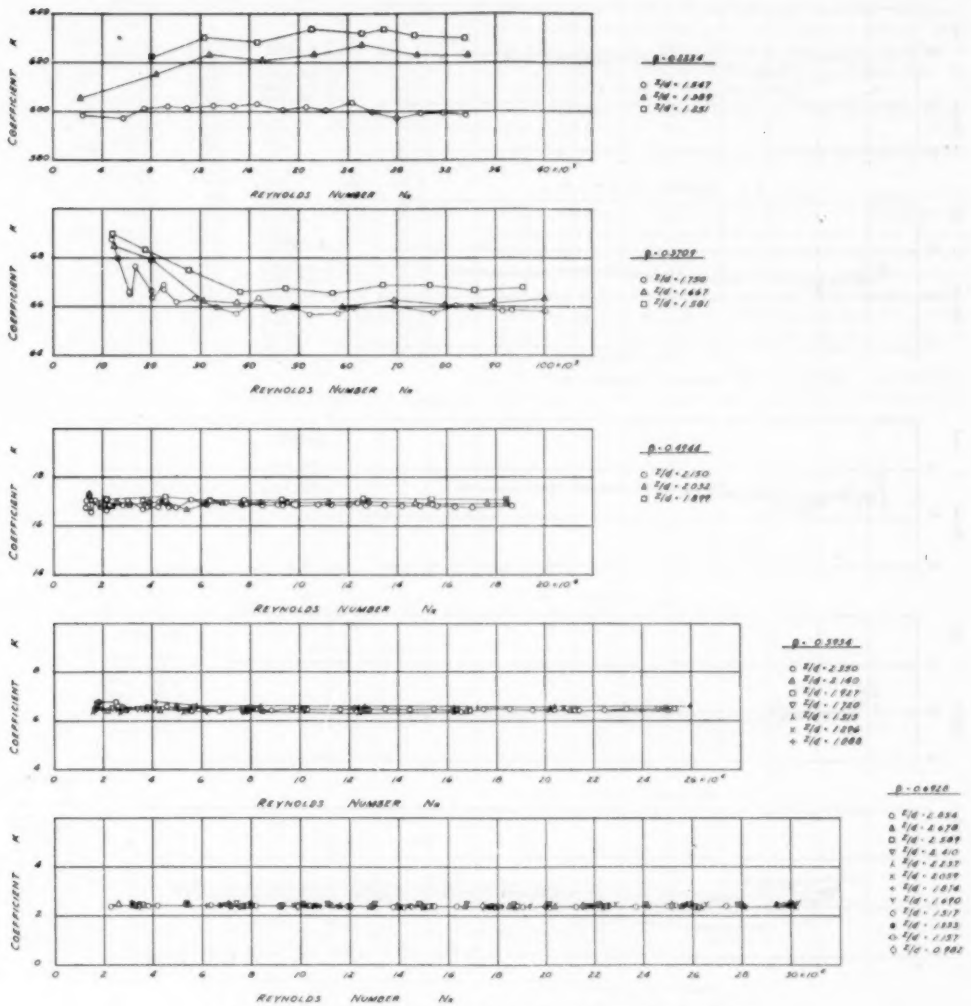

FIG. 9 PRESSURE-LOSS COEFFICIENT IN FUNCTION OF REYNOLDS NUMBER

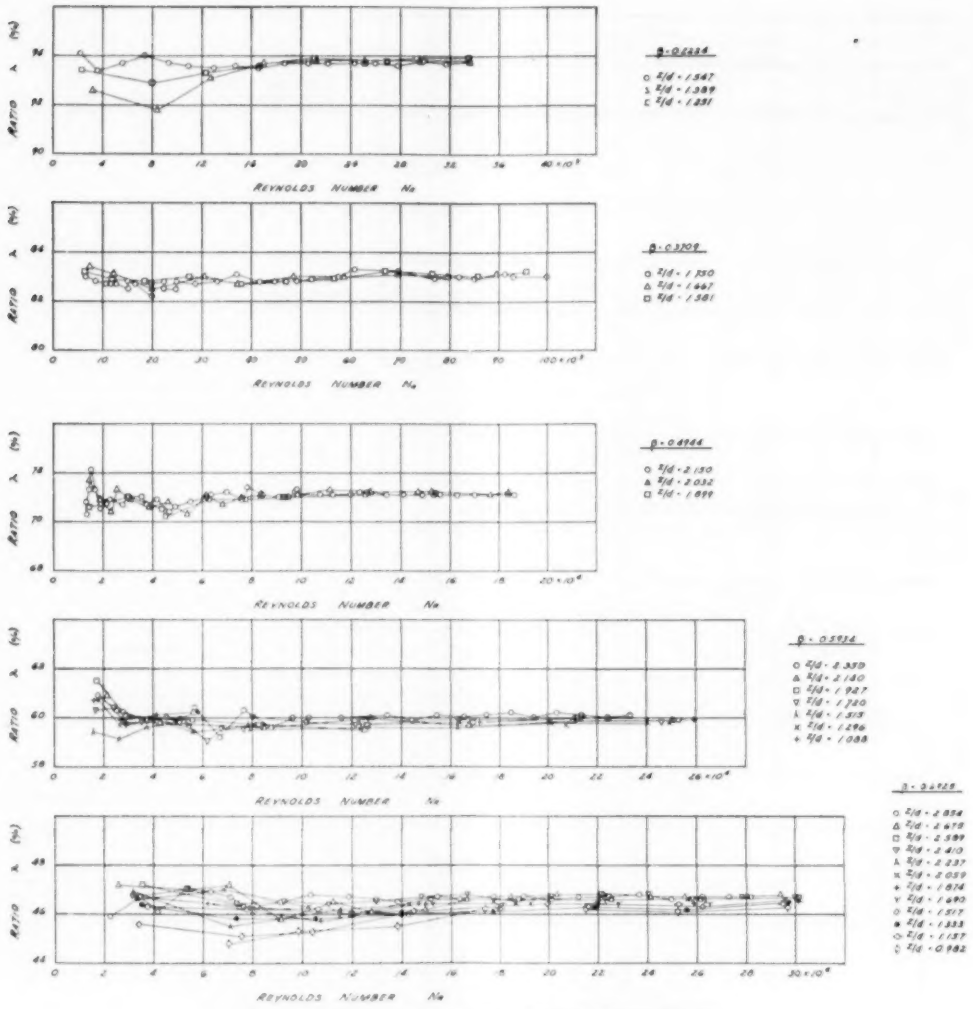

FIG. 10 PRESSURE-LOSS RATIO IN FUNCTION OF REYNOLDS NUMBER

TABLE 3 SUMMARY OF RESULTS

β	z/d	C_0	$(N_R)_0$	K'	λ'
0.2224	1.547	0.798	2200	601.0	93.7
	1.389	0.784	3200	624.0	93.8
	1.251	0.780	2300	632.0	93.9
0.3709	1.750	0.803	7000	65.9	83.0
	1.667	0.803	7000	66.2	83.0
	1.581	0.800	10000	66.8	82.1
0.4944	2.150	0.812	15000	16.80	71.1
	2.032	0.811	15000	16.95	71.2
	1.899	0.808	20000	17.10	71.1
0.5934	2.350	0.811	30000	6.46	60.1
	2.140	0.811	30000	6.46	59.9
	1.927	0.809	25000	6.46	59.9
	1.720	0.809	25000	6.46	59.9
	1.515	0.808	25000	6.46	59.8
	1.296	0.804	25000	6.55	59.8
	1.088	0.802	25000	6.60	59.9
0.6928	2.854	0.812	40000	2.40	46.7
	2.678	0.806	25000	2.40	46.7
	2.589	0.806	35000	2.40	46.6
	2.410	0.799	31000	2.40	46.7
	2.237	0.806	31000	2.40	46.5
	2.059	0.804	33000	2.40	46.6
	1.874	0.804	62000	2.40	46.4
	1.690	0.802	33000	2.40	46.4
	1.517	0.805	35000	2.40	46.4
	1.333	0.806	80000	2.40	46.3
	1.157	0.803	30000	2.40	46.3
	0.982	0.803	70000	2.40	46.2

cent of its constant value. When these figures are compared with those quoted in the introduction for Venturi tubes, it is seen that the cylindrical nozzles maintain a constant coefficient at Reynolds numbers much lower than standard devices. Furthermore, it must be observed that in many cases the values of $(N_R)_0$ would have been lower if the tests could have been extended to lower values of Reynolds number.

(*c*) The value K' of the pressure-loss coefficient at high Reynolds numbers.

(*d*) The value λ' of the pressure-loss ratio at high Reynolds numbers.

It is seen that for all values of β except the last one ($\beta = 0.6928$) the constant value of the coefficient of discharge decreased when the length ratio was below a certain limit. A concurrent increase in the value of the pressure-loss coefficient and of the pressure-loss ratio took place. This was especially true at low values of β. The values of the length ratio considered optimum are indicated in Table 4. The corresponding curves for C, K, and λ in function of Reynolds number are given in Figs. 11, 12, and 13, respectively.

The behavior of the larger nozzle ($\beta = 0.6928$) was somewhat different. A sudden drop in the value of the coefficient of discharge occurred after the first cut (from $z/d = 2.854$ to $z/d =$

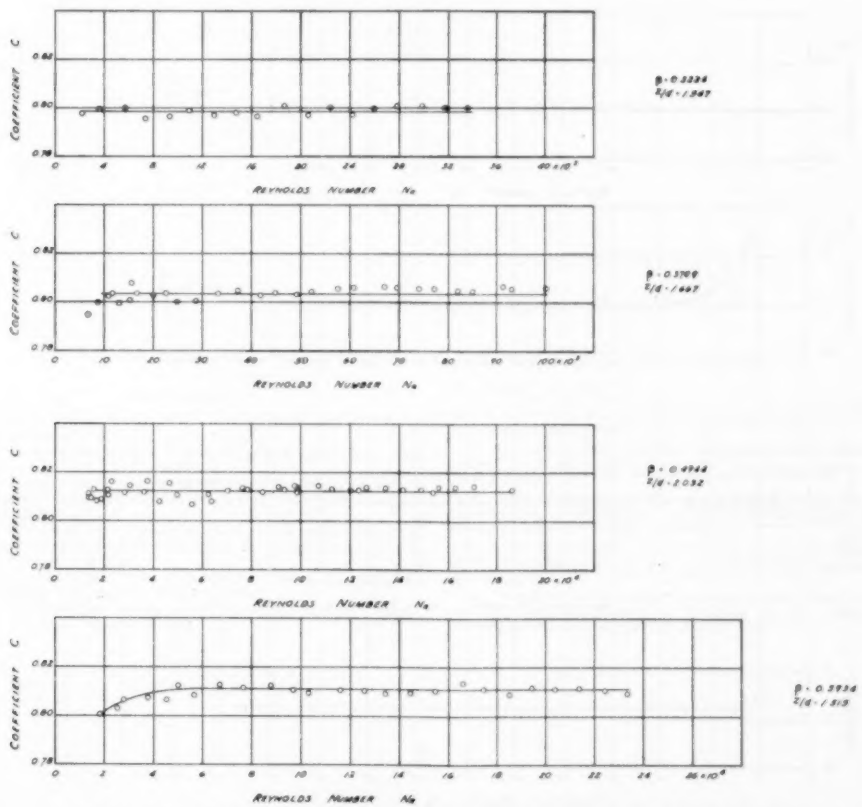

FIG. 11 COEFFICIENT OF DISCHARGE IN FUNCTION OF REYNOLDS NUMBER FOR OPTIMUM-LENGTH RATIO

TABLE 4 OPTIMUM VALUES OF z/d

β	z/d
0.2224	1.5
0.3709	1.7
0.4944	2.0
0.5934	1.5
0.6928	...

2.678). This drop amounted to almost 1 per cent of the value of the coefficient.

This coefficient then remained unchanged from $z/d = 2.678$ to $z/d = 2.589$. Another drop of approximately 1 per cent occurred at $z/d = 2.410$. Finally, for values of the length ratio equal to 2.237 and lower, the coefficient was again larger, practically within 0.5 per cent of the value for $z/d = 2.678$. Even for a value of the length ratio as low as 0.982, small change was evidenced in the value of the coefficient.

No satisfactory explanation can be offered for this behavior of the coefficient of discharge. A possible assumption would be that for the largest value of the length ratio, the fluid jet, expanding after the vena contracta completely filled the exit section of the nozzle. The expansion thus took place in two steps, namely, from the vena contracta to the nozzle cross section, then from the nozzle exit section to the pipe-line cross section. When the nozzle was cut, the length of nozzle flowing full decreased until, for a shorter length, the complete expansion of the jet took place directly from the vena contracta to the pipe diameter.

Since the variation of K and λ was very small, no optimum value of the length ratio could be assigned for $\beta = 0.6928$.

It is now planned to continue the investigation by studying the effect on the coefficient of discharge of various locations of the piezometer connections, the effect of adding a conical diffuser to the cylindrical nozzle, and the effect of roughness in the approach pipe.

ACKNOWLEDGMENTS

The authors wish to thank Builders-Providence Inc., for their sponsorship of the project. Mr. I. O. Miner, Vice-President and Chief Engineer, was of constant help and assistance.

Gratitude is also expressed to Dr. H. P. Hammond, Dean, School of Engineering, and to Dr. B. A. Whisler, Head, Department of Civil Engineering, The Pennsylvania State College.

Miss Constance Wellen and Messrs. D. H. Ruhl, A. H. Wenner, and L. H. Klotz rendered assistance at various stages of the project.

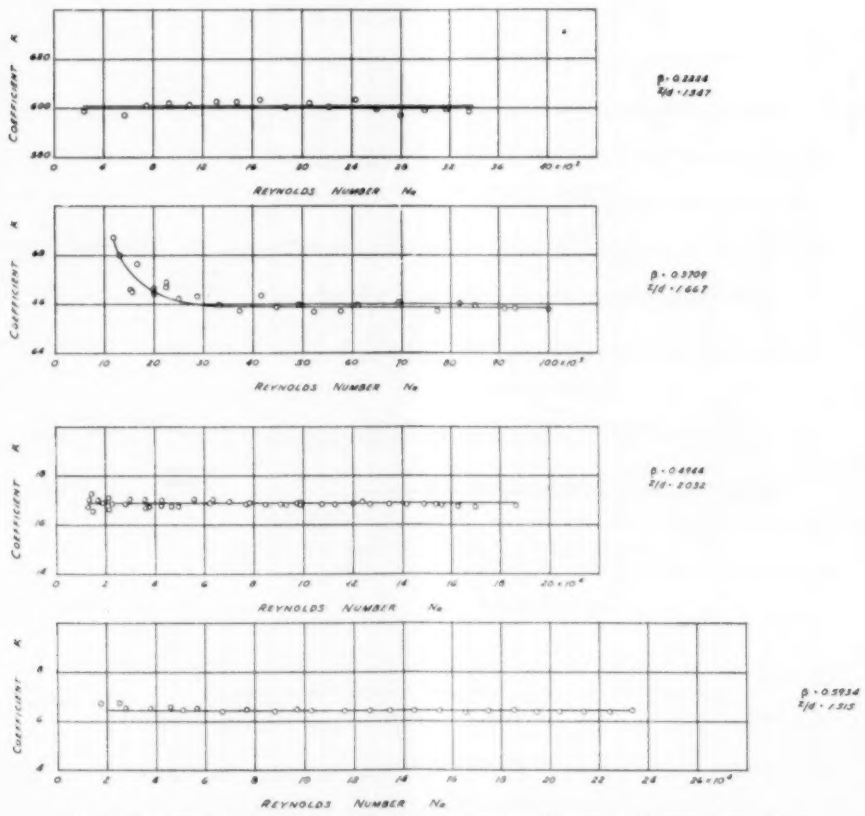

FIG. 12 PRESSURE-LOSS COEFFICIENT IN FUNCTION OF REYNOLDS NUMBER FOR OPTIMUM-LENGTH RATIO

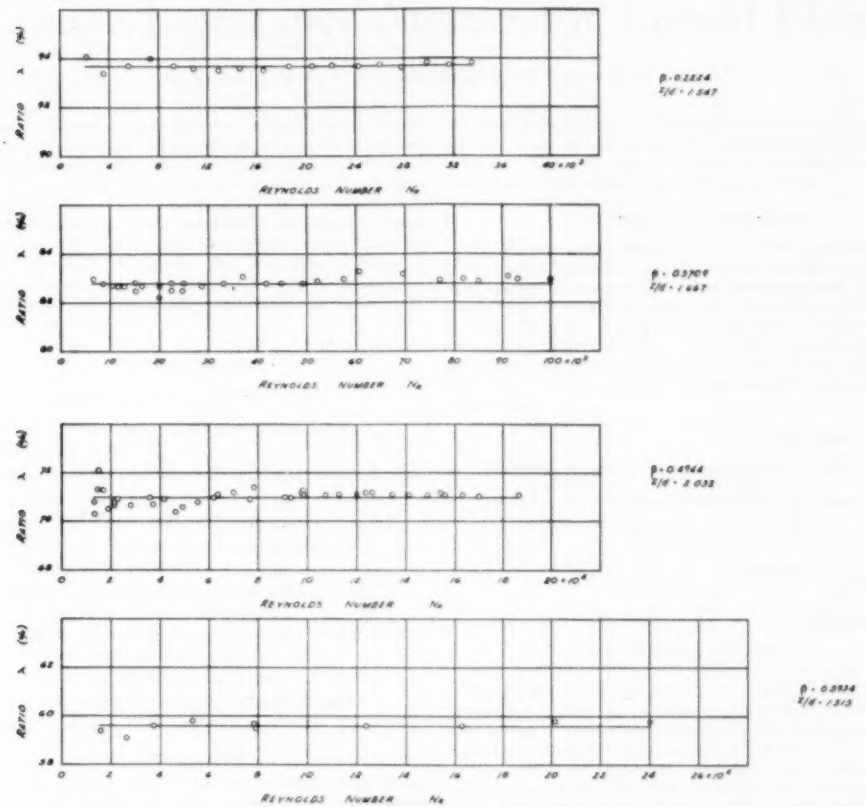

FIG. 13 PRESSURE-LOSS RATIO IN FUNCTION OF REYNOLDS NUMBER FOR OPTIMUM-LENGTH RATIO

BIBLIOGRAPHY

1 "Fluid Meters, Their Theory and Application," ASME Research Publication, 1937.

2 "Flow Measurement," British Standard Code, B.S. 1042, 1943.

3 "Regles pour la mesure des débits des fluides par tuyères et diaphragmes. Recommandations provisoires," ISA Bulletin, 9 and 12, 1935–1936.

4 "Druckausgleich in Ringkammern von Drosselgeräten," by W. Beckmann, *Forschung auf dem Gebiete des Ingenieurwesens*, vol. 8, August, 1937, pp. 192–202.

5 "La mesure des débits aux petits Nombres de Reynolds," by A. L. Jorissen, Desoer, Liege, Belgium, 1944.

6 "Discharge Coefficients of Herschel-Type Venturi Tubes," by A. L. Jorissen (to be published).

7 "Neue Düsenformen für kleinere und mittlere Reynoldszahlen," by W. Koennecke, *Forschung auf dem Gebiete des Ingenieurwesens*, vol. 9, 1938, p. 109.

8 "Durchfluss-Messung mit Drosselgeräten bei kleinen Reynoldszahlen," by W. Koennecke, *Archiv für Technisches Messen*, vol. 90, 1938, p. T-2–4.

9 "Neue Düsenformen für die Durchflussmessung bei kleinen und mittleren Reynoldszahlen," by W. Koennecke, *Archiv für Technisches Messen*, vol. 91, 1939, p. T-2–4.

10 "Messdüsenformen für kleinere und mittlere Reynoldszahlen," by W. Koennecke, *Zeitschrift des Vereines deutscher Ingenieure*, vol. 83, 1939, p. 318.

11 "Essais sur des appareils déprimogènes proposés pour la Mesure des débits aux petits Nombres de Reynolds," by Alb. Schlag, *Revue Universelle des Mines*, Belgium, February, 1951.

Linear-Resistance Meters for Liquid Flow

By R. C. SOUERS[1] and R. C. BINDER,[2] WEST LAFAYETTE, IND.

A linear or linear-resistance type of flowmeter can consist of a straight piece of pipe with a porous plug, or a resistance element and a differential gage across the porous plug. In a certain flow range the volume rate of flow through the meter is directly proportional to the pressure drop across the plug. An investigation was made of linear flowmeters with copper-wool and brass-screen disk elements; the fluid was water. The tests cover a range of plug lengths and plug specific weights. A set of dimensionless ratios is proposed for a correlation of all the data for general application.

Nomenclature

The following nomenclature is used in the paper:

A = cross-sectional area of pipe or plug normal to flow
D = diameter of fiber
e = porosity (volume of voids in plug)/(total volume of plug)
H = difference in head across plug or resistance
L = length of plug or resistance in direction of flow
P = static-pressure difference across plug or resistance
Q = volume rate of flow through plug or resistance
S = specific surface (surface area exposed to fluid)/(total volume of solid matter in resistance)
W = specific weight of plug element, equals weight of plug divided by volume of element
W_f = specific weight of fiber material in plug
μ = dynamic viscosity of fluid passing through meter
ρ = density of fluid passing through meter

Introduction

Among the different types of fluid meters is one which we call a linear or a linear-resistance type. In one form of construction this meter consists of a straight piece of pipe with a porous plug, or a resistance element, and a differential gage across the porous plug. In a certain flow range the volume rate of flow through the meter is directly proportional to the pressure drop across the plug.

The linear-resistance flowmeter has certain characteristics which may be desirable in different applications. It indicates directly the flow rate. The meter may be constructed easily and with materials readily available. If basic calibration data are established for easily duplicated plug or resistance elements, then possible users may not need to calibrate over well-established ranges.

Because of a lack of published basic data, an experimental investigation was made and material organized in order to bring out more prominently and simply the general characteristics of this type of instrument. A previous paper[3] presented data on the flow of air through meters with cotton and steel-wool plug elements. The present paper extends that work with a study of water flow through different plug-element materials.

Experimental Investigation

Fig. 1 shows a diagrammatic sketch of the apparatus used. Water passed through a straight constant-diameter pipe, and then through the porous plug. The porous plug was mounted inside a piece of smooth brass pipe, 1-in. standard pipe size (1.062 in. ID). Upstream from the porous plug was a straight length of 1-in. brass pipe 18 in. long. At the inlet to the 1-in. pipe was a straightening chamber, consisting of 20 in. of 4-in. pipe filled with 3 in. of gravel. The meter was mounted vertically with the flow up.

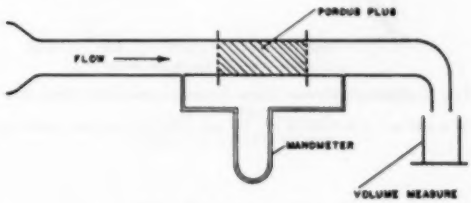

Fig. 1 Diagram of Apparatus

Three plug lengths were used, 4.25 in., 8.55 in., and 16.0 in., respectively. There was a retaining screen on each side of the porous plug. Static-pressure taps were located one pipe diameter from the retaining screen on each side of the plug.

Copper-wool and brass-screen disks were used as the plug or resistance materials. The ordinary copper wool had a rectangular fiber with average dimensions of 0.0205 × 0.00155 inch. The brass-screen disks were cut from commercial brass window screening of 16 × 16 mesh. The brass screen had a round fiber with a diameter of 0.0173 in.

Preliminary tests showed that it was necessary to deaerate the water in order to get reliable consistent data. The water was deaerated by boiling.

Figs. 2 and 3 are curves obtained from direct measurements. The middle curve in Fig. 2, for a brass-screen element, shows a linear relation between flow rate and head drop until the flow reaches about 0.075 cu ft per hr. Above this value the flow is no longer linear. Fig. 3 illustrates similar cases for copper-wool elements.

Correlation of Data

Figs. 2 and 3 illustrate the type of curves obtained with individual meters. A large number of tests were made, with different flow rates, with different plug lengths, and with different specific weights of the plug element. There is a question as to an effective organization of all the data for general application. The problem of laminar or viscous flow through porous plugs is quite complicated. A completely rational solution of this problem is

[1] Texas Beacon Laboratories, Beacon, N. Y.
[2] Professor of Mechanical Engineering, Purdue University. Mem. ASME.

Contributed by the Fluid Meters Research Committee and presented at the Annual Meeting, Atlantic City, N. J., November 25–30, 1951, of The American Society of Mechanical Engineers.
Note: Statements and opinions advanced in papers are to be understood as individual expressions of their authors and not those of the Society. Manuscript received at ASME Headquarters, September 12, 1951. Paper No. 51—A-57.

[3] "Study of Linear-Resistance Flowmeters," by F. W. Fleming and R. C. Binder, Trans. ASME, vol. 73, July, 1951, pp. 621–624.

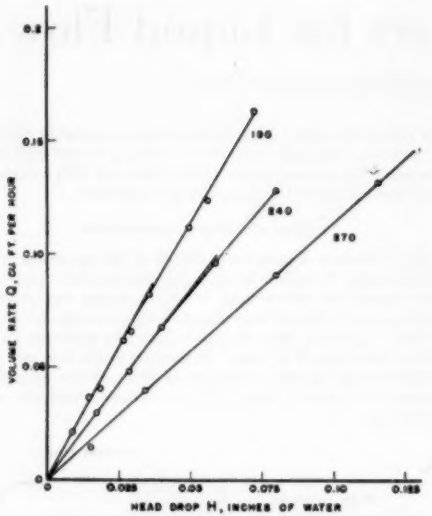

FIG. 2 CHARACTERISTICS WITH BRASS-SCREEN DISK PLUG ELEMENTS
(L is 8.56 in.; A is 0.886 sq in. Number along each curve is number of screen disks used in each meter.)

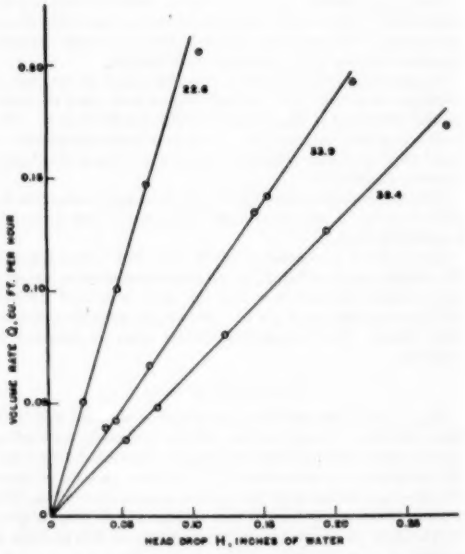

FIG. 3 CHARACTERISTICS WITH COPPER-WOOL PLUG ELEMENTS
(L is 16.0 in.; A is 0.886 sq in. Number along curve is specific weight of plug in pounds per cubic foot.)

very complicated, and, as yet, has not been fully established. Thus a dimensional analysis appears to be of direct value.

Experience with steel-wool and copper-wool meters showed promise for the use of two dimensionless ratios, $(Q\mu S^2)/(PA)$ and W/W_f. Fig. 4 shows a plot of all the tests for the copper-wool elements, using the proposed two dimensionless ratios. There is some scatter in these data, but the parameters appear useful in organizing data, at least for design studies. Fig. 5 shows a plot for the brass-screen meters using the proposed two dimensionless ratios. Fig. 6 shows a plot with log-log co-ordinates of the data in Fig. 4. The dotted line A in Fig. 6 follows data for the copper- and steel-wool flowmeters presented by Fleming and Binder.[3] The copper-wool data follow a curve which may be approximated by a hyperbola. The brass-screen data fall on a straight line, which approximates the extended leg of a hyperbola.

In dealing with pipe flow, Reynolds number is useful in es-

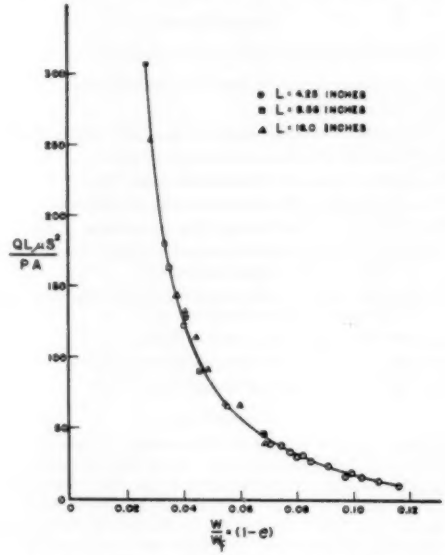

FIG. 4 CORRELATION OF DATA FOR COPPER-WOOL METERS

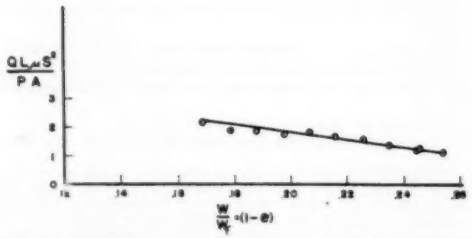

FIG. 5 CORRELATION OF DATA FOR BRASS-SCREEN-DISK METERS; L IS 8.56 IN.

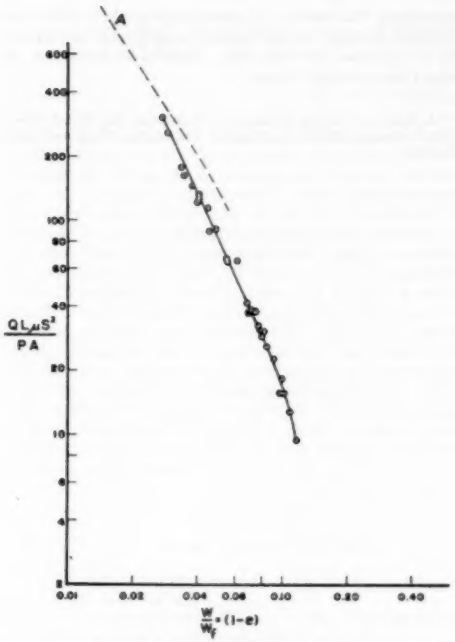

FIG. 6 CORRELATION OF DATA FOR COPPER-WOOL METERS ON LOG-LOG CO-ORDINATES

tablishing a limit for laminar or viscous flow. For the porous plug, a Reynolds number Re is defined as the dimensionless ratio

$$\mathrm{Re} = \frac{\rho Q d}{A \mu e}$$

With the use of plots of the type in Figs. 2 and 3, various Reynolds numbers were determined at the approximate limit of linearity for both copper-wool and brass-screen meters. Thus, for each material, a maximum Reynolds number Re for linear flow was determined. For brass-screen disks this maximum Reynolds number Re is about 0.5. For copper wool this maximum Reynolds number Re is about 0.9.

POSSIBLE ERRORS

Note that the foregoing data were taken only with meters in which the water was deaerated.

Various other tests with water as received directly from service lines showed no linear relation even at very low flow rates. In tests on a copper-wool meter, Fig. 7, a constant control-valve setting was used, and readings of flow rate and head loss were taken for different intervals of time. These data showed that as long as the meter was undisturbed, the head loss would increase and the flow rate would decrease with increasing time. When the meter was jarred or hammered, the head loss and flow rate would return toward the initial values.

The effect of air bubbles in a brass-screen-disk meter is shown in Fig. 8. For increments of decreasing flow, the data points did not retrace the line established for increasing flow increments. The curve has the appearance of a hysteresis loop. This loop did not appear when properly deaerated water was used.

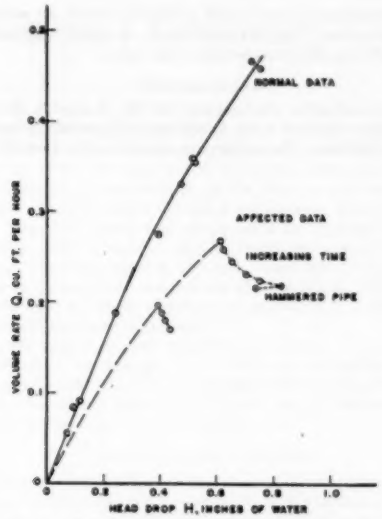

FIG. 7 EFFECTS OF AIR IN ONE COPPER-WOOL METER
(L is 4.25 in.; A is 0.886 sq in.)

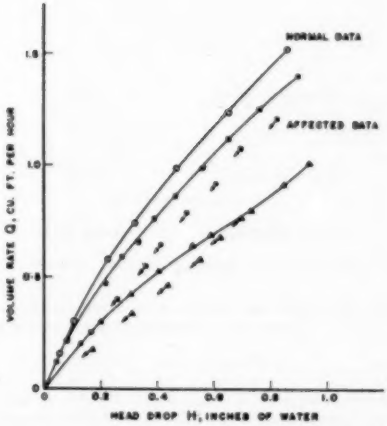

FIG. 8 EFFECTS OF AIR IN A BRASS-SCREEN-DISK METER
(L is 4.25 in.; A is 0.886 sq in.)

Thus air in a liquid linear flowmeter may have a major effect on the characteristics of the meter.

CONCLUSION

The foregoing discussion brings out some of the main features of the linear-resistance type of flowmeter for water. Basic data for two different types of plug material are presented.

A dimensional analysis yields parameters which are useful in organizing data. Air in a liquid linear flowmeter may have a major effect on the characteristics of the meter.

Acknowledgment

This investigation was suggested by Mr. Howard S. Bean in connection with work of the ASME Special Research Committee on Fluid Meters. The authors are grateful to Mr. Bean for his suggestions. The authors are grateful to Dean A. A. Potter and Prof. H. L. Solberg, both of Purdue University, for making possible the facilities for these tests. Material in this paper was adapted from a master's thesis.[4]

[4] "A Study of Linear Resistance Flowmeters for Water Flow," by R. C. Souers, MS thesis, Purdue University, West Lafayette Ind., 1951.

Oil Flow in Plain Journal Bearings

By S. A. McKEE,[1] WASHINGTON, D. C.

An analysis is given of the factors affecting the leakage of oil from the ends of plain journal bearings fed either through an oilhole or an axial groove on the unloaded side, or a circumferential groove. With bearings having an oilhole or an axial groove, the oil flow consists of two components, one resulting from the oil-feed pressure, and the other from the hydrodynamic-film pressures supporting the load. For bearings having a circumferential groove, the flow is primarily from the oil-feed pressure. The data given indicate that for any given bearing the oil flow may be expressed in terms of two dimensionless factors involving the oil-feed pressure and the bearing load. The relations between these factors and the generalized operating variable, $\mu N/P$, are given for bearings having each of the three designs of oil feed. Further investigations are suggested to provide a more complete understanding of the factors affecting end leakage of oil from plain journal bearings.

Nomenclature

The following nomenclature is used in the paper:

- D = journal diameter, in.
- L = bearing length, in.
- C = running clearance (difference between bearing diameter and journal diameter), in.
- W = total load acting on bearing, lb
- P = W/LD = pressure on projected area of bearing, psi
- N = speed of journal, rpm
- ϵ = eccentricity ratio (journal eccentricity divided by radial clearance)
- μ = absolute viscosity of lubricant at atmospheric pressure and bearing temperature, lb-min/in.^{2}
- Q = total rate of oil flow from bearing, cu in. per min
- Q' = oil flow from bearing caused by oil-feed pressure, cu in. per min
- Q'' = oil flow from bearing caused by load acting on bearing, cu in. per min
- p = oil-feed pressure (corrected for drop between gage and bearings), psi
- k_1 = dimensionless constant in Equation [2]
- $\mu N/P$ = generalized operating variable
- S = $(\mu N/P)(D/C)^2$ = Sommerfeld number

Introduction

In many modern applications the oil fed to a journal bearing serves a dual purpose. While its primary function is to act as a lubricant in the development of a load-carrying film, it also is called upon to carry away the heat generated in the bearing. As a consequence, the rate of flow of oil through a bearing is an important consideration in bearing design and operation.

This paper presents a detailed analysis of some oil-flow data obtained in a research program on the lubrication of plain journal bearings which was conducted at the National Bureau of Standards with the financial support of the National Advisory Committee for Aeronautics. Previous publications pertaining to this program[2,3,4] have dealt chiefly with the frictional characteristics, thermal behavior, and load-carrying capacity of plain journal bearings operating with forced-feed lubrication over a range of loads, speeds, and operating temperatures. That work also covered the effects of various arrangements of oilholes and grooves in the bearings and shaft.

In the present analysis, consideration is given to the factors which affect the leakage of oil when it is introduced either through an oilhole in the unloaded side of the bearing, an axial groove (parallel to axis) in the unloaded side of the bearing, or a circumferential groove in the bearing.

Factors Affecting Oil Flow

Barnard[5] pointed out that the leakage of oil from the ends of a journal bearing is caused by differences in the oil-film pressures in the axial direction. The pressures in the oil film in the bearing are influenced by two factors, namely, the oil-feed pressure, and the development of the hydrodynamic wedge which supports the load. The distribution of pressure around the journal and along the axis of a typical bearing operating at speed N and load W (see nomenclature) has the general characteristics as indicated by the curves in Fig. 1.

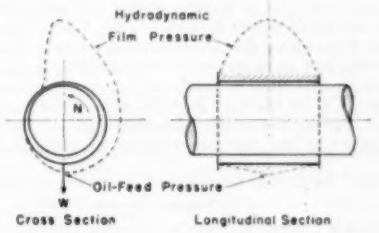

Fig. 1 Typical Pressure Distribution in Journal Bearing

For convenience, it is postulated that Q, the rate of oil flow from the bearing is represented by the equation

$$Q = Q' + Q'' \quad \ldots\ldots [1]$$

where Q' is the flow caused by the oil-feed pressure, and Q'' is the flow produced by the hydrodynamic film pressures generated in the load-supporting wedge.

Equations for the flow caused by the oil-feed pressure have

---

[1] National Bureau of Standards.

Contributed by the Lubrication Research Committee and presented at the Annual Meeting, Atlantic City, N. J., November 25–30, 1951, of The American Society of Mechanical Engineers.

Note: Statements and opinions advanced in papers are to be understood as individual expressions of their authors and not those of the Society. Manuscript received at ASME Headquarters, July 26, 1951. Paper No. 51—A-34.

[2] "Performance Characteristics of Journal Bearings With Forced-Feed Lubrication," by S. A. McKee, H. S. White, A. D. Bell, and J. F. Swindells, NACA Wartime Report ARR No. 4H15, August, 1944.

[3] "Measurements of the Combined Frictional and Thermal Behavior in Journal-Bearing Lubrication," by S. A. McKee, H. S. White, and J. F. Swindells, Trans. ASME, vol. 70, 1948, p. 409.

[4] "Oil Holes and Grooves in Plain Journal Bearings," by S. A. McKee and H. S. White, Trans. ASME, vol. 72, 1950, p. 1025.

[5] "Oil Flow in Complete Journal Bearings," by D. P. Barnard, 4th, Trans. SAE, vol. 20, 1925, p. 66.

been developed by Dennison,[6] Shaw and Macks,[7] and others for the special case of a bearing with a circumferential groove. These usually are of the form

$$Q' = k_1 \frac{pDC^3}{\mu L}(1 + 1.5\epsilon^2) \quad [2]$$

This suggests the following dimensionless functional relation for more general application

$$\frac{Q'\mu}{pC^3} = \psi_1\left(\frac{D}{C}, \frac{C}{L}, \frac{\mu N}{P}\right) \quad [3]$$

In this equation the generalized operating variable $\mu N/P$ is substituted for the quantity, $1 + 1.5\epsilon^2$.

The flow caused by the hydrodynamic-film pressures involves complex relationships among the factors involved. However, with a given bearing, operating at a given eccentricity ratio, it would be expected that the pressures generated in the oil film would depend on the load on the bearing. Accordingly, this suggests the use of the equation

$$\frac{Q''\mu}{PC^3} = \psi_2\left(\frac{D}{C}, \frac{C}{L}, \frac{\mu N}{P}\right) \quad [4]$$

which is similar to Equation [3] except that P, the load per unit projected area, is substituted for p, the oil-feed pressure.

Test Data

The oil-flow data considered here were obtained during a series of investigations using a four-bearing friction machine which has been described in detail in previous publications.[5,8,4] In this machine, a set of four equally loaded bearings is operated as a unit on a steel shaft.[8] The data presented here cover operation with sets of bearings having one oilhole (0.125 in. diam, chamfered to 0.18 in. diam at edge) directly opposite the center of the loaded side, one axial groove (0.64 in. length, 0.10 in. width, 0.04 in. depth) in the same position, or one circumferential groove (0.15 in. width, 0.075 in. depth) midway along the length of the bearing. Each design of oil feed was run with sets of bearings having two different clearances. The essential dimensions of the shaft and bearings are given in Table 1.

TABLE 1 ESSENTIAL DIMENSIONS OF SHAFTS AND BEARINGS

Design of oil feed	Bearing set	Length of bearing L, in.	Average diameter of bearing, in.	Average diameter of shaft, in.	Average clearance C, in.
1 hole in bearing	31	1.275	2.0581	2.0548	0.0033
	51	1.275	2.0599	2.0548	0.0051
Axial groove in bearing	33	1.275	2.0581	2.0548	0.0033
	53	1.275	2.0599	2.0548	0.0051
Circumferential groove in bearing	35	1.125[a]	2.0580	2.0548	0.0032
	55	1.125[a]	2.0600	2.0548	0.0052

[a] Allowance is made for circumferential groove.

Measurements of bearing diameters were made both before and after a series of tests with a given set, and the values given in the table are based on estimates of the dimensions of the bearings at the time the oil-flow data under consideration were obtained.

Not all the data obtained in a series of tests with a given set of bearings were readily applicable to the separate evaluation of the effects of oil-feed pressure or bearing load upon the oil flow from the bearing.

The most useful data for the present analysis were obtained in a series of runs operating at three different loads (W = 804, 1553, and 3008 lb), three speeds (1020, 2030, and 3040 rpm), and a number of oil-feed pressures ranging from about 10 to 60 psi. The oil used was an SAE 20 motor oil having an absolute viscosity of 70.8 centipoises at 100 F and 8.12 centipoises at 212 F. The oil-inlet temperature was maintained at 200 F. Typical examples of these data are given in Table 2.

TABLE 2 TYPICAL OIL-FLOW DATA

Bearing set	Load W, lb	Speed N, rpm	Oil-feed pressure p, psi	Bearing temperature, deg F	Rate of oil flow Q, cu in. per min
31	1553	3040	10.0	228	13.3
31	1553	3040	20.1	225	18.0
31	1553	3040	29.9	222	21.4
31	1553	3040	44.7	220	27.2
31	1553	3040	60.0	218	31.1
31	1553	2030	60.1	208	28.3
31	1553	2030	44.8	209	24.0
31	1553	2030	30.0	210	18.9
31	1553	2030	20.2	212	15.2
31	1553	2030	10.1	215	10.9
51	1553	2030	8.3	207	23.7
51	1553	2030	17.7	204	33.5
51	1553	2030	25.2	206	45.6
51	1553	2030	38.1	204	60.3
51	1553	2030	50.2	203	74.3
51	3008	2030	49.6	207	83.7
51	3008	2030	37.3	207	65.9
51	3008	2030	25.6	208	48.1
51	3008	2030	17.1	209	36.5
51	3008	2030	8.1	211	25.3
33	1553	2030	59.9	205	44.4
33	1553	2030	45.1	206	36.5
33	1553	2030	30.5	206	29.0
33	1553	2030	19.8	207	23.7
33	1553	2030	8.3	210	18.4
35	1553	2030	59.9	207	59.6
35	1553	2030	44.9	208	44.7
35	1553	2030	30.0	212	31.5
35	1553	2030	19.8	215	20.7
35	1553	2030	9.9	223	11.5

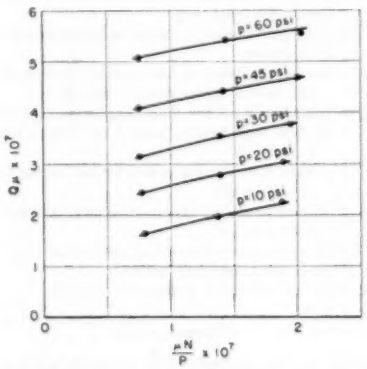

FIG. 2 OIL-FLOW DATA OBTAINED WITH 2-IN. × 1¼-IN. BEARING (C = 0.0033 IN.) WHEN OPERATING AT ONE LOAD (W = 804 LB) AND THREE SPEEDS (1020, 2030, AND 3040 RPM), USING AN SAE 20 OIL AT 200 F OIL-INLET TEMPERATURE AT OIL-FEED PRESSURES FROM 10 TO 60 PSI, AS INDICATED

Data obtained with bearing set 31 (one oilhole) operating at a load of 804 lb, three speeds, and nominal oil-feed pressures of 10, 20, 30, 45, and 60 psi are given in Fig. 2 where the quantity $Q\mu$ is plotted against the generalized operating variable $\mu N/P$. The general trend of the curves for the different oil-feed pressures (indicated in the figure) is typical of the data for all the sets of bearings operating at any one of the three loads.

[6] "Film-Lubrication Theory and Engine-Bearing Design," by E. S. Dennison, Trans. ASME, vol. 58, 1936, p. 25.

[7] "Analysis and Lubrication of Bearings," by M. C. Shaw and E. F. Macks, McGraw-Hill Book Company, Inc., New York, N. Y., 1949.

[8] Detailed information on the bearings, shaft, and operating techniques is given elsewhere.[4]

Since it is impractical to evaluate the effects of the various temperature gradients in the oil film upon the viscosity of the oil, the value for μ was chosen arbitrarily as the viscosity at atmospheric pressure at a temperature midway between the oil-inlet temperature and the average of the temperatures indicated by thermocouples fastened to the loaded side of each of the four bearings. This value for μ seems to provide better correlation than values based upon temperatures measured either by the thermocouples in the bearing shells or by thermocouples in the oil streams at the ends of the bearings.

Correlation of Data

As was mentioned previously, data such as are given in Fig. 2 may be used to separate Q into its components Q' and Q'' for any condition covered. This may be done graphically by plotting $Q\mu$ against p for any given value of $\mu N/P$. With such a plot the data fall approximately on a straight line, the slope of which is equal to $Q'\mu/p$ while the intercept at $p = 0$ equals $Q''\mu$. This separation also may be accomplished algebraically by the use of simultaneous equations.

Bearings Having One Oilhole. The results of such a separation for the two sets of bearings having one oilhole on the unloaded side and operating at the three loads and three speeds are given in Figs. 3 and 4.

In Fig. 3, $Q'\mu/pC^3$, the dimensionless factor pertaining to the oil-feed pressure, is plotted against the operating variable $P/(\mu N)$. The reciprocal of $\mu N/P$ is used since the curve for a given bearing should intersect the ordinate $P/(\mu N) = 0$ at a value of $(Q\mu)/(pC^3)$ which represents the flow with the journal running concentric with the bearing. If it is assumed that the upper portions of these curves represent conditions where the eccentricity ratio ϵ is approximately 1 and that Equation [2] may be applied to this type of bearing, then the intercepts would be four tenths of these upper values, and the curves would extend as indicated by the dotted lines.

Curves showing the relationship between $(Q''\mu)/(PC^3)$, the bearing load factor, and $\mu N/P$ are given in Fig. 4. These curves involve flow primarily on the loaded side of the bearings, hence they are extended to the zero intercept, indicating negligible flow from this cause when $\epsilon = 1$.

The data points shown in Figs. 3 and 4 are the results of computations using 5 different observed values, hence they do not indicate the correlation of the data clearly when using Equations

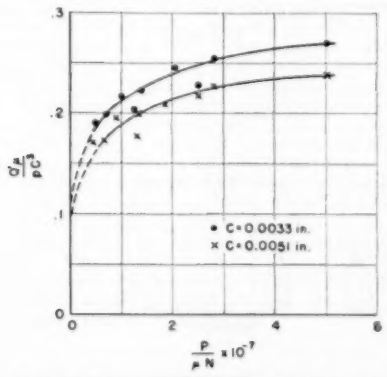

Fig. 3 Relation Between $(Q'\mu)/(pC^3)$ and $P/(\mu N)$ for 2-In. × 1½-In. Bearings Having One Oilhole (C = 0.0033 In. and 0.0051 In.)

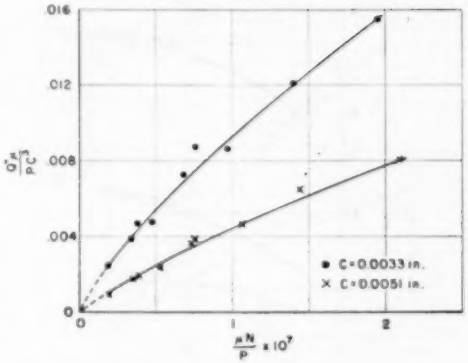

Fig. 4 Relation Between $(Q''\mu)/(PC^3)$ and $\mu N/P$ for 2-In. × 1½-In. Bearings Having One Oilhole (C = 0.0033 In. and 0.0051 In.)

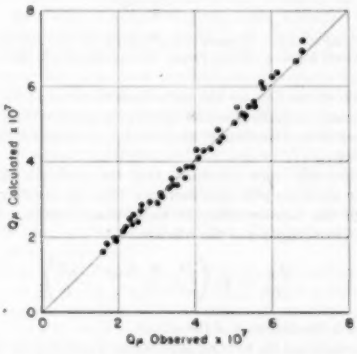

Fig. 5 Correlation of Observed Data With Calculations Based Upon Equations [1], [3], and [4] and Curves in Figs. 3 and 4

(2-in. × 1½-in. bearing having one oilhole; C = 0.0033 in.)

[1], [3], and [4]. However, in Fig. 5, where the calculated values of $Q\mu$, based on the curves in Figs. 3 and 4, are plotted against the observed values of $Q\mu$ for bearing set 31, the standard deviation between calculated and observed values is 3.1 per cent. For bearing set 51, this standard deviation is 3.3 per cent.

Comparisons of Designs of Oil Feed. Since the bearings with each design of oil feed had the same nominal clearances, length, and diameter, the curves for a given clearance provide direct comparisons of the flow characteristics of the different designs. Comparisons of the oil-feed pressure factors are given in Fig. 6, and of the bearing load factors in Fig. 7, for bearings having a nominal clearance of 0.003 in. For the bearings having a nominal clearance of 0.005 in., the corresponding curves for the different designs indicate no marked change in their relative positions.

Over the range of $P/(\mu N)$ covered, the oil-feed pressure factors for the bearings with a circumferential groove were about twice those for the axially grooved bearing and three times those obtained with the bearings having one oilhole. In this connection,

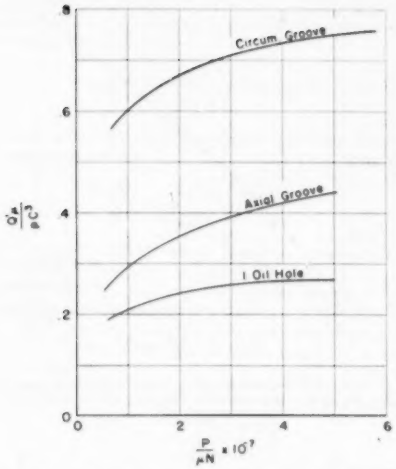

FIG. 6 $(Q'\mu)/(pC^3)$ VERSUS $P/(\mu N)$ CURVES FOR BEARINGS WITH EACH DESIGN OF OIL FEED; $C = 0.003$ IN. NOMINAL

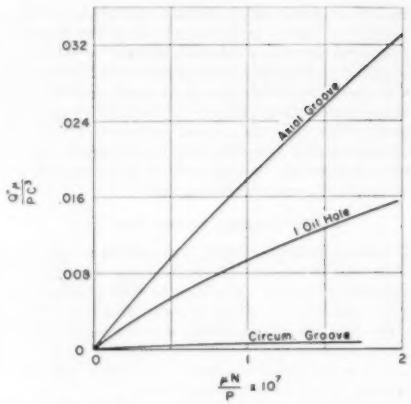

FIG. 7 $(Q'\mu)/(PC^3)$ VERSUS $\mu N/P$ CURVES FOR BEARINGS WITH EACH DESIGN OF OIL FEED; $C = 0.003$ IN. NOMINAL

the ratio of the flow for the one-oilhole bearings to the flow for the circumferentially grooved bearings is greater than would be expected from Dennison's[6] analytical treatment for this particular case.

One possible cause for this is that the motion of the journal directly over the hole may have an effect in assisting the flow through the narrow orifice at the clearance space. This suggests an investigation of the relation

$$\frac{Q'\mu}{pC^3} = \psi_2\left(\frac{D}{C}, \frac{d}{C}, \frac{L}{C}, \frac{\mu N}{p}, \frac{\mu N}{P}\right)$$

where d is the diameter of the oilhole.

In considering the bearing load factor, the flow from the axially grooved bearing was the greatest. This flow is primarily from the loaded side of the bearing, and apparently the axial groove provides a somewhat greater film thickness than the oilhole. This was noted also in the load-carrying tests previously reported,[4] where it was found that the axially grooved bearing had the lowest critical value of $\mu N/P$. The extremely low values of the bearing load factor obtained with circumferentially grooved bearings are noteworthy. A possible reason for these low values is indicated in Fig. 8 which shows the general characteristics of the longitudinal pressure distribution at the center line of the load for each of the three designs. From this figure it is seen that the single parabolic distribution of film pressures on the loaded side for the oilhole and axially grooved bearings tends to force the oil out the ends of the bearings, and hence increase the oil flow. The circumferentially grooved bearing, however, is divided by the groove into two short bearings, each of which has parabolic film-pressure distribution on the loaded side. In this case the film pressures on the inside portions of the two short bearings force the oil back into the groove. This results in a loss of the energy (from the standpoint of end leakage) that was used up originally in moving the oil axially from

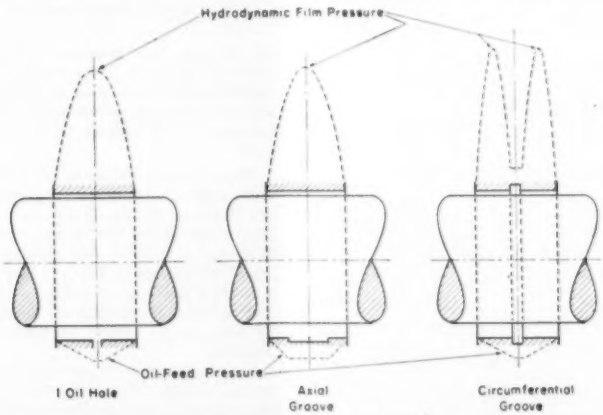

FIG. 8 PRESSURE DISTRIBUTION FOR EACH DESIGN OF OIL FEED

the groove. This loss is probably about equivalent to the gain in flow caused by the film pressures in the outer portions of the two short bearings—hence the values obtained for the bearing-load factors with this design of bearing are practically negligible.

Effect of Change in Clearance. In Fig. 9 the oil-feed pressure factor $(Q'\mu)/(pC^3)$ is plotted against the reciprocal of S, the Sommerfeld number, $S = (\mu N/P)(D/C)^2$, for the three designs of oil feed. Also, plots of the bearing load factor $(Q'\mu)/(PC^3)$, against S for the one-oil hole and axially grooved bearings are given in Fig. 10. A comparison of Fig. 3 with the one-oil hole bearing data of Fig. 9 indicates that plotting $(Q'\mu)/(pC^3)$ against $1/S$ instead of $P/(\mu N)$ tends to separate the curves rather than bring them together, as would be expected from the hydrodynamic theory. On the other hand, for a given type of bearing the bearing-load-factor data in Fig. 10 fall reasonably well on a single curve, whereas the data for bearings of different clearances fall on separate curves when plotted against $\mu N/P$ as in Fig. 4.

While such factors as accuracy of measurements in determining the clearance, choice of viscosity values used, and thermal expansion may influence the curves in Fig. 9, it is believed that

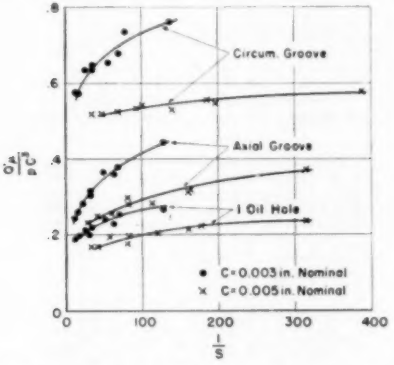

FIG. 9 RELATION BETWEEN $(Q'\mu)/(pC^3)$ AND $1/S$ FOR BEARINGS WITH EACH DESIGN OF OIL FEED

the major contributing factor to the differences shown is "out-of-roundness" possibly caused by some wear, but more probably by deformation under load. That out-of-roundness is responsible is indicated by the fact that in all the tests the oil-feed pressure factor values obtained with the bearings having the smaller clearance were proportionately larger than those obtained with the larger clearance bearings. It would be expected that the major portion of the oil flow caused by the oil-feed pressure occurs on the unloaded side of the bearing and, since a given deformation on the loaded side would have a proportionately greater effect on the clearance space on the unloaded side of the smaller clearance bearing, the effect on the flow would be in the direction shown by the differences in the $(Q'\mu)/(pC^3)$ curves. This explanation receives added support from the fact that, in cases where comparative estimates can be made, the values of $(Q'\mu)/(pC^3)$ obtained are larger than would be expected from the equations of viscous flow.

CONCLUSION

The foregoing discussion indicates that leakage of oil from the ends of plain journal bearings fed through an oilhole, or an axial groove on the unloaded side, or through a circumferential groove

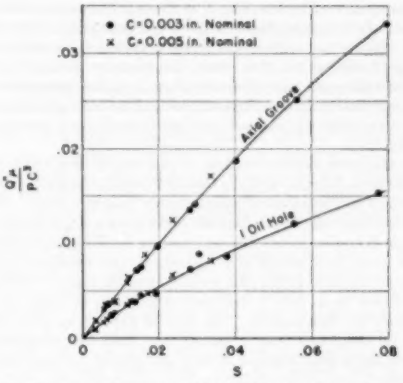

FIG. 10 RELATION BETWEEN $(Q'\mu)/(PC^3)$ AND S FOR BEARINGS HAVING ONE OILHOLE, AND AXIAL GROOVE

may be considered as consisting of two components, one resulting from the oil-feed pressure, and the other from the hydrodynamic film pressure supporting the load. In the case of a bearing with a circumferential groove, the leakage due to the hydrodynamic film pressure is negligible in comparison with that due to the oil-feed pressure, while for the other two types of bearings both causes produce appreciable leakage.

Over the range of conditions covered, the data obtained indicate that for any given bearing the end leakage of oil is defined reasonably well by Equations [3] and [4]. The differences obtained with bearings of different clearances when plotting the oil-feed pressure factor against the reciprocal of the Sommerfeld number are attributed to out-of-roundness caused chiefly by deformations under load.

While a very limited amount of other data available indicate the relations given apply also when using oils of different viscosity grade and at other oil-inlet temperatures, investigations should be made of these factors as well as the effects of changes in journal diameter and bearing length.

In further work on oil flow in plain journal bearings special emphasis should be placed on the study of flow caused by the hydrodynamic film pressures.

ACKNOWLEDGMENTS

Acknowledgment is made to Messrs. H. S. White, J. F. Swindells, and others who assisted in the NACA bearing program.

Discussion

G. B. DU BOIS.[9] This paper shows considerable progress in the study of oil flow, a problem which must be solved before we can attack the problem of estimating the operating temperature of a bearing having oil supplied under pressure.

The separation of the total oil flow into two parts, one related to the load, and the other related to the oil pressure, seems to us a valuable and necessary step. The author's method of separating these flows by graphical analysis is especially ingenious. The author is to be commended for making these oil-flow data available, and for his frank discussion of the difficulty of finding a satisfactory method of plotting the variations in oil flow.

Professor Ocvirk and the writer are also engaged in a research

[9] Professor of Mechanical Engineering, Cornell University, Ithaca, N. Y.

project sponsored by the NACA at Cornell University. We are varying the length-to-diameter ratio and measuring eccentricity ratio, friction, and oil flow. It seems to us that the variable consisting of the partial flow times the viscosity divided by the unit load times the cube of the clearance is in the right direction. However, this variable lacks terms related to the length-diameter ratio, a variation which is not apparent from the data on only one bearing.

We also have found a method of plotting oil flow which is of interest here, because we have been able to plot the author's data in Table 2 on our curve indistinguishably from our data. Thus, thanks to him, we can say that our curve gives a single line for oil flow which applies to two different bearing machines for the single oilhole case, and covers two clearances, two diameters, three length-to-diameter ratios plus variations in Zn over p. This will be included in an NACA technical note which we hope will be published in a few months. The data in Table 2, in effect, have saved us about one year of testing, and these two independent projects are a good example of how one project can supplement another.

M. D. Hersey.[10] This investigation goes far toward explaining the flow observations reported by Barnard and others. Certainly a clear physical picture of oil flow under the condition of practically uniform viscosity is a valuable aid toward understanding more complicated conditions.

Can a theoretical proof be given to show that the principle of superposition is applicable to fluid flow with variable geometry of the flow channel? The correlation of data in this paper seems to rely largely upon diagrams like Fig. 2 which are based upon a constant load. How does it work out with variable loads represented by constant values of p/P in such a diagram?

A complete dimensional analysis leads to an additional parameter p/P on the right-hand side of Equation [3]. The omission of that ratio appears to restrict our study to conditions where the journal position is not much influenced by the inlet pressure. The statement preceding Equation [4], to the effect that the film pressures generated hydrodynamically at any fixed eccentricity would depend on the load, may be questioned. This assumption is not required in the derivation of Equation [4]. Would it not be sufficient at this point to say that the eccentricity ratio depends upon $\mu N/P$?

M. Rosenblatt[11] and D. F. Wilcock.[12] We are interested in the author's separation of oil flow into two components, and although we recognize that this method is not mathematically rigorous, we agree that the data seem to indicate such a separation. His approach parallels the approach, which we used in a current paper,[13] rather closely with respect to this type of a separation. Although the bearings which we studied were different from those of the author, a comparison between the two papers is interesting.

A flux-plotting method was used to determine the film flow resulting from pressure at the oil grooves in our paper.[13] For a thin slot

$$Q_f = \frac{h^3}{12\mu}\frac{wp}{l} \text{ cu in. per min} \quad \ldots\ldots [5]$$

where

w = slot width, in.
l = slot length, in.
p = pressure, lb per in.
h = film thickness, in.
μ = viscosity, reyns

In the immediate vicinity of the groove the film thickness is nearly constant. Under these circumstances the ratio of width to length of an equivalent thin slot is determined from the small-square plot as the ratio of the number of equiflow lines to the number of equipressure lines. Thus in Fig. 11 of this discussion a plot for the author's one-hole bearing

$$\frac{w}{l} = \frac{4(4)}{6.25} = 2.56 \text{ or } Q_f = 0.213\frac{h^3p}{\mu}$$

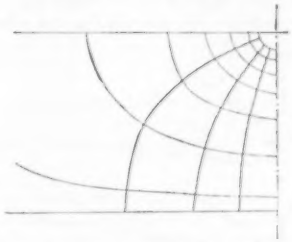

Fig. 11 Flux Plot for One-Hole Bearing

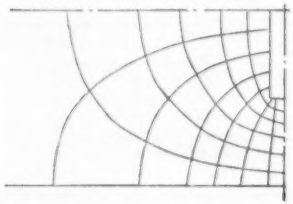

Fig. 12 Flux Plot for Axial-Groove Bearing

In Fig. 12, herewith, a plot for the author's axial-slot bearing

$$\frac{w}{l} = \frac{4(7)}{6} = 466 \text{ or } Q_f = 0.389\frac{h^3p}{\mu}$$

Now at the point of introduction of oil

$$h = \frac{c}{2}(1 + n^2) \quad \ldots\ldots [6]$$

where

c = diametrical clearance, in.
n = eccentricity

if it is assumed that the attitude curve of the journal is a semicircle. Thus

$$\frac{Q'\mu}{pc^3} = 0.213\left(\frac{1+n^2}{2}\right)^3$$

[10] Mechanical Engineer, U. S. Naval Engineering Experiment Station, Annapolis, Md. Fellow ASME. Statements and opinions are those of the writer and not to be construed as official or reflecting the views of the Navy Department.

[11] Engineer, Control Division, General Electric Company, Schenectady, N. Y.

[12] Section Engineer, Bearings and Chemical Section, Thomson Laboratory, General Electric Company, West Lynn, Mass. Mem. ASME.

[13] "Oil Flow, Key Factor in Sleeve-Bearing Performance," by D. F. Wilcock and Murray Rosenblatt, published in this issue, pp. 849–866.

for the one-hole bearing and for the axial slot bearing

$$\frac{Q'\mu}{pc^3} = 0.389\left(\frac{1+n^2}{2}\right)^2$$

Assuming that the N versus S-curves for the author's bearings are close to those for our bearings, a figure from the writers' paper[14] can be used to plot

$$\frac{Q'\mu}{pc^2} \text{ versus } \frac{1}{S}$$

curves for comparison with his data. These are shown in Fig. 13

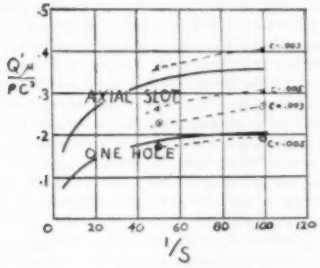

FIG. 13 PRESSURE-INDUCED FLOW
(Solid lines from Flux Plot, Dotted lines from McKee.)

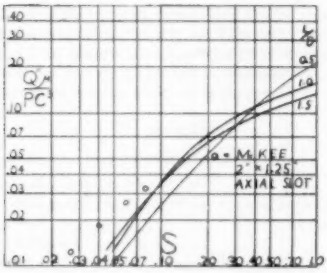

FIG. 14 FLOW IN 150-DEG BEARINGS DUE TO LOAD

of this discussion. Thus it is apparent that flux-plotting methods can be useful for predicting flow from oil grooves.

In the writers' paper, we used the term

$$q' = \frac{4Q''}{\pi NDLC} \quad \ldots\ldots [7]$$

where

Q'' = oil flow due to journal rotation cu in./min
N = rpm
D = diameter, in.
L = length, in.
C = diametrical clearance, in.

Now

$$\frac{Q''\mu}{PC^3} = \left(\frac{4Q''}{\pi NDLC}\right)\frac{\pi}{4}\frac{L}{D}\left(\frac{D}{C}\right)^2\frac{\mu N}{P} = \frac{\pi}{4}\frac{L}{D}S\,q' \ldots [8]$$

[14] See Footnote 13, Fig. 23.

Thus the theoretical curves of q' versus S in the writers' paper[15] can be put into the author's form. This is shown in Fig. 14 of this discussion, with some of the author's points for comparison. However, it must be remembered that his data are for an entirely different bearing configuration than ours and that dimensional curves of this form should be used only for similar bearing configurations.

P. R. TRUMPLER.[16] The calculation of oil flow is indeed one of the most important unsolved problems facing the bearing designer. However, the writer does not believe that the author's work will help us very much since his thinking is based on assumptions which are mostly unsatisfactory and his data are incompletely reported.

Use of the principle of similarity to set up functions of dimensionless groups is only an intermediate step between a pure guess and a complete analytical treatment based on an established mechanism. To investigate the limitations we must ask of Equations [3] and [4] of the paper whether or not the functions are complete. How about the existence of a partial oil film, which is probably avoided with oilhole and axial groove, but probably exists for the circumferential? How about the dimensions of oilhole, or the geometry of the grooves? Does not the assumption of a particular value of the viscosity μ appear to be rather arbitrary and deserve detailed explanation?

Considering the fact that the effect of variable oil viscosity is not well understood, is it not necessary to include many bearing temperatures taken at various points in the shell for the benefit of other investigators in the field? How about the dimensions of the circumferential groove?

The presupposition that dividing the oil flow into the two components Q' and Q'' will help us is open to question. Both components are dependent upon the film pressure. The partial differential equations, even for a complete film, do not permit superposition of circumferential and axial pressure components in any simple manner, because of the boundary conditions. This is an error made in all publications of which the writer is aware, underlying Equation [2], and is probably the basis for the flow-superposition idea.

If it is impossible to separate the pressure components, the usefulness of separating flow components escapes the writer.

It is believed that the entire problem of the pressure distribution in bearings with constant unidirectional load, assuming only constant viscosity, can and should be solved accurately by analytical means. This could be done for a wide variety of oil grooving. The pressure distribution would provide the solution for oil flow and load capacity at the same time. The results could then be spot-checked against experimental data. It is thought that work of this nature would provide the information which the engineer needs.

AUTHOR'S CLOSURE

While the author has no rigorous theoretical proof that it is permissible to separate the oil flow into two components, Q' and Q'', it might be well to point out that such a choice resulted from the fact that (as was mentioned in the paper) data such as is given in Fig. 2 fall in a straight line when $Q\mu$ is plotted against p for any given value of $\mu N/P$. This straight-line relationship not only provided a relatively accurate method for extrapolating to $p = 0$ but also indicated that for any given value of $\mu N/P$ (or eccentricity) any increase in p caused a proportional increase in $Q\mu$ and hence is in accord with Equation [2] which is derived from the theory of viscous flow. Accordingly, the author used this method rather than treating Q as a whole and using the variable

[15] See Footnote 14, Fig. 7.

[16] Professor, Mechanical Engineering, Illinois Institute of Technology, Chicago, Ill. Consultant, Clark Bros. Company, Inc. Mem. ASME.

p/P as suggested by Mr. Hersey. It might be mentioned also that unless this separation had been made, it is probable that the negligible "pumping effect" of the circumferentially grooved bearings would not have been noticed.

With reference to Mr. Hersey's questioning the statement regarding film pressures depending on the load, the fact that the eccentricity ratio is dependent upon $\mu N/P$ was implied by its insertion into Equation [4]. However, in this statement the author wished to point out that the same $\mu N/P$ (or eccentricity) could be obtained at different loads and the film pressures would change accordingly. For example, if we assume a given bearing is in one case operating at $N = 1000$ and $P = 200$, and in another at $N = 2000$ and $P = 400$, and either the lubricant is changed or the temperature is controlled such that the effective value for μ is the same, then the value of $\mu N/P$ would be the same in both cases, but the film pressures would be greater where $P = 400$.

In considering the case of variable loads mentioned by Mr. Hersey, it is believed that the use of the p/P parameter would not materially assist matters. In most practical bearing applications p, the oil-feed pressure, is maintained by some lubricating system usually involving a pump and a regulator for maintaining the pressure reasonably constant. Under these conditions, p is independent of the load, and, with a variable load, p/P is not a constant.

Oil Flow, Key Factor in Sleeve-Bearing Performance

By D. F. WILCOCK[1] AND MURRAY ROSENBLATT[2]

The determination and understanding of the performance characteristics of cylindrical sleeve bearings is based upon three relationships. These are (a) the viscosity-temperature characteristic of the lubricant; (b) the bearing power consumption as a function of oil-film temperature; and (c) the oil flow through the bearing as a function of Sommerfeld number. The first two are well known, and this paper is concerned primarily with the nature and quantitative determination of oil flow, together with the simplified methods for the calculation of bearing performance made possible thereby. The discussion is restricted to those bearings having oil fed under pressure to their oil-distribution grooves. Oil flows from the ends of these bearings because of the pressure in the oil grooves and because of the pressures generated in the load-carrying portion of the oil film. The second type of flow is dependent upon shaft speed. Dimensionless parameters controlling both types of flow have been calculated, and experimental results on several bearing sizes confirm the theory. A detailed study of the circumferential flow of oil in the bearing shows that Petroff's law is an excellent approximation of power loss up to an eccentricity of 0.7, and that the temperature variation in the oil film may be estimated with simple assumptions. Knowledge of bearing oil-flow characteristics permits the ready calculation of bearing performance by means of the "operating-line method."

Nomenclature

The following nomenclature is used in the paper:

A_c = chamfer flow coefficient
B = active width of oil film at any angular position in bearing, in.
C = diametral clearance, in.
C_p = heat capacity of oil, Btu/gal/deg C
D = journal diameter, in.
D_e = equivalent diameter of opening
H = power consumption of bearing, hp
K = shape coefficient for flow through a duct
L = length of bearing in axial direction, in.
M = point of minimum approach, subscript
N = journal speed, rpm
P = bearing load per square inch projected area
Q = net bearing oil flow, gpm
Q_c = oil flow through four oil-groove chamfers, gpm
Q_P = oil flow through bearing oil film due to inlet pressure, gpm
Q_R = oil flow due to rotation of journal, gpm
Q_M = circumferential oil flow past point of minimum approach, gpm
R = journal radius, in.
S = Sommerfeld number, $\left(\frac{D}{C}\right)^2 \frac{Z_2 N}{P} = 2.42 \times 10^{-9} \left(\frac{D}{C}\right)^2 \frac{\mu_2 N}{P}$
T = temperature, deg C
T_1 = inlet oil temperature, deg C
T_2 = outlet oil temperature, deg C
T_L = oil temperature at leading edge, deg C
T_T = oil temperature at trailing edge, deg C
T_M = oil temperature at point of minimum approach, deg C
ΔT = temperature rise of oil, $T_2 - T_1$
ΔT_P = temperature difference in bottom half of bearing, $T_T - T_L$
U = surface velocity of journal, ipm
W = power transfer to shaft, in-lb per min
W_p = power transfer with shaft centered (Petroff)
ΔW = error in W due to neglecting pressure-induced component of oil velocity
Z = oil viscosity, lb min per sq in.
a = chamfer dimensional radial to journal
b = chamfer dimension tangent to journal
e = journal eccentricity, in.
h = oil film thickness, in.
j = dimensionless ratio, W/W_p
k_1 = proportion of power loss in zone I, $W_1/\Sigma W$
k_2 = proportion of power loss in zone II, $W_2/\Sigma W$
l = axial length of chamfer, in.
n = eccentricity ratio, $2e/C$
p_1 = inlet oil pressure, psi
q = dimensionless oil-flow coefficient, $\frac{294\,Q_R}{NDLC}$
t = slot thickness, in.
u = oil velocity, ipm
w = slot width, in.
x = co-ordinate in direction of journal motion
z = co-ordinate in axial direction

α = acute angle between load vector and line of centers
γ = Sommerfeld substitution
θ = angle measured from load vector, in direction of motion
μ = oil viscosity, centipoises ($\mu = 4.14 \times 10^6 Z$)
μ_2 = outlet oil viscosity
ξ = ratio of corrected to uncorrected chamfer flow, $\frac{Q_c}{Q_c'}$ (Kinetic Energy Correction)
Φ = heat flow from bearing and shaft by conduction and radiation
ψ = oil viscosity-temperature function

Introduction

The methods and procedures for the analysis of the oil flow and performance characteristics of sleeve bearings described in this paper are directly applicable only to those bearings which are

[1] Section Engineer, Bearings and Chemical Section, Thomson Laboratory, General Electric Company, Lynn, Mass. Mem. ASME.
[2] Control Division, General Electric Company, Schenectady, N. Y.; formerly with Technical Education Division, General Electric Company, Schenectady, N. Y.

Contributed by the Lubrication Research Committee and presented at the Annual Meeting, Atlantic City, N. J., November 25–30, 1951, of The American Society of Mechanical Engineers.
Note: Statements and opinions advanced in papers are to be understood as individual expressions of their authors and not those of the Society. Manuscript received at ASME Headquarters, September 27, 1951. Paper No. 51—A-89.

fed by oil under pressure or which receive a copious supply of oil by some other means such as an oil ring. Bearings which are fed by oil under pressure are commonly used in modern high-speed turbines and gears, and simple but adequate means of predicting their performance accurately is needed by the designing engineer. This is particularly true where large bearings and high rotary speeds will cause abnormal temperature rises unless the design is correct. Likewise, in multiple reduction gears, where efficiency is at a premium, the multiplicity of bearings makes an accurate knowledge of bearing power consumption essential.

This paper affords methods of calculating readily both temperature rise and power consumption in bearings of the type illustrated in Fig. 1. This bearing is split into two halves. It has a cylindrical bore and large axial oil-distribution grooves located at the split, each subtending an angle of approximately 30 deg between blends with the bore. The principles outlined, however, will apply to other designs of pressure-fed bearings.

Bearings of the type illustrated are used normally where the quantity of heat generated in the bearing oil film is so large that its removal by conduction and radiation from the bearing surfaces would result in excessively high bearing temperatures. In order to avoid these excessive temperature rises, these bearings are designed so that a major proportion of the heat generated in the oil film is carried away by the oil which is caused to flow through the bearing. Since the amount of heat generated in the bearing oil film is roughly proportional to the cube of its diameter, while the heat which can be carried away at a given temperature level is proportional to the first power of the diameter, it is apparent that the larger a bearing is, the greater is the need for removing a major proportion of the generated heat by means of the oil flowing through the bearing. Because of this requirement for removing heat by means of the oil and not by radiation and conduction, a thorough knowledge of the quantity of oil which will flow through this type of bearing and of how to predict this quantity is essential if one is to predict the bearing performance.

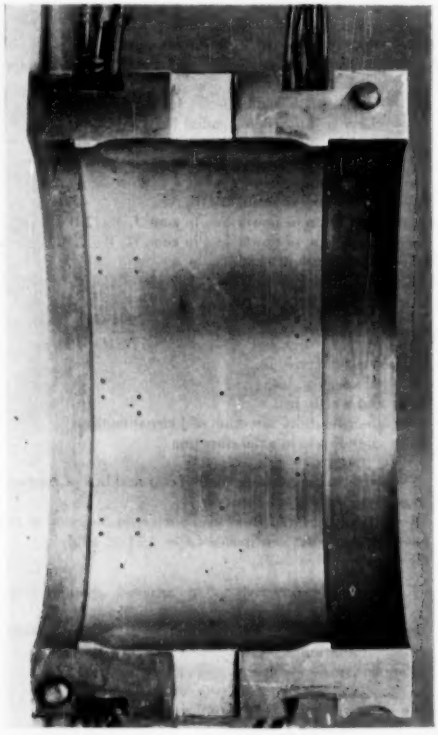

FIG. 1 LOWER HALF OF 8-IN. × 4-IN. TEST BEARING SHOWING AXIAL OIL-DISTRIBUTION GROOVES AND THERMOCOUPLE AND PRESSURE-TAP LOCATIONS

Major attention in the literature has been devoted to such things as the relations of friction factor and shaft position to the Sommerfeld number or related variables, to the pressure distribution within the oil film and the load-carrying capacity of the bearing, and to the calculation of bearing performance assuming that all heat is removed by conduction and radiation. However, Barnard (1)[1] in 1925 pointed out that in high-speed bearings where the heat generated must be removed by the oil, the bearing may be likened to a pump in which oil flow in an axial direction is due to the oil-film pressure necessary to support the bearing load and to the oil-feed pressure. He defined an "Efficiency" equal to the oil flow at zero feed pressure divided by the volume displaced circumferentially due to shear in the oil film with the shaft centered, and showed that it is related to the dimensionless variables P/ZN, D/L, and C/L.

This paper by Barnard appears to contain the essentials of a sound understanding of the mechanism of bearing oil flow, and it is surprising that his concepts have not been applied by later workers in the field. Shaw and Macks (2) calculate the oil flow at zero speed for bearings having a circumferential feed groove or a single inlet oil-feed hole and state that "flow through a stationary eccentric journal bearing should .... represent to a first approximation the flow to be expected from an actual bearing under load with the same eccentricity." Orloff (3) developed approximate equations for the flow from a bearing with a circumferential oil-feed groove, including the effects of oil-feed pressure and shaft rotation. Boyd and Robertson (4) found the oil flow through high-speed, low-load bearings with a circumferential oil groove at mid-length or with a single oil-inlet hole at the top to be substantially independent of speed and proportional to the inlet oil pressure, to the cube of the clearance, and to the reciprocal of the oil viscosity. McKee and White (5) have measured the effects of various oil-hole and groove configurations on bearing performance, oil flow, and temperature rise. Withers (6) studied oil flow through an engine main bearing and found it to be roughly proportional to the 1.3 power of speed, the square of the clearance, the square root of the inlet oil pressure, and inversely proportional to the 0.4 power of the inlet viscosity. Linn and Irons (7) found that oil flow in overshot bearings, which have a circumferential oil groove in the upper half only, has a large influence on bearing performance. In this type of bearing the oil flow is limited by an orifice in the feed line rather than by the bearing itself.

Further consideration and extension of Barnard's concept of oil flow through a bearing gives a clear picture of the phenomenon. At zero feed pressure there is a quantity of oil flowing circumferentially around the bearing which may be calculated as it is in the classical theory by adding to the flow due to shear the flow in a circumferential direction due to the pressure gradient in the oil. At zero bearing load this reduces to the shear-flow calculated with the shaft centered in the bearing. In bearings with

[1] Numbers in parentheses refer to the Bibliography at the end of the paper.

axial oil-distribution grooves such as are considered in this paper, the oil flow through the bearing which must be supplied by the oil-feed system is that oil which is forced out of the ends of the bearing due to the pressure gradients in an axial direction. This end flow may be calculated directly if the pressure gradients at the ends of the bearing are known. Thus information on end flow may be obtained from calculations by Needs (8) for 120-deg bearings, and by Waters (9), and Cameron and Wood (10) for the full journal bearing. As an alternative, the end flow may be thought of as the difference in the circumferential oil-flow rate between the points of maximum and minimum circumferential flow; and in this way the effect of shaft eccentricity in the bearing is immediately apparent. It is evident that the end flow may vary from zero when the shaft is centered to double the average circumferential flow when the eccentricity approaches one.

When the oil-feed pressure is greater than zero, an additional flow occurs due to the leakage of oil through the annular space between shaft and bearing and through the triangular-shaped openings created by the chamfers normally cut at the ends of the axial oil-feed grooves. At extremely light loads this "zero speed" oil flow Q_b is necessary to permit proper cooling of the bearing which would not have sufficient end flow at zero feed pressure.

The average outlet-oil temperature of the bearing depends upon the oil flow through the bearing, but it is equally dependent upon the bearing power consumption which in turn is a function of the oil-film viscosity. Thus it is important to know the oil-film temperature in relation to the inlet- and outlet-oil temperatures. Since the end flow from the bearing occurs only from the loaded half at zero feed pressure, it is reasonable to assume that the average film temperature in the loaded half of the bearing is equal to the average outlet-oil temperature, and measurements of oil-film temperatures have, indeed, shown this to be the case. Furthermore, the temperatures of the oil stream leaving the chamfers at the ends of the oil grooves are found to be nearly equal to the outlet-oil temperature, indicating that rather complete mixing takes place in the oil-feed grooves. In order further to understand why it is more reasonable to assume an average oil-film temperature equal to the outlet-oil temperature than to use the average of inlet- and outlet-oil temperatures, it is useful to consider the entire bearing as a mixer. Since under average conditions the end flow from a bearing is a small proportion of the circumferential flow, we may liken it to a mixer to which a small stream of cold oil is being added and from which an equal small amount of oil at the average temperature of the mixer is being withdrawn continuously. The mixer temperature is equal to the temperature of the oil being withdrawn and is above the temperature of the oil being added by an amount sufficient to carry away the heat being generated.

Thus the determination of the outlet-oil temperature determines the average oil-film viscosity and permits the prediction of bearing power consumption. If the oil flow through the bearing is known, the outlet temperature may be calculated in terms of the outlet-oil viscosity as follows, since the power consumed is proportional to viscosity

$$T_2 = T_1 + \frac{42.4H}{C_pQ} = T_1 + f(\mu_2) \quad \text{..... [1]}$$

The intersection of the line represented by Equation [1] with the viscosity-temperature curve for the particular oil to be used gives a graphical solution for the outlet-oil temperature and thence for the power consumption of the bearing. As will be shown later, the oil flow is dependent upon the oil-film viscosity because of its effect on shaft position, so that Equation [1] usually is not a straight line.

Analysis of Oil Flow

Zero Speed Flow. The zero speed flow Q_b, which is caused by the presence of a positive oil-feed pressure in the oil-distribution grooves in the bearing, has been shown to consist of two flows, namely, that oil which flows through the annular space between shaft and bearing Q_F, and that oil which flows through the chamfers at the ends of the oil-distribution grooves Q_c. In calculating Q_b, the simplifying assumption that the shaft is centered in the bearing is normally made. This assumption appears to be justified for a number of reasons, as follows:

1 When the shaft is rotating, it is roughly centered at light to moderate loads.

2 When the shaft is stationary and resting at the bottom of the bearing, the film thickness at the horizontal where the oil grooves are located is the same as for a centered shaft. Most of the flow will take place near the oil grooves.

3 Under running conditions, the zero speed conditions are obviously disturbed, and hence the calculation is approximate in any event.

4 Under low-load conditions where the zero speed flow becomes a large and important proportion of the total flow, the shaft is very nearly centered.

5 Correction for the horizontal shaft eccentricity is readily made if desired.

The oil flow through the clearance space in the bearing is proportional to the cube of the clearance and may be calculated from the general expression for the rate of flow of fluid through thin slots

$$Q = \frac{\Delta p l^3}{12Z}\left(\frac{w}{l}\right) \text{ cu in. per min} \quad \text{..... [2]}$$

The nature of the flow pattern through the clearance space may be ascertained by constructing a flux plot such as the one illustrated in Fig. 2. This shows one eighth of the developed bearing

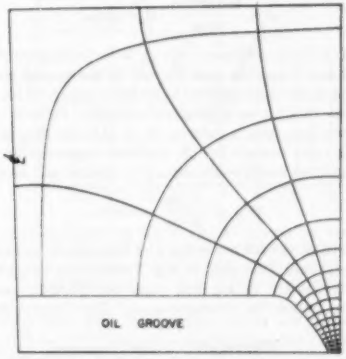

Fig. 2 Flux Plot Showing Pattern of Oil Flow Through Bearing Oil Film Due to Inlet-Oil Pressure, Assuming Shaft Centered in Bearing
(One eighth of developed bearing surface.)

surface, the minimum area of symmetry. From such a plot of orthogonal squares, the effective width to length ratio for any particular configuration of oil groove and bearing is determined for use in Equation [2]. For the particular example shown

$$\frac{w}{l} = \frac{16.2}{4} = 4.05$$

Decreasing the bearing length from 1.5 D to 0.5 D decreases w/l by only 10 per cent, for the shape of oil-feed groove illustrated, because the major portion of the flow takes place near the end of the groove. The total flow through the clearance space is 8 times that calculated by Equation [2] and, using an average value for w/l of 3.85 for the shape of oil groove illustrated, the film flow becomes

$$Q_F = \frac{5.75 \times 10^6 C^3 \Delta p}{\mu} \text{ (gpm)} \quad [3]$$

Fig. 3 shows the nature of the triangular opening created by the chamfers at the ends of the oil grooves through which a certain amount of oil leakage will occur. The flow through such a duct is given by the expression

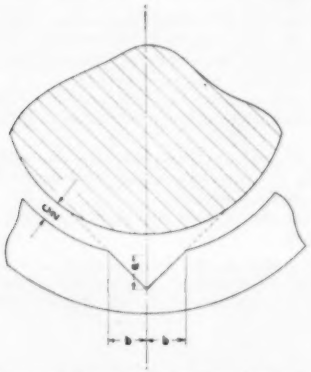

Fig. 3 Diagram of Triangular Chamfer Opening at Ends of Axial Oil Grooves

$$Q = \frac{894{,}000\ p}{K\mu l} (D_e)^2 \text{ (area)} \quad [4]$$

where K is a shape coefficient and D_e is the equivalent diameter calculated as 4 times the area divided by the wetted perimeter. K is known to be 16 for a circle, 14.25 for a square, 24 for parallel planes, and 13.3 for an equilateral triangle. Since it was not found in the literature, a value of $K = 13.0$ was determined for the 45-deg right triangle by the methods suggested by Purday (11) by applying Southwell's relaxation method and assuming

$$\nabla^2 \mu = \frac{1}{Z} \frac{\partial p}{\partial x} = \text{const} \quad [5]$$

The value of $K = 13.0$ is applied as a fair approximation to the more general case illustrated in Fig. 3 where the chamfer angle may not be exactly 45 deg and where the triangular section is extended to include the clearance space. The chamfer flow then becomes

$$Q_c^\circ = \frac{275{,}000\ a^2 b^3}{l(a + \sqrt{a^2 + b^2})^3} \frac{\Delta p}{\mu} = A_c \frac{\Delta p}{\mu} \text{ (gpm)} \quad [6]$$

Since the flow path along the chamfer is normally quite short, the pressure difference Δp used in Equation [6] must be corrected by subtracting the pressure required to accelerate the oil. Integration of the square of the velocity over the 45-deg right triangular section showed the average of the square of the velocity over the section to be 1.42 times the square of the average velocity. Therefore the average velocity head is given by

$$P_{KE} = \frac{\rho (V^2)_{avg}}{2g} = \frac{1.42\rho}{2g} \left(\frac{231\ Q_c}{60\ ab}\right)^2 \quad [7]$$

$$P_{KE} = \frac{0.0273\ \rho Q_c^2}{a^2 b^2} \quad [8]$$

However

$$Q_c = \frac{A_c(\Delta p - p_{KE})}{\mu} = Q_c^\circ - \frac{A_c P_{KE}}{\mu} \quad [9]$$

Assuming an average density of $\rho = 0.031$ lb per cu in. for paraffinic-type oils and assuming $a = b$ for the 45-deg right triangle, Equation [9] becomes

$$Q_c = Q_c^\circ - \frac{40\ Q_c^2}{l\mu} \quad [10]$$

which may be rearranged to give

$$Q_c^\circ = \frac{l\mu}{40} \left[\frac{1 - \frac{Q_c}{Q_c^\circ}}{\left(\frac{Q_c}{Q_c^\circ}\right)^2} \right] \quad [11]$$

The chart, Fig. 4, has been prepared from Equation [11] and permits determination of the proportional correction, $\xi = Q_c/Q_c^\circ$, as a function of the uncorrected chamfer flow Q_c°, and $l\mu$ the product of the length of the chamfer by the oil viscosity. The single chamfer flow then is

$$Q_c = \frac{47{,}200\ \xi \left(a + \frac{C}{2}\right)^4 p_1}{l\mu_2} \quad [12]$$

Since there are four chamfer openings, the total chamfer flow is $4\ Q_c$ if they are of equal size.

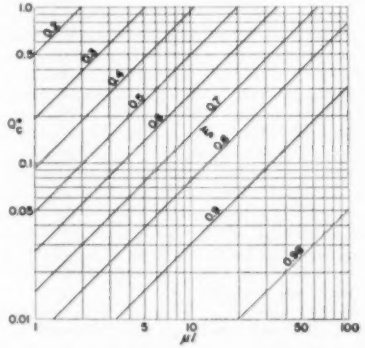

Fig. 4 Kinetic-Energy Correction for Chamfer Flow, $\xi = Q_c/Q_c^\circ$, as a Function of Q_c° and $l\mu$

Rotational Flow. The end flow from the bearing induced by rotation is a function of the axial pressure gradient existing in the oil film at the edges of the bearing. Therefore determination of the rotational flow for cylindrical bearings which have axial oil-distribution grooves requires calculation of the pressure distribution existing in the loaded half of the bearing. These calculations have been carried out in the form of numerical solutions of Reynolds equation for the centrally loaded 150-deg bearing (the lower half) and for L/D ratios of 0.5, 1.0, and 1.5. A generalized solution is obtained by first putting Reynolds equation in dimensionless form as follows

$$\frac{\partial}{\partial x'}\left(\frac{h'^3}{Z'}\frac{\partial p'}{\partial x'}\right)+\left(\frac{D}{L}\right)^2\frac{\partial}{\partial z'}\left(\frac{h'^3}{Z'}\frac{\partial p'}{\partial z'}\right)=-6\pi\frac{\partial h'}{\partial x'}\quad[13]$$

in which

$$x'=\frac{x}{D}\qquad h'=\frac{h}{C}=\frac{1+n\cos(\theta-\alpha)}{2}$$

$$Z'=\frac{Z}{Z_{avg}}\qquad z'=\frac{z}{L}$$

$$p'=\frac{p}{Z_{avg}N}\left(\frac{C}{D}\right)^2$$

The solution of Equation [13] will depend upon the length-diameter ratio, the viscosity distribution in the oil film, and the attitude measured by n and α (see Fig. 5). For a given length-diameter ratio and viscosity distribution, n and α are not independent since the journal must assume a running position such that the resultant horizontal force on the journal is zero for stable operation. Equation [13] has been solved numerically, assuming values of attitude L/D, and viscosity distribution, and remembering that the boundary conditions are that the pressure must be zero at the edges of the bearing and at the oil grooves. Any oil-feed pressure applied at the oil grooves is taken into account separately by means of the zero speed flow calculations. An exponential variation of viscosity between the leading edge and the trailing edge was assumed. The numerical solutions were obtained approximately with the aid of a d-c network analyzer choosing two values of α for each eccentricity and interpolating to obtain the conditions corresponding to a vertical load. In this way the pressure distributions for a series of values for L/D, eccentricity and viscosity distribution were obtained. A typical pressure distribution is shown in Fig. 6. From the calculated pressure distributions the dimensionless end flow

$$q=\frac{294\,Q_E}{NDLC}$$

and the total vertical load were determined by numerical integration. The results of this calculation are shown in the chart in Fig. 7 in which q is plotted as a function of Sommerfeld number S, for values of the viscosity ratio μ_L/μ_T, of 1 and 3. Lines of constant eccentricity n are also shown. It must be remembered that this chart applies specifically to bearings with two 30-deg horizontal oil grooves and that similar charts for bearings with other geometries will have to be calculated in like manner. The effect of viscosity ratio is minor.

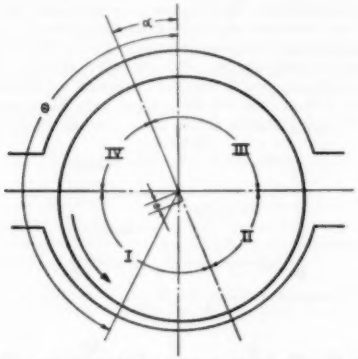

FIG. 5 SKETCH OF BEARING SHOWING FOUR ZONES OF OIL FILM
(Counterclockwise rotation.)

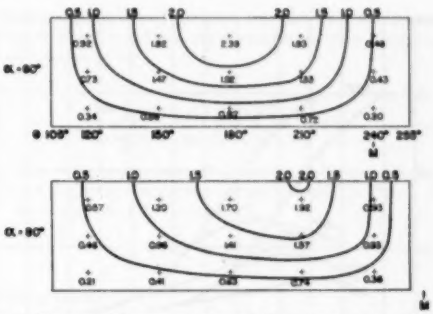

FIG. 6 PRESSURE DISTRIBUTIONS FOR $L/D = 0.5$, $n = 0.4$, $\mu_L/\mu_T = 3$, AND $\alpha = 60$ DEG AND 80 DEG IN LOADED HALF OF BEARING, AS CALCULATED ON DC BOARD
(Pressures are in dimensionless units, $p' = \frac{p}{Z_{avg}N}\left[\frac{C}{D}\right]^2$. Only half the length of bearing is shown. $\alpha = 66$ deg for horizontal equilibrium.)

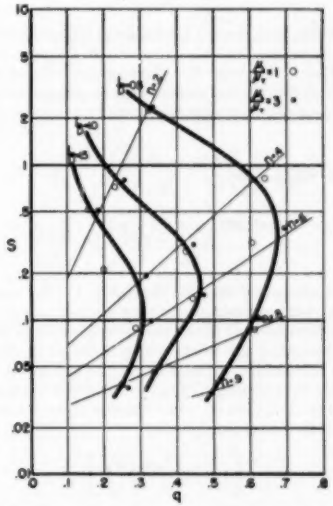

FIG. 7 DIMENSIONLESS OIL FLOW AS A FUNCTION OF SOMMERFELD NUMBER AND L/D RATIO FOR CYLINDRICAL BEARINGS WITH 30-DEG HORIZONTAL AXIAL OIL-DISTRIBUTION GROOVES
(Open circles $\mu_L/\mu_T = 1$. Solid circles, $\mu_L/\mu_T = 3$.)

The calculated values of the dimensionless oil-flow coefficient q are compared in Fig. 8 with values calculated from the papers by Cameron and Wood (10) for the 360-deg cylindrical bearing, and by Needs (8) for the 120-deg partial bearing. The comparison is made for L/D ratios of 0.5 and 1.0, and it is interesting to note that for each L/D ratio the three calculations form a family of curves in which the curve for the axial oil-groove bearing having a 150-deg arc in the loaded half lies between the curves for the 120-deg partial bearing and the 360-deg full bearing. The potential advantage in greater oil flow and lower bearing temperature to be gained from locating the oil-feed groove near the point of

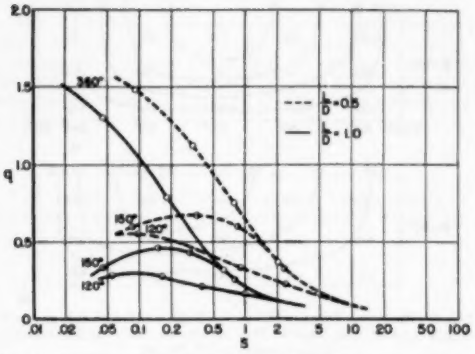

FIG. 8 COMPARISON OF DIMENSIONLESS FLOW COEFFICIENTS q FOR 120-DEG PARTIAL BEARING (NEEDS, REFERENCE 8), 150-DEG BEARING (AUTHORS), AND 360-DEG BEARING (CAMERON AND WOOD, REFERENCE 10)

maximum film thickness for low values of Sommerfeld number is apparent.

Total Flow. The total flow through the cylindrical bearing with axial oil-distribution grooves may be written as the sum of the zero speed and rotational flows giving a complete equation as follows

$$Q = Q_p + 4Q_s + Q_R = \frac{5.75 \times 10^5 C^3 p_1}{\mu_2} + 4\xi \frac{47{,}200\left(a + \frac{C}{2}\right)^4 p_1}{l\mu_2} + q\frac{NDLC}{294} \quad \ldots\ldots [14]$$

where ξ is determined from the chart, Fig. 4. The value of μ_2 is used as the best approximation to the viscosity conditions existing in the chamfers and in the clearance space when the shaft is rotating, because of the strong mixing in the oil grooves. If desired, the eccentricity of the shaft may be accounted for in the calculations by replacing $C/2$ by the true film thickness at the horizontal ($C/2 \pm e \sin \alpha$). The film-flow term, the first term in equation [14], is then multiplied by

$$\left[1 + 12\left(\frac{e \sin \alpha}{C}\right)^2\right]$$

and the second term, the chamfer flow term, is multiplied by

$$\left\{1 + 6\left[\frac{e \sin \alpha}{a + \frac{C}{2}}\right]^2 + \left[\frac{e \sin \alpha}{a + \frac{C}{2}}\right]^3\right\}$$

Rotational Flow Pattern. Some simple considerations of the pattern of oil flow within the bearing provide considerable insight into the oil flow to each of the oil-distribution grooves and into the effect of bearing load on power loss and temperature rise. In order to simplify the mathematical considerations, it will be assumed that the bearing oil-distribution grooves are compressed to a line at $\theta = 90$ deg and 270 deg; and that the energy transferred to the shaft is solely that due to the shear-induced component of oil velocity. These assumptions do not detract appreciably from the instructive nature of the results.

Considering the simplified bearing shown in Fig. 5, one sees that there are four distinct regions which may be defined in the oil film. In region I there is the convergence between the shaft and the bearing tending to compress the oil and to develop the pressures which support the external load. Under these pressures some of the oil is squeezed out the ends of the bearing and thus helps to remove the heat developed in the oil film. Slightly beyond the point of minimum approach, $\pi + \alpha$, the pressure in the oil film drops to zero gage or becomes slightly negative. Beyond this point the oil film will not develop negative absolute pressure, and the pressure remains substantially constant at or near zero. This situation has been well discussed in the literature and verified by experimental tests. Cameron and Wood (10), Cole (12), and others have pointed to the logical necessity of concluding that dp/dx must approach zero as the pressure approaches zero. If this be true and if a full laminar film were to be maintained, oil would have to be supplied to the film since the film thickness is increasing in the direction of motion in region II. This does not happen. At most, a little air or vapor is sucked in at the edges.

What then does happen in the expanding region? Since oil cannot be supplied to the film, the circumferential oil-flow rate must remain constant and at the same time shear flow must be maintained because there is at least a partial oil film and a relatively low Reynolds number. It is suggested, therefore, that the actual mechanism which occurs is somewhat as illustrated in Fig. 9 which shows that the film breaks down into a number of smaller diverging filmlets having a net cross-sectional area such

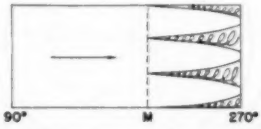

FIG. 9 SUGGESTED BREAKDOWN OF OIL FILM INTO FILMETS IN REGION II

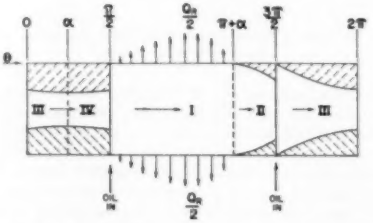

FIG. 10 DEVELOPED BEARING AREA SHOWING AREAS COVERED BY OIL FILM AT $n = 0.6$, $\alpha = 45$ DEG

that the rate of oil flow is maintained constant. Within each filmlet there must be a linear velocity profile and between the filmlets we would expect regions containing oil vapor, oil droplets, and air. The total width B of the filmlets must then be such as to maintain the flow Q_s, a constant, so that

$$B = \frac{h_x L}{h} = \frac{1 + n \cos(\theta_x - \alpha)}{1 + n \cos(\theta - \alpha)} L \quad \ldots\ldots [15]$$

where h_x is the thickness at the point where the film is full.

The complete pattern of flow postulated by the foregoing conclusion is illustrated by the developed bearing surface shown in Fig. 10 where for convenience the entire film is assumed to converge in one strip in the expanding region. Following the oil film around the bearing starting at the oil groove at 90 deg, it is compressed in region I developing a pressure and causing some end flow. In region II the film contracts inward due to the divergence of the film, but at the oil groove at 270 deg a full film is re-

stored. In region III the film thickness is still increasing and the film width contracts again. In region IV the film width begins to decrease and, although there is still not enough oil to form a complete film, the oil is gradually squeezed out to cover more surface. Enough oil to complete the formation of the full film flows in at 90 deg.

It is evident from these considerations that it is quite possible for oil flow to be in the reverse direction in the supply groove at 90 deg, the requirement being that the inlet flow at 270 deg be greater than the end flow Q. This reverse flow is observed experimentally at large eccentricities under heavy loading.

Thermal Effects

Power Consumption. Knowledge of the variable area of the bearing which is covered by oil film in regions II, III, and IV may be employed usefully in calculating the total power consumption of the bearing. It may be used further to permit estimates to be made of the variation in temperature within the bearing oil film using some reasonable assumptions.

If the simplifying assumption is made that the shear-induced component of oil velocity causes nearly all of the power transferred from the journal to the oil film, the total power so transferred may be expressed as

$$W = \int_0^{2\pi} \frac{ZU^2BRd\theta}{h} \text{ in-lb per min} \quad [16]$$

where B is a discontinuous function determined from the foregoing considerations of constant flow. It can be shown that the extent of the error introduced by neglecting the pressure-induced component of circumferential flow is given by

$$\Delta W = 2\pi PLDN\left(\frac{e\sin\alpha}{2}\right) \text{ in-lb per min} \quad [17]$$

for the torque at mid-film is given very closely by Equation [16] and ΔW represents the correction for shaft eccentricity to give shaft torque. If the journal is assumed to be running at the center of the clearance circle, Equation [16] reduces to

$$W_p = \int_0^{2\pi} \frac{ZU^2RL}{\frac{C}{2}}d\theta = \frac{4\pi ZU^2RL}{C} = \frac{2\pi^2ZN^2D^2L}{C}$$

in-lb per min ..... [18]

which is Petroff's equation. In both of these relations, Equations [16] and [18], the assumption that the oil grooves subtend a zero angle is equivalent to assuming that the turbulence in the oil groove approximately makes up for the decreased power consumption due to the depth of the oil groove. The proportional error $\Delta W/W_p$, introduced by neglecting the pressure-induced component of viscosity, may be obtained from Equations [17] and [18]

$$\frac{\Delta W}{W_p} = \frac{PC\,e\sin\alpha}{2\pi^2ZND^2} = \frac{n\sqrt{1-n^2}}{4\pi^2S} \quad [19]$$

assuming $n = \cos\alpha$. The magnitude of this error is small up to an eccentricity of 0.6 as shown in the following tabulation for $L/D = 0.5$:

n	S	$\frac{\Delta W}{W_p}$
0.2	2.4	0.002
0.4	0.8	0.012
0.6	0.33	0.037
0.8	0.085	0.143

Since the power loss with shaft centered, W_p, is calculated readily, it is useful to define the dimensionless ratio j, assuming viscosity constant, as

$$j = \frac{W}{W_p} = \frac{1}{2\pi}\int_0^{2\pi}\frac{B}{L}\left(\frac{\frac{C}{2}}{h}\right)d\theta \quad [20]$$

The total power consumption W is made up of four parts, each corresponding to one of the four regions indicated in Figs. 5 and 10. In region I, $B = L$. In region II

$$B = L\frac{h_{\min}}{h} = \frac{C}{2h}(1-n)L$$

In regions III and IV

$$B = \frac{h_{270^\circ}}{h}L = \frac{C}{2h}(1-n\sin\alpha)L$$

The proportion of the power consumption in each region to W_p may then be calculated by evaluating the following three integrals

$$\frac{W_1}{W_p} = \frac{1}{2\pi}\int_{\pi/2}^{\pi+\alpha}\frac{C}{2h}d\theta = \frac{1}{2\pi}\int_{\pi/2}^{\pi+\alpha}\frac{d\theta}{1+n\cos(\theta-\alpha)} \quad [21]$$

$$\frac{W_2}{W_p} = \frac{1}{2\pi}\int_{\pi+\alpha}^{3\pi/2}\left(\frac{C}{2h}\right)^3(1-n)d\theta = \frac{(1-n)}{2\pi}\int_{\pi+\alpha}^{3\pi/2}\frac{d\theta}{[1+\cos(\theta-\alpha)]^3} \quad [22]$$

$$\frac{W_3+W_4}{W_p} = \frac{1}{2\pi}\int_{3\pi/2}^{\pi/2}\left(\frac{C}{2h}\right)^3(1-n\sin\alpha)d\theta = \frac{1-n\sin\alpha}{2\pi}\int_{3\pi/2}^{\pi/2}\frac{d\theta}{[1+n\cos(\theta-\alpha)]^3} \quad [23]$$

These integrals may be evaluated by using the Sommerfeld substitution

$$\gamma = \cos^{-1}\left(\frac{\cos\theta+n}{1+n\cos\theta}\right) \quad [24]$$

as follows

$$\int\frac{d\theta}{1+n\cos\theta} = \frac{\cos^{-1}\gamma}{\sqrt{1-n^2}} \quad [25]$$

$$\int\frac{d\theta}{(1+n\cos\theta)^2} = \frac{\gamma-n\sin\gamma}{(1-n^2)^{3/2}} \quad [26]$$

It will be noted that it is necessary to define both the attitude angle α, and the eccentricity n, in order to determine the integrals numerically. Using the semicircular attitude curve defined by the equation, $n = \cos\alpha$, which, as can be seen from Fig. 11, is a rough approximation to the attitude curve calculated for this bearing, the integrals have been evaluated as summarized in Table 1. Values of j are obtained from the relation

$$j = \frac{W_1+W_2+W_3+W_4}{W_p} \quad [27]$$

When the values of j are plotted as a function of n, as in Fig. 12, it is seen that the simple Petroff equation is a remarkably good approximation up to eccentricities as large as 0.7. The reason that the power consumption does not increase more rapidly with n and, in fact, appears to decrease slightly at low eccentrici-

TABLE 1 VALUES OF j AND k

n	$\frac{W_1}{W_p}$	$\frac{W_2}{W_p}$	$\frac{W_1+W_2}{W_p}$	j	$k_1=\frac{W_1}{\Sigma W}$	$k_2=\frac{W_2}{\Sigma W}$
0.2	0.484	0.043	0.399	0.926	0.495	0.044
0.4	0.500	0.108	0.317	0.925	0.513	0.111
0.6	0.560	0.209	0.254	1.023	0.546	0.204
0.8	0.750	0.397	0.197	1.344	0.556	0.295
0.9	1.04	0.58	0.18	1.80	0.577	0.32

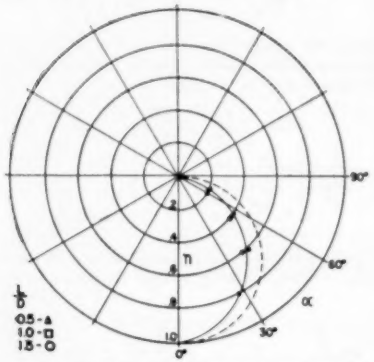

FIG. 11 CALCULATED ATTITUDE CURVE FOR CYLINDRICAL BEARINGS WITH 30-DEG HORIZONTAL AXIAL OIL GROOVES
(Dotted curve defined by equation $n = \cos \alpha$.)

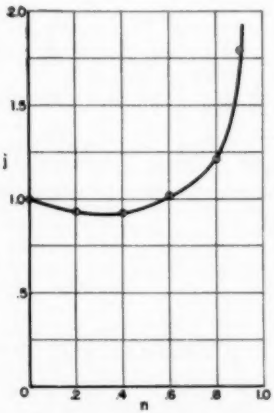

FIG. 12 POWER LOSS RELATIVE TO PETROFF'S EQUATION AS A FUNCTION OF ECCENTRICITY RATIO, n

ties, is the reduction of shearing area in the expanding portion of the oil film. While in considering the viscosity to be constant throughout the film in computing j, the heat generated under heavy loads at high eccentricities may have been overestimated, this effect is approximately compensated by neglect of the $\Delta W/W_p$ correction.

Temperature Rise. The temperature rise observed in the oil flowing through the bearing may be calculated from the power loss and the oil flow as follows

$$T_2 - T_1 = \frac{jW_p - \Phi}{QC_p}\left(\frac{1}{778 \times 12}\right) \quad [28]$$

In most calculations on large high-speed bearings it has been found reasonable to assume that Φ, representing the heat transferred from the bearing by means other than sensible heat in the oil stream, is zero. If this assumption is made, Equation [28] may be expressed as a line on a temperature-viscosity plot for a given bearing condition by substituting from Equation [18] as follows

$$T_2 = T_1 + \frac{2\pi^2 jN^2D^2L}{12 \times 778\, CQC_p} Z_2$$

$$= T_1 + 1.60 \times 10^{-11}\left(\frac{jLD^2N^2}{CQC_p}\right)\mu_2 \quad [29]$$

This is termed the "operating line" for the bearing. Note that, if as a first approximation the heat transferred by conduction and radiation is proportional to ΔT and the dependence of Q on μ_2 is neglected, a linear operating line is obtained, for if

$$\Phi = \varphi \Delta T \quad [30]$$

then

$$\Delta T = \frac{jW_p - \varphi \Delta T}{12 \times 778\, QC_p} \quad [31]$$

and

$$\Delta T = \frac{jW_p}{12 \times 778\, QC_p + \varphi}$$

$$= \frac{1.60 \times 10^{-11}\left(\frac{jLD^2N^2}{CQC_p}\right)\mu_2}{1 + \frac{\varphi}{12 \times 778\, QC_p}} \quad [32]$$

A plot of Equation [29] on the viscosity-temperature plot for the oil gives an intersection of the two curves at a point comprising the outlet-oil temperature for the bearing. The use of this procedure in calculating bearing performance will be described in detail in a later section, and is termed the "operating-line method."

Temperature Differentials Within Oil Film. At zero feed pressure, all the end flow Q_E occurs from the lower or loaded half of the bearing. The outlet-oil temperature T_2, therefore, must lie between the oil temperature at the leading edge T_L, and the oil temperature at the point of minimum approach T_M; and it will be assumed that $T_2 = (T_L + T_M)/2$. Because of the strong mixing in the oil-feed grooves between hot oil carried around the bearing and cold inlet oil, the leading-edge temperature will be higher than the inlet-oil temperature, $T_L > T_1$.

Let Q_M be the oil flow carried beyond the point of minimum approach of shaft to bearing, and let k_1 be the proportion of heat generated in zone I of the lower half. Then, assuming the heat capacity to be constant, the following equality may be written for the heat generated in zone I of the bearing

$$k_1 C_p Q\,(T_2 - T_1) = QC_p\,(T_2 - T_L) + Q_M C_p\,(T_M - T_L) \quad [33]$$

But

$$T_2 - T_L = \frac{T_L + T_M}{2} - T_L = \frac{T_M - T_L}{2} \quad [34]$$

Substituting in Equation [33] and rearranging

$$\frac{T_M - T_L}{T_2 - T_1} = \frac{\Delta T_I}{\Delta T} = \frac{2k_1}{1 + 2\frac{Q_M}{Q}} \quad [35]$$

Now

$$Q_M \cong \frac{(1-n)}{231}\left(\frac{\pi NDLC}{4}\right) \quad [36]$$

and

$$Q = \frac{q}{231}\left(\frac{\pi NDLC}{4}\right) \quad [37]$$

so that Equation [35] becomes

$$\frac{\Delta T_I}{\Delta T} = \frac{2k_1}{1 + \dfrac{2(1-n)}{q}} \quad [38]$$

Values of k_1 are given in Table 1, and values of q may be obtained from Fig. 7. A similar calculation for zone II, from which no end flow occurs, gives

$$\frac{T_T - T_M}{T_2 - T_1} = \frac{\Delta T_{II}}{\Delta T} = k_2\frac{Q}{Q_M} = \frac{k_2 q}{(1-n)} \quad [39]$$

The ratio

$$\frac{\Delta T_F}{\Delta T} = \frac{\Delta T_I + \Delta T_{II}}{\Delta T}$$

is shown as a function of n and L/D in Fig. 13, and it will be noted that except at very large eccentricities the temperature variation in the lower half of the bearing may be expected to be less than the temperature rise ΔT, of the oil passing through the bearing. Fig. 14 shows the viscosity ratios μ_1/μ_T, to be expected with medium turbine oil, $L/D = 0.5$, an inlet temperature of 40 C, and temperature rises of 10° C, 30° C, and 50° C. In general, viscosity ratios less than 4 will be experienced.

The maximum oil-film temperature is the trailing-edge temperature and may be estimated from Equations [38] and [39] as follows

$$T_T = T_2 + \frac{\Delta T_I}{2} + \Delta T_{II} = T_1 + \left[1 + \frac{k_1 q}{q + 2(1-n)} + \frac{k_2 q}{(1-n)}\right]\Delta T \quad [40]$$

Experimental Results

A series of experimental runs has been made on bearings with length-diameter ratios of 0.5, 1.0, and 1.5, using the journal-bearing test stand described by Wilcock (13) and illustrated in Fig. 15. The bearing dimensions are summarized in Table 2. The test data together with certain calculated values are given in Tables 3–9. The test apparatus permits the direct measurement of bearing torque and shaft-center displacement so that

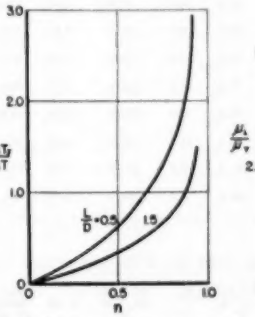

Fig. 13 Ratio of Temperature Variation in Loaded Half of Bearing to Temperature Rise in Oil Stream, as a Function of Shaft-Eccentricity Ratio

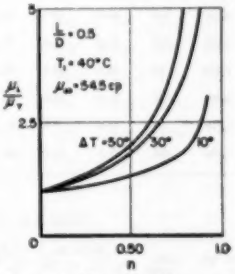

Fig. 14 Maximum Viscosity Ratio in Loaded Half of Bearing as a Function of Eccentricity Ratio and Temperature Rise in Oil Stream

TABLE 2 TEST BEARING DIMENSIONS

Bearing	Shaft diameter, in.	Bearing bore, in.			Bearing clearance, in.	Bearing length, in
		Maximum	Minimum	Average		
C	8.0010	8.0110	8.0104	8.0107	0.0097	4
D	8.0010	8.0148	8.0131	8.0136	0.0126	4
E	8.0000	8.0223	8.0190	8.0200	0.0200	4
M	3.9994	4.0036	4.0026	4.0031	0.0037	4
J	8.0010	8.0113	8.0089	8.0101	0.0091	8
G	8.0010	8.0117	8.0094	8.0014	0.0094	12
F	8.0010	8.0135	8.0108	8.0124	0.0114	12

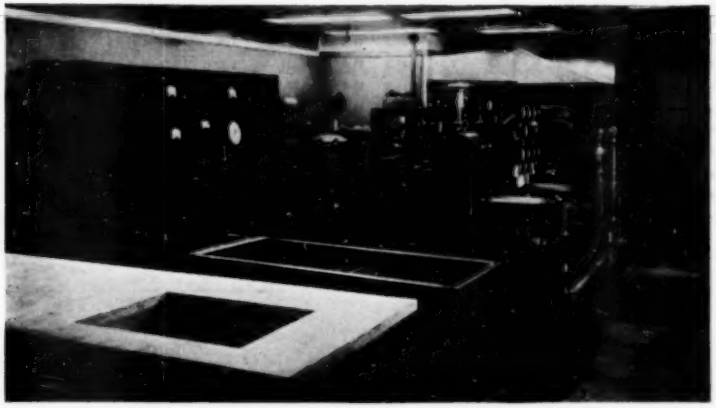

Fig. 15 Test Stand for Experimental Study of 2-In. to 8-In-Diam Sleeve Bearings
(General Electric Bearing and Lubricant Center, Thomson Laboratory, Lynn, Mass.)

TABLE 3 TEST DATA ON 8-IN. × 4-IN. × 0.0097-IN. CYLINDRICAL SLEEVE BEARING C

N, RPM	LOAD, p(PSI)	INLET OIL T_1, °C	INLET OIL p_1, PSI	OUTLET OIL T_2, °C	OUTLET OIL p_2	MAX. GRSD. RBG θ_c, TEMP., °C	Q, GPM	SHAFT TORQUE, FT. LBS.	HP	S	$j = \frac{1.35 \times 10^{7}}{p_2 N^2}$	$\phi_0 = 4\pi\left(0.23\frac{p_1}{p_2}\right)$	$Q_f = 0.529\frac{p_1}{p_2}$	Q_0	$Q - Q_0$	η
1,000	150	40.5	10.0	52	30.0	58.9	1.10	10.6	2.0	0.35	0.84	0.22	0.18	0.40	0.70	0.46
1,000	1,000	40.0	10.3	58.1	22.8	70.9	0.89	14.2	3.1	0.037	1.46	0.27	0.24	0.51	0.38	0.26
2,000	150	40.7	10.0	60.4	21.8	75.3	1.62	14.2	5.4	0.48	0.77	0.27	0.24	0.51	1.11	0.53
3,000	10	40.3	10.0	76.3	12.2	88.8	1.70	13.7	7.8	4.02	0.99	0.34	0.48	0.77	0.93	0.17
3,000	30	41.0	10.0	72.8	14.0	86.4	1.63	14.3	8.1	2.30	0.81	0.35	0.38	0.71	0.82	0.26
3,000	150	40.5	10.0	70.0	15.3	86.8	2.13	17.6	10.1	0.50	0.91	0.31	0.34	0.65	1.48	0.47
3,000	250	40.7	3.0	71.5	14.5	85.5	1.99	17.4	9.9	0.48	0.95	0.13	0.11	0.24	1.65	0.52
3,000	250	40.3	30.3	69.0	15.9	86.0	2.27	18.0	10.5	0.52	0.90	0.90	0.67	1.17	1.20	0.38
3,000	150	70.5	10.0	83.9	9.4	97.1	2.01	12.6	7.2	0.31	1.04	0.34	0.24	0.92	1.09	0.40
3,000	500	40.3	10.0	75.0	12.8	88.5	2.16	20.7	11.8	0.13	1.28	0.33	0.41	0.74	1.44	0.45
3,000	1,000	41.2	10.0	79.2	11.0	103.4	1.95	23.6	13.9	0.064	1.42	0.35	0.48	0.83	1.12	0.35
5,000	10	40.4	10.3	90.3	8.0	100.1	2.34	18.8	17.8	4.57	1.11	0.39	0.48	1.07	1.27	0.24
5,000	150	40.6	10.0	78.7	11.2	98.2	3.47	22.7	21.6	0.41	0.96	0.35	0.47	0.82	2.65	0.54
7,000	150	43.0	9.8	91.4	7.8	113.2	4.96	27.6	36.9	0.40	1.20	0.38	0.44	1.04	3.94	0.53
7,000	1,000	57.9	11.0	103.8	6.2	134.7	4.45	32.1	42.7	0.071	1.75	0.43	0.93	1.36	3.09	0.42

TABLE 4 TEST DATA ON 8-IN. × 4-IN. × 0.0126-IN. CYLINDRICAL SLEEVE BEARING D

N, RPM	LOAD, p(PSI)	INLET OIL T_1, °C	INLET OIL p_1, PSI	OUTLET OIL T_2, °C	OUTLET OIL p_2	MAX. GRSD. RBG θ_c, TEMP., °C	Q, GPM	SHAFT TORQUE, FT. LBS.	HP	S	$j = \frac{1.62 \times 10^{7}}{p_2 N^2}$	$\phi_0 = 4\pi\left(0.046\frac{p_1}{p_2}\right)$	$Q_f = 1.19\frac{p_1}{p_2}$	Q_0	$Q - Q_0$	η
250	10	39.8	10.1	39.9	54.4	48.8	0.66	3.8	0.18	0.53	0.84	0.03	0.21	0.24	0.42	1.22
250	150	39.0	10.0	40.7	52.3	48.2	0.74	8.4	0.40	0.034	1.98	0.03	0.22	0.25	0.49	1.42
500	150	39.3	10.0	43.3	45.8	48.7	1.02	9.0	0.85	0.059	1.21	0.03	0.25	0.28	0.74	1.08
500	1,000	40.4	10.8	46.3	36.5	54.0	0.86	21.0	2.0	0.0070	3.55	0.04	0.34	0.38	0.48	0.70
1,000	10	40.7	10.0	49.0	35.3	54.5	0.96	6.9	1.7	1.44	0.78	0.04	0.33	0.37	0.59	0.43
1,000	150	40.2	10.1	46.0	40.4	50.8	1.51	10.9	2.1	0.10	0.83	0.04	0.29	0.33	1.18	0.86
2,700	10	40.6	10.0	64.0	19.8	75.1	1.94	13.2	6.8	1.97	0.80	0.07	0.61	0.68	1.26	0.34
2,700	75	39.6	10.0	57.2	24.7	72.9	2.73	15.7	8.0	0.35	0.73	0.06	0.47	0.53	2.20	0.59
2,700	150	41.0	20.0	55.2	26.8	74.5	3.55	18.1	9.3	0.19	0.77	0.10	0.87	0.97	2.58	0.70
2,700	150	40.2	9.9	57.3	24.5	78.0	3.06	17.4	8.9	0.17	0.81	0.06	0.46	0.52	2.54	0.69
2,700	150	40.3	3	60.1	22.8	77.1	2.61	17.6	9.0	0.16	0.86	0.02	0.15	0.17	2.44	0.66
2,700	150	70.7	10.0	77.1	12.4	92.2	4.27	12.0	6.1	0.084	1.10	0.10	0.93	1.03	3.24	0.87
2,700	500	40.4	10.0	62.3	20.2	94.1	3.11	21.8	11.7	0.042	1.23	0.07	0.57	0.64	2.47	0.67
2,700	1,000	40.9	10.6	65.5	18.0	98.1	2.73	27.2	13.9	0.019	1.72	0.08	0.68	0.76	2.07	0.56
5,000	10	40.5	10.0	78.6	11.9	89.1	3.05	19.9	18.8	2.30	1.02	0.09	0.97	1.06	1.99	0.29
5,000	150	40.5	9.9	68.9	16.0	84.5	5.26	34.2	32.9	0.21	0.93	0.08	0.71	0.79	4.48	0.65
5,000	1,000	43.0	11.3	75.9	12.8	126.8	5.00	33.7	32.0	0.025	1.62	0.10	1.01	1.11	3.89	0.57
7,500	10	47.2	10.0	113.9	5.1	124.9	4.27	31.6	45.1	1.48	2.54*	0.14	2.25	2.39	1.98	0.19
7,500	75	44.6	10.5	86.4	9.0	102.7	6.11	42.6	60.7	0.25	1.95*	0.12	1.34	1.46	4.65	0.45
7,500	150	42.9	10.1	81.1	9.9	98.6	7.37	33.3	47.5	0.19	1.38*	0.11	1.17	1.28	6.09	0.59

*Turbulence.

TABLE 5 TEST DATA ON 8-IN. × 4-IN. × 0.0200-IN. CYLINDRICAL SLEEVE BEARING E

N, RPM	LOAD, p (PSI)	INLET OIL T_1, °C	INLET OIL p_1, PSI	OUTLET OIL T_2, °C	OUTLET OIL p_2	MAX. GROOVE RING TEMP., °C	Q, GPM	SHAFT TORQUE, FT. LBS.	HP	S	$j = \frac{2.50 \times 10^{-8}}{p_2 S^2}$	$4Q_0 = \pi\left(0.013\frac{p_1}{p_2}\right)$	$Q_p = 4.4\frac{p_1}{p_2}$	Q_0	$Q - Q_0$	q
500	150	38.7	10	39.5	52.0	42.4	1.71	9.4	0.89	0.067	1.76	0.17	0.09	1.06	0.5	0.60
1,000	10	40.2	10	42.0	50.2	49.1	2.52	7.8	1.5	1.95	0.77	0.17	0.91	1.09	1.43	0.66
1,000	150	40.5	10	44.3	45.2	50.8	2.48	11.7	2.2	0.11	1.33	0.19	1.07	1.26	1.22	0.56
1,000	500	40.0	10	46.0	40.0	50.1	2.33	15.0	2.8	0.031	1.84	0.20	1.15	1.35	0.98	0.45
3,000	150	39.8	10	53.2	29.0	75.7	5.36	19.3	11.0	0.22	1.09	0.25	1.59	1.84	3.54	0.54
3,000	150	39.8	3	55.5	27.9	75.3	4.31	16.8	10.7	0.22	1.10	0.09	0.50	0.59	3.72	0.57
3,000	150	40.4	20	51.4	33.0	76.3	6.61	19.7	11.2	0.26	0.97	0.46	3.44	3.90	2.71	0.42
3,000	150	54.4	10	63.3	20.7	79.9	6.35	15.7	8.9	0.16	1.24	0.29	2.12	2.41	3.91	0.60
3,000	150	67.4	10	74.8	14.1	88.0	7.00	12.5	7.1	0.11	1.45	0.35	3.32	3.67	3.33	0.51
6,000	10	39.8	10	63.9	20.2	80.7	7.40	25.6	26.9	4.7	0.96	0.30	2.28	2.58	4.82	0.37
6,000	75	40.2	10	62.4	21.4	83.6	9.29	28.9	32.9	0.66	1.10	0.29	2.15	2.44	6.85	0.53
6,000	150	39.8	10	62.7	20.0	88.2	9.58	28.7	32.7	0.31	1.17	0.31	2.30	2.61	6.97	0.53
6,000	500	40.4	10	67.0	17.0	101.7	9.56	31.7	36.1	0.079	1.52	0.33	2.71	3.04	6.52	0.50
9,000	10	44.9	10	97.4	7.7	142.5	9.68	46.6	79.6	2.7	3.30*	0.41	5.98	6.39	3.29	0.17
9,000	75	41.3	10	70.6	12.7	100.7	12.90	43.4	74.0	0.59	1.84*	0.36	3.62	3.98	8.92	0.46
9,000	150	43.1	10	77.7	13.2	105.4	13.87	42.6	73.0	0.28	1.76*	0.37	3.51	3.88	9.99	0.51
9,000	150	41.0	3	80.2	12.0	103.4	11.64	41.4	70.6	0.28	1.87*	0.16	1.15	1.31	10.33	0.53

* Turbulence.

TABLE 6 TEST DATA ON 4-IN. × 4-IN. × 0.0037-IN. CYLINDRICAL SLEEVE BEARING M

N, RPM	LOAD p (PSI)	INLET OIL T_1, °C	INLET OIL p_1, PSI	OUTLET OIL T_2, °C	OUTLET OIL p_2	MAX. GROOVE RING TEMP., °C	Q, GPM	SHAFT TORQUE, FT. LBS.	HP	S	$j = \frac{2.5 \times 10^{-8}}{p_2 S^2}$	$4Q_0 = \pi\left(0.013\frac{p_1}{p_2}\right)$	$Q_p = 0.020\frac{p_1}{p_2}$	Q_0	$Q - Q_0$	q
500	500	39.8	10	46.3	22.8	50.2	0.060	2.30	0.2	0.045	1.46	0.002	0.013	0.025	0.035	0.15
500	150	39.9	10	41.8	26.1	43.8	0.070	1.30	0.1	0.25	0.72	0.019	0.011	0.030	0.040	0.40
1,500	150	40.4	10	51.4	18.0	55.9	0.17	2.13	0.6	0.52	0.57	0.026	0.035	0.042	0.128	0.42
3,000	10	40.1	10	67.5	10.7	75.5	0.17	2.05	1.2	9.1	0.46	0.040	0.027	0.067	0.103	0.17
3,000	30	40.4	10	69.2	10.2	77.1	0.16	1.97	1.1	2.9	0.47	0.041	0.028	0.069	0.091	0.15
3,000	75	39.9	10	57.7	14.6	64.8	0.16	2.48	1.4	1.65	0.41	0.032	0.020	0.052	0.108	0.19
3,000	150	40.6	10	57.0	15.5	64.2	0.325	3.02	1.7	0.88	0.47	0.030	0.019	0.049	0.276	0.46
3,000	150	39.9	20	52.3	17.9	60.6	0.26	3.12	1.8	0.96	0.45	0.052	0.034	0.086	0.264	0.44
3,000	150	40.1	3	59.1	14.0	70.6	0.28	2.55	1.5	0.79	0.44	0.011	0.006	0.017	0.263	0.44
3,000	150	54.6	10	68.0	10.5	75.2	0.33	2.09	1.2	0.60	0.48	0.040	0.026	0.066	0.264	0.43
3,000	150	69.7	10	78.5	7.8	85.2	0.32	1.48	0.9	0.44	0.46	0.048	0.027	0.065	0.255	0.39
4,500	150	39.9	20	72.4	9.0	89.6	0.45	2.97	2.5	0.75	0.53	0.045	0.032	0.077	0.353	0.39
6,500	150	40.1	10	75.6	8.5	93.2	0.53	4.08	5.1	1.04	0.54	0.047	0.034	0.081	0.449	0.35
9,000	150	40.0	10	90.0	5.15	115.0	0.63	5.70	6.3	0.67	0.58	0.062	0.056	0.118	0.512	0.39
9,000	30	40.2	10	95.0	5.35	111.2	0.22	2.31	3.46	4.5	0.35	0.059	0.054	0.113	0.107	0.06
9,000	10	39.7	10	89.3	4.15	110.3	0.18	1.95	3.3	15.7	0.36	0.056	0.047	0.103	0.047	0.03

TABLE 7 TEST DATA ON 8-IN. × 8-IN. × 0.0091-IN. CYLINDRICAL SLEEVE BEARING J

N, RPM	LOAD p(PSI)	INLET OIL T_1, °C	INLET OIL P_1, PSI	OUTLET OIL T_2, °C	OUTLET OIL P_2	MAX. GROOVE TEMP., °C	Q, GPM	SHAFT TORQUE, FT. LBS.	HP	S	$J = \frac{5.03 \times 10^6 S}{p_2 R^2}$	$40_0 = 4\epsilon\left(0.29\frac{P_1}{P_2}\right)$	$Q_T = 0.45\frac{P_1}{P_2}$	Q_0	$Q - Q_0$	q
500	75	39.5	10	44.8	42.8	49.9	0.72	12.2	1.2	0.85	0.62	0.24	0.10	0.34	0.39	0.39
500	150	39.4	10	45.8	43.8	49.5	0.78	12.5	1.2	0.26	0.67	0.24	0.10	0.34	0.44	0.44
1,000	500	39.2	10	58.4	24.8	66.8	1.16	20.1	3.8	0.095	0.90	0.31	0.17	0.48	0.68	0.74
3,000	75	39.8	10	70.5	15.8	94.1	1.88	25.4	14.5	1.10	0.60	0.45	0.27	0.72	1.18	0.20
3,000	150	39.8	5	67.3	17.8	90.0	2.02	30.3	17.2	0.66	0.63	0.15	0.07	0.22	1.80	0.30
3,000	150	39.7	10	67.9	17.4	91.8	2.30	31.0	17.7	0.65	0.66	0.36	0.25	0.61	1.69	0.29
3,000	150	40.2	20	68.7	18.8	95.2	2.89	30.5	17.4	0.70	0.60	0.57	0.46	1.03	1.86	0.31
3,000	150	55.1	20	73.4	14.3	96.4	3.05	26.6	15.1	0.54	0.69	0.61	0.61	1.22	2.33	0.39
5,000	150	70.3	20	83.0	10.4	102.4	4.29	22.0	12.5	0.29	0.78	0.65	0.83	1.48	2.61	0.47
5,000	500	39.8	10	77.3	12.5	93.8	2.75	29.8	17.0	0.14	0.88	0.41	0.35	0.76	1.99	0.33
5,000	150	40.3	10	88.7	8.8	108.9	3.81	40.8	36.7	0.55	1.03	0.44	0.49	0.93	2.88	0.29
5,000	150	70.0	10	100.5	6.8	115.9	5.40	34.2	32.4	0.42	1.12	0.47	0.64	1.11	4.49	0.45
7,000	75	40.7	10	112.9	8.5	121.6	4.36	52.6	69.9	0.96	1.52	0.50	0.79	1.29	3.07	0.22
7,000	150	41.8	10	106.0	6.2	123.6	5.46	54.2	72.0	0.54	1.39	0.47	0.70	1.17	4.79	0.31
7,000	500	43.6	10	114.7	5.3	124.5	6.04	54.4	72.3	0.14	1.63	0.49	0.82	1.31	4.73	0.24

TABLE 8 TEST DATA ON 8-IN. × 12-IN. × 0.0094-IN. CYLINDRICAL SLEEVE BEARING G

N, RPM	LOAD p(PSI)	INLET OIL T_1, °C	INLET OIL P_1, PSI	OUTLET OIL T_2, °C	OUTLET OIL P_2	MAX. GROOVE TEMP., °C	Q, GPM	SHAFT TORQUE, FT. LBS.	HP	S	$J = \frac{4.03 \times 10^6 S}{p_2 R^2}$	$40_0 = 4\epsilon\left(0.66\frac{P_1}{P_2}\right)$	$Q_T = 0.45\frac{P_1}{P_2}$	Q_0	$Q - Q_0$	q
200	10	39.4	10	42.9	40.7	45.2	0.52	12.3	0.47	1.64	1.01	0.38	0.10	0.48	0.04	0.07
200	150	39.7	10	44.3	43.7	44.9	0.61	11.0	0.42	0.10	0.96	0.39	0.11	0.50	0.11	0.19
500	150	39.6	10	52.5	30.5	54.1	0.77	18.2	1.7	0.18	0.91	0.45	0.16	0.61	0.15	0.12
1,000	10	39.6	10	48.2	16.8	73.1	0.87	19.9	3.8	2.94	0.91	0.55	0.28	0.83	0.04	0.01
1,000	150	39.1	10	62.3	20.6	69.6	1.04	27.4	5.2	0.24	1.02	0.53	0.23	0.74	0.30	0 10
3,000	10	40.8	10	100.4	6.7	100.4	2.11	34.0	19.3	3.52	1.29	0.63	0.71	1.34	0.77	0.09
3,000	30	41.0	10	99.6	6.9	100.5	2.11	34.5	19.6	1.21	1.27	0.61	0.69	1.30	0.81	0.09
3,000	75	41.0	10	98.0	7.0	99.5	2.29	37.2	21.2	0.99	1.35	0.60	0.68	1.28	1.01	0.11
3,000	150	40.4	10	96.8	7.2	99.1	2.52	40.6	23.2	0.25	1.44	0.58	0.66	1.24	1.28	0.14
3,000	150	39.9	20	91.3	8.5	99.4	3.34	46.0	26.3	0.30	1.38	0.64	1.12	1.76	1.34	0.15
3,000	150	40.6	5	102.2	6.6	104.5	2.18	30.3	21.6	0.24	1.48	0.31	0.22	0.53	1.65	0.18
5,000	500	42.3	10	96.8	7.6	104.9	3.27	45.7	26.1	0.080	1.53	0.59	0.63	1.22	2.05	0.22
5,000	75	40.8	10	303.5	4.0	127.6	3.56	47.6	45.2	0.47	1.82	0.60	1.19	1.79	1.77	0.12
5,000	150	41.2	10	117.8	4.5	119.2	4.31	55.6	52.8	0.26	1.89	0.64	1.06	1.70	2.61	0.17
5,000	500	44.7	10	121.0	4.4	123.4	5.16	44.9	41.5	0.077	2.25	0.64	1.08	1.72	3.44	0.23

TABLE 9 TEST DATA ON 8-IN. × 12-IN. × 0.0114-IN. CYLINDRICAL SLEEVE BEARING F

N, RPM	LOAD p (PSI)	INLET OIL T_1, °C	INLET OIL p_1, PSI	OUTLET OIL T_2, °C	OUTLET OIL p_2	MAX. GROOVE TEMP., °C	Q, GPM	SHAFT TORQUE, FT. LBS.	BP	S	$J = \frac{0.29 \times 12^2 \times N}{p \times 2^2}$	$\frac{p_1}{p_2}$	$\frac{Q_b}{Q} = 0.85\left(0.15 + \frac{p_1}{p_2}\right)$	Q_b	$Q - Q_b$	q
200	50	44.6	10	48.5	40.0	46.6	0.65	4.8	0.2	0.99	0.58		0.13	0.21	0.34	0.31	0.42
200	150	42.9	20	43.8	43.0	44.0	1.36	10.4	0.4	0.071	1.12		0.23	0.40	0.63	0.73	0.98
200	150	44.4	10	45.9	39.0	46.0	0.97	10.6	0.4	0.064	1.26		0.13	0.22	0.35	0.62	0.79
200	150	45.2	5	45.6	40.0	47.5	0.56	10.5	0.4	0.066	1.22		0.07	0.11	0.18	0.38	0.51
500	150	44.0	10	49.2	33.5	56.9	1.41	16.8	1.6	0.14	0.93		0.15	0.25	0.40	1.01	0.54
1,000	150	46.0	10	73.2	13.0	82.3	2.96	33.4	2.9	0.11	0.95		0.25	0.42	0.67	2.08	0.54
1,000	500	44.5	10	61.3	30.0	70.3	2.02	32.2	4.1	0.050	1.09		0.21	0.42	0.63	1.39	0.57
3,000	10	45.3	10	89.0	8.8	94.5	3.95	36.5	20.9	3.33	1.38		0.29	0.97	1.26	2.69	0.24
3,000	50	45.7	10	86.5	9.7	93.5	4.15	36.8	11.0	1.20	1.17		0.28	0.80	1.14	2.99	0.27
3,000	75	44.9	10	80.5	11.2	86.7	4.39	37.5	21.4	0.86	1.04		0.27	0.76	1.03	3.36	0.30
3,000	150	45.3	10	76.2	12.7	80.4	4.96	39.6	22.6	0.31	0.96		0.26	0.67	0.93	4.03	0.36
3,000	250	70.1	10	91.1	8.4	102.4	5.77	31.9	18.2	0.21	1.17		0.30	1.01	1.31	4.46	0.40
3,000	150	45.6	5	83.0	10.3	90.7	4.50	40.6	23.2	0.25	1.22		0.17	0.41	0.58	3.92	0.35
3,000	150	45.6	20	75.6	12.9	103.2	5.77	42.9	24.4	0.32	1.09		0.64	1.32	1.34	4.41	0.40
3,000	500	44.1	10	82.3	10.7	105.7	5.51	50.3	28.6	0.079	1.45		0.27	0.79	1.06	4.45	0.40
5,000	10	49.0	10	116.7	4.4	116.7	5.62	51.4	49.0	2.70	2.16		0.35	1.95	2.30	3.54	0.19
5,000	150	49.3	10	107.7	5.8	111.9	7.79	59.9	56.8	0.24	1.91		0.32	1.47	1.79	6.00	0.32

shaft torque may be calculated. Thermocouples were used to determine the oil-film temperatures at several points.

The dimensionless oil-flow coefficients q have been calculated by first determining Q_b for each run using Equations [3] and [12]. These are plotted, for L/D ratios of 0.5, 1.0, and 1.5, as a function of the Sommerfeld number in Figs. 16, 17, and 18. The solid lines indicating the calculated q versus S curves are seen to be a fair correlation for the test results. A large part of the spread in the test results is doubtless due to errors in measurement. A small error in measuring the clearance will have a relatively large effect on q; and under conditions where Q_b is a large proportion of the total flow, an error in the measurement of Q or in the calculation of Q_b has a disproportionately large effect. It is felt, therefore, that the correlation obtained is a reasonable confirmation of the theory.

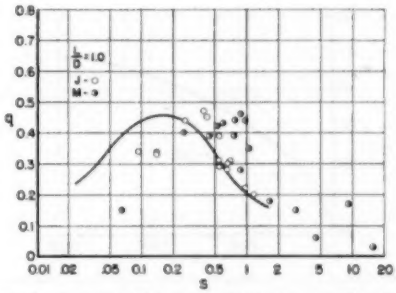

FIG. 17 COMPARISON OF EXPERIMENTAL VALUES OF q WITH CALCULATED q VERSUS S CURVE FOR $L/D = 1.0$

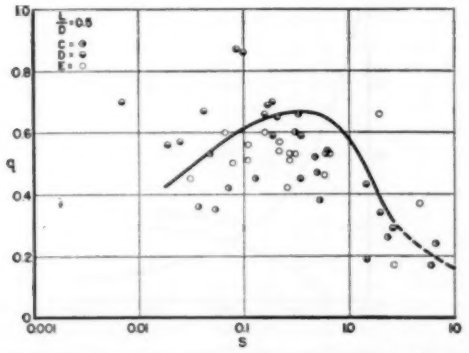

FIG. 16 COMPARISON OF EXPERIMENTAL VALUES OF q WITH CALCULATED q VERSUS S CURVE FOR $L/D = 0.5$

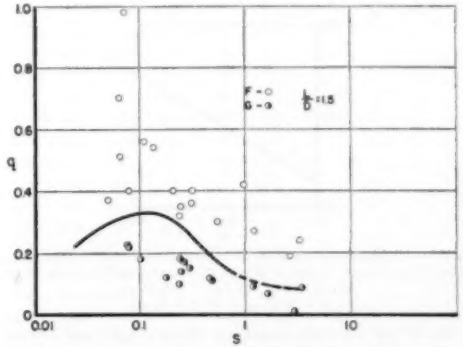

FIG. 18 COMPARISON OF EXPERIMENTAL VALUES OF q WITH CALCULATED q VERSUS S CURVE FOR $L/D = 1.5$

It is interesting to use the test data to check the approximate calculation of the effect of eccentricity on power loss, as expressed by the dimensionless coefficient j. This may be calculated from the experimental data using the following equation

$$j = \frac{2.64 \times 10^{12}\, CH}{LD^2N^2\mu_2} \qquad [41]$$

A plot of experimental values of j versus S is shown in Fig. 19 for $L/D = 0.5$ and compared with the calculated curve. The agreement appears reasonable.

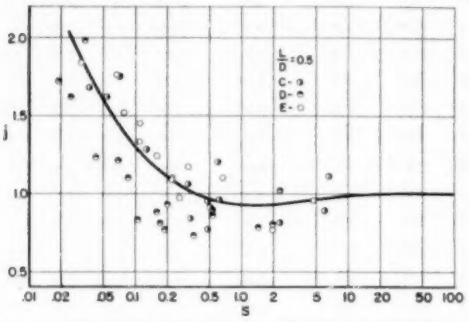

FIG. 19 COMPARISON OF EXPERIMENTAL VALUES OF j WITH CALCULATED j VERSUS S CURVE FOR $L/D = 0.5$

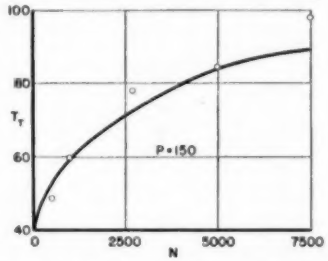

FIG. 20 COMPARISON OF MAXIMUM OBSERVED FILM TEMPERATURE WITH CALCULATED CURVE OF T_T AS A FUNCTION OF SPEED FOR BEARING D, 8 IN. × 4 IN. × 0.0126 IN.
($T_1 = 40$ C, $p_i = 10$, $P = 150$.)

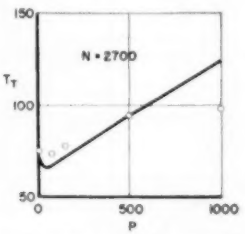

FIG. 21 COMPARISON OF MAXIMUM OBSERVED FILM TEMPERATURE WITH CALCULATED CURVE OF T_T, AS A FUNCTION OF LOAD FOR BEARING D, 8 IN. × 4 IN. × 0.0126 IN.
($T_1 = 40$ C, $p_i = 10$, $N = 2700$.)

Run D was especially completely thermocoupled and had one couple located within $^7/_{16}$ in. of the trailing edge. In Fig. 20 experimental values of T_{max} at 150 psi load are compared with the values of T_T calculated using Equation [40] over a range of speeds up to 7500 rpm, and in Fig. 21 the comparison is made at 2700 rpm over a range of loads from 10 to 1000 psi (see Table 10 for calculations of q and S). It will be seen that despite the simplifications and approximations used in deriving Equation [40], the calculations properly indicate the trends to be expected.

PREDICTION OF BEARING PERFORMANCE

The performance characteristics of cylindrical sleeve bearings with axial oil-distribution grooves at the horizontal joint can be predicted successfully using the information outlined in the preceding sections. Fundamentally this procedure involves the determination of the outlet-oil temperature and viscosity. This determination requires the solution of simultaneous equations for (*a*) the variation of oil viscosity with temperature, $\mu = \psi(T)$; and (*b*) the variation in bearing temperature with outlet-oil viscosity as given by Equation [29], which may well be termed the "operating equation" for the bearing. Since T_2 is not a simple mathematical function of μ_2 in either equation, j, Q, and C_p being functions of μ_2 in Equation [29], a graphical solution is preferred. This is done by computing two or more points on the curve of Equation [29] for suitable values of μ_2, and plotting the operating line so obtained on a viscosity-temperature chart for the oil. The intersection of the operating line with the viscosity-temperature curve of the oil is the solution for the outlet-oil temperature and viscosity.

As an example of the operating-line method, consider an 8-in-diam bearing 4 in. long with a clearance of 0.0126-in. and having 45-deg chamfer dimensions of $^1/_{64}$ in. × 0.263 in. long. This bearing is to operate at 10 psi load and 2700 rpm on an oil with a viscosity-temperature curve illustrated in Fig. 22, admitted at 10 psi and 40 C. Assuming values of μ_2 of 13, 17, and 19, the calculation is carried out as follows ($A_c = 0.040$, $C_p = 6.25$):

μ_2	Q_C	$4Q_F$	S	q	Q_B	Q	j	T_2
13	0.10	0.88	3.4	0.25	0.93	1.91	0.94	59.5
17	0.08	0.68	4.5	0.20	0.74	1.50	0.94	72.4
19	0.07	0.61	5.0	0.17	0.63	1.31	0.945	81.6

The μ_2, T_2 curve is plotted in Fig. 22, showing the desired solution at the intersection with the oil curve, $\mu_2 = 16$, $T_2 = 69$ C.

Similar procedures may be adopted for the two other types of calculations often needed by the bearing designer, namely, the calculation of bearing clearance for a given temperature rise between inlet and outlet oil; and for the calculation of either the maximum load or the minimum speed at which it is safe to oper-

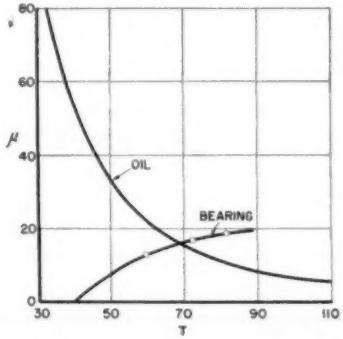

FIG. 22 VISCOSITY-TEMPERATURE CURVE FOR MEDIUM TURBINE OIL USED IN RUN D, SHOWING CALCULATED OPERATING LINE FOR $T_1 =$ 40 C, $p_i = 10$, $P = 10$, $N = 2700$, $D = 8$, $L = 4$, $C = 0.0126$

ate the bearing. For the purposes of these calculations the chart shown in Fig. 23 is useful. This shows both the eccentricity ratio n, and the power loss ratio j, as functions of the Sommerfeld number and the length-diameter ratio of the bearing. These curves are derived from Fig. 7 and Table 1.

The requirement that a bearing have a given temperature rise and outlet-oil temperature fixes the slope of the operating line, Equation [29], and the solution for bearing clearance then simply involves finding a bearing clearance which will give this slope.

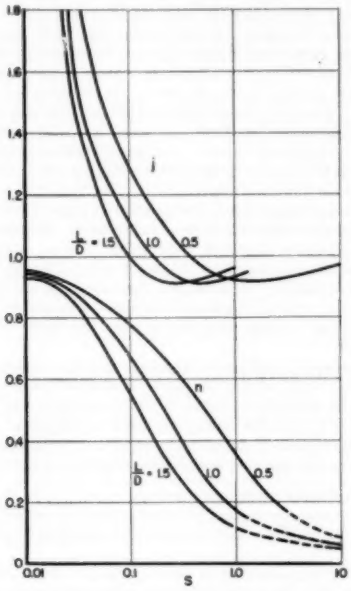

FIG. 23 ECCENTRICITY RATIO n, AND POWER-LOSS RATIO j, AS A FUNCTION OF SOMMERFELD NUMBER AND L/D RATIO, FOR CYLINDRICAL BEARINGS WITH 30-DEG AXIAL OIL GROOVES

It must be borne in mind that both j and q are functions of the Sommerfeld number which is in turn a function of the bearing clearance and outlet-oil viscosity.

A calculation of the maximum load or minimum speed which a bearing will withstand requires that the designer fix a minimum safe film thickness for the bearing. This type of calculation is carried out by first determining the minimum value of S corresponding to the maximum eccentricity ratio to be permitted, using Fig. 23. The values of j and q may then be determined from the charts, Figs. 23 and 7. The oil flow is calculated from Equation [14] as a function of μ_2, and the operating curve (Equation [29]) is then plotted on the viscosity-temperature chart for the oil as before. The value of μ_2 at the intersection of the two curves, together with the Sommerfeld number, determines the value of the maximum load or minimum speed.

Application of Bearing Computation to Design. The application of the operating-line method of computing bearing performance will be illustrated by computing the effects of clearance, bearing length, speed, and load on oil flow, temperature rise, and power consumption. A series of computations for 8-in-diam bearings is summarized in Table 10.

Bearing clearance has relatively little influence on power consumption below the turbulent region, a fact borne out by experiment (13). The computations show the following effect at 2700 rpm:

C	H	μ_2	T_2	Q
0.008	9.0	13.6	73.9	1.85
0.0126	9.6	21.2	61.0	3.11
0.020	9.6	30.6	52.0	5.47

The decreased shear rate in the larger clearance bearings is offset by the increased viscosity due to the larger oil flow.

The effect of bearing length may be examined under constant unit load or under constant total load. At constant unit load of 150 psi and 2700 rpm, the longer bearings run hotter

L/D	T_2	Q	H	H/L (hp/in.)
0.5	61	3.1	9.6	2.4
1.0	66	3.8	14.5	1.8
1.5	72	3.7	17.7	1.5

They take very little additional oil, and operate more efficiently, requiring fewer horsepower per inch. At constant total load of 4800 lb and 2700 rpm, the longer bearing is less efficient.

TABLE 10 CALCULATED PERFORMANCE OF 8-IN-DIAM CYLINDRICAL BEARINGS
(p_1 = 10, T_1 = 40 C, μ = 54 cp at 40 C, a = 0.015, l = 0.263.)

L	C	P	N	ΔQ_s	Q_r	Q_s	Q(GPM)	S	j	T_2(°C)	μ_2(CP)	H
4	0.008	150	2,700	0.07	0.22	1.56	1.85	0.09	0.94	73.9	13.6	9.0
4	0.0126	150	2,700	0.07	0.54	2.50	3.11	0.37	1.01	61.0	21.2	9.6
4	0.020	150	2,700	0.09	1.50	3.88	5.47	0.21	1.11	52.0	30.6	9.6
4	0.0126	150	500	0.04	0.29	0.13	0.76	0.13	1.21	46.5	39.2	0.73
4	0.0126	150	5,000	0.08	0.73	4.53	5.44	0.43	0.90	69.6	15.7	23.7
4	0.0126	150	7,500	0.10	0.91	6.60	7.49	0.61	0.94	76.2	12.6	41.0
8	0.0126	150	2,700	0.08	0.65	3.12	3.85	0.31	0.92	66.1	17.6	14.5
8	0.0126	75	2,700	0.08	0.72	2.23	3.03	0.56	0.91	49.8	16.0	13.0
12	0.0126	150	2,700	0.09	0.79	2.79	3.67	0.26	0.91	72.8	14.5	17.7
12	0.0126	50	2,700	0.10	0.96	1.62	2.68	0.63	0.94	78.8	12.0	15.2
4	0.0126	10	2,700	0.08	0.72	0.79	1.59	4.3	0.94	69.2	15.9	4.7
4	0.0126	50	2,700	0.07	0.56	2.02	2.65	1.1	0.92	67.0	20.5	8.5
4	0.0126	500	2,700	0.07	0.63	2.15	2.86	0.085	1.31	55.3	18.1	10.6
4	0.0126	1,000	2,700	0.09	0.74	1.91	2.74	0.041	1.68	49.8	15.6	11.7

L/D	T_2	Q	H
0.5	61	3.1	9.6
1.0	69	3.0	13.0
1.5	78	2.7	15.2

It runs hotter and has a smaller oil flow.

The effect of speed on the performance of an 8-in. × 4-in. × 0.0126-in. bearing is shown graphically in Fig. 24. Experimental points from run D are shown for comparison. The effect of load on the same bearing is illustrated in Fig. 25. Note that the outlet-oil temperature is a minimum and the oil flow a maximum at a moderate load of 100 to 150 psi.

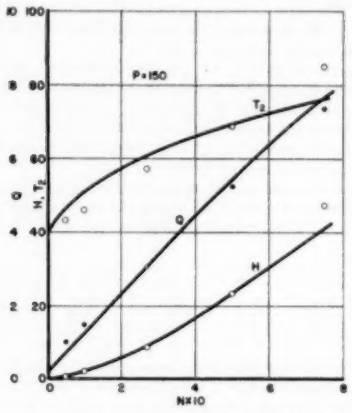

FIG. 24 COMPARISON OF EXPERIMENTAL VALUES WITH CALCULATED CURVES FOR OIL FLOW, POWER LOSS, AND OUTLET-OIL TEMPERATURE OF AN 8-IN. × 4-IN. × 0.0126-IN. BEARING (RUN D), AS A FUNCTION OF SPEED

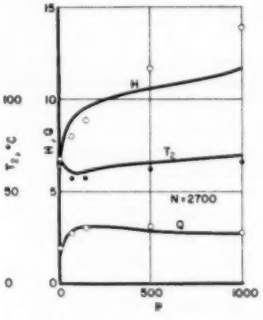

FIG. 25 EFFECT OF BEARING LOAD UPON OIL FLOW, POWER LOSS, AND OUTLET-OIL TEMPERATURE OF AN 8-IN. × 4-IN. × 0.0126-IN. BEARING
(Experimental points from run D for comparison with calculated curves.)

These illustrations of how a number of design factors affect bearing performance serve to demonstrate the utility of the prediction of bearing oil flow and the operating-line method to the designer. It will be apparent to the reader how the influence of other factors such as chamfer size, oil-groove shape, inlet-oil pressure and temperature, and oil-viscosity grade may be computed readily.

DISCUSSION

The ability to compute the quantity of oil flowing through a cylindrical bearing of known dimensions and under known operating conditions has been shown to be a key factor in the prediction of bearing performance. This is particularly true for large bearings where the loss of heat from the bearing by conduction and radiation becomes a small part of the total bearing power consumption so that the major portion of the heat loss from the bearing is by addition of sensible heat to the oil flowing through the bearing. How the knowledge of oil flow may be used in predicting bearing performance has been shown in some detail.

The reader no doubt will have noticed that while the comparison of the experimental data with the dimensionless oil flow (q versus S) curves shows considerable scatter of the experimental points, the general trend predicted by the theory is undoubtedly present. The direct comparison of computed values such as outlet-oil temperature, oil flow, and power loss with experimental values is considerably better; and this illustrates an important point which must be considered in studying the experimental values of the dimensionless variables. The computation of these dimensionless variables involves exact knowledge of many quantities which are difficult to determine precisely. Relatively small errors in bearing clearance, cylindricity, inlet-oil pressure, oil flow, and bearing alignment can cause more or less error in the calculated values. Two of the bearings, D and F, contained many pressure taps for reading oil-film pressures; and some leakage through these connections was never eliminated completely.

The designer's problem is, in general, to seek an optimum bearing design; and, despite the effects of some of the errors mentioned, the methods described in this paper offer him an easy method of solution for bearing-performance problems. The design computation seldom will agree precisely with measured bearing performance for many reasons, among which are the following:

(*a*) Approximations in the theory.

(*b*) Inaccuracies in bearing manufacture due to tolerances on bearing and shaft diameters and out-of-roundness and taper in the bearing.

(*c*) Bearing misalignment upon assembly in the machine.

(*d*) Variation in the viscosity-temperature behavior of the oil actually used from the curve used for computation.

(*e*) Variations of oil feed temperature and pressure.

(*f*) Variations in speed and load from the values assumed.

(*g*) Inability to calculate exactly the heat transfer from the bearing by conduction and radiation.

Thus it is felt that it is unnecessary to strive for great refinement in the design calculations.

On the other hand, the methods outlined in this paper do afford the designer an accurate means of comparing one design with another, of judging the effects of clearance, load, speed, base oil viscosity, inlet temperature and pressure, chamfer dimensions and oil-groove shape upon the bearing performance. Such comparisons may be made accurately without the uncertainties attendant upon the absolute values of the computed results. This method of analysis based upon the complete study of the oil-flow characteristics of a bearing design can be extended to bearings of other types, provided that the same principles are followed, and it is hoped in later papers to show how other bearings of interest to designers of high-speed machinery may be analyzed.

ACKNOWLEDGMENT

The authors wish to acknowledge with gratitude the time and facilities furnished by the General Electric Company for these studies. In particular, they wish to acknowledge their indebted-

ness to Mr. F. J. Maginniss and the Analytical Division for their warm interest and steady support for the theoretical computations. The authors also acknowledge the efforts of Messrs. Paul Lyons, William Rogers, Henry Stone, Frank Crimp, Ralph Ricketson, and Lester Dreyfuss in obtaining experimental data and assisting with their analysis.

BIBLIOGRAPHY

1 "Oil-Flow in Complete Journal Bearings," by D. P. Barnard, 4th, SAE Transactions, vol. 20, part 2, 1925, pp. 66–81; also *Industrial and Engineering Chemistry*, vol. 18, 1926, p. 460.

2 "Analysis and Lubrication of Bearings," by M. C. Shaw and E. F. Macks, McGraw-Hill Book Company, Inc., New York, N. Y., 1949.

3 "Coefficient of Friction, Oil Flow and Heat Balance of a Full Journal Bearing," by P. I. Orloff, *Aeronautial Engineer*, Moscow, USSR 9th year, January, 1935; English Translation in NACA TM 1165, October, 1947.

4 "Oil Flows and Running Temperatures of Lightly Loaded Journal Bearings," by J. Boyd and B. P. Robertson, *Lubrication Engineering*, vol. 4, April, 1948, pp. 58–62.

5 "Oil Holes and Grooves in Plain Journal Bearings," by S. A. McKee and H. S. White, Trans. ASME, vol. 72, 1950, pp. 1025–1034.

6 "Flow of Lubricating Oil From a Big-End Bearing," by J. G. Withers, *Engineering*, vol. 191, March 17, 1950, pp. 291–292.

7 "Power Losses in High-Speed Journal Bearings," by F. C. Linn and D. E. Irons, Trans. ASME, vol. 63, 1941, pp. 617–629.

8 "Effects of Side Leakage in 120-Deg Centrally Supported Journal Bearings," by S. J. Needs, Trans. ASME, vol. 56, 1934, p. 721.

9 "Characteristics of Centrally Supported Journal Bearings," by E. O. Waters, Trans. ASME, vol. 62, 1942, pp. 711–719.

10 "The Full Journal Bearing," by A. Cameron and Mrs. W. L. Wood, Proceedings of The Institution of Mechanical Engineers, vol. 161, 1949, pp. 59–64.

11 "Introduction to the Mechanics of Viscous Flow," by H. F. P. Purday, Dover Publications, New York, N. Y., 1949.

12 "Low Pressure Regions Occurring in the Hydrodynamic Lubricating Films of Journal Bearings," by J. A. Cole, *Scientific Lubrication*, vol. 3, 1951, p. 10.

13 "Turbulence in High-Speed Journal Bearings," by D. F. Wilcock, Trans. ASME, vol. 72, 1950, p. 817.

Discussion

J. A. Cole.[4] In the authors' considerations of the probable oil-flow pattern in the clearance space of a journal bearing, no allowance is made for an effect predicted by Wannier[5] and lately observed in the writer's laboratory in a transparent bearing of very large clearance ratio. The phenomenon referred to is that of reverse flow, in the form of a closed circulation in the maximum film-thickness zone of an eccentrically operating bearing. Such a reverse flow would reduce the effective divergence of the oil film in regions II and III (Figs. 5 and 10 of the paper), and convergence would effectively start well before region IV, so that a complete oil film might well be maintained, since the oil circulating in this dead space would be at a low pressure and, therefore, under no great compulsion to leak out sideways. Admittedly the lubricant sources present in the test bearings described may modify the incidence of this effect, and such a point, as well as other questions raised by the authors' stimulating discussion of bearing flow characteristics, could best be answered by visual examination of the oil film in transparent journal bearings.

The scatter in Figs. 16, 17, and 18 of the paper is rather disappointing, and it would be interesting to see more data on the effect of variation of supply pressure on oil flow than is included here, in order to apply Mr. McKee's more direct method of deducing the load or rotational component of oil flow by extrapolation to zero supply pressure as outlined in his current paper.[6]

Mayo D. Hersey.[7] A symposium on heat conditions in bearings was held at the Annual Meeting of 1941.[8] Although devoted primarily to self-contained bearings without forced lubrication, it was recommended that further research be conducted to bring out the effect of oil flow on temperature rise and load capacity. The present paper may be considered a fulfillment of those hopes.

It is interesting to compare Fig. 12 of the paper with the corresponding values for the uninterrupted sleeve bearing, as given by Equation [18] of an early paper by the writer,[9] from which, in the present notation, j was found inversely proportional to the square root of 1 minus n^2. Fig. 12 gives lower values, for example, 20 per cent less at an eccentricity ratio of 0.60, and 28 per cent less at 0.80.

One of the most useful contributions made in this paper is the concept of the bearing as a "mixer," with the tentative establishment of the outlet oil temperature as an indication of the effective film temperature. This finding is in accord with the assumption underlying the writer's equations for thermal equilibrium of high-speed bearings with controlled rates of oil flow—see Equations [12] and [13] of reference.[10] Applying Petroff's law to the function $F_1(Z)$, Newton's law of cooling to $F_2(T)$ and the equilateral hyperbola to the viscosity-temperature function $F_3(T)$ leads to an approximate solution in the form

$$T = a\left(1 + \frac{b}{a^2}\right)^{1/2} - a \qquad [42]$$

Here T (unlike the authors' notation) denotes the elevation of the film temperature above the ambient or room temperature, while a and b are defined as follows:

$$a = \frac{C_0 T_0 + Qq\,(T_0 - T_1)}{2\,(Qq + C_0)} \qquad [43]$$

$$b = \frac{T_d(QqT_1 + Z_0 B_0 N^2)}{Qq + C_0} \qquad [44]$$

In these two expressions B_0, C_0, N, Q, T_0, and Z_0 have the same meaning as in Chapter V of a book by the writer.[11] Thus, B_0 denotes the quotient of power loss divided by ZN^2 using Petroff's law; C_0 is the over-all constant in Newton's law of cooling; N the speed in revolutions per unit time (not restricted to rpm);

[4] Mechanical Engineering Research Laboratory, Lubrication Division, Thorntonhall, Glasgow, Scotland.

[5] "A Contribution to the Hydrodynamics of Lubrication," by G. H. Wannier, *Quarterly of Applied Mathematics*, vol. 8, 1950, p. 1.

[6] "Oil Flow in Plain Journal Bearings," by S. A. McKee, presented at the Annual Meeting, Atlantic City, N. J., Nov. 25–30, 1951, of The American Society of Mechanical Engineers.

[7] U. S. Naval Engineering Experiment Station, Annapolis, Md. Fellow ASME. Statements herein are personal expressions of the writer, not to be construed as official or reflecting the views of the Navy Department.

[8] "Heat Conditions in Bearings," symposium of papers by M. D. Hersey, J. T. Burwell, Jr., and G. B. Karelitz, including discussion; reprinted from Trans. ASME, vol. 64, 1942, pp. 445–455.

[9] "Laws of Lubrication of Horizontal Journal Bearings," by M. D. Hersey, *Journal of the Washington Academy of Sciences*, vol. 4, 1914, pp. 542–552 (correction required on p. 543, section 2, where "former" and "latter" should be interchanged in referring to practice of General Electric Company).

[10] "Basic Principles of Lubrication," by M. D. Hersey, pp. 19–42 of "Diesel Lubricating Oils and Basic Principles of Lubrication," ASME, 1949 (correction required in first line, p. 42, where 16 should read 8).

[11] "Theory of Lubrication," by M. D. Hersey, John Wiley & Sons, Inc., New York, N. Y., 1936; Spanish translation, containing new references, published by El Ateneo, Buenos Aires, 1947.

Q the rate of oil flow through the bearing in volume units per unit time; T_0 the elevation of the room temperature above t_0, which in turn denotes the "apparent solidifying temperature" of the oil; and Z_0 the viscosity at room temperature. The assumed viscosity relation may be written

$$Z = \frac{\text{const}}{t - t_0} = \frac{T_0 Z_0}{T + T_0} \quad \ldots\ldots\ldots\ldots [45]$$

and can be represented by a curve for Z against t or T, having a vertical asymptote at $t = t_0$ or $T = -T_0$. In addition, T_1 denotes the elevation of the oil inlet temperature above the room temperature, while q is the heat capacity of the oil per unit volume, or product of specific heat by density, expressed in mechanical units. This property is proportional to the authors' C_p and identical with h in Chapter V,[11] previously mentioned.

Since the two-constant hyperbola, Equation [45], is limited to a short temperature range, a three-constant parabola may be preferred; namely

$$Z = Z_1 - c_1(T - T_1) + c_2(T - T_1)^2 \quad \ldots\ldots\ldots [46]$$

Here Z_1 denotes the inlet viscosity, while c_1 and c_2 are empirical constants. The equilibrium temperature rise is still given by Equation [42] herewith, but with new expressions for a and b

$$a = -\frac{C_0 + Qq + (c_1 + 2c_2T_1)B_0N^2}{2c_2B_0N^2} \quad \ldots\ldots\ldots [47]$$

$$b = -\frac{QqT_1 + Z_0B_0N^2}{c_2B_0N^2} \quad \ldots\ldots\ldots\ldots [48]$$

After calculating the equilibrium temperature from Equation [42], the power loss and load capacity may be found by conventional methods. When $Q = 0$, Equations [42], [43], and [44] reduce to the forms previously given for the self-contained bearing—Equations [23], [24], and [25] in the writer's early paper,[9] for example.

The original simultaneous equations may be solved more accurately by the graphical intersection method when F_1, F_3, and F_7 are available in graphical form, as noted in a previous publication.[10] That procedure is similar to the "operating line" method used by the present authors. The limitations of simplified analytical solutions are partly compensated, however, by the qualitative insight they offer, and which can so easily be gained by varying the constants.

It is to be hoped that the methods of investigation described by the authors also can be applied to thrust bearings.

JOHN YOUNG.[12] The authors are to be congratulated for demonstrating an approach to the calculation from first principles of oil flow in a sleeve bearing. Although the difficulty they encountered in obtaining good experimental correlation shows that the problem is not yet completely solved, nevertheless a contribution of value has been made.

In calculations of this type, generally one is required to make certain simplifying assumptions—viscosity and temperature distribution, accurate geometry of the bearing, and so on—which affect the accuracy of the final result. While it is agreed that all factors which might influence the oil flow should be considered, those that affect the flow to an extent less than the percentage error already introduced by the initial assumptions should not require much attention. It is interesting, therefore to notice the importance attached by the authors to the flow in the chamfer, and the writer would like to ask if the authors could give some idea of the size of the chamfers, in the bearings which were tested, and the probable chamfer flow as a percentage of the total flow.

[12] Mechanical Engineer, Engines and Lubrication Section, National Bureau of Standards, Washington, D. C.

AUTHORS' CLOSURE

The authors are indebted to Mr. Cole for reminding the reader of the closed circulation which may occur in the maximum film-thickness zone, as a part of the discussion of oil flow. In initial studies the method of extrapolating oil flow as a function of feed pressure to zero feed pressure was employed, but as understanding increased, the more general method outlined in the paper was preferred because (*a*) it did not require a careful series of runs with no change other than feed pressure, and (*b*) methods of calculating both flow components were desired. Choosing to test bearings as they are normally produced rather than bearings made to extreme precision in the laboratory undoubtedly accounts to some degree for the lamentable scatter in Figs. 16 to 18, but the reader should also remember that several distinct bearings of widely varying clearance are plotted in each case and that the dimensionless flow coefficient q is obtained as the result of a series of calculations.

Mr. Hersey's discussion is appreciated. However, in view of the great simplicity of the graphical operating-line approach to the problem of calculating the outlet oil temperature, the analytical solution employing one of the many viscosity functions was not used. The operating-line method has proved valuable for the insight it provides into the factors affecting bearing performance. Solutions by this method using alignment charts have proved very convenient and it is hoped to publish some of them soon.

In answer to Mr. Young, the calculated chamfer flows are given in column 13, headed $4Q_c$, of Tables 3 to 9. The chamfer flows range from 2 to 75 per cent of the total oil flow, the larger percentages obtaining at low speeds and with the larger chamfers. The nominal chamfer dimension was $a = b = 1/32$ in., but since they were made by hand scraping some were larger. Each chamfer on each test bearing was measured individually, in order to obtain the average coefficients for column 13.

On the Solution of the Reynolds Equation for Slider-Bearing Lubrication—I

By A. CHARNES[1] and E. SAIBEL,[2] PITTSBURGH, PA.

An exact solution is developed for the Reynolds equation in the hydrodynamical theory of slider-bearing lubrication with side leakage for film thickness varying exponentially. This solution is in the form of a rapidly convergent series from which calculations for the pressure distribution, total bearing load, and center of pressure may be made rapidly for all values of the parameter concerned. The results are in close agreement with those which have been obtained for the plane slider bearing by cumbersome methods, and it is proposed not only to use the present solution for the plane case, but also to show the design possibilities for a much wider variety of shapes by using various portions of exponential curves.

Introduction

THE usual method of solving the problem of the slider bearing is to start from the Reynolds (1)[3] equation

$$\frac{\partial}{\partial x}\left(\frac{h^3}{\mu}\frac{\partial p}{\partial x}\right)+\frac{\partial}{\partial y}\left(\frac{h^3}{\mu}\frac{\partial p}{\partial y}\right)=6U\frac{\partial h}{\partial x} \quad \ldots\ldots [1]$$

where

p = pressure
h = thickness of the oil film
μ = coefficient of viscosity
U = velocity of the slider (assumed to be in the x-direction)
x, y = co-ordinates in plane of slider

Assuming μ to be a constant, it has been taken for granted that the simplest solution would be obtained if the thickness of the oil film h is assumed to be linear. In other words, it was thought that results would be most easily obtained if the bearing were supposed to be plane.

Such an assumption leads to the so-called Michell (2) solution which as is well known is extremely difficult to apply to practical problems. In fact, it is so intractable that numerous approximate methods have been devised to obtain numerical results. Most of these are also quite useless for general solutions of any ratio of length to width of slider or for any ratio of entrance to exit clearances, so that the problem has remained up to now in an unsatisfactory form.

It is the object of the present paper to give an exact solution of the Reynolds equation for a particular class of sliders for which the calculations are quite simple in all cases. This solution approximates to a high degree of accuracy that of Michell for the plane flat slider and may be used as an approximation to that case.

Theory

As in Michell's case, it will be assumed that μ is constant. Reynolds equation may be written in the form

$$h^3\left(\frac{\partial^2 p}{\partial x^2}+\frac{\partial^2 p}{\partial y^2}\right)+3h^2\left(\frac{\partial p}{\partial x}\frac{\partial h}{\partial x}+\frac{\partial p}{\partial y}\frac{\partial h}{\partial y}\right)=6\mu U\frac{\partial h}{\partial x} \quad [2]$$

Assuming

$$h=ae^{bx} \quad \ldots\ldots [3]$$

where a and b are known constants determined from the shape of the slider, the equation becomes

$$\frac{\partial^2 p}{\partial x^2}+\frac{\partial^2 p}{\partial y^2}+3b\frac{\partial p}{\partial x}=6\mu U\frac{b}{a^3}e^{-2bx} \quad \ldots\ldots [4]$$

and the customary boundary conditions are $p=0$ on the edges of the slider. The solution of Equation [4] may be obtained readily by assuming that

$$p(x,y)=P(x,y)+f(x) \quad \ldots\ldots [5]$$

where $f(x)$ is the particular integral and $P(x, y)$ is the complementary function. Substituting Equation [5] into Equation [4] leads to

$$\frac{\partial^2 P}{\partial x^2}+\frac{\partial^2 P}{\partial y^2}+3b\frac{\partial P}{\partial x}+\frac{d^2 f}{dx^2}+3b\frac{df}{dx}=6\mu U\frac{b}{a^3}e^{-2bx} \quad \ldots\ldots [6]$$

and if $f(x)$ is chosen so as to satisfy the equation

$$\frac{d^2 f}{dx^2}+3b\frac{df}{dx}=6\mu U\frac{b}{a^3}e^{-2bx} \quad \ldots\ldots [7]$$

then

$$\frac{\partial^2 P}{\partial x^2}+\frac{\partial^2 P}{\partial y^2}+3b\frac{\partial P}{\partial x}=0 \quad \ldots\ldots [8]$$

The boundary conditions $p=0$ on the edges of the slider become $P+f=0$ on the edges of the slider. We shall obtain two constants on solving Equation [7] which we shall choose so that P is as simple as possible on the slider edges. The best we can do is to make $f(x)=0$ at $x=0$ and $x=B$. Then $0=p=P+f=P$, at $x=0$ and $x=B$. On $y=\pm L/2$, $0=p=P+f$ means $P=-f$ there.

Solution of Equations

The solution of Equation [7] is obtained as follows:
Multiply Equation [7] through by e^{2bx} and there results

$$e^{2bx}f''(x)+3be^{2bx}f'(x)=6\mu U\frac{b}{a^3}e^{bx} \quad \ldots\ldots [9]$$

[1] Associate Professor, Department of Mathematics, Carnegie Institute of Technology.
[2] Professor of Mechanics, Department of Mathematics, Carnegie Institute of Technology. Mem. ASME.
[3] Numbers in parentheses refer to the Bibliography at the end of the paper.
Contributed by the Lubrication Research Committee and presented at the Annual Meeting, Atlantic Cty, N. J., November 25–30, 1951, of The American Society of Mechanical Engineers.
Note: Statements and opinions advanced in papers are to be understood as individual expressions of their authors and not those of the Society. Manuscript received at ASME Headquarters, July 19, 1951. Paper No. 51—A-43.

or

$$\frac{d}{dx}\left[e^{3bx}f'(x)\right] = 6\mu U\frac{b}{a^2}e^{bx} \quad [10]$$

This leads to

$$e^{3bx}f'(x) = \frac{6\mu U}{a^2}e^{bx} + k_1 \quad [11]$$

Thus

$$f(x) = -\frac{3\mu U}{a^2b}e^{-2bx} + k_1e^{-3bx} + k_2 \quad [12]$$

Using the boundary conditions $f(x) = 0$ at $x = 0$ and $x = B$ we find

$$\left.\begin{aligned} k_1 &= \frac{3\mu U}{a^2b}\frac{1-e^{-2bB}}{1-e^{-3bB}} \\ \text{and} \\ k_2 &= \frac{3\mu U}{a^2b} - k_1 = \frac{3\mu U}{a^2b}\frac{e^{-2bB}-e^{-3bB}}{1-e^{-3bB}} \end{aligned}\right\} \quad [13]$$

The problem is thus reduced to finding the solution of

$$\frac{\partial^2 P}{\partial x^2} + \frac{\partial^2 P}{\partial y^2} + 3b\frac{\partial P}{\partial x} = 0 \quad [14]$$

under the boundary conditions

$$P = 0 \text{ at } x = 0 \text{ and } x = B$$

and $P + f(x) = 0$ along $y = \pm L/2$ where $f(x)$ is given by Equation [12]. A solution by separation of variables is obtained in the customary manner by assuming

$$P = X(x)Y(y) \quad [15]$$

This leads to

$$Y'' - k^2Y = 0 \quad [16]$$

and

$$X'' + 3bX' + k^2X = 0 \quad [17]$$

where k is a constant to be determined. The solutions of these equations are respectively

$$Y = E\cosh ky + F\sinh ky \quad [18]$$

and

$$X = e^{-\frac{3bx}{2}}(C\cos mx + D\sin mx) \quad [19]$$

where

$$m = \sqrt{k^2 - \frac{9b^2}{4}}$$

Therefore the solution consists of terms of the type

$$P = e^{-\frac{3bx}{2}}(C\cos mx + D\sin mx)(E\cosh ky + F\sinh ky)$$

Setting $P = 0$ for $x = 0$ yields $C = 0$, and, because of symmetry in y, $F = 0$. Thus

$$P = Ge^{-\frac{3bx}{2}}\sin mx\cosh ky \quad [20]$$

where G is a constant.

However, $P = 0$ when $x = B$, or

$$0 = Ge^{-\frac{3b}{2}B}\sin mB\cosh ky \quad [21]$$

This is possible for a nontrivial solution where

$$mB = n\pi,\ n = 1, 2, \ldots$$

Thus

$$k = \left(\frac{n^2\pi^2}{B^2} + \frac{9b^2}{4}\right)^{1/2}$$

n being an integer. The general solution takes the form

$$P(x, y) = \sum_{n=1}^{\infty} G_n e^{-\frac{3bx}{2}}\sin\frac{n\pi}{B}x\cosh\left(\frac{n^2\pi^2}{B^2} + \frac{9b^2}{4}\right)^{1/2}y \quad [22]$$

The G will now be determined from the boundary condition $P = -f(x)$ along $y = \pm L/2$. Thus

$$\frac{3\mu U}{a^2b}e^{-2bx} - k_1e^{-3bx} - k_2 = e^{-\frac{3bx}{2}}\sum_{n=1}^{\infty} G_n\sin\frac{n\pi x}{B}\cosh\left(\frac{n^2\pi^2}{B^2} + \frac{9b^2}{4}\right)^{1/2}\frac{L}{2}$$

or

$$\frac{3\mu U}{a^2b}e^{-\frac{bx}{2}} - k_1e^{-\frac{3bx}{2}} - k_2e^{\frac{3bx}{2}} = \sum_{m=1}^{\infty} G_m\sin\frac{m\pi x}{B}\cosh\left(\frac{m^2\pi^2}{B^2} + \frac{9b^2}{4}\right)^{1/2}\frac{L}{2} \quad [23]$$

Multiplying each side of Equation [23] by $\sin(n\pi x)/B$ and integrating from $x = 0$ to $x = B$ eliminates all of the G_m except G_n and enables us to solve for G_n

$$\int_0^B\left[\frac{3\mu U}{a^2b}e^{-\frac{bx}{2}} - k_1e^{-\frac{3bx}{2}} - k_2e^{\frac{3bx}{2}}\right]\sin\left(\frac{n\pi x}{B}\right)dx = \sum_{m=1}^{\infty} G_m\cosh\left(\frac{m^2\pi^2}{B^2} + \frac{9b^2}{4}\right)^{1/2}\frac{L}{2}\int_0^B \sin\left(\frac{m\pi x}{B}\right)\sin\left(\frac{n\pi x}{B}\right)dx = G_n\cosh\left(\frac{n^2\pi^2}{B^2} + \frac{9b^2}{4}\right)^{1/2}\frac{L}{2}\frac{B}{2}$$

since the integral of these sines is 0 if $m \neq n$ and is $B/2$ if $m = n$. The result is

$$G_n = \frac{2}{B\cosh\left(\frac{n^2\pi^2}{B^2} + \frac{9b^2}{4}\right)^{1/2}\frac{L}{2}}\left\{\frac{3\mu U}{a^2b}\frac{\left(-\frac{n\pi}{B}\right)}{\left(\frac{b^2}{4} + \frac{n^2\pi^2}{B^2}\right)}\left[(-1)^ne^{-\frac{b}{2}B} - 1\right] + \frac{k_1\frac{n\pi}{B}}{\frac{9b^2}{4} + \frac{n^2\pi^2}{B^2}}\left[(-1)^ne^{-\frac{3bB}{2}} - 1\right] + \frac{k_2\frac{n\pi}{B}}{\frac{9b^2}{4} + \frac{n^2\pi^2}{B^2}}\left[(-1)^ne^{\frac{3b}{2}B} - 1\right]\right\} \quad [24]$$

The final solution is

$$p = \sum_{n=1}^{\infty} G_n e^{-\frac{3bx}{2}} \sin \frac{n\pi x}{B} \cosh \left(\frac{9b^2}{4} + \frac{n^2\pi^2}{B^2} \right)^{1/2} y + f(x) \quad [25]$$

where G_n is given by Equation [24] and $f(x)$ is given by Equations [12] and [13].

Performance Characteristics

It is now of interest to calculate the performance characteristics of the slider bearing. The characteristics treated in the present paper are the total load, center of pressure, the coefficient of friction, and the oil flow.

Total Load. The total load on the slider W is found from a straightforward calculation as follows:

Making the customary assumption, namely, that the slope of the slider is small and that consequently the vertical component of the pressure against the slider is equal to the pressure itself, we have

$$W = \int_{y=-L/2}^{L/2} \int_{x=0}^{B} p \, dx \, dy \quad [26]$$

where p is given by Equation [25]. The result is

$$W = \sum_{n=1}^{\infty} G_n \frac{\frac{2n\pi}{B}}{\left(\frac{n^2\pi^2}{B^2} + \frac{9b^2}{4} \right)^{1/2}} \sinh \left\{ \sqrt{\frac{n^2\pi^2}{B^2} + \frac{9b^2}{4}} \frac{L}{2} \right\} \left[1 - (-1)^n e^{-\frac{3bB}{2}} \right] + \left[\frac{3\mu U}{2a^2b^2} (e^{-3bB} - 1) - \frac{k_1}{3b} (e^{-3bB} - 1) + k_2 B \right] L \quad [27]$$

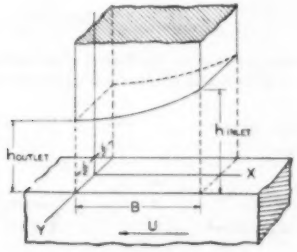

Fig. 1

Calculations

As an example of the use of the method and as a check on the accuracy of the approximation to the plane slider, we shall calculate the pressure at the center of a square slider having a ratio of film thickness at entrance to exit of 2, that is, $h_1/h_0 = 2$, see Fig. 1. Then from $h = h_0 e^{bx}$, we have

$$Bb = \log_e 2 = 0.693 \quad [40]$$

Thus

$$k_1 = 3.71 \frac{\mu UB}{h_0^2}$$

and

$$k_2 = 0.619 \frac{\mu U}{h_0^2} \quad [41]$$

For convenience we introduce the following notation

$$\left.\begin{aligned} r_n &= \frac{3\mu U}{a^2b} \frac{\frac{n\pi}{B}}{\left(\frac{b^2}{4} + \frac{n^2\pi^2}{B^2} \right)} \left[1 - (-1)^n e^{-\frac{bB}{2}} \right] \\ s_n &= \frac{k_1 \frac{n\pi}{B}}{\frac{9b^2}{4} + \frac{n^2\pi^2}{B^2}} \left[(-1) e^{-\frac{3bB}{2}} - 1 \right] \\ t_n &= \frac{k_2 \frac{n\pi}{B}}{\frac{9b^2}{4} + \frac{n^2\pi^2}{B^2}} \left[(-1)^n e^{\frac{3b}{2} B} - 1 \right] \end{aligned}\right\} \quad [42]$$

Setting $x = B/2$ and $y = 0$, we see that only the odd terms $n = 1, 3, 5$, and so forth, enter. Furthermore, it is evident that the series in Equation [25] converges very rapidly and that two terms are sufficient to yield three-figure accuracy.

We find

$$f\left(\frac{B}{2}\right) = -0.233$$

and

$$r_1 = 2.325; \quad r_3 = 0.784$$
$$S_1 = -1.441; \quad S_3 = -0.530$$
$$t_1 = -0.680; \quad t_3 = -0.25$$

all the above to be multiplied by $(\mu UB)/(h_0^2)$. Also for $n = 1$

$$\cosh \sqrt{\frac{\pi^2}{B^2} + \frac{9b^2}{4}} \frac{L}{2} = 2.70$$

and for $n = 3$, it is equal to 72.0. From these values we obtain

$$p = 0.0236 \frac{6\mu UB}{h_0^2} \quad [43]$$

This may be compared with Michell's value of $0.02218\ (6\mu UB)/(h_0^2)$, or with that found by Christopherson (4), using relaxation methods, $0.02217\ (6\mu UB)/(h_0^2)$, a difference of about 7 per cent.

Applying Equation [27] to the preceding case, we obtain

$$W = 0.0113 \frac{6\mu UB^2}{h_0^2}$$

as compared with

$$W = 0.01153 \frac{6\mu UB^2}{h_0^2} \text{ (Christopherson)}$$

and

$$W = 0.01149 \frac{6\mu UB^2}{h_0^2} \text{ (Michell)}$$

the difference being of the order of 2 per cent.

Center of Pressure

As in the calculation for the total load, it is assumed that the slope of the slider is everywhere small and that, consequently, the force acting on each element may be considered vertical.

Calling the co-ordinates of the center of pressure $(\bar{x}, 0)$, we have

$$\bar{x} = \frac{\int_0^B \int_{-L/2}^{L/2} xp\,dx\,dy}{W} \quad \ldots\ldots\ldots\ldots [28]$$

where W is the total load as calculated by Equation [27].

Using the expression for p as given by Equation [25] we find, for a typical term of the first part, namely

$$G_n e^{-\frac{3bx}{2}} \sin\frac{n\pi x}{B} \cosh\sqrt{\frac{n^2\pi^2}{B^2}+\frac{9b^2}{4}}\,y,$$

$$\int\int xp dA = \left\{\frac{2G_n}{\sqrt{\frac{n^2\pi^2}{B^2}+\frac{9b^2}{4}}} \sinh\sqrt{\frac{n^2\pi^2}{B^2}+\frac{9b^2}{4}}\,\frac{L}{2}\right\}$$

$$\left\{-\frac{(-1)^n n\pi e^{-\frac{3b}{2}B}}{\frac{9b^2}{4}+\frac{n^2\pi^2}{B^2}} - \frac{3b\frac{n\pi}{B}}{\left(\frac{9b^2}{4}+\frac{n^2\pi^2}{B^2}\right)^2}\left[(-1)^n e^{-\frac{3b}{2}B}-1\right]\right\}$$

$\ldots\ldots\ldots\ldots [29]$

This we shall designate by C_n.

The second part due to $f(x)$ in Equation [25] yields

$$\int\int xp\,dA = L\left\{\frac{3\mu U}{4a^2b^2}\left[e^{-3bB}(2bB+1)-1\right]\right.$$

$$\left. -\frac{k_1}{9b^2}\left[e^{-3bB}(3bB+1)-1\right]+\frac{k_1B^2}{2}\right\} \quad \ldots\ldots [30]$$

and this will be designated by D. Thus

$$\bar{x} = \frac{\sum_{n=1}^{\infty} C_n + D}{W} \quad \ldots\ldots\ldots\ldots [31]$$

Coefficient of Friction

The coefficient of friction, $f = F/W$ where F is the total friction force on the slider and W is the total normal force, is easily calculated. Since we have obtained W previously, see Equation [27], the calculation for F will be sufficient. This is given by

$$F = \int_0^B \int_{-L/2}^{L/2} s_x\,dx\,dy \ldots\ldots\ldots\ldots [32]$$

where

$$s_x = -\frac{\mu U}{h} - \frac{h}{2}\frac{\partial p}{\partial x} \ldots\ldots\ldots\ldots [33]$$

s_x being the shearing stress component in the x-direction.

Substituting Equation [33] into Equation [32] and using Equation [25], the integration is easily effected, the result being

$$F = \frac{4\mu UL}{ab}(e^{-bB}-1) - \frac{3ak_1L}{4}(e^{-2bB}-1)$$

$$+a\sum_{n=1}^{\infty}\frac{G_n\left(\frac{n\pi b}{B}\right)}{\left(\frac{n^2\pi^2}{B^2}+\frac{9b^2}{4}\right)^{3/2}}\left[e^{-\frac{bB}{2}}(-1)^n-1\right]\sinh\frac{L}{2}\sqrt{\frac{n^2\pi^2}{B^2}+\frac{9b^2}{4}} \quad \ldots\ldots [34]$$

The value of k_1 is given as before in Equation [13].

In the case of the infinite slider (no side leakage), this reduces to

$$F = \frac{4\mu UL}{ab}(e^{-bB}-1) - \frac{3ak_1L}{4}(e^{-2bB}-1) \ldots\ldots [35]$$

Oil Flow

In this final section, in order to complete the calculations needed for design, we compute the flow into the bearing Q and the side leakage Q_y. Finally the flow out of the bearing along the outlet edge may be found from $Q_x = Q - Q_y$.

Again the usefulness of the method developed is apparent since all of the foregoing are readily obtained and appear as rapidly convergent expressions which may easily be used for practical calculations.

It is known (7) that

$$Q = \int_{-L/2}^{L/2}\left(\frac{-h^3}{12\mu}\frac{\partial p}{\partial x}+\frac{Uh}{2}\right)_{x=B} dy \ldots\ldots [36]$$

Since

$$p = P(x, y) + f(x)$$

then

$$\left.\frac{\partial p}{\partial x}\right|_{x=B} = \left.\frac{\partial P}{\partial x}\right|_{x=B} + \left.\frac{df}{dx}\right|_{x=B}$$

From Equation [22]

$$\left.\frac{\partial P}{\partial x}\right|_{x=B} = \sum_{n=1}^{\infty} e^{-\frac{3bB}{2}} G_n \frac{n\pi}{B}(-1)^n \cosh y\sqrt{\frac{n^2\pi^2}{B^2}+\frac{9b^2}{4}}$$

and from Equation [12]

$$\left.\frac{df}{dx}\right|_{x=B} = \frac{6\mu U}{a^2}e^{-2bB} - 3bk_1e^{-2bB}$$

substituting these expressions into Equation [36] and integrating with respect to y we obtain for the total lubricant inflow at the leading edge

$$Q = \frac{1-e^{-2bB}}{1-e^{-3bB}}\cdot\frac{3LaU}{4}$$

$$-\frac{a^2e^{\frac{3bB}{2}}}{6\mu}\sum_{n=1}^{\infty}\frac{G_n(-1)^n\frac{n\pi}{B}}{\left(\frac{n^2\pi^2}{B^2}+\frac{9b^2}{4}\right)^{1/2}}\sinh\frac{L}{2}\sqrt{\frac{n^2\pi^2}{B^2}+\frac{9b^2}{4}} \quad \ldots [37]$$

To compute the side leakage Q_y it is known that (7)

$$Q_y = -2\int_0^B\left(\frac{h^3}{12\mu}\frac{\partial p}{\partial y}\right)_{y=L/2} dx \ldots\ldots [38]$$

Since $\partial p/\partial y = \partial P/\partial y$ only one term enters into the calculation. From Equation [22]

$$\left.\frac{\partial P}{\partial y}\right|_{y=L/2} = \sum_{n=1}^{\infty} e^{-\frac{3bx}{2}} G_n\sqrt{\frac{n^2\pi^2}{B^2}+\frac{9b^2}{4}}$$

$$\sin\left(\frac{n\pi x}{B}\right)\sinh\frac{L}{2}\sqrt{\frac{n^2\pi^2}{B^2}+\frac{9b^2}{4}}$$

Substituting this in Equation [38] and integrating with respect to x, we obtain for Q_y

$$Q_y = \frac{a^3}{6\mu} \sum_{n=1}^{\infty} G_n \frac{n\pi}{B} e^{\frac{3bB}{2}} \frac{(-1)^n - 1}{\sqrt{\frac{n^2\pi^2}{B^2} + \frac{9b^2}{4}}} \cdot \sinh \frac{L}{2} \sqrt{\frac{n^2\pi^2}{B^2} + \frac{9b^2}{4}} \quad \ldots\ldots [39]$$

The outflow at the trailing edge of the bearing is simply $Q - Q_y$.

Total Load for Infinitely Wide Slider

The quantity W_∞, the total load for the infinitely wide slider, has been calculated in the literature and is widely used both as an approximation for the slider of finite width and for comparison with the known solutions of finite-width sliders.

All quantities being independent of y, the basic differential Equation [1] now reduces to

$$\frac{d}{dx}\left(h^3 \frac{dp}{dx}\right) = 6\mu U \frac{dh}{dx} \quad \ldots\ldots [44]$$

This may easily be solved for the plane slider where $h = c + dx$, c and d being constants (5). However, we shall continue to assume that h varies as before, namely

$$h = ae^{bx} \quad \ldots\ldots [45]$$

The first integral of Equation [44] leads to

$$h^3 \frac{dp}{dx} = 6\mu U h + k_1' \quad \ldots\ldots [46]$$

and using Equation [45], this becomes

$$\frac{dp}{dx} = \frac{6\mu U}{a^2} e^{-2bx} + \frac{k_1'}{a^3} e^{-3bx} \quad \ldots\ldots [47]$$

Integrating again, we obtain

$$p = -\frac{3\mu U}{a^2 b} e^{-2bx} + k_1 e^{-3bx} + k_2 \quad \ldots\ldots [48]$$

where no essential generality is lost by renaming the group of constants involving k, by the single letter k_1. Since $p = 0$ when $x = 0$; and $p = 0$ when $x = B$

$$\left.\begin{aligned} 0 &= -\frac{3\mu U}{a^2 b} + k_1 + k_2 \\ 0 &= -\frac{3\mu U}{a^2 b} e^{-2bB} + k_1 e^{-3bB} + k \end{aligned}\right\} \quad \ldots\ldots [49]$$

Solving, we find, as in Equations [13]

$$\left.\begin{aligned} k_1 &= \frac{3\mu U}{a^2 b} \frac{1 - e^{-2bB}}{1 - e^{-3bB}} \\ k_2 &= \frac{3\mu U}{a^2 b} \frac{e^{-2bB} - e^{-3bB}}{1 - e^{-3bB}} \end{aligned}\right\} \quad \ldots\ldots [50]$$

Note that this pressure, as given by Equation [48], is precisely the $f(x)$ part of the pressure in the general case of the finite slider, Equation [25]. In fact, the result could have been obtained from Equation [25] by stating that p was to be independent of y.

It is interesting to compare some results using the exact solution for the flat slider of infinite width with that of the exponential slider also of infinite width:

If

$$\frac{h_{entrance}}{h_{exit}} = 2, \; W_\infty = 0.01333 \frac{6\mu UB^2}{h_0^2}$$

for the exponential slider, and

$$W_\infty = 0.0132 \frac{6\mu UB^2}{h_0^2}$$

for the flat slider. Similarly, for

$$\frac{h_{entrance}}{h_{exit}} = 3$$

Exponential slider, $W_\infty = 0.01266 \dfrac{6\mu UB^2}{h_0^2}$

Flat slider, $W_\infty = 0.0123 \dfrac{6\mu UB^2}{h_0^2}$

Comparison of Results Previously Obtained by Other Authors With Those of Present Paper

In a recent paper Boegli (6) developed an approximate method for solving the finite slider. Essentially his method is to make a one-dimensional problem out of the original one by solving along the line for which the pressure is maximum in the case of the infinite slider. He applies this approximation to both flat sliders and sliders of the type $h = h_0 a^x$, the latter being equivalent to an exponential slider discussed in the foregoing, and for which we have given the exact solution. Table 1 shows a comparison of the results of the exact solution of Michell, Boegli's approximation, and the results of the authors' analysis. Note that as the slider approaches a long narrow one in the direction of motion, Boegli's results get worse. Results obtained here maintain a small error.

TABLE 1 COMPARISON OF MICHELL'S, BOEGLI'S, AND AUTHORS' TEST RESULTS

Case	$\frac{h_{entrance}}{h_{exit}}$	$\frac{B}{L}$	W_∞*	W from Equation [27]	Boegli	W/W_∞ Calculated	Michell exact
1	2	1	0.0267	0.01130	0.421	0.423	0.434
2	3	1	0.0253	0.01209	0.493	0.477	0.460
3	2	2	0.01333	0.00246	0.168	0.1845	0.185
4	3	2	0.01266	0.00270	0.219	0.213	0.208

* Obtained from the integration of Equation [45].

It is also of interest to compare the calculations for the center of pressure. For a square slider with

$$\frac{h_{entrance}}{h_{exit}} = 3$$

namely, case 2 of Table 1, Boegli finds $\bar{x} = 0.392B$ as against $\bar{x} = 0.374B$ calculated by Michell from the exact solution for the flat slider. Using the authors' Equation [34], there results $\bar{x} = 0.385B$.

In an earlier paper Muskat, Morgan, and Meres (7) calculated several basic quantities from the exact equation for a finite flat slider by a method somewhat different from that used by Michell. We proceed now to check some of those calculations against our exact solution for the exponential slider in order to show that the results are in good agreement. Consequently it is possible through the use of the formulas derived in the paper to obtain very good approximations to the basic quantities for any ratio of width to length of slider as well as any ratio of h_{exit} to $h_{entrance}$.

TABLE 2 COMPARISON OF MUSKAT, MORGAN, AND MERES' RESULTS WITH THOSE OF THE AUTHORS

$\frac{L}{B}$	$\frac{h_0}{mB}$	S/m^2 present work	S/m^2 Muskat, et al.
∞	0.5	1.65	1.75
∞	1.0	6.25	6.0
∞	1.4	13.3	13.0
∞	2.4	49.7	48
1	0.5	3.45	3.5
1	1.0	14.75	15
1	1.4	30.5	33
1/2	0.5	7.71	8
1/2	1.0	33.9	35
1/2	1.4	71.5	73

TABLE 3 COMPARISON OF MUSKAT, MORGAN, AND MERES RESULTS WITH THOSE OF THE AUTHORS

$\frac{L}{B}$	S/m^2	f/m present work	f/m Muskat, et al.
∞	1.65	2.45	2.50
∞	6.25	5.00	5.00
∞	13.3	7.80	7.50
∞	49.7	19.9	18.0
1	3.45	4.70	5.00
1	14.75	11.1	11.0
1	30.5	17.45	17.0
1/2	7.71	9.85	9.0
1/2	33.9	24.7	24.5
1/2	71.5	37.2	39.0

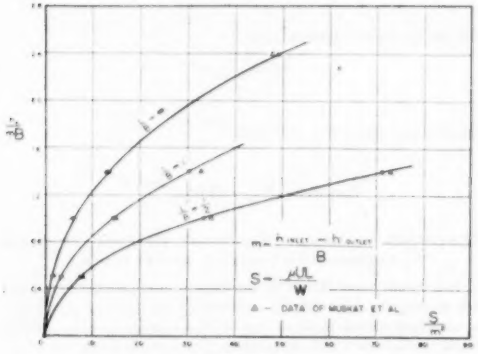

FIG. 2

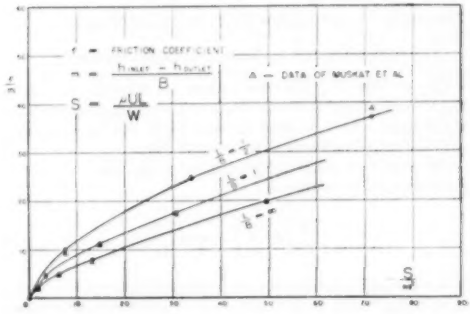

FIG. 3

We check first their (h_0/mB) versus (S/m^2) curve, where m is the slope of the flat slider, the film thickness being given by $h = mx$; also $S = \mu UL/W$ in the notation of this paper. These results are given in Table 2 and shown graphically in Fig. 2.

As a final check, consider the f/m versus S/m^2 curve, where f is the coefficient of friction, the other symbols having the significance pointed out before. The results are shown in Table 3 and are plotted in Fig. 3.

CONCLUSION

It may now readily be seen that the Reynolds equation may be solved easily for both finite and infinite sliders, that is, with and without side leakage, for a slider of exponential shape. Furthermore, all the quantities usually desired such as total load, center of pressure, coefficient of friction, oil flow, and so forth, may be found. The proposed solution is exact for the exponential slider and may be used with a high degree of accuracy of approximation for the flat slider.

Furthermore, because of the ranges in shapes possible by the use of different portions of exponential curves, the design possibilities of various modifications in slider shapes may be calculated readily from the foregoing solution.

ACKNOWLEDGMENT

The authors wish to express their thanks to Mr. Sui-Chun Ying and Mr. A. Raimondi for their assistance in the calculations and for their help in the preparation of the paper.

BIBLIOGRAPHY

1 "On the Theory of Lubrication," by O. Reynolds, Philosophical Transactions of the Royal Society of London, part 1, vol. 177, 1886, pp. 157–234.

2 "The Lubrication of Plane Surfaces," by A. G. M. Michell, *Zeitschrift für Mathematik und Physik*, vol. 52, 1905, pp. 123–137.

3 Ibid., p. 131.

4 "A New Mathematical Method for the Solution of Film Lubrication Problems," by D. G. Christopherson, Proceedings of The Institution of Mechanical Engineers, London, Eng., vol. 146, 1942, p. 126.

5 "Lubrication," by A. E. Norton, McGraw-Hill Book Company, Inc., New York, N. Y., 1942, p. 73.

6 "Hydrodynamic Lubrication of Finite Slider," by C. P. Boegli, *Journal of Applied Physics*, vol. 18, 1947, pp. 482–488.

7 "Studies in Lubrication, VII," by M. Muskat, F. Morgan, and M. W. Meres, *Journal of Applied Physics*, vol. 11, 1940, pp. 208–219

Discussion

H. J. HENRY.[4] Unfortunately, the mathematician only too often ignores the applicability of his solution to a practical problem by the average designer. His solution may be too involved and difficult for the designer. The Michell solution of the Reynolds equation in the hydrodynamical theory of slider-bearing lubrication is an example.

Obviously the authors' solution is exact only for the exponential slider, but by using their solution, performance characteristics of the slider bearing are in surprisingly close agreement with the exact solution for other shapes, particularly the flat slider. The simplification will make their method useful to the designer.

The authors' comment on the use of this solution to a class of slider bearings in which the velocity is not constant but a function of x would be greatly appreciated.

AUTHORS' CLOSURE

The authors wish to thank Dr. Henry for his interesting comments. In particular, the question he brings up regarding the solution for nonconstant velocity of the slider is one which needs careful attention.

If the velocity varies with the time, extra terms appear in the continuity equation and in the Navier-Stokes equations. If the density is assumed constant, the extra term drops out of the

[4] Director of Engineering, Chicago Pneumatic Tool Company, Franklin, Pa. Mem. ASME.

former. In the latter equations the additional terms may be important or may not be depending on the relative magnitudes of the terms involved. If both types of terms can be neglected, that is, density changes are unimportant and acceleration terms are small, we arrive again at the Reynolds equation, Equation [1] in the paper, with U a function of time. In this case the usual method of separation of variables is applicable.

If the extra terms cannot be dropped the solution must be handled differently. It is the intention of the authors to examine the latter case in the near future.

Effect of Variations in Viscosity of Lubricants Upon Timken OK and Psi Values

By I. S. KOLARIK,[1] C. A. ZEILER,[1] AND E. M. KIPP,[1] NEW KENSINGTON, PA.

The Timken lubricant tester is often used in the laboratory in establishing Timken OK loads and psi values at OK loads for lubricants of the extreme-pressure type, particularly for those used as gear lubricants. The present investigation was conducted to determine the magnitude of hydrodynamic-lubrication effects associated with viscosity in determining OK loads. The effect of rubbing speeds was also studied.

THE Timken bearing lubricant tester is one of many laboratory devices employed for the evaluation of lubricants and bearing materials. In this country the Timken machine is often used in establishing Timken OK loads and the psi values at the OK loads for lubricants of the extreme-pressure type, particularly those intended for application as gear lubricants. The Timken OK load is the maximum load which can be applied without inducing failure of the lubricant. The psi value at the OK load (the load in pounds divided by the failed area in square inches) reflects the wear occurring at this load. In this connection, Timken OK and psi values are often quoted for a wide variety of lubricants without reference to variations in the viscosities of such lubricants, the magnitude of the OK and psi values supposedly indicating the EP properties of the lubricant.

When evaluating lubricants of the extreme-pressure type, it is necessary to consider the manner in which viscosity may affect the extent of metal-to-metal contact. For this reason it is important to know whether operation of the Timken machine is affected by the hydrodynamic effects of viscosity. The rate of relative motion of the test bearing surfaces also would be involved in any effects of viscosity.

It would be misleading to compare the effectiveness of an extreme-pressure agent when added to an oil of high viscosity with that of another extreme-pressure agent when added to an oil of considerably lower viscosity if, as seems likely, the viscosity variable may affect or dominate the role played by the extreme-pressure agent. This situation has been clearly recognized in discussions by H. Blok and S. A. McKee.[2]

The only conditions under which the hydrodynamic effects associated with viscosity are neutralized in the apparatus under discussion are those when one rubbing surface removes the oil to the same extent that the other rubbing surface supplies the oil. Such a condition would be present, for example, when two identical cylinders were revolving in the same direction (both rotating clockwise, or counterclockwise) at equal revolutions per minute. Attempts to produce experimental test conditions of this type have been made only relatively recently.[3,4]

For the foregoing reasons, a preliminary investigation was made in these laboratories with the objective of determining the magnitude of hydrodynamic lubrication effects associated with viscosity in the determination of Timken OK loads. This investigation was carried out with a series of mineral oils of widely different viscosities, and containing no added oiliness, extreme pressure, or other compounds of a polar or chemically active nature. The effect of rubbing speeds was also investigated.

As will be noted, it was found that the Timken machine is sensitive in substantial degree to variations in viscosity. By suitable manipulation of the rubbing speeds and of the viscosity values of the oils under test, OK-load values, representing the full range (0 to 100 lb), of the machine were obtained.

Experimental Work

Apparatus. The Timken machine consists essentially of a means for rotating a hardened steel ring against a hardened and ground steel test block under various conditions of pressure and rubbing speed. The test block is mounted rigidly on a loading-lever arrangement with the flat side of the block perpendicular to the vertical diameter of the ring. The load lever is pivoted on a knife-edge mounted on a lower friction lever. The latter is in turn mounted on a knife-edge and provided with a stop at the unloaded end. Both levers are provided with weight hangers for application of loads. The oil is applied to the test pieces, collected, and recycled through the oil reservoir.

Test Oils. The 17 straight mineral oils employed are described by the data presented in Table 1 and represent a range in viscosity of from 59.6 SSU/100 F to a viscosity of 17,500 SSU/100 F.

TABLE 1 PHYSICAL PROPERTIES OF OILS EMPLOYED IN DETERMINATION OF TIMKEN DATA

Oil no.	Viscosity SSU/100 F	Viscosity SSU/210 F	V.I.	Specific gravity 60°/60° F	Refractive index n_D^{20}
1	59.6	34.3	43	0.8894	1.4894
1 + 2	97.9	37.9	23	....	....
1 + 4	151	41.5	40	....	....
2	219	43.6	10	0.9295	1.5103
1 + 6	374	59.1	110	....	....
2 + 6	394	53.3	63	....	....
3	527	58.3	5	0.9423	1.5161
3 + 4	626	56.7	10	....	....
1 + 6	838	88.4	110	....	....
4	903	62.0	Neg.	0.9269	1.5177
4 + 6	2140	118	75	....	....
5	3000	116	29	0.9434	1.5188
6	4680	241	100	0.9089	1.4988
7	6080	154	5	0.9482	1.5212
8	6220	218	76	0.9325	1.5200
6 + 9	8500–9000	284	82 (Approx)	....	....
9	17500	359	62	0.9540	1.5320

Procedure. The procedure for determination of OK loads corresponded to the standard Timken OK-load procedure outlined

[1] Aluminum Research Laboratories, Aluminum Company of America.

[2] "Gear Wear as Related to Viscosity of Oil," by H. Blok and S. A. McKee, in "Mechanical Wear," edited by J. T. Burwell, Jr., ASM, Cleveland, Ohio, 1950, chapter 11, pp. 199–227.

Contributed by the Lubrication Research Committee and presented at the Annual Meeting, Atlantic City, N. J., November 25–30, 1951, of The American Society of Mechanical Engineers.

Note: Statements and opinions advanced in papers are to be understood as individual expressions of their authors and not those of the Society. Manuscript received at ASME Headquarters, July 20, 1951. Paper No. 51—A-35.

[3] "Laboratory Wear Tests With Automotive Gear Lubricants," by S. A. McKee, J. F. Swindells, H. S. White, and W. Mountjoy, *Journal of Research*, U. S. National Bureau of Standards (RP 1955), vol. 42, February, 1949, pp. 125–130.

[4] "The Incremental Friction Coefficient—a Nonhydrodynamic Component of Boundary Lubrication," by J. T. Burwell, Jr., and C. D. Strang, *Journal of Applied Physics*, vol. 20, 1949, pp. 79–89.

by the Timken Roller Bearing Company, Canton, Ohio, in its instruction manual, with the single exception that the oils were not heated to 100 F prior to starting the determinations.

The loads used in the runs were applied uniformly by a mechanical load applicator. A stop watch was started at the instant the load was applied to the load lever. Unless it became evident that a score, Fig. 5, was occurring, as indicated by the characteristic sound produced, excessive "smoking" of the oil, or uneven marking on the rapidly rotating test cup, the run was continued for a total time of 10 min. The motor was then stopped, the oil cock closed, the load-lever weight removed, and the test block removed and marked with a stylus to identify the wear area.

Another unused test cup was then installed, the test block placed in the holder so as to present a fresh unused area, and the machine reassembled as before. The procedure just outlined was repeated after completion of each run. Additional load-lever weights in 2-lb increments were applied after each run, until a score was encountered.

After a lever load was obtained which resulted in a score, at any time during the 10-min test run as previously described, and as confirmed by visual inspection at the end of the run, the investigation was continued as follows to determine the exact OK load:

Additional test runs were made in 1-lb lower, then higher, increments, until duplicate loads were obtained at a lever load such that an additional 1-lb load would produce two consecutive scores or scores in two out of three runs. The highest load thus determined was taken as the OK load for the oil under test. For example, in arriving at an OK load of 10 lb for oil no. 4 + 6 (Table 1), the lever-load weights and results were as follows:

1	2 lb OK
2	4 lb OK
3	6 lb OK
4	8 lb OK
5	10 lb OK
6	12 lb Score
7	11 lb Score
8	10 lb OK
9	11 lb Score

OK load—10 lb

After the OK load was determined for an oil, the machine was disassembled, thoroughly cleaned with naphtha and prepared for the next series of runs.

The scar areas for each OK-load run were determined by examination of the scar width under a Bausch and Lomb microscope using ×40 magnification. The microscope used was a stereoscopic, wide-field, binocular type equipped with a micrometer disk mounted within one of the wide-field eye pieces; it had a range of magnification of 7 to 40 diam. The scar on the test block was first marked off at five equidistant points along the side, and the widths measured at these five points averaged. This figure was converted to inches and multiplied by the scar length of $^1/_2$ in., giving the area A for each scar.

The pressure P between the test block and test cup was calculated from the formula

$$P = 10(W+C) - 2^1/_2(B+R)$$

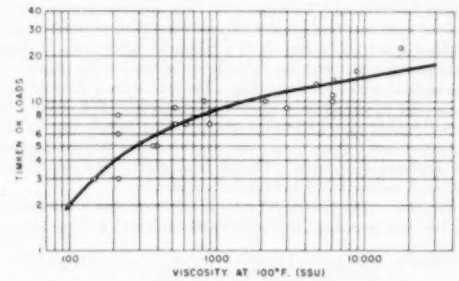

FIG. 1 EFFECT OF VARIATIONS IN VISCOSITY VALUES OF STRAIGHT PETROLEUM MINERAL OILS UPON RESULTANT TIMKEN OK LOADS

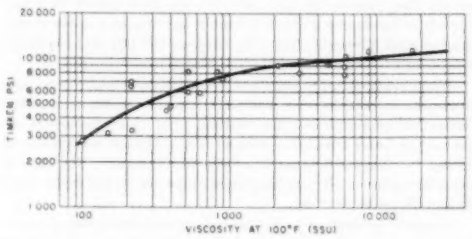

FIG. 2 EFFECT OF VARIATIONS IN VISCOSITY VALUES OF STRAIGHT PETROLEUM MINERAL OILS UPON RESULTANT TIMKEN PSI

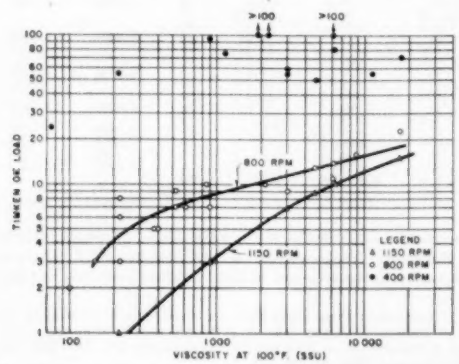

FIG. 3 EFFECT OF VARIATIONS IN VISCOSITY VALUES OF STRAIGHT PETROLEUM MINERAL OILS AND MANDREL SPEEDS UPON RESULTANT TIMKEN OK LOADS

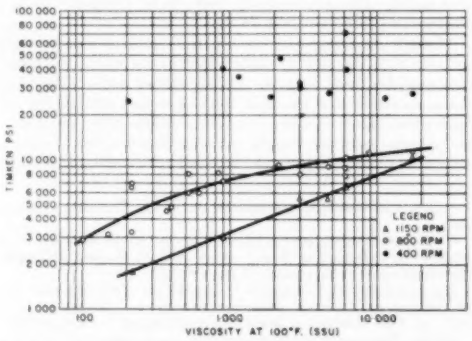

FIG. 4 EFFECT OF VARIATIONS IN VISCOSITY VALUES OF STRAIGHT PETROLEUM MINERAL OILS AND MANDREL SPEEDS UPON RESULTANT TIMKEN PSI

where W is the OK load-lever weight, $(B + R)$ the total friction-lever weight, and C the load-lever constant (1.74 for the machine used).

Pounds per square inch (psi) values were calculated by dividing the load P by the scar area A.

Test Data. Two groups of experiments were conducted. The first group involved determination of the Timken OK-load values and corresponding psi values for the 16 oils listed in Table 1. In this group of experiments the standard 800-rpm spindle speed of the machine was utilized. The results obtained are summarized graphically in Figs. 1 and 2 which are believed to be self-explanatory.

The second group of tests was similar to the first group, differing only in that two additional test-spindle speeds were used, these being, respectively, 400 rpm and 1200 rpm. These data are summarized in Figs. 3 and 4.

Discussion of Results

It is evident from the data presented that variations in OK-load values representing the full range (0 to 100 lb) of the Timken machine can be obtained by manipulation of the variables of viscosity and of rubbing speeds, and in the absence of oiliness or extreme-pressure agents. This clearly demonstrates the degree to which hydrodynamic effects may be present when employing the Timken apparatus in the evaluation of the lubricating characteristics of oils.

In instances where OK values are of interest as a possible measure of the lubricating values of oils as constituted, hydrodynamic effects may be of secondary concern, or even may be desirable since they also would be present in most practical applications. However, when the apparatus is to be used as a research tool to achieve basic understanding of the functioning of extreme-pressure-lubricant additives, then it is apparent that adequate consideration must be given to the presence of the hydrodynamic effects when using the Timken apparatus. In this connection it would also be of interest to determine whether the observed hydrodynamic effects are of concern in the presence of various types of oiliness and extreme-pressure-lubricant additives.

This investigation indicates that hydrodynamic effects must be considered if Timken test data are to be applied correctly. It would also be of interest to consider whether other lubricant-testing apparatus such as the Shell "Four-Ball," SAE machine, and others are sensitive to similar hydrodynamic effects.

Fig. 5 Typical Timken Wear Scars

Discussion

H. A. Erickson.[5] Through testing and development of a number of lubricant testing machines such as the Almen, SAE, Falex, and Four Ball, in addition to the Timken tester described in the paper, much has been learned with respect to the effects and

[5] Chief Engineer, D. A. Stuart Oil Company, Limited, Chicago, Ill.

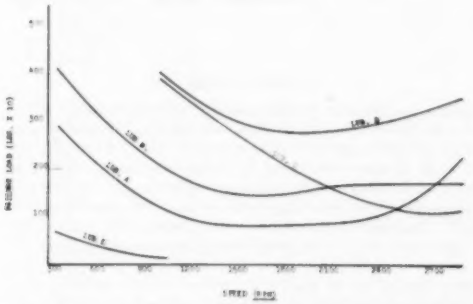

Fig. 6 Effect of Speed on Load-Carrying Ability of Four Types of Oil as Tested on Extreme-Pressure Machine

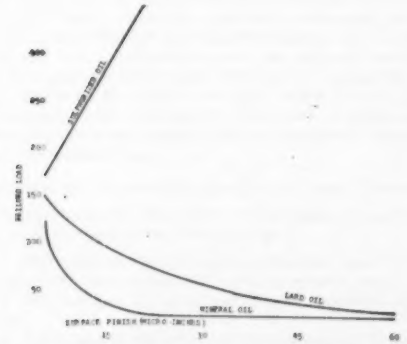

Fig. 7 Effect of Surface Finish on Load-Carrying Ability of Three Types of Oil as Tested on Extreme-Pressure Machine

behavior of extreme-pressure additives and lubricants. This is true in both the automotive and cutting-fluids fields where materials with antiweld and lubricity ability are used to impart certain desirable characteristics.

Our experience, using the machines mentioned, indicates that viscosity of the lubricant does affect the test results in the same manner as on the Timken machine reported in this paper, and any tests which are run must be compared on a like viscosity basis.

Curves A, B, C, and D in Fig. 6 of this discussion show test results of oils all blended to the same viscosity (140 at 210 F SSU), A, being a straight mineral oil; B, a balanced blend containing both antiweld and lubricity; C, an oil with only a lubricity agent; and D, one with only an antiweld agent. Lubricant E is a straight mineral oil having a viscosity of 42 SSU at 210 F or 100 SSU at 100 F.

It can be seen from these curves also that speed likewise is a factor in the load-carrying ability of the test oils and must be considered in the application of a lubricant for a specific purpose.

The curves in Fig. 7 show the results of test values as affected by the surface finish of the test members used on the machine. To make comparisons from time to time, it is well to check this variable when new test parts are received.

We feel this paper is a contribution to the field of lubrication, and the authors by their previous papers and good work in this and other societies require no further introduction.

Authors' Closure

We are appreciative of the additional data provided by Mr. Erickson tending to confirm rather broadly the results reported by us. We assume that Mr. Erickson's data in Fig. 6 represent a summary of results for more than one type of lubricant testing machine. We have investigated in a preliminary manner the effects of varying viscosities of straight mineral oils upon Shell Four Ball EP values and have found these to be substantially independent of viscosity. We certainly agree that Mr. Erickson's point with reference to comparison of lubricants upon an equivalent viscosity basis is well taken. Clearly, additional work in this field is indicated and needed.

Wet Compression in an Axial-Flow Compressor

By SHAO-LEE SOO,[1] PRINCETON, N. J.

The problem of wet compression in an axial-flow compressor was studied considering heat and mass transfer. The basic relation between the rate of compression, size of water particles, and over-all pressure ratio was obtained. The design criterion of an axial-flow compressor for wet compression was outlined. The possibility of introducing wet compression in a supersonic compressor was investigated as a two-phase Riemann shock problem.

Nomenclature

The following nomenclature is used in the paper:

A = flow area, sq ft
C_D = drag coefficient
d = diameter of particle, microns
D = diffusion coefficient, sq ft per sec
f = lb of water per lb of air
h = enthalpy, Btu per lb
h_{fg} = latent heat of evaporation, Btu per lb
J = mechanical equivalent of heat, 778.16 ft-lb/Btu
K = over-all pressure ratio
K_C = thermal conductivity, Btu/ft sec deg R
l_c = chord length, ft
L = working length of compressor, ft
M = molecular weight
m = mass, lb
n = adiabatic exponent
p = pressure, psia
P = pressure ratio before and after shock
Q = density ratio before and after shock
q = relative velocity, fps
R = universal gas constant, 1.98587 Btu/lb mole deg R
Re = Reynolds number
r_0 = radius of curvature of main stream, ft
r_r = mean radius of cascade ring, ft
S_{fg} = entropy of evaporation, Btu/lb deg R
T = temperature, deg R
t = time, sec
u = axial velocity, fps
v = specific volume, cu ft per lb
W_w = work of wet-compression, Btu pe. lb of air
W_d = work of compression of dry air, Btu per lb
w = lb of steam and water per lb of air
x, y = co-ordinates as indicated
z = axial co-ordinate, ft
Z = dimensionless axial co-ordinate as defined
V = absolute velocity, fps
α, β = blade angles as indicated
γ = stagger angle of blades
θ = angle as indicated
$\varphi = \int_0^T C_p \frac{dT}{T}$, Btu/lb deg R
η_c = adiabatic efficiency of compressor, per cent
η_w = wet-compression efficiency, per cent
η_e = equivalent adiabatic efficiency, per cent
ζ = logarithmic rate of compression, sec^{-1}
μ = viscosity, lb-mass/sec ft
σ = surface tension
Prime (′) for quantities of liquid phase
Bar (—) for vector quantities

Subscripts:

0 = inlet conditions
1 = initial conditions
2 = final conditions
a = air
d = at surface of particle of diameter d
f = liquid water
g = steam
i = ideal

Introduction

The "wet-compression" process, in which compression is made on a mixture of finely divided liquid water suspended in the air, was proposed originally by Kleinschmidt for improving the thermal efficiency and performance of gas-turbine units (1, 2).[2] It also has been suggested that a simple, efficient gas-turbine cycle of high pressure ratio can be carried out with wet compression, and in this cycle no regenerator or intercooler is necessary. This process not only has been considered as useful in marine propulsion, but also for turbojet thrust augmentation (3, 4).

In previous studies the ideal condition of continuous saturation of air-steam mixture during compression has been assumed. The assumption implies that either the mixture of air and water is very slowly compressed, such that equilibrium is maintained throughout the steps, or the diffusion rate between air and steam is infinitely large. However, considering the fact that each bulk of air is pushed through an axial-flow compressor in the order of 0.01 sec, with finite diffusion rate, the foregoing assumption tends to give theoretical results which are over-optimistic. It is the purpose of this study to correlate various factors, such as particle size, design of compressor, and so forth, to obtain a better approximation to actual conditions, and to organize a theoretical basis for design and test.

Behavior of Water-Particles in an Ideal Compressor

In order to simplify the problem, we first assume as our apparatus an ideal compressor specified as follows:

1 The compressor has an infinite number of stages with equal stage pressure ratio giving a finite over-all pressure ratio K.

2 The flow area can be adjusted to give prescribed axial velocity.

3 The adiabatic efficiency of this compressor is 100 per cent.

[1] Instructor of Thermodynamics, Princeton University. Jun. ASME.

Contributed by the Gas Turbine Power Division and presented at the Annual Meeting, Atlantic City, N. J., November 25–30, 1951, of The American Society of Mechanical Engineers.

Note: Statements and opinions advanced in papers are to be understood as individual expressions of their authors and not those of the Society. Manuscript received at ASME Headquarters, September 10, 1951. Paper No. 51—A-99.

[2] Numbers in parentheses refer to the Bibliography at the end of the paper.

4 There is an even distribution of air-water mixture across each cross section, normal to the axis.

5 The capacity of the compressor is 1 lb of air per sec, to which w lb of water is introduced.

From specification 1 in the foregoing, the pressure variation along the axial co-ordinate can be taken as exponential, or

$$p = p_0 K^{z/L} \quad \ldots [1]$$

The energy relation for a frictionless, adiabatic process can be expressed as

$$dh = v\,dp \quad \ldots [2]$$

Assuming that both the molecular concentration and temperature distribution in the neighborhood of the water particle change jumpwise from that of the liquid phase to that of the gaseous phase, Equation [2] can be expressed in terms of the components of the mixture as

$$d\varphi_a + w\,d\varphi_v - \frac{1}{T}\,d\,f(h_g - h_g' + h_{fg}') = \frac{R}{M_g}\left(\frac{M_g}{M_a} + w - f\right) d\,(\ln p) \quad \ldots [3]$$

Assuming that the water particles are relatively far apart compared with the diameter of the particles, and expressing the intermediate diameter and number of particles in terms of initial particle size and amount of liquid, the result obtained by Fuchs for evaporation rate can be expressed as (5)

$$-\frac{df}{dt} = \frac{2.564 \times 10^5}{d_0^2}\,(v_{f0} f_0)^{2/3}\,(v_f f)^{1/3}\left(\frac{T + T'}{p\sqrt{T}}\right)\left[\frac{T p_{sd}'}{T'} - \frac{p(w-f)}{(0.62188 + w - f)}\right]\left[1 + \frac{p_{sd}'}{2p}\right] \quad \ldots [4]$$

where

$$T' = T - 56.77\,\frac{h_{fg}'}{p\sqrt{T}}\left[\frac{T p_{sd}'}{T'} - \frac{p(w-f)}{(0.62188 + w - f)}\right]\left[1 + \frac{p_{sd}'}{2p}\right]$$

and

$$p_{sd}' = p_s'\,exp\,[0.09798(1251.5 - T')\,(v_{f0} v_f)^{1/3}/(d_0 T')] \quad \text{(ref. 6)}$$

In the foregoing the diffusion rate is represented as

$$D = 2.740 \times 10^{-7}\,\frac{T^{3/2}}{p}\ \text{ft}^2/\text{sec (ref. 7)}$$

the thermal conductivity of the gaseous medium is approximated by

$$K_C = 8.10 \times 10^{-9} T\ \text{Btu/ft sec deg R}$$

and the surface tension of water is approximated by

$$\sigma = 6.8933 \times 10^{-4}(1251.5 - T)\ \text{lb per ft}$$

between 500 R and 700 R.

To simplify the solution, the following quantities are introduced

$$\zeta = \frac{u}{L}\ln K \quad \ldots [5]$$

which has the dimension of sec^{-1} and is called the logarithmic rate of compression, and

$$Z = \frac{z}{L}\ln K \quad \ldots [6]$$

which is called the dimensionless axial co-ordinate. Substituting the relations represented by Equations [1], [5], and [6] into Equations [3] and [4], the latter can be simplified to

$$d(\varphi_a + w\varphi_v) - \frac{1}{T}\,d\,[f(h_g - h_g' + h_{fg}')] = \frac{R}{18.016}\,(0.62188 + w - f)\,dZ \quad \ldots [7]$$

and

$$-\frac{df}{dZ} = \frac{2.564 \times 10^5}{\zeta d_0^2 p_0}\,(v_{f0} f_0)^{2/3}\,(v_f f)^{1/3}\,\frac{(T - T')}{e^Z\sqrt{T}}\left[\frac{T\,p_{sd}'}{T'} - \frac{p_0 e^Z (w-f)}{(0.62188 + w - f)}\right]\left[1 + \frac{p_{sd}'}{2p_0 e^Z}\right] \quad \ldots [8]$$

Therefore we have altogether two independent equations; φ, h, and p_s are functions of T or T', and can be found in standard steam and gas tables (8, 9). Optimum gas-turbine-cycle efficiency requires $y = 0$ at $p = p_0 K$, while the work of compression is a minimum. The problem is, therefore, variational in nature. In other words, we have the following boundary conditions for Equations [7] and [8]

Initial:	Final:
$f_1 = f_0$	$f_2 = 0$
$T_1 = T_0$	
$Z_1 = 0$	$Z_2 = \ln K$

and

$$W = \int_1^2 dh(T, Z, f, w) = W_{min} \quad \ldots [9]$$

if w gives

$$f > 0 \quad \text{at } Z < \ln K$$
$$f = 0 \quad \text{at } Z = \ln K$$

Accurate calculations of the particle temperature in the gaseous mixture is difficult since the thermal conductivity of gaseous mixtures does not follow the ordinary law of mixture. The effect of higher concentration at the surface of a particle does not become substantial until the particle size is reduced to or below the mean free path between gaseous molecules. By dropping these two considerations together with the correction for finite vapor pressure in the last bracket of Equation [8], which, in a sense, cancels the effect of nonuniformity in the temperatures of the two phases at the same Z, the equations can be simplified to

$$d(\varphi_a + w\varphi_v) - \frac{R}{18.016}\,(0.62188 + w - f)\,dZ + \frac{fR}{18.016}\,d(\ln p_s) - d(s_{fg} f) = 0 \quad \ldots [10]$$

into which the Clapeyron relation has been introduced; and

$$-\frac{df}{dZ} = \frac{5.128 \times 10^5}{\zeta d_0^2\,p_0}\,(v_{f0} f_0)^{2/3}(v_f f)^{1/3}\,\frac{\sqrt{T}}{e^Z}\left[p_s - \frac{p_0 e^Z (w-f)}{(0.62188 + w - f)}\right] \quad \ldots [11]$$

Solutions obtained by step-by-step integration of Equations [10] and [11] are found to be good approximations (close within 5 per cent in the range of this study) of those from Equations [7] and [8].

Equation [11] shows that for a given K, results of wet com-

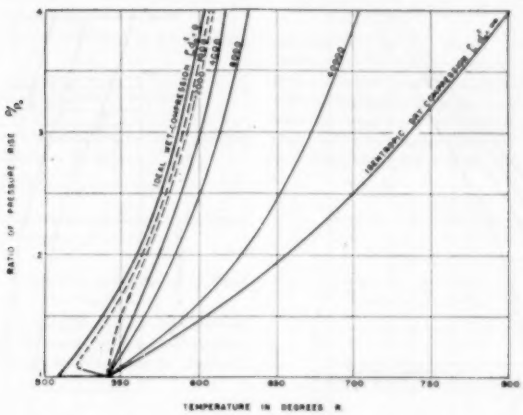

FIG. 1 *T-p* DIAGRAM OF SOLUTIONS FOR VARIOUS ζd_0^2
(T_0 = 540 R, p_0 = 14.696 psia, K = 4. Dry air and liquid water at inlet.)

pression will be the same for the same value of ζd_0^2. The limiting cases of this problem are as follows:

(*a*) $\zeta d_0^2 = 0$, or $\zeta = 0$, i.e., the mixture is very slowly compressed. Solutions obtained in this manner coincide with the results given in reference (4).

(*b*) $\zeta d_0^2 = \infty$, or $\zeta = \infty$, i.e., the mixture is very quickly compressed. It means compression of dry air as a limiting case of wet compression; the rate of compression is far greater than the rate of evaporation.

A numerical example of the complete solution of the problem for various ζd_0^2 values is presented in Fig. 1; the dotted lines indicate where the numerical integration method fails and are obtained by interpolation.

As a basis of comparison, the term "wet-compression efficiency" is introduced. It is defined as

$$\eta_w = \frac{W_d - W_w}{W_d - W_{ws}} \quad \ldots\ldots [12]$$

The diagrams of terminal temperatures, water requirements, and efficiencies of wet compression versus ζd_0^2 for various pressure ratios K, given in Figs. 2, 3, and 4 for the initial conditions indicated, show relations between the results of wet compression and d_0, ζ, and K.

BEHAVIOR OF WATER PARTICLES IN AN ACTUAL COMPRESSOR

The motion of a water particle in a given velocity field of the gaseous medium, neglecting the effect of gravitation and for small relative velocity as compared to the velocity of the main stream, can be represented by the following vector equation

$$\frac{d\bar{q}}{dt} = \frac{V_g^2}{r_0} - F\,\bar{q} \quad \ldots\ldots [13]$$

where

$$F = \frac{3\pi\mu d_0}{m} = \frac{18\mu\nu_f}{d_0} \text{ for } \mathbf{Re} < 1$$

and

$$F = \frac{\pi}{8} C_D \frac{d_0^2\, q}{\nu m} = \frac{3}{4} \frac{C_D}{d_0} \frac{\nu_f}{\nu} q \text{ for } \mathbf{Re} > 1$$

In the co-ordinate system shown in Fig. 5, representing the condition at the mean radius of the cascade ring, the paths of the main stream through a blade row can be assumed as composed of parallel circular arcs of radius r_0, and

$$r_0 = \frac{1}{2} l_c \csc \frac{1}{2} (\beta - \alpha) \quad \ldots\ldots [14]$$

and

$$V_g = u \sec (\beta - \theta) \quad \ldots\ldots [15]$$

while

$$\alpha + \beta = 2\gamma \quad \ldots\ldots [16]$$

between $\theta = 0$ and $\theta = \beta - \alpha$. It is also assumed that the state of the gaseous medium is constant for the domain under consideration and that the evaporation of the water particles does not change its diameter appreciably. Expressing Equation [13] in terms of its components in the co-ordinate system shown in Fig. 5, we have

$$\frac{dq_x}{dt} - \frac{u^2}{r_0} \tan (\beta - \theta) \sec (\beta - \theta) + F\, q_x = 0 \ldots [17]$$

$$\frac{dq_y}{dt} - \frac{u^2}{r_0} \sec (\beta - \theta) + F\, q_y = 0 \quad \ldots\ldots [18]$$

and for $\Delta x \ll r_r$

$$\frac{dq_z}{dt} - \frac{u^2}{r_r} \tan^2 (\beta - \theta) + F\, q_z = 0 \quad \ldots\ldots [19]$$

Since

$$z = r_0[\sin \beta - \sin (\beta - \theta)] \quad \ldots\ldots [20]$$

$$q_z = u - V_g \quad \ldots\ldots [21]$$

the z-component of the motion can be expressed in terms θ as

$$\frac{d^2\theta}{dt^2} + r_0 \tan(\beta - \theta) \left(\frac{d\theta}{dt}\right)^2 + F \frac{d\theta}{dt} + \frac{u^2}{r_0^2} \tan (\beta - \theta) \sec^2 (\beta - \theta) - \frac{Fu}{r_0} \sec (\beta - \theta) = 0 \quad \ldots\ldots [22]$$

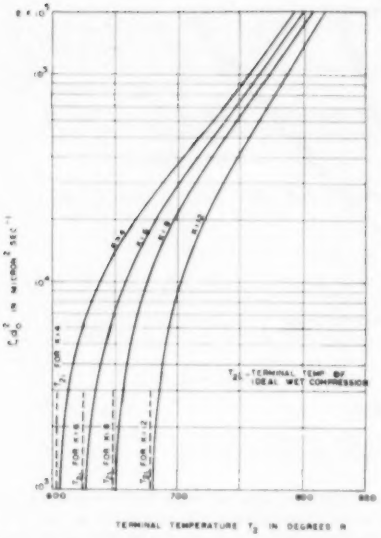

FIG. 2 TERMINAL TEMPERATURES OF WET COMPRESSION
(T_0 = 540 R, p_0 = 14.696 psia. Dry air and liquid water at inlet.)

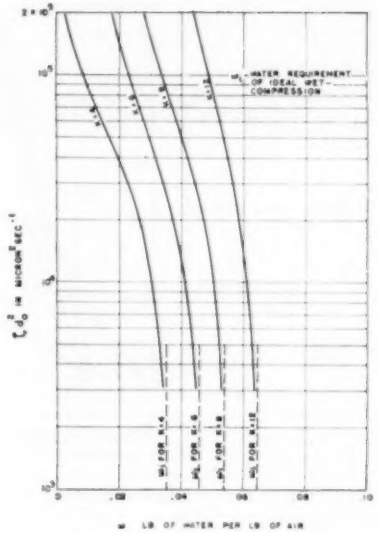

FIG. 3 WATER REQUIREMENT OF WET COMPRESSION
(T_0 = 540 R, p_0 = 14.696 psia. Dry air and liquid water at inlet.)

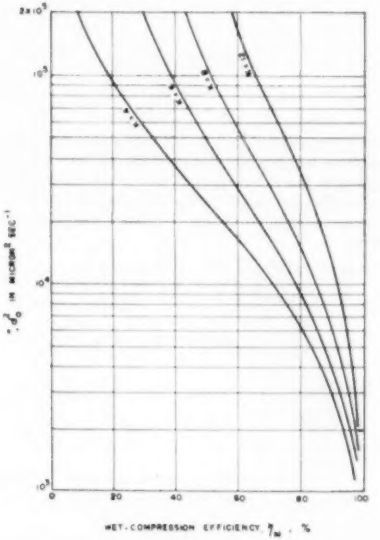

FIG. 4 WET-COMPRESSION EFFICIENCY
(T_0 = 540 R, p_0 = 14.696 psia. Dry air and liquid water at inlet.)

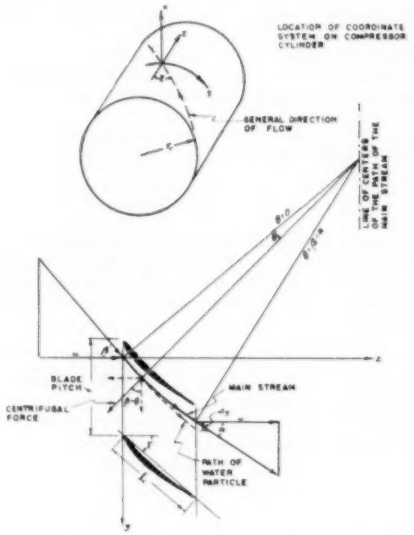

FIG. 5 CO-ORDINATE SYSTEM OF MOTIONS OF TWO-PHASE MEDIUM RELATIVE TO BLADES

which can be integrated numerically subjecting to the following initial conditions

$$t = 0, \quad \theta = 0, \quad \text{and} \quad \left(\frac{d\theta}{dt}\right)_0 = \frac{u}{r_0} \sec \beta$$

between $\theta = 0$ and $\theta = \beta - \alpha$; the value of q in the expression of F is the resultant of its components. We get

$$t = t(\theta) \quad [23]$$

The time interval in which the particle lags behind the main stream in passing through this blade row is given by

$$t = t(\beta - \alpha) - \frac{r_0}{u}(\sin \beta - \sin \alpha) \quad [24]$$

which is a simple indication of the relative velocity between the water particles and the gaseous medium. The tangential displacement of the particle from the main stream can be obtained from

$$\Delta y = \int_0^{t(\beta-\alpha)} q_y(t)\, dt \quad [25]$$

which indicates that a certain amount of the water particles will be caught by the blades. The radial displacement of the particle can be obtained from

$$\Delta x = \int_0^{t(\beta-\alpha)} q_x(t)\, dt \quad [26]$$

which indicates the amount of water particles to be thrown away to the compressor casing. The relative velocity, q, is the velocity with which a water particle hits the blade, if it does so; and, therefore, can be taken as an indication of erosion of the blade. It also affects the rate of mass transfer, which will be studied later.

The magnitude of the relative motion between the particles and the gaseous medium can be seen in the numerical example presented in Figs. 6, 7, and 8. It can be seen that for the case presented in the example, in passing through the blade row specified, the water particles of 20 microns diam move toward the blade for a distance of about $^3/_{16}$ in. This means that all particles entering within $^3/_{16}$ in. peripherally from the leading edge of the blade will be caught by the blade and cease to exist in spherical form thereafter. For a blade pitch of $1^1/_2$ in., 12 per cent of the

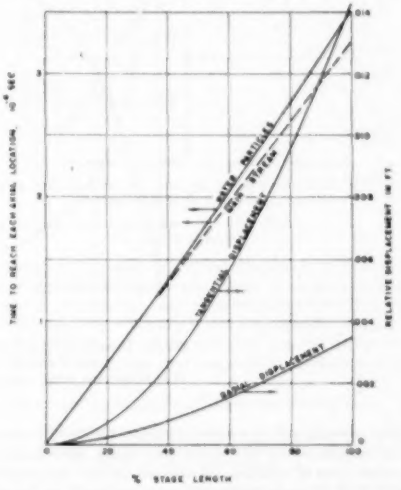

FIG. 7 RELATIVE DISPLACEMENTS BETWEEN WATER PARTICLES AND GASEOUS MEDIUM AS MIXTURE FLOWS THROUGH BLADE ROW
(Same numerical data as for Fig. 6.)

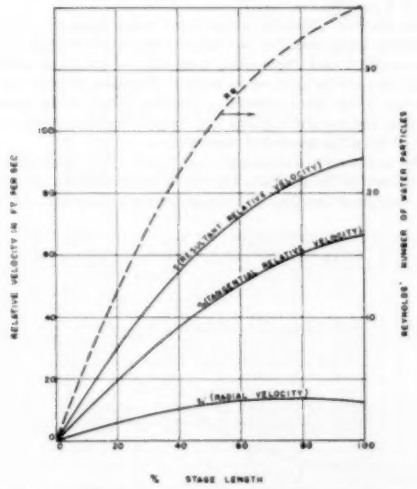

FIG. 6 RELATIVE VELOCITIES BETWEEN WATER PARTICLES AND GASEOUS MEDIUM AS MIXTURE FLOWS THROUGH BLADE ROW
(d = 20 microns. Data at mean radius of cascade ring: turning angle = $\beta - \alpha$ = 18 deg, stagger angle = γ = 42 deg, chord length = l_0 = 1.575 in., mean radius of cascade ring = r_T = 1.2 ft, axial velocity = u = 300 fps, T = 540 R, p = 14.696 psia.)

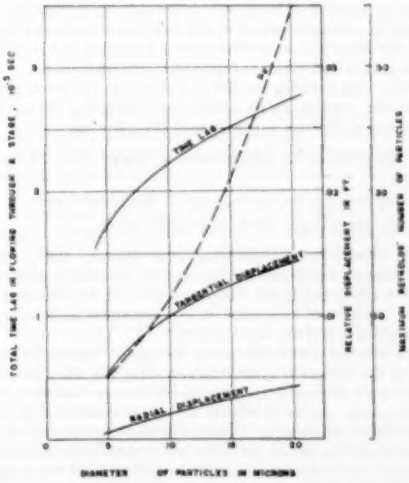

FIG. 8 RELATIVE DISPLACEMENTS AND REYNOLDS NUMBER PRODUCED ON PARTICLES OF VARIOUS SIZES IN PASSING THROUGH BLADE ROW
(Data of machine and state of mixture same as for Fig. 6.)

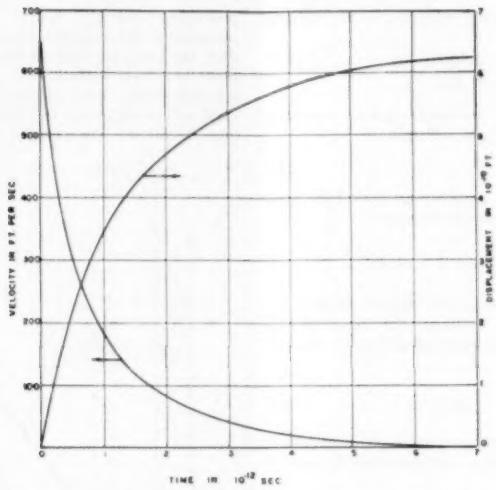

FIG. 9 DECAY OF RELATIVE VELOCITY BETWEEN WATER PARTICLES AND GASEOUS MEDIUM IN STRAIGHT FLOW
(d = 20 microns, initial relative velocity 650 fps, T = 540 R, p = 14.696 psia.)

particles probably will be caught in passing through this row and will be transferred to the compressor casing subsequently by centrifugal force of rotation. It also can be seen that radial displacement of water particles is minor compared to tangential displacement. However, this component of velocity is carried over to the next stage, while the other two components decay almost immediately at the inflection of the direction of the main stream when passing to the next blade row. This can be seen from the rapidity of decay of relative velocity between the two phases in a straight branch of the main stream as shown in Fig. 9. The magnitude of relative motion is damped out as the particles pass to high-pressure stages with reduced diameter.

Other than reducing the size of water particles, the magnitude of relative motion can be reduced by redesigning the machine, according to one or a combination of the following:

1 By reducing the axial velocity or number of rpm of the machine.

2 By reducing the turning angle of the cascade airfoil.

3 By using larger chord length of the blade.

The reasons for recommending these measures can be seen in the foregoing mathematical analysis. In designing a compressor for wet compression, the method of analysis introduced in the paper can be used as a check in selecting the stagger angle, the turning angle, and the chord length.

The effect of relative motion on the rate of evaporation can be seen in the numerical example presented in Fig. 10, which is obtained from Reynolds analogy applied to mass transfer. From the Reynolds number of relative motion, as shown in Figs. 6 and 8, this effect can be seen. However, if we adjust the rate of compression and the initial size of the water particles to maintain the condition of continuous saturation (or 100 per cent wet-compression efficiency in the preceding section) the increase of mass transfer due to relative motion is negligible.

The characteristics of a compressor designed for given pressure rise and logarithmic rate of compression when operated with various initial particle sizes can be seen in Fig. 11 in which the term "equivalent adiabatic efficiency" is defined as

$$\eta_e = \frac{W_{di}}{W_w} = \eta_c \frac{W_d}{W_w} \quad [27]$$

For high pressure ratio, an equivalent adiabatic efficiency greater than 1 is possible.

The greatest difficulty encountered when using an ordinary axial-flow compressor for wet compression is the stalling of cascade airfoils at last stages owing to greatly reduced axial velocity. There also will be an increase in blade Reynolds number and an increase in tip Mach number. The first effect is the greatest handicap because the loss due to flow disturbance tends to eliminate all the gains due to wet compression.

The usefulness of a supersonic compressor with wet compression can be seen in the diagram, Fig. 12, of normal shock conditions of a two-phase medium as compared to the Hugoniot curve of

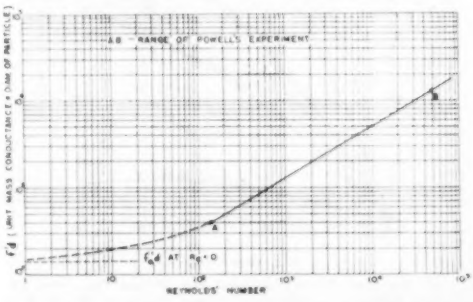

FIG. 10 EFFECT OF RELATIVE MOTION ON RATE OF MASS TRANSFER FROM WATER PARTICLE TO GASEOUS MEDIUM
(T = 540 R, p = 14.696 psia.)

dry air (13) and the isentropic curve of dry air. The curve of the two-phase medium was plotted from the "modified Rankine-Hugoniot relation" represented approximately by the following equation

$$^1/_3 (1 + P)(1 - Q) = \frac{1}{n - 1}(Q - P) - k_{fv} J(f_1 - f_2)\frac{Q}{RT_1} \quad \ldots\ldots [28]$$

The discontinuity of velocities of the liquid phase is shown in Fig. 9.

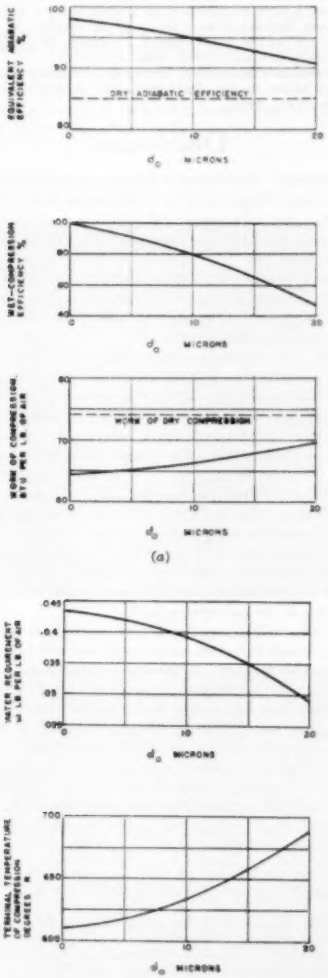

FIG. 11 CHARACTERISTICS OF WET COMPRESSORS DESIGNED FOR GIVEN PRESSURE RISE AND LOGARITHMIC RATE OF COMPRESSION, TO BE OPERATED WITH VARIOUS PARTICLE SIZES (d_0)
(ζ = 62.0, K = 4, η_c = 85 per cent, T_1 = 540 R, p_0 = 14.696 psia.)

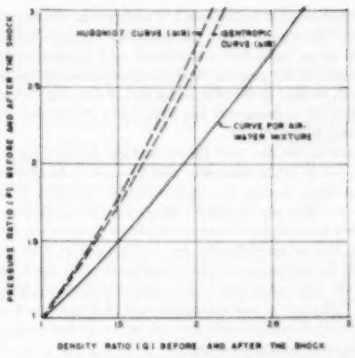

FIG. 12 NORMAL SHOCK CONDITIONS OF TWO-PHASE MEDIUM
(T_1 = 540 R, p_1 = 14.7 psia before shock.)

DISCUSSION

1 Since all the results of wet-compression vary as ζd_0^2, high ζ can be compensated for by using small d_0 to get favorable results of wet compression. Low pressure ratios also require lower ζd_0^2 to maintain high efficiency of wet compression. For $K > 12$, ideal wet compression can be achieved practically for $\zeta d_0^2 < 2000$; for $\zeta d_0^2 < 1000$, ideal wet compression can always be taken as actual.

2 The approximate ranges of ζ values in practice are

60–100 for land and marine-type compressors
200–300 for aircraft-type compressors
600 for supersonic compressors

To maintain a minimum of 70 per cent wet-compression efficiency, referring to Fig. 4, the upper limits of ζd_0^2 values for various pressure ratios are as given in Table 1

TABLE 1

K	ζd_0^2 (microns^2 sec^{-1})
4	10^4
6	1.6×10^4
8	3×10^4
12	7×10^4

Since ζ is of the order of 100 sec^{-1}, the maximum particle size permissible if any obvious thermodynamic gain is to be expected is about 20 microns diam; lower for higher ζ and lower K. This agrees with the requirements of limiting the amount of relative motion between the two phases.

3 Since economical production of a partial size below 5 microns diam is difficult, the compromise is to design compressors of comparatively low rpm, smaller turning angle, wider blade, and larger rotor radius. These requirements mean preference to a relatively large machine for a given capacity. However, as shown in Fig. 11, the gain in equivalent adiabatic efficiency made by 70 per cent wet-compression efficiency is already enormous as compared to compression of dry air. The supersonic compressor is characterized by small axial working length and high axial velocity, yet if it is designed for high pressure ratio, say, 20, the gain through this process is still indubitable.

4 In the example of Figs. 6, 7, and 8 conditions at the inlet of an axial-flow compressor are approximated. At this point the temperature and pressure of the gaseous medium are the lowest that exist in the compression process, hence both the density and the viscosity of the gaseous medium are low. The amount of relative motion will be damped out as a particle moves toward the high-

pressure end of the compressor. Considering the fact that one can control the size of water particles and the smallness of turning angle in an axial-flow compressor and comparing the state and viscosity of the gaseous medium which occur at the inlet of a compressor to that in the condenser end of a steam turbine, there will be little or no erosion of the blades of a compressor when wet compression is carried out.

5 Water is not the only liquid that can be used for wet compression, yet it is the most effective because of having the highest latent heat among the liquids (water, alcohol, benzene, n-octane, etc.) that can be used. Since the change in flow volume when other volatile fluid is used will not be as severe as in the case of water, less or no difficulty due to changes in flow characteristics will be encountered when another fluid is used instead of water. On the other hand, less thermodynamical gain is also certain. The use of wet compression in this case gives saving in both the work of compression and the latent heat of evaporation of fuel in the combustion chamber.

Conclusions

From the foregoing analysis, the following conclusions are obtained:

1 Wet compression is more efficient at high pressure ratios than at low pressure ratios when other conditions (inlet conditions, particle size d_0, and logarithmic rate of compression, ζ) are similar. For $\zeta d_0^2 < 1000$ microns $\sec^{-1}$, ideal wet compression actually can be achieved.

2 Efficient wet compression requires water particles of size below 20 microns diam. There is little or no danger of erosion of blades with particles of this order of magnitude.

3 Efficient wet compression requires a relatively slow rotational speed and a low axial velocity and, therefore, a relatively large machine for a given capacity. With proper design, 100 per cent wet-compression efficiency actually can be obtained.

4 Efficient wet compression requires a compressor specially designed for such a purpose. Ordinary compressors designed for dry air do not work well when this process is adapted. However, tolerable dry compression can be carried out in a compressor designed for wet compression.

5 The wet-compression cycle, using a volatile fuel, is advantageous for aircraft propulsion. In this case the previous statement is not important.

Acknowledgment

This paper, dealing with the theory of wet compression in an axial-flow compressor in connection with the gas-turbine cycle, was suggested by Prof. Robert V. Kleinschmidt. The author wishes to express his deepest gratitude for the privilege of pursuing this research under his guidance. It is also a pleasure to thank Prof. Howard W. Emmons and Prof. Charles H. Berry for their valuable advice toward the progress of this research. The author also wishes to express his appreciation to Mr. H. D. Emmert of the Allis-Chalmers Manufacturing Company, for his cooperation in providing practical references for this work.

Bibliography

1 "A Thermodynamic Investigation of Gas-Turbine Cycles," by R. V. Kleinschmidt, Research Memorandum No. 1–42, Bureau of Ships, Navy Department, Washington, D. C., November 9, 1942.

2 "Value of Wet-Compression in Gas-Turbine Cycles," by R. V. Kleinschmidt, *Mechanical Engineering*, vol. 69, 1947, pp. 115–116.

3 "Theoretical Analysis of Various Thrust-Augmentation Cycles for Turbojet Engines," by B. T. Lundin, NACA TN 2083, May, 1950.

4 "Theoretical Turbojet Thrust Augmentation by Evaporation of Water During Compression as Determined by Use of a Mollier Diagram," by A. M. Trout, NACA TN 2104, June, 1950.

5 "Concerning the Velocity of Evaporation of Small Droplets in a Gas Atmosphere," by N. Fuchs, NACA TM 1160, August, 1947.

6 "Thermodynamics," by J. H. Keenan, John Wiley & Sons, Inc., New York, N. Y., 1941, pp. 434–437.

7 "Absorption and Extraction," by T. K. Sherwood, McGraw-Hill Book Company, Inc., New York, N. Y., and London, England, 1937.

8 "Thermodynamic Properties of Steam," by J. H. Keenan and F. G. Keyes, John Wiley & Sons, Inc., New York, N. Y., 1936.

9 "Gas Tables," by J. H. Keenan and J. Kaye, John Wiley & Sons, Inc., New York, N. Y., 1948.

10 "Hydrodynamics," by H. Lamb, Dover Publications, New York, N. Y., 1945.

11 "Das Widerstandsprobleme," by F. Eisner, Proceedings of the Third International Congress of Applied Mechanics, Stockholm, Sweden, vol. 1, 1931, pp. 21–42.

12 "Heat Transfer Notes," by L. M. K. Boelter, V. H. Cherry, H. A. Johnson, and R. C. Martinelli, University of California Press, Berkeley and Los Angeles, Calif., 1948, chapt. 16.

13 "Notes on Mathematical Theory of Compressible Fluid Flow," by R. von Mises, Special Publication No. 2, Harvard University, Cambridge, Mass., 1949.

Discussion

A. A. Hafer.[a] The author is to be commended on some original compressor design work in a pioneering field. The writer concurs that wet compression will require new compressor-design concepts and, therefore, the approach taken by this treatise is of especial interest.

The Navy initially studied the possibility of using wet compression in gas-turbine engines in 1942, as reported by Commodore Kleinschmidt.[4] Therefore it has followed with interest developments relating to this subject.

There are two main advantages which have been associated with wet compression; that is, an increase in full-load efficiency and reduction in size per unit power output of the gas-turbine plant.[5] Several recent tests and studies indicate that the expected increase in plant efficiency has been less than expected, and in at least the case of aircraft application may result in a decrease in over-all efficiency.[6,7] Inasmuch as wet compression is used to provide thrust augmentation for short intervals in aircraft applications, the decrease in efficiency is unimportant. The author indicates several possible methods of improving the efficiency of compressors to be used for wet compression. If the adiabatic compressor efficiencies indicated in Fig. 11 of the paper can be attained in practice, a very important contribution will be made to the gas-turbine field.

It would be well to mention several mechanical complications which may result from wet compression and which must be considered by the designer. Many gas-turbine engines today use air bled from the compressor for bearing sealing and/or cooling. It is unlikely that this would be feasible with wet compression owing to the danger of contaminating the lube oil with water. Further, a control is needed which would inject the proper amount of liquid to produce saturation of the air at the compressor exit. Such a control would have to sense ambient-air temperature, relative humidity, pressure ratio, and compressor speed to provide for the proper water-injection rate, and might be a complex mechanism indeed.

[a] Lieutenant, USNR, Turbine and Gear Section, Bureau of Ships, Department of the Navy, Washington, D. C.

[4] "Value of Wet Compression in Gas Turbine Cycles," by R. V. Kleinschmidt, *Mechanical Engineering*, vol. 69, 1947, pp. 115–116.

[5] "A Thermodynamic Investigation of Gas Turbine Cycles," by R. V. Kleinschmidt, Research Memorandum No. 1–42, Bureau of Ships, Navy Department, Washington, D. C., November 9, 1942.

[6] "Theoretical Analysis of Various Thrust Augmentation Cycles for Turbojet Engines," by B. T. Lundin, NACA Technical Note 2083, May, 1950.

[7] "Kent's Mechanical Engineers' Handbook," twelfth edition, Power Section, edited by J. K. Salisbury, John Wiley & Sons, Inc., New York, N. Y., 1950.

Were continuous injection of water to be contemplated, consideration would have to be given to the purity of the water.[8] Wet-compression tests were conducted at the U. S. Naval Engineering Experiment Station at Annapolis in 1949, on the 3500-hp Allis-Chalmers gas-turbine engine. Ordinary potable or tap water was used in this test. A subsequent analysis of the tap water indicated that it contained impurities listed in Table 2 of this discussion. The total of 130 ppm of solid matter is quite typical of what may be found in the average tap water.

Figs. 13 through 17 of this discussion indicate the serious nature of the deposits which formed on the compressor blades. These views were taken after a total of 15 hr of wet-compression running at an injection rate of from 0.038 to 0.053 lb of water per lb of air. It was impossible to draw any conclusions regarding plant efficiency improvement from the data taken during these tests because of the rapid build-up of deposits on the compressor blades, with the resultant reduction in compressor efficiency. The analysis of the compressor-blade deposits is listed in Table 3 herewith.

[8] "An Introduction to the Gas Turbine," by D. G. Shepherd, D. Van Nostrand Company, Inc., New York, N. Y., 1949.

TABLE 2 ANALYSIS OF TAP WATER USED IN TESTS

Sodium sulphate, ppm	50
Sodium bicarbonates, ppm	60
Silica, ppm	8
Iron and calcium	traces
Total solids (approx.), ppm	130

TABLE 3 ANALYSIS OF COMPRESSOR-BLADE DEPOSITS

	Per cent
Convex Side of Blade	
Sodium sulphate	56
Iron oxide	4
Concave Side of Blade	
Sodium sulphate	53
Iron oxide	13

The remainder of the deposit consisted of organic material and water. The iron-oxide deposit resulted from corrosion of the compressor parts. This test certainly would confirm that distilled water is necessary for any extended wet-compression operation.

It might be of interest to examine the possibilities of wet compression as applied to gas-turbine engines for Naval service. In the lower power ratings, that is below 1000, the gas-turbine engine is used where a light, compact, simple engine is desired.

FIG. 13 LAST FOUR HIGH-PRESSURE STAGES OF COMPRESSOR STATOR SHOWING BLADE DEPOSITS

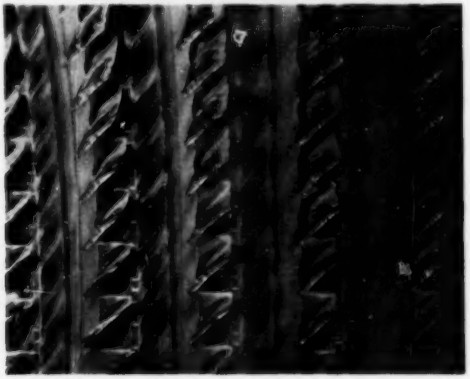

FIG. 14 COMPRESSOR STATOR INDICATING EXTENT OF BLADE-DEPOSIT BUILD-UP

FIG. 15 COMPRESSOR ROTOR-BLADE DEPOSITS VIEWED FROM HIGH-PRESSURE END

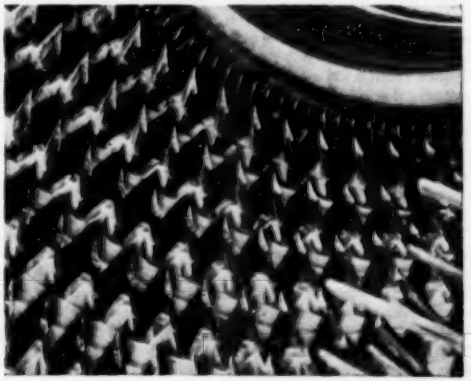

FIG. 16 LAST FIVE STAGES OF COMPRESSOR STATOR EXHIBITING BUILD-UP OF DEPOSITS ON LEADING EDGE OF BLADES

Therefore, there is in general no requirement for wet compression in this power range. Where much higher horsepower is needed, as in main propulsion, it certainly would be desirable to incorporate in the gas-turbine engine any device which will reduce the specific fuel consumption and/or result in a higher power output for a given size plant. It is, of course, necessary to consider both the size and complexity of any such device.

Probably the most serious disavantage of wet compression for Naval use is the need to use distilled water, as previously pointed out. The NACA standard for the amount of water necessary to

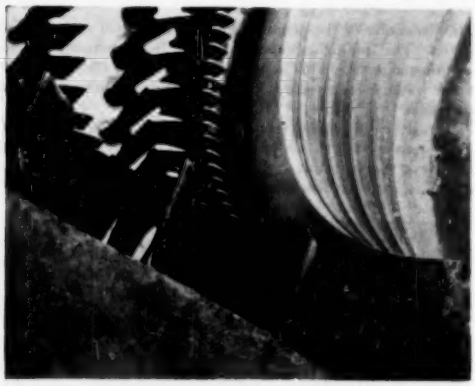

FIG. 17 HIGH-PRESSURE STATOR BLADES REVEALING DISTRIBUTION OF DEPOSITS ON CONCAVE SIDE OF BLADE

produce saturation of the air at the compressor exit is 0.048 lb of water per lb of air at 59 F. Taken at the Bureau of Ships standard ambient-air temperature of 80 F, this would be about 0.052 lb of water per lb of air. This is somewhat higher than the amount shown in Fig. 11(*b*), of the paper, but as NACA tests have indicated that practice requires a somewhat higher proportion of water than their theoretical figure, the NACA theoretical figure has been used in the following comparisons[8]: If we compare the amount of water required for wet compression in a typical gas-turbine plant with the make-up feedwater used in a standard Navy steam plant, the wet compression comes out second best by some margin. The make-up feedwater required by one class of Naval vessel averages about 0.049 gal per hp hr. Under similar conditions, a simple gas-turbine engine using wet compression would require about 0.326 gal per hp hr of injected water. This would indicate that wet compression requires roughly 6 times as much water as this particular steam plant. This number can hardly be termed a general ratio.

It can be seen that if we were to consider the amount of water required for wet compression for a gas-turbine plant of 5000 hp, operating continuously at full power, it would run into the very large figure of 39,000 gal per day for even this modest size plant. This would require the addition of 20 to 40 tons of distilling plant to the evaporator capacity of the vessel, depending upon whether steam or vapor compression were used. If a destroyer of 60,000 shp were powered solely by gas-turbine engines using wet compression, it can be seen that the size and weight of the distilling plant required for wet compression would be staggering, if it were desired to operate the vessel at full power for long periods. Commodore Kleinschmidt has mentioned[4] that it might be possible to combine a vapor-compression distilling plant with the gas-turbine plant. This is certainly possible, and could be very desirable from a thermodynamic standpoint, but it would result in an increased back pressure on the engine with consequent power loss and higher specific fuel consumption, in so far as the gas-turbine engine is concerned. It also should be remembered that to utilize wet compression to the maximum, it would be necessary to have the temperature of the injected water at least as low as the ambient-air temperature. This would require either large storage tanks or some type of refrigeration or cooling system to lower the temperature of the water as it left the distilling plant.

The Navy has one substance always available which it is desirable to exploit. This is of course an ocean full of salt water. Its consistent availability introduces a formidable competitor to wet compression in the form of intercooling. As engine length always tends to be critical in Naval applications, it may be desirable to carry out the compression process in several separate compressors or stages in large units anyway, so that intercooling is made very attractive. In fact, in a study of wet compression made by Chambadal,[9] it was indicated that wet compression appears to have no advantages over use of intercoolers in the gas-turbine cycle.

There is one application of wet compression in Naval vessels which could be very advantageous, however. This is in an application similar to that which is made in aircraft, that is, power augmentation for short periods. As indicated by Captain Simpson and Commander Sawyer,[10] the upper 80 per cent of the installed horsepower of a destroyer is used for less than 4 per cent of the operating life of the vessel. Even more surprising, the upper 60 per cent of the installed horsepower is used for less than 0.3 per cent. If a destroyer of 60,000 hp were powered by a combined steam and gas-turbine plant so that half of the power came from the gas-turbine engines, it would be feasible to obtain short bursts of power in excess of the 60,000 hp by means of wet compression. Assuming the same capacity of feed and potable water tanks as now installed, it would be possible to operate in excess of 3 hr at maximum power using wet compression. Therefore, this application of wet compression would be both feasible and desirable.

Another similar advantageous application of wet compression would be in high-speed craft powered by gas-turbine engines or a combination of Diesel and gas turbine, or gasoline and gas-turbine engines. The British MTB 5559, formerly the MGB 2009, which went into operation in 1947, is typical of this type of vessel and plant.[11] In such craft as PT boats or air-sea rescue boats, it would be extremely desirable to obtain short bursts of very high speed. Gas-turbine engines with wet compression could well perform this task.

AUTHOR'S CLOSURE

Lieutenant Hafer's discussion should be considered as an integral part of this paper in bringing out many practical aspects of a wet-compression gas-turbine power plant.

The results of recent tests, apart from uncontrolled water particle size, can be attributed to two aspects:

1 Concerning the compressor itself: The incorrect flow relation was produced by reduced flow volume at the last stages of the axial-flow compressor. Specifically, when a dry-compressor of pressure ratio as low as 4 is operated with wet compression,

[9] "The Gas Turbine Cycle With Water Injection Into the Compressor," by P. Chambadal, *Chaleur et Industrie*, vol. 30, no. 292, November, 1949, reprinted in *The Engineer's Digest*, vol. 11, no. 3, March, 1950.

[10] "The Prospects of Gas Turbines in Naval Applications," by Capt. R. T. Simpson, USN and Commander W. T. Sawyer, USN, ASME Paper 50—S-8, presented at the Annual Meeting, New York, N. Y., November 26–December 1, 1950, of THE AMERICAN SOCIETY OF MECHANICAL ENGINEERS.

[11] "Gas Turbine Propelled MGB 2009," *The Engineer*, September 5, 12, and 19, 1947.

the angle of attack at the last row of cascade airfoils is increased by the amount as indicated in Fig. 18, depending on the efficiency of wet compression expressed in terms of particle sizes. As most airfoils stall at an angle of attack greater than 20 deg, severe flow disturbance will be created. For similar compressor data at the last stage, the blade Reynolds number is increased by 67 per cent and the tip Mach number increased by 14 per cent for 100 per

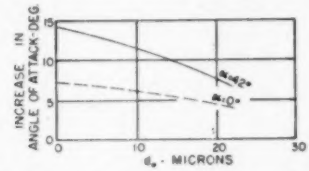

FIG. 18 CHANGES IN ANGLE OF ATTACK AT THE LAST ROW OF CASCADE AIRFOIL OF A COMPRESSOR SPECIFIED AS IN FIG. 11

cent efficient wet compression. Therefore an ordinary dry compressor can hardly be adapted for wet compression. However, a wet compressor can be operated dry (in case of failure of the water supply) with acceptable efficiency, as the losses due to reduced angle of attack and reduced Mach number are less severe. Any excessive reduction in Reynolds number should be carefully studied in designing a wet compressor which may have to operate dry.

2 Concerning the cycle as a whole: The operating pressure was too far below the optimum pressure ratio for the given turbine-inlet temperature. Fig. 19 shows the optimum-pressure ratios at various turbine-inlet temperatures of both dry and wet-compression cycles. At low-pressure ratios around 5, the wet-compression cycle is inferior to the dry cycle for the same turbine-inlet temperature. Fig. 20 shows that, for low-pressure ratios, any possible advantage due to wet compression depends on the compressor efficiency. Moreover, for the range of efficiencies of contemporary axial-flow compressors, liquid water carried into the combustion chamber due to an excessive amount of injected water always causes a loss in cycle efficiency.

In Fig. 11(*b*) the increase in water requirement due to the fact that the compressor adiabatic efficiency is 85 per cent rather than 100 per cent has been taken into account.

It will be sufficient if the control of water-injection rate simply follows the operating pressure ratio (or fuel rate) for sea level or

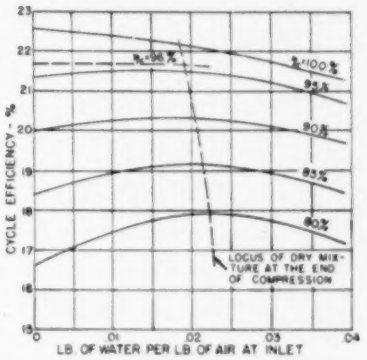

FIG. 20 EFFECT OF COMPRESSOR EFFICIENCY ON CYCLE EFFICIENCY OF WET-COMPRESSION GAS-TURBINE CYCLE
(Compressor data as in Fig. 11, turbine-inlet temperature 1200 F no regeneration.)

fixed level operation. At the same ambient temperature, the variation due to a change in relative humidity from 0 to 100 per cent is only 5 per cent for a pressure ratio of 4, and 0.5 per cent for a pressure ratio of 8. The variation in water requirement is negligible for ordinary ranges of temperature variation at sea level.

The necessity for using distilled water in carrying out wet compression is, of course, understood. If mechanical distills are used for producing distilled water at the rate of 20.4 Btu per lb,[5] the power demand is less than 1/2 per cent of the net output.

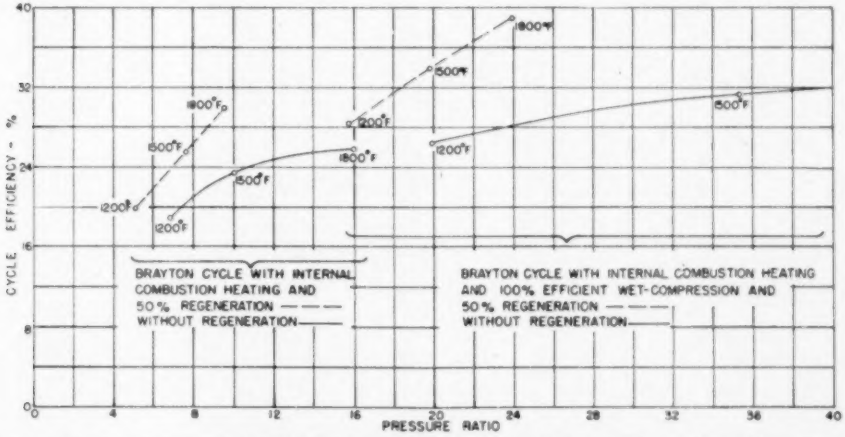

FIG. 19 OPTIMUM EFFICIENCIES OF GAS-TURBINE CYCLES BASED ON PRESSURE RATIOS AND TURBINE-INLET TEMPERATURES
(85 per cent machine efficiencies turbine-inlet temperatures are indicated on curves.)

Installation of an evaporator at the turbine exhaust is also advantageous.

It is admitted that an ordinary gas-turbine unit with effective intercooling and regeneration does give over-all efficiencies of similar order to that of a wet-compression cycle[12] not counting the space requirement. However, the gas-turbine cycle can be improved by incorporating wet compression and intercooling. The intercooling also reduces the water requirement of the wet compression.

[12] "Operating Experiences With Stationary Gas Turbines," by Paul R. Sidler, *Mechanical Engineering*, vol. 74, May, 1952, pp. 381–383.

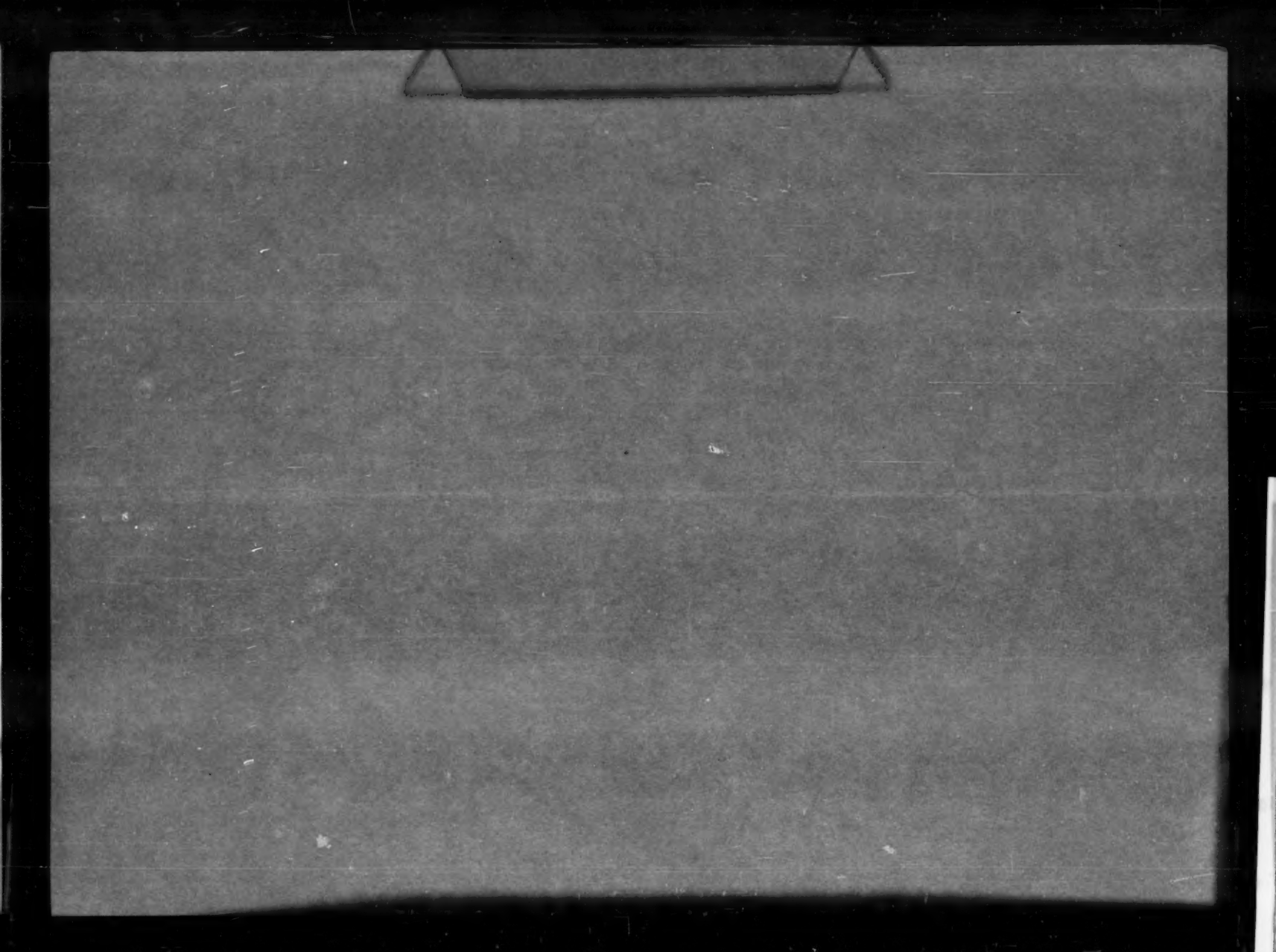

AN ASME PAPER

Its Preparation, Submission and Publication, and Presentation

To a large degree the papers prepared and presented under the ASME sponsorship are evidence by which its professional standing and leadership are judged. It follows, therefore, that to qualify for ASME sponsorship, a paper must not only present suitable subject matter, but it must be well written and conform to recognized standards of good English and literary style.

The pamphlet on "AN ASME PAPER" is designed to aid authors in meeting these requirements and to acquaint them with rules of the Society relating to the preparation and submission of manuscripts and accompanying illustrations. It also includes suggestions for the presentation of papers before Society meetings.

CONTENTS

Price 40¢. No discount allowed. *A remittance must accompany all orders for $5.00 or less. U. S. Postage Stamps are acceptable.*

THE AMERICAN SOCIETY OF MECHANICAL ENGINEERS

29 West 39th Street, New York 18, N. Y.